VNIVERSITAT DE VALÈNCIA

Shedding light on Dark Matter through 21 cm Cosmology and Reionization constraints

PhD Thesis

Pablo Villanueva Domingo

IFIC - Universitat de València - CSIC
Departament de Física Teòrica
Programa de Doctorat en Física

Under the supervision of

Olga Mena Requejo
and
Sergio Palomares Ruiz

València, June 2021

Olga Mena Requejo,
investigadora científica del Consejo Superior de Investigaciones Científicas,
y

Sergio Palomares Ruiz,
científico titular del Consejo Superior de Investigaciones Científicas,

Certifican:

Que la presente memoria, **Shedding light on Dark Matter through 21 cm Cosmology and Reionization constraints**, ha sido realizada bajo su dirección en el Instituto de Física Corpuscular, centro mixto de la Universitat de València y del CSIC, por **Pablo Villanueva Domingo**, y constituye su Tesis para optar al grado de Doctor en Física.

Y para que así conste, en cumplimiento de la legislación vigente, presenta en el Departamento de Física Teórica de la Universidad de Valencia la referida Tesis Doctoral, y firman el presente certificado.

València, a 29 de Abril de 2021,

Olga Mena Requejo Sergio Palomares Ruiz

A mis padres,
a mis abuelos
y a Inma.

. . . Y sentí vértigo y lloré,
porque mis ojos habían visto
ese objeto secreto y conjetural
cuyo nombre usurpan los hombres,
pero que ningún hombre ha mirado:
el inconcebible universo.

—Jorge Luis Borges, *El Aleph*

List of Publications

This PhD thesis is based on the following publications:

- Laura Lopez-Honorez, Olga Mena, Sergio Palomares-Ruiz and Pablo Villanueva-Domingo.
  Warm dark matter and the ionization history of the Universe [1],
  Phys. Rev., D96(10):103539, 2017.

- Pablo Villanueva-Domingo, Nickolay Y. Gnedin, and Olga Mena.
  Warm Dark Matter and Cosmic Reionization [2],
  Astrophys. J., 852(2):139, 2018.

- Pablo Villanueva-Domingo, Stefano Gariazzo, Nickolay Y. Gnedin and Olga Mena.
  Was there an early reionization component in our universe? [3],
  JCAP, 1804(04):024, 2018.

- Miguel Escudero, Laura Lopez-Honorez, Olga Mena, Sergio Palomares-Ruiz and Pablo Villanueva-Domingo.
  A fresh look into the interacting dark matter scenario [4],
  JCAP, 1806(06):007, 2018.

- Laura Lopez-Honorez, Olga Mena and Pablo Villanueva-Domingo.
  Dark Matter microphysics and 21 cm observations [5],
  Phys. Rev., D99(2):023522, 2019.

- Olga Mena, Sergio Palomares-Ruiz, Pablo Villanueva-Domingo, and Samuel J. Witte.
  Constraining the primordial black hole abundance with 21-cm cosmology [6],
  Phys. Rev., D100(4):043540, 2019.

- Pablo Villanueva-Domingo and Francisco Villaescusa-Navarro.
  Removing Astrophysics in 21 cm maps with Neural Networks [7],
  The Astrophysical Journal, 907(1):44, 2021.

Other works developed during the PhD but not included in the thesis:

- Samuel Witte, Pablo Villanueva-Domingo, Stefano Gariazzo, Olga Mena and Sergio Palomares-Ruiz.
  EDGES result versus CMB and low-redshift constraints on ionization histories [8],
  Phys. Rev., D97(10):103533, 2018.

- Pablo Villanueva-Domingo, Olga Mena and Jordi Miralda-Escudé.
  Maximum amplitude of the high-redshift 21-cm absorption feature [9],
  Phys. Rev. D101(8):083502, 2020.

- Laura Lopez-Honorez, Olga Mena, Sergio Palomares-Ruiz, Pablo Villanueva-Domingo and Samuel J. Witte.
  Variations in fundamental constants at the cosmic dawn [10],
  JCAP, 2006(06):026, 2020.

- Pablo Villanueva-Domingo and Kiyotomo Ichiki.
  21 cm Forest Constraints on Primordial Black Holes [11],
  arXiv:2104.10695

Part of Chapter 3 has been adapted for the following review:

- Pablo Villanueva-Domingo, Olga Mena and Sergio Palomares-Ruiz.
  A brief review on primordial black holes as dark matter [12],
  arXiv:2103.12087
  Submitted to *Frontiers in Astronomy and Space Sciences - section Cosmology* as an invited contribution.

Abbreviations

Acronym	Meaning
γDM	Photon Interacting Dark Matter
ΛCDM	Λ - Cold Dark Matter model
νDM	Neutrino Interacting Dark Matter
AGN	Active Galactic Nucleus
BAO	Baryonic Acoustic Oscillations
BBN	Big Bang Nucleosynthesis
BH	Black Hole
BSM	Beyond the Standard Model
CDM	Cold Dark Matter
CL	Confidence Level
CMB	Cosmic Microwave Background
DM	Dark Matter
EoR	Epoch of Reionization
FDM	Fuzzy Dark Matter
FLRW	Friedmann, Lemaître, Robertson, Walker
FZH	Furlanetto, Zaldarriaga, Hernquist
GP	Gunn, Peterson
H	Hydrogen
He	Helium
HeI	Neutral Helium
HeII	Single ionized Helium

Acronym	Meaning
HeIII	Double ionized Helium
HI	Neutral Hydrogen
HII	Ionized Hydrogen
IDM	Interacting Dark Matter
IGM	Intergalactic Medium
LSS	Large Scale Structure
LL	Lyman Limit
Lyα	Lyman α transition
MACHO	Massive Astrophysical Compact Halo Object
MHR	Miralda-Escudé, Haehnelt, Rees
MW	Milky Way
NFW	Navarro, Frenk, White
PBH	Primordial Black Hole
PS	Press, Schechter
QSO	Quasi-Stellar Object
SIDM	Self-Interacting Dark Matter
SM	Standard Model of particle physics
ST	Sheth, Tormen
WF	Wouthuysen, Field
WIMP	Weakly Interacting Massive Particle

Preface

During the last decades, our understanding of the universe has reached a remarkable level, being able to test cosmological predictions with astonishing precision. Observations of relic photons of the Cosmic Microwave Background (CMB), together with galaxy surveys, provide us with a deep comprehension of the geometry, components and chronology of the cosmos. Nonetheless, the nature of the Dark Matter (DM) still remains unknown. In this doctoral thesis, signatures of DM candidates which can leave an impact on the process of formation of structures and on the evolution of the Intergalactic Medium (IGM) are studied. The analysis of the state of ionization of the IGM, its impact on the CMB, and specially the 21 cm cosmological signal, can provide insightful information regarding the properties of the DM.

This thesis is organized in three parts. Part I is devoted to a broad introduction to the fundamentals describing the state of the art of the topics considered. The basics of the standard cosmological model and an overview of the cosmic timeline is presented in Chapter 1. In Chapter 2, the status and small-scale issues of the Cold Dark Matter (CDM) paradigm are discussed, together with the physics of two alternative non-standard DM scenarios: Warm Dark Matter (WDM) and Interacting Dark Matter (IDM). Chapter 3 examines Primordial Black Holes (PBHs) as another DM candidate, focusing on their physical properties and observational effects. The details of the 21 cm cosmological signal and its current experimental bounds are reviewed in Chapter 4. Finally, Chapter 5 is dedicated to the treatment of the IGM and the evolution of its ionization and thermal state. Part II includes the original scientific articles published during the development of the PhD, which constitute the main work of this thesis. Finally, Part III contains a summary of the main results in Spanish.

Acknowledgements

Querría comenzar estos agradecimientos por mis directores, Olga y Sergio, sin cuya guía esta tesis no habría sido posible. Gracias, Olga, por estar siempre disponible cuando lo necesitaba. Por tu atención hacia mi bienestar, tanto en el trabajo como en lo personal. Por ponerte a trabajar codo con codo conmigo, especialmente al principio, y por aportarme las herramientas para ser capaz de trabajar autónomamente. Por tu trabajo incansable y tu pasión por lo que haces, que sin duda siempre me has contagiado. Por haber apostado siempre por mí. Gracias, Sergio, por tu rigor y meticulosidad en el trabajo, por tu atención al detalle. Por las extensas discusiones sobre física que hemos tenido, ahondando con profundidad en temas a veces pasados por alto, aportándome siempre una perspectiva diferente. Por tus minuciosas y concienzudas correcciones de los artículos y de la tesis, que siempre me animaban a dar lo máximo de mí. Por tus consejos y por tu entusiasmo por la física. Solo espero que se me haya quedado algo de estas cualidades. Ha sido un auténtico placer trabajar con los dos durante estos años. Esta tesis existe gracias a vuestro apoyo y vuestra guía.

During the development of this PhD, I have had the great pleasure of visiting several wonderful places. I would like to thank the people of Fermilab, and specially Nick Gnedin, for hosting me. Thank you, Nick, for your advice and expertise, for your orientation and for encouraging me to work autonomously. Estic molt agraït també a Jordi Miralda Escudé per les estades a la Universitat de Barcelona. Ha sigut un enorme plaer discutir de física amb tu i aprendre del teu coneixement. Gràcies també a la gent del ICCUB que vau fer la meua estada tan agradable, especialment a Raphael Sadoun, Albert Sanglas i Andreu Arinyo. I owe a great debt of gratitude to Masahiro Takada-san for the hospitality at the Kavli IPMU. And also for introducing me to Kiyotomo Ichiki-san, to who I am really grateful for inviting me to the Nagoya University, and starting a fruitful collaboration. どうもありがとうございます. Querría agradecer a Paco Villaescusa Navarro por su acogida en la Universidad de Princeton y en el CCA. Gracias por iniciarme en el fascinante mundo de las redes neuronales, y por nuestras absorbentes y esperadas reuniones, donde siempre aprendo

algo nuevo. Estoy muy agradecido también a Laura Lopez Honorez por la invitación a la Universidad de Bruselas. Ha sido un placer poder trabajar contigo, aprender de ti y contagiarme de tu pasión por la física. And also thanks to the people of the ULB theory department, specially Matteo Lucca, Deanna Hopper and Rupert Coy, who made my stay really pleasing with a lot of coffee and chess games.

I would also like to thank my collaborators that I had the pleasure to work with: Stefano Gariazzo, Miguel Escudero and Sam Witte, together with the aforementioned Laura Lopez Honorez, Nick Gnedin, Jordi Miralda Escudé, Francisco Villaescusa Navarro and Kiyotomo Ichiki. Thank you all for your orientation, for the hard work and for sharing your experience and knowledge with me. I am really pleased to have had the opportunity of working with all of you.

Querría agradecer a la gente del grupo SOM por las fascinantes discusiones sobre física, tanto en los *meeting groups* como en las comidas de los viernes, donde tanto he aprendido: Nuria Rius, Pilar Hernández, Andrea Donini, Carlos Peña, Jordi Salvadó, Sam Witte, Daniel G. Figueroa, Jacobo López y Verónica Sanz. Y por supuesto, al resto de estudiantes del grupo por las experiencias compartidas durante estos años: Miguel Escudero, Héctor Ramírez, Miguel Folgado, Fer Romero, Andrea Caputo, Víctor Muñoz, Stefan Sandner y David Albandea.

Quiero agradecer a toda la gente que he tenido la oportunidad de conocer (o conocer mejor) durante los años de doctorado. Doy las gracias a Miguel Escudero y a Héctor Ramírez por vuestro apoyo en el doctorado y por las aventuras por Fermilab. Gràcies a Clara Murgui per ser una companya de despatx estupenda (encara que mai es volguera apuntar a berenar). Gracias a Brais y Lydia por haberme alegrado tantos momentos durante y después de la cuarentena. A Andrés *Posete* por tu curiosidad y tus incisivas preguntas sobre física. Obrigado Eduardo da Silva pelas conversas em português. Gracias a Víctor Muñoz por las discusiones de física, las cervezas, y por iniciarme en la fascinante cultura chilena. A Stefan, mi guiri preferido (aunque ya más valenciano que alemán), el perfecto compañero de hamburguesas y meriendas. A Juan *Lope* por nuestros locos proyectos artísticos (aunque a menudo no vayan a ninguna parte) y por avivar siempre mi lado creativo. A Miguel Folgado, por ser mi compañero de doctorado y de aventuras, por el inolvidable viaje a Japón y por los buenos momentos en el despacho y fuera de él, que sin duda continuaremos cuando lo abandonemos.

Quiero agradecer a todos los amigos que conocí en la carrera, y me han acompañado durante todos estos años, especialmente a Paco, Jaime, Bea, Dani, Laura, Álex, Kevin, Consuelo y Arturo. Gracias por vuestra amistad, ya fuese en el campus, en el camping o en los *skypes*. Aunque

hayamos tomado diferentes caminos en nuestras vidas, lo que ha unido la Física no lo ha separado el tiempo. A Dani y Cristian, por los conciertos y vuestra cálida acogida en la *torre Eiffel* durante mis meses en Barcelona. A Jose y Álvaro por todas las risas y porque rodemos muchos cortos más. Y a Pablo, por ser un amigo con quien siempre he podido contar, reírme por algún motivo y evolucionar como persona.

No puedo olvidarme de mis amigos de toda la vida: David, Irene, Javi, Jesús, Mónica, Vicente, Miguel, Sofía, Sara, Sheila y Cris, y especialmente los imprescindibles Álvaro, Dani y Juan Carlos. Ya fuese en el *cole*, en la plaza del Carmen, en el *bajo* o en la *kame*, siempre me habéis dado un lugar donde disfrutar, reírme, relajarme y desconectar de todo. Por haber crecido conmigo y haberme hecho crecer. Gracias por acompañarme y apoyarme durante tantos años.

Quiero agradecer a mi familia, tíos y primos, por todo el cariño y el apoyo que me habéis mostrado siempre. Gracias a mi yayo, que siempre lo tengo en la memoria. Agradezco a mi yaya por los veranos inolvidables en Bronchales, vividos y por venir. Al meu abuelo per les teues fascinants històries sobre la teua vida i per les teues preguntes sobre galàxies. A mi abuela por haber estimulado mi curiosidad por el mundo y la naturaleza desde que tengo uso de razón. Sin nuestras conversaciones sobre el universo, quizá esta tesis no existiría. Gracias a la gente de Novelda, y especialmente a Pili, a la Abueli y a Mamen, por hacerme sentir siempre como uno más de la familia (¡y por sus deliciosas comidas!). A mis padres por su apoyo incondicional y su cariño, por haber creído siempre en mí. Porque sin la educación que me habéis aportado, no sería lo que soy ahora.

Y por supuesto, a mi compañera de vida y amiga, Inma. Gracias por haberte convertido en un pilar fundamental para mí, y por haberme premiado con compartir nuestra vida juntos. Por tu apoyo en los malos momentos y por hacerme reír tanto en los buenos. Ambos cerramos ahora un ciclo y empezamos otro, que sin duda será igual de bueno o mejor que el presente. Y finalmente, no puedo olvidarme de Amèlie y Odín, por su cariño y sus ronroneos, que han hecho de la escritura de esta tesis un proceso mucho más agradable.

Gracias a todos los que habéis hecho posible que haya llegado hasta aquí. Esta tesis también os pertenece.

Contents

Part I

Introduction

Chapter 1

The ΛCDM Universe

1.1 Introduction

An astounding progress in our understanding of the universe has been achieved since the birth of physical cosmology, with the 1917 Einstein's article, when the universe as a whole became the subject of study [13]. The correlation between distances of galaxies and their velocities found during the next decade by Lemaître [14] and Hubble [15] led to the acceptance that the space is expanding. After the first ideas about an initial singularity proposed by Lemaître [16], it took several decades to develop the Big Bang theory. The model of a hot early universe filled by a plasma was first formulated by Alpher, Gamow and Herman [17, 18]. It implied the synthesis of light elements in the early universe, the Big Bang Nucleosynthesis (BBN), rather than from the posterior stellar nucleosynthesis. Furthermore, the hot cosmic plasma would have left a remnant radiation of relic photons from the early universe at a few Kelvin, the Cosmic Microwave Background (CMB). But it was not until the serendipitous discovery by Penzias and Wilson of an isotropic radiation at 2.73 K [19] that the scientific community took the Big Bang theory seriously.[1] The measurement of the CMB and the abundance of Helium and light elements became the unavoidable confirmations of the Big Bang model. Via the detection of the CMB anisotropies decades later, together with the galaxy surveys observing the Large Scale Structure (LSS), we have been able to accurately determine the amount of matter, and the intrinsic flat curvature of the observable cosmos.

[1] Several upper bounds and even positive measurements of the CMB temperature were obtained since 1941, although their relevance was missed for decades due to the unawareness of the Big Bang theory by experimentalists, and the ignorance of these measurements by theorists, see, e.g., [20].

On the other hand, rotational curves of galaxies and estimation of mass from the velocity dispersion through the virial theorem resulted in the awareness about a large amount of invisible matter in the universe, much more than the estimated one from stars [21]. This invisible component behaves as standard matter, in terms of gravitational interactions, but it does not radiate neither significantly interact with other known particles, and had to be of non-baryonic origin. Dark Matter (DM) soon became a fundamental ingredient of the models of structure formation and cosmic evolution. Nevertheless, the nature of the DM components still remains a conundrum. Light neutrinos were early suggested as possible candidates, but numerical simulations showed that cosmic structures would be formed in a different way than what is observed, ruling out this scenario. Several particle physics theories Beyond the Standard Model (BSM), such as Supersymmetry, predicted different candidates which may have been in thermal equilibrium with the thermal plasma, but decoupled at some moment, leaving a relic amount of weakly-interacting matter which would account for the DM. The generically known as Weakly Interacting Massive Particles (WIMPs) conform the standard DM scenario, although none of these candidates have been detected yet. Besides particles, macroscopic objects have been suggested to conform the DM, generally referred to as MACHOs. Despite its specific nature, mostly all observations seem to agree that the invisible matter is *cold*, i.e., behaving like pressureless matter with negligible temperature. These evidences have given rise to the Cold Dark Matter (CDM) paradigm, which successfully explains most of the cosmic structures we are able to see.

At the end of the last century, observation of distant galaxies via type Ia supernovae showed the accelerated expansion of the universe. This fact pointed out the existence of the last unknown cosmic ingredient, coined as Dark Energy (DE) [22, 23]. However, unlike DM, which in terms of gravitation, behaves as standard matter, the DE evolution is not consistent with any other kind of known matter. Its energy density keeps mostly constant, acting thus as a cosmological constant, as the Λ term introduced by Einstein in his seminal article [13]. However, other possible and exotic equations of state cannot be ruled out yet. Later observations from the CMB anisotropies and LSS agreed and confirmed these results. The most precise joint analysis of the Planck collaboration results with LSS data shows that only 5% of the energy content of the universe is in form of standard baryonic matter, while 26% appears as DM and 69% consists of DE [24]. These results have promoted the ΛCDM model to the state of standard cosmic paradigm, which has successfully overcame many cosmological tests. The existence of such important contributions of DM and DE imply that

most of the universe is, in some way, *dark*, and its nature mostly unknown to us.

Thanks to the measurements of CMB anisotropies and the estimation of primordial nuclei abundances, we have a clear picture of the processes involved in the early universe. We mostly understand the composition of the cosmic plasma and its evolution prior to Recombination, happening at $z \sim 1100$, when electrons and protons got bound to form neutral atoms and the CMB radiation decoupled. Any new exotic physics affecting the primordial plasma may modify the CMB or BBN abundances, and thus could be potentially probed and constrained. On the other hand, galaxy surveys such as the Sloan Digital Sky Survey (SDSS) or space based observatories, like the Hubble Space Telescope (HST), provide us with unvaluable data from the galaxies and clusters surrounding us. An outstanding breakthrough was the discovery of Baryonic Acoustic Oscillations (BAOs), which is the enhancement on correlation of galaxies at distances corresponding to the sound horizon at the CMB decoupling, by SDSS [25] and the 2dF Galaxy Redshift Survey [26], which has been subsequently measured with remarkable precision up to redshift $z \sim 2$ [27, 28]. This phenomenon is consistent with our early universe picture, and yields relevant information regarding the clustering properties of galaxies. The observation of the Lyman α (Lyα) forest, the distribution of small clouds of neutral gas producing absorption features in quasar spectra, gives us the best tool so far to probe small cosmological scales [29, 30]. All these observations can be contrasted with numerical simulations to infer how structure formation has proceeded, forming the current galaxies we see.

However, between the Recombination era and the more recent times reachable by galaxy surveys, there are some epochs in the history of the universe which still remain mainly unknown to us. It is the case of the so-called *Dark Ages*, the period of time between the decoupling of the CMB from matter (around 3.8×10^5 years after the Big Bang) and the beginning of star formation. This epoch is considered as *dark* due to the absence of observable sources of light in the universe. Despite that, its relevance in the understanding of the cosmic evolution is essential, since the onset of the growth of structure takes place in this epoch. At a given moment, approximately 10^8 years after the Big Bang, some collapsed regions were so dense that Hydrogen could ignite, giving rise to the firsts stars. The so-called Cosmic Dawn, when the earliest galaxies started to shine, also remains very uncertain. The first generation of stars, known as Population III, could have been short-lived, with no metallicity, and much more massive than the stars surrounding us, but these are too far to be directly observable with current instruments.

Lastly, the primeval galaxies filled the Inter Galactic Medium (IGM) with energetic light, which heated and ionized the universe. The observations of quasar spectra suggest that at redshift $z \simeq 6$, when the universe was nearly 7% its current age (9×10^8 years after the Big Bang), most of the IGM became completely ionized, indicating the end of the Epoch of Reionization (EoR) [31]. While the Lyα forest brings us information about the final stage of this event, how reionization started and proceeded is not completely understood yet. The nature of the sources capable of injecting so much energy into the medium is still unclear. Although galaxies could be capable of driving the process of reionization, a non-negligible contribution from quasars or from more exotic sources, such as decaying DM, cannot be ruled out. On the other hand, whereas the CMB is also modified by events after its decoupling, through the secondary anisotropies, it only provides indirect signs of these epochs. For instance, the increase in free electrons during reionization induces polarization of the CMB photons, together with a suppression in the anisotropy spectrum. Both effects are driven by the Thomson optical depth, which is an integrated quantity over all the ionization history, rather than probing specific redshifts. Therefore, measurements of the CMB do not provide us with enough information to have a precise and complete description of the EoR.

During the recent decades, a novel probe to explore the universe is gaining interest among researchers, based on the redshifted 21 cm line of Hydrogen. The hyperfine structure of the Hydrogen allows transitions with a rest frequency of 1420 MHz, or equivalently, a wavelength of 21 cm. This transition arises from the splitting of the ground state into two energy levels as a consequence of the coupling of the electron spin and the nucleus spin, in a similar way in which the coupling between the orbital angular momentum and the spin of the electron causes part of the fine structure. The interaction between both 1/2 spins mix them in two possibles levels with definite spin F: the triplet state, with $F = 1$ (parallel spins), and the singlet state, with $F = 0$ (antiparallel spins). Therefore, the third component m_F can take three values $m_F = -1, 0, 1$ in the triplet case, and only one value $m_F = 0$ for the singlet case. Since its theoretical prediction by van de Hulst in 1945 [32] and its discovery in 1951 by three different groups within a few weeks [33, 34, 35], this atomic transition has been widely observed from astrophysical sources. 21 cm surveys provided the first maps of our galaxy and the most reliable rotation curves of galaxies, which yielded ineluctable evidence of the existence of DM during the 70's.

However, the measurements so far come from nearby galaxies or gas clouds. Measuring the neutral Hydrogen of the IGM at high redshift implies a much more ambitious goal. The lifetime of the excited state is about 10^{15} s, the transitions being somewhat unfrequent, and therefore the signal

is very faint. However, the large amount of neutral Hydrogen (HI) atoms filling the IGM could compensate for this fact, resulting in a high enough number of transitions so that this signal could be observable. Moreover, most HI atoms are expected to be in its ground state, since the excited levels have lifetimes much shorter than the typical times needed for excitation. These facts may lead to a significant signal coming from hyperfine transitions at high redshift. Due to the expansion of the universe, photons emitted or absorbed at 21 cm at a given redshift z reaching the Earth would decrease its energy by a factor $1 + z$. Thus, unlike local 21 cm observations, one would seek the redshifted line, where the frequencies in the observed spectrum would indicate the epoch of absorption or emission of such photons. Notice that observations are not only restricted to galaxies, since neutral Hydrogen is spread over the medium around them, allowing to cartography the entire space. For these reasons, measurements of the redshifted 21 cm line could be an excellent way to map the IGM, allowing us to trace its three-dimensional history. The 21 cm signal is very sensitive to the temperature of the medium, and therefore it could give us information about the different stages of heating and cooling in the IGM evolution. Furthermore, since the signal would only be present if there is enough neutral Hydrogen in the universe, its detection can allow us to know the precise details of the reionization process as a function of the redshift. Therefore, 21 cm cosmology conforms a powerful and unique tool to study the Cosmic Dawn and the EoR, as well as to explore the nature of the sources of energetic radiation.

The interest in this research line has recently notably increased within the community, specially after the unexpected result of the Experiment to Detect the Global EoR Signature (EDGES) [36]. The EDGES collaboration claimed the measurement of an absorption dip centered around 78 MHz which could be consistent with the detection of the 21 cm cosmological signal, but presenting an amplitude twice as that expected from the standard scenario. This fact may imply some sort of new physics able to further cool the medium, such as DM interacting with baryons, or an extra source of radio emission. Although this observation has not been confirmed by other experiments, and it has generated strong criticism regarding the systematics and foregrounds treatment, this measurement has triggered a lot of research exploring plausible non-standard models capable of explaining such a large amplitude. While the EDGES results come from the global averaged signal over all sky, other more ambitious designs based on interferometry would be able to observe the spatial inhomogeneities of the 21 cm radiation. There is plenty of work devoted to plan and build large radio interferometers to detect this signal. Some of them are already working and collecting data, such as the Murchison Widefield Array (MWA) [37] or the LOw Frequency

Array (LOFAR) [38], which have placed stringent bounds on the maximum signal. However, the next generation of interferometric arrays such as the Hydrogen Epoch of Reionization Array (HERA) [39] and the Square Kilometer Array (SKA) [40] may be able to reach positive detections in the future, allowing us the access to unvaluable cosmic information.

The Cosmic Dawn and reionization are not only interesting due to the involved astrophysical processes, but can also provide us with more fundamental information. Star formation is hosted within DM halos, and becomes stronger in more clustered regions. More massive halos allow an earlier fragmentation and collapse into stars than lighter ones. The DM distribution determines therefore how and when galaxies form. Hence, observing these epochs may yield us valuable information regarding the DM nature, such as different alternatives to the standard CDM scenario. While CDM provides an excellent fit to current large-scale observations, a few problems arise at galactic and sub-galactic scales, which can be summarized in the fact that the CDM model predicts more structures than observed. In order to account for these issues, several alternatives to CDM have been proposed presenting a suppression in the power at small scales which could reconcile theoretical models with measurements. Instead of presureless cold matter, one could consider particles with non-negligible dispersion velocities, named Warm Dark Matter (WDM). To successfully address the unsolved questions at small scales, WDM particles should have masses of the order of the keV, much lighter than the typical GeV range of masses for WIMPs. On the other hand, Interacting Dark Matter (IDM) particles via elastic scattering with light species, such as photons or neutrinos, would produce further collisional damping and induce oscillations in the power spectrum. As a consequence, small scale fluctuations would be partly washed out, reducing the number of low mass halos, in a similar way to WDM. Such DM models with suppression of fluctuations would delay structure formation processes, leading to later Cosmic Dawn and reionization epochs. Reionization data from quasar spectra and the redshifted 21 cm line are sensitive to the timing of the onset of ionizing radiation, so they represent important tools to probe WDM and IDM scenarios.

Besides the small scale crisis, some CDM candidates could also leave important signatures in the thermal evolution of the IGM. A fascinating possibility considers Black Holes (BHs) formed in the early universe, rather than from stellar collapse, to conform the DM. The interest on Primordial Black Holes (PBHs) has been revived after the first LIGO observation of gravitational waves from BH mergers [41], which may be consistent with objects of primeval nature. The rich physics of PBHs triggers many observational effects to probe them, which allows us to constrain their masses and abundance. Besides the stringent bounds on the amount of PBHs,

these still could account for part of the DM. PBHs with solar masses would present strong accretion mechanisms. It implies that the surrounding matter would infall onto them, releasing during the process large amounts of radiation into the medium. These high energetic photons could be absorbed by the IGM, ionizing and heating the gas, and hence modifying the thermal history. These effects may be seen as a suppression of the global average or of the fluctuations of the 21 cm cosmological signal. The 21 cm power spectrum appears to be an excellent and robust probe to constrain PBH scenarios.

In this PhD thesis, the thermal evolution of the IGM has been studied, specially via the 21 cm line. The understanding of the cosmic history has been employed as a tool to explore the constituents of the DM. Several DM models which may leave relevant signatures in the cosmic evolution have been considered. It is the case of WDM and IDM scenarios, which predict a suppression of fluctuations, or PBHs, which instead imply extra energy injections, contributing to the heating and ionization. Besides these model dependent approaches, the DM impact on thermal history and matter clustering can also be studied without assuming any specific DM scenario. The possibility of early reionization epochs which may be driven by exotic DM has been studied by using CMB data. On the other hand, novel deep learning methods have been employed to seek the link between 21 cm fields and the underlying 3D matter density maps, which would provide explicit information about the DM distribution. The works included here are a sample of the capacity of reionization data and the 21 cm signal to unveil the DM properties. With the forecoming radiointerferometers, 21 cm observations may shed light on the enigmatic nature of DM.

1.2 Background cosmology

It is worth it to start by reviewing the fundamentals about the background cosmology. In General Relativity, spacetimes are determined by their *metric* tensors, $g_{\mu\nu}$, whose evolution is ruled by the Einstein Equations:

$$G_{\mu\nu} + \Lambda g_{\mu\nu} = 8\pi G_N T_{\mu\nu}, \tag{1.1}$$

where G_N is the Newton gravitational constant, $G_{\mu\nu}$ is the Einstein tensor, which accounts for the curvature of the spacetime by a combination of derivatives of the metric, and $T_{\mu\nu}$ the energy-momentum tensor, which accounts for the matter content. The constant Λ is known as the *cosmological constant*, and it is a term allowed by the symmetries in the lagrangian, and thus shall be considered (unless the asymptotic limit to the flat Minkowski metric is required, in which case it must vanish). The geometry of spacetime,

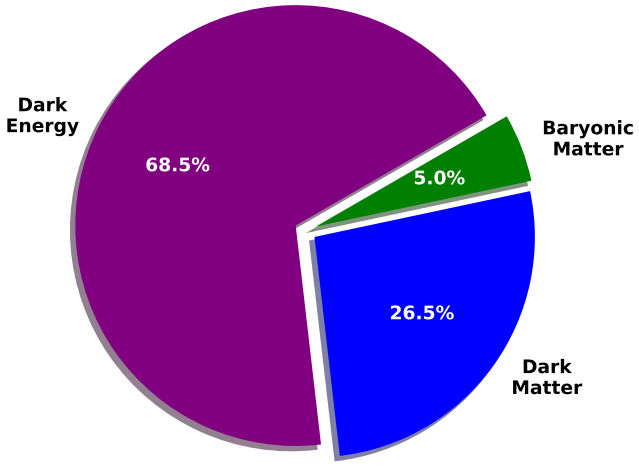

Figure 1.1: Contribution of each component to the current total energy density.

accounted for in the left-hand side of the above equation, is sourced and modified by the energy content, given by the right hand side. Equivalently, the evolution of the present matter is ruled by the curvature of spacetime.

One can apply these equations to a cosmological framework. As a first approximation, the universe appears to be statistically homogeneous and isotropic at the largest scales, which is known as the *cosmological principle*. In General Relativity, the background spacetime can be characterized by the Friedman-Lemaître-Robertson-Walker (FLRW) metric, that describes an expanding spatially homogeneous and isotropic universe. It was independently developed by Friedman [42, 43] and Lemaître [14], while in 1935, Robertson [44] and Walker [45] independently proved in a rigourous way that this metric is the unique spacetime spatially homogeneous and isotropic. The only degree of freedom present in the metric is the *expansion factor* $a(t)$, which is only function of the cosmic time t. Spatial hypersurfaces have constant curvature, which can be positive, negative or zero, leading respectively to closed, open or flat spacetimes. Observational data is consistent with a flat universe [24], as can be expected from inflation (see e.g. Ref. [46]). Therefore, along this thesis, zero curvature is assumed. The metric, written in terms of the line element ds^2, reads

$$ds^2 = g_{\mu\nu}dx^\mu dx^\nu = -dt^2 + a(t)^2\left(dr^2 + r^2 d\Omega^2\right), \tag{1.2}$$

where r is the radial comoving coordinate and $d\Omega$ is the differential solid angle. On the other hand, homogeneity and isotropy imply an energy momentum tensor of the form

$$T_{\mu\nu} = (\rho + P)U_\mu U_\nu + P g_{\mu\nu}, \tag{1.3}$$

where U_μ is the 4-velocity of the observers comoving with the fluid, and ρ and P the energy density and pressure measured in the frame of such observer. Substituting Eqs. (1.2) and (1.3) in the Einstein equations, Eq. (1.1), it is straightforward to derive the evolution equations fulfilled by the expansion factor, the so-called Friedmann equations [47]:

$$H^2 \equiv \left(\frac{\dot{a}}{a}\right)^2 = \frac{8\pi G_N}{3}\rho + \frac{\Lambda}{3} \ , \tag{1.4}$$

$$\dot{H} + H^2 = \frac{\ddot{a}}{a} = -\frac{4\pi G_N}{3}(\rho + 3P) + \frac{\Lambda}{3} \ , \tag{1.5}$$

where the dot corresponds to the derivative respect to the cosmic time, $\dot{f} = df/dt$.[2] We have implicitly defined the *expansion rate*, or Hubble parameter, as $H = \dot{a}/a$, which determines how fast the universe expands. To measure times and distances, it is customary to employ, rather than the cosmic time, the expansion factor a, or the *redshift* z, related to a and to the usual time variable as $a = 1/(1+z)$ and $dz = -cdt/(1+z)H(z)$, respectively. Either from the conservation of the energy-momentum tensor, or from Eqs. (1.4) and (1.5), we can also derive the continuity equation, which states the conservation of the total energy

$$\dot{\rho} + 3H(\rho + P) = 0 \ . \tag{1.6}$$

The total energy density and pressure are given by a sum over the different species which contribute as a source for the expansion $\rho = \sum_i \rho_i$, $P = \sum_i P_i$, with ρ_i and P_i the energy density and pressure of the species i. The equation of state $w_i = P_i/\rho_i$ determines the evolution of ρ_i, and it is characteristic for each species. In the following, we exclude interactions between different particles which may produce energy exchanges, and thus Eq. (1.6) applies to each species separately. In the case of *radiation* (i.e., massless particles such as photons, or neutrinos in the early universe), the pressure is given by $P_{rad} = (1/3)\rho_{rad}$, and thus, Eq. (1.6) without interactions lead to a dependence with the scale factor as $\rho_{rad} \propto a^{-4}$. On the other hand, non-relativistic *matter*, which encompasses both dark and baryonic matter, has negligible pressure, and hence, $\rho_m \propto a^{-3}$. The Λ contribution can be regarded as some sort of *dark energy*, with constant energy density, $\dot{\rho}_\Lambda = 0$.

Eq. (1.4) states that the expansion rate is given by the contribution of different species. It is customary to rewrite it in terms of the relative mass-energy densities with respect to the *critical density* $\rho_c(z) = 3H(z)^2/8\pi G_N$.

[2]These equations are specific cases of more general spacetimes: Eq. (1.4) (sometimes referred to as *the* Friedman equation) is the Hamiltonian constraint in the 1+3 decomposition of General Relativity, while Eq. (1.5) is a simpler case of the Raychaudhuri equation, which drives the expansion of congruences of observers (see, e.g., Ref. [48] for more details).

We thus define the *density parameters* as $\Omega_i = \rho_{i,0}/\rho_{c,0}$, where the subscript 0 indicates the current values. With this definition, the density parameters sum up to 1 in a flat universe, $\sum_i \Omega_i$, being this sum < 1 (> 1) in open (closed) universes. Taking into account radiation ($i = rad$), matter ($i = m$) and the contribution from the cosmological constant ($i = \Lambda$), on can write the expansion rate as the sum

$$H^2 = H_0^2(\Omega_{rad}(1+z)^4 + \Omega_m(1+z)^3 + \Omega_\Lambda) \ . \tag{1.7}$$

The Hubble rate evaluated today, H_0, is customarily written as $H_0 = 100\,h$ s^{-1} km Mpc^{-1}, with h the *reduced Hubble constant*, which from CMB and BAO data takes the value of $h = 0.693$ [49].[3] The Ω_i parameters are extracted from galaxy clustering measurements and CMB anisotropies observations, being the preferred values $\Omega_m = 0.315$, $\Omega_\Lambda = 0.685$ and $\Omega_{rad} = 9.04 \times 10^{-5}$ [24]. Since each of the components of the above equation has different time dependences, the cosmic timeline can be divided into eras accordingly to the dominant contribution. In the primordial universe, at high z, the $(1+z)^4$ factor of the radiation is the largest one, corresponding to the *era of radiation domination*. This is followed by the *era of matter domination*, which starts at the *matter-radiation equality*, given by $1+z_{eq} = \Omega_m/\Omega_{rad} \sim 3500$. The cosmic expansion is ruled by non-relativistic matter until $1+z_\Lambda = (\Omega_\Lambda/\Omega_m)^{1/3} \simeq 1.3$, when the *era of* Λ *domination* begins. This energy era still holds until today, after 13.8 Gyr after the Big Bang. In this thesis, we mainly focus on phenomena which take place during the matter-dominated era. Therefore, in most of the cases of interest the radiation and Λ contributions to Eq. (1.7) can be safely neglected, writing $H^2 \simeq H_0^2\Omega_m(1+z)^3$.

The matter content can be splitted into its *baryonic* and *dark* components. We can write the baryon energy density as $\rho_b = \mu m_p n_b$, with m_p the proton mass, n_b the number density of baryons and μ the mean molecular weight, which accounts for the contribution of Helium, and takes the value $\mu = 1.187$. Due to the conservation of the number of baryons, one can write $n_b = n_{b,0}(1+z)^3$, and thus the fraction to the critical density as $\Omega_b = \rho_{b,0}/\rho_{c,0}$. From the joint analysis of CMB and BAOs, the value preferred by data is $\Omega_b = 0.048$ [24]. A diagram of the current energy density contribution is shown in Fig. 1.1. On the other hand, Fig. 1.2 depicts the evolution of each energy component as a function of the scale factor, denoting the different energy domination eras.

[3] In recent years, a controversy regarding the value of the Hubble constant has arisen, since estimates from early time probes (CMB, BAOs, BBN) present a tension with local measurements from distances of galaxies, supernovae, etc. See e.g. Ref. [50] for a detailed review.

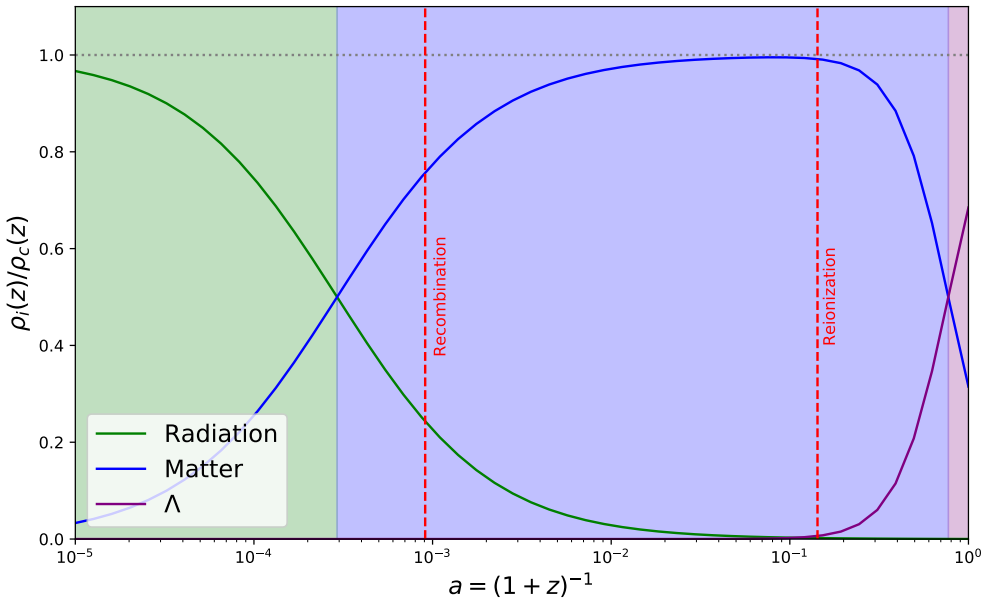

Figure 1.2: Evolution with the scale factor a of the energy density of each component relative to the total density. Recombination and the end of the EoR are indicated with vertical red lines.

Most of cosmological observations match astonishingly well with the ΛCDM model, which assumes a cosmological constant Λ as the Dark energy component, and presureless Cold Dark Matter (CDM) as the dominant matter component. The standard cosmological scenario can be described by six independent parameters, namely the baryon $\Omega_b h^2$ and the CDM $\Omega_c h^2$ energy parameters (where h is the dimensionless Hubble parameter, defined through $H_0 = 100h$ km s^{-1}Mpc^{-1}), the ratio between the sound horizon and the angular diameter distance at decoupling Θ_s, the reionization optical depth τ_T, and two parameters which determine the primordial power spectrum from inflation: the scalar spectral index n_s and the amplitude of the primordial spectrum A_s, see Ref. [24] for their current best-fit values and uncertainties.

1.3 Overview of the cosmic history

In this section we briefly review the most important milestones of the cosmic chronology, specifying the relevant epochs and the transitions among them. Simplifying the full picture, we can divide the cosmic timeline in the next phases (see, e.g., [51, 52]):

- **Primordial Universe.** Until $\sim$ 1 second after the Big Bang. This period encompassed many relevant phenomena, such as Inflation, Reheating, Baryogenesis, the Electroweak transition and the Hadronization, among others. Since we are interested in more recent times, we gloss over the details of this epoch. During the inflationary period, the energy content was dominated by some scalar field or other exotic species which led to a much faster expansion of the universe, by a factor of at least $\sim 10^{26}$, in a very short period of time, around 10^{-33} s. The fields which drove inflation decayed to the particle and radiation species in the so-called Reheating epoch, starting the radiation domination era. Thenceforth, the universe was composed by a highly homogeneous plasma, filled by a large number of species in thermal equilibrium. With the expansion and adiabatic cooling of the universe, many of these species decoupled from the cosmic plasma. The small fluctuations produced by Inflation settled the seeds where cosmic structures would grow from afterwards [46].

- **Neutrino decoupling, e^+e^- annihilation and Primordial Nucleosynthesis.** From 1 second to 10^3 minutes after the Big Bang. When the temperature of the cosmic plasma dropped to $\sim$ 1 MeV, electroweak interactions were not strong enough to maintain neutrinos in equilibrium with the rest of species. Neutrinos decoupled and thereafter evolved independently [53]. This process was closely followed by electron-positron annihilation, when photons were not energetic enough anymore to keep producing pairs through the reaction $\gamma + \gamma \to e^- + e^+$. All positrons annihilated, remaining a small fraction of electrons, and producing an extra heating of the cosmic plasma. Soon after, at $\sim$ 10 seconds, the binding energy of Deuterium could not be longer overcome by radiation. This starts the production of deuterium, which enables the formation of light elements during the so-called Primordial, or Big Bang Nucleosynthesis (BBN). As a result, protons and neutrons became bounded in nucleons, mainly in a proportion of $\sim$75% of Hydrogen and $\sim$25% Helium nuclei, by mass fraction, as well as small traces of other light elements, such as Lithium and Berilium [54, 55].

- **Matter-radiation equality.** Around $z \sim 3500$, 4.7×10^4 years after the Big Bang. Due to the different scaling of the densities with the scale factor, the matter energy content becomes as relevant as radiation at this time, becoming the dominant contribution thereafter. During the matter dominated era, small fluctuations grow much faster than during radiation domination, when they remained stalled.

- **Recombination and CMB decoupling.** Around $z \sim 1100$, 3.8×10^5 years after the Big Bang. Two fundamental related processes happened at this time. The cosmic plasma continued cooling until the photons became not energetic enough to keep electrons and protons ionized. Thus, most of the electrons and protons combined to form neutral atoms which were no longer ionized. This is the first important phase transition in the ionization state of the IGM, known as Recombination.[4] On the other hand, the decreasing number of free electrons reduced the rate of the Thomson scattering with photons of the cosmic plasma, which kept the baryonic matter coupled to radiation. Therefore, photons decoupled from baryons, evolving separately without interacting among themselves. Photons released then conform what we observe now as the Cosmic Microwave Background (CMB) [56].

- **Dark Ages.** Since $z \sim 1100$ to $z \sim 30$, from 3.7×10^5 to $\sim 10^8$ years after the Big Bang. After the CMB decoupling, the universe became transparent to radiation and mostly neutral. Due to the absence of light sources, for which is known as the Dark Ages, this period is hardly observable, except maybe via the 21 cm signal from neutral hydrogen. During these times, the growth of structures becomes important, magnifying the inhomogeneities and the collapse of matter into DM halos.

- **Cosmic Dawn.** Since $z \sim 30$ to $z \sim 10$, from $\sim 10^8$ to $\sim 5 \times 10^8$ years after the Big Bang. The first stars are formed within massive halos, yielding the most ancient galaxies and quasars. First stars are composed by nuclei formed during BBN, and thus present very low metalicity, probably conforming the so-called Population III. These stars would be more massive and short-lived than the succeeding stellar generations, the metal-poor Population II and metal-rich Population I stars. These first light sources emitted UV and X-ray radiation, heating, exciting and ionizing the surrounding medium, which should have left an imprint on the expected 21 cm signal from this period.

- **Reionization.** Since $z \sim 10$ to $z \simeq 6$, from $\sim 5 \times 10^8$ to $\sim 9 \times 10^8$ years after the Big Bang. The UV part of the spectrum emitted by the early galaxies ionized their local environment. These ionized (HII) bubbles grew until this epoch, when they started to overlap, leading eventually to a fully ionized IGM. This is the second great transition of the ionization state of the IGM after Recombination. This process leaves a suppression of the CMB power spectrum, erasing

[4] Actually, they had never been *combined* before, but this term persists for historical reasons.

the anisotropies due to the increase of free electrons. Observation of absorption features in quasar spectra (the Lyα forest and the Gunn-Peterson effect) reveals valuable information regarding the end of the overlap period, at $z \simeq 6$, although the initial stages are still poorly known. Forthcoming 21 cm experiments could allow us to explore this epoch [57, 58].

- **Λ-Matter equality.** Around $z \sim 0.3$, $\sim 10^{10}$ years after the Big Bang. The nearly constant energy density from the DE starts to dominate the energy content of the universe over matter, causing an accelerated expansion of the universe. Growth of fluctuations slowed down since then.

In Chapter 5, the thermal and ionization history during the Dark Ages, Cosmic Dawn and the EoR is detaily studied, analyzing the impact on the 21 cm cosmological signal.

Chapter 2

Non-standard Dark Matter scenarios

Although the unknown nature of Dark Matter (DM) has concerned us for decades, it is still one of the most important unsolved problems in modern physics. In order to explain structure formation at both large and small scales, several models of DM have been proposed, composed by different kinds of particles. In this chapter we review the steps which led to the requirement of DM, and the adoption of the Cold Dark Matter (CDM) paradigm. The growth of fluctuations and description of halos are summarized. Motivated by solving small scale problems present in the CDM scenario, several alternative models are reviewed, which lead to the suppression of fluctuations at small scales, discussing their impact on structure formation. We focus on two scenarios: Warm Dark Matter (WDM), such that DM particles have a non-negligible velocity dispersion, free-streaming at low scales; and Interacting Dark Matter (IDM), whose particles interact with photons or neutrinos, damping perturbations by collisional coupling.

2.1 Why Dark Matter matters

Before discussing specific DM models, we start by overviewing the historical progress of evidences of DM and the consolidation of the CDM paradigm. Some of its possible issues are outlined, motivating alternative DM candidates which are briefly summarized.

2.1.1 A historical overview

The historical development of the ideas which led to the adoption of the DM as a constituent of the universe has been widely discussed in the literature (see, e.g., Refs. [21, 59, 60, 61, 62].) Although there were hints of the existence of non-visible matter as soon as in the early 20th century (see, e.g., Ref. [21]), the firsts evidences of the existence of such matter were found in the 30s. In 1933 and 1937, Fritz Zwicky made use of the virial theorem with dispersion velocities measured in the Coma cluster, finding the presence of mass that does not emit radiation, about ∼500 times more than the standard radiative one [63, 64].[1] A similar work was performed by Sinclair Smith in 1936 with data from the Virgo cluster, also finding ∼100 times more mass than expected [65]. Horace Babcock, in his PhD thesis in 1939, presented the rotation curve of M31 (Andromeda) up to 20 kpc from its center, showing high values for the circular velocity (although he attributed it to a stronger absorption or dynamical effects in the outer parts of the galaxy) [66], and similar findings were drawn from the rotation curve of M33 by Mayall & Aller in 1942 [67]. In 1959, Kahn & Woltjer considered the relative motion between the Milky Way and Andromeda, identifying much more mass than the observed one from stellar origins in order to explain how they are approaching each other [68]. However, these first hints were not correctly interpreted by the scientific community during several decades.

It was not until the 1970s when strong evidences of the presence of invisible matter were found. Measurements of rotation curves of several galaxies in 21 cm and photometry suggested more mass than expected in the outer regions [69, 70, 71, 72, 73]. In 1973, Ostriker and Peebles performed early numerical N-body simulations, and noted that spiral rotating galaxies were unstable, unless a massive spherical halo were present [74]. Shortly after, two influential papers brought together all the mass discrepancies, evidencing the need for invisible non-baryonic matter, which would be the dominating component, and concluding that the matter density was $\Omega_m \simeq 0.2$, contrarily to the widely assumed value of $\Omega_m = 1$ at that time [75, 76]. A major breakthrough came in 1978 from the rotation curves of a set of galaxies, measured by Bosma in his PhD thesis with the 21 cm line [77], and by Rubin, Thonnard, and Ford in optical observations [78]. Both groups found flat rotation curves well beyond the observed radii of galaxies, meaning that there was invisible mass exceeding the region occupied by stars and gas. At the end of the 70's, the existence of some sort of non-radiating Dark Matter seemed unavoidable [79].

[1] This ratio is, however, an overestimation of the actual value by a factor of ~ 8, due to a wrong estimate of the Hubble parameter at that time [21].

The question then was: which kind of particles compose such invisible matter? Neutrinos seemed to be the perfect candidate for composing such DM, since they had been already measured in experiments, they do not interact with radiation, and the first neutrino oscillation measurements by that time suggested their being massive. The possibility of neutrinos as constituents of the DM was firstly pointed out in 1972 by Cowsik and McClelland [80, 81], and independently by Szalay and Marx in 1976 [82]. Neutrino masses were found to be constrained from cosmological arguments. In 1966, in the first paper considering the role of neutrinos in cosmology, Gershtein and Zeldovich derived an upper bound on the sum of the neutrino masses comparing their energy density with the critical density of the universe around $\lesssim$ 400 eV, improving by several orders of magnitude the upper bound in the muonic neutrino mass from earth-based experiments [83].[2] On the other hand, from the Pauli exclusion principle and assuming neutrino DM as the main constituent of massive halos, Tremaine and Gunn derived a lower bound for the neutrino mass of about $m_\nu > 100$ eV [86] (although it depends on Ω_m). This may be potentially inconsistent with the Gershtein-Zeldovich limit, constraining the range of neutrino masses if they constituted the DM. The announcement (later proven to be wrong) of the detection of an electron antineutrino mass around $\sim$ 30 eV [87] reinforced the possibility of neutrinos as the DM constituent [88], specially in the Moscow's Zeldovich group, who further studied the impact of neutrino *hot* DM (HDM)[3] on the growth of fluctuations [90, 91]. HDM was found to present a large free-streaming scale, erasing perturbations below it, and thus providing a *top-down* collapse, where big structures are formed before, and later fragmented to form smaller objects. However, increasingly better N-body numerical simulations during the early 80's contrasted with observations of the CfA, the first 3D galaxy survey [92], ruled out the possibility of neutrino DM, since HDM predicted much less small-scale structures than those observed in data [93].

With light neutrinos not being a plausible candidate, different alternatives were required. Peebles was the first to study the impact on fluctuations of a *cold* DM (CDM), i.e., with negligible free-streaming scale [94]. Contrary to HDM, in a CDM scenario, structure formation proceeds *bottom-up*, presenting power at all scales, and thus forming small-size objects which later merge to form larger structures, in a hierarchical way. First simulations of structure formation within the CDM framework resembled the observed clustering properties of galaxies [95], promoting CDM to a prom-

[2] Cowsik and McClelland re-derived this bound 6 years later [80], being thereafter known as the Cowsik-McClelland limit, despite presenting some mistakes in the computation [84]. The Gershtein-Zeldovich bound with current data is 94 eV $\Omega_\nu h^2$ [85].

[3] The terminology distinguishing between Hot, Warm and Cold DM according to the velocity dispersion was proposed in the mid 80's [89].

ising candidate for the non-visible matter. Collapse of matter lead to the formation of DM halos, whose abundance was well described by analytical estimates of the halo mass function, such as the Press-Schechter formalism [96], or by the Sheth-Thormen prescription, which accounts for the ellipticity of halos [97, 98]. N-body simulations showed that CDM halos have an universal density profile, well fitted by a double power law, now known as the Navarro-Frenk-White (NFW) profile after its authors [99]. This profile, valid over a large range of halo masses, scales as r^{-1} at small radii and as r^{-3} at larger distances, and is completely characterized by its virial mass and radius, and the so-called concentration parameter.

Several particle physics models were able to predict a candidate behaving as this kind of cold, collisionless and non-radiating matter. The prototype of CDM particles are the so-called WIMPs (Weakly Interacting Massive Particles) (term coined in 1985 [100]). These are heavy-mass particles with mass $\gtrsim$ 1 GeV in equilibrium with the thermal plasma in the early universe due to weak-like interactions, but decoupling at some moment, freezing out its abundance, which remained mostly constant until now. This mechanism, known as *freeze-out*, allows obtaining the current observed DM density at current times.[4] The abundance depends mostly on the cross section of the interaction, which is required to be of the order of the weak interactions to produce the observed DM density, coincidence known as the WIMP miracle. Examples of such particles are heavy thermal remnants of annihilation appearing in Supersymmetry, such as neutralinos, the supersymmetric partners of the gauge bosons, which were first considered as DM particles in 1984 [108]. Other popular candidates for CDM are scalar fields, such as axions [109], a hypothetical particle introduced through the so-called Peccei-Quinn mechanism to solve the strong CP problem in quantum chromodynamics [110]. These particles may be produced by non-thermal means, such as from the decay of topological defects or other parent particles. Other popular method is the so-called misalignment mechanism (or vacuum realignment), where the axion field is initially displaced from the vacuum and then relaxes to the potential minimum, behaving as non-relativistic matter [111]. A last group aspirant to constitute CDM, and perhaps the most obvious possibility, are MACHOs (Massive Astrophysical

[4]The freeze-out of a heavy lepton was independently proposed in five papers published in 1977 during two months by the following groups: Hut [101]; Lee and Weinberg [102] (Lee passing away shortly before the publication); Sato and Kobayashi [103]; Dicus, Kolb, and Teplitz [104]; and Vysotskii, Dolgov, and Zeldovich [105]. However, none of them realized that its relic abundance may be the one needed to constitute the non-visible DM required from astronomical observations [21, 62]. It must be noted, nevertheless, that the freeze-out mechanism, as usually happened in cosmology, had already been studied by Zeldovich and the Moscow group a decade before [106, 107] (see also Ref. [84]).

Compact Halo Objects) [112], already suggested during the 70's [113, 114]. With this term, coined by Kim Griest as opposed to WIMPs [21], a variety of objects are encompassed which would behave as non-relativistic and non-radiating matter, such as balls of Hydrogen and Helium not massive enough to initiate nuclear burning, like brown dwarfs with masses $\sim 0.01 M_\odot$ or Jupiter-like planets with masses $\sim 0.001 M_\odot$. Moreover, black hole remnants from massive stars, or Primordial Black Holes (PBHs) formed in the early universe are also included. Gravitational microlensing is one of the main tools to study them, and has strongly constrained their abundance. However, since MACHOs could only be present in the universe after the formation of first stellar and astrophysical objects, they are unable to successfully explain large scale matter fluctuations seen in the CMB and the number of baryons from BBN. An exception of that are PBHs, which represent a particularly exciting candidate, requiring a special treatment, and will be extensively discussed in Chapter 3.

On the other hand, between the hot and cold limiting cases, an intermediate *warm* scenario was also plausible, with masses around $\sim$ keV which presented a non-negligible free-streaming scale, but still consistent with data and N-body simulations. The first proposals of such WDM particles were gravitinos of mass $\sim$ 1 keV (the spin 3/2 supersymmetric partner of the graviton) in 1982 [115, 116, 117]. Although standard neutrinos were ruled out as DM candidates, other similar species may account for that. It is the case of the right-handed *sterile neutrinos*, non-interacting with Standard Model (SM) particles except by a small mixing with standard active neutrinos. Several mechanisms were suggested to produce them in the early universe from neutrino oscillations, such as the proposed by Dodelson and Widrow in 1993 through oscillations with active neutrinos out of resonance [118], or by Shi and Fuller in 1999 via resonant production [119]. Those particles would have a mass $\gtrsim$ keV, and thus would be a good candidate for WDM (or even CDM). Simulations and data at that time were not accurate enough to discern between the warm and cold scenarios, but CDM started to become the preferred alternative in the community, until becoming the standard cosmological paradigm. However, as shall be reviewed in the following, during the 90's, several problems related to structure formation at small scales challenged the CDM success, revitalizing the WDM alternative.

2.1.2 Small-scale crisis of the CDM paradigm

The CDM model has shown a great success fitting the data from the large scale structure of the universe. However, there are some discrepancies between observations and N-body simulations at galactic and subgalactic scales, which are not very well explained within the CDM paradigm. Some

of these problems arose during the 1990s, when the CDM model predicting hierarchical clustering started to become widely accepted, and N-body simulations improved their resolution to smaller scales. All of them are related to the fact that CDM scenarios predict more small scale fluctuations than those observed in data. Next, we shall review the most relevant issues. See, e.g., Refs. [120, 121] for a comprehensive overview of the subject.

- **Missing satellite issue**

  Due to the absence of a cutoff in its power spectrum, CDM models predict a lot of subhalos around massive galaxies. N-body simulations show DM self-bound clumps at all resolved scales, and many more low-mass halos than those present in observations, failing to reproduce the observed circular velocities [122, 123]. Concretely, few dozens of dwarf spheroidal satellite galaxies of the Milky Way have been observed, in contrast to the > 100 satellites present in numerical simulations [124, 125]. The observation of ultra-faint dwarf galaxies by galaxy surveys such as DES have alleviated the problem [126, 127, 128]. Many solutions to this issue have been proposed within the CDM scenario, most of them relying on the fact that not all the subhalos may be visible. Examples of them are based on a suppressed gas accretion in low-mass halos after the EoR [129], or considering supernovae feedback [130], facts which inhibit the formation of stars in small mass halos. Other proposals state that an empirical relation between stellar and halo masses can be used to correct the detection efficiency of galaxy surveys, providing the proper number of counts [131].

- **Cusp-core problem**

  A robust prediction from the CDM model which is present in all N-body simulations is the *cuspy* distribution of matter in the inner parts of halos, with density increasing abruptly at small distances from the center. More specifically, CDM density profiles usually rise as $\rho(r) \propto r^{-\gamma}$, with γ between 0.8 and 1.4 over the central radii r [132] ($\gamma \simeq 1$ in the widely used NFW profile [99]). This appears to be in contradiction with the rotation curves of most of the observed dwarf galaxies, which suggest that they must have flatter central density profiles, i.e., with $\gamma \simeq 0$, coined as *cores* [133, 134, 135]. Hydrodynamic simulations show that it may be possible to settle the problem thanks to baryonic feedback from supernova explosions and stellar winds, which would erase the central cusps [136]. A flat core could also be obtained by considering stellar and gas dynamics, by kinematically heating up DM at the centers of galaxies [137].

- **"Too-big-to-fail" problem**

  While the number of low-mass satellites have already been shown to be problematic, the most massive satellite galaxies also present some issues. One naturally would asign the brightest Milky Way (MW) galaxy satellites to the most massive subhalos present in N-body simulations. However, the Aquarius and Via Lactea simulations of the MW showed a population of ~ 10 halos very massive and dense, by a factor of ~ 5, in such a way that they would be too massive not to host bright dwarf satellites of the MW, which would be more massive than the ones actually observed [138, 125]. This could be understood by the fact that if those very massive subhalos host the brightest satellites, the deep potential wells would lead to circular velocities much larger than the observed dispersion velocity of the observed dwarf galaxies. While in low-mass halos, one can resort to baryonic effects to prevent star formation and then become non-visible, these too massive halos would be too big to fail producing stars and being visible (by baryonic feedback or any other known mechanism), and thus they should be observed. For this reason, this issue is known as the *too-big-to-fail* problem. As in the cusp-core problem, this is related to the fact that CDM tends to produce too much mass in subhalos. Although this issue was originally identified in the MW, it has also been found in the Andromeda satellites [139] and in field galaxies of the Local group, beyond the virial radius of its main galaxies [140]. In order to solve this issue, as well as baryonic feedback, interactions between the MW and its satellites, such as disk shocking or tidal stripping, have been proposed, in order to reduce the central masses of the satellites (e.g., [141]). However, simulations able to properly capture these effects need to resolve very low masses and are very challenging numerically [121].

As already stated, there are several ways to overcome the aforementioned discrepancies within the standard ΛCDM scenario. Baryonic physics, such as stellar winds or supernovae feedback, has been invoked to solve all the above problems, being plausible to account for all of them at once [142]. Other solutions rely on the poorly known mass of the MW, interpreting thus the above issues as possible indicators of a lower mass for the MW than the one assumed [143]. However, DM models different from CDM could also solve some or all of these problems, presenting an interesting and well motivated alternative.

2.1.3 Non-standard DM candidates

Despite the current efforts on detecting WIMPs, axions, or other possible CDM constituent particles, they remain undiscovered in experiments [144]. This fact, together with the observational discrepancies discussed above, motivate considering other DM models different from the standard cold paradigm. Some examples of these non-CDM candidates, and how they could account for the small-scale discrepancies, are briefly discussed in the following. These models are mostly characterized by their phenomenology in structure formation, rather than by specific particle physics theories. It is worth emphasizing that the term "non-CDM" is employed here to refer to DM scenarios which present different features at small scales, although behaving as CDM at large ones. With "non-standard", we also include candidates which can act as CDM with respect to structure formation, but differ from the archetypal WIMP scenario, as is the case of BHs formed in the early universe.

- **Warm Dark Matter (WDM)**

  In a typical WDM scenario, DM particles with masses of $\sim$ keV would lead to a substantial velocity dispersion, driving these particles to free-stream and erase fluctuations at small scales. The missing satellite problem is naturally solved, since a cutoff in the power at small scales leads to an underabundance of small structures, compared to the CDM case. As is shown in simulations, WDM can predict the required quantity of subhalos around the most massive ones [145]. Moreover, due to its dispersion velocities, WDM does naturally produce cores. However, to reproduce the observed cores, a WDM mass of ~ 0.1 keV would be required, in a range already ruled out by Lyα forest analyses [146]. Thus, non-ruled out particles with masses $\gtrsim 2$ keV would not be light enough to satisfy all the current galactic data. Finally, within a WDM scenario with $m_X \sim 2$ keV, the "too-big-to-fail" issue could be solved due to the relatively shallower profiles of the expected WDM dwarf galaxies compared to their CDM counterparts. However, thermally produced WDM particles with a higher mass particle may not be able to solve the problem satisfactorily [147].

- **Interacting Dark Matter (IDM)**

  On the other hand, collisions between DM particles and either photons or neutrinos may avoid the formation of substructures. This happens due to the collisional damping present in IDM scenarios, which, in a similar way to WDM, erase small-scale fluctuations. For this reason, IDM can also explain the low quantity of low mass halos, and

thus reconcile expectations with MW satellite observations [148]. Furthermore, as found in high resolution IDM simulations, the largest subhalos are less concentrated than those in the CDM scenario, presenting rotation curves which agree with observations for interaction cross sections of $\sigma \simeq 10^{-9}\sigma_T(\mathrm{GeV}/m_{\mathrm{DM}})$ [149], and thus accounting for the "too-big-to-fail" problem.

- **Self-Interacting Dark Matter (SIDM)**

  A widely discussed possibility considers Self-Interacting Dark Matter (SIDM), where, unlike standard collisionless CDM, DM particles present non-negligible interactions among themselves [150, 151]. These collisions would be possibly mediated by hidden gauge fields, and are a generic consequence of those models [152]. Due to scattering, heat would be transferred from high to low velocity particles, enhancing the velocity dispersion of the central regions and reducing the cuspy densities of the halos. For that reason, SIDM was proposed to solve the cusp-core problem [153], which could be explained in this way, as shown in N-body simulations [154, 155]. While the "too-big-to-fail" discrepancy may also be alleviated with SIDM [155], the amount of substructures predicted in simulations is almost identical to that in CDM, and thus the missing satellite problem would remain unsettled [156, 155].

- **Fuzzy Dark Matter (FDM)**

  Another popular example considers DM composed by an ultra light scalar field, behaving as axion-like particles (although different from the QCD axion). A specially interesting case is the so-called Fuzzy Dark Matter (FDM), which is a limit of a scalar field DM with masses $\sim 10^{-22}$ eV without self-interactions, behaving as a classical scalar field at cosmological scales [157, 158]. Its evolution is ruled by the Schrödinger equation in the expanding universe, which can be recasted in continuity and Euler-like fluid equations (the so-called Madelung equations), with an additional effective quantum potential term. This induces an effective Jeans scale (given by a macroscopic de Broglie wavelength), which further suppresses fluctuations at small scales, while FDM behaves as CDM at larger scales [159]. According to these effects, FDM has been proposed to account for the aforementioned small-scale problems [158, 160].

- **Primordial Black Holes (PBHs)**

  BHs formed in the early universe from the direct collapse of high density fluctuations conform an interesting candidate for DM, specially after the first measurement of gravitational waves from a mer-

ger of BHs by the LIGO collaboration [41]. Regarding its behavior in the formation of structures, these PBHs would mostly act as CDM, although solar mass PBHs may present an enhancement on the fluctuations at small scales due to their discrete distribution [161]. Besides that, it has been claimed that the missing satellite and too-big-to-fail problems may be also alleviated, since the presence of PBHs would imply a large population of ultra-faint dwarf galaxies, in order to be consistent with the LIGO merger rates [162, 163]. Moreover, they would present unique features which may imply different observational effects, such as PBH evaporation or emission of energetic radiation due to accretion. Given the richness of the physics involved, and the variety of phenomenological effects in the evolution of structures and the IGM, Chapter 3 is entirely dedicated to their study.

Driven by solving the above observational issues, these models become plausible candidates for DM. Additionally, some particle physics models may predict such particle candidates, also motivating their study. In this thesis, we focus on studying three of the aforementioned non-standard DM alternatives, WDM, IDM, and PBHs which can leave substantial imprints in the thermal evolution of the universe, the formation of first galaxies, the Reionization epoch and the 21 cm signal. The physical effects, constraints and impact on structure formation of WDM and IDM scenarios shall be discussed along this chapter, while PBHs are studied in the next one.

2.2 Structure formation in a nutshell

Before discussing in detail different non-CDM models, it may be useful to review the standard lore of formation of structures, summarizing the computation of linear fluctuations and the description of halos.

2.2.1 Growth of linear perturbations

In this section, we briefly review some key points regarding the growth of perturbations and the formation of structures, such as the Jeans instability and the evolution of the growth factor. The universe at the largest scales behaves as a homogeneous and isotropic fluid, as described in Sec. 1.2. However, the real universe is highly inhomogeneous at smaller scales, and the study of the evolution of deviations from the background model is needed in order to understand how the galaxies and structures we see today have been formed. The common lore of formation of structures considers

that the early universe was highly homogeneous, with small perturbations seeded from quantum fluctuations by Inflation [51]. These inhomogeneities grew along the evolution of the universe, eventually causing the formation of cosmological structures such as galaxies and clusters. Since these fluctuations were very small in the primordial universe, at early times they can be treated as linear perturbations of the Einstein Equations, which greatly simplifies their study. Although to properly treat the evolution of linear perturbations in the expanding universe, General Relativity is required, it is possible to obtain some quantitative correct results at scales inside the Hubble radius within a Newtonian framework, much easier to interpret.

Denoting with ρ the matter density, and with $\bar{\rho}$ its mean background value, the *density fluctuation*, *density contrast* or *overdensity*, δ, is defined as

$$\delta(\mathbf{x},t) = \frac{\rho(\mathbf{x},t) - \bar{\rho}(t)}{\bar{\rho}(t)}. \tag{2.1}$$

Continuity and Euler fluid equations for perturbations of the matter density δ and velocity $\mathbf{v}$ at first order in a expanding medium read [164, 165, 51, 166]

$$\dot{\delta} + \frac{1}{a}\nabla\cdot\mathbf{v} = 0, \quad \dot{\mathbf{v}} + H\mathbf{v} = -\frac{1}{a\bar{\rho}}\nabla\delta P - \frac{1}{a}\nabla\Phi, \tag{2.2}$$

where δP is the pressure perturbation and Φ the gravitational potential, which fulfills the Poisson equation,

$$\frac{1}{a^2}\nabla^2\Phi = 4\pi G_N\bar{\rho}\delta\,. \tag{2.3}$$

The a factors and the drag term $H\mathbf{v}$ account for the expanding background. The above equations can be combined, leading to an unique evolution equation for the matter overdensity δ. It is more practical to work in Fourier space, where the gradient terms are replaced by $\vec{\nabla} \to i\mathbf{k}$, having then algebraic rather than differential equations (in the spatial coordinates). Furthermore, in the linear regime, different Fourier modes evolve independently, which implies that a field at a scale $\mathbf{k}$ does not depend on other scales $\mathbf{k}'$. We define the Fourier transform of a field $\delta(\mathbf{x})$ as

$$\tilde{\delta}(\mathbf{k}) = \int d^3k\ \delta(\mathbf{x})e^{i\mathbf{k}\cdot\mathbf{x}}\,. \tag{2.4}$$

Combining and taking the Fourier transform of Eqs. (2.2) and (2.3), one obtains a single evolution equation for $\tilde{\delta}(\mathbf{k})$ as [165]

$$\ddot{\tilde{\delta}} + 2H\dot{\tilde{\delta}} + \left(\frac{c_s^2}{a^2}k^2 - 4\pi G_N\bar{\rho}\right)\tilde{\delta} = 0\ , \tag{2.5}$$

where we have used an adiabatic equation of state which relates the pressure δP and the density through the speed of sound $c_s = \delta P/\delta\rho$. Attempting

exponential solutions of the form $\tilde{\delta} \sim \exp i\omega t$, we can recognize in this equation a damped oscillator, with a frequency given by $\omega^2 = \frac{c_s^2}{a^2}k^2 - 4\pi G_N \bar{\rho}$, where the Hubble rate damps fluctuations. Two opposite terms determine this quantity: the first one is due to the thermal motion of the fluid through pressure, while the second one is a consequence of gravitational attraction. Therefore, there exist two possible behaviors: if $c_s^2 k^2/a^2 > 4\pi G_N \bar{\rho}$, then $\omega^2 > 0$, and the perturbations oscillate, and are progressively dissipated due to the H term. However, if $c_s^2 k^2/a^2 < 4\pi G_N \bar{\rho}$, the frequency acquires an imaginary value, so that the dominant solution grows exponentially. This fact indicates that the small fluctuations become unstable and grow. Matter tends to collapse by the gravitational force, increasing the density in some regions, breaking there the validity of the linear treatment. The separation between the oscillatory and collapsing regimes is governed by the (comoving) Jeans length λ_J, and its Fourier wavenumber $k_J = 2\pi/\lambda_J$, defined as

$$\lambda_J = \frac{2\pi}{k_J} = c_s \sqrt{\frac{\pi}{G_N \bar{\rho}}} \, . \tag{2.6}$$

We can define the Jeans mass as the mass within a sphere of diameter λ_J with a density equal to the background one: $M_J = (4\pi/3)\bar{\rho}(\lambda_J/2)^3$. These results can be easily interpreted: the regions of the universe with masses above the critical mass M_J (or fluctuations with wavelengths larger than λ_J) eventually collapse. On the other hand, fluctuations smaller than the Jeans scale would be dissipated and washed out.

The above equations can apply to the standard CDM case, where pressure can be safely neglected. During matter domination, $H = 2/(3t)$ and $4\pi G_N \bar{\rho} = \frac{3}{2}H^2$. Thus, Eq. (2.5) reads

$$\ddot{\tilde{\delta}} + \frac{4}{3t}\dot{\tilde{\delta}} - \frac{2}{3t^2}\tilde{\delta} = 0 \, . \tag{2.7}$$

It is possible to split the time and wavevector dependencies, defining the *growth factor* $D(z)$ as

$$\tilde{\delta}(\mathbf{k}, t) = \frac{D(t)}{D(t_*)}\tilde{\delta}(\mathbf{k}, t_*), \tag{2.8}$$

with t_* any reference time. The growth factor is usually normalized to unity at redshift 0, $D(z = 0) = 1$. Thus, it is straightforward to obtain the two solutions of the equation above, which presents a decaying mode as $D(t) \propto t^{-1}$, and a growing solution as $D(t) \propto t^{2/3} \propto a$.

During radiation domination, one should take into account the effect of radiation fluctuations sourcing the potential term. While a correct evaluation of the growth of perturbations at these epochs requires General Relativity, it is still possible to estimate the evolution of δ arguing that the

potential term in Eq. (2.5) can be neglected, since $\ddot{\delta} \sim H\dot{\delta} \sim H^2\delta$ and $\rho_m \ll \rho_\gamma \sim H^2$ [166]. Thus, since $H = 1/(2t)$, one finds

$$\dddot{\delta} + \frac{1}{t}\ddot{\delta} \simeq 0 \ , \tag{2.9}$$

whose solutions are a constant mode, and a logarithmic growing mode, $D(t) \propto \log(a)$. Contrary to the matter domination era, when matter fluctuations evolve linearly with the scale factor, during radiation domination they only slowly grow in a logarithmic way. The stagnation of growth previous to the matter-radiation equality is known as the *Mészáros effect* [167], and points out that structure formation only becomes relevant at later times, at the matter domination era.

Since linear perturbations evolve from Gaussian fluctuations, during the linear regime gaussianity still holds. It means that, as long as non-linearities are not important, since they are gaussian distributed, the density fluctuations are only characterized by the second statistical moment, given by the *two-point correlation function*, $\xi(\mathbf{x}, \mathbf{y}) = \langle \delta(\mathbf{x})\delta(\mathbf{y})\rangle$. It will be more useful to work with the Fourier transform of this quantity, known as the *matter power spectrum* $P(k, z)$, which is given by

$$\langle \widetilde{\delta}(\mathbf{k}, z)\widetilde{\delta}^*(\mathbf{k}', z)\rangle = (2\pi)^3\delta_D(\mathbf{k} - \mathbf{k}')P(k, z) \ , \tag{2.10}$$

where δ_D is the Dirac delta function and the brackets account for the average over different realizations. Statistical homogeneity enforces the appearance of the delta function, while statistical rotational invariance implies that the power spectrum depends only on the module of $\mathbf{k}$. Given the factorization of the growth function, the linear power spectrum can be written as $P(k, z) = D(z)^2P(k, 0)$. It is also customary to work with the so-called dimensionless power spectrum

$$\Delta^2(k, z) = \frac{k^3}{2\pi^2}P(k, z). \tag{2.11}$$

The initial power spectrum is determined by the primordial conditions of the universe, drawn by the inflation process. In the standard picture, inflation stretches the microscopic quantum fluctuations, which become perturbations of the fields at cosmological scales. A well-known prediction from inflationary models is the nearly scale-invariant spectrum, close to the Harrison-Zeldovich spectrum $P(k) \propto k^n$, with $n \simeq 1$ at large scales, suggested before independently by Harrison [168] and Zeldovich [169] from other arguments. This scaling can be derived from the assumption that the gravitational potential field must be scale invariant, i.e., it presents the same power at all scales. This is a desirable property to ensure that it is finite at both small and large scales. Thus, $\Delta^2_\Phi \sim$ *constant*, where Δ^2_Φ is the dimensionless power spectrum for the potential fluctuations. From the

Poisson equation in Fourier space, Eq. (2.3), $k^2\Phi \propto \delta$, and thus $k^4\Delta^2_\Phi \propto \Delta^2$, implying that $P(k) \propto k$. The preferred value for the spectral index from CMB and LSS data of $n = 0.9665 \pm 0.0038$ [24] only slightly deviates from the Harrison-Zeldovich spectrum, as inflation predicts.

The study of linear perturbations in General Relativity shows that the Fourier modes of the gravitational potential whose wavelength is larger than the horizon at the epoch of matter-radiation equality (i.e., $k < a(z_{eq})H(z_{eq})$, with z_{eq} the matter-radiation equality redshift defined in Sec. 1.2) were causally uncorrelated, and thus have remained mostly constant. As a consequence, their corresponding matter fluctuations keeps the same spectrum than the initial, roughly $\propto k$. On the other hand, those modes which had crossed the horizon before the matter-radiation equality (i.e., $k > a(t_{eq})H(t_{eq})$) become damped due to the stall of the growth of fluctuations during the radiation epoch. Moreover, baryon-photon coupling due to Thomson scattering induces some oscillations in the matter power spectrum, known as Baryon Acoustic Oscillations (BAOs). To properly predict the linear evolution and the exact shape of the power spectrum, numerical codes are required to solve the relativistic perturbation equations, such as the popular and public Boltzmann solvers CAMB (Code for Anisotropies in the Microwave Background) [170] and CLASS (Cosmic Linear Anisotropy Solving System) [171]. This description stands for standard CDM cosmologies, while other DM alternatives may present differences in the growth of the density contrast, leaving different signatures in the power spectrum. It is the case of the WDM and IDM models considered below, which present an additional cutoff or suppression at small scales, or PBHs, which may enhance the power at small scales due to shot noise, as shall be discussed in Sec. 3.2.2.

It is worth it to mention that the standard treatment of linear fluctuations considered here accounts for *isentropic* (also called *adiabatic*) perturbations, i.e., those where the entropy remains unperturbed. An additional kind of perturbations are *isocurvature* modes, where fluctuations in entropy rather than in density fields are considered (see, e.g., [30]). The current understanding of the evolution of fluctuations explains the formation of cosmic structures from adiabatic modes. However, isocurvature modes may still be relevant in some scenarios, such as PBHs, as studied in the next chapter.

2.2.2 Virial equilibrium

When fluctuations go of order unity, $\delta \sim 1$, linear perturbation theory is no longer valid, and thus non-linear approaches are required in order to

understand how cosmic structures and galaxies have formed from the small initial overdensities. Analytical approximate methods, such as the Zeldovich approximation [172], can offer relatively accurate results, although N-body simulations are needed for precise calculations. A very simple analytical prescription, although still qualitatively useful, considers that roughly spherical overdense regions expand and eventually turnaround and collapse due to the gravitational force. This picture of spherical collapse, firstly outlined by Gunn & Gott in 1972 [173], can be analytically solved, finding that the overdensity collapses to a point, reaching infinite density in a finite time. One can match the result from the extrapolation of linear theory evaluated at that collapse time, finding that, at redshift z, it corresponds to [164, 30]

$$\delta_c(z) = \frac{1.686}{D(z)} \tag{2.12}$$

for the Einstein-de Sitter universe. One can interpret this as assuming that all overdensities above that threshold at redshift z would collapse. However, the collapse to a point would be an unrealistic situation provided a slight violation of spherical symmetry or pressure effects. Instead, matter collapses to a halo, reaching a self-gravitating virial equilibrium by violent relaxation [52, 30]. From spherical collapse and the virial theorem, one can estimate the overdensity that a virialized overdensity reaches at redshift z relative to the critical density $\rho_c(z)$ defined in Sec. 1.2, as [174]

$$\Delta_{vir}(z) = 18\pi^2 + 82\,(\Omega_{\mathrm{m},z} - 1) - 39\,(\Omega_{\mathrm{m},z} - 1)^2 \ , \tag{2.13}$$

where we have defined

$$\Omega_{\mathrm{m},z} = \frac{\Omega_{\mathrm{m}}\,(1+z)^3}{\Omega_{\mathrm{m}}\,(1+z)^3 + \Omega_\Lambda} \ . \tag{2.14}$$

One can define the *virial radius* R_{vir}, related to the mass of the halo, M, by

$$M = \frac{4\pi}{3}\,\Delta_{vir}(z)\,\rho_c(z)\,R_{\mathrm{vir}}^3 \ . \tag{2.15}$$

Then,

$$\begin{aligned} R_{\mathrm{vir}}(M,z) \simeq 0.784\,h^{-1}\mathrm{kpc}\left(\frac{M}{10^8 M_\odot\,h^{-1}}\right)^{1/3} \\ \times \left(\frac{\Omega_{\mathrm{m}}}{\Omega_{\mathrm{m},z}}\,\frac{\Delta_{vir}(z)}{18\pi^2}\right)^{-1/3}\left(\frac{1+z}{10}\right)^{-1} \ . \end{aligned} \tag{2.16}$$

From the expression of the circular velocity, $V_c^2 = G_N M/R_{\mathrm{vir}}$, one can write the *virial temperature* T_{vir} as [52]

$$\begin{aligned} T_{\mathrm{vir}}(M,z) = \frac{\mu m_p V_c^2}{2k_B} \simeq 1.98\times 10^4\,\mathrm{K}\left(\frac{\mu}{0.6}\right)\left(\frac{M}{10^8 M_\odot\,h^{-1}}\right)^{2/3} \\ \times \left(\frac{\Omega_{\mathrm{m}}}{\Omega_{\mathrm{m},z}}\,\frac{\Delta_{vir}(z)}{18\pi^2}\right)^{1/3}\left(\frac{1+z}{10}\right) \ , \end{aligned} \tag{2.17}$$

being $\mu = 0.6$ the mean molecular weight of ionized IGM and $\mu = 1.22$ for the neutral one. As shall be shown, these quantities are of great interest since they roughly describe the mass and length scales of DM halos.

2.2.3 Halo Mass Function

During the Dark Ages and later times, baryons and DM surrounding primordial seeds tend to collapse and form DM halos, as N-body simulations predict. These halos could eventually host star forming galaxies and quasars, responsible for altering the IGM. It is thus of great importance to understand the abundance and mass spectrum of existing halos. The *halo mass function* accounts for the comoving number of halos per unit halo mass and volume, and can be written as [96]

$$\frac{dn}{dM} = -\frac{1}{2}\,\frac{\rho_m}{M^2}\,f(\nu)\,\frac{d\ln\sigma^2}{d\ln M}\ , \tag{2.18}$$

where $\rho_m = \Omega_m\,\rho_c$ is the average matter density in the Universe at $z = 0$, $f(\nu)$ is the so called *first-crossing distribution* and $\sigma^2 = \sigma^2(M, z)$ is the variance of the filtered density perturbations at a scale given by the mass M. The variance σ^2 is computed using linear perturbation theory, as discussed in Sec. 2.2.1. Its redshift dependence is given by the growth function, $D(z)$, normalized to 1 at $z = 0$, as $\sigma(M, z) = D(z)\sigma(M, z = 0)$. The variance at $z = 0$ and at scale R, $\sigma(M) \equiv \sigma(M, z = 0)$, reads

$$\sigma^2(M(R)) = \int \frac{d^3k}{(2\pi)^3}\,P(k)\,W^2(kR)\ , \tag{2.19}$$

where $P(k)$ is the linear power spectrum at $z = 0$ and $W(kR)$ is the Fourier transform of a filter function. Several choices are possible, being usually taken as a top-hat (TH) function in real space (i.e., a Heaviside step function), whose Fourier transform reads

$$W_{\rm TH}(kR) = \frac{3}{kR}\,\left(\sin(kR) - kR\cos(kR)\right)\ . \tag{2.20}$$

The relation of the mass M with the scale R depends on the choice of filter function. In the top-hat case, it is given by $M = \frac{4\pi}{3}\,\rho_m\,R^3$. It is worth it to note that depending on the type of filter, the mass might not be uniquely defined in terms of the scale.

On the other hand, the first-crossing distribution, $f(\nu)$, depends on the specific details on the collapse model, and is a function of $\nu = \delta_c^2(z)/\sigma^2(M)$, with $\delta_c(z)$ the linearly extrapolated overdensity for spherical collapse from Eq. (2.12). From the extended Press-Schechter, or excursion set formalism [175, 176, 177], it is possible to derive the function $f(\nu)$. The easiest

scenario, the Press-Schechter (PS) prescription, assumes spherical collapse and the condition that only overdensities above the critical density $\delta_c(z)$ are large enough to collapse to a halo. This threshold can be understood as a constant barrier, since it does not depend on the mass M. For gaussian distributed fluctuations, the former assumptions imply a first crossing distribution of the form [96]

$$f(\nu) = \sqrt{\frac{2\,\nu}{\pi}}\, e^{-\nu/2} \ , \tag{2.21}$$

Although there is general agreement of this result with the halo abundances from N-body simulations, it underpredicts the number of more massive halos, while overpredicts the low mass ones. The problem becomes even more pronounced at higher redshifts [178]. However, further improvements on the prediction of the halo mass function can be achieved by considering instead a more realistic ellipsoidal collapse model. In the excursion set-formalism, it implies a moving barrier, where the density threshold depends on the mass M. Although it cannot be computed exactly by analytical means, the Sheth-Tormen (ST) halo mass function is based on this assumption and provides a fit for the first-crossing distribution [97, 98, 179]

$$f(\nu) = A\sqrt{\frac{2\,q\,\nu}{\pi}}\left(1 + (q\,\nu)^{-p}\right)\, e^{-q\,\nu/2} \ , \tag{2.22}$$

with $p = 0.3$, $q = 0.707$ and $A = (1 + 2^{-p}\Gamma(1/2 - p)/\sqrt{\pi})^{-1} = 0.3222$. The above computations are only strictly valid for a hierarchical CDM universe. Instead, standard spherical (or elliptical) collapse does not longer apply to DM scenarios with structure suppression by free-streaming or collisional damping, effects which need to be taken into account. The proper modifications to the formalism for WDM and IDM are discussed in the following sections.

As shall be seen in Chapter 5, stellar formation and radiation fields responsible for heating and ionizing the IGM can be written in terms of the amount of halos capable of hosting star formation. Thus, a quantity of interest is the fraction of mass collapsed in halos above a mass M, which can be written in terms of the halo mass function, Eq. (2.18), as

$$f_{coll}(z, M) = \frac{1}{\rho_m}\int_M^\infty dM'\, M'\, \frac{dn(M')}{dM'} \ . \tag{2.23}$$

The relevant threshold mass for the IGM evolution is related to the minimum mass required to host star formation in a halo, as shall be discussed in Chapter 5. Using the PS prescription, Eq. (2.21), the collapsed fraction can be computed analytically, obtaining

$$f_{coll,PS}(z, M) = erfc\left(\frac{\delta_c(z)}{\sqrt{2}\sigma(M)}\right) , \tag{2.24}$$

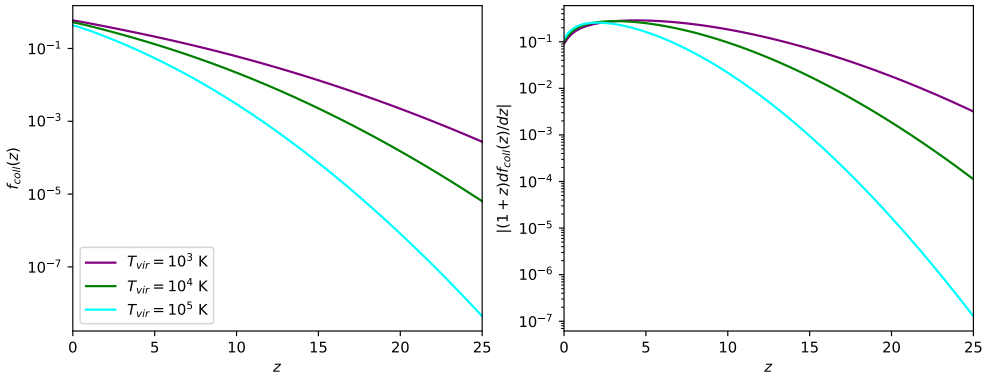

Figure 2.1: *Left:* evolution of the fraction of mass collapsed in halos above a mass corresponding to a virial temperature $T_{\rm vir}$ via Eq. (2.17), assuming a ST prescription. *Right:* derivative of the same quantity than in the left panel times $1 + z$.

where $erfc$ is the complementary error function, whereas for the ST function, Eq. (2.22), it must be computed numerically. Figure 2.1 shows the evolution of the fraction of mass collapsed and its redshift derivative for different threshold masses given by their virial temperatures.

2.3 Warm Dark Matter

As already discussed, a well motivated DM scenario considers particles with masses of the order of $\sim$ 1 keV, coined as WDM. The distinction with CDM cosmologies comes basically from its behavior at the decoupling period. In the WDM case, particles decoupled while they were still relativistic, while in the CDM case, particles had become already non-relativistic at its decoupling time. As a consequence of that, WDM particles still have some velocity dispersion, being negligible in the CDM case. Whereas at large scales, both models are indistinguishable, at small scales, due to the random thermal motion, WDM shows a suppression of power, above some cutoff scale, which washes out fluctuations. This causes a delay in structure formation and avoids a large population of small-size collapsed objects, or low-mass halos.

There are several possible candidates from particle physics theories which may behave as WDM. Supersymmetric theories predict the existence of a fermionic partner of the graviton, the gravitino, with spin 3/2 and mass $\sim$ 1 keV, which was the earliest proposal of a WDM particle as a thermal relic [116, 117]. On the other hand, right-handed sterile neutrinos are present in many Beyond the Standard Model (BSM) scenarios, and

can behave as WDM candidates [180, 181, 182]. In this decade, there was a renewed interest in sterile neutrino WDM when two independent groups reported a X-ray excess at an energy of 3.55 keV in the Chandra and XMM-Newton data from galaxy clusters [183, 184]. Since this signal is not known as an atomic line in the spectra of galaxies or clusters, it may come from a different source. It has been speculated to be originated from the decay of a sterile neutrino of mass $m_s = 7.1$ keV to an active neutrino, through the decay $\nu_s \to \nu + \gamma$. But the existence of this signal as well as its interpretation are still under discussion: further observations of galactic clusters with the Chandra ACIS [185] and with the XMM-Newton satellite [186] have found no evidence of such an excess. In addition, the signal could be due to an incomplete subtraction of atomic lines [187]. Although nowadays there is not a definite conclusion about the nature of this signal, it is expected that upcoming X-ray surveys will clarify its status.

In the following, kinetic properties of WDM, possible candidates, the free-streaming effect and the impact on the formation of cosmological structures are discussed.

2.3.1 Kinetic properties

Next, we review the general equilibrium properties of the WDM distribution. We assume that WDM is composed of particles of mass m_X which were thermally coupled to the plasma in the early universe, but became decoupled through a freeze-out mechanism while they were still relativistic [165, 188, 189]. This is contrary to the standard WIMP scenario, where DM particles decoupled when they were already non-relativistic. Considering this kind of particles as fermions, the initial distribution in phase space is given by the Fermi-Dirac function[5]

$$f_X(p) = \frac{1}{e^{pc/(k_B T_X)} + 1} \ , \tag{2.25}$$

with p the momentum and T_X the WDM temperature. While interactions were strong enough to maintain the equilibrium with the thermal plasma, WDM particles became thermally distributed, with the temperature T_X equal to the one of the plasma. After decoupling, the functional form of Eq. (2.25) becomes frozen, remaining self-similar, with the temperature redshifting as $\propto (1 + z)$. Integrating the distribution function Eq. (2.25)

[5] Although the following computations stand for fermionic DM, the final results can also apply to bosons, multiplying the number density by a factor 4/3 (since the fermionic number density is 3/4 times the bosonic one when particles are relativistic [47]).

over momentum one gets the number density of WDM particles, which reads

$$n_X = g_X \frac{3\zeta(3)}{4\pi^2} T_X^3 \ , \tag{2.26}$$

where ζ is the Riemann zeta function and g_X is the internal number of degrees of freedom, chosen as 2 for spin 1/2 particles. On the other hand, the energy density when WDM particles are non-relativistic (as currently they should behave) simply reads $\rho_X = m_X n_X$. Thus, we can relate their number density today $n_{X,0}$ with their energy density, or equivalently, with the fraction relative to the critical density, $\Omega_X = m_X n_{X,0}/\rho_c$. In addition, from Eq. (2.25) the root-mean-square velocity of the particles v_{rms} can be computed as

$$v_{rms} = \frac{\sqrt{\langle p^2 \rangle}}{m_X} = \frac{1}{m_X} \left(\frac{\int g_X d^3p \, p^2 f_X}{\int g_X d^3p f_X} \right)^{1/2} = 3.597 \, \frac{k_B T_X}{m_X} \ . \tag{2.27}$$

Since $T_X \propto (n_X/g_X)^{1/3}$, we finally can write the above result as

$$v_{rms} = 0.0437(1+z) \left(\frac{\Omega_X h^2}{0.15} \right)^{1/3} \left(\frac{m_X}{1\text{keV}} \right)^{-4/3} \text{km s}^{-1} \ , \tag{2.28}$$

which exhibits the scaling of the velocity dispersion with the mass and the abundance, explicitly showing that less massive particles present a larger velocity dispersion.

We can relate T_X with the neutrino temperature considering the entropy conservation before and after the thermal decoupling, as it is usually done with neutrino decoupling [47]. The entropy goes as $s \sim g_* T^3$, with g_* the *effective thermal number of degrees of freedom*. If thermally coupled, bosons contribute just as g to g_*, while fermions as $7/8\, g$, due to the proper phase space integral. Before DM decoupling, it takes a value $g_*(t_{dec})$. After DM decoupling, but before electron-positron annihilation, the degrees of freedom are given by electrons (2), positrons (2), neutrinos (3), antineutrinos (3) and photons (2), summing thus to $g_* = 43/4 = 10.75$. From the conservation of comoving entropy, one then finds

$$\frac{T_X}{T_\nu} = \left(\frac{43/4}{g_*(t_{dec})} \right)^{1/3} \ . \tag{2.29}$$

To relate T_X to the CMB temperature, one has to take into account that the thermal plasma is heated up by the electron-positron annihilation after neutrino decoupling, while the comoving neutrino temperature remains unchanged, leading to a relation $T_\nu = T_\gamma (4/11)^{1/3}$ [47, 165].

It is worth it to add a cautionary note regarding thermal WDM. As happens with standard neutrinos, one can constrain the mass and number of

WDM particles thermally decoupled in the early universe via the Gershtein-Zeldovich limit, enforcing that they cannot overclose the universe, i.e., $\Omega_X \lesssim 1$. The fraction of WDM can be written in terms of the mass and the temperature as

$$\Omega_X = \frac{m_X n_X}{\rho_{c,0}} \simeq \frac{m_X}{94.10\,\mathrm{eV}h^2}\left(\frac{T_X}{T_\nu}\right)^3 . \tag{2.30}$$

In order to have a thermal WDM candidate with mass of the order of ~ 1 keV accounting for all the DM ($\Omega_{\rm WDM} \simeq 0.25$), one needs $(T_X/T_\nu)^3 \sim 0.01$, implying $g_*(t_{dec}) \sim 10^3$.[6] Such a big number is much larger than the expected effective number of degrees of freedom before the electroweak transition in the SM, which is roughly ~ 100 (see, e.g., Ref. [165]). Thus, in order to be consistent with the Gershtein-Zeldovich limit, WDM particles should have decoupled in the very early universe, when some kind of new physics would present many degrees of freedom at high energies. Hence, thermal WDM, although in principle achievable, requires extra exotic physics. Despite that, it is the benchmark WDM scenario, at which most of constraints are placed. As discussed in the next section, other candidates with a thermal-like spectrum are usually considered, which may avoid the above restriction.

An additional warning must be stressed. Light particles with a thermal distribution behaving like radiation during the BBN era would enhance the radiation energy density, which has a great impact in the nucleon abundances resulting from BBN. It is quantified through the *effective number of neutrinos* N_{eff}, which takes the value of $N_{eff} = 3.044$ in the standard scenario, coming from the three neutrino species plus quantum electrodynamics corrections [54, 53] (see Ref. [190] for a recent and accurate computation). The joint analysis of BBN and CMB data from Planck agrees with that previous quantity, with an uncertainty of around the 10%, being thus well constrained [24]. Additional radiation species during BBN would contribute to N_{eff} with a factor $(T_X/T_\nu)^4 \propto g_*(t_{dec})^{-4/3}$, which must take a low value in order to be consistent with BBN and CMB results. This implies an additional reason why $g_*(t_{dec})$ must be large enough, independently on the total abundance and mass. Note however that thermal relics with $\Omega_X \sim 0.25$ and $m_X \sim 1$ keV able to be compatible with the Gershtein-Zeldovich limit would also overcome this restriction.

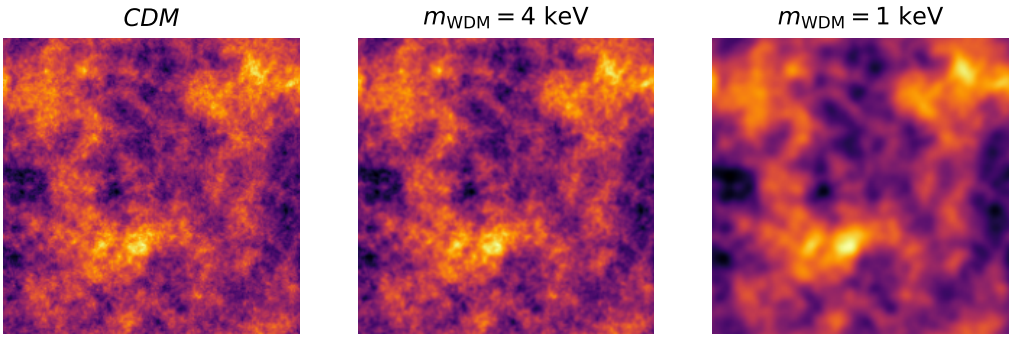

Figure 2.2: Random gaussian fields in a window of 10 Mpc/h generated by the matter power spectrum at redshift 0, for CDM (left), and WDM, with $m_{\rm WDM} = 4$ keV (middle) and $m_{\rm WDM} = 1$ keV (right), employing the power spectrum with the transfer function from Eq. (2.36). Note that lower particle masses increase the suppression scale, which erases smaller structures, and only larger fluctuations remain.

2.3.2 Free-streaming

If WDM particles are supposed to be thermally produced in the early universe (as in the WIMP scenario), they are assumed to be still relativistic at the epoch of their decoupling from the thermal plasma, but expected to become non-relativistic around the time of matter radiation equality, $t_{\rm eq}$, when the matter perturbations start to grow substantially, as discussed in Sec. 2.2.1. The free-streaming scale can be estimated as the distance a particle can travel until the matter-radiation equality $t_{\rm eq}$ [165, 191]. While the particle is relativistic, its velocity is close to the speed of light $v \sim c$. However, after a time $t_{\rm nr}$, when the temperature drops below $T_X(t_{\rm nr}) \sim m_X c^2/3$, the particle becomes non-relativistic, and hereafter its velocity decays as $v \propto a^{-1}$. Thus, the comoving distance travelled up to $t_{\rm eq}$ can be written as [165]

$$\lambda_{fs} = \int_0^{t_{\rm eq}} dt' \frac{v(t')}{a(t')} \simeq \int_0^{t_{\rm nr}} dt' \frac{c}{a(t')} + \int_{t_{\rm nr}}^{t_{\rm eq}} dt' \frac{v(t')}{a(t')}. \tag{2.31}$$

Since this process takes place in the radiation domination era, the scale factor evolves as $a(t) = a_{\rm nr}(t/t_{\rm nr})^{1/2}$, and the free-streaming length reads

$$\lambda_{fs} \simeq r_{\rm H}(t_{\rm nr}) \left(1 + \frac{1}{2} \log\left(\frac{t_{\rm eq}}{t_{\rm nr}}\right)\right), \tag{2.32}$$

where $r_{\rm H}(t_{\rm nr}) = c \int_0^{t_{\rm nr}} dt'/a(t') = 2t_{\rm nr}/a(t_{\rm nr})$ is the comoving horizon at the time $t_{\rm nr}$. From the condition $T_X(t_{\rm nr}) \sim m_X c^2/3$, since the WDM and photon

[6] In the original gravitino literature, this bound is relaxed to $g_*(t_{dec}) \sim 200$, but assuming $\Omega_{\rm WDM} = 1$, which we now know it must be lower [115].

temperatures evolve with the same dependence, $T_X \propto T_\gamma \propto a^{-1}$, one finds that $a_{\rm nr} \propto t_{\rm nr}^{1/2} \propto m_X^{-1}(T_X/T_\gamma)$, and thus, the $\lambda_{fs} \propto m_X^{-1}(T_X/T_\gamma)$. Given that, from Eq. (2.26), $n_X \propto g_X T_X^3$, and $\Omega_X = m_X n_{X,0}/\rho_{c,0}$, the scaling of the free-streaming scale goes as [192]

$$\lambda_{fs} \simeq 0.4 \left(\frac{m_X}{\rm keV}\right)^{-4/3} \left(\frac{\Omega_X h^2}{0.135}\right)^{1/3} h^{-1}{\rm Mpc}. \tag{2.33}$$

One can apply this estimate to different free-streaming species. For instance, in the case of a massive neutrino species of $m_\nu \sim$ eV, since the neutrino temperature is related to the CMB one by $T_\nu = T_\gamma (4/11)^{1/3}$ (as discussed in the previous section), one has $\Omega_\nu h^2 \simeq m_\nu/(91{\rm eV})$, and one obtains $\lambda_{fs,\nu} \simeq 10^3$ Mpc $(1{\rm eV}/m_\nu)$. If these particles formed most of the DM, which enters in the category of HDM, this estimate predicts that structures with sizes below that scale would not be formed, in contradiction with observations. However, for particles with masses around $\sim$ keV, one finds a free-streaming length of the order of $\lambda_{fs,{\rm WDM}} \sim$ 10-100 kpc, which corresponds to subgalactic sizes. This range is precisely the one required to explain the small-scale problems discussed in Sec. 2.1.2. To further illustrate this effect, Fig. 2.2 shows realizations of random gaussian fields, as the cosmological density field behaves in the linear regime, generated with the power spectrum corresponding to WDM (commented in the next section) with $m_{\rm X} = 4$ keV and WDM with $m_{\rm X} = 1$ keV, together with the CDM case, within a box of 10 Mpc/h. The small-sized fluctuations are washed out in WDM scenarios, with a greater effect the lower the mass.

The estimation of the free-streaming scale can also be carried out from the Jeans instability analysis discussed in Sec. 2.2.1. While in CDM models, pressure can be safely neglected, leading to small Jeans lengths, thermal motion of WDM models provides a larger scale above which perturbations grow. Substituting the speed of sound in Eq. (2.6) by the velocity dispersion from Eq. (2.28), one finds a scaling of the Jeans length of $\lambda_J \propto T_X/m_X \propto m_X^{-4/3}\Omega_X^{1/3}$, which is the same as the one obtained above.

The mass of WDM particles and the free-streaming scale are not univocally related, since the momentum distribution and the number density depend on the particle production mechanism. So far, throughout all the discussion, thermal relics have been assumed to constitute the WDM. However, besides thermal production through a freeze-out decoupling process from the thermal plasma, as in the WIMP scenario, WDM candidates may be produced by other mechanisms. For instance, sterile neutrinos produced at non-resonant oscillations from active neutrinos have also been proposed, by the so-called Dodelson-Widrow mechanism [118]. The distribution function for particles produced in this way has the same functional form as a thermal distribution, but suppressed by a factor which depends on the

masses of the active and sterile neutrinos. Although the original Dodelson-Widrow model as 100% of DM has been completely ruled out from Local Group galaxy counts plus X-ray observations [193], it is still considered as the archetypal sterile neutrino DM scenario. On the other hand, resonantly produced sterile neutrinos have also been proposed through the so-called Shi-Fuller mechanism, which would have a much cooler distribution function (i.e., skewed to low energies) than a thermally produced particle with the same mass [119]. Although thermal production is usually assumed for most of the bounds, it is sometimes possible to relate the constraints for non-thermal WDM to those for thermal WDM [194]. This happens, for instance, with non-resonantly-produced sterile neutrinos (as the Dodelson-Widrow mechanism), where bounds on the sterile neutrino mass m_s can be derived from constraints on the equivalent thermal relic mass m_X by the relation [195]

$$m_s = 3.90 \text{ keV} \left(\frac{m_X}{\text{keV}}\right)^{1.294} \left(\frac{0.25 \times 0.7^2}{\Omega_X h^2}\right)^{1/3} . \tag{2.34}$$

Constraints on resonantly produced sterile neutrinos (e.g., due to the Shi-Fuller mechanism) cannot be translated from thermal relic bounds and need to be studied separately. This is because there is not a single function relating the masses of both scenarios, since the relation also depends on the mixing angle [196, 197]. Generally, for the same free-streaming scale, the Shi-Fuller mechanism provides lower masses than non-resonantly produced neutrinos [198].

The most stringent observational constraints on the WDM particle mass are obtained from observations of the Lyα forest, based on the comparison of high redshift quasar spectra with hydrodynamical simulations. From QSOs spectra observed with the Keck High Resolution Echelle Spectrometer (HIRES) and the Magellan Inamori Kyocera Echelle (MIKE) spectrographs, together with SDSS data from the DR1 and DR2 data releases, this procedure has led to a limit on the mass of a WDM thermal relic of $m_X > 3.3$ keV (at the 2σ level) [199]. Making use of the SDSS-III/BOSS data, previous lower bounds where improved to $m_X > 4.09$ keV for a thermal relic, and to $m_s > 24.4$ keV for a non-resonantly produced sterile neutrino, both at the 95 % CL (although slightly weakened when Planck 2016 CMB data is also considered) [195]. A recent analysis employing eBOSS and XQ-100 Lyα data found the most stringent bounds on the thermal relic mass of $m_X > 5.3$ keV, or a limit on the non-resonantly-produced sterile neutrino mass of $m_s > 34$ keV (both at 95 % CL) [200]. The drawback of these methods is that they rely on model-dependent numerical simulations, where assumptions regarding the thermal history are taken, such as a relation between the temperature and the density, which may not be

completely accurate. Besides these Lyα forest constraints, the number of satellite galaxies of the Milky Way has also been used to explore the allowed range of masses. Since WDM predicts fewer satellite galaxies than the standard scenario, this allows rejecting masses below $m_X = 2.02$ keV (95 % CL) for a thermal relic, regardless of the specific assumptions about galaxy formation processes. This limit improves up to 3.99 keV when modeling Reionization, which suppresses dwarf galaxies formation [201]. A recent DES analysis, with new observed satellite galaxies, reject masses below 6.5 keV [128]. Anyway, MW satellite constraints strongly depend on the MW mass, whose value still presents some uncertainties [202, 203, 204]. It is worth it to keep in mind that the aforementioned bounds stand for all DM composed by WDM, but in mixed scenarios with CDM plus WDM in some amount, the bounds would weaken. In Part II of this thesis, WDM scenarios are studied with simulations of the thermal evolution of the universe, exploring how Reionization data and the 21 cm signal can constrain such models [1, 2].

2.3.3 Impact on structure formation

2.3.3.1 Linear power spectrum

The above simplified sketch allows one to understand the scaling of the free-streaming length with the mass m_X, and roughly estimate the wavelength of modes which would be affected. However, it lacks two relevant points. On the one hand, it does not take into account the logarithmic growth of perturbations during the radiation dominated era. On the other hand, the free streaming does not instantaneously switch off after $t_{\rm eq}$. A precise evaluation of the free-streaming damping requires solving numerically the evolution of linear perturbations [189]. One can write the WDM linear power spectrum in terms of a suppression relative to the CDM case characterized by the transfer function $\mathcal{T}_X^2(k)$,

$$P_X(k) = \mathcal{T}_X^2(k)\, P_{\rm CDM}(k). \tag{2.35}$$

Numerical computations from Boltzmann solver codes showed that the WDM transfer function can be fitted to the function [205]

$$\mathcal{T}_X(k) = (1 + (\alpha k)^{2\nu})^{-5/\nu}\ , \tag{2.36}$$

with $\nu = 1.12$, and the breaking scale

$$\alpha = 0.049 \left(\frac{\rm keV}{m_X}\right)^{1.11} \left(\frac{\Omega_X}{0.25}\right)^{0.11} \left(\frac{h}{0.7}\right)^{1.22} {\rm Mpc}/h\ . \tag{2.37}$$

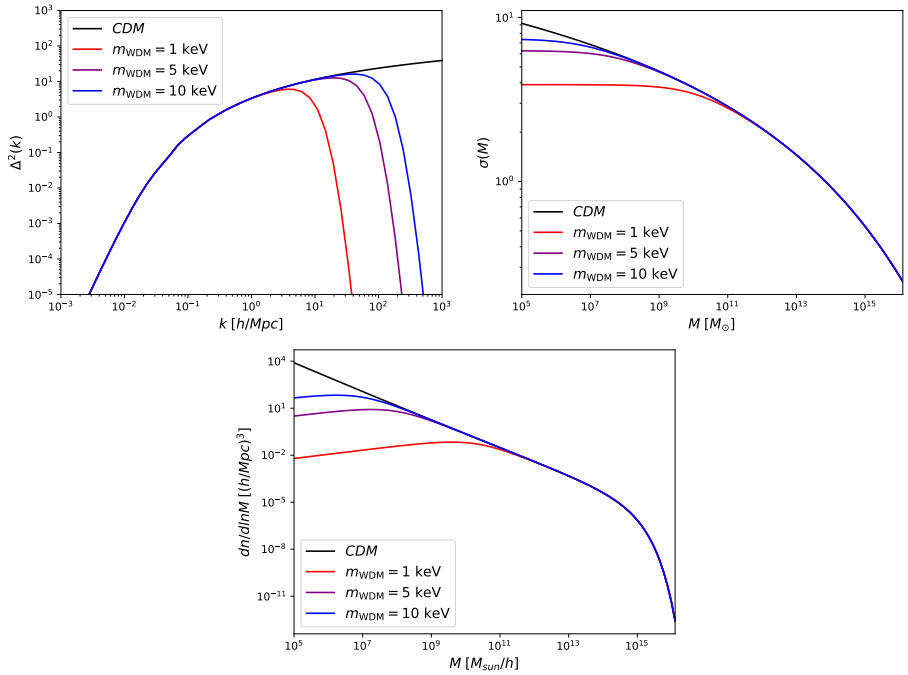

Figure 2.3: Dimensionless power spectrum (top left), variance $\sigma(M)$ (top right) and halo mass function (bottom) for CDM and three WDM models, evaluated at $z = 0$. Note the suppression at small scales, corresponding to high k in the power spectrum, and at low masses M in the variance and halo mass function.

The parameter α determines the scale where the suppression due to free streaming appears, and thus, it must be directly related to λ_{fs}. Note that our previous naive estimation of λ_{fs}, Eq. (2.33), provides a decent estimation to the accurate computation of Eq. (2.37), with a similar scaling of the parameters Ω_X and m_X. It must be stressed that this fitting formula corresponds to a thermal relic, although as it has been shown, it can be translated to some non-thermal cases via Eq. (2.34) [205]. The dimensionless power spectrum for several WDM cases is plotted in left panel of Fig. 2.3, clearly showing the damping in fluctuations above the free-streaming scale. The CDM, contrarily, keeps growing at small k, a definitory characteristic of its hierarchical behavior.

On the other hand, it is customary to define the half-mode length $\lambda_{\rm hm} = 2\pi/k_{\rm hm}$, as the scale for which $\mathcal{T}_X/\mathcal{T}_{\rm CDM} = 1/2$. From the transfer function, Eq. (2.36), this quantity reads

$$\lambda_{\rm hm} = 2\,\pi\,\alpha_X \left(2^{\nu/5} - 1\right)^{-1/(2\,\nu)} \quad , \tag{2.38}$$

while its corresponding half-mode mass $M_{\rm hm}$ is thus defined by

$$M_{\rm hm} = \frac{4\,\pi}{3}\,\rho_m\left(\frac{\lambda_{\rm hm}}{2}\right)^3 = \frac{32\,\pi^4}{3}\,\rho_m\,\alpha_X^3\left(2^{\nu/5}-1\right)^{-3/(2\,\nu)}. \tag{2.39}$$

Together with α, these scales are usually employed to reflect the lengths at which suppression effects become relevant.

2.3.3.2 Halo mass function

In order to obtain the halo mass function, one could naively employ the Press-Schechter formalism outlined in Sec. 2.2.3, making use the PS or ST halo mass functions with the WDM power spectrum. However, numerical simulations show that when doing that, N-body results are not correctly recovered, but always present a further suppression at low masses. To understand why this procedure fails, one has to recall that in the excursion set formalism, there is a mapping between linear fluctuations and non-linear ones, which can be computed from simple pressureless spherical or ellipsoidal collapse. This approach has a remarkable success for CDM, where structure formation progresses hierarchically. However, in WDM, the problem is more complicated, since pressure effects cannot be longer neglected at small scales, preventing hierarchical collapse, and the computations of simplified spherical or elliptical collapse become invalid. In order to properly treat the problem, one should re-evaluate the excursion set approach, modifying it according with the WDM nature, which involves considering a moving barrier [206]. An easier approach consists on replacing the top-hat window function by a sharp-k function (a Heaviside step function in Fourier space).[7] While in the CDM case the chosen filter does not significantly matter, with this choice in the WDM scenario, unlike with other window functions such as the top-hat filter, the halo mass function naturally tends to zero at low masses, as expected from the nature of structure formation with the free-streaming effect [191]. This procedure has a remarkable success at low redshifts, with the advantage of being simple and well motivated. However, sharp-k filters present the drawback that the mass is not univocally defined, besides the scaling $M \propto R^3$ with the filtering radius R. It requires to introduce a free parameter c so that $M = 4\pi/3c\bar{\rho}R^3$, which has to be calibrated with simulations, finding the best match to be $c \simeq 2.5$ [207].

Nevertheless, to phenomenologically match the N-body simulations, the easiest way is by modifying the ST halo mass function with the appropriate factor which gives the best fit. The authors of Ref. [192] provided a

[7] Besides this WDM issue, there are good reasons for considering the sharp-k filter. Actually, in set excursion formalism, exact analytic results for the first crossing PS distribution can only be obtained with the sharp-k filter, see, e.g., Refs. [175, 177].

functional form for that which reads

$$\frac{dn^{\rm WDM}}{dM} = \left(1 + \frac{M_{\rm hm}}{b\,M}\right)^{a} \frac{dn^{\rm ST,\,WDM}}{dM} \ . \tag{2.40}$$

The WDM halo mass function is thus given by the ST prescription $\frac{dn^{\rm ST,\,WDM}}{dM}$ (employing Eq. (2.22)), with the linear matter power spectrum corresponding to the WDM case, Eq. (2.35), multiplied by a mass-dependent term. This correction factor further suppresses the abundance at masses below $M_{\rm hm}$, and is determined by two parameters, a and b. Although the initial formulation worked with $b = 1$, it was later shown that the fit improved with $b = 0.5$, whereas $a = -0.6$ [208, 209].

As a final comment, it is worth emphasizing that modeling WDM with numerical simulations presents additional challenges with respect to CDM, such as the appearence of artificial numerical fragmentation. The existence of shot noise due to the initial random thermal velocities typical in WDM can seed unphysical overdensities at small scales. As the simulation evolves, these artificial fluctuations lead to the formation of spurious structures, producing an overabundance of low-mass halos, which is just the opposite of what is expected in a WDM scenario. This effect has been extensively discussed in the literature, and different ways to get rid off these fake halos have been proposed [210, 191, 211, 212, 213].

2.4 Interacting Dark Matter

Among the fundamental requirements of any DM candidate, it is the absence of interactions with radiation. However, it may be the case that such interactions actually exist but are so weak that are unobservable at large scales, although they could become important at smaller subgalactic scales. This exciting possibility is explored in the so-called Interacting Dark Matter (IDM) models, term which usually encompasses interactions with light particles, such as photons or neutrinos. In analogy with baryon-photon interactions via Thomson scattering, one could assume that DM particles can scatter elastically with radiation. This would induce similar effects in the growth of fluctuations of DM to those observed in the baryon sector, such as an oscillatory spectrum given by sound waves driven by radiation pressure. Furthermore, small scales would be suppressed by *collisional damping*, the analogous of Silk damping due to Thomson scattering [214]. Thus, as in the WDM case, it would result in the suppression of small-size cosmological structures, potentially having an impact on structure formation. As we shall discuss, IDM scenarios can be closely related to WDM models at the linear level, given that cosmological effects are similar. However, this sort

of degeneracy between models is broken when non-linear effects are taken into account, such as in the study of DM halos.

Photon-DM interacting scenarios have been extensively studied in the literature, either studying its impact on the CMB, large scale structure and growth of linear perturbations [215, 216, 217, 218, 219, 220] or performing N-body simulations and comparing with the observed Milky Way satellites [221, 149, 222, 209, 223]. On the other hand, the signatures of neutrino-DM interactions on the CMB and large scale structure have also been widely examined [224, 225, 226, 223, 227, 220, 228]. Henceforth in this thesis, we focus on photon-DM interactions, although we shall comment on similarities with the neutrino-DM counterpart. Throughout this section, we physically motivate these scenarios, discuss the collisional damping effects, and the signatures that IDM may leave in structure formation.

2.4.1 Particle physics motivation

An IDM scenario can arise from different fundamental or effective particle physics models. Consider, as a simple example, the case of a *hidden photon*, i.e., a vectorial gauge boson for a $U(1)$ gauge symmetry, represented by B_μ. Such a boson may arise, for instance, from Supersymmetric models or string theories [229, 230]. These particles would not interact with the SM particles, being for that reason *hidden*, but instead they could interact with DM. However, this field may also be mixed with the standard photon A_μ. Defining the field strengths as $F_{\mu\nu} = \partial_\mu A_\nu - \partial_\nu A_\mu$ and $B_{\mu\nu} = \partial_\mu B_\nu - \partial_\nu B_\mu$, one can write the lagrangian of the photon and hidden photon terms as [231, 230]

$$\mathcal{L} = -\frac{1}{4}F_{\mu\nu}F^{\mu\nu} - \frac{1}{4}B_{\mu\nu}B^{\mu\nu} + \frac{g}{2}B_{\mu\nu}F^{\mu\nu} + \mathcal{J}^\mu_{\rm em}A_\mu + \mathcal{J}^\mu_{\rm DM}B_\mu. \tag{2.41}$$

The first two terms correspond to the kinetic lagrangians of the gauge fields, while the third term accounts for a possible mixing between the standard and the hidden photon ruled by a mixing parameter g, which is allowed by the symmetries. The last terms provide the interaction between the SM and DM particles through the currents $\mathcal{J}^\mu_{\rm em}$ and $\mathcal{J}^\mu_{\rm DM}$, with A_μ and B_μ respectively. The mixing coupling is sometimes interpreted as a mixing angle, as $g = \sin(\chi)$ [230]. It is possible, however, to get rid of the mixing term by a convenient redefinition of the fields, or equivalently, changing the base A, B to diagonalize the kinetic part, as

$$A'_\mu = \sqrt{1-g^2}A_\mu \; ; \quad B'_\mu = B_\mu - gA_\mu \; . \tag{2.42}$$

Under the above change of variables, one finds that the mixing term is removed and the kinetic lagrangian becomes diagonalized:

$$\begin{aligned}\mathcal{L} = &-\frac{1}{4}F'_{\mu\nu}F'^{\mu\nu} - \frac{1}{4}B'_{\mu\nu}B'^{\mu\nu} \\ &+ \frac{1}{\sqrt{1-g^2}}\mathcal{J}^{\mu}_{\rm em}A'_{\mu} + \mathcal{J}^{\mu}_{\rm DM}\left(B'_{\mu} + \frac{g}{\sqrt{1-g^2}}A'_{\mu}\right),\end{aligned} \tag{2.43}$$

with $F'_{\mu\nu}$ and $B'_{\mu\nu}$ the field strengths for the new fields A'_{μ} and B'_{μ}. Note, however, that now the DM current gets coupled to the new photon field A'_{μ}. In this way, an effective interaction between DM particles and photons arises, determined by the coupling g. Since these processes have not been measured, this constant must be very small. Actually, predictions from Supersymmetry and string theory range between 10^{-16} and 10^{-2} [229]. The effective electric charge of the DM field would be a small non-integer quantity given by g, and the DM particles would then become *millicharged*. Note that, if the DM are composed of fermionic fields, the γDM coupling would have the same form that the interaction term in Quantum Electrodynamics, the same processes being allowed. More concretely, elastic scattering of DM particles with photons would be present, with an energy-independent cross section at low energies, in analogy with the Thomson scattering [232]. Following that argument, in millicharged DM models, the γDM cross section can be expressed as

$$\sigma_{\gamma\rm DM} = \epsilon^2\sigma_T\left(\frac{m_e}{m_{\rm DM}}\right)^2, \tag{2.44}$$

where $\sigma_T = 6.65\times10^{-25}$ cm^2 is the Thompson cross section, $\epsilon = |q|/e$ with q the DM electric charge ($q = eg/\sqrt{1-g^2}$ in the example above), e the electron charge and m_e its mass. The mass factor in the expression above comes from the fact that the Thomson cross section scales as $\sigma_T \propto m_e^{-2}$. In models such as the outlined above, however, baryon-DM scattering would also be possible, which strongly constrains these scenarios using CMB and Lyα forest [233, 234]. The upper bound obtained on the millicharge from the aforementioned analyses can be summarized as

$$\epsilon < 1.8\times10^{-6}\left(\frac{m_{\rm DM}}{\rm GeV}\right)^{1/2}, \tag{2.45}$$

which is valid for $m_{\rm DM} \gtrsim$ MeV. Other bounds can be found from solar data [235] or from accelerators [236]. Since we mostly focus on the impact of collisional damping in structure formation, the IDM scenario assumed in this thesis only considers photon-DM scattering, without baryon-DM scattering, which would have additional effects on the thermal history of the universe. Therefore, the above limit may not be applicable to our case

if non-gravitational baryon-DM interactions could be neglected. [8] Non-millicharged IDM scenarios are still possible, however. It is the case, for instance, of DM composed by axion-like particles, whose lagrangian interaction term reads $\kappa\, a\, F_{\mu\nu}F^{\rho\sigma}\epsilon^{\mu\nu\rho\sigma}$, with a the axion-like scalar field, κ the coupling constant and $\epsilon^{\mu\nu\rho\sigma}$ the Levi-Civita symbol. These scenarios present γDM scattering with interaction amplitudes scaling as $\sim \kappa^4$, while axion-baryon scattering can only happen at higher order, $\sim \kappa^4 e^4$ (at one loop), in the case that axion-baryon interaction terms are absent or negligible.[9] On the other hand, νDM interactions would not be related to millicharged particles, and in that case the bound from Eq. (2.45) does not apply. In any case, the IDM scenario treated in this thesis should be regarded as a phenomenological scenario rather than a specific particle physics model, in order to explore the consequences of collisional damping from DM interactions with light or massless particles, which may leave an imprint on the evolution of the universe and the growth of structures.

2.4.2 Collisional damping

In this section, the damping scale due to γDM interactions is derived from physical arguments.[10] Consider a DM particle immersed in the photon fluid, where both species interact. The path traveled after several successive collisions can be regarded as a random walk (see, e.g., Refs. [237, 165]), as firstly proposed by Silk in his seminal paper where collisional damping of the CMB due to baryon-photon scattering was described [214]. A photon travels a distance $\vec{r}_i$ before the i-th scattering. The net displacement $\vec{R}$ after N free paths reads $\vec{R} = \sum_i^N \vec{r}_i$. While its average vanishes (since it is a vector composed by random walks without a preferred direction), its square leads to a non-zero value. Writing the variance of each step as $\lambda_{\rm mfp}^2 = \langle|\vec{r}_i|^2\rangle$, thus, $\langle|\vec{R}|^2\rangle = N\lambda_{\rm mfp}^2$ (where products between different steps average to zero since they are not correlated) [238]. The (physical) collisional damping scale $\lambda_{\rm cd,phys}$ would be given by the total traveled distance until the decoupling time $t_{\rm dec}$, $\lambda_{\rm cd,phys}^2 \sim N\lambda_{\rm mfp}^2$. For a interaction rate of $\Gamma = n_{\rm DM}\sigma_{\gamma{\rm DM}}$, the

[8] Nevertheless, depending on the specific millicharged model, there may be still allowed regions in the parameter space where bounds could be relaxed, see, e.g., Fig. 1 of Ref. [235].

[9] Note, however, that such γDM cross section would scale with the energy as $\propto E^2$, and thus our formalism for Thomson-like scattering would not be valid, thus it must be regarded just as an illustrative example.

[10] Note that in the literature, damping effects by DM self-interactions are also sometimes considered [215, 217], although these are not covered in this thesis, restricting ourselves only to photon-induced damping.

mean-free path of a photon reads $\lambda_{\rm mfp} = \Gamma^{-1}$.[11] On the other hand, the average number of collisions during a time interval Δt is written as $N \sim c\Delta t/\lambda_{\rm mfp}$. Thus, the total distance traveled gives the comoving collisional damping scale $\lambda_{\rm cd}$ as [165, 215, 239]

$$\lambda_{\rm cd}^2 \simeq \int_0^{t_{\rm dec}} \frac{dt}{\lambda_{\rm mfp}} \frac{\lambda_{\rm mfp}^2}{a^2} = \int_0^{t_{\rm dec}} \frac{dt}{n_{\rm DM}\sigma_{\gamma{\rm DM}}a^2}, \tag{2.46}$$

where the a^2 factor makes it a squared comoving distance. The integral can be easily performed, taking into account that γDM scatterings occur during the radiation-domination era, where $a \propto t^{1/2}$. The decoupling time $t_{\rm dec}$ is defined by the relation $H(t_{\rm dec}) \sim n_{\rm DM}\sigma_{\gamma{\rm DM}}$, from which one finds $a(t_{\rm dec}) \propto \Omega_{\rm DM}\sigma_{\gamma DM}/m_{\rm DM}$. Plugging in the numbers, we find a characteristic length of

$$\lambda_{\rm cd} \sim 0.01\,{\rm Mpc}/h \left[10^8 \left(\frac{\sigma_{\gamma{\rm DM}}}{\sigma_T}\right)\left(\frac{\rm GeV}{m_{\rm DM}}\right)\right]. \tag{2.47}$$

This is a rough but still decent estimation of the correct scale, providing the same order of magnitude for the relevant cross sections, as shall be seen in Sec. 2.4.3.1. Note that the above scale grows with the combination $\sigma_{\gamma{\rm DM}}/m_{\rm DM}$, rather than with the cross section alone. This is because it depends upon the interaction rate, which goes as $n_{\rm DM}\sigma_{\gamma{\rm DM}} \propto \sigma_{\gamma{\rm DM}}/m_{\rm DM}$. Therefore, this is the relevant quantity which rules the damping effects, while in the WDM case, it is the mass of the particle. Stronger scattering (i.e., larger cross sections) imply a longer damping scale and thus deeper impact on structure formation, washing out fluctuations below it. Note that cross sections of the order $\sigma_{\gamma{\rm DM}}/\sigma_T \times (m_{\rm DM}/{\rm GeV})^{-1} \sim 10^{-8}$ would lead to damping lengths of the order of subgalactic sizes, required to account for the CDM issues discussed in Sec. 2.1.2. It must be stressed that the computation of Eq. (2.47) is too simplistic since it gloss over several additional effects which may become relevant to determine the damping scale, such as heat conduction or shear effects [217]. Finally, Eq. (2.47) may essentially work for other light or massless particles interacting with DM in thermal equilibrium with the thermal plasma in the early universe, such as neutrinos.

Based on this effect, CMB data from the Planck satellite have allowed to obtain upper bounds on the allowed elastic γDM cross sections of $\sigma_{\gamma{\rm DM}}/\sigma_T \times (m_{\rm DM}/{\rm GeV})^{-1} \lesssim 10^{-6}$ [218, 219]. However, more stringent constraints are provided from the study of satellite galaxies of the MW, which lie around $\sigma_{\gamma{\rm DM}}/\sigma_T \times (m_{\rm DM}/{\rm GeV})^{-1} \lesssim 10^{-9}$ (value that depends

[11] The photon mean free path is always much larger than the DM one, by a factor $n_\gamma/n_{\rm DM}$. For this reason we are estimating the photon damping scale rather than the DM one. As long γDM interactions are strong, DM particles remain coupled to photons and radiation fluctuations drag matter with them. Thus, the photon damping length is the relevant quantity [165].

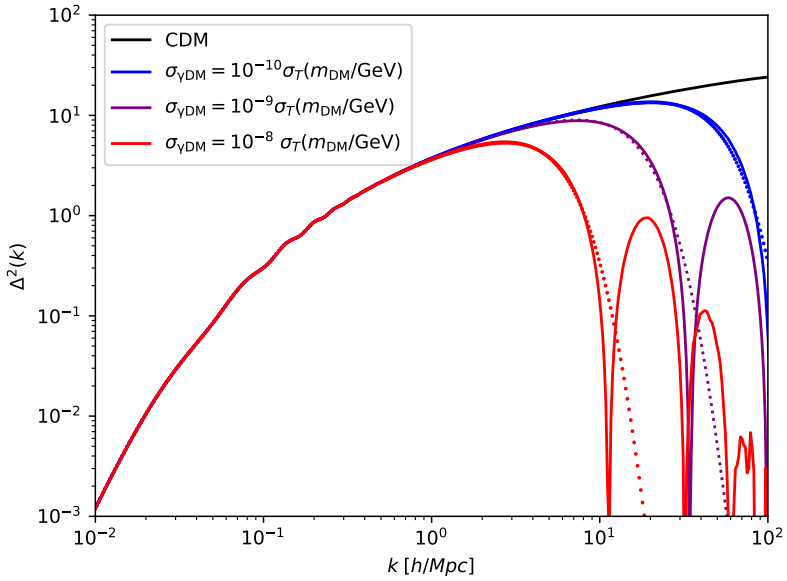

Figure 2.4: Dimensionless power spectrum for three γDM scenarios calculated with a modification of the Boltzmann solver CLASS [171] (solid curves), with the corresponding approximation using the fitting formula in Eqs. (2.36) and (2.49) (dotted curves). The transfer function approach successfully matches the first damping, and agrees with the exact computation up to the oscillatory effects appear. The equivalent WDM masses, following the correspondence from Eq. (2.50), are $0.7, 1.8, 4.7$ keV for $\sigma_{\gamma\mathrm{DM}}/\sigma_T \times (m_{\mathrm{DM}}/\mathrm{GeV})^{-1} = 10^{-8}, 10^{-9}, 10^{-10}$ respectively.

on the MW mass) [148]. On the other hand, elastic neutrino-DM scattering has been also constrained, resulting in the stringent constraints from Lyα forest $\sigma_{\nu\mathrm{DM}}/\sigma_T \times (m_{\mathrm{DM}}/\mathrm{GeV})^{-1} < 1.5 \times 10^{-9}$ [225]. In Part II of this thesis, we show how Reionization data, MW satellite galaxies and the 21 cm EDGES signal are able to provide stronger constrains on the elastic γDM cross section [4, 5].

2.4.3 Imprints on structure formation

2.4.3.1 Linear power spectrum

While the above estimate qualitatively explains the effects of collisional damping, a precise evaluation of the impact on fluctuations requires the computation of the kinetic equations including the scattering term. More specifically, interactions between photons and DM particles induce a coupling of their respective velocity fluctuations. As is derived from the integration of the Boltzmann equations, the Euler equation from Eq. (2.2) for DM

needs to be modified, including a term accounting for scattering, as [216]

$$\dot{\mathbf{v}} + H\mathbf{v} = -\frac{1}{a}\nabla\Phi + S^{-1}\,\sigma_{\gamma\mathrm{DM}}\,n_{\mathrm{DM}}\,(\mathbf{v}_\gamma - \mathbf{v})\,, \tag{2.48}$$

where $S = (\rho_{\mathrm{DM}} + p_{\mathrm{DM}})/(\rho_\gamma + p_\gamma) = (3/4)\rho_{\mathrm{DM}}/\rho_\gamma$ accounts for the ratio between momenta. While interactions are strong, the scattering term couples fluctuations of DM and photons, and the latter drag DM perturbations. On the other hand, photons present a large radiation pressure, which counteracts gravitational collapse. The compensation of both effects leads to sound waves, which results in an oscillatory behavior of the spectrum at small scales. A similar effect happens in the CDM model in the baryon-photon sector. Due to Thomson scattering, baryonic fluctuations get coupled to radiation, causing wiggles on the matter spectrum. This effect is the cause of the well-known Baryon Acoustic Oscillations (BAOs), which have been measured with large scale structure observations [25, 26, 28]. For the same reason, in γDM scenarios, DM fluctuations also present an oscillatory pattern in the power spectrum, due to the coupling of DM particles to photons, at scales which entered the horizon when these interactions were still strong. After γDM decoupling, the DM spectrum approaches the standard CDM case.

To properly predict the linear evolution of fluctuations, a numerical code is required, such as CLASS [171], which solves the Boltzmann equations hierarchy for every species in linear perturbation theory. To study IDM scenarios, the code must be properly modified, including the interaction terms between photons and DM in the hierarchy of kinetic equations, as described in Refs. [216, 218, 219]. The results of the modification of CLASS for three IDM models are shown in Fig. 2.4 in solid lines. As expected, oscillations appear below the collisional damping scale, matching the CDM case at larger scales.

Since the main effect of γDM scattering is the suppression of small scale fluctuations, an approximation of this damping can be emulated by employing the transfer function fit from Eq. (2.36), properly modified. It has been shown that this fitting formula works for IDM models, choosing $\nu = 1.2$ and parameterizing the suppression scale in terms of the γDM scattering cross section as [216]

$$\alpha_{\mathrm{IDM}} = 0.073 \left[10^8 \left(\frac{\sigma_{\gamma\mathrm{DM}}}{\sigma_T}\right)\left(\frac{\mathrm{GeV}}{m_{\mathrm{DM}}}\right)\right]^{0.48} \left(\frac{\Omega_{\mathrm{IDM}}}{0.4}\right)^{0.15} \left(\frac{h}{0.65}\right)^{1.3} \mathrm{Mpc}/h\ . \tag{2.49}$$

Note that this length agrees with the order-of-magnitude estimation of Eq. (2.47) at the relevant cross sections $\sigma_{\gamma\mathrm{DM}}/\sigma_T \times (m_{\mathrm{DM}}/\mathrm{GeV})^{-1} \sim 10^{-8}$ (although the scaling of Eq. (2.47) with the cross section is slightly different).

The power spectrum resulting from using this approach is depicted with dotted lines in Fig 2.4. Notice that it accurately matches the exact IDM power spectrum from CLASS until the damped oscillatory effects dominate at small scales. However, the transfer function approximation can provide an accurate enough description where the damping scale appears, when IDM and CDM differences show up. Furthermore, as can be seen in Fig. 2.4, the second and subsequent maxima are suppressed by more than one order of magnitude, and thus their effects in structure formation are expected to be subdominant.

Given that both IDM and WDM scenarios can be described by the same fitting formula, one can consider a correspondence between the two models which lead to an equivalent damping in the power spectrum. By equating Eqs. (2.37) and (2.49), one finds that the suppression present in a WDM model with $m_{\rm WDM}$ matches the IDM scenario with cross section $\sigma_{\gamma \rm DM}$ and mass $m_{\rm DM}$ via

$$\left(\frac{\sigma_{\gamma \rm DM}}{\sigma_T}\right)\left(\frac{\rm GeV}{m_{\rm DM}}\right) \simeq 4.1 \times 10^{-9} \left(\frac{\rm keV}{m_{\rm WDM}}\right)^{2.4} . \tag{2.50}$$

Thus, IDM and WDM scenarios related by the correspondence above give rise to similar suppression of the linear power spectrum. For instance, IDM scenarios spanning the range $\sigma_{\gamma \rm DM} \in [10^{-11} - 10^{-8}]\, \sigma_T \times (m_{\rm DM}/{\rm GeV})$ roughly correspond to WDM scenarios with $m_{\rm DM} \in [1 - 12]$ keV. For the models employed in Fig. 2.4, cross sections of $\sigma_{\gamma \rm DM}/\sigma_T \times (m_{\rm DM}/{\rm GeV})^{-1} = 10^{-8}, 10^{-9}, 10^{-10}$ correspond to WDM masses of $0.7, 1.8, 4.7$ keV respectively. The relation above allows mapping IDM to WDM scenarios, so constraints based on the linear power spectrum can be translated from one scenario to the other. However, as will be seen next, the equivalence between both scenarios is broken at the level of the halo mass function.

Although we focus on photon-DM interactions, the effects of neutrino-DM elastic scattering are found to be similar, and the induced small-scale suppression in the power spectrum can also be parameterized with the same transfer function, correcting the breaking scale as $\alpha_{\nu \rm DM} \simeq 0.8 \times \alpha_{\gamma \rm DM}$ [208].

2.4.3.2 Halo mass function

To describe the halo mass function in an IDM universe, a similar procedure to the employed with WDM (Eq. (2.40)) can be followed, although including some further modifications. Although the first suppression of the linear power spectrum in the IDM scenario looks very similar to the WDM case, and therefore can be parameterized by similar means, a key distinction between these models is that IDM presents oscillations at even smaller

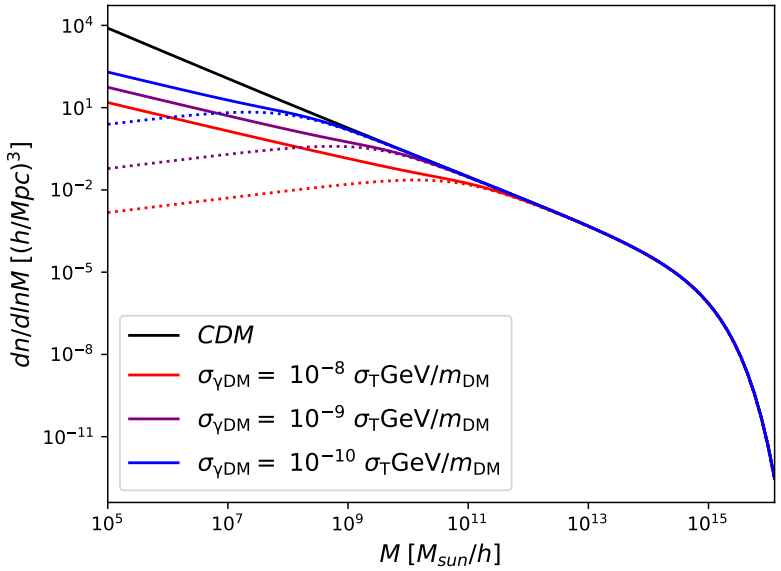

Figure 2.5: Halo mass function for CDM and three IDM models as a function of the mass, evaluated at $z = 0$. Dotted lines correspond to the WDM halo mass function with the same suppression scale.

scales, enhancing and suppressing fluctuations at growing wavenumbers. This effect induces a different behavior in the non-linear regime, affecting to the abundance of halos. As a result of these oscillations, for the same half-mode mass, low-mass halos are more abundant for IDM than for WDM [208]. Thus, to match IDM N-body simulations, an additional mass-dependent correction must be added to the halo mass function [209],

$$\frac{dn^{\rm IDM}}{dM} = \left(1 + \frac{M_{\rm hm}}{b\,M}\right)^a \left(1 + \frac{M_{\rm hm}}{g\,M}\right)^c \frac{dn^{\rm ST,\,CDM}}{dM}\,, \tag{2.51}$$

where the adopted best-fit parameters are $a = -1$, $b = 0.33$, $g = 1$, $c = 0.6$. The halo mass function $dn^{\rm ST,\,CDM}/dM$ corresponds to the standard ST first-crossing distribution considering the CDM linear power spectrum, instead of the IDM power spectrum. Note that this is different from the WDM case, where the WDM linear power spectrum explicitly appears in the halo mass function (integrated in the variance). In the IDM case, instead, the damping effects are only accounted for in the mass-dependent suppression factors of the above fit. This approach successfully matches the results from numerical simulations at $z = 0$ for cross sections around $\sigma_{\gamma\rm DM} \sim \times 10^{-9}\,\sigma_T\,(m_{\rm DM}/{\rm GeV})$ [208, 223]. The halo mass function for three IDM models is shown in Fig. 2.5 (continous colored lines), compared to the CDM (black line) and to the corresponding WDM cases, with the same half-mode mass (dotted lines). Notice that, while both scenarios present a

suppression of low-mass halos, it is more pronounced in the WDM cases, being milder for IDM. This is a consequence of the IDM oscillatory nature at small scales, which enhances low-mass halos with respect to WDM when non-linearities become important.

It has been shown that the halo mass function in νDM scenarios can be also well described by the procedure above [208]. This is because $\nu-$DM and γDM give rise to similar physics, and thus the damping effect results to be closely equivalent. More concretely, numerical simulations at $z = 0$ showed approximately the same halo mass function for the cases $\sigma_{\gamma\mathrm{DM}} = 2.9 \times 10^{-9}\,\sigma_T\,(m_{\mathrm{DM}}/\mathrm{GeV})$ and $\sigma_{\nu\mathrm{DM}} = 2.0 \times 10^{-9}\,\sigma_T\,(m_{\mathrm{DM}}/\mathrm{GeV})$, for a fixed half-mode mass [208]. This correspondence allows establishing a map between both scenarios, and estimating bounds on neutrino-DM cross sections.

Chapter 3

Primordial Black Holes

Primordial Black Holes (PBHs) conform a natural candidate for being at least one of the components of the DM. In this chapter, we shall review the basics on their formation, abundance and other properties. Some of their effects are discussed, such as the accretion of the surrounding matter or the modification of the matter fluctuations at small scales, which could leave an impact in the evolution of the universe and the formation of structures. Lastly, the most relevant constraints on their masses and abundances are discussed. For further details, see, e.g., Refs. [240, 241, 242, 243].

3.1 Foundations on PBHs

3.1.1 Motivation for the existence of PBHs

The hypothesis of the formation of PBHs in the early universe was first suggested in 1967 by Zeldovich and Novikov, who argued that PBHs would accrete radiation with catastrophic consequences and this would conflict with observational data [244]. In 1971, ignoring that previous work, Hawking proposed the standard mechanism of formation of BHs in the radiation era, by direct collapse of a highly overdense region [245]. Detailed computations of its formation mechanism by Carr and Hawking in 1974 [246] showed that the initial mass of those collapsed objects would not substantially grow by accretion, contrary to the first estimation by Zeldovich and Novikov. Later, Carr in 1975 [247] computed the abundance, mass spectrum and conditions of formation of such objects. These facts made PBHs possible candidates to account for at least part of the DM [248, 113], which at those years, as discussed in Sec. 2.1.1, started to be outlined as one fundamental problem in cosmology.

DM (partly) composed by PBHs constitutes an exciting possibility, and have attracted a great attention in the scientific community. One of the reasons is the enormous number of probes which can constrain the parameter space of PBHs, as it will be detailed in Sec. 3.3. The variety of phenomenological effects produced by PBHs allows placing stringent bounds on their abundance, usually indicated by the energy fraction of DM as PBHs, defined as $f_{\rm PBH} = \Omega_{\rm PBH}/\Omega_{\rm DM}$, with $\Omega_{\rm PBH}$ and $\Omega_{\rm DM}$ the energy parameters respect to the critical density. Moreover, since PBHs are usually expected to be formed before nucleosynthesis, BBN constraints on the baryon abundance do not apply to them, and thus can be regarded as non-baryonic DM [242]. PBH DM could be considered as a MACHO candidate, and thus constraints applying over the MACHO abundance also affect PBHs, as shall be seen in Sec. 3.3. Moreover, PBHs present unique signatures which would differentiate them from other MACHO species, such as brown dwarfs or Jupiter-like planets. Moreover, due to their primordial nature, PBHs can be accommodated with the LSS data from the CMB and the BBN bounds on the abundance of baryons, contrary to standard astrophysical MACHOs, which are unable to explain such phenomena.

Shortly after the first detection of gravitational waves from a merger of $\sim 30\,M_\odot$ BHs by LIGO [41], the question whether these could be of primordial nature was raised [249]. It has been claimed that analyses of the posterior data from gravitational wave detectors LIGO and Virgo show that the detected mergers are compatible with the hypothesis of their components being of primordial nature, although there is no strong preference over stellar BHs [163, 242, 250].

Standard astrophysical BHs are formed from the collapse of massive stars. Stellar evolution models and general relativity predict that those BHs can only be formed with masses above some threshold around $\sim 3M_\odot$, the so-called Tolman–Oppenheimer–Volkoff limit [251, 252]. This threshold arises from the condition that the degeneracy pressure of neutrons in a neutron star cannot balance its gravitational force, collapsing to a BH. In contrast, since PBHs are not formed from stars but from the direct collapse of fluctuations, in principle they could be produced with any mass. Thus, a positive measurement of a BH with a mass lower than $\sim 3M_\odot$ would be a confirmation of the existence of primordial non-stellar BHs [163].

It is generally claimed that DM formed by PBHs has the advantage that it does not require a new kind of particle, such as WIMPs, axions or sterile neutrinos. Actually, their formation is already present in standard cosmologies, although extremely unlikely. However, their production usually requires some specific inflationary scenarios or physics Beyond the Standard Model (BSM) in order to obtain a large enough abundance. The

typically considered formation mechanism of PBHs arises from the direct collapse of primordial fluctuations, whose power is enhanced at small scales as a consequence of non-slow roll inflationary dynamics, as we shall further comment on below. There are, however, other scenarios which naturally predict a population of PBHs as a result of phase transitions in the early universe. A spontaneously broken symmetry produces a phase transitions, which may lead to the formation of different topological defects, depending on the specific broken symmetry and vacuums state. Eventually, those topological defects could collapse and form PBHs, as is the case of domain walls [253, 254] or cosmic string loops [255, 256], as well as colliding vacuum bubbles [257, 253, 258]. Hence, the existence of PBHs would provide valuable hints from the still unknown physics of the very early universe.

Depending on their mass, BHs can be classified in three different groups. Stellar BHs, those which are formed after the collapse of a star, with masses from 5 to tens of solar masses. On the other hand, it is well known the existence of Super Massive Black Holes (SMBH) in most of the nuclei of galaxies, with masses ranging from 10^5 to $10^{10}\,M_\odot$, and already existing at redshifts $z > 6$. For instance, in the case of the Milky Way, its central BH has a mass of about $\sim 4 \times 10^6\,M_\odot$ [259]. A third group lies between the former, and thus called Intermediate-Mass Black Holes (IMBH), whose masses range from $\sim 10^2$ to $10^5\,M_\odot$. Contrarily to the other BH classes, there are fewer observational evidences of such objects. Nonetheless, recent LIGO and Virgo observations have found a merger event of BHs with masses ~ 60 and $\sim 80 M_\odot$, producing a remnant BH of $\sim 150\,M_\odot$, in the so far unobserved range of masses of IMBHs [260].

One of the main motivations to consider PBHs is that they could constitute the seeds for the aforementioned SMBH [261]. Such massive objects cannot be produced by the collapse of the stellar interior after a supernova explosion, whose remnants BH usually have masses ranging from 5 to tens solar masses. Moreover, although BHs can grow by accreting surrounding matter, standard accretion mechanisms can hardly explain such a large increase in the mass from stellar BHs. Although their seeds could have formed at early times ($z \gtrsim 20$), the accretion rates would be suppressed in the relatively shallow potential wells of their host halos, as well as decreased by radiative feedback effects (see, e.g., Ref. [262] for more details). However, the existence of massive enough PBHs may act as seeds for the SMBHs, from which they could have grown by accretion.

It has also been argued that PBHs could naturally explain some of the small scale problems outlined in Sec. 2.1.2. PBH DM with merger rates compatible with the LIGO measurements would lead to the formation of a large population of ultra-faint dwarf galaxies without star formation, which

could naturally explain the missing satellite and too-big-to-fail problems [162, 163].

3.1.2 Formation and conditions of collapse

The mass of a BH collapsed in the early universe depends on its formation time. A BH can be characterized by an extremely dense amount of matter in a very compact region, lying within the known as Schwarzschild radius, $R_S = 2GM_{\rm PBH}/c^2 \sim 3M_{\rm PBH}/M_\odot$ km. Thus, the mean density inside that region can be estimated to be $\rho_S = M_{\rm PBH}/(4\pi R_S^3/3) \sim 10^{18}(M/M_\odot)^{-2}$ g cm^{-3}. On the other hand, the mean density of the universe in the radiation era goes as $\rho_c \sim 10^6(t/{\rm s})^{-2}$ g cm^{-3}. In order to have PBH formation, densities at least of the order of the mean BH density, $\rho_c \sim \rho_S$, are needed. Therefore, the mass of the resulting PBHs should be of the order of the horizon mass at that time, i.e., the mass within a region of the size of the Hubble horizon, $M_{\rm PBH} \sim M_{\rm H}$ [247], which is defined as

$$M_{\rm H} = \frac{4}{3}\bar{\rho}\left(\frac{c}{H}\right)^3 = \frac{c^3}{2GH} \sim 10^{15}\ {\rm g}\ \left(\frac{t}{10^{-23}{\rm s}}\right). \tag{3.1}$$

Thus, PBHs with masses of $\sim M_\odot \simeq 2\times 10^{33}$ g would have been formed at around the QCD phase transition, at $t \sim 10^{-6}$ s, while those born at the BBN epoch, $t \sim 1$ s, would be as massive as $10^4 M_\odot$. Since the PBH mass is roughly given by the horizon one, it means that fluctuations entering the horizon can collapse into PBHs. A detailed calculation shows that $M_{\rm PBH} = \gamma M_{\rm H}$, where the proportionality factor γ depends on the details of gravitational collapse, and gets values lower than 1. Early estimates showed that it can approximated to $\gamma \simeq c_s^3 \simeq 0.2$, with $c_s = \frac{1}{3}$ the sound speed in the radiation epoch [247, 263].

We can gain insight into the process and criterion of formation of PBHs by considering a simple picture of collapse in General Relativity [240]. To simplify the problem, we can assume a spherical overdense region embedded in the expanding FLRW background. Hence, we can adopt a metric of the form

$$ds^2 = -dt^2 + a(t)^2\left(\frac{dr^2}{1-K(r)r^2} + r^2 d\Omega^2\right), \tag{3.2}$$

with $K(r)$ a positive curvature smoothly varying with the radial coordinate. This is the form of a locally closed universe, with a curvature which approaches asymptotically to $K(r) \to 0$ at large distances. In that limit, the flat FLRW limit is recovered. Since this overdense region should be much larger than the Hubble horizon, a leading order gradient expansion can be applied. Thus, neglecting derivatives of $K(r)$ in the 3-curvature of

the hypersurface with constant time, one can obtain a generalized Friedman equation from the time-time component of the Einstein equations (or Hamiltonian constraint),

$$H^2 + \frac{K(r)}{a^2} = \frac{8\pi G}{3}\rho(t,r) \tag{3.3}$$

with $H = \dot{a}/a$. Therefore, the overdensity can be written in terms of the curvature as

$$\delta = \frac{\rho - \bar{\rho}}{\bar{\rho}} = \frac{K(r)}{a^2 H^2} \tag{3.4}$$

From perturbation analysis, we know that the Jeans scale $k_J \simeq aH/c_s$, with c_s the sound speed, sets the critical length for collapse, as seen in Sec. 2.2.1. Only perturbations at scales larger than the Jeans length $2\pi/k_J$ (*i.e.*, with $k < k_J$) may be able to overcome pressure gradients and collapse. Thus, when the collapse leads to non-linear regime, $\delta \sim 1$,

$$\delta \sim 1 \Rightarrow \frac{K}{a^2 H^2} = \frac{K}{c_s^2 k_J^2} \sim 1, \tag{3.5}$$

and hence we should identify $K \sim c_s^2 k_J^2$ at the collapse regime.[1] On the other hand, as stated before, the collapse is expected to happen when perturbations enters the horizon. For a fluctuation of wavenumber k, it occurs at a time t_k, implicitly defined from $k = H(t_k)a(t_k)$. Thus, we can write the overdensity when the perturbation enters the horizon as

$$\delta(t_k) \sim \frac{K}{a(t_k)^2 H(t_k)^2} \sim c_s^2 \frac{k_J^2}{k^2}. \tag{3.6}$$

The condition of collapse $k < k_J$ enforces that $\delta(t_k) > c_s^2$. This implies that only overdensities above a certain threshold can lead to form a PBH. This minimum required overdensity is given by the speed of sound of the medium, which in the radiation dominated era, it is $c_s^2 = 1/3$. Although this is a very rough estimate, more detailed computations only slightly change the value of the threshold, which lies between $\delta_c \sim 0.3$ and 0.5 [264, 265]. Figure 3.1 shows a sketch of the process of PBH formation.

Since PBHs are formed when the fluctuation crosses the horizon, the mass of the PBH is mostly determined by the time of formation t_f given by

[1] To gain insight into this fact, one can compare it to the situation in perturbation theory, where instead of the curvature K, one has the laplacian of the gravitational potential, which in Fourier space takes the form $k^2\phi$. This is related to the density fluctuation through the Poisson equation, $k^2\phi = -4\pi G\bar{\rho}a^2\delta = -(c_s k_J)^2\delta$. Thus, when $\delta \simeq 1$, $k^2\phi \simeq (c_s k_J)^2$. In relativistic perturbation theory, the Newtonian potential is related to the curvature perturbation [47].

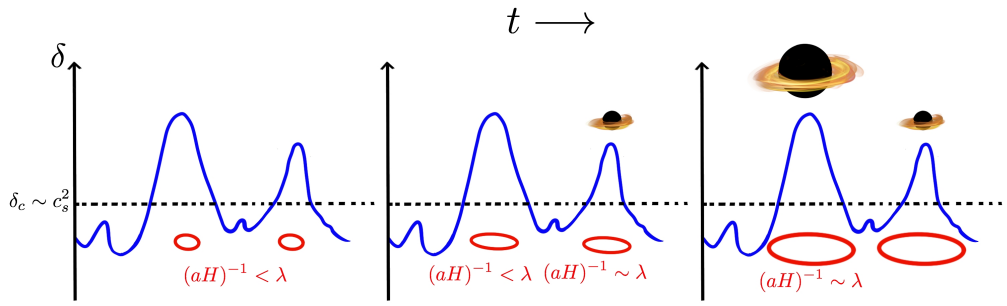

Figure 3.1: Sketch of the formation of PBHs from overdensities for three different successive moments. When fluctuations larger than a critical threshold $\delta_c \sim c_s^2$ enter the horizon, i.e., their comoving wavelength $\lambda = 2\pi/k$ (which characterizes the size of the perturbation) is of the order of the Hubble horizon $(aH)^{-1}$, the overdense region collapses and a PBH is produced. As can be seen in Eqs. (3.1) and (3.7), longer modes (large λ, low k) enter the horizon later and lead to more massive PBHs.

Eq. (3.1), and equivalently, can be related to the wavelength of the perturbation. When the mode of wavenumber k crosses the horizon, the condition $a(t_f)\, H(t_f) = k$ holds. Since the mass of the PBH is proportional to the horizon mass at the moment of formation, $M_{\rm PBH} \propto \gamma H^{-1}$. In the radiation dominated era, $H \propto a^{-2}$, and thus, $H_f \propto k^2$, obtaining the relation between the mass and the wavenumber as [240],

$$M_{\rm PBH} \simeq 30\, M_\odot \left(\frac{\gamma}{0.2}\right) \left(\frac{2.9 \times 10^5 {\rm Mpc}}{k}\right)^2 . \tag{3.7}$$

From the equation above, one can see that probing a given scale k could constrain PBH population of its corresponding mass. Furthermore, an enhancement in the power spectrum around that scale would result in a larger number of PBHs of such masses than in the standard scenario. This is the key for some inflation models with a potential which induces larger fluctuations at a range of very small scales. Different inflationary models may lead to completely different PBH scenarios. For instance, inflection points in a plateau of a single inflaton potential can lead to broad peaks in the power spectrum, which imply extended PBH mass functions [266, 267]. Other models, such as hybrid inflation, where two scalar fields are coupled, can also lead to broader peaks [268]. Furthermore, models such as the chaotic new inflation may produce two inflationary periods, giving raise to relatively narrow peaks [269, 270]. We comment more on the PBH mass function in Sec. 3.1.3. See, e.g., Ref. [240] for more information regarding inflation models.

In this thesis, we only consider PBHs formed during the radiation era. Those produced before inflation ends would have been diluted due to their

negligible density during the inflationary accelerated expansion. PBHs formed at the matter era, or in an early matter domination era previous to the radiation era, have also been considered in literature, and may have different imprints, since the conditions of collapse are less restrictive, allowing the formation from smaller inhomogeneities (see, e.g., [241]).

3.1.3 Abundance and mass function of PBHs

It is possible to estimate the initial abundance of PBHs at the moment of formation, taking into account all overdensities above the threshold of collapse $\delta_{\rm c,PBH} \simeq 1/3$. Assuming a Gaussian probability distribution $P(\delta)$ for the overdensities with variance $\sigma^2(M)$ at mass scale M (as defined in Eq. (2.19)), the initial abundance, defined as $\beta(M_{\rm H}) = \rho_{\rm PBH}(t_f)/\rho_{\rm tot}(t_f)$, reads [240, 241]

$$\beta(M_{\rm PBH}) = 2\gamma \int_{\delta_{\rm c,PBH}}^{\infty} P(\delta) d\delta = \gamma \, \mathrm{erfc}\left(\frac{\delta_{\rm c,PBH}}{\sqrt{2}\sigma(M_{\rm PBH})}\right) \tag{3.8}$$

$$\simeq \gamma \sqrt{\frac{2}{\pi}} \frac{\sigma(M_{\rm PBH})}{\delta_{\rm c,PBH}} \exp\left(-\frac{\delta^2_{\rm c,PBH}}{2\sigma^2(M_{\rm PBH})}\right), \tag{3.9}$$

where in the last equality, $\sigma(M_{\rm H}) \ll \delta_c$ has been assumed. The factor of 2 in the first equality of the above equation accounts for a fudge factor, as done in the original Press-Schechter halo mass function prescription [96]. For the standard cosmological scenario with an initial scale invariant power spectrum, at CMB scales, the amplitude of the fluctuations is around $\sigma(M_{\rm PBH}) \sim 10^{-5}$, leading to $\beta \sim 10^{-5} \exp(-10^{10})$, which is completely negligible [263]. Therefore, in order to have a relevant population of PBHs, larger values of the initial power spectrum are needed. On the other hand, the assumption of a Gaussian distribution may not be consistent with enhanced fluctuations and the presence of PBHs, and deviations from that could be unavoidable [271, 272] (except for specific inflation models presenting an inflection point [273]). Non-gaussianities could have a great impact on the initial fraction and lead to a larger population, as well as leaving further detectable signatures in gravitational waves [274].

Nonetheless, although the initial fraction β is a very small quantity, since matter and radiation scale differently with redshift, the PBH contribution can become relevant at current times. To relate that value to the current density parameters of PBHs and radiation, $\Omega_{\rm PBH}$ and Ω_γ, respectively, one has to take into account that, since PBHs behave as standard matter (dust), they scale as $\rho_{\rm PBH} \propto (1+z)^3$, while radiation goes as $\rho_\gamma \propto (1+z)^4$. Thus, relating the formation redshift with its corresponding PBH mass, we get

[243],

$$\Omega_{\rm PBH}(M) = \beta(M)(1+z_f)\Omega_\gamma \simeq \gamma^{1/2}\left(\frac{\beta(M)}{1.15\times10^{-8}}\right)\left(\frac{M}{M_\odot}\right)^{-1/2}. \quad (3.10)$$

Hence, with initial fractions as low as $\beta \sim 10^{-8}$ of solar mass BHs, the fraction of energy in PBHs would be order unity.

In principle, depending on the specific mechanism of formation, a population of PBHs with different masses could be generated. It is thus relevant to consider the mass distribution function. As commented above, the specific shape of the enhancement in the fluctuations determines the mass distribution function. Sharp peaks in the power spectrum imply approximately monochromatic PBH mass functions, while broad peaks lead to extended mass distribution functions. For simplicity, it is usually assumed in literature, as done along this thesis, that all PBHs share the same value for their masses, having therefore what is called a *monochromatic* distribution. In this case, the distribution is only determined by the fraction $f_{\rm PBH}$ and its mass $M_{\rm PBH}$, easing the computations. However, this premise may not be valid, and actually many inflationary models able to produce PBHs predict, instead, *extended* mass functions, which can span over a large range of masses. Besides the central mass and total fraction of PBHs as DM, these distributions require more parameters, such as the variance, which determines the broadness. Some common parameterizations, such as lognormal or power law functions, have been employed to effectively model generic extended mass functions, translating the usual constraints on monochromatic PBHs to these broader distributions. Besides having more freedom due to a large parameter set to fit, the constraints on extended mass functions can also be even more stringent than in the single mass case [275, 276]. Nonetheless, even with constraints forbidding $f_{\rm PBH} \sim 1$ in the monochromatic case, there are choices of the mass function which allow having all DM formed by PBHs [277].

To gain insight about the relation between the fluctuations and the mass function, consider a very sharp feature around a scale k_* in the matter power spectrum, modeled as a delta function. We then can write that contribution as $\Delta^2(k) = \Delta_*^2\, k\, \delta_D(k-k_*)$, with Δ_*^2 the amplitude. From Eq. (2.19), it is straightforward to obtain the variance as $\sigma^2(M) = \Delta_*^2 \tilde{W}^2(k_*R)$, with $M \propto R^3$, and $\tilde{W}^2(k_*R)$ the square of the Fourier transform of the window function. Regardless of the specific choice of this window function, the variance, and therefore the abundance β, present their maximum value when $R \sim k_*^{-1}$ or lower. Following the Press-Schechter prescription, one can write the mass function $df_{\rm PBH}(M)/d\ln M$ relating it to the abundance

from Eq. (3.10), as [240]

$$\frac{df_{\rm PBH}(M)}{d\ln M} d\ln M \simeq \frac{\delta^2_{\rm c,PBH}}{\sigma^2(M)} f_{\rm PBH}(M) \left|\frac{d\ln\sigma^2}{d\ln M}\right| d\ln M \ , \tag{3.11}$$

where $f_{\rm PBH}(M) = \Omega_{\rm PBH}(M)/\Omega_{\rm DM} \propto \beta(M)$. The derivative $\frac{d\ln\sigma^2}{d\ln M}$ depends on the window function but peaks at $R \sim k_*^{-1}$ (actually leading to a delta function $\delta_D(R - k_*^{-1})$ if the sharp-k filter is chosen), and therefore on the mass function too.

3.1.4 BH evaporation

In 1974, Hawking realized that, due to quantum effects in curved spacetimes, BHs may emit particles at their event horizon [278] (although Zeldovich had already proposed that rotating BHs would radiate due to the uncertainty principle [279]). The emitted radiation would have a thermal black body spectrum, with a temperature given by [278, 243]

$$T_{\rm BH} = \frac{\hbar c^3}{8\pi k_B G M} \sim 10^{-7}\ {\rm K}\ \frac{M_\odot}{M}, \tag{3.12}$$

which is known as *Hawking temperature*. Since a BH is emitting particles, it would slowly lose mass until completely evaporate. The rate of energy loss can be estimated as the product of the area of emission A times the energy density [280], as $dM/dt = -A\ \sigma_{\rm SB} T^4_{\rm BH}$, with $\sigma_{\rm SB} = \pi^2 k_B^4/(60\hbar^3 c^4)$ the Stefan-Boltzmann constant. Given that the area is that corresponding to the event horizon surface, i.e., at the Schwarzschild radius $R_S = 2GM/c^2$, it reads $A = 4\pi R_S^2 = 16\pi G^2 M^2/c^4$. Making use of the Hawking temperature from Eq. (3.12), one finds that the rate of mass loss is given by

$$\frac{dM}{dt} = -\frac{1}{15360\pi}\frac{\hbar c^4}{G^2 M^2}, \tag{3.13}$$

which can be easily integrated to obtain the lifetime of a PBH of initial mass M, which reads

$$\tau(M) = 5120\pi \frac{G^2 M^3}{\hbar c^4} \sim 10^{64}\ {\rm yr}\ \left(\frac{M}{M_\odot}\right)^3. \tag{3.14}$$

The above result imply that PBHs with smaller masses, which have higher Hawking temperature, evaporate earlier. Those with masses of $\sim 10^{15}$ g or below would have already evaporated by now, having lifetimes shorter than the age of the universe, and therefore cannot be part of the current DM. Detailed computations have to take into account the different emission rates for each particle species, as was firstly done for massless particles by Page in 1976 [281]. Currently, there are specific codes devoted to the prediction of the emitted spectra, such as `BlackHawk` [282].

3.1.5 Clustering and spin

It has been demonstrated that, if the fluctuations are originally gaussian distributed and around a relatively narrow peak, PBHs are not expected to be originated in clusters [283, 284]. It means that, initially, PBHs are Poisson (randomly) distributed on small scales, rather than presenting spatial correlations. However, either primordial non-gaussianities or a broad peak in the power spectrum could lead to a significant initial clustering [285, 286] (although it has also been argued that broad spectra would not produce appreciable clustering, see Ref. [287]). Anyway, PBHs could become bounded as the universe evolves. A proper determination of their clustering at later times is of great importance, for instance, in order to estimate their merger rates [284].

Since PBHs would be formed from the collapse of high density peaks relatively spherically symmetric, their torques and angular momentum are expected to be small [288, 289]. It is usually quantified with the dimensionless spin parameter, $\mathcal{S} = S/(GM_{\rm PBH}^2)$, where S is the spin. Estimations of $\mathcal{S}$ for PBHs show that it is a small quantity, equal or lower than 0.01 [290]. Contrary to this, astrophysical BHs are expected to have substantially larger spin parameters since the angular momentum must be conserved during the collapse of its star of origin, which are often rotating. Hence, the spin can serve as a good proxy to distinguish the nature of a population of BHs. The measurement of low spin parameters could suppose a hint for the detection of BHs of primordial formation. The latest Bayesian analysis of LIGO/Virgo mergers suggest that low values for the spin parameter are strongly preferred by data, regardless of the priors considered [250].

3.2 Signatures of PBHs

In this section, we review the most relevant effects predicted from PBHs which could leave a strong signature in the evolution of the IGM and formation of structures. These are the accretion process, which would lead to an injection of energy into the medium, and the shot-noise contribution to the power spectrum, responsible of enhancing small scale fluctuations.

3.2.1 Accretion onto PBHs

Accretion of matter onto BHs is one of the most relevant effects which can strongly impact the surrounding medium, and thus leave significant observable signatures. The process of accretion was first studied by Hoyle

and Lyttleton as a ballistic limit, neglecting the hydrodynamical, thermodynamical and pressure effects [291, 292, 293], and later by Bondi and Hoyle [294]. In these pioneer works, the accretion rate was found to depend on the relative velocity of the central point mass and the medium. The first to properly address the problem of spherical accretion, including the pressure effects, was Bondi in 1952 [295]. In the context of PBHs accreting matter in the early universe, it was shown that the expansion rate and Compton interactions played an important role [296]. The accretion process in PBHs would result in the injection of energy into the surrounding medium, which could affect its properties. Early analyses of CMB data, sensitive to changes in the IGM properties, provided stringent constraints on the PBH abundance [297]. However, posterior detailed computations showed that bounds are actually much weaker [298, 299, 300] (see Sec. 3.3 for more information regarding the observational constraints).

3.2.1.1 Spherical accretion

The physics of accretion is highly complex, but one can attempt an approximate simplified approach considering the non-relativistic limit and spherical symmetry, following the seminal work by Bondi [295, 298]. In this framework, the BH is treated as a point mass surrounded by matter, embedded in a medium which tends to constant density and pressure, ρ_∞ and P_∞, far enough from the BH. At the relevant scales, one can address the problem within Newtonian fluid mechanics. The equations governing the evolution of the density ρ and velocity $\mathbf{v}$ of the matter surrounding the PBH are the continuity and Euler equations, respectively,

$$\frac{\partial \rho}{\partial t} + \nabla \cdot (\rho \mathbf{v}) = 0, \tag{3.15}$$

$$\frac{\partial \mathbf{v}}{\partial t} + \mathbf{v} \cdot \nabla \mathbf{v} = -\frac{1}{\rho} \nabla P - \frac{G M_{\rm PBH}}{r^2} \hat{\mathbf{r}}, \tag{3.16}$$

with P the pressure, and the second term of the latter equation is the Newtonian force of gravity sourced by the central PBH, at a distance r and pointing at the radial unity vector $\hat{\mathbf{r}}$. The pressure can be related to the gas temperature T_K as $P = \rho T / m_p$ (neglecting the helium contribution for the sake of simplicity), while its gradient can be related to the speed of sound c_s as $\nabla P = c_s^2 \nabla \rho$. The simplest case to treat is considering spherical accretion, where the symmetry assumption greatly simplifies the picture, which allows extracting actual qualitative conclusions. We also assume stationary solutions, where the time derivatives can be neglected. The continuity equation can now be integrated, obtaining

$$4\pi r^2 \, \rho \, |v| = \dot{M}_{\rm PBH} = \text{constant} \ , \tag{3.17}$$

while the Euler equation reads

$$v\,\frac{dv}{dr} = -\frac{1}{\rho}\,\frac{dP}{dr} - \frac{GM_{\rm PBH}}{r^2}\ , \tag{3.18}$$

Assuming a polytropic equation of state, $P = P_\infty(\rho/\rho_\infty)^\gamma$, it is straightforward to integrate Eq. (3.18), obtaining [301]

$$\frac{1}{2}v^2 - \frac{GM}{r} + \frac{c_{s,\infty}^2}{\gamma-1}\left[\left(\frac{\rho}{\rho_\infty}\right)^{\gamma-1} - 1\right] = 0, \tag{3.19}$$

where the speed of sound at infinity is $c_{s,\infty}^2 = \gamma P_\infty/\rho_\infty$. By scrutinizing the above equations, one finds the relevant scales to be the so-called Bondi velocity, Bondi radius, and Bondi time, defined by

$$v_{\rm B} = c_{s,\infty}, \quad r_{\rm B} = \frac{GM_{\rm PBH}}{v_{\rm B}^2}, \quad t_B = \frac{r_B}{v_B} = \frac{GM_{\rm PBH}}{v_{\rm B}^3}. \tag{3.20}$$

These scales have a direct interpretation: at distances around $\sim r_B$, the accretion process starts to become important. Thus, at $\sim r_B$, the velocity reaches $v \sim c_{s,\infty}$, when the density is still close to the boundary value. It is customary to define the dimensionless accretion rate λ, as

$$\lambda = \frac{\dot{M}_{\rm PBH}}{4\pi r_B^2 \rho_\infty v_B}, \tag{3.21}$$

which in the limit commented above, should take a value ~ 1. Its actual value depends on the equation of state and other non-gravitational forces such as pressure and viscosity, but in these cases of interest, it is always of order unity.

The asymptotic values at $r \to \infty$ are $\rho \to \rho_\infty$, and by Eq. (3.17), the velocity at large radius decays as $|v| \simeq \dot{M}_{\rm PBH}/(4\pi r^2\rho_\infty) = \lambda v_B (r_B/r)^2$. The radial profiles vary depending on the equation of state considered. For instance, when the temperature evolves adiabatically, one has $T \propto \rho^{2/3}$ (see, e.g., Sec. 5.2.1), and thus $\gamma = 5/3$. Examining Eqs. (3.17) and (3.19), it can be found that the maximum accretion rate allowed is given by $\lambda_{ad} = 1/4(3/5)^{3/2} \simeq 0.12$ [298]. At low radii, the radial profiles evolve as $\rho \simeq \lambda\rho_\infty/\sqrt{2}(r_B/r)^{3/2}$, $v \simeq v_B\sqrt{2r_B/r}$ and $T \simeq T_\infty\lambda^{2/3}/2^{1/3}(r_B/r)$, where the temperature at the boundaries is related to the speed of sound as $c_{s,\infty}^2 = \gamma T_\infty/m_p$. Note that the velocity does not depend on the accretion rate λ.

The other case of interest at high redshift is when the gas temperature is coupled to the CMB one, T_γ, by efficient Compton scattering. In this case, the gas can be regarded as isothermal (it has the same temperature,

regardless of the density), $T = T_\gamma$ and then $\gamma = 1$. In analogy with the previous case, if a solution exists, the accretion rate must be lower than a maximum value given by $\lambda_{iso} = e^{3/2}/3 \simeq 1.12$. From Eqs. (3.17) and (3.19), can be easily shown that the velocity and density radial profiles are the same as in the adiabatic case,[2] while the temperature also decays as r^{-1}, but with a different prefactor [298].

In the physical relevant cases at high redshifts, the gas temperature would be between the CMB and the adiabatic evolution cases, and thus one would expect to have accretion rates between λ_{iso} and λ_{ad}. As a reference value, in the adiabatic cooling regime, $T_K \propto (1+z)^2$ (see Sec. 5.2.1), which leads to a Bondi radius of $r_B \sim 3 \times 10^{-5}\,(M_{\rm PBH}/M_\odot)(30/(1+z))^2$ kpc. It is worth noting that this distance is much larger than the scales where general relativistic effects are relevant, which can be estimated as the Schwarzschild radius of the BH, defined as $r_S = 2GM_{\rm PBH}/c^2 \simeq 3\,(M_{\rm PBH}/M_\odot)$ km, confirming the validity of the Newtonian approach.

As can be seen, the spherical symmetric case can be treated by analytic means given the equation of state, but its simplicity limits its range of validity. Firstly, it does not take into account the velocity of the BH relative to the medium, v_{rel}. The seminal Bondi's paper [295] already suggests a way to include that effect and match with the Hoyle-Lyttleton and Bondi-Hoyle results, replacing the Bondi velocity by an effective quadratic sum of velocities, $c^2_{s,\infty} \to c^2_{s,\infty} + v^2_{rel}$. One can thus write the accretion rate as

$$\dot{M}_{\rm PBH} = 4\pi\lambda\rho_\infty \frac{(GM_{\rm PBH})^2}{(c^2_{s,\infty} + v^2_{rel})^{3/2}}. \tag{3.22}$$

In the early universe, v_{rel} can be estimated as the baryon-DM relative velocity computed in linear theory. Its root-mean-square value is approximately constant before Recombination, dropping linearly with $1+z$ at later times. Hence, it can be written as [298]

$$\sqrt{\langle v_L^2 \rangle} \simeq \begin{cases} 30 \text{ km/s} & , \quad 1+z \gtrsim 10^3 \\ 30 \text{ km/s} \left(\frac{1+z}{10^3}\right) & , \quad 1+z \lesssim 10^3, \end{cases} \tag{3.23}$$

where the amplitude 30 km/s corresponds to the variance at the epoch of the CMB decoupling. On the other hand, real BHs spin, and thus form an accreting disk, being the spherical symmetric case not applicable. Even though PBH spins are expected to be small, as discussed in Sec. 3.1.5, the accreted matter may possess an angular momentum high enough to prevent the free-fall straight onto the BH and rotate around it. During the falling,

[2] Actually, this is a coincidence, other equations of state would lead to different radial profiles.

angular momentum must be conserved, which leads to the formation of an accretion disk. More specifically, an accretion disk would form if the angular momentum is large enough to keep matter orbiting at Keplerian orbits at distances much larger than the innermost stable orbits, which are roughly given by the Schwarzschild radius [302]. Applying this criterion, it has been argued that PBHs formed in the early universe would form an accretion disk if the condition $f_{\rm PBH} M_{\rm PBH}/M_\odot \ll ((1+z)/730)^3$ is fulfilled [300], which is satisfied for $M_{\rm PBH} \gtrsim M_\odot$ and a large enough abundance at the epoch of the CMB decoupling or at later times. However, some of the results outlined above are still valid as long as that the dimensionless accretion rate is properly modified. Accounting for viscosity effects and the matter outflows through jets, the typical values of order unity for λ in spherical accretion are suppressed by roughly two orders of magnitude [300].

3.2.1.2 Accretion luminosity

The relevance of the accretion mechanism resides in the fact that part of the energy carried by the inflowing matter is released later to the surrounding medium. The matter falling onto the BH is greatly accelerated, producing radiative emission of high energy photons by processes such as bremsstrahlung. The luminosity of the accreting BH is proportional to its accretion rate, and can be written as [300]

$$L_{\rm acc} = \epsilon(\dot{M}_{\rm PBH})\, \dot{M}_{\rm PBH} \ , \tag{3.24}$$

where $\epsilon(\dot{M}_{\rm PBH})$ denotes the radiative efficiency of the accretion process. This is in general a complicated function of the accretion rate $\dot{M}_{\rm PBH}$, depending on the details and geometry of the accretion mechanism. Given the luminosity, the rate of energy injected into the medium per unit volume is given by [298, 300]

$$\left(\frac{dE}{dV\,dt}\right)_{\rm inj} = L_{\rm acc}\, n_{\rm PBH} = L_{\rm acc}\, \frac{f_{\rm PBH}\, \rho_{\rm DM}}{M_{\rm PBH}} \ , \tag{3.25}$$

As a benchmark value, it is usually considered the *Eddington limit*, which is the resulting luminosity from balancing the gravitational force by pressure radiation (e.g., [30]),

$$L_{\rm Edd} = \frac{4\pi G m_p c}{\sigma_T} = 1.26 \times 10^{38} \left(\frac{M_{\rm PBH}}{M_\odot}\right) \ {\rm erg/s}. \tag{3.26}$$

The energetic efficiency of the accretion process strongly depends upon the geometry, viscosity and other hydrodynamical considerations. If the accretion disk is optically thin, most of the energy released through viscous

dissipation is radiated away, and the luminosities obtained can be close to $L_{\rm Edd}$. This was the basis of the thin disk model proposed by Shakura and Sunyaev in 1972 [303], which is able to explain the extreme brightness of many far AGNs. However, nearby BHs appear to radiate in a much less efficient way [304]. Other mechanisms have been proposed to explain such behavior, such as the Advective-Dominated-Accretion-Flow (ADAF), firstly proposed independently by Refs. [305, 306] and rediscovered years later by Refs. [307, 308, 309] (see, e.g., Ref. [310] for a review). In this scenario, the dynamics is ruled by advective currents, forming a hot thick disk or torus. Most of the emitted energy is deposited in the same accretion disk, heating it up. Thus, only a small portion of energy is injected into the surrounding medium, being the radiative process inefficient. In the ADAF scenario, the efficiency function can be fitted by a broken power-law formula of the form

$$\epsilon = \epsilon_0 \left(\frac{100\, \dot{M}_{\rm PBH}}{\dot{M}_{\rm Edd}} \right)^a , \tag{3.27}$$

where $\dot{M}_{\rm Edd} = 10\, L_{\rm Edd}$, and the slopes and amplitudes ϵ_0 and a depend on the mass range and the specific modeling of the viscosity effects [311]. Note that some previous studies in the literature assumed the case $a = 1$ [297, 298], while for such low accretion rates, it has been shown that $a \lesssim 0.6$ [311]. At a given range of masses, the final luminosity would be thus proportional to some power of the mass accretion rate. From Eqs. (3.24) and (3.27), one finds $L_{\rm acc} \propto \dot{M}_{\rm PBH}^{a+1}$, which, from Eq. (3.22), is also proportional to the inverse velocity factor $\left(c_{s,\infty}^2 + v_{\rm rel}^2\right)^{-3(a+1)/2}$. Since the DM-baryon relative velocity components are random variables gaussian distributed (and thus its modulus follows a Maxwellian distribution), one must average the total luminosity. This allows to introduce an effective velocity v_{eff}, such that $L_{\rm acc} \propto v_{eff}^{-3\,(1+a)/2}$, defined as [6, 297]

$$v_{eff} \equiv \left\langle \frac{1}{\left(c_{s,\infty}^2 + v_{rel}^2\right)^{3\,(1+a)/2}} \right\rangle^{-\frac{1}{3\,(1+a)}} \tag{3.28}$$

$$= \left[\int \frac{d^3 v_{rel}}{(2\pi \langle v_L^2 \rangle)^{3/2}} \frac{\exp\left(-\frac{v_{rel}^2}{2\langle v_L^2 \rangle}\right)}{\left(c_{s,\infty}^2 + v_{rel}^2\right)^{3\,(1+a)/2}} \right]^{-\frac{1}{3\,(1+a)}} \tag{3.29}$$

$$= c_{s,\infty} \left[\left(\frac{3}{2}\right)^{\frac{3}{2}} U\left(\frac{3}{2}, 1 - \frac{3\,a}{2}, \frac{3}{2}\mathcal{M}^{-2}\right) \mathcal{M}^{-3} \right]^{-\frac{1}{3\,(1+a)}} , \tag{3.30}$$

with $\mathcal{M} \equiv \frac{\sqrt{\langle v_L^2 \rangle}}{c_{s,\infty}}$ and $U(x;y;z)$ the confluent hypergeometric function of second kind, also known as Tricomi's function. Two limiting cases can be

obtained up to first order, depending on the ratio between velocities:

$$v_{\rm eff} \simeq \begin{cases} c_{s,\infty}\, \mathcal{M}^{1/(1+a)} \left[3\sqrt{\frac{3}{2\pi}}\, B\left(\frac{3a}{2},\frac{3}{2}\right)\right]^{-\frac{1}{3(1+a)}} & , \quad \mathcal{M} \gg 1 \\ c_{s,\infty} & , \quad \mathcal{M} \ll 1 \ , \end{cases} \tag{3.31}$$

with $B(x,y)$ the beta function. The limit $\mathcal{M} \ll 1$ holds when the gas is very hot and thus the relative velocity with respect to the environment is negligible, which is fulfilled at early times $z > 10^4$, but also after the Cosmic Dawn, when the IGM is heated up by X-ray radiation from X-ray binaries and other sources (as shall be studied in Sec. 5.2.1). The opposite limit, $\mathcal{M} \gg 1$, depends upon the specific slope a. In the usual oversimplified scenario considered in the literature, $\epsilon \propto \dot{M}_{\rm PBH}$, and thus $a = 1$, which leads to $v_{\rm eff} \sim \sqrt{c_{s,\infty} \left\langle v_L^2 \right\rangle^{1/2}}$ [297, 298].

Finally, the energy emitted in the accretion processes is deposited through different channels into the medium. Rather than the rate of energy injected, the relevant quantity is thus the energy deposition rate for each channel, which reads

$$\left(\frac{dE_c}{dV\,dt}\right)_{\rm dep} = f_c(z) \left(\frac{dE}{dV\,dt}\right)_{\rm inj} \ , \tag{3.32}$$

where the subscript c denotes the channel in which energy is deposited, namely: ionization of neutral Hydrogen or Helium, heating of the medium, or atomic excitations (where the Lyα transitions are the most relevant). The energy deposition factors $f_c(z)$ quantify the fraction of energy which goes to the different channels, and are obtained from

$$f_c(z) = \frac{H(z) \int \frac{d\ln(1+z')}{H(z')} \int d\omega\, T_c(z,z',\omega)\, L_{\rm acc}(z',\omega)}{\int d\omega\, L_{\rm acc}(z,\omega)} \ , \tag{3.33}$$

where the $T_c(z,z',\omega)$ are the transfer functions computed in Ref. [312]. The above formula integrates over the energy spectrum of the emitted luminosity, which in ADAF models can be simply parameterized as [310]

$$L_{\rm acc}(\omega) \propto \Theta(\omega - \omega_{\rm min})\, \omega^{\beta}\, \exp(-\omega/\omega_s) \ , \tag{3.34}$$

where $\omega_{\rm min} \equiv (10\, M_\odot/M_{\rm PBH})^{1/2}$ eV, $\omega_s = 200$ keV (or more generally, $\omega_s \sim \mathcal{O}(m_e)$), and β ranging in the interval $\beta \in [-1.3, -0.7]$, with the fiducial value $\beta = -1$.

3.2.2 Shot noise

As commented above, a large enough population of PBHs would require an enhancement of the fluctuations at very small scales, produced by some

inflationary mechanism, which is highly model dependent. However, the presence of PBHs can also modify the matter power spectrum by other reasons at larger scales. By the point-source nature of PBHs, one may expect a shot noise contribution to the power spectrum constant in wavenumber. This is a general feature of a discrete distribution of points with negligible spatial extension, as PBHs can be approximated. In order to understand how it arises, consider the number density of a discrete distribution of N points, given by

$$n(\mathbf{x}) = \sum_i^N \delta_D(\mathbf{x} - \mathbf{x}_i) \ . \tag{3.35}$$

Writing the mean density in a volume V as $\bar{n} = N/V$ and defining the fluctuation as $\delta(\mathbf{x}) = (n(\mathbf{x}) - \bar{n})/\bar{n}$, its Fourier transform reads

$$\tilde{\delta}(\mathbf{k}) = \int d^3x \ \delta(\mathbf{x}) \ e^{i\mathbf{k}\cdot\mathbf{x}} = \frac{1}{\bar{n}} \sum_i^N e^{i\mathbf{k}\cdot\mathbf{x}_i} - (2\pi)^3 \delta_D(\mathbf{k}). \tag{3.36}$$

Thus, for $\mathbf{k} \neq \mathbf{0}$, and writing the ensemble average $\langle ... \rangle$ as a spatial average (as implicitly done in Sec. 2.2.1), one has

$$\langle \tilde{\delta}(\mathbf{k}) \tilde{\delta}(\mathbf{k}') \rangle = \int \frac{d^3x_i}{V} \frac{1}{\bar{n}^2} \sum_i^N e^{i(\mathbf{k}+\mathbf{k}')\cdot\mathbf{x}_i} + (i \neq j \ term) \tag{3.37}$$

$$= (2\pi)^3 \delta_D^{(3)}(\mathbf{k} + \mathbf{k}') \frac{1}{\bar{n}} + (i \neq j \ term) \ . \tag{3.38}$$

While the second term gives the *proper* power spectrum for non-zero spatial separation, from the first one, a contribution arises for $\mathbf{x}_i = \mathbf{x}_j$, i.e., at zero spatial separation. Performing the integral of the first term, one gets the delta function of the second line which ensures translational invariance. Comparing to Eq. (2.10), the shot noise power spectrum therefore reads

$$P_{\rm SN}(k) = \frac{1}{\bar{n}}, \tag{3.39}$$

which is constant over wavenumbers (and thus a white noise), and inversely proportional to the number density of discrete sources. This power spectrum can be related to its real-space counterpart, the correlation function, which is a delta function in position space centered at zero distances.

On the other hand, it has been argued that these PBHs fluctuations give rise to isocurvature modes [161, 313, 314]. In general, the entropy fluctuation is defined as

$$S = \frac{\bar{\rho}_{\rm DM}\delta_{\rm DM}}{\bar{\rho}_{\rm DM} + \bar{P}_{\rm DM}} - \frac{\bar{\rho}_{rad}\delta_{rad}}{\bar{\rho}_{rad} + \bar{P}_{rad}} = \delta_{\rm DM} - \frac{3}{4}\delta_{rad} \, . \tag{3.40}$$

Isentropic (also called adiabatic) perturbations are those which $S = 0$ initially, and can be regarded as fluctuations in the density field, leaving unperturbed the equation of state of the multi-component fluid. Standard CDM composed by entirely particles behave as isentropic modes, and in the case of no PBH, then $\delta_{\rm DM} = \delta_{\rm pDM} = \frac{3}{4}\delta_{rad}$, where pDM denote particle DM. Contrarily, isocurvature perturbations are those which arise from perturbations in the equation of state, rather than in the metric, producing thus entropy, instead to the isentropic ones. Consider now a mix of particle DM and PBHs. Since the total DM density is given by its sum, $\rho_{\rm DM} = \rho_{\rm pDM} + \rho_{\rm PBH}$, the joint DM perturbation reads $\delta_{\rm DM} = (1-f_{\rm PBH})\delta_{\rm pDM} + f_{\rm PBH}\delta_{\rm PBH}$, with the particle and PBH fluctuations uncorrelated. While the particle DM would still be adiabatic, and thus $\delta_{\rm pDM} = 3\delta_{rad}/4$, the PBH perturbations may have a mix of adiabatic and isocurvature modes. Computing the entropy fluctuation, one finds $S = \delta_{\rm DM} - \frac{3}{4}\delta_{rad} = f_{\rm PBH}(\delta_{\rm PBH} - \delta_{\rm pDM})$. Given that $\delta_{\rm pDM}$ and $\delta_{\rm PBH}$ are uncorrelated, S will be in general non-zero, and therefore, an isocurvature mode arises. Since by assuming gaussian fluctuations, primordial clustering can be neglected, as discussed in Sec. 3.1.5, the isocurvature part $\delta_{\rm PBH} - \delta_{\rm pDM}$ would correspond to an initial power spectrum given by Eq. (3.39).

For general isocurvature perturbations, the transfer function, which relates the evolved power spectrum to its primordial form, can be approximated as [315]

$$T_{\rm iso} \simeq \begin{cases} \frac{3}{2}\,(1+z_{\rm eq}), & \text{for } k > k_{\rm eq} \\ 0, & \text{otherwise} \end{cases} \tag{3.41}$$

where $z_{\rm eq}$ is the redshift of matter-radiation equality, and $k_{\rm eq} = H(z_{\rm eq})/(1+z_{\rm eq})$. Therefore, the contribution of isocurvature modes only affects scales smaller than those corresponding to the matter-radiation equality era. Given that PBHs contribute to the matter overdensity as $f_{\rm PBH}\delta$, and including the growth factor defined in Sec. 2.2.1, the final contribution from the shot-noise to the matter power spectrum at redshift z can be written as [161]

$$\Delta P(k,z) = T_{\rm iso}^2\,\frac{f_{\rm PBH}^2}{n_{\rm PBH}}\,D^2(z) = \frac{9\,(1+z_{\rm eq})^2 f_{\rm PBH}\,M_{\rm PBH}}{4\,\Omega_{\rm DM}\,\rho_c}D^2(z) \tag{3.42}$$

$$\simeq 2.5\times 10^{-2} f_{\rm PBH}\left(\frac{M_{\rm PBH}}{30\,M_\odot}\right) D^2(z)\ {\rm Mpc}^3\ , \quad k > k_{\rm eq}\ , \tag{3.43}$$

where standard values for $z_{\rm eq}$ and $\Omega_{\rm DM}$ have been employed (see Sec. 1.2). It is noteworthy that the above power spectrum only depends on the joint product of the PBH fraction and the mass, instead of more complicated dependences as happens with accretion effects (see Sec. 3.2.1). Thus, the shot-noise contribution is degenerate on these two parameters.

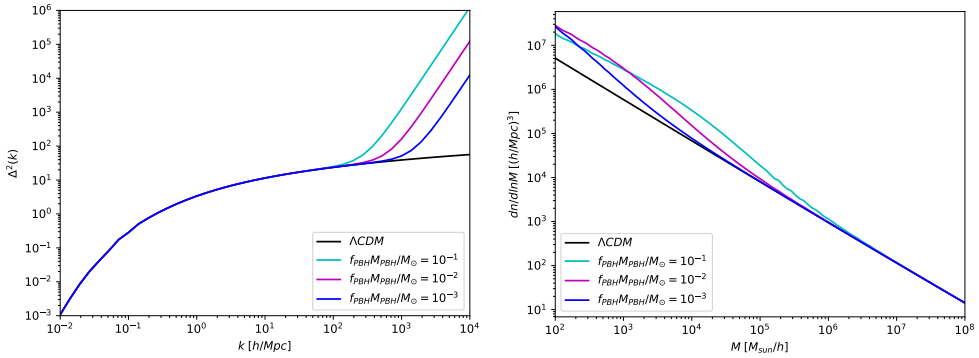

Figure 3.2: Dimensionless power spectrum (left) and halo mass function (right) at $z = 0$, for the ΛCDM case and for three PBH models with the shot-noise contribution, enhancing the power at small scales and increasing the number of low mass halos. Note that, since $P \propto k^0$ at high k, then $\Delta^2 \propto k^3$.

The inclusion of this term modifies the total matter power spectrum, and thus, the halo mass function on small scales, in analogy with the WDM and IDM cases (see Chapter 2). However, contrary to these previous DM models, low-mass halos are now enhanced instead of suppressed. For this reason, this contribution becomes only relevant for low-mass halos not large enough to cool and collapse to form stars, which are commonly known as *minihalos*. Fig. 3.2 shows the dimensionless power spectrum and the halo mass function at $z = 0$ for three models accounting for this contribution. Note that the virial mass at $T_{\rm vir} = 10^4$ K, $M \sim 10^8\, M_\odot$, the relevant scale for star-forming halos, is way above these modifications (see Eq. (2.17)).

In Part II of this thesis, the shot-noise impact on the 21 cm signal is discussed in detail [6]. Since the standard 21 cm signal is mostly ruled by the most massive star-forming halos (as shall be discussed in Chapter 5), a contribution from a high number density of minihalos may become relevant [316, 317]. However, we shall demonstrate that previous estimates neglected the effect of the heating of the IGM, which, when is consistently accounted for, suppresses the minihalo contribution, making it mostly negligible.

3.3 Observational constraints on PBHs as DM

PBHs can impact cosmology and astrophysics in a wide range of ways, leaving different observational effects which allow constraining their properties. In this section, we review the most important bounds on the current fraction of PBHs as DM, $f_{\rm PBH} = \Omega_{\rm PBH}/\Omega_{\rm DM}$, for a wide range of

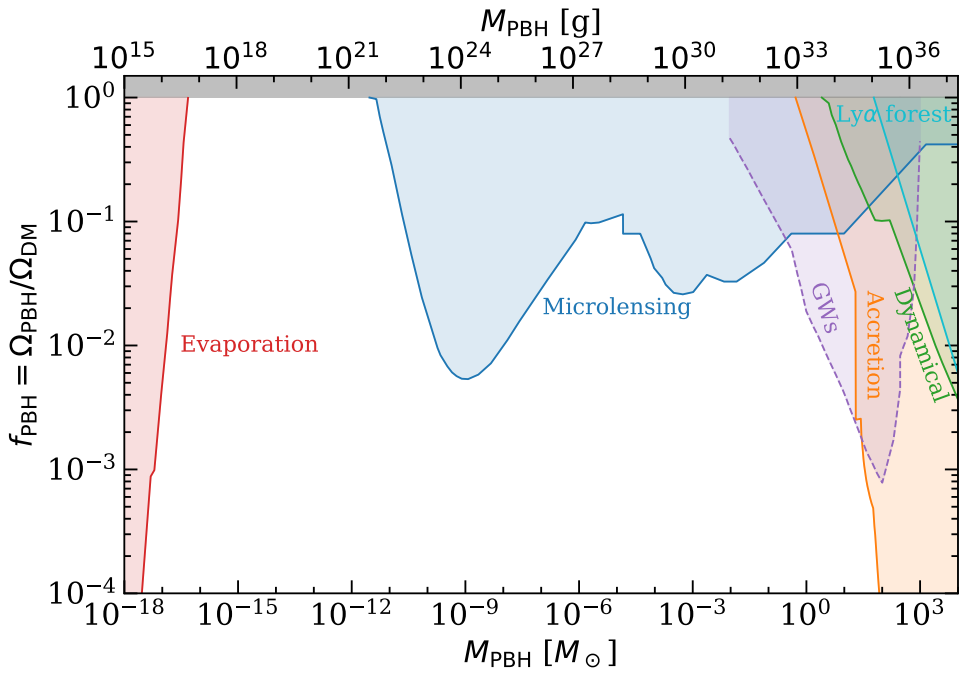

Figure 3.3: Compilation of current constraints on the PBH fraction (with respect to DM) as a function of the PBH mass, assuming a monochromatic mass function. The different probes considered are: evaporation of BHs due to Hawking radiation (red), non-observation of microlensing events (blue), merger rates from gravitational waves measurements (purple), effect of accretion on the CMB (orange), dynamical constraints, such as disruption of stellar systems by the presence of PBHs (green), and the effect of the Poisson shot noise power spectrum in the Lyα forest (cyan), see the text for more details. Limits from GWs appear with dashed lines since they could be invalidated [318]. Figure created with the publicly available `Python` code `PBHbounds`[3] [319].

masses $M_{\rm PBH}$. A collection of limits from the different probes is shown in Fig. 3.3. For a more comprehensive list of constraints, see, e.g., [243, 263, 320, 241, 242, 321].

- **Evaporation**

  As already seen, since BHs emit energy due to Hawking radiation, relatively light PBHs may be evaporating now. Those with a lifetime shorter than the age of the universe must have disintegrated nowadays, fact which forbids PBHs with $M_{\rm PBH} < M_* \simeq 4 \times 10^{14}$ g to form part of the current DM [281, 322]. Moreover, PBHs with masses small enough, although still present, should emit a strong γ-ray and cosmic ray background which could be observed. Absence of its detection strongly constrains the range of masses $M_{\rm PBH} \lesssim 10^{17}$ g. Concretely,

[3] https://github.com/bradkav/PBHbounds

the maximum fraction allowed is $f_{\rm PBH} \lesssim 2 \times 10^{-8} (M_{\rm PBH}/M_*)^{3+\epsilon}$, with $\epsilon \sim 0.1 - 0.4$ [320]. Comparable limits have been found from comparing the expected evaporation fluxes of positrons to the INTEGRAL observation of the Galactic Center 511 keV gamma-ray line [323, 324]. Diffuse supernova neutrino background searches at Super-Kamiokande are also able to set competitive constraints [325]. Considering extra contributions from electron-positron annihilations and the background modeling may set stringent bounds from the hard X-ray band [326].

- **Microlensing**

  If a compact object crosses the line of sight of a star, it may produce a so-called microlensing effect, which implies a transient and achromatic amplification of its flux. The range of masses of the objects which can produce it span from 5×10^{-10} to $\sim 100\, M_\odot$ [327, 241]. The non-detection of these events leads to stringent bounds on the maximum abundance of PBHs, as the ones found by the MACHO [328] and EROS [329] surveys in the Large and Small Magellanic Clouds, the Subaru Hyper Suprime Cam (HSC) in M31 (Andromeda) [330] and the Optical Gravitational Lensing Experiment (OGLE) in the Galactic bulge [331]. The above collaborations have placed upper bounds on the allowed fraction around $f_{\rm PBH} \lesssim 0.01 - 0.1$ in the aforementioned range of masses. Nonetheless, the existence of Earth-mass PBHs ($M_{\rm PBH} \sim 10^{-5} M_\odot$) with a fraction $f_{\rm PBH} \sim 0.03$ could explain the observation of 6 microlensing events found in the OGLE data [332], being consistent with other constraints at these range of masses [331]. Although this may constitute a hint of their existence, it cannot be regarded as a detection of PBHs, since these microlensing observations could also be explained by free-floating planets. There are, however, some caveats regarding the results of the MACHO collaboration [333], since the limits reported are model dependent and could be biased by the assumption of an over-massive halo. Moreover, the results of the MACHO and EROS projects have been found to be statistically incompatible. Therefore, these bounds are not completely reliable, and PBHs could not be definitely ruled out within these range of masses.

- **Other lensing events**

  Besides stellar microlensing, other variations of the lensing effect have been proposed to constrain such compact objects. For instance, non-smoothly distributed PBHs would produce a magnification effect of the observed light from supernovae type Ia, which constrains the PBH fraction to $f_{\rm PBH} \lesssim 0.4$ for $\gtrsim 10^{-2}\, M_\odot$ [334]. However, it has been argued [335] that former work did not account properly for the size

of supernovae, which significantly weakens the bounds in the region of first LIGO detections.[4] On the other hand, PBHs of masses $\gtrsim 10-100\,M_\odot$ may produce strong gravitational lensing of extragalactic Fast Radio Bursts (FRB). A compact object passing through could cause two different images of the same burst separated by a short time delay. The lack of observed events by future experiments like CHIME would lead to upper bounds around $f_{\rm PBH} \lesssim 0.01$ [336]. Femtolensing (i.e., lensing when the magnification depends on the wavelength of the observed light) of Gamma-Ray Bursts (GRBs) by asteroid-mass ($5\times10^{17}-10^{20}$ g) compact objects has been also proposed to constrain their abundance [337], but posterior analyses showed that GRBs are too large to be modelled as point-sources, as had been previously assumed, invalidating those bounds [338].

- **Gravitational waves**

  The observation of BH mergers by LIGO and Virgo collaborations can be employed to constrain the allowed number of PBHs. To do so, it is demanded that the predicted merger rates of PBH binaries cannot exceed the ones measured by gravitational waves. Employing data from the O1 LIGO run, tight upper bounds of $f_{\rm PBH} \lesssim 0.01$ have been found at masses between 1 and 300 $M_\odot$ [339]. However, these constraints present some caveats. It was assumed that PBH binaries are not disturbed between the moment of their formation and their merger, something which has to be yet confirmed by numerical simulations. Moreover, to derive these limits, BHs have been treated as Schwarzschild BHs, while it should be more appropriate to employ cosmological BH solutions embedded in a FLRW metric, such as the Thakurta metric [340]. This implies a time-dependent mass, and that PBH binaries created before galaxy formation would have merged at much earlier times, resulting in merger rates consistent with the LIGO data and completely avoiding these constraints [318]. Besides BH mergers, the non-observation of a stochastic gravitational wave background of mergers expected from a population of PBHs has also been used for constraining their abundance [341]. Nonetheless, the same assumptions than for those mergers have been employed, and for the same reason, they could be invalidated [318].

[4] The preprint of Ref. [334] was titled *No LIGO MACHO*, after which the former PhD advisor of one its authors replied with Ref. [335], named *LIGO Lo(g)normal MACHO*. Both titles represent a pun in Spanish language.

- **Dynamical constraints**

  Due to two-body interactions, kinetic energies of systems of different masses usually become balanced and match. If a stellar system presents in addition a MACHO population, its stars would gain kinetic energy and, due to the virial theorem, the system would expand. Therefore, the presence PBHs will dynamically heat the star clusters, making them larger and with higher velocity dispersions, leading to an eventual dissolution into its host galaxy. Populations with high mass to luminosity ratios are more sensitive to this effect, as happens with Ultra Faint Dwarf Galaxies (UFDW), which would be disrupted by the presence of PBHs. Making use of this fact, tight bounds have been obtained, $f_{\rm PBH} \sim 10^{-3}$ at $M_{\rm PBH} \sim 10^4\,M_\odot$, weakening at lower masses down to $f_{\rm PBH} \lesssim 1$ at $M_{\rm PBH} \sim 10\,M_\odot$ [342]. In a similar way, wide binary stellar systems may be perturbed by compact objects, potentially being disrupted after multiple encounters. The separation distribution of wide binaries can lead to (somewhat weak) bounds on the PBH fraction, from $f_{\rm PBH} \lesssim 1$ for $M_{\rm PBH} \simeq 3\,M_\odot$ up to $f_{\rm PBH} \lesssim 0.1$ at $M_{\rm PBH} \gtrsim 70\,M_\odot$ [343].

- **CMB constraints**

  As already stated, PBHs can emit highly energetic radiation, either as Hawking radiation from their evaporation, or from the radiation emitted by accretion. Both processes may affect the CMB spectrum mostly in two different ways: producing spectral distortions and modifying temperature anisotropies. Spectral distortions are deviations from a thermal spectrum caused by the energy injection. On the other hand, the energetic radiation can enhance the ionization rate, delay Recombination and shift the peaks of the CMB anisotropy spectrum, as well as induce more diffusion damping. The polarization spectrum can also been modified, since the increase of the fraction of free electrons would increase the Thomson optical depth and enhance the Reionization bump at large angular scales (see Sec. 5.1.3.2 for more information).

  As discussed in Sec. 3.2.1, although early CMB analyses [297] found very stringent bounds on the allowed abundance of accreting PBHs, later works revisited these computations and found much milder constraints, ranging from $f_{\rm PBH} \lesssim 1$ for $M_{\rm PBH} \sim 10$ to $f_{\rm PBH} < 3 \times 10^{-9}$ at $M_{\rm PBH} \sim 10^4\,M_\odot$ [298, 299]. The former bounds strongly depend on whether the accreted matter is ionized by collisional ionization (i.e., by collisions with free electrons) or photoionization (due to the absorption of ionizing UV photons), with the real scenario between both cases. On the other hand, while the former constraints rely on the as-

sumption of spherical accretion, accreting disks have been argued to be more realistic for PBHs. Limits in these scenarios are even tighter, finding $f_{\rm PBH} \lesssim (2M_\odot/M_{\rm PBH})^{1.6}$ [300]. Taking into account that PBHs would be immersed in DM halos with higher densities than the background, their accretion rates would be increased, also leading to more stringent constraints [344]. CMB limits from accretion are currently the most stringent ones for masses $\gtrsim 10\,M_\odot$. The caveat is their dependence upon some details of the accretion mechanisms, such as the effective velocity and the accretion rate, which may be not well understood yet.

On the other hand, the energy injection coming from evaporation would produce anisotropies and spectral distortions in the CMB spectrum, which also would bound the maximum abundance, leading to similar constraints to those obtained from the extra-galactic γ-ray background commented above [345, 346, 347]. Besides energy injection from accretion of BH evaporation, spectral distortions can also be produced by other means, such as the diffusion of photons due to Silk damping at small scales. This fact allows translating constraints on spectral distortions from FIRAS to stringent upper bounds on the PBH abundace, for masses $M_{\rm PBH} > 10^5 M_\odot$ [348].

- **Lyα forest**

  As discussed in Sec. 3.2.2, the discrete nature of PBHs would lead to a shot-noise contribution to the power spectrum, enhancing small scale fluctuations. Observations of the Lyα forest, which traces matter distribution at the smallest galactic scales, have been employed to extract limits of the maximum allowed fraction of PBHs [161]. As already commented, the shot-noise power spectrum depends on the joint product of $f_{\rm PBH}M_{\rm PBH}$, for which the upper bound $f_{\rm PBH}M_{\rm PBH} \leq 60\,M_\odot$ has been obtained [349]. The drawback of this method is on the priors of the Reionization modeling and, as any Lyα forest analysis, depends upon the details of the post-Reioniaztion IGM evolution.

Besides the aforementioned current constraints, other future probes have been suggested to constrain the abundance of PBHs. Among them, the 21 cm cosmological signal stands out as one of the most promising approaches. As already mentioned, the radiation from the hyperfine structure of the hydrogen is highly sensitive to the thermal state of the IGM, and thus, energy injection from PBH accretion or evaporation may leave strong observable signatures. The first claimed measurement of a global absorption dip by the EDGES collaboration [36] may lead to competitive bounds on the PBH abundance, either from accretion processes [350] or PBH evaporation [351, 352]. It must be noted, however, that the EDGES signal has not been

confirmed yet by other experiments, and it has been argued that it could be explained by alternative mechanisms, as will be discussed in Sec. 4.5.3. In Part II of this thesis, it is shown that forecasts of the 21 cm power spectrum data with future experiments such as HERA and SKA could potentially improve the bounds up to $f_{\rm PBH} < 10^{-2} - 10^{-6}$ for masses above $M_\odot$ [6]. The 21 cm forest observed as absorption troughs in the spectra of radio sources at $z \sim 10 - 15$ could also provide similar limits on the abundance, due to the Poisson shot noise and to the accretion heating effect, as shown in Ref. [11], not included in this thesis.

The extremely rich physics involved in the formation, evolution and distribution of PBHs implies a large number of observable effects which allow probing them. Although a myriad of constraints are present for a large range of masses, in recent years some of these limits, such as the ones coming from microlensing, femtolensing, CMB accretion or BH mergers, have been revisited and, after more detailed computations, significantly weakened or even removed. This allows opening windows in the parameter space where PBHs could still form a substantial part of the DM, if not all. On the other hand, future experiments with larger sensitivities may be able to reach yet unexplored regions in the parameter space and tighten up the current bounds. New probes, such as the 21 cm line pursued in radio interferometers like SKA, will present a promising powerful way to proof or refute the existence of solar mass BHs formed in the early universe.

Chapter 4

21 cm Cosmology

In this chapter we review the fundamentals on the 21 cm, or HI, redshifted cosmological signal. This signal arises from the spin-flip transitions in the lowest state of the Hydrogen atom. Despite its faintness due to the low emission rate, the ubiquity of Hydrogen atoms through the IGM makes it still observable with high sensitivity instrumentation. As we shall see, measuring and understanding either its global average or its fluctuations can provide highly precious information regarding the astrophysical processes which take part in the IGM, and moreover, about the DM nature, which is the focus of this thesis. In the following sections, we solve the radiative transfer equation in order to predict the 21 cm intensity, followed by an overview of the most relevant processes which determine the excitation levels of the Hydrogen. Finally, we summarize the current and forthcoming experiments devoted to detect this signal. For more details see also Refs. [353, 354, 355] for comprehensive reviews about this topic, and, e.g., Ref. [238] for fundamentals on radiative transfer.

4.1 Radiative transfer in the expanding universe

In order to predict the intensity of any radiation field, we must take into account its evolution through the IGM, accounting for emissions and absorptions in the medium. This is done by solving its Boltzmann kinetic equation, also known in this context as radiative transfer equation. The fundamental quantity is the *specific intensity* (by energy) $I(t, \nu)$ at a time

t and frequency ν, with dimensions of erg s^{-1} cm^{-2} Hz^{-1} sr^{-1}.[1] In the homogeneous expanding universe, the evolution of $I(t,\nu)$ is described by the radiative transfer equation:

$$\frac{\partial I(t,\nu)}{\partial t} + 3H(t)I(t,\nu) - H(t)\nu\frac{\partial I(t,\nu)}{\partial \nu} = -c\kappa(t,\nu)I(t,\nu) + \frac{c\epsilon(t,\nu)}{4\pi}, \quad (4.1)$$

where $H(t)$ is the Hubble rate, $\kappa(t,\nu)$ is the opacity or absorption rate, and $\epsilon(t,\nu)$ is the emissivity. The left-hand side accounts for the adiabatic evolution of the spectrum due to the expansion of the universe, while the first and second right-hand side terms account for absorptions of photons in the medium and emission of new photons, respectively. Therefore, the variation of the intrinsic intensity along its path is a competition between the loss of energy due to the interaction with the medium and the energy gained from the existing sources. Making use of the method of characteristics, we can obtain a formal solution to Eq. (4.1):

$$\begin{aligned} I(t,\nu) = &\left(\frac{a(t_*)}{a(t)}\right)^3 I\left(t_*, \frac{\nu a(t)}{a(t_*)}\right) e^{-\tau(t_*,t,\nu)} \\ &+ \frac{c}{4\pi}\int_{t_*}^{t} dt' \left(\frac{a(t')}{a(t)}\right)^3 \epsilon\left(t', \frac{\nu a(t)}{a(t')}\right) e^{-\tau(t',t,\nu)}, \end{aligned} \quad (4.2)$$

where t_* is a reference early time, and the *optical depth*, τ, is defined by

$$\tau(t',t,\nu) = c\int_{t'}^{t} dt''\kappa\left(t'', \frac{\nu a(t)}{a(t'')}\right). \quad (4.3)$$

The above dimensionless quantity denotes a measure of the total absorption along a path from time t' to t. The total intensity can therefore be interpreted as the joint combination of the initial spectrum $I(t_*, \nu a(t)/a(t_*))$ at time t_* (corresponding to a redshift z_*) damped by absorptions in the medium with the factor $e^{-\tau(t_*,t,\nu)}$, plus the integral over time of the emitted photons, whose absorptions across the medium are also taken into account through the factor $e^{-\tau(t',t,\nu)}$. It is easy to show that Eq. (4.2) is a solution of the radiative transfer equation, Eq. (4.1). Defining the operator $\mathcal{L}[...] = \frac{\partial}{\partial t} - H\nu\frac{\partial}{\partial \nu}$, notice that $\mathcal{L}[F(\xi)] = 0$, where $\xi = \nu a(t)$ and $F(\xi)$ is any function of ξ. Therefore, note that $\mathcal{L}[\tau(t',t,\nu)] = c\kappa(t,\nu)$. Writing the above solution in terms of the comoving quantities $I_c = a^3 I$ and $\epsilon_c = a^3\epsilon$

[1] The intensity can be related to the distribution function, or the photon occupation number, $f(t,\nu)$ as $I = (2h\nu^3/c^2)f$, where the factor of 2 accounts for the polarizations of the photon. With this definition, one can write the energy density of the radiation field as $u(t) = c^{-1}\int d\nu d\Omega I(t,\nu) = 2\int (d^3p)/(2\pi\hbar)^3 f(t,\nu)$, with Ω the solid angle and $p = h\nu/c$ the photon momentum.

and acting $\mathcal{L}$ over Eq. (4.2), we get

$$\mathcal{L}[I_c(t,\nu)] = -I_c\left(t_*, \frac{\nu a(t)}{a(t_*)}\right) e^{-\tau(t_*,t,\nu)} \mathcal{L}\left[\tau(t_*,t,\nu)\right] \tag{4.4}$$

$$- \frac{c}{4\pi}\int_{t_*}^{t} dt' \epsilon_c\left(t', \frac{\nu a(t)}{a(t')}\right) e^{-\tau(t',t,\nu)} \mathcal{L}\left[\tau(t',t,\nu)\right] + \frac{c}{4\pi}\epsilon_c(t,\nu) \tag{4.5}$$

$$= -c\kappa(t,\nu) I_c(t,\nu) + \frac{c}{4\pi}\epsilon_c(t,\nu), \tag{4.6}$$

which is nothing but Eq. (4.1) in a comoving form. To solve the integral of Eq. (4.2), the specific forms of the opacity and absorption are required to be known, and those can be very different depending on the processes considered. This solution not only applies to the 21 cm line, but also to the radiation fields relevant in the IGM evolution, those whose spectra span the ranges of X-rays and UV. As we shall see in Chapter 5, in these cases, photons are generated in astrophysical sources as stars, quasars and galaxies. However, in the case of the 21 cm line, emissions are produced by Hydrogen atoms throughout the neutral IGM. Henceforth, we focus on atomic transitions between a higher, excited state and a lower, ground state one, with number densities n_1 and n_0 respectively, separated by an energy $h\nu_0$. In the context of the hyperfine transition, its splitting in energy is $h\nu_0 = 5.9 \times 10^{-6}$ eV, which corresponds to a frequency of $\nu_0 = 1420$ MHz or a wavelength of 21 cm.

In order to have a measure for the relative occupation of the levels, it is customary to define the *spin temperature* T_S through the ratio between the number densities of the excited and de-excited states:

$$\frac{n_1}{n_0} = \frac{g_1}{g_0} e^{-T_*/T_S} = 3e^{-T_*/T_S}, \tag{4.7}$$

where $T_* = h\nu_0/k_B = 0.068$ K, while $g_1 = 3$ and $g_0 = 1$ denote the number of internal degrees of freedom of each state. These numbers arise from the triplet and singlet structures of the excited and de-excited levels, respectively. In all cosmological applications, $T_S \gg T_*$, implying that three out of four Hydrogen atoms are in the excited state approximately, and only one of four in the ground one. It is important to note that T_S does not refer to an actual thermodynamic temperature, but to a measure of the relative ocupation of the hyperfine levels. Equation (4.7) allows to write the population levels in terms of the spin temperature and the neutral Hydrogen number density, $n_{\rm HI}$:

$$n_1 = n_{\rm HI}\,\frac{3e^{-T_*/T_S}}{1+3e^{-T_*/T_S}}\,; \quad n_0 = n_{\rm HI}\,\frac{1}{1+3e^{-T_*/T_S}}\,. \tag{4.8}$$

The cross section of an atomic line transition is usually sharply peaked around its central frequency (although it may present relevant tails, as we

shall see with the Lyα line). Thus, it is customary to write the cross section of the transition $0 \to 1$ (being 0 and 1 the ground and excited states respectively) as $\sigma(\nu) = \sigma_{21}\phi(\nu)$, with $\phi(\nu)$ the normalized line profile, $\int d\nu\phi(\nu) = 1$, and $\sigma_{21} = 3c^2A_{10}/(8\pi\nu_0^2)$, where $A_{10} = 2.85 \times 10^{-15}s^{-1}$ is the Einstein coefficient for spontaneous emission.[2] From detailed balance, it can be related to the Einstein coefficient for stimulated emission, B_{10}, and absorption, B_{01}, as $A_{10} = 2h\nu_0^3/c^2B_{10}$ and $g_1B_{10} = B_{01}g_0$, while the normalization factor σ_{21} can also be written as $\sigma_{21} = h\nu_0/(4\pi)B_{01}$.[3] Therefore, the opacity reads

$$\kappa(\nu) = \frac{h\nu_0}{4\pi}\left(B_{01}\, n_0\, \phi(\nu) - B_{10}\, n_1\, \psi(\nu)\right) \tag{4.9}$$

$$= \frac{h\nu_0}{4\pi} B_{01}\, n_0\, \phi(\nu)\left(1 - \frac{g_0 n_1}{g_1 n_0} e^{h(\nu_0-\nu)/T_S}\right), \tag{4.10}$$

with $\psi(\nu) = \phi(\nu)e^{h(\nu_0-\nu)/T_S}$ the stimulated emission profile. The first term stands for standard absorptions by Hydrogen atoms in the ground level, while we also take into account stimulated emission by the higher level in the second term, which acts as an effective negative absorption. On the other hand, the emissivity can be written as

$$\epsilon(\nu) = h\nu_0\left(\frac{\nu}{\nu_0}\right)^3 \psi(\nu)A_{10}n_1, \tag{4.11}$$

Note that in Eqs. (4.10) and (4.11), the factors $(\nu/\nu_0)^3$ and $e^{h(\nu_0-\nu)/T}$ must be present to ensure detailed balance, i.e., in equilibrium, $\kappa(t,\nu)I_{eq}(t,\nu) = \epsilon(\nu)/(4\pi)$ implies that the equilibrium intensity $I_{eq}(t,\nu)$ becomes a black body spectrum. However, in practice, the radiation field is evaluated close to the central frequency ν_0, being thus $(\nu/\nu_0)^3 \simeq 1$ and $\psi(\nu) \simeq \phi(\nu)$. For this reason, these factors are usually dismissed. For the following derivations, it is convenient to define the source function $S(\nu)$, as

$$S(\nu) = \frac{\epsilon(\nu)}{4\pi\kappa(\nu)} = \frac{2h\nu^3}{c^2}\frac{1}{e^{h\nu/T_S} - 1} \simeq \frac{2\nu^2}{c^2}T_S, \tag{4.12}$$

where in the last equality, we have applied the Rayleigh-Jeans approximation, valid at low frequencies, where $h\nu/T_S \ll 1$. Note that the source function represents a black body spectrum with a temperature T_S. When equilibrium holds, the intensity becomes $I_{eq}(\nu) = S(\nu)$.

We shall explicitly evaluate now Eq. (4.2). Note that the frequency arguments in Eq. (4.2) are redshifted as $\nu' = \nu(1+z')/(1+z)$. It is

[2] Note that σ_{21} has units of area over time, rather than cross section units.

[3] It is worth noting that other definition of the Einstein coefficients present in the literature employs the energy density, instead of the specific intensity used here, which implies an extra factor of $4\pi/c$ (see, e.g., Ref. [356]).

appropriate then to change coordinates to integrate over frequencies, with $|dt'| = dz'/((1+z')H(z')) = d\nu'/(\nu' H(z'))$. For the hyperfine transition, the shape of the line profile $\phi(\nu)$, which includes Doppler broadening due to the thermal motions of atoms, is expected to be quite sharp, so it is safe to approximate it as a Dirac delta function around the frequency ν_0, $\phi(\nu) \simeq \delta(\nu - \nu_0)$. Exploiting this fact, we can evaluate the emission integral of Eq. (4.2) as

$$\frac{c}{4\pi}\int_{t_*}^{t} dt' \epsilon_c(t', \nu a(t)/a(t')) e^{-\tau(t',t,\nu)} = c\int_{\nu}^{\nu_*} \frac{d\nu'}{\nu' H(z')} S_c(t',\nu')\kappa(t',\nu') e^{-\tau(t',t,\nu)} \tag{4.13}$$

$$\simeq S_c(t_0,\nu_0)\int_0^{\tau(t_*,t,\nu)} d\tau e^{-\tau} = S_c(t_0,\nu_0)(1 - e^{-\tau(t_*,t,\nu)}), \tag{4.14}$$

where $\nu_* = \nu(1+z_*)/(1+z)$, t_0 is the time corresponding to $1+z_0 = (\nu_0/\nu)(1+z)$, and in the second equality we have approximated the line profile in the opacity as a delta function. On the other hand, given that $T_S \gg T_*$, the opacity from Eq. (4.10) can be approximated as

$$\kappa(\nu) \simeq \frac{h\nu_0}{4\pi} B_{01}\, n_0\, \phi(\nu) \frac{h\nu}{T_S} \simeq \frac{3c^2 A_{10}}{32\pi\nu_0^2}\, n_{\rm HI}\, \phi(\nu) \frac{h\nu}{T_S}\ , \tag{4.15}$$

where in the second equality we have written $n_0 \simeq n_{\rm HI}/4$ from Eq. (4.8), valid up to leading order in T_*/T_S. Therefore, integrating Eq. (4.3), we obtain

$$\tau(z,\nu) = \frac{3c^3 A_{10}}{32\pi\nu_0^3} \frac{x_{\rm HI}(z_0) n_{\rm H}(z_0)}{H(z_0)} \frac{T_*}{T_S(z_0)}\ , \tag{4.16}$$

where we have defined the *fraction of neutral Hydrogen* $x_{\rm HI}$ with respect to the total Hydrogen number density $n_{\rm H}$ as $x_{\rm HI} = n_{\rm HI}/n_{\rm H}$. For the shake of simplicity, this derivation is being limited to the homogeneous case, but in reality, inhomogeneities and peculiar velocities of the gas must be taken into account. It leads to a slight modification of the argument of the line profile, induced by a Doppler kinematic effect. The approximation of $\phi(\nu)$ by a delta function $\delta(\nu - \nu_0)$ considered above must then be replaced by $\delta(\nu - \nu_0(1 - \vec{\Omega}\cdot\vec{v}))$, with $\vec{\Omega}$ is the unity normalized vector along the line of sight and $\vec{v}$ the peculiar velocity of the gas. Integration of the optical depth modifies the result with an extra term depending on the derivative of the radial component of the velocity along the line of sight, $\partial_r v_r$ [354],

$$\tau(z,\nu) = \frac{3c^3 A_{10}}{32\pi\nu_0^3} \frac{x_{\rm HI}(z_0) n_{\rm H}(z_0)}{H(z_0)} \frac{T_*}{T_S(z_0)} \frac{1}{\left(1 + \frac{\partial_r v_r(z_0)}{H(z_0)}\right)} \tag{4.17}$$

$$\simeq 9.2\times 10^{-3}\ (1+\delta(z_0)) x_{\rm HI}(z_0)(1+z_0)^{3/2} \frac{(1\,{\rm K}/T_S)}{\left(1 + \frac{\partial_r v_r(z_0)}{H(z_0)}\right)}\ , \tag{4.18}$$

where we have written the Hydrogen number density as the background value $\propto (1+z)^3$ times the factor accounting for the overdensity δ, $n_{\rm H} = \bar{n}_{\rm H}(1+\delta)$. Since $T_* \ll T_S$ for the relevant regimes, the above optical depth is always much lower than unity, $\tau \ll 1$. In the following, we assume that the Hydrogen (and baryon) overdensity equals the DM one, which is an accurate approximation at the cosmological scales and redshifts of interest.

On the other hand, for the initial spectrum at t_*, the only relevant background radiation at high redshift at these frequencies is the CMB, since radio emission from astrophysical sources is expected to be several orders of magnitude lower. Therefore, we may take $I(t_*,\nu) = I_{CMB}(t_*,\nu) \simeq (2\nu^2/c^2)T_\gamma$, with $T_\gamma = 2.73$ K $(1+z)$ the CMB temperature. In the spirit of the Rayleigh-Jeans approximation, it is customary to define the *brightness temperature* $T_b(t,\nu)$ as $I(t,\nu) = (2\nu^2/c^2)T_b(t,\nu)$. Thus, in terms of brightness temperature, Eq. (4.2) reads

$$T_b(z,\nu) = T_\gamma(z)e^{-\tau(z,\nu)} + T_S(z)(1-e^{-\tau(z,\nu)}). \tag{4.19}$$

Since we are interested in the deviations from the CMB spectrum around the 21 cm line, the relevant quantity is the comoving *differential brightness temperature* δT_b, as the comoving temperature relative to the CMB one evaluated at the 21 cm frequency ν_0:

$$\delta T_b(z) = \frac{T_b(z,\nu_0) - T_\gamma(z)}{1+z} \simeq \frac{(T_\gamma(z) - T_S(z))\tau(z,\nu_0)}{1+z} \tag{4.20}$$

$$\begin{aligned} &\simeq 27\,\mathrm{mK}\, x_{\rm HI}(z)\,(1+\delta(z))\left(1-\frac{T_\gamma(z)}{T_S(z)}\right)\left(\frac{1+z}{10}\right)^{1/2} \\ &\times \left(\frac{0.15}{\Omega_m h^2}\right)^{1/2}\left(\frac{\Omega_b h^2}{0.023}\right)\frac{1}{\left(1+\frac{\partial_r v_r(z)}{H(z)}\right)}, \end{aligned} \tag{4.21}$$

where in the second identity we have used $\tau \ll 1$ and Eq. (4.18). This is the main equation for predicting the 21 cm cosmological signal, accounting for photons absorbed or emitted with frequency ν_0 at redshift z, or equivalently, being observed now at a frequency $\nu_0/(1+z)$. Thus, the observation of a frequency spectrum from the cosmological 21 cm signal actually provides a record of the history of the IGM over a range of redshifts.

Several important facts can be noted by examining Eq. (4.21). Since the signal is proportional to the neutral fraction $x_{\rm HI}$, it can be observed only if there is a significant fraction of neutral Hydrogen in the IGM. This makes it a sensitive probe for the ionization state of the medium, being a promising tool for understanding the evolution of the EoR, when the intergalactic gas becomes fully ionized. It may become especially useful to trace the end of this process, when the neutral fraction goes to zero and the overall

signal vanishes, providing a picture of the evolution of $x_{\rm HI}$. In addition, the signal gets enhanced in overdense regions as indicated by its dependence on δ, becoming also a probe for the matter density fluctuations. It must be remarked that there will be a signal only if the spin temperature differs from the CMB temperature, being observed in *absorption* if $T_S < T_\gamma$ (δT_b negative), or in *emission* if $T_S > T_\gamma$ (δT_b positive). In the limit $T_S \gg T_\gamma$, the signal saturates, and becomes independent on T_S. Finally, it is convenient to note that the velocity gradient term, negligible in the homogeneous limit, accounts for redshift distortions along the line of sight [354, 353]. In order to compute the brightness temperature for a given redshift, it is mandatory to know how T_S evolves in redshift, which will be studied in the next section.

Although not covered in this thesis, it is worth mentioning another situation of interest. Instead of employing the CMB as the radio background, one can also employ a loud radio point source, such as a quasar, as the backlight, changing T_γ in the previous analysis by the brightness temperature of the radio radiation. In that case, $T_\gamma \gg T_S$, and the signal will be seen always in absorption. The presence of clouds of neutral Hydrogen along the line of sight would imprint a set of absorption lines in the redshifted quasar spectrum, given by the distance of the gas cloud. This is the so-called *21 cm forest*, in analogy with the Lyα forest, which works under the same principle with the Lyα transition line, and stands as a promising tool to probe small scales. Since it makes use of a source with high emission in radio, it has the advantage that foregrounds are less important that when observing the signal from the IGM, which are one of its main experimental problems, as shall be discussed in Sec. 4.5.1. Moreover, it allows tracing higher redshifts than the Lyα forest due to the low 21 cm optical depths. However, the main drawback of this approach is the high uncertainty on the existence of bright enough radio sources at high redshift. See, e.g., Refs. [357, 358, 353] for more details.

4.2 Spin temperature

There are three main processes which can modify the population of the hyperfine levels and therefore determine the spin temperature, namely:

1. Absorption/emission of 21 cm photons from/to the CMB.
2. Collisions with electrons, protons and other Hydrogen atoms.
3. Resonant scattering of Lyα photons that cause a spin flip via an intermediate excited state (Wouthuysen-Field effect).

Each of these processes may produce spin-flip transitions, exciting or de-exciting the Hydrogen atom. The kinetic equations for the population of each level must account for all these effects, and can be written as

$$\begin{aligned}\dot{n}_1 + 3Hn_1 &= -(\dot{n}_0 + 3Hn_0) \\ &= (C_{01} + P_{01} + B_{01}\bar{I})n_0 - (C_{10} + P_{10} + A_{10} + B_{10}\bar{I})n_1 \ ,\end{aligned} \tag{4.22}$$

where the term $3H$ accounts for the adiabatic expansion, $\bar{I} = (1/4\pi)\int d\Omega \int d\nu \phi(\nu) I(\nu) \simeq I(\nu_0)$ is the angle-averaged radiation field evaluated at the 21 cm line, and C_{10} and P_{10} are the de-excitation rates (per atom) from collisions and Lyα scattering, respectively, while C_{01} and P_{01} are their corresponding excitation rates. Given that the rates of these processes are much faster than the Hubble timescale, the spin temperature is given to a very good approximation by the equilibrium balance of these effects,

$$n_1(C_{10} + P_{10} + A_{10} + B_{10}\bar{I}) = n_0(C_{01} + P_{01} + B_{01}\bar{I}) \ , \tag{4.23}$$

Due to detailed balance in collisional coupling, we can relate the de-excitation and excitation coefficients to the *kinetic temperature* T_K of the gas. For that, consider only collisional coupling, where the evolution equation takes the form: $\dot{n}_1 + 3Hn_1 = C_{01}n_0 - C_{10}n_1$. In the equilibrium case at temperature T_K (indicated by the superindex eq), the left hand side of this equation vanishes, leading to the relation between the excitation and de-excitation rates:

$$\frac{C_{01}}{C_{10}} = \left(\frac{n_1}{n_0}\right)^{eq} = \frac{g_1}{g_0} e^{-T_*/T_K} \simeq 3\left(1 - \frac{T_*}{T_K}\right) \ , \tag{4.24}$$

where in the last equality we have used the fact that $T_* \ll T_K$ for all temperatures of interest. Analogously, we can *define* the effective *color temperature* of the UV radiation field, T_c, as

$$\frac{P_{01}}{P_{10}} \equiv \frac{g_1}{g_0} e^{-T_*/T_c} \simeq 3\left(1 - \frac{T_*}{T_c}\right) , \tag{4.25}$$

which can be related to the temperature of the Lyα radiation field, as indicated in Sec. 4.3.3. From Eqs. (4.7) and (4.23), employing the relations above, together with the fact that $T_* \ll T_S$, and using the Rayleigh-Jeans approximation for the CMB radiation field, $\bar{I} \simeq 2k_B T_\gamma \nu_0^2/c^2$, it is straightforward to show that the spin temperature T_S can be written as [353]

$$T_S^{-1} = \frac{T_\gamma^{-1} + x_c T_K^{-1} + x_\alpha T_c^{-1}}{1 + x_c + x_\alpha} \ , \tag{4.26}$$

where we have defined the collisional and Lyα *coupling coefficients* x_c and x_α as[4]

$$x_c = \frac{C_{10}T_*}{A_{10}T_\gamma} \; ; \quad x_\alpha = \frac{P_{10}T_*}{A_{10}T_\gamma} \; . \tag{4.27}$$

From Eq. (4.26), it can be seen that if collisions or Lyα are efficient enough, the spin temperature *couples* to the kinetic or color temperature, respectively, being close to the CMB one otherwise. In most cases of interest, since the Lyα optical depth is large, Lyα scattering is efficient enough to maintain the equilibrium with the gas, and the color temperature is close to the kinetic one, $T_c \simeq T_K$. We compute the color temperature properly from the radiation field in Sec. 4.3.3 and show the limit $T_c \simeq T_K$ explicitly. Then, generally, T_S will take values between the kinetic and the CMB temperatures.

In the next subsections we discuss in some detail the physics involved in the above coupling mechanisms. Before that, it is convenient to emphasize that, although we have several quantities with units of temperature, some of them are not truly thermodynamic temperatures. For instance, T_b is a measure of radio intensity, T_S measures the relative occupation numbers of the two hyperfine levels, and T_c describes the photon distribution in the vicinity of the Lyα transition, behaving as an effective brightness temperature for the Lyα radiation. Only the CMB blackbody temperature T_γ and the gas kinetic one T_K are genuine thermodynamic temperatures.

4.2.1 Collisional coupling

Collisions of neutral Hydrogen atoms with other IGM species, such as free protons, electrons and other H atoms, may induce spin-flips transitions in the hyperfine levels. These processes dominate during the Dark Ages, when the background gas density is still high, but become negligible at the epoch of star formation. The collisional de-excitation coefficient C_{10} must include the three species mentioned above, and can be written as

$$C_{10} = \sum_i n_i \kappa_{i\mathrm{H}} = n_{\mathrm{HI}}\kappa_{\mathrm{HH}} + n_e\kappa_{e\mathrm{H}} + n_p\kappa_{p\mathrm{H}} \; , \tag{4.28}$$

where n_i is the number density of each species i and $\kappa_{i\mathrm{H}}$ the scattering rate between the neutral Hydrogen and each species i. These rates can be obtained integrating the cross section of each process, by a quantum mechanical calculation, as is done in [354, 362]. We make use of the tabulated

[4]The spin temperature can also be written as $T_S = (T_\gamma + y_c T_K + y_\alpha T_c)/(1 + y_c + y_\alpha)$, with the coupling coefficients given by $y_i = x_i T_\gamma / T_K$. This convention is also widely employed in the literature and will be used in some articles of Part II.

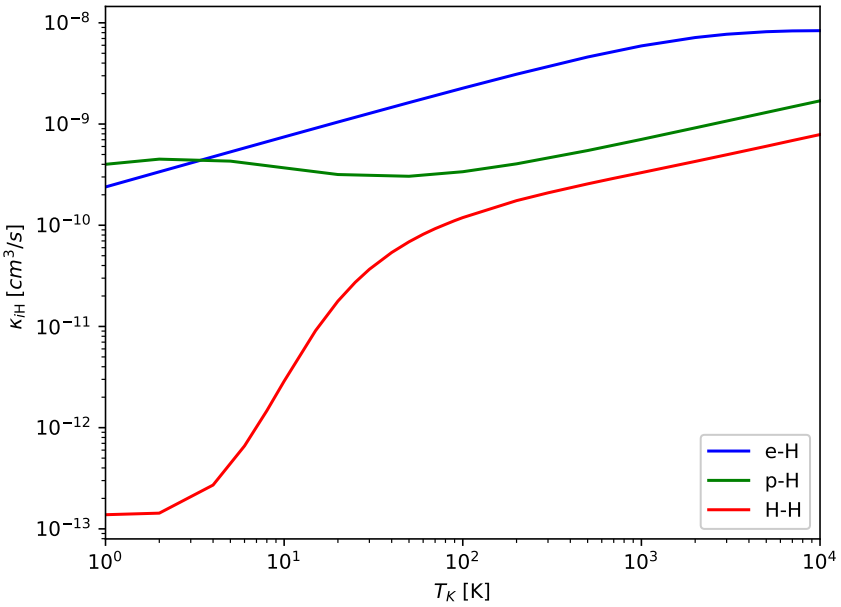

Figure 4.1: Scattering rates between the different species as a function of temperature: e-H ([359], blue line), p-H ([360], green line), and H-H ([361], red line) collisions.

values as a function of T_K provided by Ref. [359] for the electron-Hydrogen rate $\kappa_{e\mathrm{H}}$, and by Refs. [361, 363] for Hydrogen-Hydrogen collisions, κ_{HH} (see also the fits proposed in Refs. [364, 365]). The proton-Hydrogen rate κ_{pH} can be approximated for $T_K \gtrsim 100$ K as $\kappa_{pH} \simeq 2.0\,\kappa_{HH}$ [360], although for quantitative computations the tabulated data from Ref. [360] is used. However, since in Eq. (4.28) is weighted by the ionized fraction, it becomes subdominant at low ionization states, becoming relevant only at low temperatures. Figure 4.1 shows the scattering rates as a function of temperature from the tabulated data. We can safely neglect collisions with other species, such as Helium, since it is usually in a spin singlet state. This fact forbids spin exchange, unless it can be excited to the triplet state, something very unlikely in the thermal state of the IGM [354, 366]. It must be remarked that, although the collisional coupling process becomes irrelevant after the Dark Ages for the global 21 cm signal, it can be locally important at overdense regions, where collisions are enhanced by the term $1 + \delta$ present in the number densities.

4.2.2 Wouthuysen-Field effect

Collisional coupling of the 21 cm line can only be efficient at large densities, and thus, in the bulk of the IGM becomes negligible at late times, after $z \sim 30$. However, once star formation begins, resonant scattering

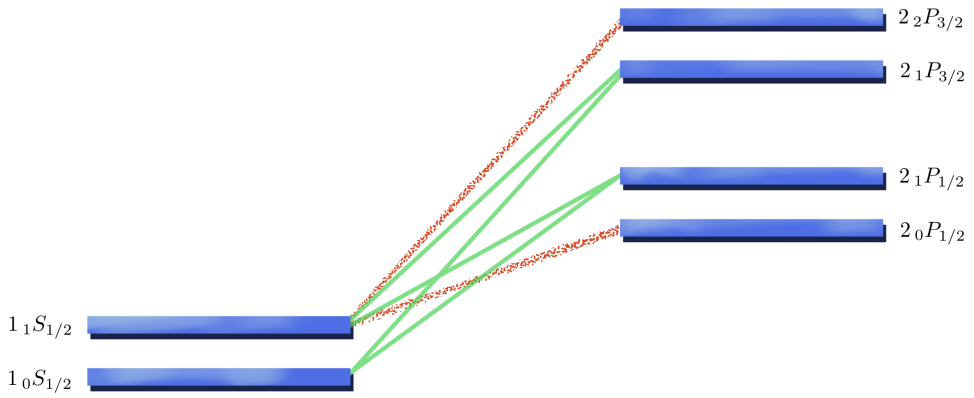

Figure 4.2: Hyperfine structure of the 1S and 2P levels of the Hydrogen atom and relevant transitions for the Wouthuysen-Field effect. Solid green lines represent transitions which cause spin flips, while dotted red lines are allowed transitions not contributing to spin flips.

of Lyα photons provides a second channel to modify the spin temperature. This coupling mechanism was discovered independently by Siegfried A. Wouthuysen in 1952 [301] and by George B. Field in 1958 [367], and named after them as the Wouthuysen-Field (WF) effect. It enables transitions between hyperfine levels of the ground 1S state to the 2P level, which can cause an effective spin flip. With F denoting the hyperfine spin state, the dipole selection rules impose restrictions over the possible spin changes ΔF, allowing those transitions which fulfill $\Delta F = 0, \pm 1$, except $F = 0 \rightarrow 0$. These are showed in Fig. 4.2, with the notation $n_F L_J$, being n, L and J the principal, orbital and total angular momentum quantum numbers. For example, suppose a Hydrogen atom initially in the singlet state $1_0S_{1/2}$ which absorbs a Lyα photon, being excited into any of the central 2P hyperfine states. The de-excitation due to emission of another Lyα photon may relax the atom to its initial state, but also to the triplet ground state $1_1S_{1/2}$, causing an effective spin flip. Note that not all the allowed transitions lead to a spin flip in the 1S state, i.e. the levels $2_0P_{1/2}$ and $2_2P_{3/2}$ do not contribute to the spin flips.

We can outline a simple example to illustrate mathematically the behavior of this mechanism. Consider an atom with the hyperfine states of the ground state, n_1, n_0, and also an effective excited state, n_2, which corresponds to the 2P levels. Neglecting stimulated emission[5] and collisional

[5]This is a fair approximation at Lyα frequencies for the relevant temperatures of the IGM post-Recombination, since $e^{h\nu_{Ly\alpha}/T_K} \gg 1$, being thus equivalent to replace the Bose-Einstein distribution function by the Maxwell-Boltzmann one.

coupling, the dynamical evolution of the occupation number is driven by the equation:

$$\dot{n}_2 + 3Hn_2 = B_{02}I_{02}n_0 + B_{12}I_{12}n_1 - (A_{21} + A_{20})n_2 \ , \tag{4.29}$$

where B_{ij}, A_{ij} and I_{ij} are the absorption and emission Einstein coefficients, and the radiation flux evaluated at the transition $i \to j$. Given the short lifetime of the 2P state, we can approximate the above equation by the equilibrium case, solving for n_2:

$$n_2 \simeq \frac{B_{02}I_{02}n_0 + B_{12}I_{12}n_1}{A_{21} + A_{20}} \ . \tag{4.30}$$

Therefore, the change in n_1 due to transitions between the excited levels is given by:

$$\begin{aligned} &(\dot{n}_1 + 3Hn_1)\,|_{\mathrm{Ly}\alpha} = A_{21}n_2 - B_{12}I_{12}n_1 \\ &\simeq A_{21}\frac{B_{02}I_{02}}{A_{21} + A_{20}}n_0 - A_{20}\frac{B_{12}I_{12}}{A_{21} + A_{20}}n_1 \equiv P_{01}n_0 - P_{10}n_1 \ , \end{aligned} \tag{4.31}$$

where in the last equality, we have related the flux and Einstein coefficients for the $0, 1 \leftrightarrow 2$ transitions with the excitation and de-excitation coefficients P_{10} and P_{01}. In reality, the situation is slightly more complicated since there is not only one excited state but two hyperfine levels in the 2P state which contribute to spin flips, $2_1P_{3/2}$ and $2_1P_{1/2}$, but the reasoning is the same. Relating the Einstein coefficients for the different states, it is straightforward to obtain the final de-excitation rate as [368]

$$P_{10} = \frac{4P_\alpha}{27} \ , \tag{4.32}$$

where P_α is the Lyα scattering rate, defined as:

$$P_\alpha = 4\pi \int d\nu \sigma_\alpha(\nu) J(\nu) \ , \tag{4.33}$$

being J the specific intensity by number, related to $I(\nu)$ as $I = h\nu J(\nu)$. The cross section of the Lyα transition, $\sigma_\alpha(\nu)$, can be written as $\sigma_\alpha(\nu) = \sigma_0\varphi_\alpha(\nu)$, being $\sigma_0 = \frac{\pi e^2}{m_e c} f_\alpha$, with $f_\alpha = 0.4162$ the oscillator strength of the Lyα transition, and $\varphi_\alpha(\nu)$ its line profile.[6] Since $\varphi_\alpha(\nu)$ is a peaked function around the Lyα transition, P_α can be estimated to be proportional to the radiation flux evaluated at the Lyα frequency, J_α, as $P_\alpha \sim 4\pi\sigma_0 J_\alpha$. However, Doppler broadening and the tails of the distribution are actually important. Furthermore, resonant scattering around the Lyα line induces an absorption feature which must be properly calculated. Hence, the determination of the radiation spectrum becomes mandatory for a precise evaluation of P_α, and is treated in the following section.

[6] One can also define the Lyα cross section analogously to the 21 cm line with the spontaneous emission coefficient $A_\alpha = 6.25 \times 10^8$ s^{-1}, as $\sigma_0 = 3c^2 A_\alpha/(8\pi\nu_\alpha^2)$.

4.3 Lyα line scattering

As stated in the previous section, the spin temperature dynamics, and therefore the 21 cm signal, strongly depends on the Lyα flux, its correct estimation being necessary. It is thus compulsory to solve the radiative transfer around that line, by employing a kinetic equation similar to Eq. (4.1). These transitions are, however, short lived, and absorptions of photons are quickly followed by emissions, being the full picture a scattering process which redistributes frequencies of the spectrum. Scattering around the Lyα line has been broadly studied in the literature for decades [369, 370, 371, 372, 373]. The kinetic equation for the comoving flux of photons J (with units of s^{-1} cm^{-2} Hz^{-1} sr^{-1}) can be written as

$$\frac{\partial J(\nu)}{\partial t} - H\nu\frac{\partial J(\nu)}{\partial \nu} = c\, n_{\rm HI}\, \sigma_0 \left[\int d\nu' \mathcal{R}(\nu',\nu) J(\nu') - \varphi(\nu) J(\nu) + \mathcal{C}\Delta\nu_D^{-1}\psi(\nu)\right], \tag{4.34}$$

where the two first terms in the right-hand side correspond to the scattering part, while the last term accounts for line injection. Here, as in most of applications, isotropic scattering has been assumed, although angle-dependent cross section may be considered [369]. Note also that stimulated emission has been neglected, as usual when dealing with the Lyα line, although it is easy to include its effect in the kinetic equation [373]. The *scattering kernel*, or redistribution function, $\mathcal{R}(\nu',\nu)$, drives the frequency variation of the scattered photons, and fulfills the normalization condition $\int d\nu' \mathcal{R}(\nu,\nu') = \varphi(\nu)$, which ensures number conservation in the scattering term. The specific shape of $\mathcal{R}(\nu,\nu')$ depends upon the line profile $\varphi(\nu)$ and the details of the redistribution mechanism [374]. Regarding the last term, relative to injection of photons in the line, $\mathcal{C}$ is the rate at which they are produced, while $\psi(\nu)$ stands for the spectral profile, usually taken as a Dirac delta function (normalized to $\int d\nu \psi(\nu) = \Delta\nu_D$ for later convenience).

Rather than working with the frequency, it is useful to employ as variable the normalized frequency $x = (\nu - \nu_\alpha)/\Delta\nu_D$, defining the Doppler broadening frequency as $\Delta\nu_D = \nu_\alpha\sqrt{2k_B T_K/(m_H c^2)}$, which characterizes the width of the line due to thermal Doppler effect[7]. Accordingly, we define the dimensionless line profile and scattering kernel as $\phi(x) = \Delta\nu_D\varphi(\nu)$ and $R(x',x) = (\Delta\nu_D)^2\mathcal{R}(\nu',\nu)$ respectively, with the proper normalization conditions $\int dx\, \phi(x) = 1$ and $\int dx' R(x',x) = \phi(x)$. Given that the frequency variation during these scattering processes is small, the redistribution func-

[7] If one computes the same quantity for the 21 cm line, given that it linearly scales with the frequency, one finds that it is a factor $\sim 6\times10^{-7}$ lower than the Lyα Doppler broadening. That is one of the reasons why one can safely approximate the 21 cm line profile as a Dirac delta function for most of applications in Sec. 4.1, while the broadening of the Lyα line can be of great relevance, as shown in this section.

tion can be expanded following a Fokker-Planck procedure, which allows performing the integral of Eq. (4.34) as [369, 370]

$$\int dx' R(x', x) J(x') \simeq \phi(x) J(x) + \frac{1}{2}\frac{\partial}{\partial x}\left[\phi(x)\left(\frac{\partial J(x)}{\partial x} + 2\eta(x) J(x)\right)\right], \tag{4.35}$$

where the second term in the expansion accounts for the thermal recoil, with $\eta(x) = h\nu_\alpha/\sqrt{2 m_H c^2 k_B T_K} - (x + x_0)^{-1}$, being $x_0 = \nu_\alpha/\Delta\nu_D$. The last term $(x + x_0)^{-1}$ in η ensures detailed balance, although for the forthcoming computations can be neglected. The Fokker-Planck expansion of Eq. (4.35) simplifies enormously the treatment of the scattering process, since, instead of an integro-differential equation, it allows writing a differential one, much easier to solve. As we are interested in the spectrum around the Lyα line, we can approximate the term $\nu\partial/\partial\nu J(x) \simeq (\nu_\alpha/\Delta\nu_D)\partial/\partial x J(x)$ in Eq. (4.34). On the other hand, a relevant quantity in Lyα radiative transfer is its optical depth, usually known as the *Gunn-Peterson optical depth*, which can be computed from Eq. (4.3) for the Lyα transition approximating the line profile as a Dirac delta function [375]:

$$\tau_{\rm GP} = \frac{c\,\sigma_0\, n_{\rm HI}(z)}{H(z)\nu_\alpha} \simeq 5.0 \times 10^5\, x_{\rm HI}(z)(1+\delta)\left(\frac{1+z}{7}\right)^{3/2}. \tag{4.36}$$

This quantity is of great importance for the Lyα forest and the study of the ionization state of the IGM, as shall be discussed in Chapter 5. Within this section, we neglect the overdensity factor δ since we focus on the homogeneous computation. Defining the *Sobolev parameter* γ_S as the inverse of the Gunn-Peterson optical depth, $\gamma_S = \tau_{\rm GP}^{-1} = H\nu_\alpha/(c\sigma_0 n_{\rm HI})$, the final line scattering equation reads

$$\frac{\Delta\nu_D}{c n_{\rm HI}\sigma_0}\frac{\partial J(x)}{\partial t} - \gamma_S\frac{\partial J(x)}{\partial x} = \frac{1}{2}\frac{\partial}{\partial x}\left[\phi(x)\left(\frac{\partial J(x)}{\partial x} + 2\eta J(x)\right)\right] + \mathcal{C}\psi(x). \tag{4.37}$$

Note that Eq. (4.37) is consistent with detailed balance, i.e., the equilibrium spectrum $J(\nu) = 2\nu^2/c^2 \exp[-h\nu/(k_B T_K)]$ is a solution when the right hand side is equal to zero and there are no injections. Furthermore, when integrating over frequency, the scattering part (i.e., setting aside the injection term) fulfills number conservation by construction (the frequency integral of Eq. (4.37) vanishes), given that the right-hand side term is a total derivative. Spin exchange due to hyperfine interactions can affect the above result, but it is easily included by making the substitution $\gamma_S \to \gamma_S(1 + T_{se}/T_K)^{-1}$ and $\eta \to \eta(1 + T_{se}/T_S)/(1 + T_{se}/T_K)$, with $T_{se} = (2/9)T_K\nu_{21}/\Delta\nu_D^2 = 0.40$ K the spin-exchange characteristic temperature [376, 372, 371].

4.3.1 Modification of the spectrum

For the time scales of interest, we can just focus on stationary solutions, when the time derivative of Eq. (4.37) can be neglected:

$$\frac{\partial}{\partial x}\left[\phi(x)\frac{\partial J(x)}{\partial x} + 2(\gamma_S + \eta\phi(x))J(x)\right] = -2\mathcal{C}\psi(x). \tag{4.38}$$

The above equation is easily integrated, and since it is linear in J, our complete solution will be given by the sum of the continuum spectrum, $J_c(x)$ (i.e., the solution of the homogeneous equation, without injections), plus the injected photons near the line center, $J_i(x)$ (the non-homogeneous solution). Continuum photons correspond to those emitted between Lyα and Lyβ transitions, and then redshift to the Lyα line. On the other hand, injected photons are those between the Lyβ and the Lyman limit (13.6 eV), which can excite an atom reaching a Lyman series line, and thereafter being converted to Lyα photons when the atom decays [370]. It is worth noting that some radiative cascades can finish in the two-photon transition 2S $\rightarrow$ 1S, and do not contribute to Lyα injections [371, 377]. Imposing the proper boundary conditions, far away from the center of the line, the integration constants can be determined. In the continuum case, (*i.e.*, $\mathcal{C} = 0$), there are photons with energies between Lyβ and Lyα redshifting, and thus far enough from the resonance, we have $J_c(x) \rightarrow J_{c,\infty}$ for $\nu \rightarrow \pm\infty$, getting

$$\phi(x)\frac{\partial J_c(x)}{\partial x} + 2(\gamma_S + \eta\phi(x))J_c(x) = 2\gamma_S J_{c,\infty}. \tag{4.39}$$

On the other hand, in the injected case, new photons are produced at the Lyα line, which can redshift towards lower energies, but higher energy photons cannot be produced (except from the scattering process, only relevant near the resonance). Thus, for $\nu \rightarrow \infty$, we expect $J_i(x) \rightarrow 0$, while for $\nu \rightarrow -\infty$ we write $J_i(x) \rightarrow J_{i,\infty}$[8]. Hence, taking $\psi(x) = \delta_D(x)$ as the injection profile[9], one finds $\mathcal{C} = \gamma_S J_{i,\infty}$ and

$$\phi(x)\frac{\partial J_i(x)}{\partial x} + 2(\gamma_S + \eta\phi(x))J_i(x) = 2\gamma_S J_{i,\infty}(1 - \Theta(x)). \tag{4.40}$$

Note that if the scattering terms are neglected (i.e., the terms with $\phi(x)$), the injected spectrum can be easily solved, being $J_i(x) = J_{i,\infty}(1 - \Theta(x))$. The above equations can be integrated, obtaining the solution for continuum photons, and for injected photons with $x < 0$, as

$$J(x) = J_\infty\left(1 - 2\,\eta\int_0^\infty dy \exp\left[-2\,\eta\,y - 2\,\gamma_S\int_{x-y}^{x}\frac{dx'}{\phi(x')}\right]\right), \tag{4.41}$$

[8] Note the slight abuse of notation, denoting $J_{i,\infty}$ instead of $J_{i,-\infty}$, in order to unify notation with the continous case.

[9] Employing other broader distributions has little impact on the resulting spectrum [370].

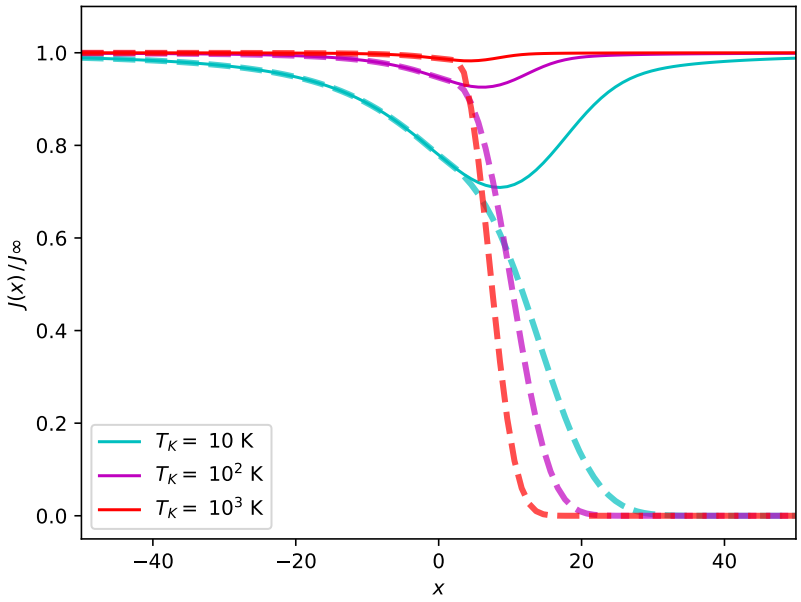

Figure 4.3: Spectrum for continuum (continuous lines) and injected (dashed lines) photons around the Lyα line, for three different temperatures at redshift $z = 10$.

while the solution for injected photons with $x > 0$ is

$$J(x) = J(0) \exp\left[-2\,\eta\,x - 2\,\gamma_S \int_0^x \frac{dx'}{\phi(x')}\right]. \tag{4.42}$$

While for some results we have assumed $\phi(x)$ to be very sharp, the evaluation of the spectrum requires a more precise form of the line profile. Its proper shape implies a Lorentzian function, accounting for the resonance, convolved with a Maxwell-Boltzmann distribution, responsible for the thermal broadening, giving rise to the so-called *Voigt distribution* (e.g., Ref. [370])

$$\phi(x) = \frac{a}{\pi^{3/2}} \int_{-\infty}^{\infty} dy\, \frac{e^{-y^2}}{(x-y)^2 + a^2}, \tag{4.43}$$

where $a = A_\alpha/(8\pi\Delta\nu_D)$. Examples of the solutions of Eq. (4.41) and Eq. (4.42) employing the Voigt distribution for three temperatures at a fixed redshift $z = 10$ are shown in Fig. 4.3. Note that the absorption feature due to scattering effects is more prominent for lower temperatures in the continuum case, while it broadens the suppression in the injected spectrum. At higher temperatures, the modification of the continuum spectrum gets milder, while the falloff in injected photons is sharper. In both cases, scattering effects become weaker at higher temperatures, approaching the no-scattering limit (constant and step function spectrum, respectively for continuum and injected photons).

4.3.2 Lyα scattering rate

The deviation of the Lyα intensity due to line scattering can be quantified defining the quantity

$$S_{\alpha,a} = \int dx \phi(x) \frac{J_{a,\nu}(x)}{J_{a,\infty}}, \tag{4.44}$$

for $a = c, i$. Note that $S_{\alpha,a}$ depends only on the shape of the spectrum and not on its normalization. Then, the Lyα scattering rate can be written from Eq. (4.33) as

$$P_\alpha = 4\pi\sigma_0 \int dx \phi(x) J(x) = 4\pi\sigma_0 S_\alpha J_{\alpha,\infty}, \tag{4.45}$$

where it has been implicitly summed over the continuum and injected contributions. Hence, from Eqs. (4.27), (4.32) and (4.45), the Lyα coupling coefficient can be written as

$$x_\alpha = \frac{16\pi\sigma_0 T_*}{27 A_{10} T_\gamma} S_\alpha J_{\alpha,\infty}, \tag{4.46}$$

which shall be used to compute the spin temperature. The flux far from the line, $J_{\alpha,\infty}$, is determined by the astrophysical model and cosmological evolution, and it will be computed in the next chapter. However, the factor S_α is only determined by the integrated spectrum, and therefore it does not depend on the specific astrophysical parameters, being a function of the temperature and redshift (or, more specifically, of temperature and the Sobolev parameter γ_S). This quantity accounts for scattering effects in the flux, and is usually of order ~ 1. The integrals of Eqs. (4.39) and (4.42) cannot be solved analytically, although there are numerical fits for $S_{\alpha,a}$ in the literature, such as the one from Ref. [371], employed in the code `21cmFAST` [378] (widely used in Part II). It is possible however to approximate the shape of the line profile to obtain analytic results, as done in the so-called *wing approximation*, with a remarkable agreement with numerical computations [376, 372]. Although that solution is given in terms of hypergeometric functions, an accurate fit following this approximation can be derived [376], writing

$$S_\alpha \simeq \exp\left[-1.79\,\alpha\right], \tag{4.47}$$

with $\alpha = \eta \left(3A_\alpha/(8\pi\Delta\nu_D\gamma_S)\right)^{1/3} = 0.717 T_K^{-2/3} (\tau_{GP}/10^6)^{1/3}$ [10]. From this it can be seen that S_α is close to unity at large temperatures and low optical depths (which correspond to low redshifts in a mostly neutral medium, see

[10] Other approximate fits slightly more accurate can be found in Ref. [372].

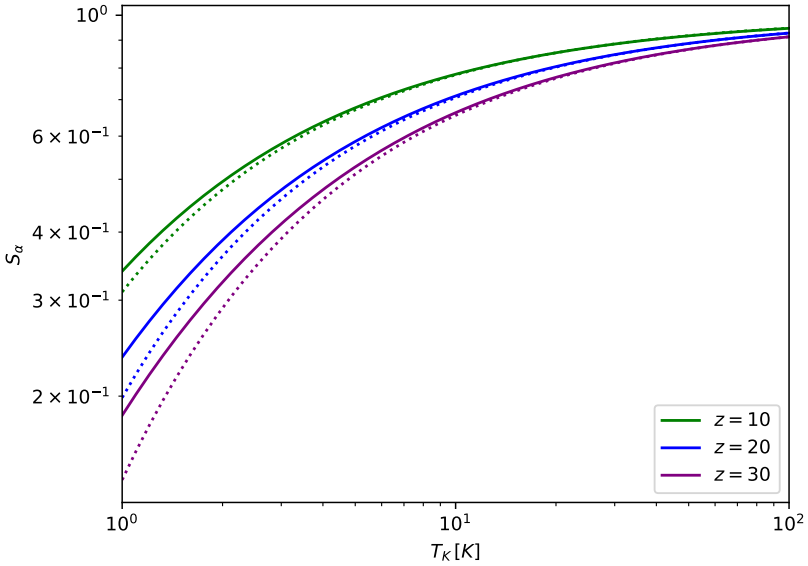

Figure 4.4: S_α (for continuum photons) as a function of the kinetic temperature T_K, at several redshifts. Continuous lines stand for the exact case, while dotted lines correspond to the simple fit from Eq. (4.47) [376].

Eq. (4.36)), being damped in the opposite case. This behavior can be verified in Fig. 4.4, which depicts the variation of S_α with the temperature at different redshifts, for the exact calculation (i.e., integrating Eq. (4.41)) and for the fit in Eq. (4.47). In the shown cases, spin exchange effects have been neglected, which is a good enough approximation as long as $T_K, T_S \gg T_{se} = 0.40$ K. Otherwise, S_α depends on T_S, via the modifications of η and γ_S described above.

4.3.3 Color temperature

Although the Lyα spectrum is not an equilibrium spectrum, and therefore it does not have a definite temperature, one can define an effective *color temperature* as [372]

$$\frac{h}{k_B T_c(\nu)} \equiv -\frac{1}{f(\nu)} \frac{df(\nu)}{d\nu}, \tag{4.48}$$

where $f(\nu) = J/(2\nu^2/c^2)$ is the photon occupation number. Note that, with the above definition, if T_c is a constant of the frequency, one recovers a thermal spectrum with that temperature (a Maxwell-Boltzmann distribution for high energies, since stimulated emission is neglected). It must be emphasized that the color temperature from Eq. (4.48) would not have to be necessarily the same as the one implicitly defined in Eq. (4.25). However, it can be shown that both temperatures coincide if the Lyα line profile

is narrow enough [379]. One can employ the calculations from the previous section to predict the color temperature for Eq. (4.48) (and equivalently for Eq. (4.25) if the previous argument holds). Employing Eq. (4.39), this temperature can be written as

$$\frac{h}{k_B T_c(x)} = \frac{2\eta}{\Delta\nu_D} + \frac{2\gamma_S}{\Delta\nu_D \phi(x)} \left(1 - \frac{J_\infty}{J(x)}\right). \tag{4.49}$$

Including the effect of spin exchange (*i.e.*, substituting $\gamma_S \to \gamma_S(1 + T_{se}/T_K)^{-1}$ and $\eta \to \eta(1 + T_{se}/T_S)/(1 + T_{se}/T_K)$, as commented above), and evaluating the color temperature at the center of the line, one gets

$$T_c = T_K \left[\left(\frac{1 + T_{se}/T_S}{1 + T_{se}/T_K} \right) + \frac{\gamma_S \left(1 + T_{se}/T_K\right)^{-1}}{\eta\phi(0)} \left(1 - \frac{J_\infty}{J(0)}\right) \right]^{-1}, \tag{4.50}$$

where it can be shown that the second term becomes negligible at both low and high temperatures [372]. The above one is an implicit equation: one needs T_c to compute T_S with Eq. (4.26), but T_c also depends on T_S. Therefore, it has to be solved by an iterative procedure, as done in `21cmFAST` [378]. From the previous equation, we can see that when the coupling to the kinetic temperature is efficient enough, $T_c \simeq T_K$ is a good approximation, as stated in Sec. 4.2. In any case, since $T_K, T_S \gg T_{se}$ in most cases of interest, T_K is a very good approximation for the color temperature even without a strong Lyα coupling.

4.3.4 Lyα heating

Scattering around the Lyα line, besides modifying the spectral shape of the radiation field, can also produce an additional heating contribution to the gas temperature. Part of the energy of the Lyα photon can be left in the atom as thermal energy, although depending on the gas temperature, the atoms can also lose energy in this process, becoming a cooling mechanism. This contribution was firstly studied in Ref. [380], under the assumption of neglecting the thermal motion of the atoms. This simplification overestimated the real heating rate, as was shown by the authors of Ref. [370], who calculated it properly from the kinetic equation.

In order to derive the heating contribution from scatterings around the Lyα line, we have to multiply the kinetic equation Eq. (4.37) by the energy $h\nu$ and integrate over frequency. In the case of injected photons, we have to take into account the energy carried by the photons injected in the line, $h\nu_\alpha \dot{n}_\alpha$ [381], where $\dot{n}_\alpha = 4\pi n_{\rm HI}\sigma_0 \mathcal{C}$ is the rate of change in the number of photons, obtained from the integration of Eq. (4.37) over frequency. This contribution vanishes in the case of considering only continuum photons,

since scattering processes conserve photon number. Thus, for either the continuum, $k = c$, or injected case, $k = i$, the heating rate of the gas by Lyα scattering reads

$$\mathcal{Q}|_{\mathrm{Ly}\alpha,\mathrm{k}} = -\frac{4\pi}{c}\int d\nu\, h\nu\, \left(\frac{\partial J}{\partial t} - H\nu\frac{\partial J}{\partial \nu}\right) + h\nu_\alpha \dot{n}_\alpha \tag{4.51}$$

$$= -4\pi n_{\mathrm{HI}}\sigma_0 \int d\nu\, h\nu\, \frac{1}{2}\frac{\partial}{\partial x}\left[\phi\left(\frac{\partial J}{\partial x} + 2\eta J\right)\right] \tag{4.52}$$

$$= 4\pi n_{\mathrm{HI}}\sigma_0 h\Delta\nu_D \int d\nu\, \frac{1}{2}\phi\left(\frac{\partial J}{\partial x} + 2\eta J\right), \tag{4.53}$$

where in the last equality we have integrated by parts. We have also taken into account the fact that the spectral profile vanishes far away from the resonance. Employing Eq. (4.39) for continuum photons, or Eq. (4.40) for injected ones, we can write the heating rate for each channel as [370, 372, 382]

$$\mathcal{Q}|_{\mathrm{Ly}\alpha,\mathrm{c}} = \frac{4\pi H h\nu_\alpha \Delta\nu_D}{c}\, \mathcal{I}_k\, J_\infty^{(k)}, \tag{4.54}$$

where $k = c, i$, and we have defined the continuum and injected heating integrals, $\mathcal{I}_c$ and $\mathcal{I}_i$ respectively, as

$$\mathcal{I}_c = \int_{-\infty}^{\infty} dx\, \frac{(J_{c,\infty} - J_c(x))}{J_{c,\infty}} \tag{4.55}$$

and

$$\mathcal{I}_i = \int_{-\infty}^{0} dx\, \frac{(J_{i,\infty} - J_i(x))}{J_{i,\infty}} - \int_0^{\infty} dx \frac{J_i(x)}{J_{i,\infty}}. \tag{4.56}$$

The integrals I_c and I_i encode the details on the scattering effects and, as happened with the S_α factor, do not depend on the normalization, but only on the redshift and the temperature, or equivalently, on the temperature and the Sobolev parameter γ_S. Numerical fits for these quantities, based on the wing approximation, can be found in Ref. [372]. The importance of this heating mechanism in the evolution of the IGM is however mild, as shall be discussed in the next chapter.

4.4 21 cm power spectrum

The most obvious measurement of the 21 cm signal comes from averaging the incoming radiation from all sky directions, which is known as the *global signal* $\overline{\delta T_b}$, corresponding to take the mean value of Eq. (4.21). While this spatially averaged signature could provide a superb source to

understand the IGM evolution, it lacks some information about inhomogeneities. The signal is enhanced in overdense regions, and thus sensitive to the pattern of the cosmic web and distribution of galaxies and halos. Processes such as X-ray heating and reionization are expected to be highly inhomogeneous, since radiation fields would expand around galaxies, and their complex behavior cannot be completely encoded in a spatially averaged quantity. Moreover, the main experimental caveats to measure the global signal are the strong foregrounds from the galactic synchrotron emission and the effect of the ionosphere, which are more easily removed if different spatial scales are considered, as shall be discussed in Sec. 4.5. It is therefore mandatory to study not only the global signal but also its spatial fluctuations, via higher order statistics. The two-point correlation function is the most obvious choice. Given that radiointerferometers extract information about the Fourier modes of the signal, it is natural to work in Fourier space, rather than in real space, employing thus the power spectrum, as done in Sec. 2.2.1 for the matter density field. The two-point statistics are of remarkable importance, since for gaussian fields, they present all the information of the distribution.

Defining the normalized fluctuation of the 21 cm signal from Eq. (4.21) as

$$\delta_{21}(z,\mathbf{r}) = \frac{\delta T_b(z,\mathbf{r}) - \overline{\delta T_b}(z)}{\overline{\delta T_b}(z)}, \tag{4.57}$$

one can take its Fourier transform, as defined in Chapter 2, denoted as $\widetilde{\delta}_{21}(z,\mathbf{k})$. Therefore, equivalently to Eq. (2.10), the 21cm differential brightness temperature power spectrum is defined as

$$\langle \widetilde{\delta}_{21}(z,\mathbf{k}) \widetilde{\delta}^*_{21}(z,\mathbf{k}') \rangle \equiv (2\pi)^3 \delta^{\mathrm{D}}(\mathbf{k}-\mathbf{k}') P_{21}(z,k) \ . \tag{4.58}$$

In the previous equation, the delta function accounts for invariance under translations. On the other hand, invariance under rotations imply that the power spectrum only depends on the modulus of the wavevector $\mathbf{k}$. These facts are the consequences of statistical homogeneity and isotropy, respectively. Instead of P_{21}, it is customary to work with the dimensionless power spectrum, defined as $\Delta^2_{21}(k,z) = (k^3/2\pi^2) P_{21}(k,z)$. Since this quantity may present singularities when $\overline{\delta T_b}(z)$ vanishes, we rather employ the product $\overline{\delta T_b}^2(z)\Delta^2_{21}(k,z)$, which has units of temperature squared.

One can gain insight into the different contributions to the brightness temperature field by linearizing Eq. (4.21). Employing the spin temperature equation, Eq. (4.26), the fluctuation of the 21 cm signal can be written as [354, 353]

$$\delta_{21} = \beta\delta + \beta_x\delta_x + \beta_\alpha\delta_\alpha + \beta_T\delta_T - \delta_{\partial v}, \tag{4.59}$$

with each δ_i accounts for the fluctuations of the different fields: δ for the matter density field, δ_x for the neutral fraction, δ_α for the Lyα flux, δ_T

for the kinetic temperature of the gas and $\delta_{\partial v}$ for the line-of-sight gradient of the peculiar velocities. The functions β_i weight the importance of each fluctuation in the 21 cm one, and a straightforward computation shows

$$\beta = 1 + \frac{x_c}{x_{\rm tot}(1 + x_{\rm tot})}, \tag{4.60}$$

$$\beta_x = 1 + \frac{x_c^{\rm HH} - x_c^{\rm eH}}{x_{\rm tot}(1 + x_{\rm tot})}, \tag{4.61}$$

$$\beta_\alpha = \frac{x_\alpha}{x_{\rm tot}(1 + x_{\rm tot})}, \tag{4.62}$$

$$\beta_T = \frac{T_\gamma}{T_K - T_\gamma} + \frac{1}{x_{\rm tot}(1 + x_{\rm tot})} \left(x_c^{\rm eH} \frac{d \ln \kappa_{10}^{\rm eH}}{d \ln T_K} + x_c^{\rm HH} \frac{d \ln \kappa_{10}^{\rm HH}}{d \ln T_K} \right), \tag{4.63}$$

with $x_{\rm tot} = x_\alpha + x_c$, and $x_c^{\rm eH}$ and $x_c^{\rm HH}$ accounting only for the eH and HH contributions to the collisional coupling, respectively. Therefore, fluctuations in the brightness temperature can be regarded as a weighted sum over the fluctuations of the different fields on which it depends. To derive the previous equations, $T_c = T_K$ has been assumed for the sake of simplicity, which is a reasonable assumption, as stated in the previous section.

The unity terms of β and β_x come from the proportionality of the brightness temperature to the density and the ionization fraction, respectively, while the second term includes the contribution from collisional coupling, only relevant at high redshifts or overdense regions. The first term of the temperature coefficient β_T accounts for how fast the spin temperature changes under fluctuations in T_K, while the second one comes from the temperature dependence on the collisional coupling coefficients. The first one presents a singularity when $T_K = T_\gamma$, but this is unphysical and disappears in the quantity $\overline{\delta T_b}^2(z)\Delta_{21}^2(k, z)$. The β_α is proportional to the Lyα coupling coefficient. Understanding the behavior of these coefficients can shed light on the evolution of the power spectrum, which shall be discussed in the next chapter.

In principle, it is possible to study the evolution of first order perturbations, by linearizing the evolution equations of the temperature and ionization fraction (which shall be explained in the next chapter), as done with the matter density field. This approach has been followed in the literature [383, 384], but since IGM processes become non-linear at some moment, its range of validity is limited. Although we shall compute the 21 cm power spectrum from the non-linear evolved fields in our numerical simulations, it is useful to overview these linear quantities to qualitatively understand the evolution of the power spectrum.

It can be argued that the different δ_i may be proportional to the overdensity δ in the linear limit. This is easily seen in the case of the temperature perturbation δ_T, before the onset of heating, as long as the sound speed is spatially constant. Writing the pressure as $P = \rho k_B T_K/\mu$, with μ the molecular weight and ρ the mass density, $c_s^2 = dP/d\rho = k_B T_K/\mu + (\rho k_B/\mu) dT_K/d\rho$ and thus $\delta_T = (\rho/T_K) dT_K/d\rho\delta = [c_s^2/(k_B T_K/\mu) - 1]\,\delta$ [383]. From the linearized ionization equation, before the galactic sources are switched on, the evolution is dictated by recombinations, whose rate is proportional to δ, and thus $\delta_x \propto \delta$ (the details of ionization evolution shall be properly discussed in the next chapter). When X-rays are starting to be efficiently emitted, the previous arguments would not be valid. Nevertheless, X-ray photons are radiated from the galaxies placed at the overdensities, and thus would also be related to δ. An analogous reasoning can be applied to the Lyα flux, δ_α. Finally, in linear theory, the redshift-space distortions term can be easily computed, getting $\delta_{\partial v} \simeq -\cos^2\theta f\delta$, where θ is the angle between the direction of the line of sight and the wavevector, and $f = d\ln D/d\ln a$ ($= 1$ in the Einstein-de Sitter universe) [30], with D the growth factor defined in 2.2.1. Therefore, the 21 cm power spectrum approximately traces the matter power spectrum, weighted by combinations of the β_i functions. However, the actual behavior of the different fluctuations implies extra dependences with the scale for each δ_i, since astrophysical processes are highly inhomogeneous [384]. For this reason, the matter power spectrum cannot be trivially extracted from the 21 cm one.

Finally, it is noteworthy that, unlike the CMB, the 21 cm signal is expected to be non-gaussian. This is due to the growth of perturbations into the non-linear regime, where deviations from gaussianity are developed (as happens in standard perturbation theory at higher order, see, e.g., [385]). Therefore, the power spectrum could not provide the full statistical information about its fluctuations. Although not considered in this thesis, other summary statistics have been exploited in the literature, and could be extremely useful to understand the signal. For instance, the bispectrum (three-point correlation function in Fourier space) encodes information not only about the magnitude of the field but also about its complex phases (which is related to the filamentarity) [386, 387, 388]. On the other hand, Minkowski functionals supply information regarding the morphology and shapes of the structures, especially useful to gain insight into the growth of HII bubbles during the EoR [389, 390, 391, 392].

4.5 Observational tests of the 21 cm cosmological signature

The observation of the redshifted HI cosmological signal is one of the greatest challenges in current observational astronomy. Thus, the requisites to measure this signature need to be critically evaluated. Given the strong foregrounds and the faintness of the signal, achieving a great sensitivity is a crucial point, and large collecting areas and long integration times are needed. Unlike the CMB, 21 cm photons may provide snapshots for different redshifts, which allows attempting a 3D tomographic view of the IGM. In order to make a 3D map of the universe and to obtain information from different epochs, broadband antennas are required, spanning over a large range of frequencies. As already stated, photons observed at a frequency ν are redshifted from its absorption or emission by the hyperfine transition with a frequency $\nu_0 = 1420$ MHz at redshift z, such that $\nu = \nu_0/(1+z)$. Therefore, the range of frequencies observed provides information from a given epoch (although higher redshifts can also be reached employing Fourier modes along the line of sight in scale dependent measurements [393]).

Depending on the task, either single stations or interferometric arrays of antennas could be employed to detect radio frequencies. One of the key differences between both approaches is the spatial resolution. In a single antenna, usually designated as *dish* (although often they do not have that shape), the angular resolution θ is determined by the wavelength λ of the observed radiation and the characteristic size of the antenna L, as [393]

$$\theta \simeq \frac{\lambda}{L}\,. \tag{4.64}$$

On the other hand, instead of employing one unique dish, it is possible to employ interferometric techniques to correlate many of them, acting as a huge effective antenna which enlarges the collecting area. These telescopes are known as *interferometers*, and are characterized, among other parameters, by the number of antennas and the maximum baseline distance, which is roughly the maximum length covered by the array. The observation of a given Fourier mode can be performed by the correlation of a pair of antennas separated by a baseline distance b. In this case, the angular resolution reads

$$\theta \simeq \frac{\lambda}{b}\,. \tag{4.65}$$

While single dish experiments usually have sizes of tens of meters (being the Green Bank Telescope with 100 m the largest of the world [394]), interferometers may spread over tens of kilometers, which allow them to reach much

larger resolutions. Selecting pairs of antennas with different baseline distances, distinct Fourier modes could be probed. For this reason, in order to observe the 21 cm fluctuations, interferometers are the proper choice. However, these installations may be extremely expensive. Experiments committed to measure the global average signal do not need such a high resolution, and could work with single dishes. In the case of the interferometers, the maximum baseline is of great relevance since it sets the maximum angular resolution which can be achieved at a given wavelength. And equivalently, the minimum baseline between two antennas determines the largest spatial scales which interferometers are sensitive to. More explicitly, the wavenumber k is proportional to the baseline distance b [355], and thus, inversely proportional to the angular resolution θ. In interferometers, the size of antennas has also a great importance since it determines, together with the number of elements, the total collecting area. The larger it is, the better the sensitivity gets, and the fainter the signals that can be detected are. Finally, from the equations above it can be noticed that the wavelength of observation also determines the observable scale. As a consequence, low frequency radiation, redshifted from older epochs such as the Dark Ages, cannot be as well resolved as photons with larger frequencies.

4.5.1 Foregrounds

Unlike the CMB, whose temperature is relatively free from foregrounds at the observed frequencies, in the case of the 21 cm line they become the major issue to overcome. These contaminants can be 3 or 4 orders of magnitude larger than the cosmological brightness temperature, which makes understanding its behavior mandatory in order to extract cosmological information.

There are two main sources of foregrounds from cosmic origins [355]: *i)* galactic foregrounds, given by diffuse synchrotron and free-free emission from the Milky Way (such as thermal bremsstrahlung of free electrons scattering off free ions without being captured), and *ii)* extragalactic foregrounds, as radio emission from Active Galactic Nuclei (AGN) and star-forming galaxies. While the former are mostly important at large scales, being important for angular scales larger than a degree, the latter dominates at smaller scales. The synchrotron emission in the Milky Way is produced by relativistic cosmic-ray electrons accelerated in supernovae remnants and other sources, which typically present a power law energy spectrum. This implies that their synchrotron emission has also a power-law spectral shape [238]. Since the galactic plane contains most of stars, supernovae are more common there, where cosmic rays originate. This leads to a stronger synchrotron emission along this plane. On the other hand, AGN are powered

by accretion of matter onto a central supermassive BH, which can present strong radio emission. Star forming galaxies can also present synchrotron and free-free emission in a similar way to the Milky Way. In each case, power laws can describe their spectra. Therefore, in both galactic and extragalactic foregrounds, given the characteristic spectra of AGN, synchrotron and free-free emission, both contributions are expected to be smoothly varying in frequency, which is a key point for their removal. The characteristic decaying power-law shape provides larger foregrounds at lower frequencies, which makes harder to detect signals from distant epochs, such as the Dark Ages, whose photons have redshifted more.

Employing scale-dependent statistics, such as the power spectrum, allows removing the foregrounds much more easily than in the global signal case. This is because, at some scales, gradients in the inhomogeneous signal could present a sharp evolution. This is, for instance, what happens at the edges of the ionized bubbles, where the signal varies abruptly along short distances. These sudden changes contrast with the astrophysical foregrounds, which vary much more smoothly, due to the synchrotron and free-free spectra, which can be easily separated from the cosmological signal.

Besides the cosmic foregrounds, the presence of the ionosphere can also impact the observed signal. It is specially important at the lowest radio frequencies, becoming an even harder task to observe signals from distant epochs, such as the Dark Ages. The most effective way to mitigate their effect would be to observe from outside the Earth, as proposed in several telescopes discussed in the following sections.

In interferometric searches, an alternative to foreground removal is *foreground avoidance*, based on observing modes where foregrounds are suppressed. The Fourier space can be decomposed in wavenumbers parallel and perpendicular to the line of sight, $(k_\parallel, k_\perp)$. The frequency axis corresponds to the line of sight direction. Thus, spectrally smooth foregrounds would be mostly compacted in the lowest $k_\parallel$ modes. This defines a region in the Fourier space, where foregrounds are restricted, and then can be avoided by looking away. However, due to chromatic instrumental effects which imprint unsmooth spectral features, the dominance of foregrounds extends towards large $k_\perp$ at higher $k_\parallel$, shaping a *wedge* in Fourier space [395]. Luckily, this region is relatively well delimited, allowing to evade the contaminated modes. Foreground avoidance presents an advantage since allows to elude possible biases from foregrounds fitting. The drawback of this method is that the number of accessible scales becomes significantly reduced. The subtleties of this procedure are discussed in, e.g., Refs. [393, 396, 397].

4.5.2 Global signal experiments

Attempting to measure the global averaged signal is one of the primary goals of observational 21 cm cosmology. These measurements correspond to the monopole in a spherical harmonics decomposition, typical in CMB studies. Experiments designed to detect the global signature do not need to resolve spatial details on the sky, and are thus commonly carried out by single antennas that have wide beams, rather than large interferometric arrays, as happens with experiments focused on measuring fluctuations (although there are exceptions, such as LEDA, as discussed below). For the very same reason, these experiments can also employ coarser frequency channels with larger bandwidths, with no need for a spectral resolution as large as the experiments searching for fluctuations. The mitigation of cosmic and ionosphere foregrounds, which requires a precise calibration, becomes the greatest challenge. However, an epoch of rapid reionization, with an abrupt drop in the signal, may be different enough from the smoothly varying foregrounds, fact which has been used to rule out too fast and sharp reionization processes, placing constraints on the timing and duration of the EoR. The most relevant experiments pursuing the global signature are listed in what follows (see, e.g., Refs. [398, 399] for more details).

- The Experiment to Detect the Global EoR Signature (EDGES) [400] is located at Murchison Radio-astronomy Observatory in Western Australia, and composed by a single dipole antenna. Early measurements were able to rule out very rapid EoR [401]. The most remarkable result was announced in 2018, when its team reported the evidence of an absorption profile in the low-band spectrum (50-100 MHz), centered around 78 MHz (corresponding to $z \sim 17$), with an amplitude of ~ 0.5 K [36]. This deep trough is roughly twice the maximum predicted within the context of the ΛCDM model. The implications and caveats of this measurement are discussed in Sec. 4.5.3. Regardless of this absorption feature, high-band measurements spanning 90-190 MHz [402] have been employed to constrain the astrophysical parameter space from Cosmic Dawn to the EoR [403, 404, 405].

- The Shaped Antenna to measure the background RAdio Spectrum (SARAS) [406] was sited at the Raman Research Institute in India, although it has been its upgraded version, SARAS 2 [407] at Timbaktu Collective in Southern India, the one which have offered more competitive results. Using its observations at frequencies 110-200 MHz, rapid periods of reionization have been constrained [408]. Furthermore, SARAS 2 has ruled out several astrophysical models which present a very cold IGM at the epoch of the Cosmic Dawn, which

would lead to large amplitudes in the global signal [408, 409]. Note that this may be in tension with the EDGES results.

- The Large-Aperture Experiment to Detect the Dark Ages (LEDA) [410, 411] is placed on the Long Wavelength Array stations at Owens Valley Radio Observatory (OVRO-LWA), in California, USA. Unlike other global signal single-antenna experiments, it is formed by ~ 250 dipole antennas spread over an area of ~ 200 m of diameter, constituting an interferometric array capable of observing frequencies between 30 and 88 MHz, which may probe the Cosmic Dawn epoch (redshifts $16 < z < 34$). LEDA observations allowed to place limits on the amplitude and width of the 21 cm absorption profile at $z \sim 20$ [412].

- The Dark Ages Polarimeter Pathfinder (DAPPER) [413, 414] is an ambitious space based project to put into orbit a spacecraft in the dark side of the Moon, avoiding therefore the ionosphere foregrounds. Unlike the previous experiments, it is at the planning stage and has not been built yet. It is designed to operate at very low frequencies, between 10-110 MHz, being able in principle to reach the Dark Ages, at redshifts $z \sim 36 - 83$. It was preceded by the proposal of the Dark Ages Radio Explorer (DARE) [415, 416].

4.5.3 The EDGES affair

The reported absorption profile by the EDGES collaboration in the low-band spectrum (50-100 MHz) has supposed a major result in the last years, given its unexpected shape. In order to explain such a deep absorption trough, there are two main possibilities, as can be seen from equation Eq. (4.21): either *i)* the spin temperature (and thus the kinetic one) is very cold, or *ii)* the CMB background T_γ has extra contributions at radio frequencies.

Standard evolution histories within the ΛCDM scenario limit the coldest kinetic temperature attainable, since the only cooling process efficient at this regime is due to adiabatic expansion, $T_K \propto a^{-2}$. Figure 4.5 shows a sample of such extremely optimistic scenario in blue, with the largest possible amplitude within the standard picture, compared to the EDGES result in red. Even with the spin temperature completely coupled to the adiabatic one at these epochs, the largest possible signals could not exceed ~ -250 mK at $z \sim 17$. The issue gets worse for more realistic scenarios, as the one shown in purple, where heating of the IGM and the non-perfect coupling of the spin temperature to the kinetic one have been taken into account properly (as shall be reviewed in Chapter 5). The EDGES measurement may thus imply that extra cooling processes are present during the Cosmic

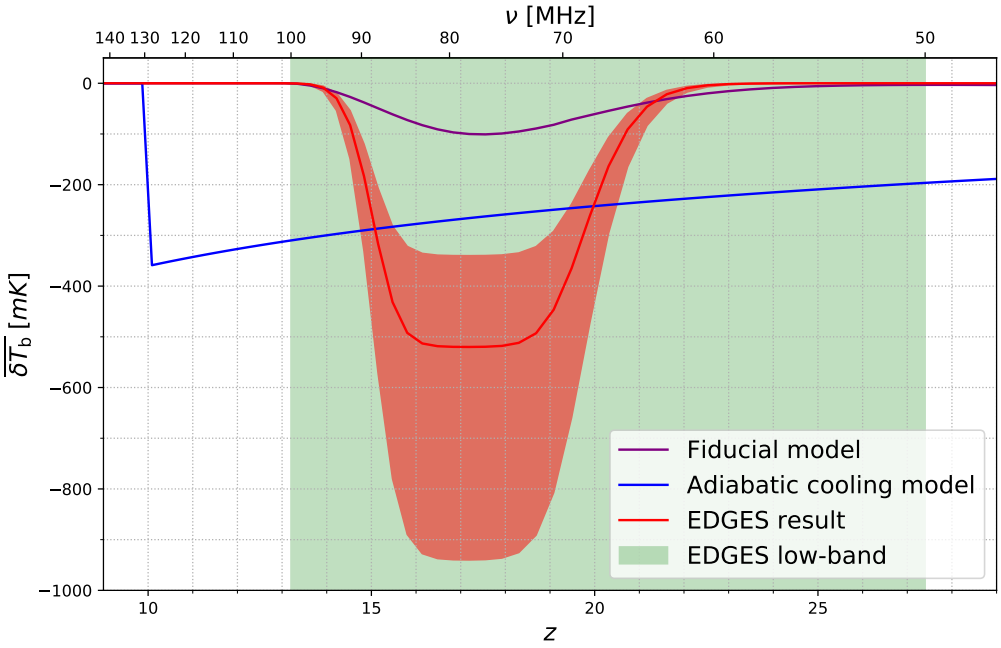

Figure 4.5: Global 21 cm brightness temperature for the best fit to explain the EDGES absorption feature shown in red, with its 99% CL interval [36]. EDGES low-band data lie in the range covered by the green region. For comparison, an extreme case with adiabatic cooling, T_S completely coupled to T_K and instantaneous reionization at $z \sim 10$ is also included in blue, as well as a fiducial model shown in purple computed from `21cmFAST` [378] such that it presents the absorption dip at roughly the same redshifts (see Chapter 5 for a detailed discussion on the evolution of the brightness temperature and the astrophysical processes involved).

Dawn and Dark Ages to drive the spin temperature to such a low value. Following this idea, many authors have proposed non-standard scenarios to achieve a cooler IGM. This is the case of DM-baryon interactions, which would transfer thermal energy from the gas to the DM particles [417, 418, 419, 420, 421, 422]. An early Dark Energy period could provide an earlier decoupling of the gas temperature from the Compton interactions, giving more time to cool adiabatically [423].

The excess of radio radiation at the epoch of the Cosmic Dawn has also been suggested as a possible way to increase T_γ and thus explain the EDGES signal [424]. However, it has been argued that the diffuse radio background from astrophysical origins, by either synchrotron or inverse-Compton scattering due to relativistic electrons, seems unlikely to explain the signal. This is because the radio emissivity required to enhance T_γ should be enlarged by a factor from 10^3 to 10^6 respect to the local $z = 0$ estimates [425, 426]. However, the existence of soft photon emission at low radio frequencies from light DM, such as axion-like particles, may account

for the required background [427, 428, 429]. Accretion onto intermediate-mass black holes has also been proposed to produce the required extra radio emission [430, 431].

Besides trying to explain the signal, the EDGES result has also been used to constrain different DM models, such as DM annihilation [432, 433], DM decay [434], WDM [435, 436], PBHs [350, 351, 352] or FDM [437, 436]. In Part II of this thesis, an example of this is shown, constraining IDM and WDM models making use of the timing of the EDGES signal [5]. The consistency of the EDGES result with other experimental constraints from EoR and CMB have also been explored, even though that work is not included in this thesis [8].

Thus, although some (exotic) solutions may be able to explain the EDGES result, it also presents some controversy within the scientific community for other reasons. It has not been confirmed yet by other experiments. Observations of SARAS 2 at similar range of frequencies have ruled out models which should show such a deep absorption trough, being in tension with the EDGES finding [408, 409]. The shape of the signal extracted from the data is also highly non-trivial and not well understood. The absorption model to fit the data employed in [36] was chosen to be a flattened gaussian, with no clear interpretation from physical grounds. The broad dip suggests a relatively extended epoch around $z \sim 17$ with constant temperature, which can not be explained within current IGM evolutionary models. In fact, when one attempts to accommodate the astrophysical modeling of the signal to the EDGES data, the width of the absorption dip can only be fitted in models with high heating, opposite to what is required to obtain large amplitudes, suggesting an additional inconsistency between the measurement and canonical astrophysical scenarios [8].

In addition, several caveats regarding the treatment of foregrounds and calibration have been claimed, which could invalidate the measurement. Although the EDGES calibration has been carefully scrutinized by the team during 10 years, some concerns about possible systematics have been raised. A possible ground plane artifact may produce such a broad absorption signal, as was shown by Ref. [438]. This would induce one or several resonances in the data, which could be confused with a cosmological signal. The authors found that three of these resonant features with no 21 cm signal provided a fit as good as the one obtained by EDGES. Remarkably, the best-fit resonant frequencies were in good agreement with those estimated for a ground plane artifact, considering the dimensions of the square patch and properties of the soil.

Furthermore, Ref. [439] found that different foreground and absorption models could fit the EDGES signal. It was shown that the best fit paramet-

ers for the ionospheric foregrounds employed by EDGES were not physical, since they imply optical depths and temperatures of the ionosphere with negative values. In addition, it was found that two gaussians or a sinusoidal feature with no absorption signal can provide a fit to the spectrum as good as the one presented by the EDGES collaboration. These non-cosmological features could be a consequence of some sort of overlooked systematics, such as the one proposed by [438].

The authors of Ref. [440] further analyzed these questions, by employing a Bayesian evidence-based comparison over a broad amount of models. They discussed different models for the signal, including physical motivated ones from simulations varying astrophysical parameters. Cosmic and ionospheric foregrounds, as well as possible calibration errors with sinusoidal shapes, were also considered. It was found that models including calibration systematics were decisively preferred. Moreover, models with amplitudes consistent with the standard cosmological scenario were present among the best fitting models. Furthermore, they did not find strong evidence to favor models exhibiting 21 cm signal over those without one. All these facts place reasonable doubts about whether it is possible to infer an actual 21 cm cosmological measurement from the EDGES data.

All the above references show the great impact that the EDGES result have left on the astrophysics and cosmology communities. However, the aforementioned caveats place important concerns regarding the validity of this measurement, which can only be confirmed by upcoming observations from future radiotelescopes.

4.5.4 21 cm power spectrum experiments

Although detecting the global signature is of significative importance, the information which can be extracted from it is limited, and the experimental challenges and caveats are numerous. For this reason, most observational efforts are devoted to detect the spatial fluctuations of the 21 cm signal, which would enable a multi-scale view of the Hydrogen map, and an easier removal of the foregrounds. Interferometry based on large arrays of antennas conforms the proper tool to access small scales. Interferometers offer a natural way to directly estimate the power spectrum of an astronomical image. This is because the voltage induced in a pair of antennas can be correlated, providing the visibility, which is nothing but the Fourier transform of the perceived intensity of the radiation [458, 355]. Moreover, as already mentioned, foregrounds can be more easily treated than when dealing with global measurements.

Facility	Location	ν [MHz]	z	$N_{\rm ant}$	$b_{\rm max}$ [km]
GMRT	India	50-1420	0-27	30	30
MWA	Australia	70-90, 135-195	15-19, 6-10	128	5
LOFAR	Netherlands	30-80, 120-190	17-46, 6-11	50–60	50
PAPER	South Africa	110-180	7–12	64	0.210
OVRO-LWA	USA	27-88	15-52	288	< 1.5
LEDA	USA	45-88	15-30	256	< 10
HERA*	South Africa	50-250	5-27	350	< 1
SKA-low*	Australia	50-350	4-27	$\sim 10^5$	65
SKA-mid*	South Africa	350-15.3$\times 10^3$	0-4	197	150

Table 4.1: List of current and future interferometers attempting to measure the spatial fluctuations of the 21 cm signal, including its location, range of frequencies of operation ν, accessible redshifts z, number of antennas $N_{\rm ant}$, and maximum baseline attainable $b_{\rm max}$. Experiments marked with an asterisk (*) are not completed yet. Note that LEDA, despite being an interferometer, is devoted to detect the global signal rather than 21 cm fluctuations.

The achieved sensitivity is subject to different aspects of the experimental design and systematics. It is also limited by the spatial scales and redshifts to be observed. Among the possible sources of noise, the most important one is thermal noise. Thermal fluctuations in the apparatus produce a gaussian white-noise signal (i.e., scale independent) characterized by its root-mean-square $T_{N,rms}$ [458]. Thus, the thermal noise at a single baseline goes as $\overline{\delta T_b}^2(z)\Delta^2_{21}(k,z) \sim k^3 T^2_{N,rms}$. This implies that the sensitivity worsens at very small scales. Furthermore, due to the factor to convert from angles and bandwidth to cosmological distances, this noise also increases with redshift, roughly as $(1+z)^{5/2}$ [459]. Therefore, distant sources (i.e., remote epochs) become more difficult to observe by a limitation in the sensitivity, and not only by the effect of foregrounds. In order to calculate the sensitivity of a full interferometric array, one must sum up the contributions by each baseline over all the Fourier modes. Combining independent k modes, the sensitivity can be improved, with a noise dependence of $\sim k^{5/2}$ rather than k^3. Moreover, if different baselines measure the same Fourier modes, having redundant observations, the total noise decreases with the number of antennas as $N^{-1}_{\rm ant}$. This dependence is easy to interpret, given that the power spectrum is a sort of variance, which typically decreases with $N^{-1}_{\rm ant}$ when independent measurements are taken into account. It is thus auspicious to have interferometers with a large number of dishes,

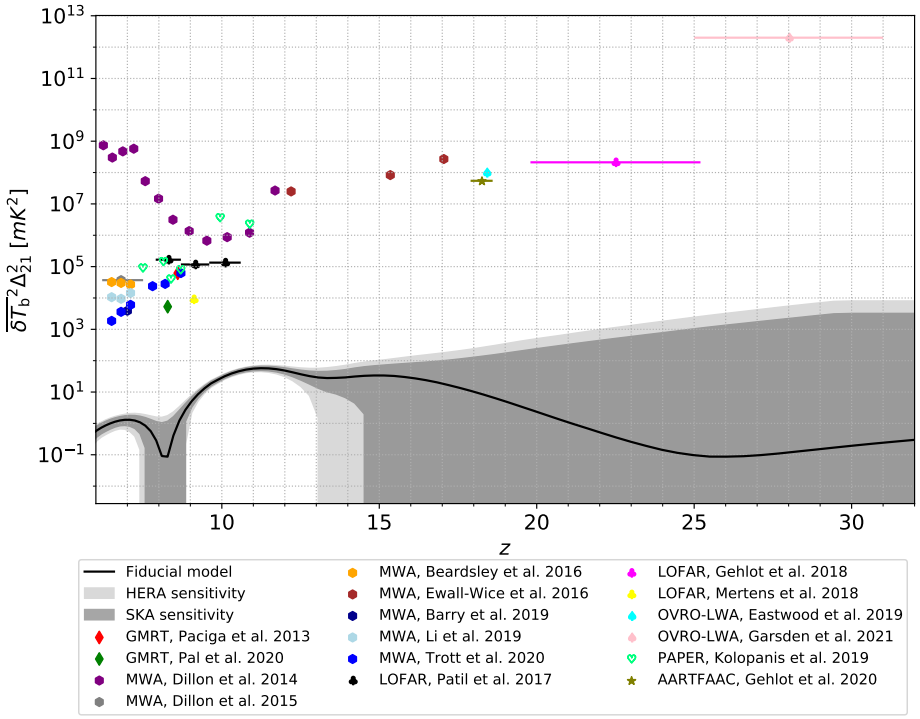

Figure 4.6: Summary of upper limits on the 21 cm power spectrum. The dots denote the bounds found by the experiments GMRT [441, 442], MWA [397, 443, 444, 445, 446, 447, 448], LOFAR [449, 450, 451], OVRO-LWA [452, 453], PAPER [454] and AARTFAAC (an extension to LOFAR) [455]. Most of them lie between the wavenumbers $k = 0.1$ and $0.5\ h$/Mpc, except the ones from Refs. [442] and [450] (note also that Ref. [449] presents stronger limits at $k = 0.053\ h$/Mpc). The continuous black line corresponds to a fiducial theoretical model computed with `21cmFAST` [378], at $k = 0.2\ h$/Mpc (details regarding its evolution and the astrophysical modeling are discussed in Chapter 5). Gray bands depict the forecasted sensitivities for the HERA and SKA experiments, computed via the code `21cmSense`[11] [456]. The script to generate this figure has been made publicly available[12] [457].

placed at regular grids to probe the same Fourier modes, in order to improve the sensitivity, see Refs. [458, 459] for more details on these regards.

Thus far, none of the existing experiments has achieved a detection of the 21 cm fluctuations from the pre-EoR universe (although some cross-correlation with other probes have been detected from the post-EoR low redshift universe, as discussed below). However, current radiointerferometers have placed remarkable upper limits on the amplitude of the fluctuations, increasingly tighter over the years, which have constrained the possible thermal evolution histories. The current upper bounds are shown in Fig. 4.6, together with a fiducial model of the 21 cm power spectrum. In the

[11] https://github.com/jpober/21cmSense
[12] https://github.com/PabloVD/21cmBounds

following, we comment on the interferometer experiments which have been able to place constraints on the 21 cm fluctuations amplitude from epochs between the Cosmic Dawn and the EoR, which are also listed in Tab. 4.1. For more information, see, e.g., Refs. [393, 355, 398, 460].

- The Giant Metrewave Radio Telescope (GMRT) [461] is an array located in Maharashtra, India, for low-frequency general purposes. It consists of 30 dishes of 45 m of diameter, spread over 25 km. It allows observing in 6 frequency bands, covering from 50 to 1420 MHz. Reionization and post-EoR epochs have been studied with this instrument, being pioneer in the treatment of foregrounds and their removal employing spatial correlations. Although not optimized for the cosmological 21 cm signal, it has been the first one to place upper limits at redshifts relevant for the EoR, at $z \sim 9$ [462], being subsequently revised (and significantly weakened) [441]. A stringent constraint has also been recently proposed at $z \simeq 8$ [442].

- The Murchison Widefield Array (MWA) [37] is located in the Murchison Radio-astronomy Observatory, at the Western Australian desert. It consisted of 128 elements in its Phase I (2013-2016), being increased to 256 with longer baselines since 2016. Each of these elements is formed by a tile of 4×4 grid of crossed dipole antennas, ranging from 70 to 300 MHz. The MWA has published several upper limits covering a broad range of epochs, from the EoR, at redshifts $z \sim 6$ to 11 [397, 443, 444, 446, 447, 448], to Cosmic Dawn [445], constraining redshifts $z \sim 12, 15$ and 17.

- The Donald C. Backer Precision Array for Probing the Epoch of Reionization (PAPER) [463, 464] is an interferometer designed and optimized for observations of the EoR, operating between 100 and 200 MHz. It consisted of two stations, a preliminary one with 32 antennas sited at Green Bank, West Virginia, USA, for testing, and the main installations for scientific research with 64 antennas placed at the South African Karoo desert. Its team pioneered ways to improve the sensitivity, proposing methods such as maximizing redundant observations of the same Fourier modes to reduce the noise [458], and the so-called delay spectrum technique to avoid foregrounds [465]. It provided several upper limits at the EoR [466, 467, 468]. However, posterior re-analysis of their data showed errors in their analysis related to the covariance matrices and to an underestimation of the level of signal loss, which invalidated these limits [469, 470]. Nevertheless, they were later updated properly accounting for these errors, significantly weakening the bounds [454] (see [355] for further details on this issue). The PAPER experiment is already deccomissioned,

but its infrastructure in South Africa currently serves for the HERA interferometer.

- The LOw Frequency Array (LOFAR) [38] is a multi-purpose interferometer focused on low frequencies sited at the Netherlands[13]. It includes two types of antennas, covering high-band (110-250 MHz) and low-band (10-90 MHz) observations. While the low-band elements are standard dipole antennas, the high-band ones consist of a tile of 16 individual antennas. Upper limits on the 21 cm power spectrum have been placed using its observations, both at the EoR, covering redshifts $z \sim 8$ to 10 [449, 451], and at the Cosmic Dawn, reaching redshifts from $z \sim 19$ to 25 [450]. An add-on real time transient detector facility appended to LOFAR called Amsterdam-ASTRON Radio Transients Facility And Analysis Center (AARTFAAC) [472] has recently found a stringent upper limit at $z \simeq 18$ [455]. An extension of LOFAR coined NenUFAR, located in Nançay, France, is ongoing, which may serve as a pathfinder for future experiments such as SKA [473].

- The Owens Valley Radio Observatory Long Wavelength Array (OVRO-LWA) is sited in Owens Valley, California, USA. It is formed by 288 dipole antennas spanning from 27 to 85 MHz, arranged in an pseudo-random disposition in a compact core of 200 m of diameter, being thus well suited for transient searches such as gamma ray bursts or exoplanets. Besides that, it has also been employed for constraining the 21 cm fluctuations, finding an upper limit at $z \simeq 18$ [452], and recently in the range $25 < z < 31$, being this one the bound located at the farthest redshift so far [453]. The LEDA facilities are also located at the OVRO-LWA.

All of the aforementioned upper limits on the amplitude of fluctuations are placed at a range of scales spanning $0.1\,h\mathrm{Mpc}^{-1} < k < 1\,h\mathrm{Mpc}^{-1}$ (although the LOFAR ones include also modes down to $k \sim 0.01\ h\mathrm{Mpc}^{-1}$), and are about 2 orders of magnitude larger than the expected fiducial models for the 21 cm signal [393]. Besides the interferometers mentioned above, some single dish experiments have been employed to constrain the 21 cm fluctuations at low redshift, from the post-reionization universe. Although these epochs lie beyond the scope of this thesis, it is worth mentioning some results due to their significance. The Green Bank Telescope (GBT)

[13]The Netherlands has a long tradition related to the 21 cm signal. Among other achievements, it was Dutch astronomers, van de Hulst and Wouthuysen, who predicted the hyperfine transition and the Lyα coupling, respectively, becoming aware of the astronomical importance of the 21 cm signal in radioastronomy. Furthermore, Muller, Oort and Van de Hulst observed the first rotation curve and HI map of the Milky Way, showing for the first time its spiral arms. See Ref. [471] for more information.

[394], located at Green Bank, West Virginia, USA, is the world's largest fully steerable radio telescope, with 100-meter diameter. Operating at frequencies between 100 and 115 GHz, it has been the first to detect 21 cm fluctuations in the post-EoR universe, via cross-correlations with other surveys: with the optical galaxy survey DEEP2 at $z \simeq 0.5 - 1.1$ [474], and WiggleZ at $z \sim 0.8$ [475]. The Parkes Radio Telescope [476] in New South Wales, Australia, has 64-meter diameter, and detects frequencies from 1230 to 1530 MHz. Similarly to the GBT, the cross-correlation of its observations with those from the 2dF galaxy survey provided detections of the cosmological HI line at redshifts $0.057 < z < 0.098$ [477].

On the other hand, several radiointerferometers are expected to be built within this decade, which may have enough sensitivity to attain a positive detection of the signal in the next few years. Some of them are devoted to perform HI *line intensity mapping*, i.e., measuring the integrated 21 cm emission from unresolved gas clouds, accessing clumpy neutral regions in the post-reionization era, up to $z \sim 2.5$. Examples of these are the Canadian CHIME [478], HIRAX in South Africa [479], the Tianlai experiment in China [480] or the BINGO observatory in South America [481]. Among the proposals for studying the Cosmic Dawn and EoR periods, here we highlight two interferometers which by their sensitivity and international effort, may become a great step forward towards the detection of the HI signature.

- The Hydrogen Epoch of Reionization Array (HERA) [39] is placed at the same facilities than PAPER in the Karoo desert, South Africa, specifically designed to observe the EoR. For that, it will observe in a range between 50 and 250 MHz, and is expected to have 350 dishes with 14 m diameter each, when completed. It has been deployed following the ideas developed for PAPER, with a highly redundant array to enhance the sensitivity. Although not finished yet, it is already running and collecting data.

- The Square Kilometer Array (SKA) [40], is the most ambitious radiointerferometer designed so far, with the world's largest area (~ 1 km^2) when completed. It will consist of two different facilities operating at different frequencies. On the one hand, SKA-low will be comprised of $\sim 10^5$ antennas grouped into stations in the Murchison Radio-astronomy Observatory at the Western Australian desert, spanning frequencies from 50 to 350 MHz. The SKA-mid, on the other hand, will be formed by 197 dishes in the South African Karoo desert, observing frequencies from 350 MHz to 15.3 GHz. The pseudo-random arrangement of antennas will allow reaching baselines up to 150 and 65 km, respectively. It will employ the facilities previously occupied by MWA and HERA. Although far from being finished yet,

pathfinder telescopes are already constructed and gathering data, such as MeerKAT in South Africa [482] and ASKAP in Australia [483].

- The Farside Array for Radio Science Investigations of the Dark ages and Exoplanets (FARSIDE) is a proposal for building an interferometric array based on the Moon [484], in addition to the orbiting satellite DAPPER. It would be composed by 128 dipoles across a 10 km^2 area. Covering from 0.1 to 40 MHz, it is aimed to detect the faint 21 cm power spectrum during the Dark Ages. Contrary to previous interferometers, it is still an idea under design and its construction has not started yet.

The above lists of current and future interferometers are not intended to be comprehensive, but to provide an outlook of experimental status, as well as about the increasing efforts of the scientific community for pursuing the cosmological 21 cm signal. A lot of work remains to be done, but these are exciting times for seeking the hyperfine line of the IGM.

Chapter 5

Evolution of the Intergalactic Medium

The physics of the IGM is highly rich and complex. Its study is fundamental in order to understand how and when galaxies formed, evolving from a mostly homogeneous fluid towards the cosmic web of galaxies and quasars immersed in an ionized medium we can see today. At $z \sim 1100$, the CMB decouples from the thermal plasma, marking the beginning of the so-called Dark Ages. After Recombination, most atoms become neutral, only a small fraction of free electrons remaining. The gas temperature keeps cooling, coupled to the photon temperature due to Compton scattering until $z \sim 150$, when these interactions become inefficient. Thereafter, the gas cools adiabatically. During the Dark Ages, overdensities around primordial seeds keep growing, leading eventually to the formation of galaxies. The newly born stars emit highly energetic radiation capable of altering the IGM evolution.

In order to understand the IGM evolution in detail, full numerical simulations are required, properly computing the hydrodynamics and radiative transfer, which are very expensive computationally wise. However, some semi-analytical approximations can be assumed, which simplify significantly the picture, and allow us to gain insight into the physical processes involved. Simplifying the full picture, we can treat the IGM as a two-phase medium [353]. One of the phases is the mostly neutral IGM, characterized by the gas temperature $T_K(\mathbf{x}, z)$, and the free electron fraction $x_e(\mathbf{x}, z)$, which accounts for the free electrons remaining from Recombination. After the onset of star formation, energetic X-ray radiation can reach these neutral areas, heating and ionizing the gas, although still remaining mostly neutral. On the other hand, the immediately surrounding regions of galaxies and ionizing sources are expected to be almost completely ionized, forming HII bubbles. Once

the star formation processes are efficient enough, these bubbles can grow and eventually merge among them, ionizing the full IGM during the so called Epoch of Reionization (EoR). We characterize the fraction of volume occupied by the HII bubbles with the ionized *filling factor* Q_i, where the local ionization fraction is ~ 1. In these completely ionized regions, temperatures reach $\sim 10^4$ K, where atomic cooling peaks. Therefore, the global ionization fraction including the (mostly) neutral IGM plus the HII regions can be written as

$$\bar{x}_i = Q_i + (1 - Q_i)\bar{x}_e,$$

where $\bar{x}_e$ is the spatial average over $x_e(\mathbf{x}, z)$ (in the neutral IGM). Hence, during the EoR, the mostly neutral IGM becomes completely ionized. The two-phase IGM is a simplification of the real IGM, but accurate enough and widely employed in semi-analytical computations, as in the code `21cmFAST` [378, 485], which is widely employed throughout this thesis. In this chapter, we review the evolution of the ionized fraction and gas temperature at each phase, discussing the different sources of energy injection, as well as the current constraints on the reionization epoch. For further details, there are many reviews in the literature treating the physics of reionization and the IGM, see Refs. [52, 486, 487, 488, 57, 58].

5.1 Ionized IGM

In this section, we discuss the details of the reionization processes, starting by considering only the globally averaged ionized fraction, and commenting latter on the effects of inhomogeneities. Current observational constraints on the EoR are summarized at the end of the section.

5.1.1 Global Reionization

The evolution of the HII number density $n_{\rm HII}(\mathbf{x}, t)$ is given by its continuity equation (e.g., [487]):

$$\frac{dn_{\rm HII}}{dt} + 3Hn_{\rm HII} = \Gamma_{\rm HI} n_{\rm HI} - \alpha_A n_{\rm HII} n_e, \tag{5.1}$$

where the left-hand side stands for the adiabatic evolution and the right-hand side accounts for the interplay between ionizations and recombinations, being $\Gamma_{\rm HI}$ the *ionization rate* and α_A the so-called *case-A recombination* coefficient. Peculiar velocities may also be taken into account, but we neglect them in this derivation for the sake of simplicity. The recombination coefficient considered depends upon the medium. In neutral IGM, ionizing

photons are rapidly absorbed, and transitions to the ground state do not effectively contribute to the ionization. This is the so-called *case-B recombination*, where recombinations to the ground state are excluded. Contrarily, the HII phase is a thin medium where these UV photons can freely travel through. For this reason, employing case-A recombination there is more adequate, such that recombinations to the lowest state are taken into account [354]. In this case, the coefficient takes the value $\alpha_A = 4.2 \times 10^{-13}\text{cm}^3\ \text{s}^{-1}$, evaluated at $T_K = 10^4$ K, a factor of ~ 2 larger than case-B.

We characterize the state of ionization of the IGM by means of the fraction of ionized volume, defining the filling factor as the volume-average of the HII fraction in the ionized medium: $Q_i = \langle x_{\rm HII} \rangle$, where $x_{\rm HII} = n_{\rm HII}/n_{\rm H}$. This quantity provides the fraction of volume of the IGM which is completely ionized by UV photons. To obtain an evolution equation for Q_i, we must spatially average the above equation. Since in this phase, both Hydrogen and Helium are mostly ionized, $n_e \simeq (1+\chi) n_{\rm HII}$, with $\chi = \mathfrak{f}_{\rm He}/\mathfrak{f}_{\rm H}$, with $\mathfrak{f}_{\rm H} = n_{\rm H}/n_b = 0.92$ and $\mathfrak{f}_{\rm He} = n_{\rm He}/n_b = 0.08$ the fraction of Hydrogen and Helium atoms per baryon, respectively.[1] Decomposing the HII number density as $n_{\rm HII} = x_{\rm HII}\, \bar{n}_{\rm H}\, (1+\delta)$, with δ the density contrast respect to the mean value, as defined in Sec. 2.2.1, the squared averaged HII density can be written as

$$\langle n_{\rm HII}^2 \rangle \simeq C\, Q_i\, \bar{n}_{\rm H}^2, \tag{5.2}$$

where we have approximated $\langle x_{\rm HII}^2 \rangle \simeq \langle x_{\rm HII} \rangle = Q_i$, given that $x_{\rm HII}$ takes values very close to 1 in these mostly ionized regions. The *clumping factor* $C = \langle n_{\rm H}^2 \rangle / \langle n_{\rm H} \rangle^2 = \langle (1+\delta)^2 \rangle$ accounts for the fact that the IGM is not completely homogeneous and has a density distribution. These inhomogeneities have an impact in the ionization history through this clumping factor, since recombinations are enhanced in overdense regions. There are several prescriptions to compute this coefficient, depending on the specific definition and method of simulation, and it depends upon the scale at which it is evaluated [489, 490]. While the modeling of the clumping factor is highly challenging, most estimations predict values of order unity at the redshifts of interest [491, 492].

We focus now on the ionizing term of Eq. (5.1). As long as the mean free path is much smaller than the size of the universe, or equivalently, the opacity κ is larger than the expansion rate, $1/\kappa \ll c/H$, ionizing photons are absorbed soon after being released. This is the so-called *on-the-spot* approximation, which can be safely used for the ionizing field at the EoR. Employing J and ε as the flux and comoving emissivity by number, respect-

[1] Doubly-ionized Helium, HeIII, can be usually neglected for the redshifts of interest, due to its high ionization threshold.

ively,[2] this simplification implies that Eq. (4.1) can be replaced by

$$0 \simeq -c\kappa J + \frac{c(1+z)^3\varepsilon}{4\pi}. \tag{5.3}$$

Hence, the ionizing UV flux, $J_{\rm UV}(\nu)$ (in units of $\rm s^{-1}\ keV^{-1}\ cm^{-2}\ sr^{-1}$), reads

$$J_{\rm UV}(\nu) \simeq \frac{(1+z)^3\varepsilon(\nu)}{4\pi\kappa(\nu)} \tag{5.4}$$

with $\kappa(\nu) = \sigma_{\rm HI}(\nu)n_{\rm HI}$ and $\sigma_{\rm HI}(\nu)$ the photoionization cross section for Hydrogen. Introducing the above flux in the source term of Eq. (5.1), one obtains:

$$n_{\rm HI}\Gamma_{\rm HI} = 4\pi n_{\rm HI}\int_{\nu_{\rm HI}}^{\infty} d\nu\,\sigma_{\rm HI}(\nu)J_{\rm UV}(\nu) \simeq (1+z)^3\int_{\nu_{\rm HI}}^{\infty} d\nu\,\varepsilon(\nu) = \dot{n}_\gamma, \tag{5.5}$$

with $\dot{n}_\gamma$ the proper rate density of emitted photons and $h\nu_{\rm HI} = 13.6$ eV the threshold ionization energy for Hydrogen. Thus, spatially averaging Eq. (5.1), and making use of the results from Eqs. (5.2) and (5.5), we obtain the evolution equation for the filling factor,

$$\frac{dQ_i}{dt} = \frac{\dot{n}_\gamma}{\bar{n}_{\rm H}} - \frac{Q_i}{\bar{t}_{rec}}, \tag{5.6}$$

being $\bar{t}_{rec}^{-1} = \alpha_A(1+\chi)C\bar{n}_{\rm H}$ the mean recombination time. The source term $\dot{n}_\gamma$ is completely determined by the emissivity, which can be modeled as proportional to the comoving *star formation rate* $\dot{\rho}_*$,

$$\varepsilon(\nu) = \mathcal{N}(\nu)f_{esc}\frac{\dot{\rho}_*}{\mu m_p} = \mathcal{N}(\nu)f_* f_{esc}\bar{n}_{b,0}\frac{df_{coll}(z, M_*)}{dt}, \tag{5.7}$$

with f_* the fraction of baryon into stars, f_{esc} the fraction of photons which escape from the galaxies to the IGM, μ the mean baryonic weight and $\mathcal{N}(\nu)$ the the number of emitted photons per baryon per frequency unit, which accounts for the energy spectrum and it is usually assumed to be a power-law function. In the second equality we have written the star formation rate $\dot{\rho}_*$ in terms of the derivative of the the fraction of mass collapsed in halos above a mass M_*, f_{coll}, defined in Eq. (2.23). Here, since we assume that ionizing photons come from stars within galaxies, $M_*(z)$ should be taken as the minimum mass required to host star formation in a halo. Therefore, only halos with masses large enough to host star formation can contribute to the UV flux. Using the Press-Schechter prescription, Eq. (2.21), the fraction of collapsed mass can be computed analytically,

[2] Note that in Sec. 4.1, I and ϵ were the flux and emissivity by energy, rather than by number, i.e., with an additional factor $h\nu$.

obtaining Eq. (2.24), while for the Sheth-Tormen function, Eq. (2.22), it must be computed numerically. This threshold can be related to the *minimum virial mass* $M_{\rm vir}^{\rm min}$ corresponding to a virial temperature $T_{\rm vir}^{\rm min}$, which can be defined from Eq. (2.17) as [52]

$$M_{\rm vir}^{\rm min}(z) = 10^8 \left(\frac{T_{\rm vir}^{\rm min}}{1.98\times10^4\,{\rm K}}\frac{0.6}{\mu}\right)^{3/2}\left(\frac{1+z}{10}\right)^{-3/2} M_\odot/h\ , \tag{5.8}$$

where μ is the mean molecular weight which is equal to 1.2 (0.6) for a neutral (fully ionized) primordial gas. The minimum virial temperature is usually chosen at the atomic cooling threshold, $T_{\rm vir}^{\rm min} \simeq 10^4$ K, minimum value required to have an efficient atomic cooling, allowing the gas to fragment, condense and form stars. However, molecular cooling would be relevant in metal-free clouds, cradle of the so-called Population III stars, a hypothetical first generation of very massive stars lacking metals. The formation of H_2 would present the most important mechanism to lose thermal energy, leading to lower values of the temperature, down to $\sim 10^3$ K [52, 58]. Given the uncertainty on the stellar population and cooling mechanism in halos, in the following we consider either $T_{\rm vir}^{\rm min}$ or $M_{\rm vir}^{\rm min}$ as a free parameter. The density rate of ionizing photons is then

$$\dot{n}_\gamma(z) = N_{\gamma/b} f_* f_{esc} \bar{n}_b(z) \frac{df_{coll}(z, M_{\rm vir}^{\rm min})}{dt}, \tag{5.9}$$

being $N_{\gamma/b} = \int_{\nu_{\rm HI}} d\nu \mathcal{N}(\nu)$ the number of ionizing photons per baryon. Note that this formalism is specially appropriate for high redshifts, since at later times, $z < 10$, mergers of halos can also contribute to star formation [353]. Eq. (5.6) can thus be rewritten as

$$\frac{dQ_i}{dt} = \xi \frac{df_{coll}}{dt} - \frac{Q_i}{\bar{t}_{rec}}, \tag{5.10}$$

being ξ the *ionization efficiency*, defined as the product of the astrophysical parameters

$$\xi = N_{\gamma/b} f_* f_{esc} \frac{1}{f_{\rm H}}. \tag{5.11}$$

This is the final equation that must be solved in order to predict the evolution of the ionized medium during the reionization era.[3] A further simplification can be taken when recombinations are slow enough. Assuming that the product $N_{\gamma/b} f_* f_{esc}$ is redshift independent, we can formally solve Eq. (5.10) as [494]

$$Q_i(z) = \frac{\xi\ f_{coll}(z, M_{\rm vir}^{\rm min})}{1 + N_{rec}}, \tag{5.12}$$

[3] Eq. (5.10) can also apply to the post-reionization era by accounting for the residual neutral clouds in the ionized IGM as an extra term in the opacity, correctly reproducing the redshift evolution [493].

where $N_{rec} = Q_i(z)^{-1} \int_z (dt/dz')dz' Q_i(z') \bar{t}_{rec}^{-1}(z')$ is the mean cumulative number of recombinations per Hydrogen atom. The filling factor is therefore proportional to the fraction of matter collapsed in star-forming halos, with an efficiency factor given by a product of astrophysical parameters. In principle, these parameters may be redshift and mass dependent, but due to the uncertainties in their values and for the sake of simplicity, we shall consider them as constant both in mass and in redshift. The number of ionizing photons per baryon $N_{\gamma/b}$ can be estimated from the spectrum and the initial mass function of stars, which depend upon the details of star formation (burst formation or continuous) and on their metallicity [495, 496]. Making use of the present-day initial mass function of low-metallicity stars, known as Population II stars, $N_{\gamma/b} \sim 4 \times 10^3$. Nonetheless, it can reach $\sim 10^5$ if metal-free and very massive stars of $> 10^2 M_\odot$, the so-called Population III, are considered as the initial composition. Regarding the fraction of baryons into stars, previous works on the comparison of the star formation rate with the one derived from UV luminosity function measurements (see, e.g., Refs. [497, 498] and references therein), as well as radiation-hydrodynamic simulations of high-redshift galaxies (see, e.g., Ref. [499]), have found values of this quantity around $f_* \sim 0.01$. On the other hand, most photons produced in a galaxy would remain within, being consumed in ionizing its neutral matter. Nonetheless, a small fraction of photons, encoded by f_{esc}, could escape from the galactic boundaries into the IGM and contribute to the reionization mechanism. The estimation of this parameter is challenging since it depends on the distribution of column densities and galactic morphologies. Although it is neither well observed nor well modeled, it takes typical values of $f_{esc} \sim 0.1$ (see, e.g., Ref. [487] and references therein). Finally, in Eq. (5.12), the mean number of recombinations N_{rec} can also be taken as a free parameter, provided that it does not vary much with time. It is expected to take low values, $N_{rec} < 1$ (e.g., Ref. [500]). Note that, at least as far as ionization is concerned, the relevant quantity is the product of these parameters, and not the specific value of each one. It also implies degeneracies between these parameters, which could only be broken if other observables besides the ionization fraction are considered. Due to the lack of observations of galaxies at high redshifts, these parameters are still poorly constrained and remain highly uncertain, and thus ξ is usually taken as a free parameter. For the default values commented above with Population II stars, the fiducial value for the ionizing efficiency is $\xi \simeq 40$. Therefore, from Eqs. (5.6) or (5.12), one can conclude that the parameters ξ and $M_{\rm vir}^{\rm min}$ (or $T_{\rm vir}^{\rm min}$) rule the ionization history, and completely determine the filling factor in this simple picture of global ionization.

To roughly estimate the conditions at which the IGM becomes completely ionized, one can see in Fig. 2.1 that $f_{coll}(z, M_{\rm vir}^{\rm min}) \sim 0.1$ at $z \sim 6$

for $T_{\rm vir}^{\rm min} = 10^4$ K. Thus, from Eq. (5.12), to ensure that the IGM becomes completely ionized at that redshift, as expected from data, it is required that $\xi \gtrsim 10$, which roughly agrees with the above estimation with the fiducial values. To properly evaluate the evolution of the filling factor, one must numerically solve Eqs. (5.6) or (5.12). Examples of ionization histories, computed with `21cmFAST` [378, 485], can be found in Fig. 5.1, for several values of the relevant astrophysical parameters, ξ and $M_{\rm vir}^{\rm min}$. The plot shows also the current observational constraints on the ionized fraction, which will be explained in Sec. 5.1.3. The minimum virial masses of $M_{\rm vir}^{\rm min} = 10^8$ and $10^9\, M_\odot/h$ have been chosen to correspond to minimum virial temperatures of $T_{\rm min}^{\rm vir} = 10^4$ (atomic cooling threshold) and 10^5 K respectively at $1 + z \simeq 10$. On the other hand, the considered values of the ionizing factor $\xi = 4$ and 10 may be related to Population II ($N_{\gamma/b} = 4\times10^3$) and Population III ($N_{\gamma/b} = 10^5$) stars, respectively, in case $f_* \simeq 0.01$ and $f_{esc} \simeq 0.1$. Notice that both parameters are somewhat degenerate, since increasing (decreasing) the ionizing efficiency (the minimum virial mass) leads to an earlier reionization period. Efficiencies of $\xi \gtrsim 4$ with threshold masses of $\lesssim 10^9\, M_\odot/h$ are needed in order to have the universe ionized at $z \sim 6$, as indicated by data (see Sec. 5.1.3). Molecular cooling, with $T_{\rm min}^{\rm vir} \sim 10^3$ K, may lead to a very early reionization era inconsistent with observations, unless extremely low ionizing efficiencies were considered.

Many candidates have been considered as the sources of reionization. QSOs (Quasi-Stellar Objects, also known as quasars) have been largely considered, since they are among the brightest sources in the universe, being able to emit in the UV range. However, their number density drops at high redshifts, and seems to be not enough to contribute significantly to the global ionization of the IGM, accounting only for 1-5% of the required ionizing background [501]. Standard galaxies become then the preferred option, since we have observational confirmation of bright galaxies for $z \gtrsim 6$ up to $z \sim 11$ thanks to the Hubble Space Telescope (HST) Ultra Deep Field [502, 503]. Future telescopes such as the JWST [504] could be able to detect farther and fainter galaxies. Given the slope of the typical luminosity function, dwarf faint galaxies may be the most relevant ones for producing an ionizing background due to their high abundance [58]. Regarding the stellar components, early redshift stars responsible for reionization may belong to the Population II group, whose stars present low metallicity, about one tenth of the solar metallicity. However, the first stars of the universe could have had even lower metallicities, being mostly composed only by Hydrogen and Helium, the most abundant elements after Primordial Nucleosynthesis. The so-called Population III stars would constitute a metal-free first stellar generation, rather different to the other known stellar types [58]. The lack of heavy elements reduces the cooling capability of the initial collapsing cloud,

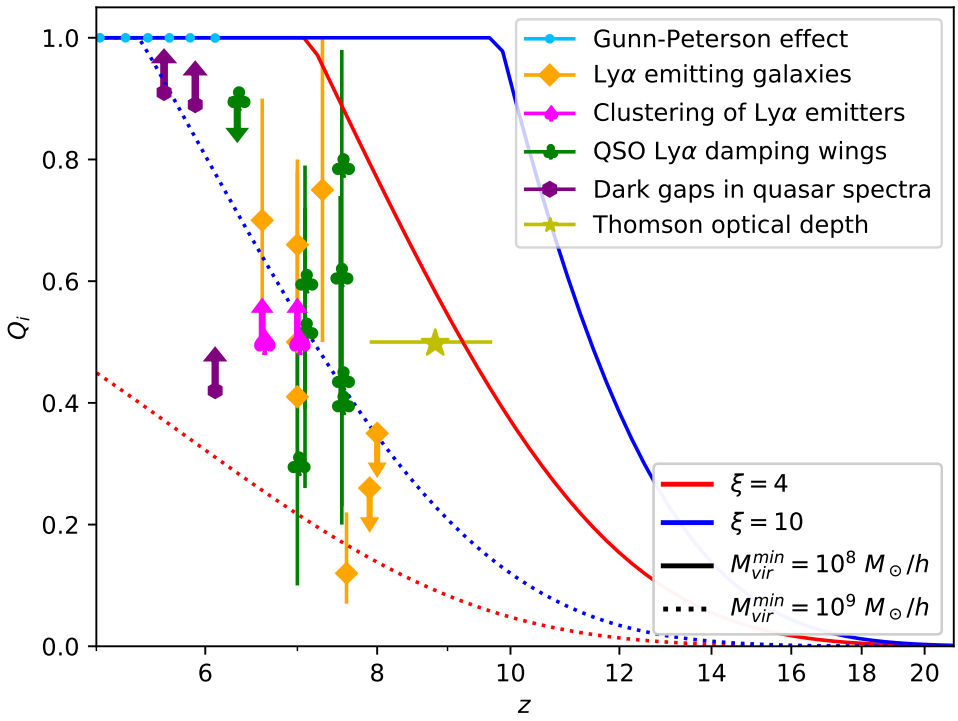

Figure 5.1: Evolution of the filling factor Q_i as a function of redshift, for different values of $M_{\rm vir}^{\rm min}$ and ξ. The included observational data is listed in Tab. 5.1 and explained in Sec. 5.1.3, arising from different probes: Gunn-Peterson effect, Lyα emission in galaxies, damping wings in Lyα spectra from QSOs, dark gaps in quasar spectra and estimates from the Thomson optical depth of the CMB. The upwards (downwards) arrows denote lower (upper) limits on Q_i.

leading to much more massive stars than the usually observed, with hotter central temperatures. As stated above, the number of emitted photons could be larger than in the Population II case. Moreover, the cooling of the gas happens by H_2 formation, leading to lower virial temperatures. This kind of stars has not been directly observed, yet some indirect evidences are already present [505].

5.1.2 Inhomogeneous Reionization

The discussion above stands for a global reionization scenario, and it is useful to predict the average ionized volume. However, numerical simulations agree on the fact that reionization is highly inhomogeneous [506, 507]. In principle, only hydrodynamic simulations with detailed radiative transfer can account for the complex physics of the inhomogeneous reionization process. However, several semi-analytical procedures have been proposed in the literature in order to account for inhomogeneities with good agreement

with numerical simulations (see, e.g., Ref. [508] for a comparison). In Ref. [509], the *FZH model*[4] was proposed in order to understand the growth of ionized regions, making use of the excursion set formalism. The basic idea is to promote Eq. (5.12) to be scale dependent, writing the filling factor $Q_i(z;\delta,M)$ of a region with a mass M and an overdensity δ (smoothed within the scale given by M) as

$$Q_i(z;\delta,M) = \frac{\xi\, f_{coll,cond}(z, M_{\rm vir}^{\rm min};\delta,M)}{1+N_{rec}}, \tag{5.13}$$

where the global collapsed fraction has been replaced by the *conditional* one, $f_{coll,cond}(z, M_{\rm vir}^{\rm min};\delta,M)$, the fraction of mass in collapsed objects above M_* at a redshift z within a region of mass scale M and overdensity δ. For the Press-Schechter function, this reads

$$f_{coll,cond}(z, M_{\rm vir}^{\rm min};\delta,M) = erfc\left(\frac{\delta_c(z)-\delta}{\sqrt{2(\sigma(M_{\rm vir}^{\rm min})^2-\sigma(M)^2)}}\right). \tag{5.14}$$

This is equivalent to assume that the ionized mass is proportional to the mass of collapsed objects, with the proportionality constant $\xi/(1+N_{rec})$. Therefore, as done in the standard excursion-set formalism [175], a point of space $\mathbf{x}$ with a density contrast $\delta(\mathbf{x})$ smoothed over a scale M is asigned to an ionized region of mass M if M is the largest scale at which the condition $Q_i(z;\delta(\mathbf{x}),M) \geq 1$ is fulfilled. This is equivalent to the criterion $\xi f_{coll,cond}(z, M_{\rm vir}^{\rm min};\delta(\mathbf{x}),M)/(1+N_{rec}) \geq 1$, where this last inequality imposes a condition over δ in the ionized bubbles, implying that only regions dense enough are capable of self-ionize, i.e the condition:

$$\delta \geq \delta_c(z) - erfc^{-1}\left((1+N_{rec})/\xi)\sqrt{2(\sigma(M_*)^2-\sigma(M)^2)}\right) \tag{5.15}$$

must hold within the region in order to be ionized. Note that the expression above is valid only for the PS prescription. For these reasons, this is considerered as an *inside-out* scenario of reionization, where, on average, high-density regions are firstly ionized. The threshold overdensity at a scale M can be considered a moving barrier to construct a HII mass function in the excursion set formalism [509]. This prescription is well suited for numerical implementation and it is computationallt very efficient, since it only needs to filter the density field, marking as ionized the cells above the threshold at a given filter scale. For this reason, it is the method used in many codes such as `21cmFAST` [378]. It has been shown to be in good agreement with more computationally expensive radiative transfer codes at scales $\gtrsim 1$ Mpc [510].

[4] After its authors Furlanetto, Zaldarriaga and Hernquist.

There are other analytical models to treat inhomogenous reionization, such as the known as *MHR model*[5] proposed in [511]. In this prescription, it is assumed that only regions with overdensities above a certain treshold remain neutral, as a consequence of an enhanced recombination rate. Contrarily to the FZH model, this is an *outside-in* scenario, where the most dense regions ionize later. Although it may seem in contradiction with FZH, the application of MHR is appropriate in the later stages of reionization, when only small overdense spots of the IGM remain neutral. Moreover, it is evaluated in a single, small scale, instead of the multiscale approach of FZH, which is able to describe the morphology of the reionization process on large scales. Both methods can be combined and provide an accurate description of the reionization from different perspectives [508].

Finally, although our focus in this thesis is on semi-analytic methods to solve the ionization history, a proper determination of the IGM evolution requires more accurate though computationally expensive methods. Some of them involve N-body simulations to compute the density fields and halo population, combined with a detailed radiative transfer treatment, via, e.g., adaptive ray tracing algorithms [512, 513]. However, hydrodynamic radiative transfer simulations are the most reliable at the smallest scales, able to reach spatial resolutions of $\sim$ 100 pc - $\sim$ 10 kpc, although are limited to boxes of tens of Mpc. They account for different baryonic effects absent in other prescriptions, which may include stellar and supernovae feedback, star formation, fully coupled three-dimensional radiative transfer and detailed cooling and heating for the metal enriched gas [514, 515, 516]. Radiative transfer can be treated by three main approaches, namely employing moments methods (e.g., [517]), Monte Carlo sampling (e.g., [518]) or ray tracing (e.g., [519]). See Refs. [520, 521] for detailed comparisons between codes and radiative transfer methods, and also, e.g., Refs. [522, 523] for overviews and more details on this topic.

5.1.3 Constraints on the Epoch of Reionization

Currently, several estimations of the global ionized fraction of the IGM at different redshifts have been performed. Although the end of reionization is well determined, the precise evolution at lower redshifts becomes much more uncertain, being some of the estimations strongly dependent on the underlying assumed models. In this section we review some of the most important methods to bound the onset and timing of the EoR. Table 5.1 shows a summary of the most important constraints, which are also plotted in Fig. 5.1.

[5] After Miralda-Escudé, Haehnelt and Rees.

Data	Redshift	Q_i	Reference
Gunn-Peterson effect	5.03	$0.9999451^{+0.0000142}_{-0.0000165}$	Fan et al., 2006 [524]
	5.25	$0.9999330^{+0.0000207}_{-0.0000244}$	
	5.45	$0.9999333^{+0.0000247}_{-0.0000301}$	
	5.65	$0.9999140^{+0.0000365}_{-0.0000460}$	
	5.85	$0.9998800^{+0.0000408}_{-0.0000490}$	
	6.10	0.99957 ± 0.00030	
Dark gaps in quasar spectra	5.6	>0.91	McGreer et al., 2015 [525]
	5.9	>0.89	
	6.1	>0.42	
Lyα Emission in Galaxies	7	$0.66^{+0.12}_{-0.09}$	Schenker et al., 2014 [526]
	8	< 0.35	
	6.6	0.7 ± 0.2	Konno et al., 2018 [527]
	7	$0.5^{+0.3}_{-0.1}$	Inoue et al., 2018 [528]
	~ 7	$0.41^{+0.15}_{-0.11}$	Mason et al., 2018 [529]
	7.3	0.75 ± 0.25	Itoh et al., 2018 [530]
	7.6 ± 0.6	$0.12^{+0.10}_{-0.05}$	Hoag et al., 2019 [531]
	7.9 ± 0.6	< 0.26	Mason et al., 2019 [532]
Clustering of Lyα Emitters	6.6	$\gtrsim 0.5$	McQuinn et al., 2007 [533]
	6.6	$\gtrsim 0.5$	Ouchi et al., 2010 [534]
	7	$\gtrsim 0.5$	Sobacchi and Mesinger, 2015 [535]
QSO Lyα damping wings	6.24-6.42	<0.9 (2σ)	Schroeder et al., 2013 [536]
	7.00	$0.30^{+0.23}_{-0.20}$	Wang et al., 2020 [537]
	7.09	$0.60^{+0.19}_{-0.21}$	Greig et al., 2017 [538]
	7.52	$0.61^{+0.13}_{-0.22}$	Yang et al., 2020 [539]
	7.54	$0.79^{+0.19}_{-0.17}$	Greig et al., 2018 [540]
	7.54	$0.44^{+0.18}_{-0.21}$ (95% CL)	Bañados et al., 2018 [541]
	7.09	0.52 ± 0.26	Davies et al., 2018 [542]
	7.54	$0.40^{+0.23}_{-0.20}$	
Thomson Optical Depth	8.8 ± 0.9	0.5	Adam et al., 2016 [543]
	$\tau_T = 0.0519^{+0.0030}_{-0.0079}$		Aghanim et al., 2020 [24]

Table 5.1: List of representative constraints on Q_i at 1σ (unless stated otherwise). Data points are plotted in Fig. 5.1, see, e.g., Refs. [544, 545] for comprehensive (though slightly outdated) compilations of data.

5.1.3.1 Gunn-Peterson effect

The first, and one of the most important probes of the EoR, is the Gunn-Peterson effect, named after the physicists who predicted it in 1965 [546]. Due to the fact that most of the Hydrogen atoms in the IGM are in their fundamental state, the relevant transitions are those which relate its ground state with the excited ones, as the Lyα transition. Many astrophysical objects like galaxies and quasars can emit high energy radiation which, due to the expansion of the universe, redshift to lower frequencies along its journey. In their passing across the IGM, these photons could eventually redshift to the wavelength corresponding to the Lyα transition. Thus, any neutral Hydrogen atom around could absorb it, preventing us from seeing it. Since the IGM is densely filled by Hydrogen atoms, these absorptions would be likely even if a considerable fraction of Hydrogen atoms were ionized. The efficiency of this absorption is given by the optical depth of the Lyα transition, the so-called Gunn-Peterson optical depth $\tau_{\rm GP}$, already computed in Eq. (4.36), which can be approximated as $\tau_{\rm GP} \simeq 5.0\times10^5\, x_{\rm HI}\,((1+z)/7)^{3/2}$. From that formula, one can clearly see that the medium is optically thick ($\tau_{\rm GP} > 1$) unless it is highly ionized, e.g. $x_{\rm HI} < 10^{-5}$ at $z \sim 6$. Hence, observing QSO spectra embedded in a mostly neutral IGM, we would see an absorption trough (known as *Gunn-Peterson trough*) just above the Lyα transition (since photons are redshifted from higher frequencies). However, we actually can observe light from relatively distant quasars without this expected suppression, up to $z \sim 6$, when a significant damping in the spectrum appears. This means that, for $z \lesssim 6$, essentially there is no neutral gas in the IGM, being most of the atoms in a highly ionized state. For higher redshifts, however, the medium appears to be still predominantly neutral. This transition between these two regimes is the so-called EoR.

The first evidence of this GP trough at $z \sim 6$ was reported in Ref. [31] from spectroscopic observations of quasars in the Keck Observatory. The Gunn-Peterson effect has been extensively used in order to constrain the end of this epoch, observing the light emitted by distant quasars. The detection of the Gunn-Peterson trough in the spectra allows us to determine the ionized fraction with great precision. This method was used in Ref. [524] to estimate the neutral fraction $1 - Q_i$ between $\sim 10^{-5}$ and $\sim 10^{-4}$ at six different redshifts $z = 5.03$, 5.25, 5.45, 4.65, 5.85 and 6.10, by means of the observation of spectra of 19 bright quasars. These measurements are not, however, model-independent, since assumptions such as the temperature-density relation of the IGM or the PDF of overdensities were assumed.

On the other hand, there is a related method to constrain the ionized fraction less subject to the modeling of the IGM. In Ref. [525], lower limits on Q_i were placed from the distribution of dark gaps in quasar spectra

at redshifts 5.6, 5.9 and 6.1 [525] (indicated in Tab. 5.1 as *dark gaps in quasar spectra*). These results were achieved by determining the fraction of binned spectra in Lyα and Lyβ forests which were dark, i.e., presented zero flux. Although less restrictive, these are robust limits obtained in a model-independent way, unlike the estimations from Ref. [524]. All these data indicate that reionization has to be completed by $z \sim 6$. It is worth mentioning that observations of the Lyα forest work under the same idea than the GP effect. While the GP trough is a deep suppression of the spectrum due to a not completely neutral IGM, the Lyα forest arises from neutral clouds of gas embedded in the ionized IGM, which imprint narrow absorption dips in the QSO spectrum determined by their size. This allows to tightly constrain the residual neutral fraction in the post-EoR universe via estimations of the optical depth [547, 548, 549].

5.1.3.2 Thomson Optical Depth

Once reionization has started, the increase in the number of free electrons makes Thomson scattering to be relevant again, as it happened before the Recombination era. This scattering isotropizes the radiation field, being the angular power spectrum of the CMB suppressed by a damping factor $e^{-2\tau_T}$, where τ_T is the Thomson optical depth, defined as

$$\tau_T = \int \frac{cdz}{(1+z)H(z)} \sigma_T \, n_e(z) \ , \tag{5.16}$$

with $\sigma_T = 0.6652 \times 10^{-24}$ cm^2 the Thomson cross section. This damping enforces the radiation field to become isotropic for large enough τ_T, erasing anisotropies. As a consequence, the reionization epoch leaves imprints on the CMB spectrum, being τ_T the quantity which characterizes its impact. This is one of the six parameters of the baseline ΛCDM cosmological model, determined with great precision by the Planck mission [550]. Although in the temperature TT spectrum there is a degeneracy between the Thomson optical depth and the amplitude of the primordial fluctuations, it is broken in the polarization of the CMB spectrum, since Thomson scattering induces polarization at low multipoles [551]. Parameterizing the evolution of Q_i with z as a tanh function, the latest Planck analysis offers a value for this quantity of [24]

$$\tau_T = 0.0519^{+0.0030}_{-0.0079} \ , \tag{5.17}$$

making use of the low-l EE modes likelihood. Previous Planck analyses [543] evaluated also the beginning, the final and the duration of reionization based on a slightly larger, earlier estimation of the optical depth, $\tau_{T,2016} = 0.058 \pm 0.012$. Within the *tanh* parameterization, the reionization process occurs suddenly enough around a characteristic redshift of $z_{re} = 8.8 \pm 0.9$

(where the ionization fraction reaches 50%), with a total duration of $\Delta z < 4.6$ (at 95% CL), with the additional constraint that the IGM must be fully ionized at $z < 6$, due to the Gunn-Peterson effect. These results change only slightly if an asymmetric power-law parameterization is assumed, rather than a *tanh* function [543]. Besides the functional parameterization, other approaches have been used in the literature to exploit the τ_T constraint, such as the PCA (Principal Component Analysis) decomposition [552, 553, 554, 3], the PCHIP (Piecewise Cubic Hermite Interpolating Polynomial) [3] or CMB plus reionization modeling [555]. In Part II of this thesis, CMB data is exploited in order to reconstruct the ionization history by means of the aforementioned PCA and PCHIP analyses, studying the plausibility of an early reionization period [3].

Measurements of the Thomson optical depth constitute a robust indication of reionization and allow us to parameterize some general properties of the EoR. However, in order to infer timing, duration or patchiness aspects of the EoR, specific parameterizations are needed, since this does not provide us with information about the evolution of the free electron fraction at each redshift, but instead about its integral along time.

5.1.3.3 Other constraints

While the Gunn-Peterson trough and the CMB measurements provide the most robust bounds on the EoR, other methods may also lead to constraints on the ionization history. The most relevant ones are summarized in the following.

- **Lyα emission in galaxies**

  One of the most profitable approaches is based on the observation of Lyα emitting galaxies, usually presenting large star formation rates, which can constitute a successful approach for exploring how reionization has proceeded at higher redshifts ($z \gtrsim 7$) [556]. The Subaru Hyper Suprime-Cam has provided measurements of thousands of luminosities of Lyα emitters through several wavelength bands, which allows placing constraints on the reionization history. Examples of this are the survey SILVERRUSH [557], from which several estimates of the neutral fraction have been derived at redshifts $z = 6.6$ [527] and $z = 7.3$ [528], and the CHORUS survey [558], which has provided constraints at $z \simeq 7$ [530]. Other constraints rely on Lyα emission from faint Lyman break galaxy candidates, those detected by a drop in the spectrum at frequencies above the Lyman limit, caused because ionizing photons are absorbed in their local environment. The detection and non-detection of Lyα emission in such galaxies allows placing

bounds around $z \sim 7$ [526, 529], $z \sim 7.6$ [531] and $z \sim 8$ [526, 532]. All the above results indicate that reionization is not yet complete at those epochs, $z \sim 7$. One of the caveats of employing Lyα emitters to infer the ionization fraction is that radiative transfer modeling is needed, these results being, therefore, quite sensitive to the assumptions considered and to the details of the numerical implementations.

- **Clustering of Lyα emitters**

  Constraints closely related to the above ones can be derived from the clustering properties of Lyα emitters, rather than their luminosity functions. An enhancement in the clustering of Lyα emitters could be regarded as a consequence of reionization, since radiation from clumped galaxies would suffer less absorption than from isolated ones. This effect can be hardly mimicked via other processes, thus indicating the progress of the EoR. It has allowed to place lower limits on the ionized fraction at $z = 6.6$ [533, 534] and $z \simeq 7$ [535]. The main difficulty of this method is that these estimates require a great number of Lyα emitters, in order to properly infer the clustering properties.

- **Lyα damping wing**

  Lyα photons absorbed in the tails (*damping wings*) of the cross section instead of the resonance could also provide a powerful probe of the EoR. Lyα cross section can be modeled by a Voigt profile, Eq. (4.43), which near the resonance behaves similar to a Gaussian distribution, but far enough from the center of the line, decays much slower as a Lorentzian function. One can split the optical depth in two different contributions, one from the center of the line, and the other from the tails of the distribution, which is a smoother function of the frequency. The strength of the damping wing absorption strongly depends on the neutral fraction of the environment, fact which allows placing constraints on Q_i [559, 560]. Taking advantage of its spectral smoothness, it was possible to set upper limits on Q_i between $z = 6.24$ and 6.42 [536]. Stronger bounds can be obtained by studying the absorption on the red side of the Lyα line, where resonant absorption is negligible, and thus must be produced at the tails. The discovery of four of the farthest observed quasars has allowed placing constraints using that method at redshifts $z = 7.00$ [537], $z = 7.09$ [538, 542], $z = 7.52$ [539] and $z = 7.54$ [540, 541, 542]. The derivation of all these constraints based on the Lyα damping wing also rely on radiative transfer and hydrodynamical simulations. For the same redshifts, different methodologies and model assumptions may provide differing constraints (see Tab. 5.1).

On the other hand, there is recent evidence of overlapping ionized bubbles around three galaxies at $z \sim 7.7$ from spectroscopic observations [561]. Finally, as commented in the previous chapter, although the 21 cm signal have not been measured at these redshifts, some constraints have been obtained on the duration and completion redshift of the EoR. The EDGES high-band observations are capable of ruling out too abrupt and rapid reionization processes [403]. Other compilations of ionization data can be found in Refs. [544, 545].

5.2 Neutral IGM

In this section, the relevant physics of the neutral IGM is outlined. Before ionized regions around each galaxy grow and merge, the surrounding medium is still in a neutral state, with a remnant ionized fraction from Recombination. The astrophysical processes taking part in galaxies and other sources can produce X-ray radiation capable of reaching areas far beyond the galaxies, altering its thermal and ionization state. Moreover, Lyα radiation is expected to fill the neutral medium, of great importance for the 21 cm signal. In the following, we comment on the heating, ionization and Lyα flux present in the mostly neutral IGM.

5.2.1 Heating of the IGM

From energy conservation, one can derive a differential equation which determines the kinetic temperature of the gas, T_K. The thermal evolution equation reads (e.g., Ref. [562])

$$\frac{dT_K}{dt} + 2HT_K - \frac{2}{3}\frac{T_K}{(1+\delta)}\frac{d\delta}{dt} + \frac{T_K}{1+x_e}\frac{dx_e}{dt} = \frac{2\mathcal{Q}}{3\,n_b(1+x_e)}\,, \tag{5.18}$$

where $\mathcal{Q}$ is the total heating rate per unit volume. The second and third terms of the left-hand side account for adiabatic expansion, the fourth one induces changes in the temperature given by the ionization variation, whereas the right-hand side term includes any possible interacting process which can cool down or heat up the gas. Note that, in the absence of heating/cooling $\mathcal{Q}$ terms, the above equation can be anallitically solved, obtaining $T_K \propto a^{-2}(1+\delta)^{2/3}/(1+x_e)$. In the homogeneous, post-recombination limit, we have the well-known adiabatic cooling evolution $T_K \propto a^{-2}$ as a consequence of the expansion of the universe.

There are several possibles sources of heating and cooling in the IGM which contribute to $\mathcal{Q}$. In the following, we shall comment on the most

relevant ones to take into account. While in this section, only the standard processes are considered, further heating terms may arise from exotic DM scenarios, such as accretion in PBHs. The heating effects in that case are widely discussed in Part II of this thesis [6].

5.2.1.1 Compton cooling

Compton scattering $e + \gamma \leftrightarrow e + \gamma$ is the responsible of the coupling between matter and radiation in the early universe. Even after the decoupling of the CMB, the gas is still affected by scatterings with photons, due to the large number of photons compared to baryons, enforcing the gas temperature T_K to be equal to the CMB temperature T_γ. The corresponding cooling rate can be derived from the Boltzmann equation for the Compton scattering, after performing a Fokker-Planck expansion (similar to Eq. (4.35)) and obtaining the so-called Kompaneets equation [563]. Integrating it, the Compton cooling rate is obtained [164],

$$\mathcal{Q}|_{Compton} = \frac{4\sigma_T n_e \rho_\gamma}{m_e c} (T_\gamma - T_K) \,, \tag{5.19}$$

where $\rho_\gamma = (\pi^2/15) T_\gamma^4$ is the CMB energy density. This result was first derived in Ref. [564]. At high redshifts, when Compton cooling is very efficient and there are no other relevant sources of heating, the gas temperature is coupled to the CMB temperature $T_K \to T_\gamma \propto (1+z)$. However, due to the expansion of the universe, there is a moment when the adiabatic cooling term becomes dominant, and the Compton interactions no longer can couple both temperatures. This thermal decoupling happens at a redshift z_D when both rates (adiabatic and Compton) are similar

$$2HT_K|_{z_D} \sim \left. \frac{2\mathcal{Q}|_{Compton}}{3k_B n_b(z_D)(1+x_e^\infty)} \right|_{z_D} \tag{5.20}$$

$$\Rightarrow \; 1 + z_D \simeq \left(\frac{45 m_e H_0 \sqrt{\Omega_m}}{4\pi^2 \sigma_T T_{\gamma,0} x_e^\infty} \right) \simeq 150, \tag{5.21}$$

where we have employed $x_e^\infty \simeq 3 \times 10^{-4}$ as the leftover free electron fraction from Recombination, which is roughly constant, as estimated in Sec. 5.2.2 or computed via publicly available Recombination codes such as RECFAST [565]. Therefore, we expect an adiabatic evolution of the kinetic temperature $T_K \propto (1+z)^2$ for redshifts below $z_D \sim 150$, as long as no other heating sources are present.

5.2.1.2 X-ray heating

After the onset of star formation, some astrophysical objects such as high mass X-ray binaries in starbust galaxies, supernova remnants or black holes in mini-quasars may emit a strong background radiation at UV and X-ray frequencies [566, 353]. Given that the ionization cross section can be approximated as $\sigma(\nu) \propto \nu^{-3}$ (see, e.g., Ref. [30]), the mean free path of photons goes as $\lambda_{mfp} \sim \nu^3$. While UV photons have a lower mean free path and are absorbed in the neighborhood of astrophysical sources, ionizing their environment, the more energetic X-rays can travel much farther, being able to reach the mostly neutral IGM, distant from galaxies. Photons with $\sim$ keV energies can therefore be absorbed, transferring their energy either to ionization, heating or atomic transitions.

Solving the radiative transfer equation for X-rays, Eq. (4.1), it is possible to obtain obtain the specific X-ray intensity (by number) $J_{\rm X}$ (in units of s^{-1} keV^{-1} cm^{-2} sr^{-1}),[6] which reads

$$J_{\rm X}(z,\nu) = \frac{(1+z)^2}{4\pi}\int_z^\infty dz' \frac{dt}{dz'}\,(1+z')\varepsilon_{\rm X}(\nu')\,e^{-\tau_{\rm X}(\nu,z,z')}\,, \tag{5.22}$$

where $\nu' = \nu(1+z')/(1+z)$ is the comoving frequency at emission, and $\tau_{\rm X}(\alpha, m_e)$ is the IGM optical depth from z' to z. This factor accounts for the attenuation of the X-ray flux through the IGM. In analogy to Eq. (5.7), the comoving specific X-ray emissivity $\epsilon_{\rm X}(z,\nu)$ is modeled as

$$\varepsilon_{\rm X}(\nu) = \frac{L_{\rm X}(\nu)}{h\nu\,{\rm SFR}}\dot{\rho}_* = \frac{L_{\rm X}(\nu)}{h\nu\,{\rm SFR}} f_*\bar{\rho}_{b,0}\frac{df_{coll}(z, M_{\rm vir}^{\rm min})}{dt}, \tag{5.23}$$

where $L_{\rm X}/{\rm SFR}$ is the specific differential X-ray luminosity normalized to the star formation rate escaping the host galaxies (in units of erg s^{-1} Hz^{-1} $M_\odot^{-1}$ yr), whose spectral shape can be assumed to be a power law, $L_{\rm X} \propto (\nu/\nu_0)^{-\gamma_{\rm X}}$, with ν_0 a threshold frequency. The slope takes values around $\gamma_{\rm X} \simeq 1$, ranging between 0.8 and 1.5, depending on the specific X-ray source [566, 494, 567]. High-redshift X-ray emitters are not directly observed yet, and thus we shall consider the luminosity normalization as a free parameter, given by the integrated luminosity (per SFR) over the energy band $(2-10$ keV), $L_{\rm X[2-10\ keV]}/{\rm SFR}$.[7] We shall take as a fiducial value the extrapolation from nearby starbusts galaxies, $L_{\rm X[2-10\ keV]}/{\rm SFR} = 3.4\times10^{40}$

[6] Note that other convention in the literature denotes with $J_{\rm X}$ the flux by energy, rather than by number, having thus units of erg s^{-1} keV^{-1} cm^{-2}, and implying an extra factor of $h\nu$. For that quantity, we employ I.

[7] There are other parameterizations to account for the normalization, such as those followed in the early versions of `21cmFAST` code [378]. Instead of the luminosity, the heating efficiency ξ_X was chosen, defined as the number of X-ray photons per solar mass in stars, which can be easily related to $L_{\rm X[2-10\ keV]}/{\rm SFR}$.

erg s^{-1} $M_\odot^{-1}$ yr [566, 494]. More recent estimates agree with that default value, showing luminosities from X-ray compact binaries between 10^{39} and 10^{40} erg s^{-1} $M_\odot^{-1}$ yr between redshifts 0 and 4 [568]. The threshold frequency ν_0 is tipically assumed to lie between $h\nu_0 = 300$ and 500 eV, but its specific value is less relevant given is degeneracy with $L_{\mathrm{X[2-10\ keV]}}/\mathrm{SFR}$ and the slope γ_X. Frequencies below ν_0 are locally absorbed in the nearby region of the emitting source, and do not reach the IGM. Comparing to Eq. (5.23), one can see that the X-ray escape fraction is effectively set to 1, since most of the X-rays are able to get away galaxies due to the high mean free path.

The heating rate by X-ray sources is thus given by

$$\mathcal{Q}|_X(z) = 4\pi\, n_b(z) \int_{\nu_0}^{\infty} d\nu\, J_{\mathrm{X}}(z,\nu) \sum_j (h\nu - E_j^{\mathrm{th}}) f_{\mathrm{heat}}\, f_j\, x_j\, \sigma_j(\nu)\ , \quad (5.24)$$

where σ_j are the photoionization cross-sections of species j, and f_{heat} accounts for the fraction of energy from X-rays that is converted into heat in the IGM, using the fit from Ref. [569]. Since evaluating the integrals of Eqs. (5.22) and (5.24) together with the optical depth can be quite time-consuming, some numerical implementations (such as the one followed in the `21cmFAST` code [570, 378, 485]) approximate the absorption factor $e^{-\tau_{\mathrm{X}}}$ to speed-up the computation. Given its exponential form, we can assume that all photons with optical depth large enough, $\tau_{\mathrm{X}} > 1$, are easily absorbed in the medium, whereas photons with $\tau_{\mathrm{X}} \leq 1$ are able to travel without being absorbed. It is equivalent to approximate the absorption factor as a Heaviside step function, $e^{-\tau_{\mathrm{X}}} \simeq \theta\,[1 - \tau_{\mathrm{X}}(\nu, z, z')]$, avoiding to integrate over the optical depth,

$$\mathcal{Q}|_X(z) = (1+z)^2 n_b(z) \int_z^{\infty} dz' \frac{dt}{dz'}(1+z') \int_{Max[\nu_0,\nu_{\tau=1}]}^{\infty} d\nu \sum_j (h\nu - E_j^{\mathrm{th}}) f_{\mathrm{heat}} \times f_j\, x_j\, \sigma_j(\nu) \varepsilon_{\mathrm{X}}(\nu')\ , \quad (5.25)$$

where $\nu_{\tau=1}$ is the frequency where the optical depth equals unity.

The function f_{heat} accounts for the fraction of X-ray energy deposited as heating. Other amounts of this energy are absorbed in form of ionization and excitation, having therefore the corresponding fractions f_{ion} and f_{exc}. Although these functions depend on the X-ray energy and the ionization fraction x_e, they saturate at energies $\gtrsim 100$ eV, having a function of only x_e [571, 569]. A rough approximation gives [572]

$$f_{\mathrm{heat}} \sim \frac{1+2x_e}{3}, \quad f_{\mathrm{ion}} \sim f_{\mathrm{exc}} \sim \frac{1-x_e}{3}. \quad (5.26)$$

Then, in mostly neutral media, the energy splits equally in the three channels, while it is mainly deposited as heating when the ionization is high.

To gain insight about the impact of X-rays in the temperature evolution, we can estimate the total heating by taking the on-the-spot approximation in the flux (i.e., employing Eq. (5.4) in Eq. (5.24)), getting a simpler heating rate (e.g., [494]),

$$\mathcal{Q}|_X(z) = \frac{L_{\mathrm{X[2-10\ keV]}}}{\mathrm{SFR}}\, f_* f_{\mathrm{heat}}\, \rho_b(z)\, \frac{df_{coll}(z, M_{\mathrm{vir}}^{\mathrm{min}})}{dt}. \tag{5.27}$$

Thus, the increase in temperature per baryon in a Hubble time is

$$\begin{aligned}\frac{2\,\mathcal{Q}|_X}{3\,H\,n_b} \simeq 10\,\mathrm{K}\, &\left(\frac{-(1+z)df_{coll}(z, M_*)/dz}{10^{-3}}\right) \\ &\times \left(\frac{L_{\mathrm{X[2-10\ keV]}}/\mathrm{SFR}}{3.4\times 10^{40} erg\cdot s^{-1} M_\odot^{-1} yr}\right)\left(\frac{f_*}{0.01}\right)\left(\frac{f_{\mathrm{heat}}}{0.2}\right),\end{aligned} \tag{5.28}$$

assuming $df_{coll}(z, M_{\mathrm{vir}}^{\mathrm{min}})/dt/H(z) = -(1+z)df_{coll}(z, M_{\mathrm{vir}}^{\mathrm{min}})/dz \simeq 10^{-3}$ as a fiducial value at $z \simeq 20$. Note that, given the growth of the collapse factor, the above formula increases by an order of magnitude at $z \simeq 15$, as can be noticed in Fig. 2.1. As a further estimation, ignoring adiabatic terms and changes in the ionization fraction in the temperature equation, Eq. (5.18), we can integrate the temperature taking Eq. (5.27) as the source in order to estimate the order of magnitude increase in temperature generated by X-rays, $\Delta T|_X(z)$,

$$\Delta T|_X(z) = \frac{2}{3}\frac{L_{\mathrm{X[2-10\ keV]}}}{\mathrm{SFR}}\, f_* f_{\mathrm{heat}}\, \mu m_p\, \Delta f_{coll}(z, M_*) \tag{5.29}$$

$$\begin{aligned}&\simeq 10^4 \mathrm{K}\, \Delta f_{coll}(z, M_{\mathrm{vir}}^{\mathrm{min}}) \left(\frac{L_{\mathrm{X[2-10\ keV]}}/\mathrm{SFR}}{3.4\times 10^{40} erg\cdot s^{-1} M_\odot^{-1} yr}\right) \\ &\times \left(\frac{f_*}{0.01}\right)\left(\frac{f_{\mathrm{heat}}}{0.2}\right),\end{aligned} \tag{5.30}$$

where we have assumed the fiducial values $L_{\mathrm{X[2-10\ keV]}}/\mathrm{SFR} \simeq 3.4 \times 10^{40} erg s^{-1} M_\odot^{-1} yr$, $f_{\mathrm{heat}} \simeq 0.2$ and $f_* \simeq 0.01$ [494]. Therefore, an increase in the collapse fraction of $\Delta f_{coll}(z, M_{\mathrm{vir}}^{\mathrm{min}}) \sim 1$ would lead to heat up the medium by $\sim 10^4$ K. Note however, that the on-the-spot scenario would only be accurate for low redshifts, when the mean free path is much shorter than the Hubble length, and for quantitative computations, Eq. (5.24) (or Eq. (5.25)) must be used. Figure 5.2 shows the temperature prediction for different astrophysical models, computed with `21cmFAST`. As can be seen, the minimum virial temperature sets the timing of the onset of heating, being earlier for lower threshold masses, as lower mass halos are allowed to host star formation. On the other hand, the X-ray luminosity determines

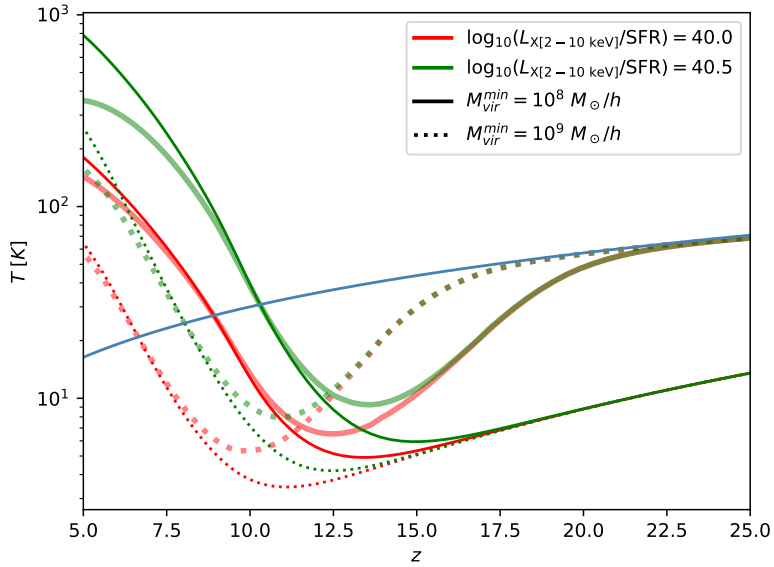

Figure 5.2: Evolution of the relevant temperatures as a function of redshift, for different values of the minimum virial mass and X-ray luminosity per star formation rate (in units of erg $s^{-1} M_\odot^{-1}$yr). Thin lines stand for the kinetic temperature of the gas T_K, thick lines for the spin temperature T_S, while the blue line corresponds to the CMB temperature T_γ.

the strenght of heating. The spin temperature, treated in Sec. 4.2, is also shown, being coupled to the kinetic one by means of scattering of Hydrogen atoms by Lyα radiation, whose flux is commented in Sec. 5.2.3.

5.2.1.3 21 cm heating

Recently, a new heating channel was proposed based on CMB photons interacting via the 21 cm line [382]. The absorption and emission of CMB photons by the hyperfine levels in Hydrogen atoms can also transfer some thermal energy in the process. Its corresponding heating rate can be written as [382]

$$\mathcal{Q}|_{21} = \frac{3}{4}\, n_H\, x_{\rm HI}\, x_{CMB}\, A_{10}\, T_*\, \left(\frac{T_\gamma}{T_S} - 1\right), \tag{5.31}$$

where $x_{CMB} = (1 - e^{-\tau_{21}})/\tau_{21} \simeq 1$, where the 21 cm optical depth τ_{21} is small. Note that this heating implicitly depends on the Lyα flux, and therefore on the astrophysical parameters, through T_S. Given the factor $T_\gamma/T_S - 1$, this heating rate turns on when T_S deviates from T_γ, during the Lyα coupling period, vanishing however when the hyperfine transitions are driven by CMB photons. Since this epoch (partly) coincides with the onset of X-ray heating, it has a subdominant impact on the thermal history of the IGM, unless X-ray emitters are quite faint [9]. Note that in the limit when

the medium is very hot, and the CMB is cooler than the IGM, $T_\gamma/T_K < 1$, and cooling instead of heating takes place. The maximum possible cooling from this source appears in the limit when T_γ/T_K can be neglected, and thus $T_\gamma/T_S - 1 \simeq -1$.

One can easily estimate quantitatively this effect. Approximating the color temperature to the kinetic one (which is a fair assumption, as commented in Sec. 4.3.3), we can write

$$\frac{T_\gamma}{T_S} - 1 \simeq \frac{x_\alpha}{1 + x_\alpha} \left(\frac{T_\gamma}{T_K} - 1 \right). \tag{5.32}$$

In Sec. 5.2.3.1, the Lyα coupling coefficient is estimated as $x_\alpha \sim 0.5$ at $z \sim 20$ in the fiducial model. The largest possible values for T_γ/T_K are reached when heating sources are not efficient enough and the kinetic temperature still cools adiabatically, having $T_\gamma/T_K = (1 + z_D)/(1 + z)$. Then, at $z \sim 20$, $T_\gamma/T_K \sim 7$ and $T_\gamma/T_S - 1 \sim 2$. In real scenarios, heating sources could be already important at these times to produce temperature deviations from the adiabatic evolution, lowering this value. Therefore, it must be taken as an upper limit. Hence, the heat per baryon and per Hubble time reads

$$\frac{2\,\mathcal{Q}|_{21}}{3\,H\,n_b} \simeq \frac{1}{2}\, \text{ʃ}_H\, \frac{A_{10}\,T_*}{H} \left(\frac{T_\gamma}{T_S} - 1 \right) \tag{5.33}$$

$$\simeq 3\ \text{K} \left(\frac{21}{1+z} \right)^{3/2} \left(\frac{T_\gamma/T_S - 1}{2} \right), \tag{5.34}$$

which is roughly an order of magnitude lower than the corresponding X-ray heat from Eq. (5.28). For lower redshifts, this difference even increases: while the X-ray heating increases by an order of magnitude at $z \simeq 15$, Eq. (5.34) would reach as much as ~ 20 K at the same epoch, if the assumption of adiabatic evolution is still valid (which should not be true, since heating sources could already be important) and the Lyα coupling is completely efficient. These considerations make the 21 cm heating term negligible in most of astrophysical scenarios, and consequently, is usually not considered, as happens in `21cmFAST`. It must be remarked, however, that if X-ray luminosities are much lower than expected, this would be the dominant heating channel at high redshifts. Furthermore, it could also be relevant for even higher redshifts, deep in the Dark Ages, when collisional coupling becomes efficient, allowing the factor $T_\gamma/T_S - 1$ to deviate from 0.

5.2.1.4 Lyα heating

Lyα scattering with atoms can transfer a fraction of energy from radiation to the gas, with a contribution from continuum and injected photons.

The heating rate, already computed in Sec. 4.3.4, reads

$$\mathcal{Q}|_{\mathrm{Ly}\alpha,\mathrm{k}} = \frac{4\pi H h\nu_\alpha \Delta\nu_D}{c} J_{\infty,k} I_k = n_b h \Delta\nu_D H \frac{J_{\infty,k}}{J_0} I_k \ , \tag{5.35}$$

where k stands for $k = c$, *continuum*, or $k = i$, *injected* photons, and $J_0(z) = c\bar{n}_b(z)/(4\pi\nu_\alpha)$ the intensity corresponding to one photon per baryon [370]. The integrals I_c and I_i encode the details of the scattering effects and depend on the temperature and the Gunn-Peterson optical depth τ_{GP} (the optical depth of Lyα photons redshifting through the IGM). For these quantities, we use the fits provided by Ref. [372].

It is straightforward to estimate the efficiency of Lyα photons to heat the medium. For the ranges of interest, epochs between $z \sim 30$ and $z \sim 10$, and for temperatures between ~ 10 K and ~ 100 K, the heating integrals $|I_k|$ are of the order of ~ 10 or lower [372]. The rate is proportional to the energy $h\Delta\nu_D \simeq 0.5\,\mathrm{K}\sqrt{T_K/(10^2\mathrm{K})}$. Employing the estimate of $J_\infty/J_0 \sim 3\times10^{-2}$ at $z \sim 20$ from Sec. 5.2.3.1, we obtain a heating per baryon in a Hubble time of

$$\frac{2\,\mathcal{Q}|_{\mathrm{Ly}\alpha,\mathrm{k}}}{3\,H\,n_b} = \frac{2}{3} h\Delta\nu_D \frac{J_{\infty,k}}{J_0} I_k \tag{5.36}$$

$$\simeq 0.1\ \mathrm{K} \left(\frac{T_K}{10^2\mathrm{K}}\right)^{1/2} \left(\frac{J_\infty/J_0}{3\times10^{-2}}\right) \left(\frac{I_k}{10}\right) \ , \tag{5.37}$$

Note that this is two orders of magnitude lower than the estimation from X-rays in Eq. (5.28), and also lower than the 21 cm contribution, Eq. (5.34). This difference even increases for lower redshifts, when X-rays are more efficient. Moreover, the term of injected photons cool the gas rather than heating it at these temperatures and redshifts, which counteracts in some amount the continuum term. Therefore, Lyα scatterings only mildly heat up the gas compared to absorption of X-rays, see Refs. [382, 9] for further comparisons. As happens with the 21 cm heating rate, with realistic X-ray luminosities this heating channel becomes subdominant and in practice (as done in `21cmFAST`) is usually neglected.

5.2.2 Ionization evolution

The evolution of the local ionized fraction of the neutral IGM, $x_e(\mathbf{x}, z) \equiv n_e/n_b$, is given by the interplay between ionizations of H and He atoms, and recombinations of positive ions. Part of the discussion is similar to that of Sec. 5.1.1, with few differences. Since the neutral IGM is a thick medium where most of ionizing photons are fastly absorbed, the recombinations to the ground state do not effectively account for the net ionized fraction, and

then case B recombination must be employed, rather than case A [354]. Moreover, the ionization of the neutral IGM is produced by X-ray photons with a mean free path long enough to escape beyond the galaxy environment, instead of ionizing UV photons locally absorbed. For that reason, the on-the-spot approximation is not as good estimate as in Sec. 5.1.1, and the proper ionization rate should be computed. Considering Eq. (5.1) and the equivalent ones for HeI and HeIII, and taking into account that conservation of charge implies $n_e = n_{\rm HII} + n_{\rm HeII} + 2n_{\rm HeIII}$, we can derive the evolution equation for x_e:

$$\frac{dx_e}{dt} = \Lambda_{\rm ion} - \alpha_{\rm B}\, C\, x_e^2\, n_b\, \text{ſ}_{\rm H}\ , \tag{5.38}$$

where $\alpha_{\rm B} \simeq 2.6 \times 10^{-13} (T_K/10^4 K)^{-0.7} cm^3 s^{-1}$ is the case-B recombination, and C is the clumping factor (evaluated at the scale on the scale of the simulation cell). The total ionization rate $\Lambda_{\rm ion}$ is given by the joint contribution of the ionizing rates Γ_j of each species j, with $n_b \Lambda_{\rm ion} = \sum_j \Gamma_j n_j$, and can be written as

$$\Lambda_{\rm ion} = \sum_j 4\pi x_j \text{ſ}_j \int_{\nu_0}^{\infty} d\nu\, \sigma_j(\nu)\, F_j\, J_X(\nu), \tag{5.39}$$

where J_X is the X-ray flux, given by Eq. (5.22), F_j accounts for the contribution from primary and secondary ionizations, and the summation goes over the different degrees of ionization $j = {\rm HI, HeI, HeII}$. In the neutral IGM, we can assume the same degree of ionization of the species HII and HeII, thus $n_{\rm HII}/n_{\rm H} \simeq n_{\rm HeII}/n_{\rm He} \simeq x_e$, the fraction of HeIII being negligible. Therefore, in the equation above we can write $x_{\rm HI} = x_{\rm HeI} = 1 - x_e$ and $x_{\rm HeII} = x_e$. The factors F_j read [378]:

$$F_j = 1 + (h\nu - E_j^{th}) \left(\frac{f_{\rm ion,HI}}{E_{\rm HI}^{th}} + \frac{f_{\rm ion,HeI}}{E_{\rm HeI}^{th}} + \frac{f_{\rm ion,HeII}}{E_{\rm HeII}^{th}} \right), \tag{5.40}$$

being E_j^{th} the threshold energy for each species, and $f_{\rm ion,j}$ the fraction of the electron's energy going into secondary ionizations of species j. We employ the fits derived in Ref. [571] for the functions $f_{\rm ion,j}$, which can be roughly approximated by Eq. (5.26) for HI, being suppressed by an order of magnitude for Helium. The unity term in the equation above stands for primary ionizations, while the second term accounts for secondary ones. These secondary ionizations are produced by electrons which, after receiving energy from a X-ray photon, become very fast and non-thermal, colliding and distributing their energy in several channels until thermalizing.

It is possible to sketch the x_e evolution in some approximate limits. Before the formation of X-ray sources and after Recombination, only a leftover fraction remained ionized. One can easily estimate the evolution of this remnant by neglecting ionizing sources in Eq. (5.38). In this simple limit, the

differential equation can be easily integrated, obtaining a slowly decaying function of redshift towards a constant value. For the recombination coefficient, it can be assumed that $T_K \simeq T_{\gamma,0}(1+z)$ (with $T_{\gamma,0} = 2.73$ K) due to Compton cooling, valid for high redshifts (as shown in Sec. 5.2.1.1). Since Recombination takes place at $z_{\rm R} \sim 10^3$, when the universe was still completely ionized, $x_e(z_{\rm R}) \sim 1$, hence, the remnant ionized fraction for redshifts much lower than $z_{\rm R}$ is given by

$$x_e \simeq \frac{H_0\sqrt{\Omega_m}}{\alpha_B(T_{\gamma,0})n_{\rm H,0}(1+z_{\rm R})^{0.8}} \simeq 3\times 10^{-4}, \tag{5.41}$$

which remarkably coincides with the precise estimation from Recombination codes such as RECFAST [565].[8] On the other hand, this fraction grows again when starbust galaxies or other sources start injecting X-ray photons to the medium. Following the same procedure of Sec. 5.2.1.2, we can treat the ionization rate using the on-the-spot approximation, to rouhgly estimate the impact of X-rays on x_e. Similarly to Eq. (5.27), and neglecting secondary ionizations, we get

$$\Lambda_{\rm ion} \simeq \frac{L_{\rm X[2-10\ keV]}}{\rm SFR} f_* \frac{\mu m_p}{h\nu_0} \frac{df_{coll}(z,M_*)}{dt}. \tag{5.42}$$

Neglecting recombinations, we can solve Eq. (5.38), obtaining

$$\begin{aligned}\Delta x_e(z) \sim 10^{-2}\Delta f_{coll}(z,M_*) &\left(\frac{L_{\rm X[2-10\ keV]}/{\rm SFR}}{3.4\times 10^{40} erg\cdot s^{-1} M_\odot^{-1} yr}\right) \\ &\times \left(\frac{f_*}{0.01}\right)\left(\frac{500eV}{h\nu_0}\right).\end{aligned} \tag{5.43}$$

Note that for the fiducial values considered, the increase in x_e would be somewhat mild. This fact, compared to the discussion in Sec. 5.1, indicates that the progress of reionization processes must be mostly driven by the expansion and overlap of HII bubbles due to UV radiation, rather than the effect of X-rays in the mostly neutral regions, which has a moderate impact. For more quantitative computations, however, a full and precise determination of x_e is required and must be computed properly.

5.2.3 Lyα flux

One of the most relevant quantities for the determination of the spin temperature is the Lyα flux, J_α, responsible of the WF effect commented in

[8] It has to be emphasized that at $z \sim 150$, the Compton coupling is not efficient anymore, and the kinetic temperature deviates from the CMB one, as commented above, but taking this into account would not alter the order-of-magnitude estimate.

Sec. 4.2.2. There are two main sources which are able to produce a relevant flux in the IGM at the redshifts of interest: the redshifted radiation from stellar emission, providing a flux $J_{\alpha,*}$, and X-ray excitation, $J_{\alpha,X}$. The total flux is then given by the sum $J_\alpha = J_{\alpha,*} + J_{\alpha,X}$. These mechanims are reviewed in the following.

5.2.3.1 Stellar emission

Once the first stars in the universe are formed, they release radiation background between the Lyman limit and the Lyα frequency. Due to the expansion of the universe, these photons can redshift to Ly-n resonances, and eventually lead to a $2p \rightarrow 1s$ transition through a decaying cascade. Due to the high optical depth of the IGM, photons redshifting to Lyman resonances are always absorbed. When a photon reaches the Ly-n resonance at redshift z, it can be emitted at $z_{max,n} > z$, which is the maximum emission redshift so that a photon reaches the Ly-n resonance at redshift z:

$$1 + z_{max,n} = (1+z)\,\frac{\nu_{n+1}}{\nu_n} = (1+z)\,\frac{1-\frac{1}{(n+1)^2}}{1-\frac{1}{n^2}}, \tag{5.44}$$

where the Ly-n frequency is $\nu_n = \nu_{LL}(1-n^{-2})$, with $\nu_{LL} = 13.6$ eV$/h$ the Lyman limit frequency. As stated in Sec. 4.3.1, some radiative cascades do not contribute to the Lyα flux, since they terminate in the 2s $\rightarrow$ 1s transition. We thus define the probability to generate a Lyα photon after the absorption by the n level as the recycled fraction of level n, $f_{rec}(n)$ [377]. This quantity can be easily computed by means of an iterative algorithm from the selection rules and the decay rates. The total Lyα flux can be written in terms of the photon comoving emissivity $\varepsilon_\alpha(\nu, z)$ as [377, 573]

$$J_{\alpha,*} = \frac{c(1+z)^2}{4\pi} \sum_{n=2}^{n_{max}} f_{rec}(n) \int_z^{z_{max,n}} dz' \frac{\varepsilon_\alpha(\nu'_n, z')}{H(z')}\ , \tag{5.45}$$

where the emission frequency is $\nu'_n = \nu_n(1+z')/(1+z)$.

Following the procedure of Sec. 5.1, we can employ a simple model for the emissivity, proportional to the comoving star formation rate density $\dot{\rho}_*(z)$ [574],

$$\varepsilon_\alpha(\nu, z) = \mathcal{N}(\nu)\frac{\dot{\rho}_*(z)}{\mu m_p} = \mathcal{N}(\nu) f_* \bar{n}_{b,0} \frac{df_{coll}(z, M_*)}{dt}\ , \tag{5.46}$$

where $\mathcal{N}(\nu)$ is the the number of emitted photons per frequency. The radiation spectral distribution in frequencies can be taken as a piecewise power law between each n and $n+1$ Lyman levels,

$$\mathcal{N}(\nu) = N_n \frac{(\beta_n+1)\nu_\alpha^{\beta_n}}{(\nu_{n+1}^{\beta_n+1} - \nu_n^{\beta_n+1})} \left(\frac{\nu}{\nu_\alpha}\right)^{\beta_n}\ , \quad \nu_n \leq \nu \leq \nu_{n+1}, \tag{5.47}$$

with $\nu_\alpha = (3/4)\nu_{LL}$ the Lyα frequency, N_n the number of photons emitted between the n and $n+1$ resonances and β_n the spectral index, whose numerical values can be derived from stellar synthesis models [575, 574]. The function above is normalized as $\int_{\nu_n}^{\nu_{n+1}} d\nu \mathcal{N}(\nu) = N_n$, while the normalization of the total spectrum gives the total number of photons emitted between the Lyα and the Lyman limit $\int_{\nu_\alpha}^{\nu_{LL}} d\nu \mathcal{N}(\nu) = \sum_n N_n = N_{\rm tot}$. For Population II (or low-metallicity) stars, $N_{\rm tot} \simeq 9690$, out of which 6520 photons are emitted between Lyα and Lyβ lines [575, 574]. For very massive and metal-free Population III stars, $N_{\rm tot} \simeq 4800$, with 2670 photons between Lyα and Lyβ [495]. However, given the lack of observations of high-redshifts galaxies, the mass distribution, metallicity and therefore the spectrum of these sources is still highly uncertain. Hence, $N_{\rm tot}$ may be considered as a free parameter, which is usually proportional to the number of ionizing photons $N_{\gamma/b}$. In `21cmFAST`, the fiducial scenario assumes Population II stars, which have $N_{\gamma/b} = 4 \times 10^3$, that, with the spectrum of Eq. (5.47), corresponds to a value of $N_{tot} \simeq 9690$.

As a side note, an emissivity proportional to ν^{-1} (normalized as $\mathcal{N}(\nu) = N_{tot}/\ln(4/3)\,\nu^{-1}$) allows to solve analytically the integral of Eq. (5.45), obtaining the following Lyα flux [9]:

$$J_{\alpha,*}(z) = \frac{c\bar{n}_b(z) f_* N_{tot}}{4\pi\nu_\alpha ln(4/3)} \sum_{n=2}^{n_{max}} f_{rec}(n) \frac{\nu_\alpha}{\nu_n} \left(f_{coll}(z, M_*) - f_{coll}(z_{max,n}, M_*)\right) \ . \tag{5.48}$$

This flux differs by less than 10% from the one computed with the piecewise power-law spectrum presented above, and given its analytical form, can provide insight about the flux evolution. Profiting from the formula above, it is possible to estimate the production of Lyα photons in the high redshift universe. Writing the intensity corresponding to one photon per baryon $J_0(z) = c\bar{n}_b(z)/(4\pi\nu_\alpha)$ as a reference value [370], it is is possible to give an order-of-magnitude approximation for the Lyα flux as

$$J_{\alpha,*}(z) \sim 3 \times 10^{-2} J_0(z) \left(\frac{N_{tot}}{9690}\right) \left(\frac{f_*}{0.01}\right) \left(\frac{f_{coll}(z, M_*)}{10^{-4}}\right), \tag{5.49}$$

where the fiducial value taken for N_{tot} corresponds to Pop II stars, as commented above, and $f_{coll}(z, M_*) \simeq 10^{-4}$ for a minimum virial temperature of 10^4 K at $z \simeq 20$ (see Fig. 2.1). With this result, the Lyα coupling coefficient from Eq. (4.46) reads

$$x_\alpha \simeq 14.5 \times S_\alpha \frac{J_{\alpha,*}(z)}{J_0(z)} \left(\frac{1+z}{21}\right)^2 \tag{5.50}$$

$$\sim 0.5\, S_\alpha \left(\frac{1+z}{21}\right)^2 \left(\frac{N_{tot}}{9690}\right) \left(\frac{f_*}{0.01}\right) \left(\frac{f_{coll}(z, M_*)}{10^{-4}}\right), \tag{5.51}$$

where, as stated in Sec. 4.3.2, S_α is an order 1 function accounting for the details of radiative transfer. Therefore, we see that, for these fiducial astrophysical parameters, the WF coefficient approaches $x_\alpha \sim 1$ at $z \simeq 20$, implying an efficient WF effect and thus a strong coupling between the spin temperature and the kinetic one from there on.

5.2.3.2 X-ray excitation

Similarly to what happens with secondary ionizations, absorption of energetic X-ray photons can lead to collisional excitation by fast electrons of Hydrogen atoms, producing a Lyα photon at the de-excitation [384]. The corresponding flux of this mechanism can be written as

$$J_{\alpha,X} = \frac{cn_b(z)}{4\pi h\nu_\alpha H\nu_\alpha} 4\pi \int_{\nu_0}^{\infty} d\nu\, J_{\rm X}(z,\nu) \sum_j (h\nu - E_j^{\rm th}) f_{{\rm Ly}\alpha}\, f_j\, x_j\, \sigma_j(\nu), \quad (5.52)$$

where $f_{{\rm Ly}\alpha}$ is the fraction of electron energy which is deposited as Lyα excitations, whose value is close to the total excitations fraction, $f_{\rm exc}$, as $f_{{\rm Ly}\alpha} \simeq 0.8 f_{\rm exc}$ [569]. In the high energy limit, where $f_{\rm exc}$ saturates to constant values of energy, the expression above can be approximated as

$$J_{\alpha,X} \simeq \frac{c}{4\pi h\nu_\alpha H\nu_\alpha} \frac{f_{{\rm Ly}\alpha}}{f_{\rm heat}} \mathcal{Q}|_X(z) = J_0(z) \frac{f_{{\rm Ly}\alpha}}{f_{\rm heat}} \frac{\mathcal{Q}|_X(z)}{H h\nu_\alpha n_b(z)} \quad (5.53)$$

with $f_{{\rm Ly}\alpha} \simeq f_{\rm heat}$ at high energies [569]. As we have done for the heating and ionization in the previous subsections, we can apply the on-the-spot approximation in the X-ray flux of the equation above, to estimate the rough contribution of this term to the total Lyα background. Employing Eq. (5.27), one can find

$$\begin{aligned} J_{\alpha,X}(z) \simeq 10^{-4} J_0(z) & \left(\frac{-(1+z) df_{coll}(z, M_*)/dz}{10^{-3}} \right) \\ & \times \left(\frac{L_{\rm X[2-10\ keV]}/{\rm SFR}}{3.4 \times 10^{40} erg \cdot s^{-1} M_\odot^{-1} yr} \right) \left(\frac{f_*}{0.01} \right) \left(\frac{f_{{\rm Ly}\alpha}}{0.2} \right), \end{aligned} \quad (5.54)$$

where we have evaluated $df_{coll}(z, M_*)/dt/H(z) = -(1+z) df_{coll}(z, M_*)/dz \simeq 10^{-3}$ as a fiducial value at $z \simeq 20$ for a minimum virial temperature of 10^4 K. Note that this flux is about 2 orders of magnitude lower than the estimated one from Eq. (5.49), and therefore, only appears as a subdominant contribution to the overall flux. However, quantitative computations must still consider it for a precise evaluation of the WF coupling epoch.

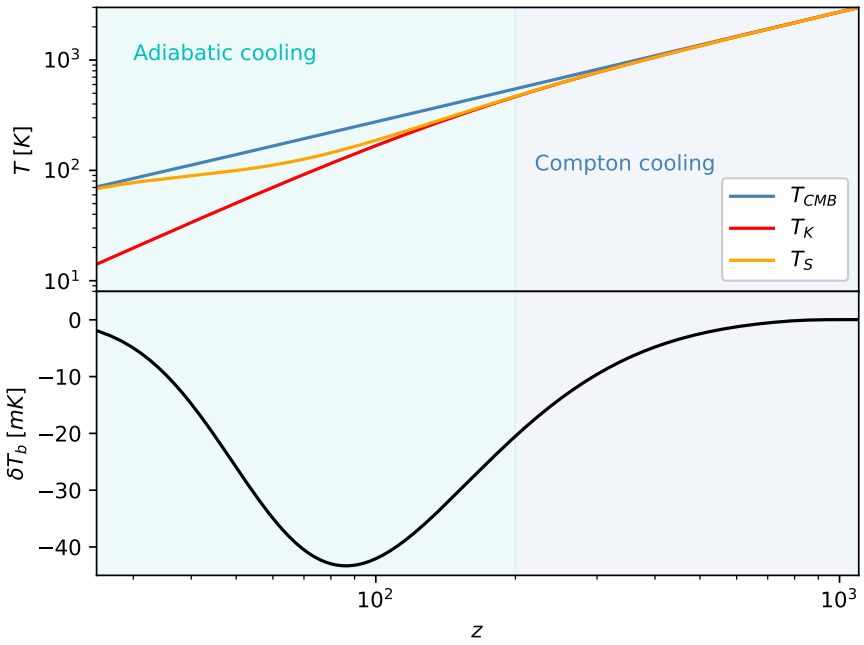

Figure 5.3: Evolution of the CMB, kinetic and spin temperatures (top panel) and global brightness temperature (bottom panel) as a function of redshift during the Dark Ages.

5.3 Evolution of the 21 cm line

In this section an overview of the most important phases of the thermal history of the universe is presented. The different epochs, driven by the heating and ionization processes studied in the previous sections, may be probed by means of the 21 cm line, either from its global sky average or from the power spectrum described in Sec. 4.4. It is worth writing here explicitly the global brightness temperature, $\overline{\delta T}_b$, taking the background quantities in Eq. (4.21)[9] and assuming the default cosmological parameters:

$$\overline{\delta T}_b \simeq 27\,\mathrm{mK}\, x_{\mathrm{HI}} \left(1 - \frac{T_\gamma}{T_S}\right) \left(\frac{1+z}{10}\right)^{1/2} \tag{5.55}$$

Figure 5.3 shows the evolution of the CMB, kinetic and spin temperatures (top panel) and global brightness temperature (bottom panel) during the Dark Ages. After that period, more complex astrophysical modeling is needed. Fig. 5.4 presents the evolution of the CMB, kinetic and spin temperatures (top panel), global brightness temperature (medium panel)

[9]Strictly, the global signal must be obtained from averaging the brightness temperature fields from simulations, rather than by replacing in Eq. (4.21) the background values, which may induce slightly different results. This average has been analytically treated, making use of the probability distribution for the density, in Ref. [9]. In any case, the conclusions regarding the IGM history outlined in this section are unaltered.

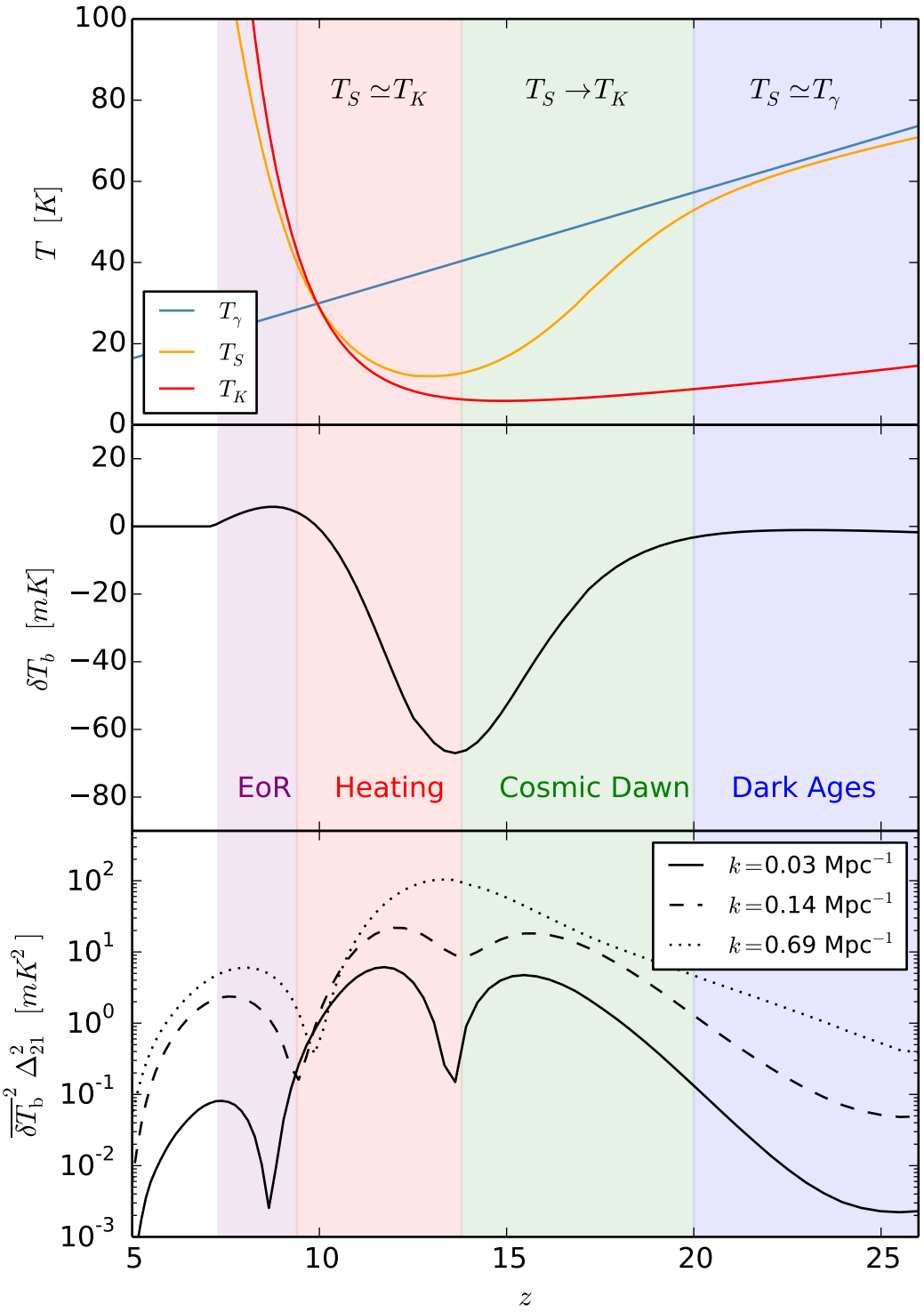

Figure 5.4: Evolution of the CMB, kinetic and spin temperatures (top panel), global brightness temperature (medium panel) and 21 cm power spectrum (bottom panel) as a function of redshift.

and 21 cm power spectrum (bottom panel) for a standard thermal history, computed from a `21cmFAST` simulation. The power spectrum is evaluated at three differentt scales, $k = 0.03$, 0.14, $0.69\,\mathrm{Mpc}^{-1}$. The specific astrophysical model assume Population II stars, with the parameters $M_{\rm vir}^{\rm min} = 10^8 M_\odot$, $L_{\rm X[2-10\ keV]}/\mathrm{SFR} = 10^{40.5}$, $N_{\gamma/b} = 4 \times 10^3$ and $f_* = 0.01$. By inspecting the 21 cm signal, it is possible to identify the following epochs:

1. **Dark Ages and collisional coupling.** Firstly, after Recombination, happening at $z \sim 1100$, the gas temperature evolves still coupled to the CMB, due to Compton cooling (discussed in Sec. 5.2.1.1). When the kinetic temperature departs from the CMB one, evolving adiabatically, the still high density of the IGM induces collisional coupling discussed in Sec. 4.2.1. Hence, the spin temperature is expected to be coupled to the gas by that process, producing an absorption dip in the brightness temperature, Eq. (5.55). This absorption regime persists as long as the gas is dense enough to produce sufficient collisions, whereupon CMB photons drive again the spin temperature and the signal reduces its amplitude. Such signal would be hard to detect due to its small amplitude and high redshift range (or equivalently, low frequencies). Figure 5.3 depicts this period, specifying when the gas temperature evolves by Compton cooling or adiabatically.

2. **End of the Dark Ages.** After the collisional coupling period but at high enough redshifts, $z > 20$, there are not enough stars formed yet, and thus the hyperfine transitions are mainly driven by absorption and emission of CMB photons. The spin temperature is therefore coupled again to the CMB temperature, which cools as $1 + z$, and thus the brightness temperature remains close to zero. However, given the growth of fluctuations, the 21 cm power spectrum starts to increase. Meanwhile, since the gas is already thermally decoupled from the CMB, its kinetic temperature continues cooling adiabatically as $(1 + z)^2$. The blue region in Fig. 5.4 represents this era.

3. **Cosmic Dawn and WF effect.** Once the first stars are born, they start to emit UV radiation which redshift to Lyman resonances. These photons scatter with neutral Hydrogen atoms with a high cross section, causing spin-flip transitions and modifying the hyperfine level populations. This effect, the so-called WF effect already studied in Sec. 4.2.2, couples the spin temperature to the kinetic temperature of the gas, which in this epoch is still cooling adiabatically. The factor T_γ/T_S of Eq. (5.55) leads to an absorption profile in the brightness temperature. The peak in the power spectrum indicates the summit of the Lyα fluctuations. In Fig. 5.4, this epoch is depicted by the green area.

4. **Heating of the IGM.** When there is enough X-ray radiation emitted from starbusts and other sources, the IGM begins to be heated, increasing T_K, and therefore the spin temperature too, which is expected to be mostly coupled to T_K at this time due to the WF effect. This reduces the depth of the peak of the global signal, and eventually leads to a transition between the absorption regime to an emission regime when $T_S > T_\gamma$. The largest fluctuations in heating are indicated in the peak of the power spectrum. The red area corresponds to this phase in Fig. 5.4.

5. **Epoch of Reionization.** Finally, when the ionized bubbles around each light source grow enough to overlap, the IGM moves into a fully ionized phase. Since the global signal is proportional to the ionized fraction, it begins to decrease until it dissappears at the end of the EoR. The peak in the power spectrum roughly corresponds to this moment. The purple area of Fig. 5.4 illustrates this period.

It is possible to gain insight into the milestones in the evolution of the 21 cm power spectrum shown in Fig. 5.4 by inspecting the behavior of the β_i coefficients defined in Sec. 4.4. As can be noticed from the examination of β_α, this coefficient is small until the Lyα flux becomes strong enough. After that, when Lyα coupling dominates, $x_{\rm tot} \simeq x_\alpha$ and β_α decays again. This leaves a peak in β_α, and also in the power spectrum around the onset of Lyα radiation (see, e.g., Fig. 9 of Ref. [354]). This peak traces the epoch of the Cosmic Dawn, and is seen in Fig. 5.4. The β_T coefficient presents a similar behavior. Neglecting the collisional term, with the proper normalization to avoid the singularity, it reads

$$\overline{\delta T_b}\beta_T \propto \left(1 - \frac{T_\gamma}{T_S}\right)\frac{T_\gamma}{T_K - T_\gamma} = \frac{x_{\rm tot}}{1 + x_{\rm tot}}\frac{T_\gamma}{T_K}, \tag{5.56}$$

The kinetic temperature is expected to cool adiabatically, until the X-ray radiation becomes efficient to heat the IGM, and T_K grows. At that moment, T_K gets its lower value, and thus T_γ/T_K the maximum. On the other hand, the factor $x_{\rm tot}/(1 + x_{\rm tot}) \simeq x_\alpha/(1 + x_\alpha)$ grows until it saturates to 1 when $x_\alpha \gg 1$. Both contributions place a maximum in this term of the power spectrum, which marks the heating epoch. This maximum does not have to occur exactly when T_K is minimum, due to the $x_{\rm tot}/(1 + x_{\rm tot})$ term. Finally, the existence of a third peak indicating the EoR can also be easily interpreted. One has to bear in mind that, as commented in Sec. 5.1, the ionization process occurs due to the growth of completely ionized HII bubbles onto the neutral IGM, and is hence a highly inhomogeneous process. However, both the mostly neutral IGM and the universe after

reionization present homogeneous ionization fractions ($\sim 10^{-4}$ and ~ 1, respectively), with small deviations from the mean ionization value. During the transition between the two periods, the non-homogeneous expansion of HII bubbles enhance the spatial fluctuations, which are reduced again when EoR is nearly complete. Fluctuations must present then a peak, which is also reflected on the 21 cm power spectrum. The qualitative behavior of the power spectrum at the different scales is similar, although at smaller scales, the heating and Lyα peaks spread and merge.

As can be seen from the previous discussion, both the 21 cm global signal and its power spectrum could provide us with a superb tool to study the thermal history of the IGM: from the birth of the first stars (that can be related to the beginning of the absorption regime) to the end of reionization (which we could date when the signal vanishes), passing through the onset of the IGM heating (linked to the position of the absorption dip and the transition between absorption and emission regimes). Observing and understanding this evolution would provide us with highly relevant information about the astrophysical processes which take place during these times, and more importantly, about the processes of structure formation and the nature of the Dark Matter component, which is the focus of this thesis.

Bibliography

[1] L. Lopez-Honorez, O. Mena, S. Palomares-Ruiz and P. Villanueva-Domingo, *Warm dark matter and the ionization history of the Universe*, *Phys. Rev.* **D96** (2017) 103539, [1703.02302]. Cited on page i, 41, 209, 212, 350, and 354.

[2] P. Villanueva-Domingo, N. Y. Gnedin and O. Mena, *Warm Dark Matter and Cosmic Reionization*, *Astrophys. J.* **852** (2018) 139, [1708.08277]. Cited on page i, 41, 210, 349, and 351.

[3] P. Villanueva-Domingo, S. Gariazzo, N. Y. Gnedin and O. Mena, *Was there an early reionization component in our universe?*, *JCAP* **04** (2018) 024, [1712.02807]. Cited on page i, 132, 211, and 352.

[4] M. Escudero, L. Lopez-Honorez, O. Mena, S. Palomares-Ruiz and P. Villanueva-Domingo, *A fresh look into the interacting dark matter scenario*, *JCAP* **1806** (2018) 007, [1803.08427]. Cited on page i, 49, 212, and 353.

[5] L. Lopez-Honorez, O. Mena and P. Villanueva-Domingo, *Dark matter microphysics and 21 cm observations*, *Phys. Rev.* **D99** (2019) 023522, [1811.02716]. Cited on page i, 49, 110, 213, and 354.

[6] O. Mena, S. Palomares-Ruiz, P. Villanueva-Domingo and S. J. Witte, *Constraining the primordial black hole abundance with 21-cm cosmology*, *Phys. Rev.* **D100** (2019) 043540, [1906.07735]. Cited on page i, 69, 73, 79, 135, 213, and 355.

[7] P. Villanueva-Domingo and F. Villaescusa-Navarro, *Removing Astrophysics in 21 cm Maps with Neural Networks*, ApJ **907** (Jan., 2021) 44, [2006.14305]. Cited on page i, 214, 350, and 356.

[8] S. Witte, P. Villanueva-Domingo, S. Gariazzo, O. Mena and S. Palomares-Ruiz, *EDGES result versus CMB and low-redshift constraints on ionization histories*, *Phys. Rev.* **D97** (2018) 103533, [1804.03888]. Cited on page ii, and 110.

[9] P. Villanueva-Domingo, O. Mena and J. Miralda-Escudé, *Maximum amplitude of the high-redshift 21-cm absorption feature*, *Physical Review D* **101** (Apr, 2020) . Cited on page ii, 139, 141, 145, and 147.

[10] L. Lopez-Honorez, O. Mena, S. Palomares-Ruiz, P. Villanueva-Domingo and S. J. Witte, *Variations in fundamental constants at the cosmic dawn*, J. Cosmology Astropart. Phys. **2020** (June, 2020) 026, [2004.00013]. Cited on page ii.

[11] P. Villanueva-Domingo and K. Ichiki, *21 cm Forest Constraints on Primordial Black Holes*, 2104.10695. Cited on page ii, and 79.

[12] P. Villanueva-Domingo, O. Mena and S. Palomares-Ruiz, *A brief review on primordial black holes as dark matter*, 2103.12087. Cited on page ii.

[13] A. Einstein, *Kosmologische Betrachtungen zur allgemeinen Relativitätstheorie*, *Sitzungsberichte der Königlich Preußischen Akademie der Wissenschaften (Berlin* (Jan., 1917) 142–152. Cited on page 3, and 4.

[14] G. Lemaître, *Un Univers homogène de masse constante et de rayon croissant rendant compte de la vitesse radiale des nébuleuses extra-galactiques*, *Annales de la Société Scientifique de Bruxelles* **47** (Jan., 1927) 49–59. Cited on page 3, and 10.

[15] E. Hubble, *A Relation between Distance and Radial Velocity among Extra-Galactic Nebulae*, *Proceedings of the National Academy of Science* **15** (Mar., 1929) 168–173. Cited on page 3.

[16] G. Lemaître, *The Beginning of the World from the Point of View of Quantum Theory.*, Nature **127** (May, 1931) 706. Cited on page 3.

[17] R. A. Alpher, H. Bethe and G. Gamow, *The origin of chemical elements*, *Phys. Rev.* **73** (Apr, 1948) 803–804. Cited on page 3.

[18] R. A. Alpher and R. Herman, *Evolution of the Universe*, Nature **162** (Nov., 1948) 774–775. Cited on page 3.

[19] A. A. Penzias and R. W. Wilson, *Measurement of the Flux Density of CAS a at 4080 Mc/s.*, ApJ **142** (Oct., 1965) 1149. Cited on page 3.

[20] P. J. E. Peebles, J. Page, Lyman A. and R. B. Partridge, *Finding the Big Bang*. 2009. Cited on page 3.

[21] G. Bertone and D. Hooper, *History of dark matter*, *Reviews of Modern Physics* **90** (Oct., 2018) 045002, [1605.04909]. Cited on page 4, 18, 20, and 21.

[22] A. G. Riess, A. V. Filippenko, P. Challis, A. Clocchiatti, A. Diercks, P. M. Garnavich et al., *Observational Evidence from Supernovae for an Accelerating Universe and a Cosmological Constant*, AJ **116** (Sept., 1998) 1009–1038, [astro-ph/9805201]. Cited on page 4.

[23] S. Perlmutter, G. Aldering, G. Goldhaber, R. A. Knop, P. Nugent, P. G. Castro et al., *Measurements of Ω and Λ from 42 High-Redshift Supernovae*, ApJ **517** (June, 1999) 565–586, [astro-ph/9812133]. Cited on page 4.

[24] Planck collaboration, N. Aghanim et al., *Planck 2018 results. VI. Cosmological parameters*, *Astron. Astrophys.* **641** (2020) A6, [1807.06209]. Cited on page 4, 10, 12, 13, 30, 37, 129, and 131.

[25] D. J. Eisenstein, I. Zehavi, D. W. Hogg, R. Scoccimarro, M. R. Blanton, R. C. Nichol et al., *Detection of the Baryon Acoustic Peak in the Large-Scale Correlation Function of SDSS Luminous Red Galaxies*, ApJ **633** (Nov., 2005) 560–574, [astro-ph/0501171]. Cited on page 5, and 50.

[26] S. Cole, W. J. Percival, J. A. Peacock, P. Norberg, C. M. Baugh, C. S. Frenk et al., *The 2dF Galaxy Redshift Survey: power-spectrum analysis of the final data set and cosmological implications*, MNRAS **362** (Sept., 2005) 505–534, [astro-ph/0501174]. Cited on page 5, and 50.

[27] M. Ata et al., *The clustering of the SDSS-IV extended Baryon Oscillation Spectroscopic Survey DR14 quasar sample: first measurement of baryon acoustic oscillations between redshift 0.8 and 2.2*, *Mon. Not. Roy. Astron. Soc.* **473** (2018) 4773–4794, [1705.06373]. Cited on page 5.

[28] A. de Mattia et al., *The Completed SDSS-IV extended Baryon Oscillation Spectroscopic Survey: measurement of the BAO and growth rate of structure of the emission line galaxy sample from the anisotropic power spectrum between redshift 0.6 and 1.1*, 2007.09008. Cited on page 5, and 50.

[29] M. Dijkstra, *Saas-Fee Lecture Notes: Physics of Lyman Alpha Radiative Transfer*, 1704.03416. Cited on page 5.

[30] H. Mo, F. C. van den Bosch and S. White, *Galaxy Formation and Evolution*. 2010. Cited on page 5, 30, 31, 68, 103, and 136.

[31] R. H. Becker, X. Fan, R. L. White, M. A. Strauss, V. K. Narayanan, R. H. Lupton et al., *Evidence for Reionization at z∼6: Detection of a Gunn-Peterson Trough in a z=6.28 Quasar*, *AJ* **122** (Dec., 2001) 2850–2857, [astro-ph/0108097]. Cited on page 6, and 130.

[32] H. C. van de Hulst, *Radiogolven uit het wereldruim: II. Herkomst der radiogolvenRadiogolven uit het wereldruim: II. Herkomst der radiogolvenRadio waves from space.*, *Nederlandsch Tijdschrift voor Natuurkunde* **11** (Jan., 1945) 210–221. Cited on page 6.

[33] H. I. Ewen and E. M. Purcell, *Observation of a Line in the Galactic Radio Spectrum: Radiation from Galactic Hydrogen at 1,420 Mc./sec.*, Nature **168** (Sept., 1951) 356. Cited on page 6.

[34] C. A. Muller and J. H. Oort, *Observation of a Line in the Galactic Radio Spectrum: The Interstellar Hydrogen Line at 1,420 Mc./sec., and an Estimate of Galactic Rotation*, Nature **168** (Sept., 1951) 357–358. Cited on page 6.

[35] J. L. Pawsey, *Observation of a Line in the Galactic Radio Spectrum: The Interstellar Hydrogen Line at 1,420 Mc./sec., and an Estimate of Galactic Rotation*, Nature **168** (Sept., 1951) 358. Cited on page 6.

[36] J. D. Bowman, A. E. E. Rogers, R. A. Monsalve, T. J. Mozdzen and N. Mahesh, *An absorption profile centred at 78 megahertz in the sky-averaged spectrum*, *Nature* **555** (2018) 67–70. Cited on page 7, 78, 107, 109, and 110.

[37] J. D. Bowman, I. Cairns, D. L. Kaplan, T. Murphy, D. Oberoi, L. Staveley-Smith et al., *Science with the murchison widefield array*, *Publications of the Astronomical Society of Australia* **30** (2013) . Cited on page 7, and 114.

[38] M. P. van Haarlem, M. W. Wise, A. W. Gunst, G. Heald, J. P. McKean, J. W. T. Hessels et al., *Lofar: The low-frequency array*, *Astronomy and Astrophysics* **556** (Jul, 2013) A2. Cited on page 8, and 115.

[39] A. P. Beardsley, M. F. Morales, A. Lidz, M. Malloy and P. M. Sutter, *Adding context to James Webb Space Telescope surveys with current and future 21cm radio observations*, *Astrophys. J.* **800** (2015) 128, [1410.5427]. Cited on page 8, and 116.

[40] G. Mellema et al., *Reionization and the cosmic dawn with the Square Kilometre Array*, *Exper. Astron.* **36** (2013) 235–318, [1210.0197]. Cited on page 8, and 116.

[41] LIGO Scientific Collaboration and Virgo Collaboration collaboration, B. P. Abbott, R. Abbott, T. D. Abbott, M. R. Abernathy, F. Acernese, K. Ackley et al., *Observation of gravitational waves from a binary black hole merger*, *Phys. Rev. Lett.* **116** (Feb, 2016) 061102. Cited on page 8, 26, 56, and 348.

[42] A. Einstein, *Bemerkung zu der Arbeit von A. Friedmann „Über die Krümmung des Raumes“*, *Zeitschrift fur Physik* **11** (Dec., 1922) 326–326. Cited on page 10.

[43] A. Friedmann, *Über die Möglichkeit einer Welt mit konstanter negativer Krümmung des Raumes*, *Zeitschrift fur Physik* **21** (Dec., 1924) 326–332. Cited on page 10.

[44] H. P. Robertson, *Kinematics and World-Structure*, ApJ **82** (Nov., 1935) 284. Cited on page 10.

[45] A. G. Walker, *On Milne's Theory of World-Structure*, *Proceedings of the London Mathematical Society* **42** (Jan., 1937) 90–127. Cited on page 10.

[46] D. Baumann, *Inflation*, in *Theoretical Advanced Study Institute in Elementary Particle Physics: Physics of the Large and the Small*, pp. 523–686, 2011. 0907.5424. DOI. Cited on page 10, and 14.

[47] S. Dodelson, *Modern cosmology*. 2003. Cited on page 11, 35, 36, and 59.

[48] G. F. R. Ellis, R. Maartens and M. A. H. MacCallum, *Relativistic Cosmology*. 2012. Cited on page 11.

[49] L. Pogosian, G.-B. Zhao and K. Jedamzik, *Recombination-independent determination of the sound horizon and the Hubble constant from BAO*, *Astrophys. J. Lett.* **904** (2020) L17, [2009.08455]. Cited on page 12.

[50] E. Di Valentino, O. Mena, S. Pan, L. Visinelli, W. Yang, A. Melchiorri et al., *In the Realm of the Hubble tension – a Review of Solutions*, 2103.01183. Cited on page 12.

[51] V. Mukhanov, *Physical Foundations of Cosmology*. 2005, 10.2277/0521563984. Cited on page 13, and 27.

[52] R. Barkana and A. Loeb, *In the beginning: The First sources of light and the reionization of the Universe*, *Phys. Rept.* **349** (2001) 125–238, [astro-ph/0010468]. Cited on page 13, 31, 120, and 123.

[53] J. Lesgourgues, G. Mangano, G. Miele and S. Pastor, *Neutrino Cosmology*. Cambridge University Press, 2, 2013. Cited on page 14, and 37.

[54] F. Iocco, G. Mangano, G. Miele, O. Pisanti and P. D. Serpico, *Primordial Nucleosynthesis: from precision cosmology to fundamental physics*, *Phys. Rept.* **472** (2009) 1–76, [0809.0631]. Cited on page 14, and 37.

[55] C. Pitrou, A. Coc, J.-P. Uzan and E. Vangioni, *Precision big bang nucleosynthesis with improved Helium-4 predictions*, *Phys. Rept.* **754** (2018) 1–66, [1801.08023]. Cited on page 14.

[56] W. Hu, *CMB temperature and polarization anisotropy fundamentals*, *Annals Phys.* **303** (2003) 203–225, [astro-ph/0210696]. Cited on page 15.

[57] A. Ferrara and S. Pandolfi, *Reionization of the Intergalactic Medium*, *Proc. Int. Sch. Phys. Fermi* **186** (2014) 1–57, [1409.4946]. Cited on page 16, and 120.

[58] J. H. Wise, *Cosmic reionisation*, *Contemporary Physics* **60** (Apr, 2019) 145–163. Cited on page 16, 120, 123, and 125.

[59] R. H. Sanders, *The Dark Matter Problem: A Historical Perspective*. 2010. Cited on page 18.

[60] J. G. de Swart, G. Bertone and J. van Dongen, *How dark matter came to matter*, *Nature Astronomy* **1** (Mar., 2017) 0059, [1703.00013]. Cited on page 18.

[61] C. S. Frenk and S. D. M. White, *Dark matter and cosmic structure*, *Annalen der Physik* **524** (Oct., 2012) 507–534, [1210.0544]. Cited on page 18.

[62] P. J. E. Peebles, *Origin of the CDM Paradigm*, 2018. Cited on page 18, and 20.

[63] F. Zwicky, *Die Rotverschiebung von extragalaktischen Nebeln*, *Helvetica Physica Acta* **6** (Jan., 1933) 110–127. Cited on page 18.

[64] F. Zwicky, *On the Masses of Nebulae and of Clusters of Nebulae*, ApJ **86** (Oct., 1937) 217. Cited on page 18.

[65] S. Smith, *The Mass of the Virgo Cluster*, ApJ **83** (Jan., 1936) 23. Cited on page 18.

[66] H. W. Babcock, *The rotation of the Andromeda Nebula*, *Lick Observatory Bulletin* **498** (Jan., 1939) 41–51. Cited on page 18.

[67] N. U. Mayall and L. H. Aller, *The Rotation of the Spiral Nebula Messier 33.*, ApJ **95** (Jan., 1942) 5. Cited on page 18.

[68] F. D. Kahn and L. Woltjer, *Intergalactic Matter and the Galaxy.*, ApJ **130** (Nov., 1959) 705. Cited on page 18.

[69] V. C. Rubin and J. Ford, W. Kent, *Rotation of the Andromeda Nebula from a Spectroscopic Survey of Emission Regions*, ApJ **159** (Feb., 1970) 379. Cited on page 18.

[70] K. C. Freeman, *On the Disks of Spiral and S0 Galaxies*, ApJ **160** (June, 1970) 811. Cited on page 18.

[71] D. H. Rogstad and G. S. Shostak, *Gross Properties of Five Scd Galaxies as Determined from 21-CENTIMETER Observations*, ApJ **176** (Sept., 1972) 315. Cited on page 18.

[72] R. N. Whitehurst and M. S. Roberts, *High-Velocity Neutral Hydrogen in the Central Region of the Andromeda Galaxy*, ApJ **175** (July, 1972) 347. Cited on page 18.

[73] M. S. Roberts and A. H. Rots, *Comparison of Rotation Curves of Different Galaxy Types*, A&A **26** (Aug., 1973) 483–485. Cited on page 18.

[74] J. P. Ostriker and P. J. E. Peebles, *A Numerical Study of the Stability of Flattened Galaxies: or, can Cold Galaxies Survive?*, ApJ **186** (Dec., 1973) 467–480. Cited on page 18.

[75] J. P. Ostriker, P. J. E. Peebles and A. Yahil, *The Size and Mass of Galaxies, and the Mass of the Universe*, ApJ **193** (Oct., 1974) L1. Cited on page 18.

[76] J. Einasto, A. Kaasik and E. Saar, *Dynamic evidence on massive coronas of galaxies*, Nature **250** (July, 1974) 309–310. Cited on page 18.

[77] A. Bosma, *The distribution and kinematics of neutral hydrogen in spiral galaxies of various morphological types*. PhD thesis, -, Jan., 1978. Cited on page 18.

[78] V. C. Rubin, J. Ford, W. K. and N. Thonnard, *Extended rotation curves of high-luminosity spiral galaxies. IV. Systematic dynamical properties, Sa -> Sc.*, ApJ **225** (Nov., 1978) L107–L111. Cited on page 18.

[79] S. M. Faber and J. S. Gallagher, *Masses and mass-to-light ratios of galaxies.*, ARA&A **17** (Jan., 1979) 135–187. Cited on page 18.

[80] R. Cowsik and J. McClelland, *An Upper Limit on the Neutrino Rest Mass*, Phys. Rev. Lett. **29** (Sept., 1972) 669–670. Cited on page 19.

[81] R. Cowsik and J. McClelland, *Gravity of Neutrinos of Nonzero Mass in Astrophysics*, ApJ **180** (Feb., 1973) 7–10. Cited on page 19.

[82] A. S. Szalay and G. Marx, *Neutrino rest mass from cosmology*, *Astron. Astrophys.* **49** (1976) 437–441. Cited on page 19.

[83] S. S. Gershtein and Y. B. Zel'dovich, *Rest Mass of Muonic Neutrino and Cosmology*, *ZhETF Pisma Redaktsiiu* **4** (Sept., 1966) 174. Cited on page 19.

[84] A. D. Dolgov, *Three P's in Cosmology: Progress, Problems, and Perspectives*, *EPJ Web Conf.* **71** (2014) 00040. Cited on page 19, and 20.

[85] A. D. Dolgov, *Neutrinos in cosmology*, Phys. Rep. **370** (Nov., 2002) 333–535, [hep-ph/0202122]. Cited on page 19.

[86] S. Tremaine and J. E. Gunn, *Dynamical role of light neutral leptons in cosmology*, Phys. Rev. Lett. **42** (Feb., 1979) 407–410. Cited on page 19.

[87] V. A. Lubimov, E. G. Novikov, V. Z. Nozik, E. F. Tretyakov and V. S. Kosik, *An estimate of the ν_e mass from the β-spectrum of tritium in the valine molecule*, *Physics Letters B* **94** (July, 1980) 266–268. Cited on page 19.

[88] J. R. Bond, G. Efstathiou and J. Silk, *Massive neutrinos and the large-scale structure of the universe*, *Phys. Rev. Lett.* **45** (Dec, 1980) 1980–1984. Cited on page 19.

[89] J. R. Bond, J. Centrella, A. S. Szalay and J. R. Wilson, *Dark matter and shocked pancakes*, in *Formation and Evolution of Galaxies and Large Structures in the Universe* (J. Audouze and J. Tran Thanh Van, eds.), vol. 117 of *NATO Advanced Study Institute (ASI) Series C*, p. 87, Jan., 1984. Cited on page 19.

[90] A. G. Doroshkevich, Y. B. Zeldovich, R. A. Syunyaev and M. Y. Khlopov, *Astrophysical implications of the neutrino rest mass. II - The density-perturbation spectrum and small-scale fluctuations in the microwave background. III - Nonlinear growth of perturbations and the missing mass*, *Pisma v Astronomicheskii Zhurnal* **6** (Aug., 1980) 457–469. Cited on page 19.

[91] A. G. Doroshkevich, M. I. Khlopov, R. A. Sunyaev, A. S. Szalay and I. B. Zeldovich, *Cosmological impact of the neutrino rest mass*, *Annals of the New York Academy of Sciences* **375** (Dec., 1981) 32–42. Cited on page 19.

[92] M. Davis, J. Huchra, D. W. Latham and J. Tonry, *A survey of galaxy redshifts. II. The large scale space distribution.*, ApJ **253** (Feb., 1982) 423–445. Cited on page 19.

[93] S. D. M. White, C. S. Frenk and M. Davis, *Clustering in a neutrino-dominated universe*, ApJ **274** (Nov., 1983) L1–L5. Cited on page 19.

[94] P. J. E. Peebles, *Large-scale background temperature and mass fluctuations due to scale-invariant primeval perturbations*, ApJ **263** (Dec., 1982) L1–L5. Cited on page 19.

[95] M. Davis, G. Efstathiou, C. S. Frenk and S. D. M. White, *The evolution of large-scale structure in a universe dominated by cold dark matter*, ApJ **292** (May, 1985) 371–394. Cited on page 19.

[96] W. H. Press and P. Schechter, *Formation of galaxies and clusters of galaxies by selfsimilar gravitational condensation*, *Astrophys. J.* **187** (1974) 425–438. Cited on page 20, 32, 33, and 61.

[97] R. K. Sheth and G. Tormen, *Large scale bias and the peak background split*, *Mon. Not. Roy. Astron. Soc.* **308** (1999) 119, [astro-ph/9901122]. Cited on page 20, and 33.

[98] R. K. Sheth, H. J. Mo and G. Tormen, *Ellipsoidal collapse and an improved model for the number and spatial distribution of dark matter haloes*, *Mon. Not. Roy. Astron. Soc.* **323** (2001) 1, [astro-ph/9907024]. Cited on page 20, and 33.

[99] J. F. Navarro, C. S. Frenk and S. D. M. White, *A Universal Density Profile from Hierarchical Clustering*, ApJ **490** (Dec., 1997) 493–508, [astro-ph/9611107]. Cited on page 20, and 22.

[100] G. Steigman and M. S. Turner, *Cosmological constraints on the properties of weakly interacting massive particles*, *Nuclear Physics B* **253** (Jan., 1985) 375–386. Cited on page 20.

[101] P. Hut, *Limits on masses and number of neutral weakly interacting particles*, *Physics Letters B* **69** (July, 1977) 85–88. Cited on page 20.

[102] B. W. Lee and S. Weinberg, *Cosmological lower bound on heavy-neutrino masses*, Phys. Rev. Lett. **39** (July, 1977) 165–168. Cited on page 20.

[103] K. Sato and M. Kobayashi, *Cosmological Constraints on the Mass and the Number of Heavy Lepton Neutrinos*, *Progress of Theoretical Physics* **58** (Dec., 1977) 1775–1789. Cited on page 20.

[104] D. A. Dicus, E. W. Kolb and V. L. Teplitz, *Cosmological upper bound on heavy-neutrino lifetimes*, Phys. Rev. Lett. **39** (July, 1977) 168–171. Cited on page 20.

[105] M. I. Vysotskii, A. D. Dolgov and I. B. Zeldovich, *Cosmological limits on the masses of neutral leptons*, *ZhETF Pisma Redaktsiiu* **26** (Aug., 1977) 200–202. Cited on page 20.

[106] Y. B. Zeldovich, *Survey of Modern Cosmology*, *Advances in Astronomy and Astrophysics* **3** (Jan., 1965) 241–379. Cited on page 20.

[107] Y. B. Zeldovic, L. B. Okun and S. B. Pikelner, *Quarks, astrophysical and physico-chemical aspects*, *Physics Letters* **17** (July, 1965) 164–166. Cited on page 20.

[108] J. Ellis, J. S. Hagelin, D. V. Nanopoulos, K. Olive and M. Srednicki, *Supersymmetric relics from the big bang*, *Nuclear Physics B* **238** (June, 1984) 453–476. Cited on page 20.

[109] J. Preskill, M. B. Wise and F. Wilczek, *Cosmology of the Invisible Axion*, *Phys. Lett. B* **120** (1983) 127–132. Cited on page 20.

[110] R. D. Peccei and H. R. Quinn, CP *conservation in the presence of pseudoparticles*, *Phys. Rev. Lett.* **38** (Jun, 1977) 1440–1443. Cited on page 20.

[111] D. J. E. Marsh, *Axion cosmology*, Phys. Rep. **643** (July, 2016) 1–79, [1510.07633]. Cited on page 20.

[112] K. Griest, *The Search for the Dark Matter: WIMPs and MACHOs*, in *Texas/PASCOS '92: Relativistic Astrophysics and Particle Cosmology* (C. W. Akerlof and M. A. Srednicki, eds.), vol. 688, p. 390, Jan., 1993. hep-ph/9303253. DOI. Cited on page 21.

[113] P. Meszaros, *Primeval black holes and galaxy formation.*, A&A **38** (Jan., 1975) 5–13. Cited on page 21, and 55.

[114] S. D. M. White and M. J. Rees, *Core condensation in heavy halos: a two-stage theory for galaxy formation and clustering.*, MNRAS **183** (May, 1978) 341–358. Cited on page 21.

[115] H. Pagels and J. R. Primack, *Supersymmetry, cosmology, and new physics at teraelectronvolt energies*, *Phys. Rev. Lett.* **48** (Jan, 1982) 223–226. Cited on page 21, and 38.

[116] J. R. Bond, A. S. Szalay and M. S. Turner, *Formation of galaxies in a gravitino-dominated universe*, *Phys. Rev. Lett.* **48** (Jun, 1982) 1636–1639. Cited on page 21, and 34.

[117] G. R. Blumenthal, H. Pagels and J. R. Primack, *Galaxy formation by dissipationless particles heavier than neutrinos*, Nature **299** (Sept., 1982) 37–38. Cited on page 21, and 34.

[118] S. Dodelson and L. M. Widrow, *Sterile neutrinos as dark matter*, *Phys. Rev. Lett.* **72** (Jan, 1994) 17–20. Cited on page 21, and 39.

[119] X. Shi and G. M. Fuller, *New Dark Matter Candidate: Nonthermal Sterile Neutrinos*, Phys. Rev. Lett. **82** (Apr., 1999) 2832–2835, [astro-ph/9810076]. Cited on page 21, and 40.

[120] A. Del Popolo and M. Le Delliou, *Small Scale Problems of the ΛCDM Model: A Short Review*, *Galaxies* **5** (Feb., 2017) 17, [1606.07790]. Cited on page 22.

[121] J. S. Bullock and M. Boylan-Kolchin, *Small-Scale Challenges to the ΛCDM Paradigm*, ARA&A **55** (Aug., 2017) 343–387, [1707.04256]. Cited on page 22, and 23.

[122] A. Klypin, A. V. Kravtsov, O. Valenzuela and F. Prada, *Where Are the Missing Galactic Satellites?*, ApJ **522** (Sept., 1999) 82–92, [astro-ph/9901240]. Cited on page 22.

[123] B. Moore, T. Quinn, F. Governato, J. Stadel and G. Lake, *Cold collapse and the core catastrophe*, MNRAS **310** (Dec., 1999) 1147–1152, [astro-ph/9903164]. Cited on page 22.

[124] M. Boylan-Kolchin, J. S. Bullock and M. Kaplinghat, *The Milky Way's bright satellites as an apparent failure of ΛCDM*, MNRAS **422** (May, 2012) 1203–1218, [1111.2048]. Cited on page 22.

[125] M. Boylan-Kolchin, J. S. Bullock and M. Kaplinghat, *Too big to fail? The puzzling darkness of massive Milky Way subhaloes*, MNRAS **415** (July, 2011) L40–L44, [1103.0007]. Cited on page 22, and 23.

[126] K. Bechtol, A. Drlica-Wagner, E. Balbinot, A. Pieres, J. D. Simon, B. Yanny et al., *Eight New Milky Way Companions Discovered in First-year Dark Energy Survey Data*, ApJ **807** (July, 2015) 50, [1503.02584]. Cited on page 22.

[127] A. Drlica-Wagner, K. Bechtol, E. S. Rykoff, E. Luque, A. Queiroz, Y. Y. Mao et al., *Eight Ultra-faint Galaxy Candidates Discovered in Year Two of the Dark Energy Survey*, ApJ **813** (Nov., 2015) 109, [1508.03622]. Cited on page 22.

[128] DES collaboration, E. O. Nadler et al., *Milky Way Satellite Census. III. Constraints on Dark Matter Properties from Observations of Milky Way Satellite Galaxies*, 2008.00022. Cited on page 22, and 41.

[129] J. S. Bullock, A. V. Kravtsov and D. H. Weinberg, *Reionization and the Abundance of Galactic Satellites*, ApJ **539** (Aug., 2000) 517–521, [astro-ph/0002214]. Cited on page 22.

[130] A. Dekel and J. Silk, *The Origin of Dwarf Galaxies, Cold Dark Matter, and Biased Galaxy Formation*, ApJ **303** (Apr., 1986) 39. Cited on page 22.

[131] S. Y. Kim, A. H. G. Peter and J. R. Hargis, *Missing Satellites Problem: Completeness Corrections to the Number of Satellite Galaxies in the Milky Way are Consistent with Cold Dark Matter Predictions*, Phys. Rev. Lett. **121** (Nov., 2018) 211302, [1711.06267]. Cited on page 22.

[132] J. F. Navarro, A. Ludlow, V. Springel, J. Wang, M. Vogelsberger, S. D. M. White et al., *The diversity and similarity of simulated cold dark matter haloes*, MNRAS **402** (Feb., 2010) 21–34, [0810.1522]. Cited on page 22.

[133] B. Moore, *Evidence against dissipation-less dark matter from observations of galaxy haloes*, Nature **370** (Aug., 1994) 629–631. Cited on page 22.

[134] R. A. Flores and J. R. Primack, *Observational and Theoretical Constraints on Singular Dark Matter Halos*, ApJ **427** (May, 1994) L1, [astro-ph/9402004]. Cited on page 22.

[135] S.-H. Oh, D. A. Hunter, E. Brinks, B. G. Elmegreen, A. Schruba, F. Walter et al., *High-resolution Mass Models of Dwarf Galaxies from LITTLE THINGS*, AJ **149** (June, 2015) 180, [1502.01281]. Cited on page 22.

[136] S. Mashchenko, J. Wadsley and H. M. P. Couchman, *Stellar Feedback in Dwarf Galaxy Formation*, *Science* **319** (Jan., 2008) 174, [0711.4803]. Cited on page 22.

[137] J. I. Read, M. G. Walker and P. Steger, *Dark matter heats up in dwarf galaxies*, *Mon. Not. Roy. Astron. Soc.* **484** (2019) 1401–1420, [1808.06634]. Cited on page 22.

[138] M. Boylan-Kolchin, J. S. Bullock and M. Kaplinghat, *The Milky Way's bright satellites as an apparent failure of ΛCDM*, *Mon. Not. Roy. Astron. Soc.* **422** (2012) 1203–1218, [1111.2048]. Cited on page 23.

[139] E. J. Tollerud, M. Boylan-Kolchin and J. S. Bullock, *M31 satellite masses compared to ΛCDM subhaloes*, MNRAS **440** (June, 2014) 3511–3519, [1403.6469]. Cited on page 23.

[140] E. N. Kirby, J. S. Bullock, M. Boylan-Kolchin, M. Kaplinghat and J. G. Cohen, *The dynamics of isolated Local Group galaxies*, MNRAS **439** (Mar., 2014) 1015–1027, [1401.1208]. Cited on page 23.

[141] A. Zolotov, A. M. Brooks, B. Willman, F. Governato, A. Pontzen, C. Christensen et al., *Baryons Matter: Why Luminous Satellite Galaxies have Reduced Central Masses*, ApJ **761** (Dec., 2012) 71, [1207.0007]. Cited on page 23.

[142] A. Del Popolo and M. Le Delliou, *A unified solution to the small scale problems of the ΛCDM model II: introducing parent-satellite interaction*, J. Cosmology Astropart. Phys. **2014** (Dec., 2014) 051, [1408.4893]. Cited on page 23.

[143] J. Wang, C. S. Frenk, J. F. Navarro, L. Gao and T. Sawala, *The missing massive satellites of the Milky Way*, MNRAS **424** (Aug., 2012) 2715–2721, [1203.4097]. Cited on page 23.

[144] T. Lin, *Dark matter models and direct detection*, *PoS* **333** (2019) 009, [1904.07915]. Cited on page 24.

[145] M. R. Lovell, V. Eke, C. S. Frenk, L. Gao, A. Jenkins, T. Theuns et al., *The haloes of bright satellite galaxies in a warm dark matter universe*, MNRAS **420** (Mar., 2012) 2318–2324, [1104.2929]. Cited on page 24.

[146] A. V. Macciò, S. Paduroiu, D. Anderhalden, A. Schneider and B. Moore, *Cores in warm dark matter haloes: a Catch 22 problem*, MNRAS **424** (Aug., 2012) 1105–1112, [1202.1282]. Cited on page 24.

[147] A. Schneider, D. Anderhalden, A. V. Maccio and J. Diemand, *Warm dark matter does not do better than cold dark matter in solving small-scale inconsistencies.*, MNRAS **441** (June, 2014) L6–L10, [1309.5960]. Cited on page 24.

[148] C. Bœhm, J. A. Schewtschenko, R. J. Wilkinson, C. M. Baugh and S. Pascoli, *Using the Milky Way satellites to study interactions between cold dark matter and radiation*, *Mon. Not. Roy. Astron. Soc.* **445** (2014) L31–L35, [1404.7012]. Cited on page 25, and 49.

[149] J. A. Schewtschenko et al., *Dark matter-radiation interactions: the structure of Milky Way satellite galaxies*, *Mon. Not. Roy. Astron. Soc.* **461** (2016) 2282–2287, [1512.06774]. Cited on page 25, and 45.

[150] E. D. Carlson, M. E. Machacek and L. J. Hall, *Self-interacting Dark Matter*, ApJ **398** (Oct., 1992) 43. Cited on page 25.

[151] S. Tulin and H.-B. Yu, *Dark Matter Self-interactions and Small Scale Structure*, *Phys. Rept.* **730** (2018) 1–57, [1705.02358]. Cited on page 25.

[152] A. Loeb and N. Weiner, *Cores in Dwarf Galaxies from Dark Matter with a Yukawa Potential*, *Phys. Rev. Lett.* **106** (2011) 171302, [1011.6374]. Cited on page 25.

[153] D. N. Spergel and P. J. Steinhardt, *Observational Evidence for Self-Interacting Cold Dark Matter*, Phys. Rev. Lett. **84** (Apr., 2000) 3760–3763, [astro-ph/9909386]. Cited on page 25.

[154] M. Rocha, A. H. G. Peter, J. S. Bullock, M. Kaplinghat, S. Garrison-Kimmel, J. Onorbe et al., *Cosmological Simulations with Self-Interacting Dark Matter I: Constant Density Cores and Substructure*, *Mon. Not. Roy. Astron. Soc.* **430** (2013) 81–104, [1208.3025]. Cited on page 25.

[155] M. Vogelsberger, J. Zavala and A. Loeb, *Subhaloes in self-interacting galactic dark matter haloes*, MNRAS **423** (July, 2012) 3740–3752, [1201.5892]. Cited on page 25.

[156] E. D'Onghia and A. Burkert, *The Failure of self-interacting dark matter to solve the overabundance of dark satellites and the soft core question*, *Astrophys. J.* **586** (2003) 12–16, [astro-ph/0206125]. Cited on page 25.

[157] W. Hu, R. Barkana and A. Gruzinov, *Fuzzy Cold Dark Matter: The Wave Properties of Ultralight Particles*, Phys. Rev. Lett. **85** (Aug., 2000) 1158–1161, [astro-ph/0003365]. Cited on page 25.

[158] L. Hui, J. P. Ostriker, S. Tremaine and E. Witten, *Ultralight scalars as cosmological dark matter*, Phys. Rev. D **95** (Feb., 2017) 043541, [1610.08297]. Cited on page 25.

[159] J.-W. Lee, *Brief History of Ultra-light Scalar Dark Matter Models*, in *European Physical Journal Web of Conferences*, vol. 168 of *European Physical Journal Web of Conferences*, p. 06005, Jan., 2018. 1704.05057. DOI. Cited on page 25.

[160] X. Du, C. Behrens and J. C. Niemeyer, *Substructure of fuzzy dark matter haloes*, *Mon. Not. Roy. Astron. Soc.* **465** (2017) 941–951, [1608.02575]. Cited on page 25.

[161] N. Afshordi, P. McDonald and D. N. Spergel, *Primordial Black Holes as Dark Matter: The Power Spectrum and Evaporation of Early Structures*, ApJ **594** (Sept., 2003) L71–L74, [astro-ph/0302035]. Cited on page 26, 71, 72, and 78.

[162] S. Clesse and J. García-Bellido, *The clustering of massive Primordial Black Holes as Dark Matter: measuring their mass distribution with Advanced LIGO*, *Phys. Dark Univ.* **15** (2017) 142–147, [1603.05234]. Cited on page 26, and 58.

[163] S. Clesse and J. García-Bellido, *Seven hints for primordial black hole dark matter*, *Physics of the Dark Universe* **22** (Dec., 2018) 137–146, [1711.10458]. Cited on page 26, 56, and 58.

[164] P. J. E. Peebles, *Principles of Physical Cosmology*. 1993. Cited on page 27, 31, and 135.

[165] E. W. Kolb and M. S. Turner, *The Early Universe*, *Front. Phys.* **69** (1990) 1–547. Cited on page 27, 35, 36, 37, 38, 47, and 48.

[166] D. Baumann, *Cosmology lecture notes*. Cited on page 27, and 29.

[167] P. Meszaros, *The behaviour of point masses in an expanding cosmological substratum.*, A&A **37** (Dec., 1974) 225–228. Cited on page 29.

[168] E. R. Harrison, *Fluctuations at the Threshold of Classical Cosmology*, Phys. Rev. D **1** (May, 1970) 2726–2730. Cited on page 29.

[169] Y. B. Zeldovich, *A hypothesis, unifying the structure and the entropy of the Universe*, MNRAS **160** (Jan., 1972) 1P. Cited on page 29.

[170] A. Lewis, A. Challinor and A. Lasenby, *Efficient computation of CMB anisotropies in closed FRW models*, *Astrophys. J.* **538** (2000) 473–476, [astro-ph/9911177]. Cited on page 30.

[171] J. Lesgourgues, *The Cosmic Linear Anisotropy Solving System (CLASS) I: Overview*, 1104.2932. Cited on page 30, 49, and 50.

[172] Y. B. Zel'Dovich, *Reprint of 1970A&A.....5...84Z. Gravitational instability: an approximate theory for large density perturbations.*, A&A **500** (Mar., 1970) 13–18. Cited on page 31.

[173] J. E. Gunn and I. Gott, J. Richard, *On the Infall of Matter Into Clusters of Galaxies and Some Effects on Their Evolution*, ApJ **176** (Aug., 1972) 1. Cited on page 31.

[174] G. L. Bryan and M. L. Norman, *Statistical properties of X-ray clusters: Analytic and numerical comparisons*, *Astrophys. J.* **495** (1998) 80, [astro-ph/9710107]. Cited on page 31.

[175] J. R. Bond, S. Cole, G. Efstathiou and N. Kaiser, *Excursion set mass functions for hierarchical Gaussian fluctuations*, *Astrophys. J.* **379** (1991) 440. Cited on page 32, 43, 127, and 349.

[176] A. R. ZENTNER, *The excursion set theory of halo mass functions, halo clustering, and halo growth*, *International Journal of Modern Physics D* **16** (May, 2007) 763–815. Cited on page 32.

[177] M. Maggiore and A. Riotto, *The halo mass function from excursion set theory. i. gaussian fluctuations with non-markovian dependence on the smoothing scale*, *The Astrophysical Journal* **711** (Feb, 2010) 907–927. Cited on page 32, and 43.

[178] V. Springel, S. D. M. White, A. Jenkins, C. S. Frenk, N. Yoshida, L. Gao et al., *Simulations of the formation, evolution and clustering of galaxies and quasars*, astro-ph/0504097. Cited on page 33.

[179] R. K. Sheth and G. Tormen, *An Excursion set model of hierarchical clustering : Ellipsoidal collapse and the moving barrier*, *Mon. Not. Roy. Astron. Soc.* **329** (2002) 61, [astro-ph/0105113]. Cited on page 33.

[180] K. N. Abazajian et al., *Light Sterile Neutrinos: A White Paper*, 1204.5379. Cited on page 35.

[181] M. Drewes et al., *A White Paper on keV Sterile Neutrino Dark Matter*, *JCAP* **01** (2017) 025, [1602.04816]. Cited on page 35.

[182] K. N. Abazajian, *Sterile neutrinos in cosmology*, *Phys. Rept.* **711-712** (2017) 1–28, [1705.01837]. Cited on page 35.

[183] E. Bulbul, M. Markevitch, A. Foster, R. K. Smith, M. Loewenstein and S. W. Randall, *Detection of an Unidentified Emission Line in the Stacked X-Ray Spectrum of Galaxy Clusters*, ApJ **789** (July, 2014) 13, [1402.2301]. Cited on page 35.

[184] A. Boyarsky, O. Ruchayskiy, D. Iakubovskyi and J. Franse, *Unidentified Line in X-Ray Spectra of the Andromeda Galaxy and Perseus Galaxy Cluster*, Phys. Rev. Lett. **113** (Dec., 2014) 251301, [1402.4119]. Cited on page 35.

[185] F. Hofmann, J. S. Sanders, K. Nandra, N. Clerc and M. Gaspari, *7.1 keV sterile neutrino constraints from X-ray observations of 33 clusters of galaxies with Chandra ACIS*, A&A **592** (Aug., 2016) A112, [1606.04091]. Cited on page 35.

[186] S. Bhargava et al., *The XMM Cluster Survey: new evidence for the 3.5 keV feature in clusters is inconsistent with a dark matter origin*, *Mon. Not. Roy. Astron. Soc.* **497** (2020) 656–671, [2006.13955]. Cited on page 35.

[187] T. Jeltema and S. Profumo, *Discovery of a 3.5 keV line in the Galactic Centre and a critical look at the origin of the line across astronomical targets*, MNRAS **450** (June, 2015) 2143–2152, [1408.1699]. Cited on page 35.

[188] R. Barkana, Z. Haiman and J. P. Ostriker, *Constraints on Warm Dark Matter from Cosmological Reionization*, ApJ **558** (Sept., 2001) 482–496, [astro-ph/0102304]. Cited on page 35.

[189] P. Bode, J. P. Ostriker and N. Turok, *Halo formation in warm dark matter models*, *Astrophys. J.* **556** (2001) 93–107, [astro-ph/0010389]. Cited on page 35, and 41.

[190] J. J. Bennett, G. Buldgen, P. F. De Salas, M. Drewes, S. Gariazzo, S. Pastor et al., *Towards a precision calculation of $N_{\rm eff}$ in the Standard Model II: Neutrino decoupling in the presence of flavour oscillations and finite-temperature QED*, 2012.02726. Cited on page 37.

[191] A. Schneider, R. E. Smith and D. Reed, *Halo Mass Function and the Free Streaming Scale*, *Mon. Not. Roy. Astron. Soc.* **433** (2013) 1573, [1303.0839]. Cited on page 38, 43, and 44.

[192] A. Schneider, R. E. Smith, A. V. Macciò and B. Moore, *Nonlinear Evolution of Cosmological Structures in Warm Dark Matter Models*, *Mon. Not. Roy. Astron. Soc.* **424** (2012) 684, [1112.0330]. Cited on page 39, and 43.

[193] S. Horiuchi, P. J. Humphrey, J. Onorbe, K. N. Abazajian, M. Kaplinghat and S. Garrison-Kimmel, *Sterile neutrino dark matter bounds from galaxies of the Local Group*, *Phys. Rev. D* **89** (2014) 025017, [1311.0282]. Cited on page 40.

[194] S. Colombi, S. Dodelson and L. M. Widrow, *Large scale structure tests of warm dark matter*, *Astrophys. J.* **458** (1996) 1, [astro-ph/9505029]. Cited on page 40.

[195] J. Baur, N. Palanque-Delabrouille, C. Yèche, C. Magneville and M. Viel, *Lyman-alpha forests cool warm dark matter*, J. Cosmology Astropart. Phys. **2016** (Aug., 2016) 012, [1512.01981]. Cited on page 40.

[196] A. Schneider, *Astrophysical constraints on resonantly produced sterile neutrino dark matter*, J. Cosmology Astropart. Phys. **2016** (Apr., 2016) 059, [1601.07553]. Cited on page 40.

[197] J. Baur, N. Palanque-Delabrouille, C. Yèche, A. Boyarsky, O. Ruchayskiy, É. Armengaud et al., *Constraints from Ly-α forests on non-thermal dark matter including resonantly-produced sterile neutrinos*, J. Cosmology Astropart. Phys. **2017** (Dec., 2017) 013, [1706.03118]. Cited on page 40.

[198] K. N. Abazajian, *Neutrinos in Astrophysics and Cosmology: Theoretical Advanced Study Institute (TASI) 2020 Lectures*, in *Theoretical Advanced Study Institute in Elementary Particle Physics: The Obscure Universe: Neutrinos and Other Dark Matters*, 2, 2021. 2102.10183. Cited on page 40.

[199] M. Viel, G. D. Becker, J. S. Bolton and M. G. Haehnelt, *Warm dark matter as a solution to the small scale crisis: New constraints from high redshift Lyman-α forest data*, Phys. Rev. D **88** (Aug., 2013) 043502, [1306.2314]. Cited on page 40.

[200] N. Palanque-Delabrouille, C. Yèche, N. Schöneberg, J. Lesgourgues, M. Walther, S. Chabanier et al., *Hints, neutrino bounds, and WDM constraints from SDSS DR14 Lyman-α and Planck full-survey data*, J. Cosmology Astropart. Phys. **2020** (Apr., 2020) 038, [1911.09073]. Cited on page 40.

[201] O. Newton, M. Leo, M. Cautun, A. Jenkins, C. S. Frenk, M. R. Lovell et al., *Constraints on the properties of warm dark matter using the satellite galaxies of the Milky Way*, *arXiv e-prints* (Nov., 2020) arXiv:2011.08865, [2011.08865]. Cited on page 41.

[202] W. Wang et al., *Estimating the dark matter halo mass of our Milky Way using dynamical tracers*, *Mon. Not. Roy. Astron. Soc.* **453** (2015) 377–400, [1502.03477]. Cited on page 41.

[203] M. Cautun, A. Benítez-Llambay, A. J. Deason, C. S. Frenk, A. Fattahi, F. A. Gómez et al., *The milky way total mass profile as inferred from Gaia DR2*, MNRAS **494** (May, 2020) 4291–4313, [1911.04557]. Cited on page 41.

[204] T. K. Fritz, A. Di Cintio, G. Battaglia, C. Brook and S. Taibi, *The mass of our Galaxy from satellite proper motions in the Gaia era*, MNRAS **494** (June, 2020) 5178–5193, [2001.02651]. Cited on page 41.

[205] M. Viel, J. Lesgourgues, M. G. Haehnelt, S. Matarrese and A. Riotto, *Constraining warm dark matter candidates including sterile neutrinos and light gravitinos with WMAP and the Lyman-alpha forest*, *Phys. Rev.* **D71** (2005) 063534, [astro-ph/0501562]. Cited on page 41, and 42.

[206] A. J. Benson, A. Farahi, S. Cole, L. A. Moustakas, A. Jenkins, M. Lovell et al., *Dark matter halo merger histories beyond cold dark matter - I. Methods and application to warm dark matter*, MNRAS **428** (Jan., 2013) 1774–1789, [1209.3018]. Cited on page 43.

[207] A. Schneider, *Structure formation with suppressed small-scale perturbations*, *Mon. Not. Roy. Astron. Soc.* **451** (2015) 3117–3130, [1412.2133]. Cited on page 43.

[208] J. A. Schewtschenko, R. J. Wilkinson, C. M. Baugh, C. Bœhm and S. Pascoli, *Dark matter-radiation interactions: the impact on dark matter haloes*, *Mon. Not. Roy. Astron. Soc.* **449** (2015) 3587–3596, [1412.4905]. Cited on page 44, 51, 52, and 53.

[209] Á. Moliné, J. A. Schewtschenko, S. Palomares-Ruiz, C. Bœhm and C. M. Baugh, *Isotropic extragalactic flux from dark matter annihilations: lessons from interacting dark matter scenarios*, *JCAP* **1608** (2016) 069, [1602.07282]. Cited on page 44, 45, and 52.

[210] J. Wang and S. D. M. White, *Discreteness effects in simulations of Hot/Warm dark matter*, *Mon. Not. Roy. Astron. Soc.* **380** (2007) 93–103, [astro-ph/0702575]. Cited on page 44.

[211] R. E. Angulo, O. Hahn and T. Abel, *The Warm DM halo mass function below the cut-off scale*, *Mon. Not. Roy. Astron. Soc.* **434** (2013) 3337, [1304.2406]. Cited on page 44.

[212] A. Hobbs, J. Read, O. Agertz, F. Iannuzzi and C. Power, *Novel Adaptive softening for collisionless N-body simulations: eliminating spurious haloes*, *Mon. Not. Roy. Astron. Soc.* **458** (2016) 468–479, [1503.02689]. Cited on page 44.

[213] A. Banerjee and N. Dalal, *Simulating nonlinear cosmological structure formation with massive neutrinos*, *JCAP* **1611** (2016) 015, [1606.06167]. Cited on page 44.

[214] J. Silk, *Cosmic Black-Body Radiation and Galaxy Formation*, ApJ **151** (Feb., 1968) 459. Cited on page 44, and 47.

[215] C. Bœhm, P. Fayet and R. Schaeffer, *Constraining dark matter candidates from structure formation*, *Phys. Lett.* **B518** (2001) 8–14, [astro-ph/0012504]. Cited on page 45, 47, and 48.

[216] C. Bœhm, A. Riazuelo, S. H. Hansen and R. Schaeffer, *Interacting dark matter disguised as warm dark matter*, *Phys. Rev.* **D66** (2002) 083505, [astro-ph/0112522]. Cited on page 45, and 50.

[217] C. Boehm and R. Schaeffer, *Constraints on dark matter interactions from structure formation: Damping lengths*, *Astron. Astrophys.* **438** (2005) 419–442, [astro-ph/0410591]. Cited on page 45, 47, and 48.

[218] R. J. Wilkinson, J. Lesgourgues and C. Bœhm, *Using the CMB angular power spectrum to study Dark Matter-photon interactions*, *JCAP* **1404** (2014) 026, [1309.7588]. Cited on page 45, 48, and 50.

[219] J. Stadler and C. Bœhm, *Constraints on γ-CDM interactions matching the Planck data precision*, J. Cosmology Astropart. Phys. **2018** (Oct., 2018) 009, [1802.06589]. Cited on page 45, 48, and 50.

[220] J. J. Stadler, *How dark is dark matter? Robust limits on dark matter - radiation interactions from cosmological observations*. PhD thesis, Durham U., 2019. Cited on page 45.

[221] C. Boehm, J. A. Schewtschenko, R. J. Wilkinson, C. M. Baugh and S. Pascoli, *Using the Milky Way satellites to study interactions between cold dark matter and radiation.*, MNRAS **445** (Nov., 2014) L31–L35, [1404.7012]. Cited on page 45.

[222] J. A. Schewtschenko, R. J. Wilkinson, C. M. Baugh, C. Bœhm and S. Pascoli, *Dark matter-radiation interactions: the impact on dark matter haloes*, MNRAS **449** (June, 2015) 3587–3596, [1412.4905]. Cited on page 45.

[223] J. A. Schewtschenko, *Cosmological Simulations with Dark Matter from beyond the Standard Model*. PhD thesis, Durham U., 2016. Cited on page 45, and 52.

[224] G. Mangano, A. Melchiorri, P. Serra, A. Cooray and M. Kamionkowski, *Cosmological bounds on dark-matter-neutrino interactions*, Phys. Rev. D **74** (Aug., 2006) 043517, [astro-ph/0606190]. Cited on page 45.

[225] R. J. Wilkinson, C. Bœhm and J. Lesgourgues, *Constraining Dark Matter-Neutrino Interactions using the CMB and Large-Scale Structure*, *JCAP* **1405** (2014) 011, [1401.7597]. Cited on page 45, and 49.

[226] M. Escudero, O. Mena, A. C. Vincent, R. J. Wilkinson and C. Bœhm, *Exploring dark matter microphysics with galaxy surveys*, *JCAP* **1509** (2015) 034, [1505.06735]. Cited on page 45.

[227] J. Stadler, C. Bœhm and O. Mena, *Comprehensive study of neutrino-dark matter mixed damping*, J. Cosmology Astropart. Phys. **2019** (Aug., 2019) 014, [1903.00540]. Cited on page 45.

[228] M. R. Mosbech, C. Boehm, S. Hannestad, O. Mena, J. Stadler and Y. Y. Y. Wong, *The full Boltzmann hierarchy for dark matter-massive neutrino interactions*, 2011.04206. Cited on page 45.

[229] K. R. Dienes, C. F. Kolda and J. March-Russell, *Kinetic mixing and the supersymmetric gauge hierarchy*, *Nucl. Phys. B* **492** (1997) 104–118, [hep-ph/9610479]. Cited on page 45, and 46.

[230] A. Mirizzi, J. Redondo and G. Sigl, *Microwave Background Constraints on Mixing of Photons with Hidden Photons*, *JCAP* **03** (2009) 026, [0901.0014]. Cited on page 45.

[231] B. Holdom, *Two U(1)'s and Epsilon Charge Shifts*, *Phys. Lett. B* **166** (1986) 196–198. Cited on page 45.

[232] M. E. Peskin and D. V. Schroeder, *An Introduction to quantum field theory*. Addison-Wesley, Reading, USA, 1995. Cited on page 46.

[233] S. D. McDermott, H.-B. Yu and K. M. Zurek, *Turning off the Lights: How Dark is Dark Matter?*, *Phys. Rev. D* **83** (2011) 063509, [1011.2907]. Cited on page 46.

[234] C. Dvorkin, K. Blum and M. Kamionkowski, *Constraining Dark Matter-Baryon Scattering with Linear Cosmology*, *Phys. Rev.* **D89** (2014) 023519, [1311.2937]. Cited on page 46.

[235] N. Vinyoles and H. Vogel, *Minicharged Particles from the Sun: A Cutting-Edge Bound*, *JCAP* **1603** (2016) 002, [1511.01122]. Cited on page 46, and 47.

[236] P. Agrawal et al., *Feebly-Interacting Particles:FIPs 2020 Workshop Report*, 2102.12143. Cited on page 46.

[237] W. Hu, *Lecture Notes on CMB Theory: From Nucleosynthesis to Recombination*, 0802.3688. Cited on page 47.

[238] G. B. Rybicki and A. P. Lightman, *Radiative Processes in Astrophysics*. 1986. Cited on page 47, 81, and 105.

[239] C. Boehm, P. Fayet and R. Schaeffer, *Constraining the strength of dark matter interactions from structure formation*, in *Dark Matter in Astro- and Particle Physics, DARK 2002* (H. V. Klapdor-Kleingrothaus and R. D. Viollier, eds.), pp. 333–344, Jan., 2002. astro-ph/0205406. Cited on page 48.

[240] M. Sasaki, T. Suyama, T. Tanaka and S. Yokoyama, *Primordial black holes—perspectives in gravitational wave astronomy*, *Class. Quant. Grav.* **35** (2018) 063001, [1801.05235]. Cited on page 55, 58, 60, 61, and 63.

[241] A. M. Green and B. J. Kavanagh, *Primordial Black Holes as a dark matter candidate*, *J. Phys. G* **48** (2021) 4, [2007.10722]. Cited on page 55, 61, 74, and 75.

[242] B. Carr and F. Kühnel, *Primordial Black Holes as Dark Matter: Recent Developments*, *Annual Review of Nuclear and Particle Science* **70** (Oct., 2020) annurev, [2006.02838]. Cited on page 55, 56, and 74.

[243] B. J. Carr, K. Kohri, Y. Sendouda and J. Yokoyama, *New cosmological constraints on primordial black holes*, Phys. Rev. D **81** (May, 2010) 104019, [0912.5297]. Cited on page 55, 62, 63, and 74.

[244] Y. B. Zel'dovich and I. D. Novikov, *The Hypothesis of Cores Retarded during Expansion and the Hot Cosmological Model*, Soviet Ast. **10** (Feb., 1967) 602. Cited on page 55.

[245] S. Hawking, *Gravitationally collapsed objects of very low mass*, MNRAS **152** (Jan., 1971) 75. Cited on page 55.

[246] B. J. Carr and S. W. Hawking, *Black holes in the early Universe*, MNRAS **168** (Aug., 1974) 399–416. Cited on page 55.

[247] B. J. Carr, *The primordial black hole mass spectrum.*, ApJ **201** (Oct., 1975) 1–19. Cited on page 55, and 58.

[248] G. F. Chapline, *Cosmological effects of primordial black holes*, Nature **253** (Jan., 1975) 251–252. Cited on page 55.

[249] S. Bird, I. Cholis, J. B. Muñoz, Y. Ali-Haïmoud, M. Kamionkowski, E. D. Kovetz et al., *Did LIGO Detect Dark Matter?*, Phys. Rev. Lett. **116** (May, 2016) 201301, [1603.00464]. Cited on page 56.

[250] J. Garcia-Bellido, J. F. Nuño Siles and E. Ruiz Morales, *Bayesian analysis of the spin distribution of LIGO/Virgo black holes*, *arXiv e-prints* (Oct., 2020) arXiv:2010.13811, [2010.13811]. Cited on page 56, and 64.

[251] R. C. Tolman, *Static Solutions of Einstein's Field Equations for Spheres of Fluid*, *Physical Review* **55** (Feb., 1939) 364–373. Cited on page 56.

[252] J. R. Oppenheimer and G. M. Volkoff, *On Massive Neutron Cores*, *Physical Review* **55** (Feb., 1939) 374–381. Cited on page 56.

[253] J. Garriga, A. Vilenkin and J. Zhang, *Black holes and the multiverse*, J. Cosmology Astropart. Phys. **2016** (Feb., 2016) 064, [1512.01819]. Cited on page 57.

[254] H. Deng, J. Garriga and A. Vilenkin, *Primordial black hole and wormhole formation by domain walls*, J. Cosmology Astropart. Phys. **2017** (Apr., 2017) 050, [1612.03753]. Cited on page 57.

[255] S. Hawking, *Black Holes From Cosmic Strings*, *Phys. Lett. B* **231** (1989) 237–239. Cited on page 57.

[256] A. Polnarev and R. Zembowicz, *Formation of primordial black holes by cosmic strings*, *Phys. Rev. D* **43** (Feb, 1991) 1106–1109. Cited on page 57.

[257] S. W. Hawking, I. G. Moss and J. M. Stewart, *Bubble collisions in the very early universe*, *Phys. Rev. D* **26** (Nov, 1982) 2681–2693. Cited on page 57.

[258] H. Deng and A. Vilenkin, *Primordial black hole formation by vacuum bubbles*, J. Cosmology Astropart. Phys. **2017** (Dec., 2017) 044, [1710.02865]. Cited on page 57.

[259] Gravity Collaboration, R. Abuter, A. Amorim, M. Bauböck, J. P. Berger, H. Bonnet et al., *A geometric distance measurement to the Galactic center black hole with 0.3% uncertainty*, A&A **625** (May, 2019) L10, [1904.05721]. Cited on page 57.

[260] LIGO Scientific Collaboration and Virgo Collaboration collaboration, R. Abbott, T. D. Abbott, S. Abraham, F. Acernese, K. Ackley, C. Adams et al., *Gw190521: A binary black hole merger with a total mass of* 150 $M_\odot$, *Phys. Rev. Lett.* **125** (Sep, 2020) 101102. Cited on page 57.

[261] B. Carr and J. Silk, *Primordial black holes as generators of cosmic structures*, MNRAS **478** (Aug., 2018) 3756–3775, [1801.00672]. Cited on page 57.

[262] M. Volonteri, *Formation of supermassive black holes*, *The Astronomy and Astrophysics Review* **18** (Apr, 2010) 279–315. Cited on page 57.

[263] A. M. Green, *Primordial Black Holes: sirens of the early Universe*, *arXiv e-prints* (Mar., 2014) arXiv:1403.1198, [1403.1198]. Cited on page 58, 61, and 74.

[264] A. M. Green, A. R. Liddle, K. A. Malik and M. Sasaki, *New calculation of the mass fraction of primordial black holes*, Phys. Rev. D **70** (Aug., 2004) 041502, [astro-ph/0403181]. Cited on page 59.

[265] I. Musco, *Threshold for primordial black holes: Dependence on the shape of the cosmological perturbations*, Phys. Rev. D **100** (Dec., 2019) 123524, [1809.02127]. Cited on page 59.

[266] J. García-Bellido and E. Ruiz Morales, *Primordial black holes from single field models of inflation*, *Physics of the Dark Universe* **18** (Dec., 2017) 47–54, [1702.03901]. Cited on page 60.

[267] J. García-Bellido, *Massive Primordial Black Holes as Dark Matter and their detection with Gravitational Waves*, in *Journal of Physics Conference Series*, vol. 840 of *Journal of Physics Conference Series*, p. 012032, May, 2017. 1702.08275. DOI. Cited on page 60.

[268] S. Clesse and J. García-Bellido, *Massive primordial black holes from hybrid inflation as dark matter and the seeds of galaxies*, Phys. Rev. D **92** (July, 2015) 023524, [1501.07565]. Cited on page 60.

[269] J. Yokoyama, *Chaotic new inflation and formation of primordial black holes*, *Phys. Rev. D* **58** (Sep, 1998) 083510. Cited on page 60.

[270] R. Saito, J. Yokoyama and R. Nagata, *Single-field inflation, anomalous enhancement of superhorizon fluctuations and non-Gaussianity in primordial black hole formation*, J. Cosmology Astropart. Phys. **2008** (June, 2008) 024, [0804.3470]. Cited on page 60.

[271] G. Franciolini, A. Kehagias, S. Matarrese and A. Riotto, *Primordial black holes from inflation and non-Gaussianity*, J. Cosmology Astropart. Phys. **2018** (Mar., 2018) 016, [1801.09415]. Cited on page 61.

[272] V. De Luca, G. Franciolini, A. Kehagias, M. Peloso, A. Riotto and C. Ünal, *The ineludible non-Gaussianity of the primordial black hole abundance*, J. Cosmology Astropart. Phys. **2019** (July, 2019) 048, [1904.00970]. Cited on page 61.

[273] V. Atal and C. Germani, *The role of non-gaussianities in Primordial Black Hole formation*, *Phys. Dark Univ.* **24** (2019) 100275, [1811.07857]. Cited on page 61.

[274] R.-g. Cai, S. Pi and M. Sasaki, *Gravitational Waves Induced by non-Gaussian Scalar Perturbations*, *Phys. Rev. Lett.* **122** (2019) 201101, [1810.11000]. Cited on page 61.

[275] B. Carr, M. Raidal, T. Tenkanen, V. Vaskonen and H. Veermäe, *Primordial black hole constraints for extended mass functions*, Phys. Rev. D **96** (July, 2017) 023514, [1705.05567]. Cited on page 62.

[276] N. Bellomo, J. L. Bernal, A. Raccanelli and L. Verde, *Primordial black holes as dark matter: converting constraints from monochromatic to extended mass distributions*, J. Cosmology Astropart. Phys. **2018** (Jan., 2018) 004, [1709.07467]. Cited on page 62.

[277] B. V. Lehmann, S. Profumo and J. Yant, *The maximal-density mass function for primordial black hole dark matter*, *Journal of Cosmology and Astroparticle Physics* **2018** (Apr, 2018) 007–007. Cited on page 62.

[278] S. W. Hawking, *Black hole explosions?*, Nature **248** (Mar., 1974) 30–31. Cited on page 63.

[279] S. W. Hawking, *A brief history of time. From the Big Bang to Black Holes*. 1988. Cited on page 63.

[280] M. C. Lopresto, *Some Simple Black Hole Thermodynamics*, *The Physics Teacher* **41** (May, 2003) 299–301. Cited on page 63.

[281] D. N. Page, *Particle emission rates from a black hole. II. Massless particles from a rotating hole*, Phys. Rev. D **14** (Dec., 1976) 3260–3273. Cited on page 63, and 74.

[282] A. Arbey and J. Auffinger, *BlackHawk: A public code for calculating the Hawking evaporation spectra of any black hole distribution*, *Eur. Phys. J. C* **79** (2019) 693, [1905.04268]. Cited on page 63.

[283] Y. Ali-Haïmoud, *Correlation Function of High-Threshold Regions and Application to the Initial Small-Scale Clustering of Primordial Black Holes*, Phys. Rev. Lett. **121** (Aug., 2018) 081304, [1805.05912]. Cited on page 64.

[284] V. Desjacques and A. Riotto, *Spatial clustering of primordial black holes*, Phys. Rev. D **98** (Dec., 2018) 123533, [1806.10414]. Cited on page 64.

[285] T. Suyama and S. Yokoyama, *Clustering of primordial black holes with non-Gaussian initial fluctuations*, *Progress of Theoretical and Experimental Physics* **2019** (Oct., 2019) 103E02, [1906.04958]. Cited on page 64.

[286] G. Ballesteros, P. D. Serpico and M. Taoso, *On the merger rate of primordial black holes: effects of nearest neighbours distribution and clustering*, J. Cosmology Astropart. Phys. **2018** (Oct., 2018) 043, [1807.02084]. Cited on page 64.

[287] A. Moradinezhad Dizgah, G. Franciolini and A. Riotto, *Primordial black holes from broad spectra: abundance and clustering*, J. Cosmology Astropart. Phys. **2019** (Nov., 2019) 001, [1906.08978]. Cited on page 64.

[288] T. Chiba and S. Yokoyama, *Spin Distribution of Primordial Black Holes*, *PTEP* **2017** (2017) 083E01, [1704.06573]. Cited on page 64.

[289] M. Mirbabayi, A. Gruzinov and J. Noreña, *Spin of Primordial Black Holes*, *JCAP* **03** (2020) 017, [1901.05963]. Cited on page 64.

[290] V. De Luca, V. Desjacques, G. Franciolini, A. Malhotra and A. Riotto, *The initial spin probability distribution of primordial black holes*, J. Cosmology Astropart. Phys. **2019** (May, 2019) 018, [1903.01179]. Cited on page 64.

[291] F. Hoyle and R. A. Lyttleton, *The effect of interstellar matter on climatic variation*, *Proceedings of the Cambridge Philosophical Society* **35** (Jan., 1939) 405. Cited on page 65.

[292] F. Hoyle and R. A. Lyttleton, *On the accretion of interstellar matter by stars*, *Proceedings of the Cambridge Philosophical Society* **36** (Jan., 1940) 325. Cited on page 65.

[293] F. Hoyle and R. A. Lyttleton, *On the physical aspects of accretion by stars*, *Proceedings of the Cambridge Philosophical Society* **36** (Jan., 1940) 424. Cited on page 65.

[294] H. Bondi and F. Hoyle, *On the mechanism of accretion by stars*, MNRAS **104** (Jan., 1944) 273. Cited on page 65.

[295] H. Bondi, *On spherically symmetrical accretion*, MNRAS **112** (Jan., 1952) 195. Cited on page 65, and 67.

[296] M. Ricotti, *Bondi Accretion in the Early Universe*, ApJ **662** (June, 2007) 53–61, [0706.0864]. Cited on page 65.

[297] M. Ricotti, J. P. Ostriker and K. J. Mack, *Effect of Primordial Black Holes on the Cosmic Microwave Background and Cosmological Parameter Estimates*, ApJ **680** (June, 2008) 829–845, [0709.0524]. Cited on page 65, 69, 70, and 77.

[298] Y. Ali-Haïmoud and M. Kamionkowski, *Cosmic microwave background limits on accreting primordial black holes*, *Phys. Rev.* **D95** (2017) 043534, [1612.05644]. Cited on page 65, 66, 67, 68, 69, 70, and 77.

[299] B. Horowitz, *Revisiting Primordial Black Holes Constraints from Ionization History*, *arXiv e-prints* (Dec., 2016) arXiv:1612.07264, [1612.07264]. Cited on page 65, and 77.

[300] V. Poulin, P. D. Serpico, F. Calore, S. Clesse and K. Kohri, *CMB bounds on disk-accreting massive primordial black holes*, *Phys. Rev.* **D96** (2017) 083524, [1707.04206]. Cited on page 65, 68, and 78.

[301] S. A. Wouthuysen, *On the excitation mechanism of the 21-cm (radio-frequency) interstellar hydrogen emission line.*, AJ **57** (Jan., 1952) 31–32. Cited on page 66, and 91.

[302] E. Agol and M. Kamionkowski, *X-rays from isolated black holes in the Milky Way*, *Mon. Not. Roy. Astron. Soc.* **334** (2002) 553, [astro-ph/0109539]. Cited on page 68.

[303] N. I. Shakura and R. A. Sunyaev, *Black holes in binary systems. Observational appearance*, *Astron. Astrophys.* **24** (1973) 337–355. Cited on page 69.

[304] R. Narayan, *Why Do AGN Lighthouses Switch Off?*, in *Lighthouses of the Universe: The Most Luminous Celestial Objects and Their Use for Cosmology* (M. Gilfanov, R. Sunyeav and E. Churazov, eds.), p. 405, Jan., 2002. astro-ph/0201260. DOI. Cited on page 69.

[305] S. Ichimaru, *Bimodal behavior of accretion disks - Theory and application to Cygnus X-1 transitions*, *Astrophys. J.* **214** (1977) 840–855. Cited on page 69.

[306] M. J. Rees, E. S. Phinney, M. C. Begelman and R. D. Blandford, *Ion supported tori and the origin of radio jets*, *Nature* **295** (1982) 17–21. Cited on page 69.

[307] R. Narayan and I. Yi, *Advection dominated accretion: Underfed black holes and neutron stars*, *Astrophys. J.* **452** (1995) 710, [astro-ph/9411059]. Cited on page 69.

[308] R. Narayan and I. Yi, *Advection-dominated Accretion: A Self-similar Solution*, ApJ **428** (June, 1994) L13, [astro-ph/9403052]. Cited on page 69.

[309] M. A. Abramowicz, X. Chen, S. Kato, J.-P. Lasota and O. Regev, *Thermal Equilibria of Accretion Disks*, ApJ **438** (Jan., 1995) L37, [astro-ph/9409018]. Cited on page 69.

[310] F. Yuan and R. Narayan, *Hot accretion flows around black holes*, *Ann. Rev. Astron. Astrophys.* **52** (2014) 529–588, [1401.0586]. Cited on page 69, and 70.

[311] F.-G. Xie and F. Yuan, *The radiative efficiency of hot accretion flows*, *Mon. Not. Roy. Astron. Soc.* **427** (2012) 1580, [1207.3113]. Cited on page 69.

[312] T. R. Slatyer, *Indirect Dark Matter Signatures in the Cosmic Dark Ages II. Ionization, Heating and Photon Production from Arbitrary Energy Injections*, *Phys. Rev.* **D93** (2016) 023521, [1506.03812]. Cited on page 70.

[313] J. R. Chisholm, *Clustering of primordial black holes: Basic results*, Phys. Rev. D **73** (Apr., 2006) 083504, [astro-ph/0509141]. Cited on page 71.

[314] D. Inman and Y. Ali-Haïmoud, *Early structure formation in primordial black hole cosmologies*, *Phys. Rev. D* **100** (2019) 083528, [1907.08129]. Cited on page 71.

[315] J. A. Peacock, *Cosmological physics*. Cambridge University Press, 1999, 10.1017/CBO9780511804533. Cited on page 72.

[316] J.-O. Gong and N. Kitajima, *Small-scale structure and 21cm fluctuations by primordial black holes*, *JCAP* **1708** (2017) 017, [1704.04132]. Cited on page 73, 214, and 355.

[317] J.-O. Gong and N. Kitajima, *Distribution of primordial black holes and 21cm signature*, *JCAP* **1811** (2018) 041, [1803.02745]. Cited on page 73, 214, and 355.

[318] C. Boehm, A. Kobakhidze, C. A. J. O'hare, Z. S. C. Picker and M. Sakellariadou, *Eliminating the LIGO bounds on primordial black hole dark matter*, *JCAP* **03** (2021) 078, [2008.10743]. Cited on page 74, and 76.

[319] B. J. Kavanagh, *bradkav/pbhbounds: Release version*, Nov., 2019. 10.5281/zenodo.3538999. Cited on page 74.

[320] B. Carr, F. Kühnel and M. Sandstad, *Primordial black holes as dark matter*, Phys. Rev. D **94** (Oct., 2016) 083504, [1607.06077]. Cited on page 74, and 75.

[321] B. Carr, K. Kohri, Y. Sendouda and J. Yokoyama, *Constraints on Primordial Black Holes*, *arXiv e-prints* (Feb., 2020) arXiv:2002.12778, [2002.12778]. Cited on page 74.

[322] B. J. Carr, K. Kohri, Y. Sendouda and J. Yokoyama, *Constraints on primordial black holes from the Galactic gamma-ray background*, Phys. Rev. D **94** (Aug., 2016) 044029, [1604.05349]. Cited on page 74.

[323] W. DeRocco and P. W. Graham, *Constraining Primordial Black Hole Abundance with the Galactic 511 keV Line*, *Phys. Rev. Lett.* **123** (2019) 251102, [1906.07740]. Cited on page 75.

[324] R. Laha, *Primordial Black Holes as a Dark Matter Candidate Are Severely Constrained by the Galactic Center 511 keV γ -Ray Line*, *Phys. Rev. Lett.* **123** (2019) 251101, [1906.09994]. Cited on page 75.

[325] B. Dasgupta, R. Laha and A. Ray, *Neutrino and positron constraints on spinning primordial black hole dark matter*, *Phys. Rev. Lett.* **125** (2020) 101101, [1912.01014]. Cited on page 75.

[326] J. Iguaz, P. D. Serpico and T. Siegert, *Isotropic X-ray bound on Primordial Black Hole Dark Matter*, 2104.03145. Cited on page 75.

[327] B. Paczynski, *Gravitational Microlensing by the Galactic Halo*, ApJ **304** (May, 1986) 1. Cited on page 75.

[328] C. Alcock, R. A. Allsman, D. R. Alves, T. S. Axelrod, A. C. Becker, D. P. Bennett et al., *MACHO Project Limits on Black Hole Dark Matter in the 1-30 M_{solar} Range*, ApJ **550** (Apr., 2001) L169–L172, [astro-ph/0011506]. Cited on page 75.

[329] P. Tisserand, L. Le Guillou, C. Afonso, J. N. Albert, J. Andersen, R. Ansari et al., *Limits on the Macho content of the Galactic Halo from the EROS-2 Survey of the Magellanic Clouds*, A&A **469** (July, 2007) 387–404, [astro-ph/0607207]. Cited on page 75.

[330] H. Niikura, M. Takada, N. Yasuda, R. H. Lupton, T. Sumi, S. More et al., *Microlensing constraints on primordial black holes with Subaru/HSC Andromeda observations*, *Nature Astronomy* **3** (Apr., 2019) 524–534, [1701.02151]. Cited on page 75.

[331] H. Niikura, M. Takada, S. Yokoyama, T. Sumi and S. Masaki, *Constraints on Earth-mass primordial black holes from OGLE 5-year microlensing events*, Phys. Rev. D **99** (Apr., 2019) 083503, [1901.07120]. Cited on page 75.

[332] P. Mróz, A. Udalski, J. Skowron, R. Poleski, S. Kozłowski, M. K. Szymański et al., *No large population of unbound or wide-orbit Jupiter-mass planets*, Nature **548** (Aug., 2017) 183–186, [1707.07634]. Cited on page 75.

[333] M. R. S. Hawkins, *A new look at microlensing limits on dark matter in the Galactic halo*, A&A **575** (Mar., 2015) A107, [1503.01935]. Cited on page 75.

[334] M. Zumalacárregui and U. Seljak, *Limits on Stellar-Mass Compact Objects as Dark Matter from Gravitational Lensing of Type Ia Supernovae*, Phys. Rev. Lett. **121** (Oct., 2018) 141101, [1712.02240]. Cited on page 75, and 76.

[335] J. Garcia-Bellido, S. Clesse and P. Fleury, *LIGO Lo(g)Normal MACHO: Primordial Black Holes survive SN lensing constraints*, *arXiv e-prints* (Dec., 2017) arXiv:1712.06574, [1712.06574]. Cited on page 75, and 76.

[336] J. B. Muñoz, E. D. Kovetz, L. Dai and M. Kamionkowski, *Lensing of fast radio bursts as a probe of compact dark matter*, *Phys. Rev. Lett.* **117** (Aug, 2016) 091301. Cited on page 76.

[337] A. Barnacka, J. F. Glicenstein and R. Moderski, *New constraints on primordial black holes abundance from femtolensing of gamma-ray bursts*, Phys. Rev. D **86** (Aug., 2012) 043001, [1204.2056]. Cited on page 76.

[338] A. Katz, J. Kopp, S. Sibiryakov and W. Xue, *Femtolensing by dark matter revisited*, J. Cosmology Astropart. Phys. **2018** (Dec., 2018) 005, [1807.11495]. Cited on page 76.

[339] Y. Ali-Haïmoud, E. D. Kovetz and M. Kamionkowski, *Merger rate of primordial black-hole binaries*, Phys. Rev. D **96** (Dec., 2017) 123523, [1709.06576]. Cited on page 76.

[340] S. N. G. Thakurta, *Kerr metric in an expanding universe.*, *Indian Journal of Physics* **55B** (Jan., 1981) 304–310. Cited on page 76.

[341] Z.-C. Chen and Q.-G. Huang, *Distinguishing primordial black holes from astrophysical black holes by Einstein Telescope and Cosmic Explorer*, J. Cosmology Astropart. Phys. **2020** (Aug., 2020) 039, [1904.02396]. Cited on page 76.

[342] T. D. Brandt, *Constraints on MACHO Dark Matter from Compact Stellar Systems in Ultra-faint Dwarf Galaxies*, ApJ **824** (June, 2016) L31, [1605.03665]. Cited on page 77.

[343] M. A. Monroy-Rodríguez and C. Allen, *The End of the MACHO Era, Revisited: New Limits on MACHO Masses from Halo Wide Binaries*, ApJ **790** (Aug., 2014) 159, [1406.5169]. Cited on page 77.

[344] P. D. Serpico, V. Poulin, D. Inman and K. Kohri, *Cosmic microwave background bounds on primordial black holes including dark matter halo accretion*, *Physical Review Research* **2** (May, 2020) 023204, [2002.10771]. Cited on page 78.

[345] V. Poulin, J. Lesgourgues and P. D. Serpico, *Cosmological constraints on exotic injection of electromagnetic energy*, *JCAP* **03** (2017) 043, [1610.10051]. Cited on page 78.

[346] S. Clark, B. Dutta, Y. Gao, L. E. Strigari and S. Watson, *Planck Constraint on Relic Primordial Black Holes*, *Phys. Rev. D* **95** (2017) 083006, [1612.07738]. Cited on page 78.

[347] S. K. Acharya and R. Khatri, *CMB spectral distortions constraints on primordial black holes, cosmic strings and long lived unstable particles revisited*, *JCAP* **02** (2020) 010, [1912.10995]. Cited on page 78.

[348] T. Nakama, B. Carr and J. Silk, *Limits on primordial black holes from μ distortions in cosmic microwave background*, *Phys. Rev. D* **97** (2018) 043525, [1710.06945]. Cited on page 78.

[349] R. Murgia, G. Scelfo, M. Viel and A. Raccanelli, *Lyman-<mml:math display="inline"><mml:mrow><mml:mi>α</mml:mi></mml:mrow></mml:math> Forest Constraints on Primordial Black Holes as Dark Matter*, Phys. Rev. Lett. **123** (Aug., 2019) 071102, [1903.10509]. Cited on page 78.

[350] A. Hektor, G. Hutsi, L. Marzola, M. Raidal, V. Vaskonen and H. Veermäe, *Constraining primordial black holes with the EDGES 21-cm absorption signal*, *Phys. Rev.* **D98** (2018) 023503, [1803.09697]. Cited on page 78, and 110.

[351] S. Clark, B. Dutta, Y. Gao, Y.-Z. Ma and L. E. Strigari, *21 cm limits on decaying dark matter and primordial black holes*, *Phys. Rev. D* **98** (2018) 043006, [1803.09390]. Cited on page 78, and 110.

[352] A. Halder and S. Banerjee, *Bounds on Abundance of Primordial Black Hole and Dark Matter from EDGES 21cm Signal*, 2102.00959. Cited on page 78, and 110.

[353] J. R. Pritchard and A. Loeb, *21-cm cosmology*, *Rept. Prog. Phys.* **75** (2012) 086901, [1109.6012]. Cited on page 81, 87, 88, 101, 119, 123, and 136.

[354] S. Furlanetto, S. P. Oh and F. Briggs, *Cosmology at Low Frequencies: The 21 cm Transition and the High-Redshift Universe*, *Phys. Rept.* **433** (2006) 181–301, [astro-ph/0608032]. Cited on page 81, 85, 87, 89, 90, 101, 121, 142, and 150.

[355] A. Mesinger, *The Cosmic 21-cm Revolution; Charting the first billion years of our universe*. 2019, 10.1088/2514-3433/ab4a73. Cited on page 81, 105, 111, and 114.

[356] B. T. Draine, *Physics of the Interstellar and Intergalactic Medium*. 2011. Cited on page 84.

[357] S. R. Furlanetto and A. Loeb, *The 21 Centimeter Forest: Radio Absorption Spectra as Probes of Minihalos before Reionization*, ApJ **579** (Nov., 2002) 1–9, [astro-ph/0206308]. Cited on page 87.

[358] S. Furlanetto, *The 21 Centimeter Forest*, *Mon. Not. Roy. Astron. Soc.* **370** (2006) 1867–1875, [astro-ph/0604223]. Cited on page 87.

[359] S. R. Furlanetto and M. R. Furlanetto, *Spin-exchange rates in electron-hydrogen collisions*, MNRAS **374** (Jan., 2007) 547–555, [astro-ph/0608067]. Cited on page 90.

[360] S. R. Furlanetto and M. R. Furlanetto, *Spin exchange rates in proton-hydrogen collisions*, MNRAS **379** (July, 2007) 130–134, [astro-ph/0702487]. Cited on page 90.

[361] B. Zygelman, *Hyperfine Level-changing Collisions of Hydrogen Atoms and Tomography of the Dark Age Universe*, ApJ **622** (Apr., 2005) 1356–1362. Cited on page 90.

[362] F. J. Smith, *Hydrogen atom spin-change collisions*, Planet. Space Sci. **14** (Oct., 1966) 929–936. Cited on page 89.

[363] A. C. Allison and A. Dalgarno, *Spin Change in Collisions of Hydrogen Atoms*, ApJ **158** (Oct., 1969) 423. Cited on page 90.

[364] H. Liszt, *The spin temperature of warm interstellar H I*, A&A **371** (May, 2001) 698–707, [astro-ph/0103246]. Cited on page 90.

[365] M. Kuhlen, P. Madau and R. Montgomery, *The Spin Temperature and 21 cm Brightness of the Intergalactic Medium in the Pre-Reionization era*, ApJ **637** (Jan., 2006) L1–L4, [astro-ph/0510814]. Cited on page 90.

[366] C. M. Hirata and K. Sigurdson, *The spin-resolved atomic velocity distribution and 21-cm line profile of dark-age gas*, MNRAS **375** (Mar., 2007) 1241–1264, [astro-ph/0605071]. Cited on page 90.

[367] G. B. Field, *Excitation of the Hydrogen 21-CM Line*, *Proceedings of the IRE* **46** (Jan., 1958) 240–250. Cited on page 91.

[368] A. Meiksin, *Detecting the Epoch of First Light in 21-CM Radiation*, in *Perspectives on Radio Astronomy: Science with Large Antenna Arrays* (M. P. van Haarlem, ed.), p. 37, Jan., 2000. Cited on page 92.

[369] G. B. Rybicki and I. P. dell'Antonio, *The Time Development of a Resonance Line in the Expanding Universe*, *"Astrophys. J."* **427** (June, 1994) 603, [astro-ph/9312006]. Cited on page 93, and 94.

[370] X.-L. Chen and J. Miralda-Escudé, *The spin - kinetic temperature coupling and the heating rate due to Lyman - alpha scattering before reionization: Predictions for 21cm emission and absorption*, *Astrophys. J.* **602** (2004) 1–11, [astro-ph/0303395]. Cited on page 93, 94, 95, 96, 99, 100, 141, and 145.

[371] C. M. Hirata, *Wouthuysen-Field coupling strength and application to high-redshift 21 cm radiation*, *Mon. Not. Roy. Astron. Soc.* **367** (2006) 259–274, [astro-ph/0507102]. Cited on page 93, 94, 95, and 97.

[372] S. Furlanetto and J. R. Pritchard, *The Scattering of Lyman-series Photons in the Intergalactic Medium*, *Mon. Not. Roy. Astron. Soc.* **372** (2006) 1093–1103, [astro-ph/0605680]. Cited on page 93, 94, 97, 98, 99, 100, and 141.

[373] G. B. Rybicki, *Improved fokker-planck equation for resonance line scattering*, *Astrophys. J.* **647** (2006) 709–718, [astro-ph/0603047]. Cited on page 93.

[374] D. G. Hummer and G. B. Rybicki, *The Sobolev Approximation for Line Formation with Partial Frequency Redistribution*, ApJ **387** (Mar., 1992) 248. Cited on page 93.

[375] A. Loeb and S. R. Furlanetto, *The First Galaxies in the Universe*. 2013. Cited on page 94.

[376] L. Chuzhoy and P. R. Shapiro, *Uv pumping of hyperfine transitions in the light elements, with application to 21-cm hydrogen and 92-cm deuterium lines from the early universe*, *Astrophys. J.* **651** (2006) 1–7, [astro-ph/0512206]. Cited on page 94, 97, and 98.

[377] J. R. Pritchard and S. R. Furlanetto, *Descending from on high: lyman series cascades and spin-kinetic temperature coupling in the 21 cm line*, *Mon. Not. Roy. Astron. Soc.* **367** (2006) 1057–1066, [astro-ph/0508381]. Cited on page 95, and 144.

[378] A. Mesinger, S. Furlanetto and R. Cen, *21cmFAST: A Fast, Semi-Numerical Simulation of the High-Redshift 21-cm Signal*, *Mon. Not. Roy. Astron. Soc.* **411** (2011) 955, [1003.3878]. Cited on page 97, 99, 109, 113, 120, 125, 127, 136, 137, 142, and 349.

[379] P. C. Breysse, Y. Ali-Haïmoud and C. M. Hirata, *Ultimate frontier of 21-cm cosmology*, *Phys. Rev. D* **98** (2018) 043520, [1804.10626]. Cited on page 99.

[380] P. Madau, A. Meiksin and M. J. Rees, *21-CM tomography of the intergalactic medium at high redshift*, *Astrophys. J.* **475** (1997) 429, [astro-ph/9608010]. Cited on page 99.

[381] A. Oklopčić and C. M. Hirata, *Lyα heating of inhomogeneous high-redshift intergalactic medium*, *The Astrophysical Journal* **779** (Dec, 2013) 146. Cited on page 99.

[382] T. Venumadhav, L. Dai, A. Kaurov and M. Zaldarriaga, *Heating of the intergalactic medium by the cosmic microwave background during cosmic dawn*, *Phys. Rev.* **D98** (2018) 103513, [1804.02406]. Cited on page 100, 139, and 141.

[383] S. Naoz and R. Barkana, *Growth of linear perturbations before the era of the first galaxies*, MNRAS **362** (Sept., 2005) 1047–1053, [astro-ph/0503196]. Cited on page 102, and 103.

[384] J. R. Pritchard and S. R. Furlanetto, *21-cm fluctuations from inhomogeneous X-ray heating before reionization*, MNRAS **376** (Apr., 2007) 1680–1694, [astro-ph/0607234]. Cited on page 102, 103, and 146.

[385] F. Bernardeau, S. Colombi, E. Gaztañaga and R. Scoccimarro, *Large-scale structure of the Universe and cosmological perturbation theory*, Phys. Rep. **367** (Sept., 2002) 1–248, [astro-ph/0112551]. Cited on page 103.

[386] S. Majumdar, J. R. Pritchard, R. Mondal, C. A. Watkinson, S. Bharadwaj and G. Mellema, *Quantifying the non-Gaussianity in the EoR 21-cm signal through bispectrum*, *Mon. Not. Roy. Astron. Soc.* **476** (2018) 4007–4024, [1708.08458]. Cited on page 103.

[387] S. Majumdar, M. Kamran, J. R. Pritchard, R. Mondal, A. Mazumdar, S. Bharadwaj et al., *Redshifted 21-cm Bispectrum I: Impact of the Redshift Space Distortions on the Signal from the Epoch of Reionization*, 2007.06584. Cited on page 103.

[388] A. Saxena, S. Majumdar, M. Kamran and M. Viel, *Impact of dark matter models on the EoR 21-cm signal bispectrum*, *Mon. Not. Roy. Astron. Soc.* **497** (2020) 2941–2953, [2004.04808]. Cited on page 103.

[389] S. Yoshiura, H. Shimabukuro, K. Takahashi and T. Matsubara, *Studying topological structure of 21-cm line fluctuations with 3D Minkowski functionals before reionization*, *Mon. Not. Roy. Astron. Soc.* **465** (2017) 394–402, [1602.02351]. Cited on page 103.

[390] L. Gleser, A. Nusser, B. Ciardi and V. Desjacques, *The morphology of cosmological reionization by means of Minkowski functionals*, *Mon. Not. Roy. Astron. Soc.* **370** (2006) 1329–1338, [astro-ph/0602616]. Cited on page 103.

[391] A. Kapahtia, P. Chingangbam, S. Appleby and C. Park, *A novel probe of ionized bubble shape and size statistics of the epoch of reionization using the contour Minkowski Tensor*, *JCAP* **10** (2018) 011, [1712.09195]. Cited on page 103.

[392] K. Kakiichi, S. Majumdar, G. Mellema, B. Ciardi, K. L. Dixon, I. T. Iliev et al., *Recovering the HII region size statistics from 21-cm tomography*, *Mon. Not. Roy. Astron. Soc.* **471** (2017) 1936–1954, [1702.02520]. Cited on page 103.

[393] A. Liu and J. R. Shaw, *Data Analysis for Precision 21 cm Cosmology*, PASP **132** (June, 2020) 062001, [1907.08211]. Cited on page 104, 106, 114, and 115.

[394] R. M. Prestage, K. T. Constantikes, T. R. Hunter, L. J. King, R. J. Lacasse, F. J. Lockman et al., *The green bank telescope*, *Proceedings of the IEEE* **97** (2009) 1382–1390. Cited on page 104, and 116.

[395] A. Datta, J. D. Bowman and C. L. Carilli, *Bright Source Subtraction Requirements for Redshifted 21 cm Measurements*, ApJ **724** (Nov., 2010) 526–538, [1005.4071]. Cited on page 106.

[396] E. Chapman, S. Zaroubi, F. B. Abdalla, F. Dulwich, V. Jelić and B. Mort, *The Effect of Foreground Mitigation Strategy on EoR Window Recovery*, *Mon. Not. Roy. Astron. Soc.* **458** (2016) 2928–2939, [1408.4695]. Cited on page 106.

[397] J. S. Dillon, A. Liu, C. L. Williams, J. N. Hewitt, M. Tegmark, E. H. Morgan et al., *Overcoming real-world obstacles in 21 cm power spectrum estimation: A method demonstration and results from early murchison widefield array data*, *Phys. Rev. D* **89** (Jan, 2014) 023002. Cited on page 106, 113, and 114.

[398] L. Koopmans, R. Barkana, M. Bentum, G. Bernardi, A.-J. Boonstra, J. Bowman et al., *Peering into the Dark (Ages) with Low-Frequency Space Interferometers*, *arXiv e-prints* (Aug., 2019) arXiv:1908.04296, [1908.04296]. Cited on page 107, and 114.

[399] A. Liu, J. R. Pritchard, M. Tegmark and A. Loeb, *Global 21 cm signal experiments: A designer's guide*, Phys. Rev. D **87** (Feb., 2013) 043002, [1211.3743]. Cited on page 107.

[400] J. D. Bowman, A. E. E. Rogers and J. N. Hewitt, *Toward Empirical Constraints on the Global Redshifted 21 cm Brightness Temperature During the Epoch of Reionization*, ApJ **676** (Mar., 2008) 1–9, [0710.2541]. Cited on page 107.

[401] J. D. Bowman and A. E. E. Rogers, *A lower limit of $\Delta z>0.06$ for the duration of the reionization epoch*, Nature **468** (Dec., 2010) 796–798, [1209.1117]. Cited on page 107.

[402] R. A. Monsalve, A. E. E. Rogers, J. D. Bowman and T. J. Mozdzen, *Calibration of the EDGES High-Band Receiver to Observe the Global 21-cm Signature from the Epoch of Reionization*, *Astrophys. J.* **835** (2017) 49, [1602.08065]. Cited on page 107.

[403] R. A. Monsalve, A. E. E. Rogers, J. D. Bowman and T. J. Mozdzen, *Results from EDGES High-band. I. Constraints on Phenomenological Models for the Global 21 cm Signal*, ApJ **847** (Sept., 2017) 64, [1708.05817]. Cited on page 107, and 134.

[404] R. A. Monsalve, B. Greig, J. D. Bowman, A. Mesinger, A. E. E. Rogers, T. J. Mozdzen et al., *Results from EDGES High-Band: II. Constraints on Parameters of Early Galaxies*, *Astrophys. J.* **863** (2018) 11, [1806.07774]. Cited on page 107.

[405] R. A. Monsalve, A. Fialkov, J. D. Bowman, A. E. E. Rogers, T. J. Mozdzen, A. Cohen et al., *Results from EDGES High-Band: III. New Constraints on Parameters of the Early Universe*, *Astrophys. J.* **875** (2019) 67, [1901.10943]. Cited on page 107.

[406] N. Patra, R. Subrahmanyan, A. Raghunathan and N. Shankar, *SARAS: a precision system for measurement of the Cosmic Radio*

Background and signatures from the Epoch of Reionization, *Exper. Astron.* **36** (2013) 319–370, [1211.3800]. Cited on page 107.

[407] S. Singh, R. Subrahmanyan, N. U. Shankar, M. S. Rao, B. S. Girish, A. Raghunathan et al., *SARAS 2: a spectral radiometer for probing cosmic dawn and the epoch of reionization through detection of the global 21-cm signal*, *Experimental Astronomy* **45** (Apr., 2018) 269–314, [1710.01101]. Cited on page 107.

[408] S. Singh, R. Subrahmanyan, N. Udaya Shankar, M. Sathyanarayana Rao, A. Fialkov, A. Cohen et al., *First Results on the Epoch of Reionization from First Light with SARAS 2*, ApJ **845** (Aug., 2017) L12, [1703.06647]. Cited on page 107, 108, and 110.

[409] S. Singh et al., *SARAS 2 constraints on global 21-cm signals from the Epoch of Reionization*, *Astrophys. J.* **858** (2018) 54, [1711.11281]. Cited on page 108, and 110.

[410] L. J. Greenhill and G. Bernardi, *HI Epoch of Reionization Arrays*, 1201.1700. Cited on page 108.

[411] D. C. Price, L. J. Greenhill, A. Fialkov, G. Bernardi, H. Garsden, B. R. Barsdell et al., *Design and characterization of the Large-aperture Experiment to Detect the Dark Age (LEDA) radiometer systems*, MNRAS **478** (Aug., 2018) 4193–4213, [1709.09313]. Cited on page 108.

[412] G. Bernardi, J. T. L. Zwart, D. Price, L. J. Greenhill, A. Mesinger, J. Dowell et al., *Bayesian constraints on the global 21-cm signal from the Cosmic Dawn*, MNRAS **461** (Sept., 2016) 2847–2855, [1606.06006]. Cited on page 108.

[413] J. O. Burns et al., *Dark Cosmology: Investigating Dark Matter \& Exotic Physics in the Dark Ages using the Redshifted 21-cm Global Spectrum*, 1902.06147. Cited on page 108.

[414] J. Burns et al., *Global 21-cm Cosmology from the Farside of the Moon*, 2103.05085. Cited on page 108.

[415] J. O. Burns et al., *Probing the First Stars and Black Holes in the Early Universe with the Dark Ages Radio Explorer (DARE)*, *Adv. Space Res.* **49** (2012) 433–450, [1106.5194]. Cited on page 108.

[416] J. O. Burns, J. Lazio, S. Bale, J. Bowman, R. Bradley, C. Carilli et al., *Probing the first stars and black holes in the early Universe with the Dark Ages Radio Explorer (DARE)*, *Advances in Space Research* **49** (Feb., 2012) 433–450, [1106.5194]. Cited on page 108.

[417] R. Barkana, *Possible interaction between baryons and dark-matter particles revealed by the first stars*, *Nature* **555** (2018) 71–74, [1803.06698]. Cited on page 109.

[418] J. B. Muñoz and A. Loeb, *A small amount of mini-charged dark matter could cool the baryons in the early Universe*, *Nature* **557** (2018) 684, [1802.10094]. Cited on page 109.

[419] J. B. Muñoz, C. Dvorkin and A. Loeb, *21-cm Fluctuations from Charged Dark Matter*, *Phys. Rev. Lett.* **121** (2018) 121301, [1804.01092]. Cited on page 109.

[420] A. Fialkov, R. Barkana and A. Cohen, *Constraining Baryon–Dark Matter Scattering with the Cosmic Dawn 21-cm Signal*, *Phys. Rev. Lett.* **121** (2018) 011101, [1802.10577]. Cited on page 109.

[421] A. Berlin, D. Hooper, G. Krnjaic and S. D. McDermott, *Severely Constraining Dark Matter Interpretations of the 21-cm Anomaly*, *Phys. Rev. Lett.* **121** (2018) 011102, [1803.02804]. Cited on page 109.

[422] M. S. Mahdawi and G. R. Farrar, *Constraints on Dark Matter with a moderately large and velocity-dependent DM-nucleon cross-section*, *JCAP* **10** (2018) 007, [1804.03073]. Cited on page 109.

[423] J. C. Hill and E. J. Baxter, *Can Early Dark Energy Explain EDGES?*, *JCAP* **08** (2018) 037, [1803.07555]. Cited on page 109.

[424] C. Feng and G. Holder, *Enhanced Global Signal of Neutral Hydrogen Due to Excess Radiation at Cosmic Dawn*, ApJ **858** (May, 2018) L17, [1802.07432]. Cited on page 109.

[425] P. Sharma, *Astrophysical radio background cannot explain the EDGES 21-cm signal: constraints from cooling of non-thermal electrons*, MNRAS **481** (Nov., 2018) L6–L10, [1804.05843]. Cited on page 109.

[426] J. Mirocha and S. R. Furlanetto, *What does the first highly-redshifted 21-cm detection tell us about early galaxies?*, *Mon. Not. Roy. Astron. Soc.* **483** (2019) 1980–1992, [1803.03272]. Cited on page 109.

[427] S. Fraser et al., *The EDGES 21 cm anomaly and properties of dark Matter*, *Phys. Lett.* **B785** (2018) 159–164, [1803.03245]. Cited on page 110.

[428] M. Pospelov, J. Pradler, J. T. Ruderman and A. Urbano, *Room for New Physics in the Rayleigh-Jeans Tail of the Cosmic Microwave Background*, *Phys. Rev. Lett.* **121** (2018) 031103, [1803.07048]. Cited on page 110.

[429] T. Moroi, K. Nakayama and Y. Tang, *Axion-photon conversion and effects on 21 cm observation*, *Physics Letters B* **783** (Aug., 2018) 301–305, [1804.10378]. Cited on page 110.

[430] A. Ewall-Wice, T. C. Chang, J. Lazio, O. Dore, M. Seiffert and R. A. Monsalve, *Modeling the radio background from the first black holes at cosmic dawn: Implications for the 21 cm absorption amplitude*, *Astrophys. J.* **868** (2018) 63, [1803.01815]. Cited on page 110.

[431] A. Ewall-Wice, T.-C. Chang and T. J. W. Lazio, *The Radio Scream from Black Holes at Cosmic Dawn: A Semi-Analytic Model for the Impact of Radio Loud Black-Holes on the 21 cm Global Signal*, *Mon. Not. Roy. Astron. Soc.* **492** (2020) 6086–6104, [1903.06788]. Cited on page 110.

[432] G. D'Amico, P. Panci and A. Strumia, *Bounds on Dark Matter annihilations from 21 cm data*, *Phys. Rev. Lett.* **121** (2018) 011103, [1803.03629]. Cited on page 110.

[433] H. Liu and T. R. Slatyer, *Implications of a 21-cm signal for dark matter annihilation and decay*, *Phys. Rev.* **D98** (2018) 023501, [1803.09739]. Cited on page 110.

[434] A. Mitridate and A. Podo, *Bounds on Dark Matter decay from 21 cm line*, *JCAP* **1805** (2018) 069, [1803.11169]. Cited on page 110.

[435] M. Safarzadeh, E. Scannapieco and A. Babul, *A limit on the warm dark matter particle mass from the redshifted 21 cm absorption line*, *Astrophys. J.* **859** (2018) L18, [1803.08039]. Cited on page 110.

[436] A. Schneider, *Constraining noncold dark matter models with the global 21-cm signal*, Phys. Rev. D **98** (Sept., 2018) 063021, [1805.00021]. Cited on page 110.

[437] A. Lidz and L. Hui, *Implications of a prereionization 21-cm absorption signal for fuzzy dark matter*, Phys. Rev. D **98** (July, 2018) 023011, [1805.01253]. Cited on page 110.

[438] R. F. Bradley, K. Tauscher, D. Rapetti and J. O. Burns, *A Ground Plane Artifact that Induces an Absorption Profile in Averaged Spectra from Global 21 cm Measurements, with Possible Application*

to EDGES, ApJ **874** (Apr., 2019) 153, [1810.09015]. Cited on page 110, and 111.

[439] R. Hills, G. Kulkarni, P. D. Meerburg and E. Puchwein, *Concerns about modelling of the EDGES data*, Nature **564** (Dec., 2018) E32–E34, [1805.01421]. Cited on page 110.

[440] P. H. Sims and J. C. Pober, *Testing for calibration systematics in the EDGES low-band data using Bayesian model selection*, MNRAS **492** (Feb., 2020) 22–38, [1910.03165]. Cited on page 111.

[441] G. Paciga, J. G. Albert, K. Bandura, T.-C. Chang, Y. Gupta, C. Hirata et al., *A simulation-calibrated limit on the H I power spectrum from the GMRT Epoch of Reionization experiment*, MNRAS **433** (July, 2013) 639–647, [1301.5906]. Cited on page 113, and 114.

[442] S. Pal, S. Bharadwaj, A. Ghosh and S. Choudhuri, *Demonstrating the Tapered Gridded Estimator (TGE) for the Cosmological HI 21-cm Power Spectrum using* 150 MHz *GMRT observations*, *Mon. Not. Roy. Astron. Soc.* **501** (2021) 3378–3391, [2012.04998]. Cited on page 113, and 114.

[443] J. S. Dillon, A. R. Neben, J. N. Hewitt, M. Tegmark, N. Barry, A. P. Beardsley et al., *Empirical covariance modeling for 21 cm power spectrum estimation: A method demonstration and new limits from early murchison widefield array 128-tile data*, *Phys. Rev. D* **91** (Jun, 2015) 123011. Cited on page 113, and 114.

[444] A. P. Beardsley, B. J. Hazelton, I. S. Sullivan, P. Carroll, N. Barry, M. Rahimi et al., *First Season MWA EoR Power spectrum Results at Redshift 7*, ApJ **833** (Dec., 2016) 102, [1608.06281]. Cited on page 113, and 114.

[445] A. Ewall-Wice, J. S. Dillon, J. N. Hewitt, A. Loeb, A. Mesinger, A. R. Neben et al., *First limits on the 21 cm power spectrum during the Epoch of X-ray heating*, MNRAS **460** (Aug., 2016) 4320–4347, [1605.00016]. Cited on page 113, and 114.

[446] N. Barry et al., *Improving the Epoch of Reionization Power Spectrum Results from Murchison Widefield Array Season 1 Observations*, 1909.00561. Cited on page 113, and 114.

[447] W. Li, J. C. Pober, N. Barry, B. J. Hazelton, M. F. Morales, C. M. Trott et al., *First Season MWA Phase II Epoch of Reionization Power Spectrum Results at Redshift 7*, ApJ **887** (Dec., 2019) 141, [1911.10216]. Cited on page 113, and 114.

[448] C. M. Trott et al., *Deep multiredshift limits on Epoch of Reionization 21 cm power spectra from four seasons of Murchison Widefield Array observations*, *Mon. Not. Roy. Astron. Soc.* **493** (2020) 4711–4727, [2002.02575]. Cited on page 113, and 114.

[449] A. H. Patil, S. Yatawatta, L. V. E. Koopmans, A. G. de Bruyn, M. A. Brentjens, S. Zaroubi et al., *Upper Limits on the 21 cm Epoch of Reionization Power Spectrum from One Night with LOFAR*, ApJ **838** (Mar., 2017) 65, [1702.08679]. Cited on page 113, and 115.

[450] B. K. Gehlot, F. G. Mertens, L. V. E. Koopmans, M. A. Brentjens, S. Zaroubi, B. Ciardi et al., *The first power spectrum limit on the 21-cm signal of neutral hydrogen during the Cosmic Dawn at z = 20-25 from LOFAR*, MNRAS **488** (Sept., 2019) 4271–4287, [1809.06661]. Cited on page 113, and 115.

[451] F. G. Mertens et al., *Improved upper limits on the 21-cm signal power spectrum of neutral hydrogen at $z \approx 9.1$ from LOFAR*, *Mon. Not. Roy. Astron. Soc.* **493** (2020) 1662–1685, [2002.07196]. Cited on page 113, and 115.

[452] M. W. Eastwood, M. M. Anderson, R. M. Monroe, G. Hallinan, M. Catha, J. Dowell et al., *The 21 cm Power Spectrum from the Cosmic Dawn: First Results from the OVRO-LWA*, AJ **158** (Aug., 2019) 84, [1906.08943]. Cited on page 113, and 115.

[453] H. Garsden, L. Greenhill, G. Bernardi, A. Fialkov, D. C. Price, D. Mitchell et al., *A 21-cm power spectrum at 48 MHz, using the Owens Valley Long Wavelength Array*, 2102.09596. Cited on page 113, and 115.

[454] M. Kolopanis, D. C. Jacobs, C. Cheng, A. R. Parsons, S. A. Kohn, J. C. Pober et al., *A Simplified, Lossless Reanalysis of PAPER-64*, ApJ **883** (Oct., 2019) 133, [1909.02085]. Cited on page 113, and 114.

[455] B. K. Gehlot, F. G. Mertens, L. V. E. Koopmans, A. R. Offringa, A. Shulevski, M. Mevius et al., *The AARTFAAC Cosmic Explorer: observations of the 21-cm power spectrum in the EDGES absorption trough*, MNRAS **499** (Oct., 2020) 4158–4173, [2010.02269]. Cited on page 113, and 115.

[456] J. Pober, *21cmSense: Calculating the sensitivity of 21cm experiments to the EoR power spectrum*, Sept., 2016. Cited on page 113.

[457] P. Villanueva-Domingo, *21cmbounds*, Mar., 2021. 10.5281/zenodo.4579904. Cited on page 113.

[458] A. Parsons, J. Pober, M. McQuinn, D. Jacobs and J. Aguirre, *A Sensitivity and Array-configuration Study for Measuring the Power Spectrum of 21 cm Emission from Reionization*, ApJ **753** (July, 2012) 81, [1103.2135]. Cited on page 111, 112, 113, and 114.

[459] J. C. Pober, A. R. Parsons, D. R. DeBoer, P. McDonald, M. McQuinn, J. E. Aguirre et al., *The Baryon Acoustic Oscillation Broadband and Broad-beam Array: Design Overview and Sensitivity Forecasts*, AJ **145** (Mar., 2013) 65, [1210.2413]. Cited on page 112, and 113.

[460] J. Raste, G. Kulkarni, L. C. Keating, M. G. Haehnelt, J. Chardin and D. Aubert, *Implications of the $z > 5$ Lyman-α forest for the 21-cm power spectrum from the epoch of reionization*, 2103.03261. Cited on page 114.

[461] G. Swarup, S. Ananthakrishnan, V. K. Kapahi, A. P. Rao, C. R. Subrahmanya and V. K. Kulkarni, *The giant metre-wave radio telescope*, *Current Science* **60** (1991) 95–105. Cited on page 114.

[462] G. Paciga, T.-C. Chang, Y. Gupta, R. Nityanada, J. Odegova, U.-L. Pen et al., *The GMRT Epoch of Reionization experiment: a new upper limit on the neutral hydrogen power spectrum at $z\approx 8.6$*, MNRAS **413** (May, 2011) 1174–1183, [1006.1351]. Cited on page 114.

[463] A. R. Parsons et al., *The Precision Array for Probing the Epoch of Reionization: 8 Station Results*, *Astron. J.* **139** (2010) 1468, [0904.2334]. Cited on page 114.

[464] A. Parsons, M. McQuinn, D. Jacobs, J. Aguirre and J. Pober, *A Sensitivity and Array-Configuration Study for Measuring the Power Spectrum of 21cm Emission from Reionization*, *Astrophys. J.* **753** (2012) 81, [1103.2135]. Cited on page 114.

[465] A. R. Parsons, J. C. Pober, J. E. Aguirre, C. L. Carilli, D. C. Jacobs and D. F. Moore, *A Per-baseline, Delay-spectrum Technique for Accessing the 21 cm Cosmic Reionization Signature*, ApJ **756** (Sept., 2012) 165, [1204.4749]. Cited on page 114.

[466] J. C. Pober et al., *Opening the 21cm EoR Window: Measurements of Foreground Isolation with PAPER*, *Astrophys. J.* **768** (2013) L36, [1301.7099]. Cited on page 114.

[467] D. C. Jacobs et al., *Multi-redshift limits on the 21cm power spectrum from PAPER*, *Astrophys. J.* **801** (2015) 51, [1408.3389]. Cited on page 114.

[468] Z. S. Ali et al., *PAPER-64 constraints on reionization: The 21cm power spectrum at z =8.4*, *Astrophys. J.* **809** (2015) 61, [1502.06016]. Cited on page 114.

[469] C. Cheng, A. R. Parsons, M. Kolopanis, D. C. Jacobs, A. Liu, S. A. Kohn et al., *Characterizing Signal Loss in the 21 cm Reionization Power Spectrum: A Revised Study of PAPER-64*, ApJ **868** (Nov., 2018) 26, [1810.05175]. Cited on page 114.

[470] Z. S. Ali, A. R. Parsons, H. Zheng, J. C. Pober, A. Liu, J. E. Aguirre et al., *Erratum: "PAPER-64 Constraints on Reionization: The 21 cm Power Spectrum at z = 8.4" (<A href="http://doi.org/10.1088/0004-637x/809/1/61">2015, ApJ, 809, 61</A>)*, ApJ **863** (Aug., 2018) 201. Cited on page 114.

[471] H. van Woerden and R. G. Strom, *The beginnings of radio astronomy in the Netherlands*, *Journal of Astronomical History and Heritage* **9** (June, 2006) 3–20. Cited on page 115.

[472] P. Prasad, F. Huizinga, E. Kooistra, D. van der Schuur, A. Gunst, J. Romein et al., *The AARTFAAC All-Sky Monitor: System Design and Implementation*, *Journal of Astronomical Instrumentation* **5** (Dec., 2016) 1641008, [1609.04205]. Cited on page 115.

[473] P. Zarka, M. Tagger, L. Denis, J. N. Girard, A. Konovalenko, M. Atemkeng et al., *Nenufar: Instrument description and science case*, in *2015 International Conference on Antenna Theory and Techniques (ICATT)*, pp. 1–6, 2015. DOI. Cited on page 115.

[474] T.-C. Chang, U.-L. Pen, K. Bandura and J. B. Peterson, *An intensity map of hydrogen 21-cm emission at redshift z∼0.8*, Nature **466** (July, 2010) 463–465. Cited on page 116.

[475] K. W. Masui, E. R. Switzer, N. Banavar, K. Bandura, C. Blake, L. M. Calin et al., *Measurement of 21 cm Brightness Fluctuations at z ∼0.8 in Cross-correlation*, ApJ **763** (Jan., 2013) L20, [1208.0331]. Cited on page 116.

[476] L. Staveley-Smith, W. E. Wilson, T. S. Bird, M. J. Disney, R. D. Ekers, K. C. Freeman et al., *The Parkes 21 CM multibeam receiver*, PASA **13** (Nov., 1996) 243–248. Cited on page 116.

[477] C. J. Anderson, N. J. Luciw, Y. C. Li, C. Y. Kuo, J. Yadav, K. W. Masui et al., *Low-amplitude clustering in low-redshift 21-cm intensity maps cross-correlated with 2dF galaxy densities*, MNRAS **476** (May, 2018) 3382–3392, [1710.00424]. Cited on page 116.

[478] A. Liu, H. C. Chiang, A. Crites, J. Sievers and R. Hložek, *High-redshift 21cm Cosmology in Canada*, in *Canadian Long Range Plan for Astronony and Astrophysics White Papers*, vol. 2020, p. 12, Oct., 2019. 1910.03153. DOI. Cited on page 116.

[479] L. B. Newburgh, K. Bandura, M. A. Bucher, T. C. Chang, H. C. Chiang, J. F. Cliche et al., *HIRAX: a probe of dark energy and radio transients*, in *Ground-based and Airborne Telescopes VI* (H. J. Hall, R. Gilmozzi and H. K. Marshall, eds.), vol. 9906 of *Society of Photo-Optical Instrumentation Engineers (SPIE) Conference Series*, p. 99065X, Aug., 2016. 1607.02059. DOI. Cited on page 116.

[480] X. Chen, *The Tianlai Project: a 21CM Cosmology Experiment*, in *International Journal of Modern Physics Conference Series*, vol. 12 of *International Journal of Modern Physics Conference Series*, pp. 256–263, Mar., 2012. 1212.6278. DOI. Cited on page 116.

[481] C. A. Wuensche, a. pre=" and the" BINGO Collaboration, *The BINGO telescope: a new instrument exploring the new 21 cm cosmology window*, in *Journal of Physics Conference Series*, vol. 1269 of *Journal of Physics Conference Series*, p. 012002, July, 2019. 1803.01644. DOI. Cited on page 116.

[482] M. G. Santos, M. Cluver, M. Hilton, M. Jarvis, G. I. G. Jozsa, L. Leeuw et al., *Meerklass: Meerkat large area synoptic survey*, 2017. Cited on page 117.

[483] D. McConnell, C. L. Hale, E. Lenc, J. K. Banfield, G. Heald, A. W. Hotan et al., *The rapid askap continuum survey i: Design and first results*, *Publications of the Astronomical Society of Australia* **37** (2020) . Cited on page 117.

[484] J. Burns et al., *A Lunar Farside Low Radio Frequency Array for Dark Ages 21-cm Cosmology*, 2103.08623. Cited on page 117.

[485] J. Park, A. Mesinger, B. Greig and N. Gillet, *Inferring the astrophysics of reionization and cosmic dawn from galaxy luminosity functions and the 21-cm signal*, *Mon. Not. Roy. Astron. Soc.* **484** (2019) 933, [1809.08995]. Cited on page 120, 125, and 137.

[486] A. A. Meiksin, *The Physics of the Intergalactic Medium*, *Rev. Mod. Phys.* **81** (2009) 1405–1469, [0711.3358]. Cited on page 120.

[487] T. R. Choudhury, *Analytical Models of the Intergalactic Medium and Reionization*, *Current Science* **97** (Sept., 2009) 841, [0904.4596]. Cited on page 120, and 124.

[488] N. Y. Gnedin, *Modeling Physical Processes at Galactic Scales and Above*, *Saas-Fee Advanced Course* **43** (Jan., 2016) 1, [1412.5184]. Cited on page 120.

[489] K. Finlator, S. P. Oh, F. Özel and R. Davé, *Gas clumping in self-consistent reionization models*, *Monthly Notices of the Royal Astronomical Society* **427** (Nov, 2012) 2464–2479. Cited on page 121.

[490] G. C. So, M. L. Norman, D. R. Reynolds and J. H. Wise, *Fully Coupled Simulation of Cosmic Reionization. II. Recombinations, Clumping Factors, and the Photon Budget for Reionization*, *ApJ* **789** (July, 2014) 149, [1311.2152]. Cited on page 121.

[491] A. A. Kaurov and N. Y. Gnedin, *Recombination clumping factor during cosmic reionization*, *The Astrophysical Journal* **787** (May, 2014) 146. Cited on page 121.

[492] A. A. Kaurov and N. Y. Gnedin, *Cosmic reionization on computers. iii. the clumping factor*, *The Astrophysical Journal* **810** (Sep, 2015) 154. Cited on page 121.

[493] P. Madau, *Cosmic Reionization After Planck and Before JWST: An Analytic Approach*, *Astrophys. J.* **851** (2017) 50, [1710.07636]. Cited on page 123.

[494] S. Furlanetto, *The Global 21 Centimeter Background from High Redshifts*, *Mon. Not. Roy. Astron. Soc.* **371** (2006) 867–878, [astro-ph/0604040]. Cited on page 123, 136, 137, and 138.

[495] V. Bromm, R. P. Kudritzki and A. Loeb, *Generic spectrum and ionization efficiency of a heavy initial mass function for the first stars*, *The Astrophysical Journal* **552** (May, 2001) 464–472. Cited on page 124, and 145.

[496] E. Zackrisson, C.-E. Rydberg, D. Schaerer, G. Östlin and M. Tuli, *The spectral evolution of the first galaxies. i.james webb space telescopedetection limits and color criteria for population iii galaxies*, *The Astrophysical Journal* **740** (Sep, 2011) 13. Cited on page 124.

[497] N. Leite, C. Evoli, M. D'Angelo, B. Ciardi, G. Sigl and A. Ferrara, *Do Cosmic Rays Heat the Early Intergalactic Medium?*, *Mon. Not. Roy. Astron. Soc.* **469** (2017) 416–424, [1703.09337]. Cited on page 124.

[498] A. Lidz and L. Hui, *Implications of a prereionization 21-cm absorption signal for fuzzy dark matter*, *Phys. Rev. D* **98** (2018) 023011, [1805.01253]. Cited on page 124.

[499] J. H. Wise, V. G. Demchenko, M. T. Halicek, M. L. Norman, M. J. Turk, T. Abel et al., *The birth of a galaxy – III. Propelling reionization with the faintest galaxies*, *Mon. Not. Roy. Astron. Soc.* **442** (2014) 2560–2579, [1403.6123]. Cited on page 124.

[500] A. Mesinger, A. Ferrara and D. S. Spiegel, *Signatures of X-rays in the early Universe*, *Mon. Not. Roy. Astron. Soc.* **431** (2013) 621, [1210.7319]. Cited on page 124.

[501] R. L. Grissom, D. R. Ballantyne and J. H. Wise, *On the contribution of active galactic nuclei to reionization (Research Note)*, *Astron. Astrophys.* **561** (2014) A90, [1312.1358]. Cited on page 125.

[502] R. S. Ellis, R. J. McLure, J. S. Dunlop, B. E. Robertson, Y. Ono, M. A. Schenker et al., *The Abundance of Star-forming Galaxies in the Redshift Range 8.5-12: New Results from the 2012 Hubble Ultra Deep Field Campaign*, *ApJL* **763** (Jan., 2013) L7, [1211.6804]. Cited on page 125.

[503] P. A. Oesch, G. Brammer, P. G. v. Dokkum, G. D. Illingworth, R. J. Bouwens, I. Labbé et al., *A remarkably luminous galaxy atz= 11.1 measured withhubble space telescopegrism spectroscopy*, *The Astrophysical Journal* **819** (Mar, 2016) 129. Cited on page 125.

[504] J. P. Gardner et al., *The James Webb Space Telescope*, *Space Sci. Rev.* **123** (2006) 485, [astro-ph/0606175]. Cited on page 125.

[505] D. Sobral, J. Matthee, B. Darvish, D. Schaerer, B. Mobasher, H. Röttgering et al., *Evidence for PopIII-like stellar populations in the most luminous Lyα emitters at the epoch of reionisation: spectroscopic confirmation*, *Astrophys. J.* **808** (2015) 139, [1504.01734]. Cited on page 126.

[506] O. Zahn, A. Mesinger, M. McQuinn, H. Trac, R. Cen and L. E. Hernquist, *Comparison of reionization models: radiative transfer simulations and approximate, seminumeric models*, *Monthly Notices of the Royal Astronomical Society* **414** (Apr, 2011) 727–738. Cited on page 126.

[507] N. Y. Gnedin, *Cosmic reionization on computers. i. design and calibration of simulations*, *The Astrophysical Journal* **793** (Sep, 2014) 29. Cited on page 126.

[508] A. A. Kaurov, *On improving analytical models of cosmic reionization for matching numerical simulation*, *The Astrophysical Journal* **831** (Nov, 2016) 198. Cited on page 127, and 128.

[509] S. Furlanetto, M. Zaldarriaga and L. Hernquist, *The Growth of HII regions during reionization*, *Astrophys. J.* **613** (2004) 1–15, [astro-ph/0403697]. Cited on page 127, and 349.

[510] O. Zahn, A. Mesinger, M. McQuinn, H. Trac, R. Cen and L. E. Hernquist, *Comparison Of Reionization Models: Radiative Transfer Simulations And Approximate, Semi-Numeric Models*, *Mon. Not. Roy. Astron. Soc.* **414** (2011) 727, [1003.3455]. Cited on page 127.

[511] J. Miralda-Escudé, M. Haehnelt and M. J. Rees, *Reionization of the Inhomogeneous Universe*, *ApJ* **530** (Feb., 2000) 1–16, [astro-ph/9812306]. Cited on page 128.

[512] H. Trac and R. Cen, *Radiative transfer simulations of cosmic reionization. 1. Methodology and initial results*, *Astrophys. J.* **671** (2007) 1, [astro-ph/0612406]. Cited on page 128.

[513] K. L. Dixon, I. T. Iliev, G. Mellema, K. Ahn and P. R. Shapiro, *The Large-Scale Observational Signatures of Low-Mass Galaxies During Reionization*, *Mon. Not. Roy. Astron. Soc.* **456** (2016) 3011–3029, [1512.03836]. Cited on page 128.

[514] N. Y. Gnedin, *Cosmic Reionization On Computers I. Design and Calibration of Simulations*, *Astrophys. J.* **793** (2014) 29, [1403.4245]. Cited on page 128, 210, 349, and 351.

[515] H. Xu, J. H. Wise, M. L. Norman, K. Ahn and B. W. O'Shea, *Galaxy Properties and UV Escape Fractions during the Epoch of Reionization: Results from the Renaissance Simulations*, ApJ **833** (Dec., 2016) 84, [1604.07842]. Cited on page 128.

[516] A. Doussot, H. Trac and R. Cen, *SCORCH. II. Radiation-hydrodynamic Simulations of Reionization with Varying Radiation Escape Fractions*, *Astrophys. J.* **870** (2019) 18, [1712.04464]. Cited on page 128.

[517] N. Y. Gnedin and T. Abel, *Multi-dimensional cosmological radiative transfer with a Variable Eddington Tensor formalism*, New A **6** (Oct., 2001) 437–455, [astro-ph/0106278]. Cited on page 128.

[518] B. Ciardi, A. Ferrara, S. Marri and G. Raimondo, *Cosmological reionization around the first stars: Monte Carlo radiative transfer*, *Mon. Not. Roy. Astron. Soc.* **324** (2001) 381, [astro-ph/0005181]. Cited on page 128.

[519] J. H. Wise and T. Abel, *ENZO+MORAY: radiation hydrodynamics adaptive mesh refinement simulations with adaptive ray tracing*, MNRAS **414** (July, 2011) 3458–3491, [1012.2865]. Cited on page 128.

[520] I. T. Iliev, B. Ciardi, M. A. Alvarez, A. Maselli, A. Ferrara, N. Y. Gnedin et al., *Cosmological radiative transfer codes comparison project - I. The static density field tests*, MNRAS **371** (Sept., 2006) 1057–1086, [astro-ph/0603199]. Cited on page 128.

[521] I. T. Iliev, D. Whalen, G. Mellema, K. Ahn, S. Baek, N. Y. Gnedin et al., *Cosmological radiative transfer comparison project - II. The radiation-hydrodynamic tests*, MNRAS **400** (Dec., 2009) 1283–1316, [0905.2920]. Cited on page 128.

[522] H. Y. Trac and N. Y. Gnedin, *Computer Simulations of Cosmic Reionization*, *Advanced Science Letters* **4** (Feb., 2011) 228–243, [0906.4348]. Cited on page 128.

[523] A. Mesinger, *Reionization and Cosmic Dawn: theory and simulations*, *IAU Symp.* **333** (2017) 3–11, [1801.02649]. Cited on page 128.

[524] X.-H. Fan et al., *Constraining the evolution of the ionizing background and the epoch of reionization with z 6 quasars. 2. a sample of 19 quasars*, *Astron. J.* **132** (2006) 117–136, [astro-ph/0512082]. Cited on page 129, 130, and 131.

[525] I. McGreer, A. Mesinger and V. D'Odorico, *Model-independent evidence in favour of an end to reionization by $z \approx 6$*, *Mon. Not. Roy. Astron. Soc.* **447** (2015) 499–505, [1411.5375]. Cited on page 129, 130, and 131.

[526] M. A. Schenker, R. S. Ellis, N. P. Konidaris and D. P. Stark, *Line Emitting Galaxies Beyond a Redshift of 7: An Improved Method for Estimating the Evolving Neutrality of the Intergalactic Medium*, *Astrophys. J.* **795** (2014) 20, [1404.4632]. Cited on page 129, and 133.

[527] A. Konno, M. Ouchi, T. Shibuya, Y. Ono, K. Shimasaku, Y. Taniguchi et al., *SILVERRUSH. IV. Lyα luminosity functions at*

$z = 5.7$ and 6.6 studied with ~1300 Lyα emitters on the 14-21 deg^2 sky, PASJ **70** (Jan., 2018) S16, [1705.01222]. Cited on page 129, and 132.

[528] A. K. Inoue, K. Hasegawa, T. Ishiyama, H. Yajima, I. Shimizu, M. Umemura et al., *SILVERRUSH. VI. A simulation of Lyα emitters in the reionization epoch and a comparison with Subaru Hyper Suprime-Cam survey early data*, PASJ **70** (June, 2018) 55, [1801.00067]. Cited on page 129, and 132.

[529] C. A. Mason, T. Treu, M. Dijkstra, A. Mesinger, M. Trenti, L. Pentericci et al., *The Universe Is Reionizing at $z \sim 7$: Bayesian Inference of the IGM Neutral Fraction Using Lyα Emission from Galaxies*, *Astrophys. J.* **856** (2018) 2, [1709.05356]. Cited on page 129, and 133.

[530] R. Itoh, M. Ouchi, H. Zhang, A. K. Inoue, K. Mawatari, T. Shibuya et al., *CHORUS. II. Subaru/HSC Determination of the Lyα Luminosity Function at $z = 7.0$: Constraints on Cosmic Reionization Model Parameter*, ApJ **867** (Nov., 2018) 46, [1805.05944]. Cited on page 129, and 132.

[531] A. Hoag, M. Bradač, K. Huang, C. Mason, T. Treu, K. B. Schmidt et al., *Constraining the Neutral Fraction of Hydrogen in the IGM at Redshift 7.5*, ApJ **878** (June, 2019) 12, [1901.09001]. Cited on page 129, and 133.

[532] C. A. Mason et al., *Inferences on the timeline of reionization at $z \sim 8$ from the KMOS Lens-Amplified Spectroscopic Survey*, *Mon. Not. Roy. Astron. Soc.* **485** (2019) 3947–3969, [1901.11045]. Cited on page 129, and 133.

[533] M. McQuinn, L. Hernquist, M. Zaldarriaga and S. Dutta, *Studying reionization with Lyα emitters*, MNRAS **381** (Oct., 2007) 75–96, [0704.2239]. Cited on page 129, and 133.

[534] M. Ouchi, K. Shimasaku, H. Furusawa, T. Saito, M. Yoshida, M. Akiyama et al., *Statistics of 207 Lyα Emitters at a Redshift Near 7: Constraints on Reionization and Galaxy Formation Models*, ApJ **723** (Nov., 2010) 869–894, [1007.2961]. Cited on page 129, and 133.

[535] E. Sobacchi and A. Mesinger, *The clustering of Lyman α emitters at $z \approx 7$: implications for reionization and host halo masses*, MNRAS **453** (Oct., 2015) 1843–1854, [1505.02787]. Cited on page 129, and 133.

[536] J. Schroeder, A. Mesinger and Z. Haiman, *Detection of Gunn-Peterson Damping Wings in High-z Quasar Spectra: Evidence for Incomplete Reionization*, *Mon. Not. Roy. Astron. Soc.* **428** (2013) 3058, [1204.2838]. Cited on page 129, and 133.

[537] F. Wang, F. B. Davies, J. Yang, J. F. Hennawi, X. Fan, A. J. Barth et al., *A Significantly Neutral Intergalactic Medium Around the Luminous z = 7 Quasar J0252-0503*, ApJ **896** (June, 2020) 23, [2004.10877]. Cited on page 129, and 133.

[538] B. Greig, A. Mesinger, Z. Haiman and R. A. Simcoe, *Are we witnessing the epoch of reionization at z=7.1 from the spectrum of J1120+0641?*, *Mon. Not. Roy. Astron. Soc.* **466** (2017) 4239–4249, [1606.00441]. Cited on page 129, and 133.

[539] J. Yang, F. Wang, X. Fan, J. F. Hennawi, F. B. Davies, M. Yue et al., *Pōniuā'ena: A Luminous z = 7.5 Quasar Hosting a 1.5 Billion Solar Mass Black Hole*, ApJ **897** (July, 2020) L14, [2006.13452]. Cited on page 129, and 133.

[540] B. Greig, A. Mesinger and E. Bañados, *Constraints on reionisation from the z=7.5 QSO ULASJ1342+0928*, 1807.01593. Cited on page 129, and 133.

[541] E. Banados et al., *An 800-million-solar-mass black hole in a significantly neutral Universe at redshift 7.5*, *Nature* **553** (2018) 473–476, [1712.01860]. Cited on page 129, and 133.

[542] F. B. Davies et al., *Quantitative Constraints on the Reionization History from the IGM Damping Wing Signature in Two Quasars at z > 7*, *Astrophys. J.* **864** (2018) 142, [1802.06066]. Cited on page 129, and 133.

[543] Planck collaboration, R. Adam et al., *Planck intermediate results. XLVII. Planck constraints on reionization history*, *Astron. Astrophys.* **596** (2016) A108, [1605.03507]. Cited on page 129, 131, and 132.

[544] B. E. Robertson et al., *New Constraints on Cosmic Reionization from the 2012 Hubble Ultra Deep Field Campaign*, *Astrophys. J.* **768** (2013) 71, [1301.1228]. Cited on page 129, and 134.

[545] R. J. Bouwens et al., *Reionization after Planck: The Derived Growth of the Cosmic Ionizing Emissivity now matches the Growth of the Galaxy UV Luminosity Density*, *Astrophys. J.* **811** (2015) 140, [1503.08228]. Cited on page 129, and 134.

[546] J. E. Gunn and B. A. Peterson, *On the Density of Neutral Hydrogen in Intergalactic Space.*, *ApJ* **142** (Nov., 1965) 1633–1636. Cited on page 130.

[547] A. Songaila, *The Evolution of the intergalactic medium transmission to redshift six*, *Astron. J.* **127** (2004) 2598, [astro-ph/0402347]. Cited on page 131.

[548] C.-A. Faucher-Giguère, J. X. Prochaska, A. Lidz, L. Hernquist and M. Zaldarriaga, *A Direct Precision Measurement of the Intergalactic Lyα Opacity at 2 <= z <= 4.2*, ApJ **681** (July, 2008) 831–855, [0709.2382]. Cited on page 131.

[549] G. D. Becker, J. S. Bolton, P. Madau, M. Pettini, E. V. Ryan-Weber and B. P. Venemans, *Evidence of patchy hydrogen reionization from an extreme Lyα trough below redshift six*, *Mon. Not. Roy. Astron. Soc.* **447** (2015) 3402, [1407.4850]. Cited on page 131.

[550] Planck collaboration, Y. Akrami et al., *Planck 2018 results. I. Overview and the cosmological legacy of Planck*, *Astron. Astrophys.* **641** (2020) A1, [1807.06205]. Cited on page 131.

[551] S. Zaroubi, *The epoch of reionization*, *Astrophysics and Space Science Library* (Sep, 2012) 45–101. Cited on page 131.

[552] W. Hu and G. P. Holder, *Model - independent reionization observables in the CMB*, *Phys. Rev. D* **68** (2003) 023001, [astro-ph/0303400]. Cited on page 132.

[553] M. J. Mortonson and W. Hu, *Model-independent constraints on reionization from large-scale CMB polarization*, *Astrophys. J.* **672** (2008) 737–751, [0705.1132]. Cited on page 132.

[554] C. H. Heinrich, V. Miranda and W. Hu, *Complete Reionization Constraints from Planck 2015 Polarization*, *Phys. Rev. D* **95** (2017) 023513, [1609.04788]. Cited on page 132, 212, and 353.

[555] D. K. Hazra, D. Paoletti, F. Finelli and G. F. Smoot, *Joining bits and pieces of reionization history*, *Phys. Rev. Lett.* **125** (Aug, 2020) 071301. Cited on page 132.

[556] M. Dijkstra, *Lyman Alpha Emitting Galaxies as a Probe of Reionization*, *Publ. Astron. Soc. Austral.* **31** (2014) 40, [1406.7292]. Cited on page 132.

[557] M. Ouchi, Y. Harikane, T. Shibuya, K. Shimasaku, Y. Taniguchi, A. Konno et al., *Systematic Identification of LAEs for Visible Exploration and Reionization Research Using Subaru HSC (SILVERRUSH). I. Program strategy and clustering properties of ~2000 Lyα emitters at z = 6-7 over the 0.3-0.5 Gpc^2 survey area*, PASJ **70** (Jan., 2018) S13, [1704.07455]. Cited on page 132.

[558] A. K. Inoue, S. Yamanaka, M. Ouchi, I. Iwata, K. Shimasaku, Y. Taniguchi et al., *CHORUS. I. Cosmic HydrOgen Reionization Unveiled with Subaru: Overview*, PASJ **72** (Dec., 2020) 101, [2011.07211]. Cited on page 132.

[559] J. Miralda-Escudé, *Reionization of the Intergalactic Medium and the Damping Wing of the Gunn-Peterson Trough*, ApJ **501** (July, 1998) 15–22, [astro-ph/9708253]. Cited on page 133.

[560] A. Mesinger, Z. Haiman and R. Cen, *Probing the Reionization History Using the Spectra of High-Redshift Sources*, ApJ **613** (Sept., 2004) 23–35, [astro-ph/0401130]. Cited on page 133.

[561] V. Tilvi, S. Malhotra, J. E. Rhoads, A. Coughlin, Z. Zheng, S. L. Finkelstein et al., *Onset of cosmic reionization: Evidence of an ionized bubble merely 680 myr after the big bang*, *The Astrophysical Journal* **891** (Feb, 2020) L10. Cited on page 134.

[562] L. Hui and N. Y. Gnedin, *Equation of state of the photoionized intergalactic medium*, MNRAS **292** (Nov., 1997) 27–42, [astro-ph/9612232]. Cited on page 134.

[563] A. S. Kompaneets, *The Establishment of Thermal Equilibrium between Quanta and Electrons*, *Soviet Journal of Experimental and Theoretical Physics* **4** (May, 1957) 730–737. Cited on page 135.

[564] R. Weymann, *Diffusion Approximation for a Photon Gas Interacting with a Plasma via the Compton Effect*, *Physics of Fluids* **8** (Nov., 1965) 2112–2114. Cited on page 135.

[565] S. Seager, D. D. Sasselov and D. Scott, *A New Calculation of the Recombination Epoch*, *ApJL* **523** (Sept., 1999) L1–L5, [astro-ph/9909275]. Cited on page 135, and 143.

[566] S. P. Oh, *Reionization by Hard Photons. I. X-Rays from the First Star Clusters*, *ApJ* **553** (June, 2001) 499–512, [astro-ph/0005262]. Cited on page 136, and 137.

[567] S. Sazonov and I. Khabibullin, *The intrinsic collective X-ray spectrum of luminous high-mass X-ray binaries*, *Mon. Not. Roy. Astron. Soc.* **468** (2017) 2249–2255, [1703.03354]. Cited on page 136.

[568] P. Madau and T. Fragos, *Radiation Backgrounds at Cosmic Dawn: X-Rays from Compact Binaries*, *Astrophys. J.* **840** (2017) 39, [1606.07887]. Cited on page 137.

[569] S. R. Furlanetto and S. J. Stoever, *Secondary ionization and heating by fast electrons*, MNRAS **404** (June, 2010) 1869–1878, [0910.4410]. Cited on page 137, and 146.

[570] A. Mesinger and S. Furlanetto, *Efficient Simulations of Early Structure Formation and Reionization*, *Astrophys. J.* **669** (2007) 663, [0704.0946]. Cited on page 137.

[571] J. M. Shull and M. E. van Steenberg, *X-ray secondary heating and ionization in quasar emission-line clouds*, *ApJ* **298** (Nov., 1985) 268–274. Cited on page 137, and 142.

[572] X.-L. Chen and M. Kamionkowski, *Particle decays during the cosmic dark ages*, *Phys. Rev. D* **70** (2004) 043502, [astro-ph/0310473]. Cited on page 137.

[573] F. Haardt and P. Madau, *Radiative transfer in a clumpy universe. iv. new synthesis models of the cosmic uv/x-ray background*, *The Astrophysical Journal* **746** (Feb, 2012) 125. Cited on page 144.

[574] R. Barkana and A. Loeb, *Detecting the earliest galaxies through two new sources of 21cm fluctuations*, *Astrophys. J.* **626** (2005) 1–11, [astro-ph/0410129]. Cited on page 144, and 145.

[575] C. Leitherer, D. Schaerer, J. D. Goldader, R. M. G. Delgado, C. Robert, D. F. Kune et al., *Starburst99: Synthesis Models for Galaxies with Active Star Formation*, *Apjs* **123** (July, 1999) 3–40, [astro-ph/9902334]. Cited on page 145.

[576] P. Villanueva-Domingo, *Pablovd/21cmdeeplearning: 21cmdeeplearning*, Mar., 2021. 10.5281/zenodo.4569964. Cited on page 215, and 356.

Part II

Scientific Research

Summary of the results

Part I of this thesis has been devoted to introduce the cosmological impact of several non-canonical DM models, as well as to overview the relevant physics of the IGM evolution and the 21 cm line. Part II comprises the original research work carried out during the development of this PhD thesis. In order to ease its reading and to provide a concise guideline including the key points of each article, we briefly summarize in what follows the research manuscripts that this thesis comprises.

1. **Warm dark matter and the ionization history of the Universe**

   Reference [1] studies the impact of WDM scenarios on the thermal and ionization evolution of the IGM. Due to the free streaming effect of $\sim$ keV particles, the formation of structures is suppressed on small scales with respect to the standard CDM case, as described in detail in Sec. 2.3. This implies a reduction in the number of star forming low-mass halos, capable of emitting UV and X-ray radiation responsible for ionizing and heating the IGM. The decrease of the number of such sources leads to a delay of the cosmic dawn, the heating epoch and the EoR. Making use of semi-analytical simulations, employing the formalism described in Chap. 5, the evolution of the kinetic temperature and the ionization fraction is computed for several WDM scenarios, varying the WDM mass between 1 and 4 keV, a physically motivated range to account for the small-scale issues outlined in Sec. 2.1.2. Given that the thermal history of the IGM is very sensitive to the stellar and radiative processes involved, we also consider different astrophysical scenarios. Three astrophysical parameters are modified, namely the minimum virial temperature (related to the minimum mass to host star formation), the UV ionizing efficiency and the X-ray heating efficiency (directly related to the X-ray luminosity).

   The results of the ionization fraction from simulations have been confronted with observational bounds on the state of ionization during the EoR. Two kinds of data are taken into account, a subset of the compilation discussed in Sec. 5.1.3. On the one hand, constraints

and lower limits on the ionization fraction at redshifts $8 \geq z \gtrsim 6$ from quasar spectra and Lyα emitting galaxies are considered. On the other hand, we also employ the Thomson optical depth inferred from the CMB anisotropies. It is shown that bounds employing only CMB data are less restrictive than those from the ionization state at some redshift, given that the Thomson optical depth is an integrated quantity, rather than a redshift dependent constraint. We find that some astrophysical parameters are strongly degenerate among them, and also with the WDM mass. More specifically, the delay of the EoR present in a WDM model can be approximately mimicked either by a high ionization efficiency (which boost an earlier reionzation) or by a lower minimum virial temperature (so that lower mass halos could form stars and contribute to emit ionizing radiation). For that reason, lower limits on the WDM mass obtained by this method are weaker than those from the Lyα forest, although still capable of bounding its value down to ~ 1 keV.

2. **Warm Dark Matter and Cosmic Reionization**

In order to dive deeper in the phenomenology of WDM, Ref. [2] further investigates the impact of WDM models on the cosmological evolution and formation of structures. In this case, accurate hydrodynamical simulations are employed, rather than semi-analytic computations, providing thus more reliable results. We make use of the framework of Cosmic Reionization on Computers (CROC) [514], which represents the state of the art in the numerical modeling of the EoR, properly modifying the initial power spectrum in order to include the characteristic suppression of WDM scenarios. A WDM mass of $m_{\rm WDM} = 3$ keV is assumed, value which lies around the constraints from Lyα forest observations.

Different reionization observables are computed in order to explore the impact of the free streaming scale, such as the halo mass function and the galaxy UV luminosity functions, which show both a suppression (at low masses and high magnitudes, respectively) with respect to the CDM case. While current telescopes are not able to discriminate among CDM and WDM cases, the upcoming JWST telescope, capable of reaching the faint end of the galaxy luminosity function, could provide the key to constrain such WDM masses. The effect on the cumulative probability distribution function for the effective Lyα opacity $\tau_{\rm GP}$ in the post-EoR IGM is also discussed, finding that, compared to the CDM scenario at a given redshift, the WDM case presents more extended tails toward high $\tau_{\rm GP}$, which correspond to

high density regions, since they are ionized later. Compared to Lyα forest data, it favors the CDM case, although it is not clear whether tunning the astrophysical parameters in WDM scenarios could improve its agreement with data. Finally, the 21 cm power spectrum is also computed, showing an interplay between a suppression due to the free streaming and an enhancement because of the delayed reionization in the WDM case. This leads to a non-trivial behavior, which makes it hardly detectable by the first generation of experiments.

3. **Was there an early reionization component in our universe?**

   The ionization history of the universe during the EoR is far from being well determined. Although most of the bounds are consistent with a relatively fast reionization process ending at $z \sim 6$, an early contribution, for example from non-canonical DM scenarios injecting energy into the medium, may still be possible. In Ref. [3], this question is examined under the light of Planck CMB data. The ionization history is modeled in order to be consistent with the the power spectrum of the EE polarization modes of the CMB, which is sensitive to reionization at low multipoles. Several methods are employed in order to emulate the evolution of the ionized fraction. Firstly, functional parameterizations are considered, such as the frequently used redshift-symmetric and the redshift-asymmetric parameterizations. On the other hand, an approach based on the Principal Component Analysis (PCA) is applied, extracting the eigenmodes from the Fisher matrix of the C_l components of the EE spectrum. Those with the smallest variances are expected to carry the most valuable cosmological information. A subset of these eigenfunctions is employed as a basis to recover the ionization history around a given fiducial model, either assuming a constant value or one of the aforementioned parameterizations. A third method based on Piecewise Cubic Hermite Interpolating Polynomial (PCHIP) is employed, considering as free parameters the ionized fraction at several different redshifts, which are smoothly interpolated via the PCHIP method.

   We compare the different approaches to recover the ionization history with a Monte Carlo Markov Chain (MCMC) analysis, showing that some of them prefer an early reionization component, including some oscillatory pattern, such as using the PCA combination summed to a fiducial model. However, when the PCA combination is included as an argument of the parameterization, exploiting its functional form, the resulting history is smoother and does not show an early onset. The application of the frequentist Akaike information and the Bayesian in-

formation criteria confirms that none of them in particular is preferred over the other possible formulations, and thus an early reionization is not preferred by CMB data, contrary to previous claims [554].

4. **A fresh look into the interacting dark matter scenario**

In Ref. [4], phenomenological DM models involving elastic scattering with photons, coined as Interacting Dark Matter (IDM), are discussed in the context of the thermal evolution of the IGM and the number of satellite galaxies of the MW. In this case, as shown in Sec. 2.4, the coupling between DM particles and photons produces a collisional damping effect, inducing a suppression and an oscillatory pattern at the smallest scales, in a similar way as the power spectrum is modified by the baryon-photon coupling. This effect can reduce the number of small scale structures and low mass halos, similarly to WDM. The magnitude of this damping is determined by the elastic scattering cross section over the DM particle mass, $\sigma_{\gamma\mathrm{DM}}/m_{\mathrm{DM}}$.

Semi-analytic simulations of the thermal and ionization state of the IGM have been carried out in order to investigate the signatures of IDM scenarios. Suppressing the growth of structures due to collisional damping retards the formation of first stars and galaxies, delaying all astrophysical processes such as X-ray heating and reionization. Analogously to the findings in Ref. [1] regarding the WDM mass, the IDM cross section is strongly degenerated with several astrophysical parameters, mainly the ionization efficiency and the minimum virial temperature. On the other hand, the number of expected subhalos is computed, which in an IDM scenario is reduced with respect to the CDM scenario. This fact allows to constrain the elastic cross section when compared to the observed MW satellite galaxies. The satellite galaxies constraint, however, strongly depends upon the assumed MW total mass, which is not completely well determined yet, and within its expected mass range, the bounds on the cross section can vary up to one order of magnitude. By combining this upper limit with the bounds from the IGM ionization history, some astrophysical degeneracies can be broken.

5. **Dark Matter microphysics and 21 cm observations**

The EDGES collaboration claimed the detection of the global 21 cm signal, presenting an absorption dip with an amplitude of roughly 500

mK, which doubles the expectations in the standard ΛCDM. As discussed in Sec. 4.5.3, astrophysical modeling seems unlikely to account for such large amplitude, possibly requiring non-standard scenarios with extra cooling mechanism to explain this absorption. Nevertheless, the timing of the EDGES absorption signal, perfectly consistent with standard ΛCDM predictions, can be employed in order to constrain other non-canonical scenarios which may impact the IGM history. In Ref. [5], two aspects of the redshift location of the EDGES signal are exploited in order to constrain IDM and WDM models, which are capable of delaying the onset of star formation during the cosmic dawn.

On the one hand, the minimum of the global 21 cm brightness temperature computed from simulations is demanded to appear not later than the EDGES absorption dip, located at $z \simeq 17$. On the other hand, by examining the beginning of the absorption regime in the EDGES data, one can infer when the Lyα coupling must be strong enough to deviate the spin temperature from the CMB one via the WF effect (as reviewed in Sec. 4.2). Following that idea, in order to be consistent with data, one can assume that the Lyα coupling coefficient must become order one at $z \simeq 20$. Therefore, it is possible to rule out IDM and WDM models which present a too delayed absorption epoch and cannot fulfill the above conditions. Both aforementioned criteria allow extracting competitive constraints on both the WDM mass and the IDM cross section. These bounds strongly depend upon the specific astrophysical scenario, weakening the limits in scenarios with low virial temperatures. Nonetheless, assuming the default scenario of Pop II stars with a virial temperature of 10^4 K as the source of the Lyα radiation, the obtained bounds from the EDGES timing largely improve the ones from other astrophysical probes.

6. **Constraining the primordial black hole abundance with 21-cm cosmology**

Reference [6] studies in detail the cosmological effects of the existence of PBHs as part of the DM in the 21 cm cosmological signal. As overviewed in Sec. 3.2, there are two main consequences of solar mass PBHs for the IGM evolution. On the one hand, the presence of PBHs in the early universe would imply an additional contribution to the matter power spectrum given by a shot noise spectrum independent on the scale, due to their discrete nature, which evolves as an isocurvature mode. This would magnify the formation of structures at small scales, where this term becomes dominant with respect to the standard adia-

batic fluctuations. Hence, this enhancement mostly affects minihalos, low mass halos not massive enough to initiate star formation. The expected 21 cm sky-average brightness temperature coming from these minihalos is computed, which differs from the standard IGM global signal. It is shown that, even with the shot noise enhancement, it would not be enough to produce a detectable signal, contrary to previous claims in the literature [316, 317].

On the other hand, like standard astrophysical BHs, PBHs would accrete their surrounding matter. During the infall onto the PBH, particles may be greatly accelerated, releasing UV and X-ray radiation to the environment. These photons would inject energy into the medium when absorbed, further heating and ionizing it. We compute the 21 cm signal arising from the local environment of PBHs, demonstrating that it would be well below observable sensitivities. However, energetic radiation can escape from the nearby surroundings of PBHs and be deposited into the IGM, leaving a strong signature on the 21 cm global signal and power spectrum from the IGM. Due to the further ionization and the hotter medium, the absorption amplitude of the brightness temperature and its fluctuations would be suppressed, leading to an emission regime in the most extreme cases. We run a MCMC analysis with semi-analytical simulations of the IGM 21 cm signal varying the fraction of PBHs as DM, $f_{\rm PBH}$, and their mass, $M_{\rm PBH}$, together with four astrophysical parameters. The expected sensitivities of the upcoming interferometers HERA and SKA are employed in order to explore the region of the PBH parameter space which may be probed by such experiments. We show that current bounds on the PBH abundance in the range $1 - 10^3 M_\odot$, coming from microlensing and the impact of accretion of the CMB, could be potentially improved up to two orders of magnitude by future 21 cm power spectrum observations.

7. **Removing Astrophysics in 21 cm maps with Neural Networks**

The 21 cm line stands as a promising tool to map the distribution of matter in the universe, given that it allows tracing the location of neutral Hydrogen, which tracks the DM clumps. This may allow eventually achieving tomographic 3D density maps of the IGM. However, the link between the HI and DM density distribution is not unequivocal, since the brightness temperature strongly relies on the thermal and ionization state of the medium. Furthermore, once reionization is advanced, the signal from HII regions is mostly suppressed. In Ref. [7], we attempt to recover the underlying matter density field from

a 21 cm map, making use of machine learning methods. Specifically, a Convolutional Neural Network (CNN) based on the so-called U-Net architecture [576] is trained with 1000 numerical simulations of the brightness temperature field and its corresponding density maps, aimed to learn how to recover the latter from the former. These simulations include different initial conditions for each realization, varying also three relevant astrophysical parameters, in order to become robust to distinct astrophysical scenarios.

It is shown that, once it is trained, the CNN is able to successfully extract the density field from a given 21 cm map. To test its accuracy, several statistics of the matter density are computed, such as the power spectrum, the cross-correlation coefficient or the probability distribution function, matching the corresponding ones from the true maps within a few percent down to scales $k \sim 2$ Mpc^{-1}. The network can be applied to maps on different redshift, although its performance worsens at low redshifts, $z \sim 10$, when reionization is already ongoing and the link between the HI and the DM distribution becomes more diffuse. Furthermore, part of the trained layers of the network are employed to predict the underlying astrophysical parameters, showing that the CNN actually learns astrophysical information, substracting it from the 21 cm signal in order to predict the density field.

PHYSICAL REVIEW D **96,** 103539 (2017)

Warm dark matter and the ionization history of the Universe

Laura Lopez-Honorez,[1] Olga Mena,[2] Sergio Palomares-Ruiz,[2] and Pablo Villanueva-Domingo[2]
[1]*Service de Physique Théorique, CP225, Université Libre de Bruxelles, Bld du Triomphe, and Theoretische Natuurkunde, Vrije Universiteit Brussel and The International Solvay Institutes, Pleinlaan 2, B-1050 Brussels, Belgium*
[2]*Instituto de Física Corpuscular (IFIC), CSIC-Universitat de València, Apartado de Correos 22085, E-46071, Spain*
(Received 28 March 2017; published 27 November 2017)

In warm dark matter scenarios structure formation is suppressed on small scales with respect to the cold dark matter case, reducing the number of low-mass halos and the fraction of ionized gas at high redshifts and thus, delaying reionization. This has an impact on the ionization history of the Universe and measurements of the optical depth to reionization, of the evolution of the global fraction of ionized gas and of the thermal history of the intergalactic medium, can be used to set constraints on the mass of the dark matter particle. However, the suppression of the fraction of ionized medium in these scenarios can be partly compensated by varying other parameters, as the ionization efficiency or the minimum mass for which halos can host star-forming galaxies. Here we use different data sets regarding the ionization and thermal histories of the Universe and, taking into account the degeneracies from several astrophysical parameters, we obtain a lower bound on the mass of thermal warm dark matter candidates of $m_X > 1.3$ keV, or $m_s > 5.5$ keV for the case of sterile neutrinos nonresonantly produced in the early Universe, both at 90% confidence level.

DOI: 10.1103/PhysRevD.96.103539

I. INTRODUCTION

The appearance of the first generation of galaxies, when the Universe was a few hundred million years old, led to the end of the so-called dark ages of the Universe. The ultraviolet (UV) photons emitted in these galaxies, gradually ionized the neutral hydrogen which had rendered the Universe transparent following the epoch of recombination, in a process known as reionization [1]. However, so far, the exact moment when cosmic reionization took place is not precisely known [2].

The reionization transition in the late Universe increases the number density of free electrons, n_e, which can scatter the cosmic microwave background (CMB), with a probability related to the optical depth at reionization, τ, i.e., the line-of-sight integral of n_e weighted with the Thomson cross section, and dominated by single-ionized hydrogen and helium states. The effect of free electrons on the CMB temperature anisotropies leads to a suppression of the acoustic peaks by a factor $e^{-2\tau}$ at scales within the horizon at the reionization period, a signature which is very degenerate with the amplitude of the primordial power spectrum, A_s. Nevertheless, the reionization process creates linear polarization on the CMB spectrum due to the scattering between free electrons and the large-scale CMB quadrupole. This signature, usually dubbed as the "reionization bump," with the induced polarized power scaling as τ^2 (see, e.g., Fig. 2 of Ref. [3]), and peaks at scales larger than the horizon size at the reionization period, resulting in a determination of τ almost free of degeneracies (see Ref. [3] or corresponding chapter in Ref. [2] for an exhaustive description of the epoch of reionization (EoR) and its impact on the CMB). Measurements by the Wilkinson Microwave Anisotropy Probe (WMAP) of the optical depth to reionization, $\tau = 0.089 \pm 0.014$, indicated an early-reionization scenario ($z_{\rm re} = 10.6 \pm 1.1$) [4], requiring the presence of sources of reionization at $z \gtrsim 10$. This value of τ was somehow in tension with observations of Lyman-α (Ly-α) emitters at $z \simeq 7$ [5–9], which instead pointed out to reionization being complete by $z \simeq 6$. Nevertheless, the results presented by the Planck collaboration in the 2015 public data release, including the large-scale (low-ℓ) polarization observations of the Low Frequency Instrument (LFI) [10] together with Planck temperature and lensing data, indicate that $\tau = 0.066 \pm 0.016$ [11] (see also Ref. [12]). Therefore, analyses of the Planck data questioned the need for high-redshift sources of reionization [13–17]. More recently, an analysis from the Planck collaboration, where unaccounted systematics in the large angular scale polarization data from the High Frequency Instrument (HFI) have been carefully modeled and removed [18,19], has provided a measurement of the reionization optical depth of $\tau = 0.055 \pm 0.009$ [18] based exclusively on the polarization (commonly named as the *EE*) spectrum measurements.

Despite its potential to unravel the mean polarization redshift, the measurement of τ provides only integrated information on the free electron fraction x_e and not on its precise redshift evolution, i.e., redshift tomography is not possible (see, e.g., Ref. [20]). In order to fully characterize

such an evolution, upcoming and future measurements of the 21 cm hyperfine transition of neutral hydrogen, which maps its distribution at different redshifts (and thus the distribution of x_e), are highly relevant (see, e.g., Refs. [21–24]).

Awaiting future cosmological measurements of the 21 cm transition line, it is important to exploit our current knowledge of the evolution of the total ionized fraction at late times, $\bar{x}_i$. In particular, the redshift dependence of $\bar{x}_i$ allows performing independent and crucial tests of the dark matter (DM) properties, as the free-streaming of light particles at late times could generate differences on the matter power spectrum with respect to the standard cold dark matter (CDM) case. These differences could provide information concerning different particle physics models [25–27]. In this regard, much work has been devoted in the literature to set constraints on annihilations/decays of DM particles from effects on the cosmic ionization history [11,28–67]. In this work, on another hand, we focus instead on testing the possibility of warm dark matter (WDM) via measurements of the ionization fraction close to the EoR (see also Refs. [68,69]). WDM scenarios offer a very interesting alternative to the standard CDM paradigm, as they provide an explanation of large-scale observations, while alleviating the small-scale problems of the CDM standard picture, i.e., the missing satellite [70,71], the too-big-to-fail [72], and the core-cusp [73,74] problems.[1] Since WDM particles have non-negligible velocities at high redshifts, structure formation is suppressed at scales below the DM's free-streaming length, delaying the halo and star formation periods. It is precisely this suppression in the growth of small scale structures what allows solving some of the problems of CDM cosmologies mentioned above [25,78–92]. Furthermore, if the WDM candidate is identified with a keV sterile neutrino, this could provide the origin for the recently observed X-ray signals in galaxy clusters, the galactic center and the cosmic X-ray background [93–96].

Currently, the most stringent constraints on the WDM particle mass are obtained from the comparison of Lyα forest power spectra observed from distant quasars to the results obtained with hydrodynamical simulations in the non-linear regime, using a power-law temperature-density relation [97]. In combination with CMB data, this technique provides lower limits on the WDM mass of $m_X > 4.17$ keV for a thermal relic[2] and $m_s > 25.0$ keV for a nonresonantly produced sterile neutrino, both at 95% confidence level (CL) [98], improving upon previous bounds [99–105]. Even more stringent limits are found when adding the power spectrum measured for $z = 4.2$ and $z = 4.6$ with the high-resolution HIRES/MIKE spectrographs, $m_X > 4.65$ keV (and correspondingly $m_s > 28.8$ keV) [98] and $m_X > 5.3$ keV [106]. Other bounds obtained from halo counts at high redshifts [107–112], using the stellar mass function to reproduce the Tully-Fisher relation [113] or from high-redshift gamma-ray bursts [114], are slightly weaker. Let us mention as well that the latest Planck optical depth τ data has also offered a unique opportunity to improve the existing bounds on reionization driven by a sterile neutrino WDM, produced via resonant oscillations, that could explain the observed x-ray features at ∼3.5 keV (see, e.g., Ref. [115] for a recent and complete analysis of such a possibility).

In this work, instead, we adopt a different approach and focus on an *universal* aspect of WDM cosmologies, namely, the delay caused in the reionization process due to the free-streaming of DM particles. We shall constrain the WDM scenario via the most recent measurement of τ from the Planck collaboration [18], together with other constraints on the reionization level at different redshifts. The small-scale suppression of the matter power spectrum, typical in WDM cosmologies, delays structure formation and consequently, the EoR [116–118]. Exploiting this effect by means of the seminumerical modeling provided by the 21 CMFAST code [119,120], we shall derive a lower bound on the mass of the WDM particles, devoting special attention to existing degeneracies among the ionization efficiency of UV photons, the number of x-ray photons per solar mass in stars and the minimum virial mass (or temperature) above which halos can start hosting galaxies.

The structure of the paper is as follows. Section II presents the modeling of the WDM power spectrum and the resulting halo mass function. Section III contains the description of the ionization processes and of the different parameters we consider in our analysis, including a discussion of the crucial parameter degeneracies. In Sec. IV A we describe the data used in our numerical analysis and the results can be found in Sec. IV B. We draw our conclusions in Sec. V.

II. WARM DARK MATTER HALO MASS FUNCTION

In general, WDM scenarios encompass DM candidates having non-negligible velocities at high redshifts, so the growth of structures is suppressed below a free-streaming length of typically one Mpc. When WDM particles are thermally produced, they are assumed to be relativistic at the epoch of decoupling, in contrast to the standard WIMP scenario, but nonrelativistic at the time of matter radiation equality, $t_{\rm eq}$, where substantial growth of perturbations becomes possible. A crude estimate of the free-streaming

[1]It has been argued that some of these problems could possibly be solved once baryonic physics is properly accounted for (see, e.g., Refs. [75,76]), or via CMB spectral distortions (see the recent Ref. [77]).

[2]These particles would decouple early in the Universe and their temperature today should be lower than that of active neutrinos, so that $m_X n_X/n_\nu = m_X (T_X/T_\nu)^3 = 94.1 \Omega_{\rm DM} h^2$ eV, where n_X and n_ν are the number densities of the WDM particle and of active neutrinos and T_X and T_ν are the corresponding temperatures today.

length can then be obtained computing the distance over which such a particle can travel until $t_{\rm eq}$ [121]. This simplified approach allows one to understand that the free-streaming length decreases with increasing m_X but it misses some important points: the logarithmic growth of perturbations during the radiation dominated era and the fact that free-streaming does not instantaneously switch off after $t_{\rm eq}$. One is thus led to make use of a numerical Boltzmann code so as to accurately account for free-streaming [25]. The resulting suppression of the linear matter power spectrum has been fitted,[3] and can be characterized by [99]

$$T_{\rm WDM}(k) = (1 + (\alpha k)^{2\nu})^{-5/\nu}, \quad (1)$$

such that the WDM power spectrum can be written in terms of that for CDM as

$$P_{\rm WDM}(k) = P_{\rm CDM}(k) T^2_{\rm WDM}(k), \quad (2)$$

with $\nu = 1.12$ and the breaking scale

$$\alpha = 0.049 \left(\frac{\rm keV}{m_X}\right)^{1.11} \left(\frac{\Omega_X}{0.25}\right)^{0.11} \left(\frac{h}{0.7}\right)^{1.22} {\rm Mpc}/h, \quad (3)$$

where WDM has been assumed to account for all the DM and to be a thermal relic (see also Ref. [99] for nonthermal relics).

Around the time of reionization, of interest for this paper, perturbations have long gone nonlinear and high-resolution N-body simulations are required to obtain the halo mass function, i.e., the number of halos per unit mass as a function of mass and redshift, which is defined as [123]

$$\frac{dn(M,z)}{dM} = \frac{\rho_{m,0}}{M^2} \frac{d\ln\sigma^{-1}}{d\ln M} f(\sigma), \quad (4)$$

where $n(M,z)$ is the (comoving) halo number density, $\rho_{m,0} = \Omega_{m,0}\rho_{c,0}$ is the average matter density in the Universe today ($z = 0$), $\sigma^2 = \sigma^2(M,z)$ is the variance of density perturbations and it is a function of the halo mass M and redshift z, and the function $f(\sigma)$ is the first crossing distribution and represents the fraction of mass that has collapsed to form halos per unit interval in $\ln\sigma^{-1}$. The first analytical derivation of $f(\sigma)$, which is expected to be a universal function, by Press-Schechter, assumed a spherical collapse model. They also used the linear growth of primordial fluctuations to calculate the fraction of mass in virialized objects more massive than a given mass by relating it to the fraction of the volume in which the smoothed initial density field is above some threshold density [124,125]. However, within this model, the number of halos is underpredicted for high masses and low redshifts and overpredicted for low masses and redshifts [126–129]. An improvement was achieved by Sheth and Tormen (ST) using the same Press-Schechter formalism but with an ellipsoidal collapse model instead [130–132], resulting in the first crossing distribution $f(\sigma)$ to be given by [130]

$$f(\sigma) = A\sqrt{\frac{2q}{\pi}}\left(1 + \left(\frac{\sigma^2}{q\delta_c^2}\right)^p\right)\left(\frac{\delta_c}{\sigma}\right) e^{-\frac{q\delta_c^2}{2\sigma^2}}, \quad (5)$$

where $q = 0.707$ and $p = 0.3$ were obtained by fitting the results of the GIF simulations [133], $A = 0.322$ is the normalization constant so that $\int f(\sigma) d\ln\sigma^{-1} = 1$, and $\delta_c = 1.686$ is the critical overdensity required for collapse at $z = 0$. Although Ref. [132] later proposed $q = 0.75$ in order to reduce the discrepancies with the results of Ref. [123] at large masses, we will use $q = 0.707$ for our default CDM ST halo mass function, following Refs. [83,134,135]. On the other hand, we use $q = 1$ as our default value for WDM scenarios,[4] value that has been shown to match WDM simulations [134,135]. We use the default conditional mass function in 21 CMFAST, which is based on the hybrid prescription of Refs. [136,137].

In principle, the differences between WDM and CDM scenarios are encoded, via the modification of the matter power spectrum, in the root-mean-square (rms) variance of density perturbations, which is defined as

$$\sigma^2(M(R),z) = \left(\frac{D(z)}{D(0)}\right)^2 \int \frac{d^3k}{(2\pi)^3} P(k) |W(kR)|^2, \quad (6)$$

where the redshift dependence is driven by the linear growth function, $D(z)$, $P(k)$ is the linear power spectrum at $z = 0$ computed following Eq. (2) for WDM and $W(kR)$ is the Fourier transform of a filter function. For CDM the filter function is usually taken to be a spherical top-hat (TH) function in real space, on a scale $R^3 = 3M/(4\pi\rho_{m,0})$, i.e.,

$$W_{\rm TH}(kR) = \frac{3}{kR}(\sin(kR) - 3\cos(kR)). \quad (7)$$

Although it has been used previously [122], this appears to be inadequate to describe WDM cosmologies [88,116,134], for which there is a cutoff in the matter power spectrum at small masses. With this choice of filter, the halo mass function increases with decreasing mass, contrary to what is found in WDM simulations. This can be understood by the fact that for a given scale R a large range of unsuppressed scales k contributes to σ^2 and hence to the halo mass function [138]. Instead, it has been argued that the redshift evolution of the WDM suppression of power at

[3]Note that the parametrization used in Ref. [122] is obtained from Ref. [25].

[4]Note that the default values used in 21 CMFAST are $q = 0.73$, $p = 0.175$, and $A = 0.353$ (also used to describe WDM cosmologies [122]), from Ref. [123].

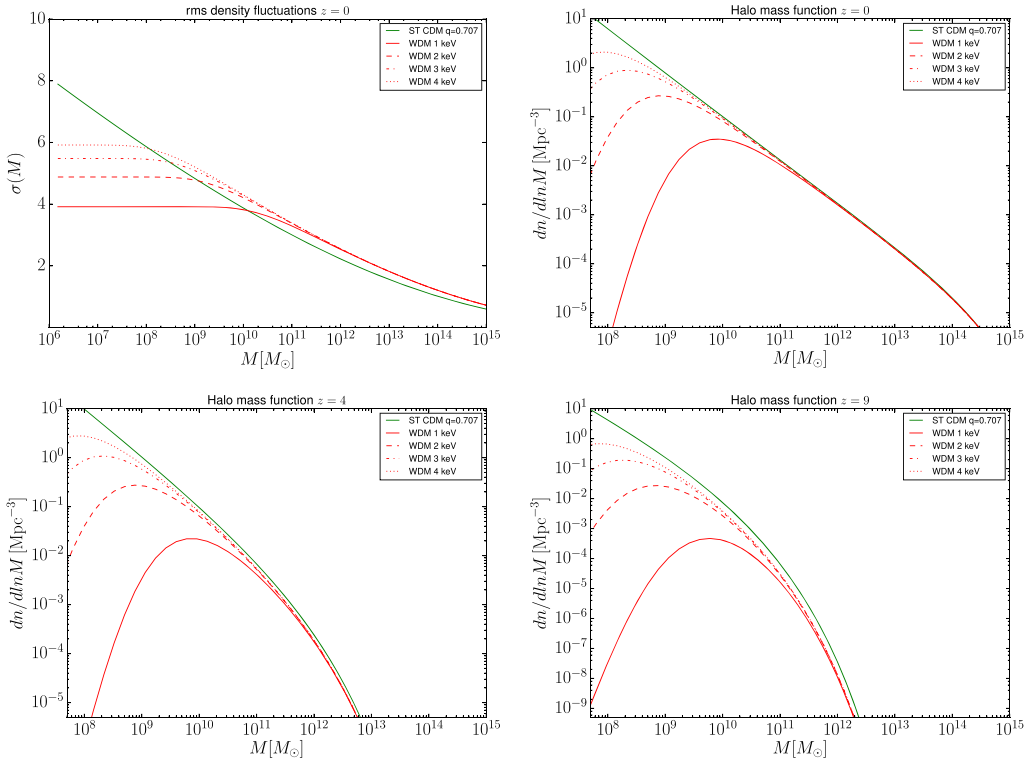

FIG. 1. Root-mean-square density fluctuation $\sigma(M)$ at $z = 0$ (top-left panel). Halo mass functions for CDM and WDM at $z = 0$ (top-right panel), $z = 4$ (bottom-left panel), and $z = 9$ (bottom-right panel). For CDM we use $q = 0.707$, see Eq. (5), and a spherical top-hat filter in real space. For WDM, we use $q = 1$ and a spherical top-hat filter in k-space.

small scales observed in N-body simulations is better accounted for by using a sharp-k window, i.e., a spherical top-hat window in k-space [88,134],

$$W_{\mathrm{SK}}(kR) = \Theta(1 - kR), \tag{8}$$

where Θ is the Heaviside function. With this choice of window function, the halo mass function can be written as

$$\frac{dn_{\mathrm{SK}}}{dM_{\mathrm{SK}}} = \frac{1}{2}\frac{\rho_{m,0}}{M_{\mathrm{SK}}^2} f(\sigma_{\mathrm{SK}}) \frac{1}{2\pi^2\sigma_{\mathrm{SK}}^2} \frac{P(1/R_{\mathrm{SK}})}{R_{\mathrm{SK}}^3} \frac{d\ln R_{\mathrm{SK}}}{d\ln M_{\mathrm{SK}}}, \tag{9}$$

where, in this work, f is given by Eq. (5). In the case, of the spherical top-hat filter in real space, the mass assignment for each scale R_{SK} is unambiguously defined. In contrast, in the case of the sharp-k filter, the mass is not well defined given a scale in real space and needs to be constrained from the results of simulations. Except from the dependence $M_{\mathrm{SK}} \propto R_{\mathrm{SK}}^3$, guaranteed by the spherical symmetry of the filter, a free parameter c has to be introduced such that

$$M_{\mathrm{SK}} = \frac{4\pi}{3}\rho_m (cR_{\mathrm{SK}})^3. \tag{10}$$

In this work, we take $c = 2.5$ to match the halo mass functions obtained from simulations [88,135]. In the following, we will thus us a TH filter for CDM and a SK filter for WDM, and we have accordingly modified the 21 CMFAST code.[5]

Figure 1 depicts the mass dependence of the rms of matter density fluctuations, $\sigma(M)$, and of the halo mass function in WDM scenarios for the range of WDM masses considered in this work. We compare the results for the CDM case with $q = 0.707$ and a TH filter to those

[5]We stress again that to describe the suppression at small scales in WDM scenarios, only the window function (and the power spectrum), but not the first crossing distribution, is different from the standard Sheth-Tormen approach in CDM scenarios. We also stress that the modifications to the code described above are slightly different from those introduced in Ref. [122].

corresponding to WDM scenarios with $q = 1$ and a SK filter. With a TH window function used to describe the CDM case, $\sigma_{\rm TH}(M_{\rm TH})$ increases monotonically with decreasing values of $M_{\rm TH}$. In contrast, for the WDM SK window function, the rms variance increases monotonically for large masses, while it becomes constant for small masses to account for the free-streaming effects. This is illustrated in the top-left panel of Fig. 1. The transition between these two regimes is dictated by the abruptness of the cutoff in the linear WDM power spectrum. Notice that, although the shape of $\sigma(M)$ at large masses is similar for WDM and CDM scenarios, their values differ. One should thus take this into account when normalizing the results obtained from 21 CMFAST [119,120].[6] The other three panels of Fig. 1 show the resulting halo mass function at redshift $z = 0$ (top-right panel), $z = 4$ (bottom-left panel), and $z = 9$ (bottom-right panel). The flattening of $\sigma(M)$ for low halo masses directly induces the suppression of the halo mass function in the WDM cases. For large halo masses, a similar mass dependence for both WDM and CDM at $z = 0$ is found. Let us mention, as reported in Refs. [134,135], that the sharp-k model typically underestimates the halo abundance at large halo masses especially at large redshifts, even though the discrepancy with the data is greatly reduced for halos defined by a spherical overdensity halo finder algorithm. Thus, the halo mass function model for WDM used here does not exactly reproduce the CDM behavior for large halo masses.

Notice that the model for WDM halo mass function of Ref. [135], which is the one we follow, is very similar to the one used in Ref. [88] except from one point. Based on Ref. [116], the authors of Ref. [88] argue that, due to the WDM residual thermal velocity dispersion at the time of collapse, the growth of collapsing overdensities is suppressed below an effective Jeans mass M_J. Below that mass, the critical overdensity for collapse is larger than in CDM scenarios, so the halo mass function is further suppressed. As mentioned in Refs. [134,135], such a Jeans mass is however expected to drop significantly once the Universe enters the matter-dominated era and to damp perturbations on scales much lower than the free-streaming length. However, this is already accounted for in the above treatment of the WDM case. Thus, in our treatment of the WDM halo mass function, we do not include the effect of late time velocity contributions and we have modified accordingly the 21 CMFAST code to ensure that no extra Jeans mass cutoff at a given M_J has been imposed. As a final note, we stress that the halo mass function we use provides a good description of the outcome from numerical simulations up to redshift $z = 5$ [135], even if significant uncertainties are still present. At higher redshifts we have to rely on extrapolations.

[6]For the best fit of the cosmological parameters, $\sigma_8(z=0)|_{\rm TH} = 0.82$ using the TH filter in real space, while $\sigma_8(z=0)|_{\rm SK} = 0.48$ using the SK filter.

III. IONIZATION AND THERMAL HISTORIES AND WARM DARK MATTER

As mentioned in the introduction, our goal is to constrain WDM models evaluating the impact on the ionization history of the Universe. For this, we study the evolution of the total ionized fraction $\bar{x}_i$. For that purpose, we make use of the publicly available code 21 CMFAST that, based on excursion set formalism, perturbation theory and analytic prescriptions, generates semianalytic simulations of the evolved density, peculiar velocity, halo and ionization fields. This code has specially been developed with the purpose of studying variations in the 21 cm signal due to the change in a given set of astrophysical and cosmological parameters. Here we use this code in order to evaluate the ionization fraction evolution around (before) the time of reionization. Notice that $\bar{x}_i(\mathbf{x}, z)$ is obtained from two separate contributions. In the *ionized* IGM (once first sources have lighted on) the ionization level is characterized by $Q_{\rm HII} = \zeta_{\rm UV} f_{\rm coll}(> M_{\rm vir}^{\rm min})$ where $Q_{\rm HII}$ denotes the covering factor of the fully ionized HII regions, $\zeta_{\rm UV}$ characterizes the UV ionization efficiency (see below) and $f_{\rm coll}(> M_{\rm vir}^{\rm min})$ is the fraction of mass collapsed into halos with mass large enough ($> M_{\rm vir}^{\rm min}$) to host star-forming galaxies. The latter is defined in terms the halo mass function introduced in the previous section as

$$f_{\rm coll}(> M_{\rm vir}^{\rm min}) = \int_{M_{\rm vir}^{\rm min}} \frac{M}{\rho_{m,0}} \frac{dn}{dM} dM. \tag{11}$$

On the other hand, the local ionized fraction of the *neutral* IGM, $x_e(\mathbf{x}, z)$ can be written as

$$\frac{dx_e(\mathbf{x}, z)}{dz} = \frac{dt}{dz}(\Lambda_{\rm ion} - \alpha_{\rm A} C x_e^2 n_b \bar{\mathfrak{f}}_{\rm H}), \tag{12}$$

where $n_b = \bar{n}_{b,0}(1+z)^3(1+\bar{\delta}_b(\mathbf{x}, z))$ is the baryon number density, $\Lambda_{\rm ion}$ the ionization rate, $\alpha_{\rm A}$ the case-A recombination coefficient,[7] $C \equiv \langle n_e^2 \rangle / \langle n_e \rangle^2$ is the clumping factor, with n_e the electron number density, and

[7]Case-A recombination involves a sum over all recombination coefficients (including recombinations to the ground state) and it is typically used for optically thin media. In this case, one expects that all produced recombination photons escape the system without giving rise to ionization. Case-A is appropriate in the highly-ionized low-redshift Universe, where most of the recombinations are actually taking place in dense, partially neutral gas, so-called Lyman-limit systems (LLS). In this case, photons resulting from ground state recombinations are likely to be absorbed locally, inside the LLS and do not contribute to the ionization balance in the diffuse IGM [139]. However, notice that considering case-A or case-B recombination has a negligible impact on the results presented here.

$\mathfrak{f}_H = n_H/n_b$ is the hydrogen number fraction. Equation (12) is solved numerically by means of the 21 CMFAST code, briefly described above.

The total ionized fraction reads (see, e.g., Ref. [140])

$$\bar{x}_i \simeq Q_{\rm HII} + (1 - Q_{\rm HII})x_e. \quad (13)$$

Notice that for the purpose of this work the most relevant contribution to $\bar{x}_i$ is $Q_{\rm HII}$ that drives the ionization fraction around the reionization time. Once the ionization history is at hand, one can compute the optical depth to reionization, defined as

$$\tau = \sigma_T \int \tilde{x}_i n_b dl, \quad (14)$$

where σ_T is the Thomson cross-section and dl is the line-of-sight proper distance.

A. Free astrophysics parameters

For the sake of simplicity and for comparison purposes with other works, we shall describe the ionization history of the IGM in terms of a reduced number of quantities, namely the WDM mass m_X, the ionization efficiency of UV photons $\zeta_{\rm UV}$, the minimum virial temperature $T_{\rm vir}^{\rm min}$ (or equivalently the minimum virial mass $M_{\rm vir}^{\rm min}$, see below) and the x-ray efficiency $\zeta_{\rm X}$. In order to obtain the evolution of $\bar{x}_i(z)$ we make use of the publicly available code 21 CMFAST [119,120].[8] Concerning the range considered for the WDM particle mass in the case of thermal relics, we restrict ourselves to the few keV region, $m_X \in [1-4]$ keV, where previous related analyses have been focused on.

As mentioned above, the UV ionizing efficency $\zeta_{\rm UV}$ fixes the ionization fraction in the ionized IGM. It can be reexpressed in terms of the fraction of ionizing photons escaping their host galaxy $f_{\rm esc}$, the number of ionizing photons per stellar baryons inside stars N_γ, the fraction of baryons that form stars $f_\star$, and the mean number of recombinations per baryon $\bar{n}_{\rm rec}$,[9] as [140]

$$\zeta_{\rm UV} \simeq 30\left(\frac{N_\gamma}{4400}\right)\left(\frac{f_{\rm esc}}{0.1}\right)\left(\frac{f_\star}{0.1}\right)\left(\frac{1.5}{1+\bar{n}_{\rm rec}}\right). \quad (15)$$

As already noted in Ref. [122], suppressing the photon-production efficiency can have similar effects on ionization observables, as for WDM the abundance of low mass halos is suppressed. We allow $\zeta_{\rm UV}$ to vary in the range $\zeta_{\rm UV} \in [5, 105]$ (see, e.g., Ref. [24] for the bounds that could be obtained on this parameter from future 21 cm observations). Let us emphasize that for the purpose of this work, we have not modified the criterium encoded in 21 CMFAST for a region to be considered ionized[10] namely:

$$\zeta_{\rm UV} f_{\rm coll} > 1, \quad (16)$$

with $\zeta_{\rm UV}$ assumed to be constant with redshift for simplicity.

Another parameter we allow to vary is $T_{\rm vir}^{\rm min}$,[11] which is the threshold temperature for halos hosting star-forming galaxies. The default value in the numerical code 21 CMFAST is $T_{\rm vir}^{\rm min} = 10^4$ K, as lower temperatures have been shown to be insufficient to efficiently cool the halo gas through atomic cooling [144–148]. The choice of $T_{\rm vir}^{\rm min}$ can be translated into a minimum virial halo mass value [1]

$$M_{\rm vir}^{\rm min}(z) \simeq 10^8 \left(\frac{T_{\rm vir}^{\rm min}}{2\times 10^4 {\rm K}}\right)^{3/2}\left(\frac{1+z}{10}\right)^{-3/2} M_\odot, \quad (17)$$

which implies, e.g., $M_{\rm vir}^{\rm min} \simeq 3\times 10^7\ M_\odot$ at a redshift $z = 10$ for $T_{\rm vir}^{\rm min} = 10^4$ K. Following the upper limit $T_{\rm vir}^{\rm min} \sim 2\times 10^5$ K quoted in Refs. [140,149], we shall restrict ourselves to the range $T_{\rm vir}^{\rm min} \in [10^4 - 10^5]$ K.

Finally, we also vary modestly the number of X-ray photons per solar mass in stars, dubbed as $\zeta_{\rm X}$ (see, e.g., Refs. [120,150]). We consider two values: $\zeta_{\rm X} = 10^{56} M_\odot^{-1}$ and $5\times 10^{56} M_\odot^{-1}$, which approximately correspond to $N_{\rm X} \simeq 0.1$ and 0.5 X-ray photons per stellar baryon. Although this range is consistent with the observed integrated 0.5–8 keV luminosity at $z = 0$ [151], we note that significant uncertainties exist [152–154]. Nevertheless, given the degeneracies in the current analysis,[12] we restrict $\zeta_{\rm X}$ to that limited range.

B. Parameter degeneracies

In Fig. 2 we show the total ionized fraction, $\bar{x}_i$, as a function of redshift for different reionization histories. In both panels we illustrate the redshift evolution of $\bar{x}_i$ for four values of the WDM particle mass: $m_X = 1$ keV (black curves), 2 keV (red curves), 3 keV (blue curves), and 4 keV (magenta curves); and for three values of the UV ionizing

[8] Except for the astrophysics parameters mentioned here, we use the 21 CMFAST default settings for our simulations (for the version we use, we have a $(200\ {\rm Mpc})^3$ comoving box with a 900^3 grid).

[9] In WDM models, the rate of recombinations in the smallest halos is smaller than in CDM models, which could make reionization to occur earlier than in CDM models. Nevertheless, note that $\bar{n}_{\rm rec}$ is included in our definition of $\zeta_{\rm UV}$, although the trading-off of these parameters is, in general, non-trivial [141,142].

[10] Notice that [143] pointed out that the excursion set formalism, used in 21 CMFAST, tracks the average collapsed mass fraction $f_{\rm coll}$ instead of the stochastic source count which can give rise to a nonconservation of photons.

[11] We take the same threshold temperature $T_{\rm vir}^{\rm min}$ for halos hosting ionizing and X-ray sources.

[12] In the case of $\bar{x}_i(z)$, a value of $\zeta_{\rm X}$ larger than the range considered here can be approximately traded off for a larger value of $T_{\rm vir}^{\rm min}$ or a lower value of $\zeta_{\rm UV}$.

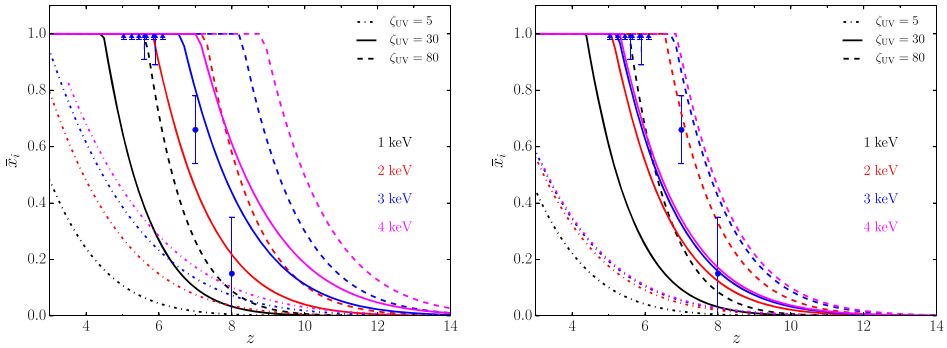

FIG. 2. Total ionized fraction, $\bar{x}_i$, as a function of redshift for different reionization histories, for four values of the WDM particle mass: $m_{\rm WDM} = 1$ keV (black curves), 2 keV (red curves), 3 keV (blue curves), and 4 keV (magenta curves); and for three possible values of the UV ionizing efficiency: $\zeta_{\rm UV} = 5$ (dotted curves), 30 (solid curves), and 80 (dashed curves); fixing the minimum virial temperature to $T_{\rm vir}^{\rm min} = 10^4$ K (left panel) and $T_{\rm vir}^{\rm min} = 10^5$ K (right panel). For all cases we use $\zeta_{\rm X} = 10^{56} M_\odot^{-1}$. We also illustrate some of the measurements and limits currently available on $\bar{x}_i$ at a number of redshifts. See the main text for details.

efficiency $\zeta_{\rm UV} = 5$ (dotted curves), 30 (solid curves), and 80 (dashed curves). In the left panel, the minimum virial temperature is fixed to $T_{\rm vir}^{\rm min} = 10^4$ K whereas in the right panel it is fixed to $T_{\rm vir}^{\rm min} = 10^5$ K. In both panels, we also depict some of the measurements and limits currently available on $\bar{x}_i$, that are described in the following section. Notice that, while both panels have been produced for a value of the X-ray efficiency $\zeta_{\rm X} = 10^{56} M_\odot^{-1}$, the results are not very sensitive to this parameter, given the limited range considered here.[13] Notice also that there exists a degeneracy between $\zeta_{\rm UV}$ and m_X. Indeed, a lower value of the WDM mass, which implies a larger small-scale suppression and thus, a larger departure from the CDM picture, would delay structure formation and therefore the entire reionization process, and this can be compensated by a larger UV ionization efficiency. For instance, for $T_{\rm vir}^{\rm min} = 10^4$ K, the $\bar{x}_i(z)$ curves for the $m_X = 2$ keV, $\zeta_{\rm UV} = 80$ case (red dashed curve) and those for the $m_X = 4$ keV, $\zeta_{\rm UV} = 30$ case (magenta solid curve) are almost identical and they are constrained exactly in the same way from measurements and limits on $\bar{x}_i(z)$. Notice that the $\zeta_{\rm UV}$ and m_X degeneracy cannot broken by using the Planck results for the optical depth to reionization because τ is an integrated quantity of $\bar{x}_i$ over redshift.

Measurements of the IGM temperature $T_{\rm K}(z)$ could help in alleviating some of the degeneracies discussed above. For instance, the IGM temperature is expected to be more sensitive than $\bar{x}_i$ to $\zeta_{\rm X}$, since this is the fundamental parameter which rules the heating of the gas. However, usual temperature data are derived from the Lyman-α forest measurements in the fully ionized phase [155,156], regime where we cannot reliably compute the IGM temperature using 21 CMFAST [119,120]. A complete and proper calculation of the IGM temperature would require computational expensive hydrodynamical simulations, which are beyond the scope of this work.

[13]This is expected, as in scenarios in which the usual parameters have values close to the canonical ones, x-rays only account for a few percent of the total fraction of ionization. On the other hand, a larger contribution from x-rays can have an important impact on more extreme scenarios [140].

IV. NUMERICAL ANALYSIS

A. Data sets

The optical depth from the last-scattering surface to reionization, τ, provides information of the integrated ionization history of the Universe and impacts the CMB spectrum, so that constraints on the reionization period can be obtained by means of its determination with CMB data. For our numerical analyses, we have imposed a Gaussian prior on the Planck result: $\tau = 0.055 \pm 0.009$ [18]. We compute the redshift evolution of the total ionized fraction, $\bar{x}_i(z)$, using the 21 CMFAST code [119,120], as previously explained, and in this way we determine the value of τ for each of the models studied here. In order to add the Planck prior, we have modified the CAMB (Code for Anisotropies in the Microwave Background) Boltzmann solver code [157] to allow for any possible ionization history, including those corresponding to WDM scenarios, for which we also employ the 21 CMFAST code to compute the reionization history as a function of redshift.

For deriving bounds using the ionization history of the Universe, we use some of the measurements compiled in Ref. [16]. One set of data uses the Gunn-Peterson optical depth from bright quasars at six different redshifts, $z = 5.03$, 5.25, 5.45, 4.65, 5.85, 6.10 [158], whereas another one makes use of the distribution of dark gaps in quasar spectra at $z = 5.6$ and $z = 5.9$ [159]. Both sets of

data indicate that reionization is complete by $z \sim 6$. On the other hand, the observations of Lyα emission in star-forming galaxies at higher redshifts ($z \gtrsim 7$), if the behavior at lower redshifts is extrapolated [5,6,9,160–170], indicates that reionization is not complete at those high redshifts. In this work we consider recent results at $z = 7$ and $z = 8$ [8], which use the models of Ref. [162]. In practice, given the precision of our numerical simulations, the Gunn-Peterson measurements imply that reionization should be fully completed at the quoted redshifts and we take their 1σ interval as lower bounds. All these measurements of the total ionized fraction are depicted in Fig. 2, and are included in our numerical analyses in the next section.

Therefore, in practice, we compute two χ^2, one for each type of data, and add them up. In the case of the low-redshift data of the ionization fraction, as indicated, we only consider lower bounds. In practice, for each model, at the redshifts corresponding to the data points, there is no contribution to the χ^2 if $\bar{x}_i(z)$ is larger than the measured lower bound.

B. Results

In the following, we present our results exploiting the data previously described and the simulations performed with the 21 CMFAST code. The redshift at which simulations start is $z = 35$, which roughly corresponds to the epoch when the first bright sources begin to appear. The simulations stop at $z = 3$, when reionization is expected to be complete. Due to the fact the runs are computationally expensive, we have made a grid in the parameter space and we have restricted ourselves to the following values: $m_X = 1,\ 1.5,\ 2,\ 3,\ 4$ keV, $\zeta_{\rm UV} = 5,\ 30,\ 42.5,\ 55,\ 80,\ 105$, $T_{\rm vir}^{\rm min} = 10^4$ K, 5×10^4 K and 10^5 K, and $\zeta_{\rm X} = 10^{56} M_\odot^{-1}$ and $5 \times 10^{56} M_\odot^{-1}$. We first start describing the different constraints obtained individually by each of the data sets considered. After that, we present the combined bounds, i.e., those obtained when the measurements of the optical depth to reionization τ and $\bar{x}_i(z)$ are simultaneously considered. This approach helps to understand our final constraints and it also justifies the combination of the different data sets considered here since, as we show, there is no tension among these data sets.

We start with the limits on our parameters obtained from measurements of $\bar{x}_i(z)$ at low redshifts. Focusing on the $(m_X, \zeta_{\rm UV})$ plane, we find the allowed regions to be rather independent of the adopted value of the number of x-ray photons per solar mass in stars, $\zeta_{\rm X}$. In the top panels of Fig. 3, we depict the regions allowed at 90% CL from $\bar{x}_i(z)$ data only, corresponding to $\zeta_{\rm X} = 5 \times 10^{56} M_\odot^{-1}$, and three possible values of the minimum virial temperature $T_{\rm vir}^{\rm min} = 10^4$ K (left panel), 5×10^4 K (middle panel), and 10^5 K (right panel). By comparing the results in the three panels, one can clearly see the effect of the nontrivial dependence of $\bar{x}_i(z)$ on the minimum virial temperature, as the allowed regions shift to lower values of $\zeta_{\rm UV}$ for lower values of $T_{\rm vir}^{\rm min}$. This is because a lower minimum virial temperature

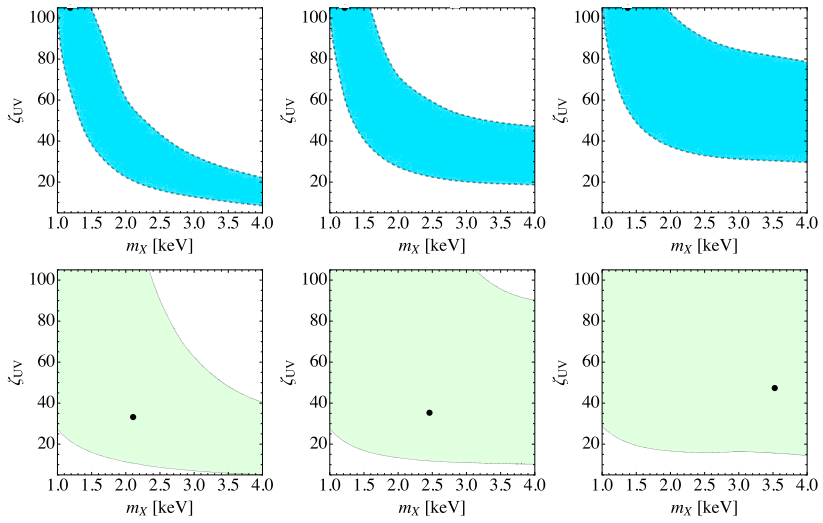

FIG. 3. Contours in the $(m_X, \zeta_{\rm UV})$ plane corresponding to 90% CL, for three values of the minimum virial temperature: $T_{\rm vir}^{\rm min} = 10^4$ K (left-column panels), 5×10^4 K (middle-column panels), and 10^5 K (right-column panels). The number of X-ray photons per solar mass in stars is $\zeta_{\rm X} = 5 \times 10^{56} M_\odot^{-1}$ in all panels. The best-fit value is indicated with a black point. Top panels: using only $\bar{x}_i(z)$ data. Bottom panels: using only the Planck measurement of the optical depth, $\tau = 0.055 \pm 0.009$ [18].

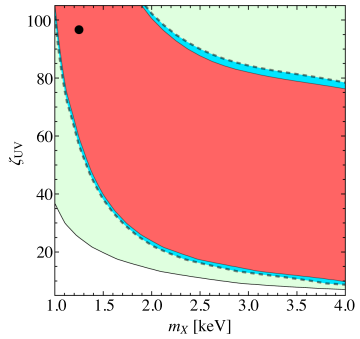

FIG. 4. Contours in the (m_X, ζ_{UV}) plane corresponding to 90% CL, for the two data sets shown in Fig. 3: $\bar{x}_i(z)$ (light blue region) and τ (light green region), after profiling over T_{vir}^{min} and ζ_X, and the resulting contour obtained from the combination of them (red region). The global best-fit value in $m_X = 1.25$ keV and $\zeta_{UV} = 96.6$ is indicated with a black point.

imply an earlier reionization time, which then would requires a lower UV heating efficiency. The best-fit value when using this set of data is obtained for $m_X = 1.2$ keV, $\zeta_{UV} = 105$, and $T_{vir}^{min} = 10^4$ K, with very little sensitivity to the value of ζ_X (the χ^2 is very flat in the direction of this parameter for the range we consider).

Given that the optical depth τ only provides information on the integrated ionization history of the Universe, constraints based on its measurement are less restrictive than those obtained by using the redshift evolution of $\bar{x}_i$ (shown in the top panels of Fig. 3). This can be seen in the bottom panels of Fig. 3 where we use the Planck result for τ and, analogously to the top panels, we depict the 90% CL allowed contour in the (m_X, ζ_{UV}) plane for $\zeta_X = 5 \times 10^{56} M_\odot^{-1}$ and three values of the minimum virial temperature $T_{vir}^{min} = 10^4$ K (left panel), 5×10^4 K (middle panel) and 10^5 K (right panel). As expected, qualitatively, a very similar behavior to that in the top panels of Fig. 3 is obtained and likewise, these bounds are also insensitive to the specific value of the parameter ζ_X within the range we consider. Quantitatively, the allowed regions are larger. In this case, the low-m_X allowed contours remain basically unaffected by changes in the minimum virial temperature, as reionization is considerably delayed and high UV efficiencies are always needed, regardless of the value of T_{vir}^{min}. With this measurement, the best-fit value is obtained for $m_X = 1.6$ keV, $\zeta_{UV} = 58$ and $T_{vir}^{min} = 2.9 \times 10^4$ K, and it is independent on the value of ζ_X (in the range we consider for this parameter).

In Fig. 4 we show the 90% CL contours in the (m_X, ζ_{UV}) plane after profiling over the minimum virial temperature T_{vir}^{min} and the x-ray efficiency ζ_X, obtained for the two different data sets described above: the global ionization fraction $\bar{x}_i(z)$ (light blue region), and the optical depth τ (light green region), together with the final bounds after combining these data sets (red region). Note that the χ^2 is very flat along the direction of m_X in the allowed region, which is an indication of the strong degeneracy between the WDM mass and other astrophysical parameters as ζ_{UV} and T_{vir}^{min}. The presence of these degeneracies makes completely impossible to bound the WDM particle mass. We find the global best-fit value in $m_X = 1.25$ keV and $\zeta_{UV} = 96.6$.

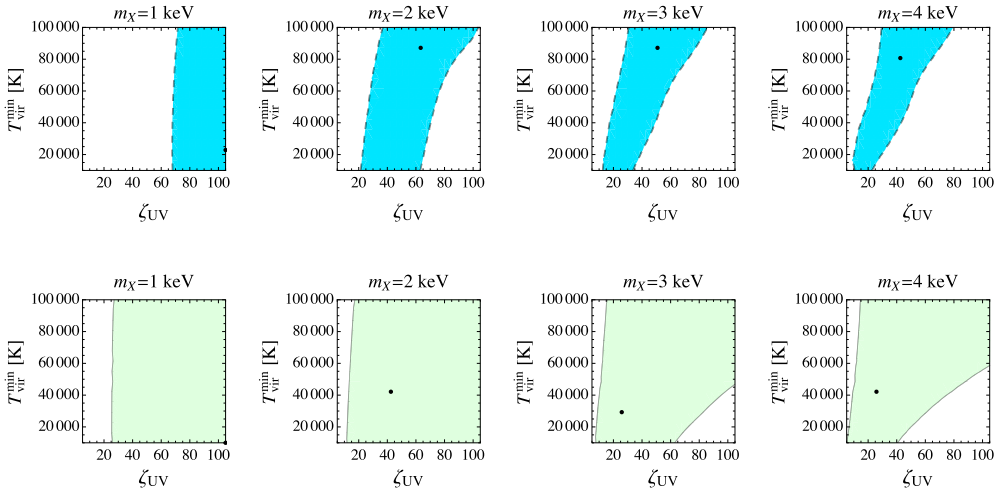

FIG. 5. The top (bottom) panel shows the 90% CL allowed regions from the analyses to $\bar{x}_i(z)$ (optical depth, τ) measurements in the $(\zeta_{UV}, T_{vir}^{min})$ plane for four values of the WDM mass m_X, profiling over ζ_X. The best-fit values are indicated with black points.

One can check the complete consistence between both data sets, as could be expected, since the optical depth is mainly given by the integral of $\bar{x}_i(z)$ over redshift.

In order to further explore the degeneracies between the different parameters, and how the IGM quantities depend on the precise value of the WDM mass, we illustrate the 90% CL contours arising from our numerical analyses in the ($\zeta_{\rm UV}$, $T_{\rm vir}^{\rm min}$) plane for different values of the WDM mass. In Fig. 5 we show the corresponding χ^2 results from the fits to the ionization fraction of the universe (top panel) and of the reionization optical depth (bottom panel), profiled over $\zeta_{\rm X}$, for four different values of the WDM mass: $m_X = 1$, 2, 3, and 4 keV. Notice that a lower m_X would imply a delayed reionization history and therefore a larger value of the UV efficiency would be required. Figure 5 shows the strong degeneracies between these three parameters ($\zeta_{\rm UV}$, $T_{\rm vir}^{\rm min}$ and m_X). We do not show the (ζ_X, $T_{\rm vir}^{\rm min}$) and ($\zeta_{\rm UV}$, ζ_X) planes, because, as he have pointed out earlier, $\bar{x}_i$ and τ are almost insensitive to changes in ζ_X for the range of interest.

Let us finally comment that measurements of the Lyα power spectrum can be also used to constrain simultaneously the WDM mass and the IGM thermal history, inferred from the suppression of power in the matter spectrum and via Jeans and Doppler broadening of the absorption lines [171,172], respectively. By means of this method the density of neutral hydrogen can be estimated and then used to extract the total matter density. Indeed, for a given DM scenario, the recently observed cutoff in the Lyα flux power spectrum can be related to the IGM thermal history [104,173] via a temperature-density relation [97], obtaining more constraining results than the ones presented here [98–106].

V. CONCLUSIONS

Our knowledge of the reionization of the Universe is still obscure. Measurements of the CMB provide information on the so-called optical depth to reionization. The most recent analysis from the Planck collaboration using the Planck HFI obtained a relatively low value, $\tau = 0.055 \pm 0.009$ [18], based exclusively on the spectrum polarization data. Additional (nonintegrated) information on the ionization history of the Universe can also be extracted from measurements of the Gunn-Peterson optical depth or of the damping absorption wings in bright quasar spectra, or from the prevalence of Lyα emission in the spectra of high-redshift galaxies. In addition, measurements of the thermal history, sensitive to the ionization history, are also important.

Another crucial ingredient to understand the formation of structure at late times is the DM nature. While CDM models can satisfactorily explain large scale structure observations, there are a number of discrepancies at small scales between observations and CDM predictions. This small-scale crisis of the CDM paradigm could be alleviated in WDM scenarios for which the associated free-streaming length is larger and thus, fluctuations at small scales would be suppressed, potentially explaining the missing satellite [70,71], too-big-to-fail [72], and the core-cusp [73,74] problems. Reionization in WDM cosmologies would be delayed for this very same effect: halo formation processes would be delayed, and so would the onset of reionization. However, the details of reionization are not known accurately and precise determinations of the number of X-ray photons per solar mass in stars, the UV ionization efficiency and the minimum virial temperature that sets the threshold mass for halos to host star-forming galaxies are only moderately constrained.

In this work, we have considered measurements of the reionization optical depth and the Universe's ionized fraction to constrain the mass of the DM particle in WDM scenarios. Using the 21 CMFAST code [119,120], we have performed simulations of different ionization histories in WDM cosmologies, including their corresponding halo mass function, discussed in Sec. II. As described in Sec. III, we have considered four free parameters: the WDM mass, the number of X-ray photons per solar mass in stars, the minimum virial temperature for halos to host galaxies and the UV ionization efficiency. However, there are important degeneracies among these parameters. For instance, the lower the WDM mass the larger the free-streaming length and thus, the longer structure formation delays, which in turn can be compensated by a larger UV ionizing efficiency or a smaller minimum virial temperature. Therefore, given the degeneracies among some of the astrophysical parameters that drive the ionization processes and the WDM mass, i.e., the suppression of the matter power spectrum, obtaining constraints on the minimum mass of the WDM particle with this approach is a difficult task, and therefore our results cannot compete with those obtained from measurements of the IGM temperature in the post-reionization era [98–106].

Finally, let us stress that future measurements of the 21 cm hyperfine transition of neutral hydrogen, which would map its distribution at different redshifts [and thus the distribution of $\bar{x}_i(z)$], are expected to constitute a very useful tool to understand the ionization history of the Universe, and could allow us to further test predictions from WDM models [122,174–178] or even to disentangle the potential signals from DM annihilations or decays in CDM scenarios [35–37,39,41,42,49,54,60,63,67].

ACKNOWLEDGMENTS

We thank A. Mesinger and J. Miralda-Escudé for clarifications and enlightening discussions. We also thank A. C. Vincent, who took part on the initial stages of this work, for useful comments. L. L. H. is supported by the FNRS-FRS and also acknowledges partial support by the Université Libre de Bruxelles, the Vrije Universiteit Brussel (VUB), the Belgian Federal Science Policy Office through the Interuniversity Attraction Pole P7/37,

the IISN and the Strategic Research Program *High-Energy Physics* of the VUB. O. M. and P. V. D. are supported by PROMETEO II/2014/050 and by the Spanish Grant No. FPA2014–57816-P of the MINECO. S. P. R. is supported by a Ramón y Cajal contract, by the Spanish MINECO under Grant No. FPA2014-54459-P and by the Generalitat Valenciana under grant PROMETEOII/2014/049. O. M., S. P. R., and P. V. D. are also supported by the MINECO Grant No. SEV-2014-0398 and by the European Union's Horizon 2020 research and innovation program under the Marie Skłodowska-Curie grant agreements No. 690575 and 674896. S. P. R. is also partially supported by the Portuguese FCT through the CFTP-FCT Unit 777 (PEst-OE/FIS/UI0777/2013).

[1] R. Barkana and A. Loeb, Phys. Rep. **349**, 125 (2001).
[2] A. Mesinger, *Understanding the Epoch of Cosmic Reionization*, Astrophysics and Space Science Library, Vol. 423 (Springer, New York, 2016).
[3] C. L. Reichardt, in *Understanding the Epoch of Cosmic Reionization: Challenges and Progress*, edited by A. Mesinger (Springer International Publishing, New York, 2016), Vol. 423.
[4] G. Hinshaw *et al.* (WMAP Collaboration), Astrophys. J. Suppl. Ser. **208**, 19 (2013).
[5] D. P. Stark, R. S. Ellis, K. Chiu, M. Ouchi, and A. Bunker, Mon. Not. R. Astron. Soc. **408**, 1628 (2010).
[6] T. Treu, K. B. Schmidt, M. Trenti, L. D. Bradley, and M. Stiavelli, Astrophys. J. **775**, L29 (2013).
[7] L. Pentericci *et al.*, Astrophys. J. **793**, 113 (2014).
[8] M. A. Schenker, R. S. Ellis, N. P. Konidaris, and D. P. Stark, Astrophys. J. **795**, 20 (2014).
[9] V. Tilvi, C. Papovich, S. L. Finkelstein, J. Long, M. Song, M. Dickinson, H. C. Ferguson, A. M. Koekemoer, M. Giavalisco, and B. Mobasher, Astrophys. J. **794**, 5 (2014).
[10] N. Aghanim *et al.* (Planck Collaboration), Astron. Astrophys. **594**, A11 (2016).
[11] P. A. R. Ade *et al.* (Planck), Astron. Astrophys. **594**, A13 (2016).
[12] M. Lattanzi, C. Burigana, M. Gerbino, A. Gruppuso, N. Mandolesi, P. Natoli, G. Polenta, L. Salvati, and T. Trombetti, J. Cosmol. Astropart. Phys. 02 (2017) 041.
[13] A. Mesinger, A. Aykutalp, E. Vanzella, L. Pentericci, A. Ferrara, and M. Dijkstra, Mon. Not. R. Astron. Soc. **446**, 566 (2015).
[14] T. R. Choudhury, E. Puchwein, M. G. Haehnelt, and J. S. Bolton, Mon. Not. R. Astron. Soc. **452**, 261 (2015).
[15] B. E. Robertson, R. S. Ellis, S. R. Furlanetto, and J. S. Dunlop, Astrophys. J. **802**, L19 (2015).
[16] R. J. Bouwens, G. D. Illingworth, P. A. Oesch, J. Caruana, B. Holwerda, R. Smit, and S. Wilkins, Astrophys. J. **811**, 140 (2015).
[17] S. Mitra, T. R. Choudhury, and A. Ferrara, Mon. Not. R. Astron. Soc. **454**, L76 (2015).
[18] N. Aghanim *et al.* (Planck Collaboration), Astron. Astrophys. **596**, A107 (2016).
[19] R. Adam *et al.* (Planck Collaboration), Astron. Astrophys. **596**, A108 (2016).
[20] M. J. Mortonson and W. Hu, Astrophys. J. **672**, 737 (2008).
[21] S. Furlanetto *et al.*, arXiv:0902.3259.
[22] J. R. Pritchard and A. Loeb, Rep. Prog. Phys. **75**, 086901 (2012).
[23] S. R. Furlanetto, in *Understanding the Epoch of Cosmic Reionization: Challenges and Progress*, edited by A. Mesinger (Springer International Publishing, New York, 2016), Vol. 423, p. 247.
[24] A. Liu, J. R. Pritchard, R. Allison, A. R. Parsons, U. Seljak, and B. D. Sherwin, Phys. Rev. D **93**, 043013 (2016).
[25] P. Bode, J. P. Ostriker, and N. Turok, Astrophys. J. **556**, 93 (2001).
[26] R. Adhikari *et al.*, J. Cosmol. Astropart. Phys. 01 (2017) 025.
[27] L. Hui, J. P. Ostriker, S. Tremaine, and E. Witten, Phys. Rev. D **95**, 043541 (2017).
[28] J. A. Adams, S. Sarkar, and D. W. Sciama, Mon. Not. R. Astron. Soc. **301**, 210 (1998).
[29] S. H. Hansen and Z. Haiman, Astrophys. J. **600**, 26 (2004).
[30] E. Pierpaoli, Phys. Rev. Lett. **92**, 031301 (2004).
[31] X.-L. Chen and M. Kamionkowski, Phys. Rev. D **70**, 043502 (2004).
[32] N. Padmanabhan and D. P. Finkbeiner, Phys. Rev. D **72**, 023508 (2005).
[33] L. Zhang, X.-L. Chen, Y.-A. Lei, and Z.-G. Si, Phys. Rev. D **74**, 103519 (2006).
[34] M. Mapelli, A. Ferrara, and E. Pierpaoli, Mon. Not. R. Astron. Soc. **369**, 1719 (2006).
[35] Y. A. Shchekinov and E. O. Vasiliev, Mon. Not. R. Astron. Soc. **379**, 1003 (2007).
[36] S. R. Furlanetto, S. P. Oh, and E. Pierpaoli, Phys. Rev. D **74**, 103502 (2006).
[37] M. Valdés, A. Ferrara, M. Mapelli, and E. Ripamonti, Mon. Not. R. Astron. Soc. **377**, 245 (2007).
[38] L. Zhang, X. Chen, M. Kamionkowski, Z.-G. Si, and Z. Zheng, Phys. Rev. D **76**, 061301 (2007).
[39] L. Chuzhoy, Astrophys. J. **679**, L65 (2008).
[40] A. Natarajan and D. J. Schwarz, Phys. Rev. D **78**, 103524 (2008); **81**, 089905(E) (2010).
[41] D. T. Cumberbatch, M. Lattanzi, and J. Silk, Phys. Rev. D **82**, 103508 (2010).
[42] A. Natarajan and D. J. Schwarz, Phys. Rev. D **80**, 043529 (2009).
[43] A. V. Belikov and D. Hooper, Phys. Rev. D **80**, 035007 (2009).
[44] S. Galli, F. Iocco, G. Bertone, and A. Melchiorri, Phys. Rev. D **80**, 023505 (2009).

[45] T. R. Slatyer, N. Padmanabhan, and D. P. Finkbeiner, Phys. Rev. D **80**, 043526 (2009).
[46] G. Huetsi, A. Hektor, and M. Raidal, Astron. Astrophys. **505**, 999 (2009).
[47] M. Cirelli, F. Iocco, and P. Panci, J. Cosmol. Astropart. Phys. 10 (2009) 009.
[48] T. Kanzaki, M. Kawasaki, and K. Nakayama, Prog. Theor. Phys. **123**, 853 (2010).
[49] Q. Yuan, B. Yue, X.-J. Bi, X. Chen, and X. Zhang, J. Cosmol. Astropart. Phys. 10 (**2010**) 023.
[50] J. Hisano, M. Kawasaki, K. Kohri, T. Moroi, K. Nakayama, and T. Sekiguchi, Phys. Rev. D **83**, 123511 (2011).
[51] S. Galli, F. Iocco, G. Bertone, and A. Melchiorri, Phys. Rev. D **84**, 027302 (2011).
[52] D. P. Finkbeiner, S. Galli, T. Lin, and T. R. Slatyer, Phys. Rev. D **85**, 043522 (2012).
[53] G. Giesen, J. Lesgourgues, B. Audren, and Y. Ali-Haimoud, J. Cosmol. Astropart. Phys. 12 (2012) 008.
[54] M. Valdés, C. Evoli, A. Mesinger, A. Ferrara, and N. Yoshida, Mon. Not. R. Astron. Soc. **429**, 1705 (2013).
[55] T. R. Slatyer, Phys. Rev. D **87**, 123513 (2013).
[56] L. López-Honorez, O. Mena, S. Palomares-Ruiz, and A. C. Vincent, J. Cosmol. Astropart. Phys. 07 (2013) 046.
[57] S. Galli, T. R. Slatyer, M. Valdés, and F. Iocco, Phys. Rev. D **88**, 063502 (2013).
[58] R. Diamanti, L. López-Honorez, O. Mena, S. Palomares-Ruiz, and A. C. Vincent, J. Cosmol. Astropart. Phys. 02 (2014) 017.
[59] M. S. Madhavacheril, N. Sehgal, and T. R. Slatyer, Phys. Rev. D **89**, 103508 (2014).
[60] C. Evoli, A. Mesinger, and A. Ferrara, J. Cosmol. Astropart. Phys. 11 (2014) 024.
[61] T. R. Slatyer, Phys. Rev. D **93**, 023527 (2016).
[62] M. Kawasaki, K. Nakayama, and T. Sekiguchi, Phys. Lett. B **756**, 212 (2016).
[63] L. López-Honorez, O. Mena, A. Moliné, S. Palomares-Ruiz, and A. C. Vincent, J. Cosmol. Astropart. Phys. 08 (2016) 004.
[64] H. Liu, T. R. Slatyer, and J. Zavala, Phys. Rev. D **94**, 063507 (2016).
[65] I. M. Oldengott, D. Boriero, and D. J. Schwarz, J. Cosmol. Astropart. Phys. 08 (2016) 054.
[66] T. R. Slatyer and C.-L. Wu, Phys. Rev. D **95**, 023010 (2017).
[67] V. Poulin, J. Lesgourgues, and P. D. Serpico, J. Cosmol. Astropart. Phys. 03 (2017) 043.
[68] A. Lapi and L. Danese, J. Cosmol. Astropart. Phys. 09 (2015) 003.
[69] W.-W. Tan, F. Y. Wang, and K. S. Cheng, Astrophys. J. **829**, 29 (2016).
[70] A. A. Klypin, A. V. Kravtsov, O. Valenzuela, and F. Prada, Astrophys. J. **522**, 82 (1999).
[71] B. Moore, S. Ghigna, F. Governato, G. Lake, T. Quinn, J. Stadel, and P. Tozzi, Astrophys. J. **524**, L19 (1999).
[72] M. Boylan-Kolchin, J. S. Bullock, and M. Kaplinghat, Mon. Not. R. Astron. Soc. **422**, 1203 (2012).
[73] B. Moore, T. R. Quinn, F. Governato, J. Stadel, and G. Lake, Mon. Not. R. Astron. Soc. **310**, 1147 (1999).
[74] V. Springel, J. Wang, M. Vogelsberger, A. Ludlow, A. Jenkins, A. Helmi, J. F. Navarro, C. S. Frenk, and S. D. M. White, Mon. Not. R. Astron. Soc. **391**, 1685 (2008).
[75] A. Fattahi *et al.*, arXiv:1607.06479.
[76] M. R. Lovell, V. Gonzalez-Perez, S. Bose, A. Boyarsky, S. Cole, C. S. Frenk, and O. Ruchayskiy, Mon. Not. R. Astron. Soc. **468**, 2836 (2017).
[77] T. Nakama, J. Chluba, and M. Kamionkowski, Phys. Rev. D **95**, 121302 (2017).
[78] A. Knebe, J. E. G. Devriendt, A. Mahmood, and J. Silk, Mon. Not. R. Astron. Soc. **329**, 813 (2002).
[79] P. Colin, O. Valenzuela, and V. Avila-Reese, Astrophys. J. **673**, 203 (2008).
[80] J. Zavala, Y. P. Jing, A. Faltenbacher, G. Yepes, Y. Hoffman, S. Gottlöber, and B. Catinella, Astrophys. J. **700**, 1779 (2009).
[81] R. E. Smith and K. Markovic, Phys. Rev. D **84**, 063507 (2011).
[82] M. R. Lovell, V. Eke, C. S. Frenk, L. Gao, A. Jenkins, T. Theuns, J. Wang, S. D. M. White, A. Boyarsky, and O. Ruchayskiy, Mon. Not. R. Astron. Soc. **420**, 2318 (2012).
[83] A. Schneider, R. E. Smith, A. V. Macciò, and B. Moore, Mon. Not. R. Astron. Soc. **424**, 684 (2012).
[84] M. R. Lovell, C. S. Frenk, V. R. Eke, A. Jenkins, L. Gao, and T. Theuns, Mon. Not. R. Astron. Soc. **439**, 300 (2014).
[85] R. Kennedy, C. Frenk, S. Cole, and A. Benson, Mon. Not. R. Astron. Soc. **442**, 2487 (2014).
[86] C. Destri, H. J. de Vega, and N. G. Sánchez, Phys. Rev. D **88**, 083512 (2013).
[87] R. E. Angulo, O. Hahn, and T. Abel, Mon. Not. R. Astron. Soc. **434**, 3337 (2013).
[88] A. J. Benson, A. Farahi, S. Cole, L. A. Moustakas, A. Jenkins, M. Lovell, R. Kennedy, J. Helly, and C. Frenk, Mon. Not. R. Astron. Soc. **428**, 1774 (2013).
[89] A. Kamada, N. Yoshida, K. Kohri, and T. Takahashi, J. Cosmol. Astropart. Phys. 03 (**2013**) 008.
[90] M. R. Lovell, S. Bose, A. Boyarsky, S. Cole, C. S. Frenk, V. Gonzalez-Perez, R. Kennedy, O. Ruchayskiy, and A. Smith, Mon. Not. R. Astron. Soc. **461**, 60 (2016).
[91] A. D. Ludlow, S. Bose, R. E. Angulo, L. Wang, W. A. Hellwing, J. F. Navarro, S. Cole, and C. S. Frenk, Mon. Not. R. Astron. Soc. **460**, 1214 (2016).
[92] L. Wang, V. Gonzalez-Perez, L. Xie, A. P. Cooper, C. S. Frenk, L. Gao, W. A. Hellwing, J. Helly, M. R. Lovell, and L. Jiang, Mon. Not. R. Astron. Soc. **468**, 4579 (2017).
[93] E. Bulbul, M. Markevitch, A. Foster, R. K. Smith, M. Loewenstein, and S. W. Randall, Astrophys. J. **789**, 13 (2014).
[94] A. Boyarsky, O. Ruchayskiy, D. Iakubovskyi, and J. Franse, Phys. Rev. Lett. **113**, 251301 (2014).
[95] A. Boyarsky, J. Franse, D. Iakubovskyi, and O. Ruchayskiy, Phys. Rev. Lett. **115**, 161301 (2015).
[96] N. Cappelluti *et al.*, arXiv:1701.07932.
[97] L. Hui and N. Y. Gnedin, Mon. Not. R. Astron. Soc. **292**, 27 (1997).
[98] C. Yèche, N. Palanque-Delabrouille, J. Baur, and H. du Mas des Bourboux, J. Cosmol. Astropart. Phys. 06 (2017) 047.
[99] M. Viel, J. Lesgourgues, M. G. Haehnelt, S. Matarrese, and A. Riotto, Phys. Rev. D **71**, 063534 (2005).

[100] U. Seljak, A. Makarov, P. McDonald, and H. Trac, Phys. Rev. Lett. **97**, 191303 (2006).
[101] M. Viel, J. Lesgourgues, M. G. Haehnelt, S. Matarrese, and A. Riotto, Phys. Rev. Lett. **97**, 071301 (2006).
[102] M. Viel, G. D. Becker, J. S. Bolton, M. G. Haehnelt, M. Rauch, and W. L. W. Sargent, Phys. Rev. Lett. **100**, 041304 (2008).
[103] A. Boyarsky, J. Lesgourgues, O. Ruchayskiy, and M. Viel, J. Cosmol. Astropart. Phys. 05 (2009) 012.
[104] M. Viel, G. D. Becker, J. S. Bolton, and M. G. Haehnelt, Phys. Rev. D **88**, 043502 (2013).
[105] J. Baur, N. Palanque-Delabrouille, C. Yèche, C. Magneville, and M. Viel, J. Cosmol. Astropart. Phys. 08 (2016) 012.
[106] V. Iršič *et al.*, Phys. Rev. D **96**, 023522 (2017).
[107] F. Pacucci, A. Mesinger, and Z. Haiman, Mon. Not. R. Astron. Soc. **435**, L53 (2013).
[108] C. Schultz, J. Oñorbe, K. N. Abazajian, and J. S. Bullock, Mon. Not. R. Astron. Soc. **442**, 1597 (2014).
[109] P. Dayal, A. Mesinger, and F. Pacucci, Astrophys. J. **806**, 67 (2015).
[110] N. Menci, N. G. Sánchez, M. Castellano, and A. Grazian, Astrophys. J. **818**, 90 (2016).
[111] N. Menci, A. Grazian, M. Castellano, and N. G. Sánchez, Astrophys. J. **825**, L1 (2016).
[112] N. Menci, A. Merle, M. Totzauer, A. Schneider, A. Grazian, M. Castellano, and N. G. Sanchez, Astrophys. J. **836**, 61 (2017).
[113] X. Kang, A. V. Maccio, and A. A. Dutton, Astrophys. J. **767**, 22 (2013).
[114] R. S. de Souza, A. Mesinger, A. Ferrara, Z. Haiman, R. Perna, and N. Yoshida, Mon. Not. R. Astron. Soc. **432**, 3218 (2013).
[115] S. Bose, C. S. Frenk, J. Hou, C. G. Lacey, and M. R. Lovell, Mon. Not. R. Astron. Soc. **463**, 3848 (2016).
[116] R. Barkana, Z. Haiman, and J. P. Ostriker, Astrophys. J. **558**, 482 (2001).
[117] R. S. Somerville, J. S. Bullock, and M. Livio, Astrophys. J. **593**, 616 (2003).
[118] N. Yoshida, A. Sokasian, L. Hernquist, and V. Springel, Astrophys. J. **591**, L1 (2003).
[119] A. Mesinger and S. Furlanetto, Astrophys. J. **669**, 663 (2007).
[120] A. Mesinger, S. Furlanetto, and R. Cen, Mon. Not. R. Astron. Soc. **411**, 955 (2011).
[121] E. W. Kolb and M. S. Turner, Front. Phys. **69**, 1 (1990).
[122] M. Sitwell, A. Mesinger, Y.-Z. Ma, and K. Sigurdson, Mon. Not. R. Astron. Soc. **438**, 2664 (2014).
[123] A. Jenkins, C. S. Frenk, S. D. M. White, J. M. Colberg, S. Cole, A. E. Evrard, H. M. P. Couchman, and N. Yoshida, Mon. Not. R. Astron. Soc. **321**, 372 (2001).
[124] W. H. Press and P. Schechter, Astrophys. J. **187**, 425 (1974).
[125] J. R. Bond, S. Cole, G. Efstathiou, and N. Kaiser, Astrophys. J. **379**, 440 (1991).
[126] V. Springel *et al.*, Nature (London) **435**, 629 (2005).
[127] K. Heitmann, D. Higdon, C. Nakhleh, and S. Habib, Astrophys. J. **646**, L1 (2006).
[128] Z. Lukic, K. Heitmann, S. Habib, S. Bashinsky, and P. M. Ricker, Astrophys. J. **671**, 1160 (2007).
[129] W. A. Watson, I. T. Iliev, A. D'Aloisio, A. Knebe, P. R. Shapiro, and G. Yepes, Mon. Not. R. Astron. Soc. **433**, 1230 (2013).
[130] R. K. Sheth and G. Tormen, Mon. Not. R. Astron. Soc. **308**, 119 (1999).
[131] R. K. Sheth, H. J. Mo, and G. Tormen, Mon. Not. R. Astron. Soc. **323**, 1 (2001).
[132] R. K. Sheth and G. Tormen, Mon. Not. R. Astron. Soc. **329**, 61 (2002).
[133] G. Kauffmann, J. M. Colberg, A. Diaferio, and S. D. M. White, Mon. Not. R. Astron. Soc. **303**, 188 (1998).
[134] A. Schneider, R. E. Smith, and D. Reed, Mon. Not. R. Astron. Soc. **433**, 1573 (2013).
[135] A. Schneider, Mon. Not. R. Astron. Soc. **451**, 3117 (2015).
[136] R. Barkana and A. Loeb, Astrophys. J. **609**, 474 (2004).
[137] R. Barkana and A. Loeb, Mon. Not. R. Astron. Soc. **384**, 1069 (2008).
[138] J. A. Schewtschenko, R. J. Wilkinson, C. M. Baugh, C. Bœhm, and S. Pascoli, Mon. Not. R. Astron. Soc. **449**, 3587 (2015).
[139] J. Miralda-Escudé, Astrophys. J. **597**, 66 (2003).
[140] A. Mesinger, A. Ferrara, and D. S. Spiegel, Mon. Not. R. Astron. Soc. **431**, 621 (2013).
[141] B. Yue and X. Chen, Astrophys. J. **747**, 127 (2012).
[142] A. Rudakovskiy and D. Iakubovskyi, J. Cosmol. Astropart. Phys. 06 (2016) 017.
[143] A. Paranjape, T. R. Choudhury, and H. Padmanabhan, Mon. Not. R. Astron. Soc. **460**, 1801 (2016).
[144] A. E. Evrard, Astrophys. J. **363**, 349 (1990).
[145] A. Blanchard, D. Valls-Gabaud, and G. A. Mamon, Astron. Astrophys. **264**, 365 (1992).
[146] M. Tegmark, J. Silk, M. J. Rees, A. Blanchard, T. Abel, and F. Palla, Astrophys. J. **474**, 1 (1997).
[147] Z. Haiman, T. Abel, and M. J. Rees, Astrophys. J. **534**, 11 (2000).
[148] B. Ciardi, A. Ferrara, F. Governato, and A. Jenkins, Mon. Not. R. Astron. Soc. **314**, 611 (2000).
[149] B. Greig and A. Mesinger, Mon. Not. R. Astron. Soc. **449**, 4246 (2015).
[150] P. Christian and A. Loeb, J. Cosmol. Astropart. Phys. 09 (2013) 014.
[151] S. Mineo, M. Gilfanov, and R. Sunyaev, Mon. Not. R. Astron. Soc. **419**, 2095 (2012).
[152] E. Treister, K. Schawinski, M. Volonteri, P. Natarajan, and E. Gawiser, Nature (London) **474**, 356 (2011).
[153] L. L. Cowie, A. J. Barger, and G. Hasinger, Astrophys. J. **748**, 50 (2012).
[154] A. R. Basu-Zych *et al.*, Astrophys. J. **762**, 45 (2013).
[155] E. Puchwein, J. S. Bolton, M. G. Haehnelt, P. Madau, G. D. Becker, and F. Haardt, Mon. Not. R. Astron. Soc. **450**, 4081 (2015).
[156] G. D. Becker, J. S. Bolton, M. G. Haehnelt, and W. L. W. Sargent, Mon. Not. R. Astron. Soc. **410**, 1096 (2011).
[157] A. Lewis, A. Challinor, and A. Lasenby, Astrophys. J. **538**, 473 (2000).
[158] X.-H. Fan, M. A. Strauss, R. H. Becker, R. L. White, J. E. Gunn, G. R. Knapp, G. T. Richards, D. P. Schneider, J. Brinkmann, and M. Fukugita, Astron. J. **132**, 117 (2006).

[159] I. McGreer, A. Mesinger, and V. D'Odorico, Mon. Not. R. Astron. Soc. **447**, 499 (2015).
[160] M. R. Santos, Mon. Not. R. Astron. Soc. **349**, 1137 (2004).
[161] S. Malhotra and J. E. Rhoads, Astrophys. J. **617**, L5 (2004).
[162] M. McQuinn, L. Hernquist, M. Zaldarriaga, and S. Dutta, Mon. Not. R. Astron. Soc. **381**, 75 (2007).
[163] A. Mesinger and S. Furlanetto, Mon. Not. R. Astron. Soc. **386**, 1990 (2008).
[164] D. P. Stark, R. S. Ellis, and M. Ouchi, Astrophys. J. **728**, L2 (2011).
[165] A. Fontana *et al.*, Astrophys. J. **725**, L205 (2010).
[166] M. Dijkstra, A. Mesinger, and S. Wyithe, Mon. Not. R. Astron. Soc. **414**, 2139 (2011).
[167] L. Pentericci *et al.*, Astrophys. J. **743**, 132 (2011).
[168] Y. Ono *et al.*, Astrophys. J. **744**, 83 (2012).
[169] J. Caruana, A. J. Bunker, S. M. Wilkins, E. R. Stanway, M. Lacy, M. J. Jarvis, S. Lorenzoni, and S. Hickey, Mon. Not. R. Astron. Soc. **427**, 3055 (2012).
[170] J. Caruana, A. J. Bunker, S. M. Wilkins, E. R. Stanway, S. Lorenzoni, M. J. Jarvis, and H. Ebert, Mon. Not. R. Astron. Soc. **443**, 2831 (2014).
[171] N. Y. Gnedin and L. Hui, Mon. Not. R. Astron. Soc. **296**, 44 (1998).
[172] T. Theuns, J. Schaye, and M. Haehnelt, Mon. Not. R. Astron. Soc. **315**, 600 (2000).
[173] A. Garzilli, A. Boyarsky, and O. Ruchayskiy, Phys. Lett. B **773**, 258 (2017).
[174] A. Loeb and M. Zaldarriaga, Phys. Rev. Lett. **92**, 211301 (2004).
[175] A. Mesinger, A. Ewall-Wice, and J. Hewitt, Mon. Not. R. Astron. Soc. **439**, 3262 (2014).
[176] T. Sekiguchi and H. Tashiro, J. Cosmol. Astropart. Phys. 08 (2014) 007.
[177] H. Shimabukuro, K. Ichiki, S. Inoue, and S. Yokoyama, Phys. Rev. D **90**, 083003 (2014).
[178] I. P. Carucci, F. Villaescusa-Navarro, M. Viel, and A. Lapi, J. Cosmol. Astropart. Phys. 07 (2015) 047.

The Astrophysical Journal, 852:139 (7pp), 2018 January 10 https://doi.org/10.3847/1538-4357/aa9ff5

Warm Dark Matter and Cosmic Reionization

Pablo Villanueva-Domingo[1], Nickolay Y. Gnedin[2,3,4], and Olga Mena[1]
[1] Instituto de Física Corpuscular (IFIC), CSIC-Universitat de València, Apartado de Correos 22085, E-46071, Spain
[2] Particle Astrophysics Center, Fermi National Accelerator Laboratory, Batavia, IL 60510, USA; gnedin@fnal.gov
[3] Kavli Institute for Cosmological Physics, The University of Chicago, Chicago, IL 60637 USA
[4] Department of Astronomy & Astrophysics, The University of Chicago, Chicago, IL 60637 USA
Received 2017 September 18; revised 2017 November 8; accepted 2017 December 4; published 2018 January 16

Abstract

In models with dark matter made of particles with keV masses, such as a sterile neutrino, small-scale density perturbations are suppressed, delaying the period at which the lowest mass galaxies are formed and therefore shifting the reionization processes to later epochs. In this study, focusing on Warm Dark Matter (WDM) with masses close to its present lower bound, i.e., around the 3 keV region, we derive constraints from galaxy luminosity functions, the ionization history and the Gunn–Peterson effect. We show that even if star formation efficiency in the simulations is adjusted to match the observed UV galaxy luminosity functions in both CDM and WDM models, the full distribution of Gunn–Peterson optical depth retains the strong signature of delayed reionization in the WDM model. However, until the star formation and stellar feedback model used in modern galaxy formation simulations is constrained better, any conclusions on the nature of dark matter derived from reionization observables remain model-dependent.

Key words: cosmology: theory – galaxies: formation – intergalactic medium – large-scale structure of universe – methods: numerical

1. Introduction

The current canonical cosmological model, the so-called Λ-Cold Dark Matter (ΛCDM) scenario, assumes that dark matter is made of totally cold weakly interacting particles, representing ∼26% of the universe mass-energy density. This very simple framework provides an accurate description of both large-scale structure observations (Alam et al. 2017) and the temperature and polarization anisotropies of the Cosmic Microwave Background (CMB) measured with unprecedented precision by the *Planck* satellite (Ade 2016). However, the precise microphysics and, ultimately, the nature of dark matter remains undiscovered (Bertone et al. 2005; Bergstrom 2012). Particle physics models cover a very wide range for possible masses, interactions, and free-streaming scales for the dark matter particles. The last property is probably the most interesting one for cosmological and astrophysical observations. Free-streaming allows the dark matter particles to propagate out of density perturbations, suppressing the growth of structure at scales smaller than a characteristic scale. For practical purposes, such a scale is totally irrelevant for CDM particles. However, there are a number of well-motivated hypothesized particles (such as sterile neutrinos) for which its free-streaming nature is very relevant and cannot be neglected when computing our universe's structure formation history.

Besides the fact that particle physics provides excellent *theoretically*-motivated dark matter candidates with non-negligible free-streaming scales, there also exist several *observational* indications that are sometimes interpreted as the so-called "small-scale crisis" of the ΛCDM model (see Bullock & Boylan-Kolchin 2017, for the recent review). These further motivate the search for alternatives to the standard CDM scenario: abundances and kinematics of gravitationally bound structures predicted in purely collisionless, not-accounting-for-any-baryonic-physics numerical simulations of the ΛCDM paradigm are not consistent with several observational measures of analogous quantities in the Local Group and other nearby galaxies (Klypin et al. 1999; Moore et al. 1999; Boylan-Kolchin et al. 2012). Plenty of work has been devoted to trying to resolve these existing controversies at galactic and sub-galactic scales (Lovell et al. 2012, 2014, 2016, 2017; Vogelsberger et al. 2012; Sawala et al. 2013, 2016; Polisensky & Ricotti 2014; Fattahi et al. 2016; Schewtschenko et al. 2016; Wang et al. 2017; Nakama et al. 2017). Among the possible solutions, a Warm Dark Matter (WDM) candidate with a ∼keV mass will have a non-negligible free-streaming scale, providing one of several potential explanations. Furthermore, claims of the detection of a monochromatic line at 3.56 keV in X-ray data toward the Andromeda and Perseus Cluster were reported in Bulbul et al. (2014), Boyarsky et al. (2014). Such a line has been identified as the radiative decay of a WDM keV sterile neutrino into a photon plus an active neutrino state ($\nu_s \rightarrow \gamma\nu$). The Ly$\alpha$ power spectra from distant quasars has been shown to provide a robust tool where to test and extract the most constraining bounds on the mass of a thermal WDM relic (Viel et al. 2005, 2006, 2008, 2013; Seljak et al. 2006; Boyarsky et al. 2009; Baur et al. 2016; Iršič et al. 2017; Yèche et al. 2017), albeit it is subject to potential uncertainties in the modeling of dynamics and thermodynamics of the Inter Galactic Medium (IGM) at low and intermediate redshifts.

In this work, we focus on the constraints on the WDM mass around the 3 keV region (where current constraints lie (Iršič et al. 2017; Yèche et al. 2017)) from the reionization period (Barkana et al. 2001; Somerville et al. 2003; Yoshida et al. 2003; Yue & Chen 2012; Pacucci et al. 2013; Mesinger et al. 2014; Schultz et al. 2014; Lapi & Danese 2015; Bose et al. 2016, 2017; Menci et al. 2016; Corasaniti et al. 2017; Dayal et al. 2017; Lopez-Honorez et al. 2017), when the ultraviolet photons emitted by the first forming galaxies ionized the neutral IGM. With its free-streaming nature, WDM particles wash out small-scale overdensities, delaying the formation of the lowest mass galaxies (which are among the

main sources of ionizing photons), and, consequently, shifting the reionization processes to later epochs.

We make use of extensive hydrodynamical simulations, which model the complex physics involved in the cosmic reionization processes. Therefore, we self-consistently account for a wide range of physical effects such as star formation and stellar feedback, non-equilibrium ionization of hydrogen and helium, etc. (Gnedin 2014); several of them are highly degenerate with the WDM free-streaming nature. We then compare the results arising from our hydrodynamical simulations to a set of reionization-related observables. We consider measurements of the UV galaxy luminosity functions (Bouwens et al. 2015), the ionization fraction of the universe (Fan et al. 2006), and distributions of the Gunn–Peterson optical depth (Becker et al. 2015).

All in all, our calculations show that, while there is little hope in distinguishing among several possible WDM scenarios and the canonical ΛCDM case using current astronomical measurements of the observables listed above, future observations with the *James Webb Space Telescope* (*JWST*; Gardner et al. 2006) may reach the required sensitivity to differentiate WDM from CDM in reionization observables, if systematic uncertainties due to currently poorly known reionization ingredients, such as stellar feedback, can be reduced and kept under control by, e.g., future progress in constraining galaxy formation models.

2. WDM Cosmologies

WDM is characterized by having non-negligible thermal velocities at high redshifts, suppressing the growth of structures on scales below a free-streaming length, which depends on the mass of the WDM particle m_X, and it is typically of the order of 100 kiloparsecs for keV WDM candidates. The free-streaming scale can be computed as the distance over which such a particle can travel until the time of matter radiation equality $t_{\rm eq}$ (Kolb & Turner 1990; Schneider et al. 2012), while more accurate predictions require numerical simulations (Bode et al. 2001). In contrast to the standard WIMP scenario, WDM particles are still relativistic at the decoupling epoch, but non-relativistic at $t_{\rm eq}$, when substantial growth of perturbations becomes possible. Hereafter, we consider that all the dark matter is warm and that it was thermally decoupled in the early universe. Predictions for non-thermal relics as non-resonantly produced sterile neutrinos can be easily related to our results (c.f. Viel et al. 2005).

The WDM free-streaming nature leads to a CDM-like power spectrum with a cutoff, which is around a scale 10^{10} (10^{8}) $M_\odot$ for $m_X \simeq 1$ (3) keV, below Milky Way-like galaxy sizes. Consequently, the WDM power spectrum, $P_{\rm WDM}(k)$, can be written in terms of that for CDM $P_{\rm CDM}(k)$ through a transfer function $T_{\rm WDM}(k)$, which accounts for the suppression on small scales (Bode et al. 2001):

$$P_{\rm WDM}(k) = T^2_{\rm WDM}(k)\, P_{\rm CDM}(k). \quad (1)$$

This transfer function has to be obtained from a numerical Boltzmann code in order to accurately account for free-streaming. A common fit is given by Bode et al. (2001), Viel et al. (2005)

$$T_{\rm WDM}(k) = (1 + (\alpha k)^{2\nu})^{-5/\nu}, \quad (2)$$

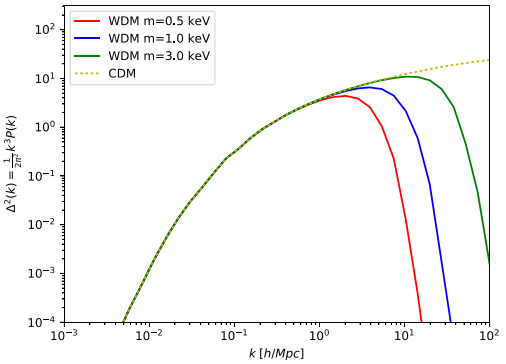

Figure 1. Dimensionless linear power spectrum $\Delta^2(k) = \frac{1}{2\pi^2}k^3P(k)$ for several values of the WDM particle mass m_X, together with the ΛCDM case.

with $\nu = 1.12$ and the breaking scale

$$\alpha = 0.049\left(\frac{\rm keV}{m_X}\right)^{1.11}\left(\frac{\Omega_X}{0.25}\right)^{0.11}\left(\frac{h}{0.7}\right)^{1.22} {\rm Mpc}\ h^{-1}, \quad (3)$$

being Ω_X the dark matter density fraction over the critical density, and h is the reduced Hubble constant. Other parameterizations have been used in the literature, such as that of Villaescusa-Navarro & Dalal (2011), who present a different choice of the breaking scale α in terms of the free-streaming length. The dependence of the dimensionless power spectrum $\Delta^2(k) = \frac{1}{2\pi^2}k^3P(k)$ on the WDM particle mass m_X is shown in Figure 1 for several values of m_X. Notice that, the lighter the particle is, the smaller is the value of k at which the suppression of the power spectrum appears.

3. Simulations and Their Calibration

For modeling the formation of cosmic structure and the process of reionization, we use numerical technology from the Cosmic Reionization On Computers (CROC) project (Gnedin 2014; Gnedin & Kaurov 2014). These simulations include a wide range of physical effects that are relevant for accurately modeling the cosmic reionization, such as the dynamics of dark matter and cosmic gas, star formation and stellar feedback, non-equilibrium ionization of hydrogen and helium, fully coupled three-dimensional radiative transfer, radiation-field-dependent cooling and heating functions for the metal enriched cosmic gas, etc. (see Gnedin 2014, for more details).

As the primary effect of WDM is on small spatial and mass scales, in this paper we only use simulations in computational boxes of 20 h^{-1} Mpc on a side. As our results demonstrate, it would simply be a waste of computational resources to use larger boxes. Specifically, we use the simulations from the "Caiman" series introduced in Gnedin et al. (2017). The primary advantage of these new series over the original simulations from Gnedin (2014) is that the new runs include corrections for weak numerical convergence (Gnedin 2016a) and, hence, deliver numerically converged results. Specifically, we use *Planck* cosmology; the mass resolution of our simulations is $M_{\rm l} = 7 \times 10^6 M_\odot$ and the spatial resolution is kept fixed in physical units to 100 pc, just as in Gnedin et al. (2017).

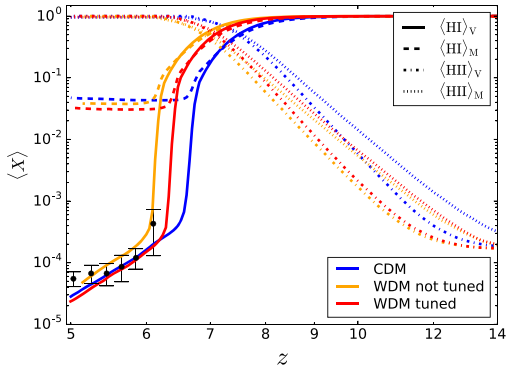

Figure 2. Ionization histories for a single realization (A) of the CDM model (blue lines), the WDM model with identical physical and numerical parameters ("not *tuned* WDM," orange lines) and the WDM model with 50% higher star formation efficiency ("*tuned* WDM," red lines). Solid (dotted–dashed) lines correspond to the volume-weighted H I (H II) fraction, while dashed (dotted) lines correspond to the mass-weighted H I (H II) fraction. The measurements are from Fan et al. (2006).

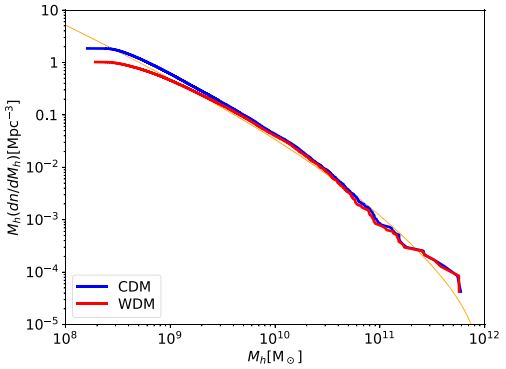

Figure 3. Halo mass function for the CDM (blue) and WDM (red) case as well as theoretical expectation (orange) using Tinker et al. (2008) fitting formula. We avoid artificial numerical fragmentation, typical of WDM simulations, due to our particular refinement criterion.

We use three sets of simulations in this paper. The pure CDM set (the same one used in Gnedin et al. 2017) includes six independent realizations (labeled A–F) that are combined in computing averaged quantities to approximate true averages over the infinite universe. The second set includes a single realization (A) of a WDM model with all physical and numerical parameters kept identical to the CDM case. Finally, the third set includes four out of six independent realizations (A, B, D, E) with the WDM model and star formation efficiency increased by a factor of 1.5 (or, equivalently, the gas depletion time decreased by a factor 1.5) compared to the CDM case. The particular choice of these four realizations is motivated by the property that the average over them in the pure CDM simulation set for all of the quantities considered in this paper is virtually identical to analogous averages over all six realizations. Hence, these four realizations serve as a good approximation to the average universe.

The reason for adjusting the star formation efficiency is given in Figure 2. It shows ionization histories for the first realization (A) for the three simulations sets we consider. The original CROC CDM simulations were calibrated against the diverse observational data to ensure the best achievable (not necessarily good) match. In particular, they match the observed mean opacity in the spectra of high-redshift quasars from Fan et al. (2006). The WDM model with identical physical and numerical parameters does not match these data, because the lack of small-scale power reduces star formation and, hence, ionizing emissivity of dwarf galaxies. But parameters like star formation efficiency and ionizing emissivity are phenomenologically adjustable parameters; they cannot yet be constrained from the first principles. Hence, the WDM simulations need to be re-calibrated again to ensure the best possible match with the data, in order to be a viable theoretical model.

We have performed such re-calibration, and it turns out that it is only sufficient to increase the star formation efficiency by 50%, while keeping fixed all other physical and numerical parameters to the previously calibrated values. Ionization history for the *tuned* WDM model is also shown in Figure 2 with the red lines. As one can see, it offers an identically good fit to Fan et al. (2006) data. We shall elaborate further on this point in our Results section.

In the remainder of this paper, we will show that such a *tuned* WDM model also fits some (but not all) observational constraints as well as the best-calibrated CDM model. Hence, hereafter we will only compare the CDM simulation set and the simulations set of the re-calibrated WDM model; we will drop the qualification *tuned* for clarity, as the proper comparison between the two models is for their best-calibrated realizations, not between models with the same physical and numerical parameters (in which case one of them would not be properly calibrated).

A particular challenge in modeling Warm or Hot Dark Matter with simulations is artificial numerical fragmentation, which has been extensively discussed in the literature (Wang & White 2007; Angulo et al. 2013; Schneider et al. 2013; Banerjee & Dalal 2016). Shot noise due to initial random thermal velocities can seed unphysical overdensities at small scales, which lead to the formation of spurious structures as the simulation evolves. As a result, there is an unphysical overabundance of low-mass halos, just the opposite from what is expected for a WDM model.

There exist several numerical approaches for suppressing this artificial fragmentation (Angulo et al. 2013; Hobbs et al. 2016). In this work, we adopt an alternative, simpler approach that is sufficient for our purpose, but may not be applicable for higher mass resolution simulations. CROC simulations use the Adaptive Refinement Tree (ART) code (Kravtsov 1999; Kravtsov et al. 2002; Rudd et al. 2008) that implements an Adaptive Mesh Refinement technique. The mesh refinement and de-refinement strategies are essentially user-definable; in CROC simulations, refinement is implemented in a quasi-Lagrangian manner, striving to keep the mass per cell approximately constant, but the refinement is performed only on the gas density and not on the dark matter density. Because artificial numerical fragmentation typically produces halos with masses too small to contain any appreciable amount of baryons (Okamoto et al. 2008; Lovell et al. 2014), the computational mesh (and, hence all gravity calculations) is not refined at the potential locations of such halos, and thus they simply do not form in CROC simulations. This is apparent from Figure 3,

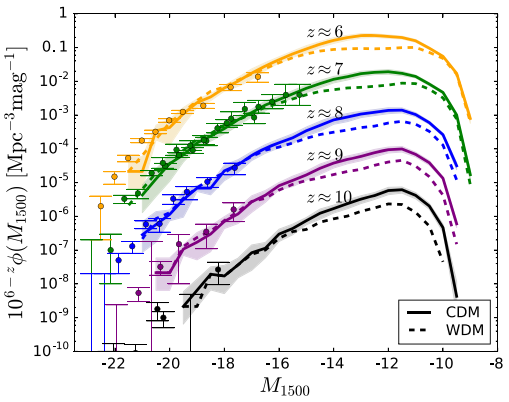

Figure 4. Galaxy UV luminosity functions at five different redshifts for CDM (solid) and WDM (dashed) simulations. Colored bands show the rms variations between four independent realizations (shown for the CDM case only). Points with error bars from Bouwens et al. (2015).

which shows halo mass functions for the CDM and WDM simulations with identical numerical parameters.

It is important to note here that the simulations presented in Figure 3 have limited mass resolution, resolving halos down to $M_h \approx 3 \times 10^8 M_\odot$ (the mass at which the simulated CDM halo mass function deviates from the theoretical expectation). It is possible that for higher resolution simulations, artificial numerical fragmentation would appear even with our choice of refinement criteria.

4. Results

4.1. Galaxy Luminosity Functions

Galaxy UV luminosity functions represent one of the best observables to constrain the properties of reionization sources. Current *HST* observations have managed to measure UV magnitudes ~ -15 at $z \lesssim 8$ and reach redshifts $z \sim 10$ (Bouwens et al. 2015). Despite their high sensitivity, the current observations are still insensitive to the faint end of the UV luminosity function for the range of galaxy luminosities affected by the nature of dark matter. In Gnedin (2016b), it was shown that simulations agree well with current measurements, and that the usual Schechter fit can provide a good description of the luminosity functions over the currently measured range of luminosities.

Figure 4 depicts one of the main results of this study. We plot the simulated UV galaxy luminosity functions for $z = 6$, 7, 8, 9, and 10, together with current observations from Bouwens et al. (2015). The solid lines depict the CDM scenario, while the dashed lines show the predictions for a WDM particle with a mass $m_X = 3$ keV. Notice that both models match well each other *and* the existing measurements; however, at lower luminosities, the WDM model predicts fewer galaxies, as expected. It is worth highlighting that (a) there is a difference between the CDM and WDM cosmologies for magnitudes ~ -14 and further beyond, and (b) this difference is almost redshift independent.

The current observations have not yet reached this crucial region, and existing data do not allow us to distinguish among the CDM and WDM models. However, the future *JWST* observations will be able to probe galaxy luminosity functions at redshifts $z \sim 8$–10 down to magnitudes ~ -13 by taking advantage of gravitational lensing effects. Whether these observations will be able to actually constraint the nature of dark matter is, however, unclear, due to inherent theoretical uncertainty in predicting galaxy luminosity functions at these faint magnitudes. We expand on this subject further in the Conclusions section.

Another feature of modeled galaxy luminosity function in Figure 4 is the steep turnover at $M_{1500} \approx -10$. This turnover is only weakly sensitive to the nature of dark matter and is highly model dependent. It is caused by the primary assumption made in CROC simulations that stars form predominantly in molecular gas. As halos with masses below about $10^8 M_\odot$ contain little molecular gas, they contribute respectively little to star formation (and, hence to UV luminosity). This result, we emphasize again, is a theoretical assumption, not a known fact. Several recent large computational projects achieved a similar level of precision in matching observational constraints to the CROC projects, and they all predict the turnover to occur at widely varying luminosities (Bouwens et al. 2017). Hence, the location and the shape of the turnover cannot be considered as a reliable theoretical prediction and will have to be constrained by future observations.

4.2. Ionization History

The ionization history of the universe may also offer a tool to constrain the dark matter nature. The ionization history is given by the volume filling factor of the ionized hydrogen $Q_{\rm H\,II}$, whose evolution follows the reionization equation of Madau et al. (1999):

$$\frac{dQ_{\rm H\,II}}{dt} = \frac{\dot{n}_{\rm ion}}{n_{\rm H}} - \frac{Q_{\rm H\,II}}{\bar{t}_{\rm rec}}, \tag{4}$$

where $\dot{n}_{\rm ion}$ is the globally averaged rate of production of hydrogen ionizing photons, which can be related with the star formation rate $\dot{\rho}_*$ through (Robertson et al. 2015)

$$\dot{n}_{\rm ion} = f_{\rm esc}\, \xi_{\rm ion}\, \dot{\rho}_*, \tag{5}$$

where $f_{\rm esc}$ is the effective escape fraction of ionizing photons and $\xi_{\rm ion}$ is the ionizing photon production efficiency per unit star formation rate.

As previously stated, in WDM cosmologies, free-streaming of dark matter particles suppresses small-scale fluctuations, delaying structure formation and, therefore, the onset of the overall reionization process. The effect will be more pronounced for smaller WDM masses (see Figure 1). However, after a quick inspection of Equation (5), one can notice that the eventual smaller ionized fraction in the presence of a WDM particle could be easily accommodated by an increase of the star formation rate/effective escape fraction of ionizing photons, leaving unchanged the volume filling factor. Therefore, as anticipated in Section 3 and illustrated in Figure 2, it is always possible to match the ionization history of a given WDM cosmology to that expected in the standard CDM picture and be perfectly consistent with SDSS high-redshift quasars observations at $5.74 < z < 6.42$ (Fan et al. 2006).

While Figure 2 shows that some differences between our CDM and WDM models remain even after tuning, it is unlikely to be a detectable difference, as we have only tuned the star formation efficiency. There exist many more parameters that

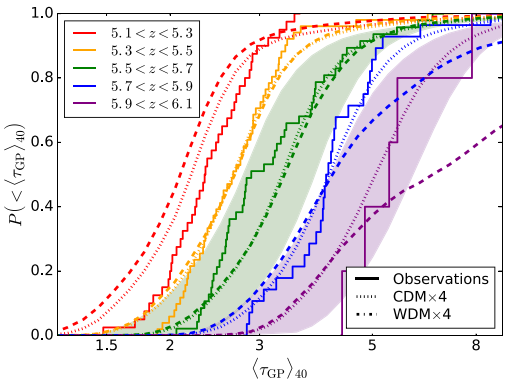

Figure 5. Probability distribution functions for the effective IGM opacity in 40 h^{-1}Mpc sight line segments from our simulations. Solid lines correspond to CDM, dashed to WDM. Colored bands show the rms variations between four independent realizations (shown for the CDM case for $5.5 < z < 5.7$ and $5.9 < z < 6.1$ bins only). Observational data are from Becker et al. (2015) and Gnedin et al. (2017). Later reionization in the WDM model is easily detectable by the data.

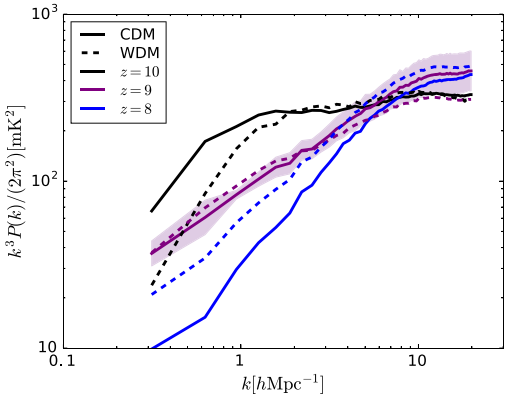

Figure 6. Power spectra of redshifted 21 cm emission for CDM (solid) and WDM (dashed) models, at several redshifts where the signal is sufficiently high. The purple band shows the rms variation between four independent realizations (shown for the CDM case at $z = 9$ only).

can also be tuned in the simulations (cosmological parameters, feedback models, ionizing efficiency, etc.) to achieve an even better agreement between CDM and WDM models.

4.3. Post-reionization IGM

Galaxy UV luminosity functions offer a strong constraint on the sources of ionizing photons during reionization. Another observational probe of the final stages of reionization and its immediate aftermath comes from the observations of absorption spectra of high-redshift quasars. With the sample of quasars discovered at $z > 6$ exceeding 100 (Bañados et al. 2016), one cannot only accurately measure the mean Gunn–Peterson opacity (as shown in Figure 2), but also determine their full probability distribution functions (PDFs; Becker et al. 2015).

Resonant scattering in the Lyα line of (remaining after reionization residual) neutral hydrogen depletes the observed flux from a distant quasar by a factor $e^{-\tau}$, being τ the Gunn–Peterson optical depth. The value of τ is highly (quadratically) sensitive to the distribution of neutral hydrogen $n_{\rm H\,I}$ along a given line of sight. In order to have a statistical description of the Lyα opacity, one usually averages the normalized flux over a number of lines of sight $\langle F\rangle$. It is customary to define an effective averaged optical depth $\tau_{\rm eff}$ as

$$\tau_{\rm eff} = -\ln\langle F\rangle_L, \tag{6}$$

where L is the distance along the line of sight over which the averaging is performed.

We compute from our simulations the PDF of $\tau_{\rm eff}$ and its cumulative distribution $P(\leqslant\tau_{\rm eff})$, i.e., the probability of having an optical depth lower than $\tau_{\rm eff}$. We test our predictions against the measurements obtained by Becker et al. (2015) in Figure 5, with averaging performed over sight line segments of comoving length $L = 40\,h^{-1}$ Mpc, as in Gnedin et al. (2017), who demonstrated that this segment length is reliably modeled by CROC simulations. Because the optical depth increases with redshift, the cumulative probability distribution is shifted to higher values of τ, as z increases.

The effect of the WDM free-streaming nature on the Gunn–Peterson optical depth is easy to understand: as reionization is delayed in the WDM case, the higher density (and, hence, higher optical depth) regions get ionized later (Miralda-Escudé et al. 2000; Kaurov 2016), extending the high $\tau_{\rm eff}$ tail toward larger values. The lower density regions, which have been ionized early enough, follow similar ionization states in both CDM and WDM models. While with the existing data, the CDM scenario is favored, it is at present unclear if the discrepancy can be eliminated by appropriately tweaking star formation and stellar feedback models in the WDM scenario. Nevertheless, a smaller WDM mass than the one considered here (for instance, a lighter WDM particle with $m_X \sim 2$ keV) would only increase the discrepancy with observations, and therefore such a scenario appears increasingly unlikely.

Both models also fail to match observations at $z < 5.3$. This discrepancy was noted in the first CROC papers (Gnedin 2014; Gnedin & Kaurov 2014) and was interpreted as a failure of the adopted stellar feedback model.

4.4. Redshifted 21 cm Emission

Another potential strong constraint on the process of reionization is offered by the redshifted 21 cm emission from neutral hydrogen. While the idea to use that emission as a probe of reionization has been around for a long time (see Pritchard & Loeb 2012 for a recent review), only recently interesting observational constraints have been placed by Murchison Widefield Array (MWA; Dillon et al. 2014, 2015) and Donald C. Backer Precision Array for Probing the Epoch of Reionization (PAPER; Parsons et al. 2014; Ali et al. 2015; Jacobs et al. 2015; Pober et al. 2015).

In Figure 6, we show simulated power spectra of redshifted 21 cm emission (the currently most favorable statistical probe of the reionization signal) at several redshifts. In order to understand the behavior of the 21 cm power spectrum P_{21}, we have to recall that the power spectrum depends both on the matter overdensity δ and on the neutral fraction $x_{\rm H\,I}$. At the higher redshifts ($z \sim 10$), before reionization starts, the power spectrum in WDM cosmologies is suppressed with respect to the CDM case due to the free-streaming nature of the WDM

particle. At redshifts of $z \simeq 8$, the reionization process has already started in the CDM model, reducing the hydrogen neutral fraction and diminishing the 21 cm power spectrum signal. That is not the case for the WDM cosmology, in which the entire reionization process is delayed. The interplay between the free streaming and the delayed reionization present in the WDM scenario explains the decrease at $z = 8$ and the increase at $z = 10$ at scales $k \sim 1\ h\ \mathrm{Mpc}^{-1}$ in the WDM 21 cm power spectrum relative the CDM model. Consequently, even if the differences between the CDM and WDM models are non-trivial, they are probably not large enough to be detectable by the first generation of experiments.

5. Conclusions

WDM scenarios with free-streaming scales of ∼Mpc, while giving excellent predictions for the measurements of the large-scale structure of the universe, also offer an appealing solution to several unresolved difficulties in the standard CDM paradigm, such as the so-called "small-scale crisis" (missing satellite, too-big-to-fail, and core-cusp problems) and the controversial detection of a monochromatic line at 3.56 keV in X-ray data. Furthermore, particle physics renders many well-motivated theoretical scenarios in which WDM candidates arise naturally (e.g., sterile neutrinos).

It is therefore timely to explore what the reionization history of the universe can currently tell about the nature of dark matter, specifically focusing on a WDM particle mass of ∼3 keV, the present lower bound from CMB and Lyα forest power spectra. The formation of cosmic structure and the process of reionization are sufficiently realistically simulated via the CROC project (Gnedin 2014; Gnedin & Kaurov 2014). These simulations account for the dynamics of dark matter and cosmic gas, star formation and stellar feedback, non-equilibrium ionization of hydrogen and helium, fully coupled three-dimensional radiative transfer, and radiation-field-dependent cooling and heating functions for the metal enriched cosmic gas. Three sets of simulations have been produced: the canonical CDM cosmology case, a WDM model with identical parameters to the CDM case, and a WDM model in which the star formation rate is increased by a factor of 1.5.

We have shown that the lack of small-scale power in WDM cosmology (relative to the equivalent CDM case) due to the non-negligible free-streaming length of WDM particle considerably delays the reionization processes. However, a higher star formation efficiency (or, equivalently, a lower gas depletion time) compensates for the WDM-suppressed small-scale structure, leading to nearly identical (within the currently observationally constrained range) galaxy luminosity functions in the CDM and WDM cases. Such tuning of the star formation efficiency in our simulations is perfectly justified, as this quantity still remains a parameter, adjustable within reasonable bounds, which currently can be derived neither from the first principles nor from observational constraints.

A so tuned WDM model never-the-less underpredicts (as compared to the pure CDM case) the abundance of galaxies with UV magnitudes below about −15, the range of galactic luminosities well within reach of the soon-to-be-launched *JWST* telescope (which is expected to measure the faint end of the galaxy UV luminosity function down to $M_{\mathrm{UV}} \simeq -13$). The WDM model also differs significantly from the CDM case in the predicted redshifted 21 cm emission.

Clustering and luminosity functions of Lyα emitters (Konno et al. 2017; Ouchi et al. 2017) may offer another possible test of WDM scenarios. In practice, such a test strongly relies on comparisons with analytical models and therefore is a highly model-dependent probe of reionization.

However, by far the most significant signature of delayed reionization in the WDM case is the distribution of Gunn–Peterson optical depth in the spectra of high-redshift quasars—perhaps the most constraining observational data on cosmic reionization today. Both the Planck value of the Thomson optical depth (Adam et al. 2016; Aghanim et al. 2016) and the ionization state of low density IGM significantly constrain reionization history with the existing data. Both of those constraints push reionization to lower redshifts. This push is, however, resisted by the observational constraints on the ionization state of higher density gas (i.e., higher τ_{eff} tail of Gunn–Peterson optical depth distributions). Hence, the overall shape of PDFs of τ_{eff} is strongly constraining. In particular, our WDM model fails that observational test by a large margin even after adjusting the star formation efficiency.

Despite all of these observational signatures, the question of whether the nature of dark matter can be constrained by observational tests of cosmic reionization remains open. In our simulations, we tuned the star formation efficiency to reproduce the observed UV luminosity functions in both CDM and WDM models, but galaxy formation simulations include much more uncertainty than just one parameter—the full model of star formation and stellar feedback is largely unconstrained. For example, it is possible that some other change to the stellar feedback model adopted in the simulations may reduce the feedback strength and make the WDM model more consistent with observations. However, such a change must be highly non-trivial, as the stellar feedback in CROC simulations is already too weak: it fails to reduce star formation by $z = 5$ sufficiently to match the Gunn–Peterson data for $z < 5.3$.

Thus, whether reionization observables can actually be used to constraint the nature of dark matter ultimately depends on the ability of future simulations to predict the shape of galaxy luminosity function precisely—a strict requirement, only possible if the physics of star formation and stellar feedback in these dwarf, high-redshift galaxies can be constrained sufficiently accurately. The field of galaxy formation is seeing lighting speed progress in modeling stellar feedback, but the required precision in modeling galaxy luminosity functions remains a high order, and only the future will show whether that order can be fulfilled.

O.M. and P.V.D. would like to thank the Fermilab Theoretical Physics Department for hospitality. O.M. and P.V.D. are supported by PROMETEO II/2014/050, by the Spanish Grants SEV-2014-0398 and FPA2014–57816-P of MINECO and by the European Union's Horizon 2020 research and innovation program under the Marie Skłodowska-Curie grant agreements No. 690575 and 674896.

This manuscript has been authored in part by Fermi Research Alliance, LLC under contract No. DE-AC02-07CH11359 with the U.S. Department of Energy, Office of Science, Office of High Energy Physics. The United States Government retains and the publisher, by accepting the article for publication, acknowledges that the United States Government retains a non-exclusive, paid-up, irrevocable, world-wide license to publish or reproduce the published form

of this manuscript, or allow others to do so, for United States Government purposes. This research used resources of the Argonne Leadership Computing Facility, which is a DOE Office of Science User Facility supported under Contract DE-AC02-06CH11357. An award of computer time was provided by the Innovative and Novel Computational Impact on Theory and Experiment (INCITE) program. This research is also part of the Blue Waters sustained-petascale computing project, which is supported by the National Science Foundation (awards OCI-0725070 and ACI-1238993) and the state of Illinois. Blue Waters is a joint effort of the University of Illinois at Urbana-Champaign and its National Center for Supercomputing Applications. This work made extensive use of the NASA Astrophysics Data System and arXiv.org preprint server.

References

Adam, R., Aghanim, N., Ashdown, M., et al. 2016, A&A, 596, A108
Ade, P. A. R., Roca-Fàbrega, S., de Bruijne, J., & Prusti, T. 2016, A&A, 594, A13
Aghanim, N., Ashdown, M., Aumont, J., et al. 2016, A&A, 596, A107
Alam, S., Ata, M., Bailey, S., et al. 2017, MNRAS, 470, 2617
Ali, Z. S., Parsons, A. R., Zheng, H., et al. 2015, ApJ, 809, 61
Angulo, R. E., Hahn, O., & Abel, T. 2013, MNRAS, 434, 3337
Bañados, E., Venemans, B. P., Decarli, R., et al. 2016, ApJS, 227, 11
Banerjee, A., & Dalal, N. 2016, JCAP, 1611, 015
Barkana, R., Haiman, Z., & Ostriker, J. P. 2001, ApJ, 558, 482
Baur, J., Palanque-Delabrouille, N., Yèche, C., Magneville, C., & Viel, M. 2016, JCAP, 1608, 012
Becker, G. D., Bolton, J. S., Madau, P., et al. 2015, MNRAS, 447, 3402
Bergstrom, L. 2012, AnP, 524, 479
Bertone, G., Hooper, D., & Silk, J. 2005, PhR, 405, 279
Bode, P., Ostriker, J. P., & Turok, N. 2001, ApJ, 556, 93
Bose, S., Frenk, C. S., Hou, J., Lacey, C. G., & Lovell, M. R. 2016, MNRAS, 463, 3848
Bose, S., Hellwing, W. A., Frenk, C. S., et al. 2017, MNRAS, 464, 4520
Bouwens, R. J., Illingworth, G. D., Oesch, P. A., et al. 2015, ApJ, 803, 34
Bouwens, R. J., Oesch, P. A., Illingworth, G. D., Ellis, R. S., & Stefanon, M. 2017, ApJ, 843, 129
Boyarsky, A., Lesgourgues, J., Ruchayskiy, O., & Viel, M. 2009, JCAP, 0905, 012
Boyarsky, A., Ruchayskiy, O., Iakubovskyi, D., & Franse, J. 2014, PhRvL, 113, 251301
Boylan-Kolchin, M., Bullock, J. S., & Kaplinghat, M. 2012, MNRAS, 422, 1203
Bulbul, E., Markevitch, M., Foster, A., et al. 2014, ApJ, 789, 13
Bullock, J. S., & Boylan-Kolchin, M. 2017, ARA&A, 55, 343
Corasaniti, P. S., Agarwal, S., Marsh, D. J. E., & Das, S. 2017, PhRvD, 95, 083512
Dayal, P., Choudhury, T. R., Bromm, V., & Pacucci, F. 2017, ApJ, 836, 16
Dillon, J. S., Liu, A., Williams, C. L., et al. 2014, PhRvD, 89, 023002
Dillon, J. S., Neben, A. R., Hewitt, J. N., et al. 2015, PhRvD, 91, 123011
Fan, X.-H., Strauss, M. A., Becker, R. H., et al. 2006, AJ, 132, 117
Fattahi, A., Navarro, J. F., Sawala, T., et al. 2016, MNRAS, submitted
Gardner, J. P., Mather, J. C., Clampin, M., et al. 2006, SSRv, 123, 485
Gnedin, N. Y. 2014, ApJ, 793, 29
Gnedin, N. Y. 2016a, ApJ, 821, 50
Gnedin, N. Y. 2016b, ApJL, 825, L17
Gnedin, N. Y., Becker, G. D., & Fan, X. 2017, ApJ, 841, 26
Gnedin, N. Y., & Kaurov, A. A. 2014, ApJ, 793, 30
Hobbs, A., Read, J., Agertz, O., Iannuzzi, F., & Power, C. 2016, MNRAS, 458, 468
Iršič, V., Viel, M., Haehnelt, M. G., et al. 2017, PhRvD, 96, 023522
Jacobs, D. C., Pober, J. C., Parsons, A. R., et al. 2015, ApJ, 801, 51
Kaurov, A. A. 2016, ApJ, 831, 198
Klypin, A. A., Kravtsov, A. V., Valenzuela, O., & Prada, F. 1999, ApJ, 522, 82
Kolb, E. W., & Turner, M. S. 1990, FrP, 69, 1
Konno, A., Ouchi, M., Shibuya, T., et al. 2017, arXiv:1705.01222
Kravtsov, A. V. 1999, PhD thesis, New Mexico State Univ.
Kravtsov, A. V., Klypin, A. A., & Hoffman, Y. 2002, ApJ, 571, 563
Lapi, A., & Danese, L. 2015, JCAP, 1509, 003
Lopez-Honorez, L., Mena, O., Palomares-Ruiz, S., & Domingo, P. V. 2017, PhRvD, 96, 103539
Lovell, M. R., Bose, S., Boyarsky, A., et al. 2016, MNRAS, 461, 60
Lovell, M. R., Eke, V., Frenk, C., et al. 2012, MNRAS, 420, 2318
Lovell, M. R., Frenk, C. S., Eke, V. R., et al. 2014, MNRAS, 439, 300
Lovell, M. R., Gonzalez-Perez, V., Bose, S., et al. 2017, MNRAS, 468, 2836
Madau, P., Haardt, F., & Rees, M. J. 1999, ApJ, 514, 648
Menci, N., Grazian, A., Castellano, M., & Sanchez, N. G. 2016, ApJL, 825, L1
Mesinger, A., Ewall-Wice, A., & Hewitt, J. 2014, MNRAS, 439, 3262
Miralda-Escudé, J., Haehnelt, M., & Rees, M. J. 2000, ApJ, 530, 1
Moore, B., Quinn, T. R., Governato, F., et al. 1999, ApJL, 524, L19
Nakama, T., Chluba, J., & Kamionkowski, M. 2017, PhRvD, 95, 121302
Okamoto, T., Gao, L., & Theuns, T. 2008, MNRAS, 390, 920
Ouchi, M., Harikane, Y., & Shibuya, T. 2017, eprint (arXiv:1704.07455)
Pacucci, F., Mesinger, A., & Haiman, Z. 2013, MNRAS, 435, L53
Parsons, A. R., Liu, A., Aguirre, J. E., et al. 2014, ApJ, 788, 106
Pober, J. C., Ali, Z. S., Parsons, A. R., et al. 2015, ApJ, 809, 62
Polisensky, E., & Ricotti, M. 2014, MNRAS, 437, 2922
Pritchard, J. R., & Loeb, A. 2012, RPPh, 75, 086901
Robertson, B. E., Ellis, R. S., Furlanetto, S. R., & Dunlop, J. S. 2015, ApJL, 802, L19
Rudd, D. H., Zentner, A. R., & Kravtsov, A. V. 2008, ApJ, 672, 19
Sawala, T., Frenk, C., Fattahi, A., et al. 2016, MNRAS, 457, 1931
Sawala, T., Frenk, C. S., Crain, R. A., et al. 2013, MNRAS, 431, 1366
Schewtschenko, J. A., Baugh, C. M., Wilkinson, R. J., et al. 2016, MNRAS, 461, 2282
Schneider, A., Smith, R. E., Macciò, A. V., & Moore, B. 2012, MNRAS, 424, 684
Schneider, A., Smith, R. E., & Reed, D. 2013, MNRAS, 433, 1573
Schultz, C., Oñorbe, J., Abazajian, K. N., & Bullock, J. S. 2014, MNRAS, 442, 1597
Seljak, U., Makarov, A., McDonald, P., & Trac, H. 2006, PhRvL, 97, 191303
Somerville, R. S., Bullock, J. S., & Livio, M. 2003, ApJ, 593, 616
Tinker, J., Kravtsov, A. V., Klypin, A., et al. 2008, ApJ, 688, 709
Viel, M., Becker, G. D., Bolton, J. S., et al. 2008, PhRvL, 100, 041304
Viel, M., Becker, G. D., Bolton, J. S., & Haehnelt, M. G. 2013, PhRvD, 88, 043502
Viel, M., Lesgourgues, J., Haehnelt, M. G., Matarrese, S., & Riotto, A. 2005, PhRvD, 71, 063534
Viel, M., Lesgourgues, J., Haehnelt, M. G., Matarrese, S., & Riotto, A. 2006, PhRvL, 97, 071301
Villaescusa-Navarro, F., & Dalal, N. 2011, JCAP, 1103, 024
Vogelsberger, M., Zavala, J., & Loeb, A. 2012, MNRAS, 423, 3740
Wang, J., & White, S. D. M. 2007, MNRAS, 380, 93
Wang, L., Gonzalez-Perez, V., Xie, L., et al. 2017, MNRAS, 468, 4579
Yèche, C., Palanque-Delabrouille, N., Baur, J., & du Mas des Bourboux, H. 2017, JCAP, 1706, 047
Yoshida, N., Sokasian, A., Hernquist, L., & Springel, V. 2003, ApJL, 591, L1
Yue, B., & Chen, X. 2012, ApJ, 747, 127

Journal of Cosmology and Astroparticle Physics
An IOP and SISSA journal

Was there an early reionization component in our universe?

Pablo Villanueva-Domingo,[a] **Stefano Gariazzo,**[a] **Nickolay Y. Gnedin**[b,c,d] **and Olga Mena**[a]

[a]Instituto de Física Corpuscular (IFIC), CSIC-Universitat de València, Apartado de Correos 22085, E-46071, Spain
[b]Particle Astrophysics Center, Fermi National Accelerator Laboratory, Batavia, IL 60510, U.S.A.
[c]Kavli Institute for Cosmological Physics, The University of Chicago, Chicago, IL 60637, U.S.A.
[d]Department of Astronomy & Astrophysics, The University of Chicago, Chicago, IL 60637, U.S.A.

E-mail: pablo.villanueva@ific.uv.es, gariazzo@ific.uv.es, gnedin@fnal.gov, omena@ific.uv.es

Received December 15, 2017
Accepted March 26, 2018
Published April 6, 2018

Abstract. A deep understanding of the epoch of reionization is still missing in our knowledge of the universe. While future probes will allow us to test the precise evolution of the free electron fraction from redshifts between $z \simeq 6$ and $z \simeq 20$, at present one could ask what kind of reionization processes are allowed by present cosmic microwave background temperature and polarization measurements. An early contribution to reionization could imply a departure from the standard picture where star formation determines the reionization onset. By considering a broad class of possible reionization parameterizations, we find that current data do not require an early reionization component in our universe and that only one marginal class of models, based on a particular realization of reionization, may point to that. In addition, the frequentist Akaike information criterion (AIC) provides strong evidence against alternative reionization histories, favoring the most simple reionization scenario, which describes reionization by means of only one (constant) reionization optical depth τ.

Keywords: cosmological parameters from CMBR, reionization

ArXiv ePrint: 1712.02807

 https://doi.org/10.1088/1475-7516/2018/04/024

JCAP04(2018)024

Contents

JCAP04(2018)024

1 Introduction

The epoch of reionization is the interval of time during which the cosmic gas evolves from an almost completely neutral state (neglecting the recombination leftovers) to an ionized state. This ionization process is believed to happen due to the onset of star formation at redshifts $z \simeq 12$, and it is believed to last until $z \simeq 6$. Several astrophysical observables (quasars [1, 2], Lyman α emitters [3–7], γ ray bursts [8, 9]) seem to agree with this hypothesis. However, the precise details of the overall reionization process still remain obscure. The main reason is that the currently available most precise information on the reionization period comes from cosmic microwave background (CMB) measurements through a redshift-integrated quantity. During reionization, the number density of free electrons which can scatter the CMB, n_e, increases. As a consequence, the reionization optical depth τ increases according to a line of-sight integral of n_e, generating a suppression of the CMB peaks at any scale within the horizon at the reionization period. This suppression, however, can be easily compensated with an enhancement of the primordial power spectrum amplitude, A_s. A much better and cleaner measurement of τ can be obtained via measurements of the CMB polarization, which is linearly affected by reionization (see e.g. refs. [10–13] for seminal works and [14] for a recent review). The latest measurements of the Planck collaboration provide a value of $\tau = 0.055 \pm 0.009$ [15, 16] based exclusively on the CMB polarization spectrum. This value of τ is in a much better agreement than previous WMAP [17] and Planck [18] estimates with observations of Lyman-α (Ly-α) emitters at $z \simeq 7$ [3–7], which require that reionization is complete by $z \simeq 6$. Even if now cosmological and astrophysical tests of the reionization process seem to agree, the measurement of τ provides only integrated information on the free electron fraction x_e, and not on its precise redshift evolution. Consequently, the same measured value of τ may correspond to very different reionization histories.

Traditionally, the most commonly exploited model for the time evolution of the free electron fraction, $x_e(z)$, uses a step-like transition, implemented via a hyperbolic tangent [19]. Model independent attempts have been carried out in several works in the past [13, 20–28] and also more recently [29–31], based either on a redshift-node decomposition of $x_e(z)$ or on a principal component analysis (PCA) of the CMB polarization angular power spectrum. More concretely, using the latter approach, the authors of [29] claimed that Planck 2015 data

favors a high-redshift ($z > 15$) component to the reionization optical depth. The quoted 2σ evidence would come from the excess in power in the low multipole range of the Planck 2015 CMB polarization spectrum. Accordingly to their results, the functional form of the usual step-like model prevents a priori for such an early component in the reionization history of our universe. However, the authors of [30], using a different method, which implements reionization through a non-parametric reconstruction that uses a piecewise cubic Hermite interpolating polynomial (`PCHIP`), find only marginal evidence for extended reionization histories. Since an early component in the reionization history $x_e(z)$ (or, in other words, a high redshift contribution to the reionization optical depth τ) may either imply the need for a high-redshift population of ionizing sources (hypothesis that will be tested by the future James Webb Space Telescope [32]), or give hints about a possible energy injection from dark matter annihilations or decays [33–47], or accreting massive primordial black holes [48–52], it is mandatory to robustly establish what current data prefer, regardless of the model used to describe the redshift evolution of the free electron fraction.

Here we first analyze several possible parameterizations for reionization (PCA with several fiducial cosmologies and the `PCHIP` method) and explore the corresponding constraints on the reionization history of the universe. We then shall exploit tools related to model selection among competing models, using both the Akaike information criterion (AIC) and the Bayesian information criterion (BIC), which will allow us to quantitatively decide which model is currently preferred and whether it exists or not an indication for an early reionization component in our universe.

The structure of the paper is as follows. We start by discussing the different reionization approaches that we shall test against current data in section 2. In section 3 we describe the cosmological observations exploited in our numerical analyses, whose results are shown in section 4. Our conclusions are summarized in section 5.

2 Reionization histories

In the following, we will derive the constraints on the reionization history of our universe from cosmological observations exploring several possible scenarios, focusing on a possible early reionization component in our universe. For that, we shall exploit the reionization optical depth:

$$\tau(z) = \int_z^\infty dz' \frac{c\, dt'}{dz'} (n_{\rm e}(z') - n_{\rm e,0}(z')) \sigma_{\rm T} \ , \tag{2.1}$$

where $n_{\rm e}(z) = n_{\rm H}(0)(1+z)^3 x_{\rm e}(z)$ and $n_{\rm e,0}(z) = n_{\rm H}(0)(1+z)^3 x_{\rm e,0}(z)$, being $n_{\rm H}(0)$ the number density of hydrogen at present, $x_{\rm e}(z)$ the free electron fraction and $x_{e,0}(z)$ the free electron fraction leftover from the recombination epoch (see e.g. [53–55]). Therefore, eq. (2.1) just accounts for the cumulative Compton optical depth after recombination, subtracting the pre-reionization contribution.

2.1 Canonical scenarios

We start describing the free electron fraction by means of the most simple and commonly exploited parameterizations in the literature, i.e. the so-called *redshift-symmetric* and *redshift-asymmetric* parameterizations (see e.g. [16]).

- *Redshift-symmetric* parameterization.

  The most economical and widely employed approach to describe the reionization process in our universe assumes that the free electron fraction follows a step-like function,

JCAP04(2018)024

taking the recombination leftover value at high redshifts and becoming close to one at low redshifts, and being described by the hyperbolic tangent function [19]

$$x_e^{\tanh}(z) = \frac{1+f_{\rm He}}{2}\left(1+\tanh\left[\frac{y(z_{\rm re})-y(z)}{\Delta y}\right]\right), \tag{2.2}$$

where $y(z) = (1+z)^{3/2}$, $\Delta y = 3/2(1+z_{\rm re})^{1/2}\Delta z$, and Δz is the width of the transition, fixed in the following to $\Delta z = 0.5$. This parametrization is named "redshift symmetric" because the redshift interval between the beginning of reionization and its half completion equals the corresponding one between half completion and the reionization offset, and it is the default one implemented in Boltzmann solver codes such as `CAMB`[1] [56]. This parameterization, as well as the following ones, also accounts for the first ionization of helium $f_{\rm He} = n_{\rm He}/n_{\rm H}$, assumed to happen at the same time than that of hydrogen. The full helium reionization is modeled via another hyperbolic tangent function with $z_{\rm re,He} = 3.5$ and $\Delta z = 0.5$. Therefore, the only free parameter in this simple approach is the reionization redshift $z_{\rm re}$. When this redshift-symmetric parameterization is used as the fiducial model in our PCA analyses (see next subsection), we fix $z_{\rm re} = 8.8$, following the results quoted in ref. [16].

- *Redshift-asymmetric* reionization.

  Besides the previous case, alternative reionization parameterizations with a non redshift-symmetric transition have been proposed in the literature. One of the most flexible choices, which shows good agreement with current measurements from quasars, Lyα emitters and star-forming galaxies, is represented by a power law, described via three parameters [16, 57]:

$$x_e^{\rm asym}(z) = \begin{cases} 1+f_{\rm He} & \text{for } z < z_{\rm end}, \\ (1+f_{\rm He})\left(\frac{z_{\rm early}-z}{z_{\rm early}-z_{\rm end}}\right)^{\alpha} & \text{for } z_{\rm end} < z < z_{\rm early}, \\ 0 & \text{for } z > z_{\rm early}. \end{cases} \tag{2.3}$$

  Following Planck 2016 reionization analyses [16], when using this redshift-asymmetric model as a fiducial model in our PCA analyses, we shall fix the redshift at which the first sources in our universe switch on, $z_{\rm early} = 20$, the redshift at which reionization is fully complete, $z_{\rm end} = 6$, and the exponent $\alpha = 6.10$.

2.2 Principal component analysis (PCA)

The second method we follow here to model the reionization process is the principal component analysis (PCA) approach of refs. [13, 20–25], exploited more recently in refs. [29, 31]. Following these previous works, we discretize the redshift range from $z_{\rm min} = 6$ to $z_{\rm max} = 30$ in N_z bins of width of $\delta z = 0.25$. We set the ionization fraction to $x_e = 0$ for $z \geq z_{\rm max}$, when the reionization processes have not started yet, while for $z \leq 6$ we assume fully ionized hydrogen and singly ionized helium, i.e. $x_e = 1 + f_{\rm He}$. The full helium reionization is modeled as aforementioned. This approach makes use of the Fisher information matrix [58], that we compute as:

$$F_{ij} = \sum_{\ell=2}^{\ell_{\rm max}} \frac{1}{\sigma^2_{C_\ell}} \frac{\partial C_\ell}{\partial x_e(z_i)} \frac{\partial C_\ell}{\partial x_e(z_j)} = \sum_{\ell=2}^{\ell_{\rm max}} \left(\ell+\frac{1}{2}\right) \frac{\partial \ln C_\ell}{\partial x_e(z_i)} \frac{\partial \ln C_\ell}{\partial x_e(z_j)}, \tag{2.4}$$

[1] Code for Anisotropies in the Microwave Background (CAMB).

JCAP04(2018)024

where the C_ℓ are the components of the large angle EE polarization spectrum. The sum above is truncated at $\ell_{\rm max} = 100$, because the reionization imprint is mostly located in the lowest modes of the CMB polarization spectrum. In eq. (2.4) we have used the well-known result for the cosmic variance: $\sigma^2_{C_\ell} = C^2_\ell\, 2/(2\ell+1)$. Having the Fisher matrix, we can diagonalize it and find that the eigenfunctions are the principal components $S_\mu(z)$ and the eigenvalues are proportional to the inverse of the estimated variance of each eigenmode, σ^2_μ. Using the normalization of ref. [20], we can write the Fisher matrix as

$$F_{ij} = \frac{1}{(N_z+1)^2}\sum_{\mu=1}^{N_z}\frac{1}{\sigma^2_\mu}S_\mu(z_i)S_\mu(z_j)\ . \tag{2.5}$$

We sort the different eigenfunctions in order to have the smallest uncertainties at the lowest modes, being therefore the $\mu = 1$ case the best constrained mode. Due to completeness and orthogonality of the principal components, the following properties are fulfilled:

$$\int_{z_{\rm min}}^{z_{\rm max}} dz\, S_\mu(z)S_\nu(z) = (z_{\rm max} - z_{\rm min})\delta_{\mu\nu}\,, \tag{2.6}$$

$$\sum_{\mu=1}^{N_z} S_\mu(z_i)S_\mu(z_j) = (N_z+1)\delta_{ij}\,. \tag{2.7}$$

Since the width of the bins is chosen to be sufficiently small, in practice we can replace the integrals over redshift by discrete sums. One of the ideas behind the PCA approach is that one can write redshift-dependent quantities such as the ionization fraction as a linear combination of the principal components. Since the lowest modes have the smallest uncertainties, we truncate the sum, using only the first 5 principal components, following ref. [20]. We apply the PCA analysis to the ionization history in two different ways, which are explained below.

- *Case A*

  In the first PCA approach, named *PCA-A* in what follows, the reionization history reads as

  $$x_e^A(z) = x_{\rm e}^{\rm fid}(z) + \sum_\mu m_\mu^A S_\mu(z)\ . \tag{2.8}$$

  Given a fiducial model $x_{\rm e}^{\rm fid}(z)$, and knowing the amplitudes derived from the Fisher matrix (see eq. (2.4)), one can recover an arbitrary ionization history using a PCA analysis. This is the standard approach adopted in refs. [20, 29] in order to constrain the ionization history with CMB data. Following [20], we can derive upper and lower bounds for each amplitude m_μ:

  $$m_\mu^\pm = \int_{z_{\rm min}}^{z_{\rm max}} dz \frac{S_\mu(z)[x_e^{\rm max} - 2x_e^{\rm fid}(z)] \pm x_e^{\rm max}|S_\mu(z)|}{2(z_{\rm max} - z_{\rm min})}\ . \tag{2.9}$$

  Additionally, in order to guarantee physical ionization histories, the choice of our amplitudes m_μ has to fulfill the condition $0 \le x_e(z) \le 1 + f_{\rm He}$ at any redshift z.[2]

[2]Notice that this constraint for physicality is stronger than that followed in ref. [29], as any unphysical model will be retained for the Monte Carlo analyses.

JCAP04(2018)024

- *Case B*

  In the second of our PCA analyses, named *PCA-B*, we choose a different approach to the standard PCA analysis described above, in which the free electron fraction is proportional to the fiducial model plus the PCA decomposition. Here, we exploit the functional form of the fiducial model in order to test other possible reionization parameterizations. Following this idea, for the redshift-symmetric, *tanh* description, we insert the PCA decomposition inside the argument of the hyperbolic tangent:

$$x_e^{B,\tanh}(z) = \frac{1+f_{\rm He}}{2}\left(1+\tanh\left[\frac{y(z_{\rm re})-y(z)}{\Delta y}+\sum_\mu m_\mu^B S_\mu(z)\right]\right) . \tag{2.10}$$

  Notice that we recover the fiducial *tanh* model by setting the amplitudes m_μ to 0. We perform an analogous replacement for the redshift-asymmetric parameterization:

$$x_e^{B,\rm asym}(z) = \begin{cases} 1+f_{\rm He} & \text{for } z < z_{\rm end}, \\ (1+f_{\rm He})\left(\left(\frac{z_{\rm early}-z}{z_{\rm early}-z_{\rm end}}\right)+\sum_\mu m_\mu^B S_\mu(z)\right)^\alpha & \text{for } z_{\rm end} < z < z_{\rm early}, \\ 0 & \text{for } z > z_{\rm early}. \end{cases} \tag{2.11}$$

  We take for the specific parameters of the *tanh* and *asym* cases the fiducial values given in section 2.1.

2.3 PCHIP

The third and last method we adopt in order to describe the reionization history is based on a non-parametric form for the free electron fraction $x_e(z)$, which is described using the function values $x_e(z_i)$ in a number n of fixed redshift points $z_1, \ldots, z_n$. Following the procedure adopted for the PCA analyses, we fix the function to be a constant both at low redshifts ($z \leq 6$) and at high redshifts ($z \geq 30$). The first and the last redshift nodes we use to parameterize the function at intermediate redshifts are therefore $z_1 = 6$ and $z_n = 30$, where we also want the function to be continuous: as a consequence, the values $x_e(z_1) = 1 + f_{\rm He}$ and $x_e(z_n) = 0$ are fixed and the number of varying parameters that describe $x_e(z)$ is always $n-2$. We consider a case with a total of $n = 7$ nodes (5 free parameters), located at redshifts

$$z_i \in \{6,\ 7,\ 8.5,\ 10,\ 13,\ 20,\ 30\}\,, \tag{2.12}$$

in order to have the same number of free parameter than in the PCA cases.

The function $x_e(z)$ at $z \neq z_i$ is computed through an interpolation among its values in the nodes. We employ the "piecewise cubic Hermite interpolating polynomial" (`PCHIP`) [59, 60] in a very similar way to refs. [61–64], where the `PCHIP` function was adopted to describe the power spectrum of initial curvature perturbations, or the more recent work of [30], where the `PCHIP` method has also been used to model the evolution of $x_e(z)$. The idea behind the `PCHIP` function is similar to that of the natural cubic spline, with the difference that the monotonicity of the series of interpolating points must be preserved. Spurious oscillations that may be introduced by the standard spline are avoided by imposing a condition on the first derivative of the function in the nodes, which must be zero if there is a change in the monotonicity of the point series. A more detailed discussion on the `PCHIP` function can be found in the appendix of ref. [61].

JCAP04(2018)024

Summarizing, the free electron fraction in the PCHIP case is described by:

$$x_e(z) = \begin{cases} 1 + f_{\rm He} & \text{for } z \leq z_1, \\ \texttt{PCHIP}(z;\ x_e(z_1),\ \ldots,\ x_e(z_n)) & \text{for } z_1 < z < z_n, \\ 0 & \text{for } z \geq z_n, \end{cases} \tag{2.13}$$

where n will be 7 and the redshifts z_i are reported in eq. (2.12).

For the values of the function in the varying nodes, which are the free reionization parameters in our Markov chain Monte Carlo analyses, we impose a linear prior $0 \leq x_e(z_i) \leq 1 + f_{\rm He}$, with $i = 2,\ \ldots,\ n-1$. This ensures that the free electron fraction is always positive and smaller than its value today. The value of the reionization optical depth τ that we report in our results is derived from eq. (2.1).

3 Cosmological data

We use Planck satellite 2015 measurements of the CMB temperature, polarization, and cross-correlation spectra [18, 65] to derive the constraints on the possible reionization histories.[3] More precisely, we exploit both the high-ℓ ($30 \leq \ell \leq 2508$) and the low-ℓ ($2 \leq \ell \leq 29$) TT likelihoods based on the reconstructed CMB maps and we include the Planck polarization likelihoods in the low-multipole regime ($2 \leq \ell \leq 29$), plus the high-multipole ($30 \leq \ell \leq 1996$) EE and TE likelihoods.[4] All these CMB likelihood functions depend on several nuisance parameters (e.g. residual foreground contamination, calibration, and beam-leakage [18, 66]), which have been properly considered and marginalized over. To derive constraints on the reionization history and related parameters, we have modified the Boltzmann equations solver CAMB code [56] and apply Markov chain Monte Carlo (MCMC) methods by means of an adapted version of the CosmoMC package [67]. As for current constraints, we consider a minimal version of the ΛCDM model, described by the following set of parameters:

$$\{\omega_{\rm b},\ \omega_{\rm c},\ \Theta_{\rm s},\ \ln(10^{10} A_{\rm s}),\ n_{\rm s}\}\,, \tag{3.1}$$

where $\omega_{\rm b} \equiv \Omega_{\rm b} h^2$ and $\omega_{\rm c} \equiv \Omega_{\rm c} h^2$ represent the physical baryon and cold dark matter energy densities, $\Theta_{\rm s}$ is the angular scale of recombination, $A_{\rm s}$ is the primordial power spectrum amplitude and $n_{\rm s}$ the spectral index. Notice that we do not have τ among the parameters included in our analyses, as τ is a derived parameter. Instead, we will add the additional parameters describing the PCA and PCHIP reionization models, that will lead to the constraints presented in what follows.

4 Results

Figure 1 shows the most relevant results from our analyses of Planck 2015 temperature and polarization data assuming different reionization histories. As aforementioned, we shall focus on the cumulative redshift distribution function of the reionization optical depth, eq. (2.1). A large departure from 0 at redshifts $z > 10$ would indicate evidence for an early reionization contribution, and therefore for non-standard reionization sources as, for instance, energy

[3] We make use of the publicly available Planck likelihoods [66], see www.cosmos.esa.int/web/planck/pla.

[4] The latest reionization constraints from the Planck collaboration do not consider the TE data in the analyses, due to its larger cosmic variance and its weaker dependence on the reionization optical depth, when compared to EE measurements, see [16].

JCAP04(2018)024

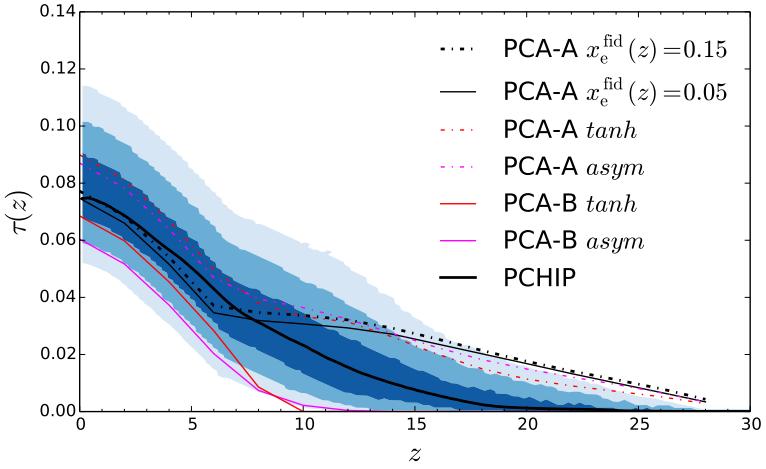

Figure 1. Cumulative redshift evolution of the reionization optical depth $\tau(z)$ for several possible reionization scenarios. The black thin solid and dot-dashed lines illustrate the PCA-A scenario for the case of two fiducial models constant in redshift. The two upper dot-dashed lines refer also to the PCA-A parameterization but with redshift-dependent fiducial models. The two lower colored solid lines depict the PCA-B scenarios, while the thick solid black line and the blue contours show the mean value and the 1, 2 and 3σ allowed regions within the `PCHIP` prescription.

injection from dark matter annihilations or from matter accretion on massive primordial black holes. Notice that the PCA-A method of ref. [29], in which the PCA decomposition is added linearly to a fiducial $x_e^{fid}(z)$, leads *always* to an early contribution to the optical depth τ, i.e. τ is significantly different from 0 at $z > 10$, in contrast to standard reionization scenarios. Furthermore, the presence of this early contribution is independent of the fiducial model, as we can see from the four PCA-A cases depicted in figure 1, which provide the same predictions at $z > 10$, differing only mildly at small redshifts, regardless whether the fiducial model is a constant function or it depends on the redshift instead.

In order to unravel the origin of this early reionization component present when using the PCA-A description, several tests have been carried out. Firstly, we have eliminated the physical limits in the PCA amplitudes, finding very similar results. Secondly, we have simulated mock Planck data with the hyperbolic tangent description and then fitted these data to a PCA-A modeling, using different fiducial models. We always find two bumps in the recovered x_e, see figure 2, one located between $z = 10$ and $z = 15$ and a second one located between $z = 20$ and $z = 25$. Upcoming measurements from the Planck satellite could disentangle if this early reionization component is truly indicated by the data or instead it is due to the adopted modeling or to other effects (i.e. systematics).

Furthermore, this early reionization component is definitely absent when other possible reionization histories are used in the analyses. For instance, in the case of PCA-B parameterizations (see eqs. (2.10) and (2.3)), there is no early reionization contribution, as $\tau(z)$ is negligibly small for $z > 10$. The same happens for the `PCHIP` method, in which the mean reconstructed value of $\tau(z)$ is also very small at high redshifts, showing little evidence for an

JCAP04(2018)024

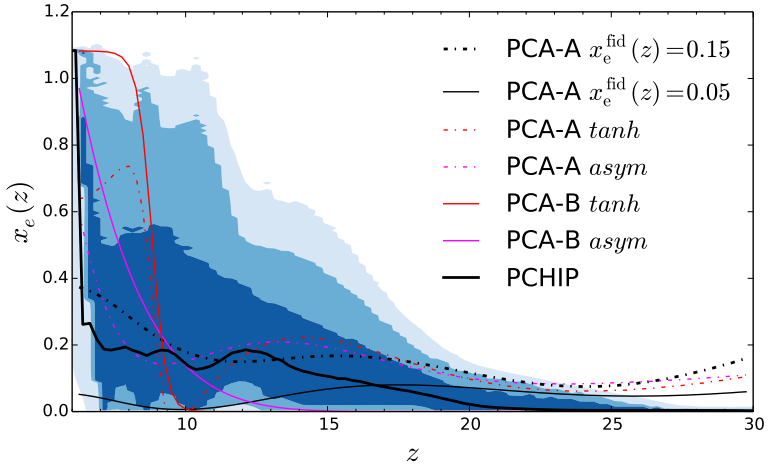

Figure 2. Free electron fraction as a function of the redshift for several possible reionization scenarios. Line styles and colors are the same as in figure 1.

early reionization component (see also ref. [30]). Notice that the value of τ today is smaller in the PCA-B approaches than in the PCA-A and PCHIP descriptions. However, this behavior is the expected one, as the PCA-B scenarios are very close to those explored by the Planck collaboration in ref. [16], where it was found that the current value of τ is 0.058 ± 0.012 for the hyperbolic tangent case, in perfect agreement with our findings here, even if we make use of the 2015 Planck likelihood only (the mean value is $\tau = 0.068$ for the very same model). The differences between the PCA-A and PCA-B cases can be understood from the fact that the case B imposes a more restrictive functional form on the ionization history.

The findings above are fully consistent with our limits on the free electron fraction $x_e(z)$ at a given redshift. Figure 2 shows the free electron fraction for the PCHIP parameterization together with the other PCA-A and PCA-B models explored here. The color coding is identical to that used in figure 1. Notice that for the PCA-A models the free electron fraction is almost constant in the redshift interval $z = 10 - 30$, as a consequence of the choice of the fiducial model, and therefore there will always be an early reionization component *within this approach*. However, when considering either the PCHIP or the PCA-B models, the free electron fraction is significantly smaller than 0.2 for redshifts above $z = 15$ and it is almost negligible above $z = 20$. Therefore, the fact that current CMB observations need an early contribution to reionization is highly questionable, as it strongly depends on the framework used to analyze the data. Using Planck CMB temperature and polarization data within the PCHIP analysis, we find $x_e < 0.90$, < 0.49 and < 0.13 at 2σ in the nodes at $z = 10$, 13 and 20, respectively. Fluctuations in the lower 1σ limits shown in figure 2 are numerical artifacts that appear when computing the error bands at intermediate positions between the fixed PCHIP nodes and cannot be considered as significant. Figure 3 shows the 68% and 95% CL allowed regions for the amplitudes of the PCHIP nodes, i.e. the $x_e(z)$ at the redshifts listed in eq. (2.12), from the Planck CMB measurements considered here. A quick inspection of figure 3 tells us that all the amplitudes are perfectly compatible with a vanishing value. Only

JCAP04(2018)024

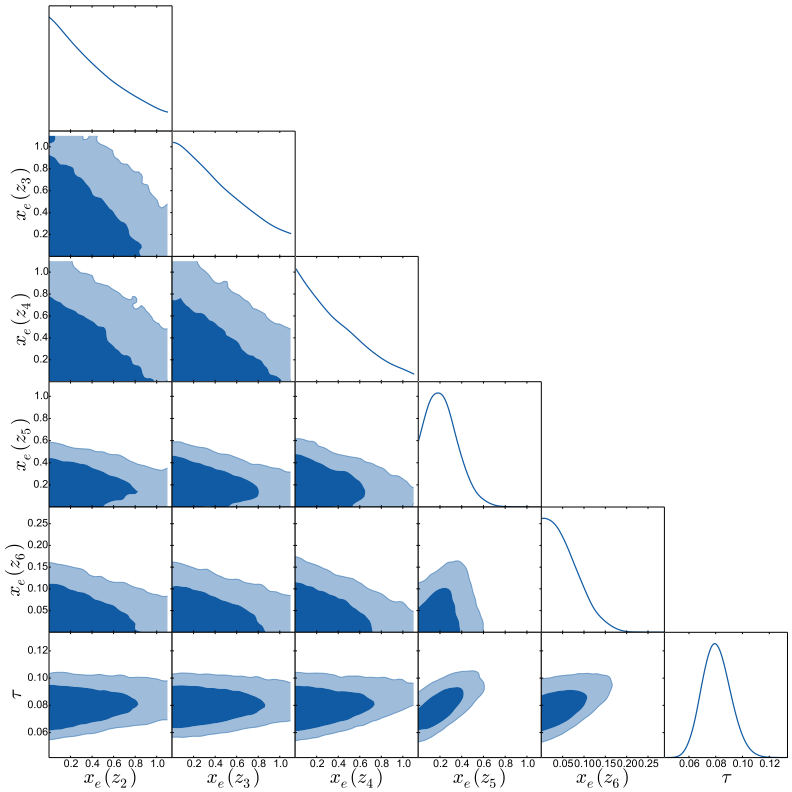

Figure 3. 68% and 95% CL allowed regions from the Planck CMB measurements considered here on the amplitudes in the PCHIP approach, together with the one-dimensional posterior probability distributions.

one of them, m_5, the node corresponding to $z = 13$, shows a very mild departure from 0. However, this mild departure is far from being a significant effect, as it barely appears at 1σ. We can therefore conclude that there is no evidence for a high redshift component in $x_{\rm e}(z)$. Notice also from figure 3 that, in general, the PCHIP amplitudes are anti-correlated among themselves. We also illustrate the derived distribution for the value of the reionization optical depth, $\tau_{\rm PC}$, which is significantly correlated with the nodes at the higher redshifts. Even a modest increase of $x_{\rm e}$ at $z = 13$ or at $z = 20$ would imply a significant shift towards larger values of the current reionization optical depth.

In order to further assess our findings above, we adopt here two information criteria which have been widely exploited in astrophysical and cosmological contexts (see refs. [68, 69] for details), namely the frequentist Akaike information criterion (AIC)

$$\mathrm{AIC} \equiv -2 \ln \mathcal{L}_{\rm max} + 2k \,, \tag{4.1}$$

which establishes that the penalty term between competing models is twice the number of

JCAP04(2018)024

free parameters in the model, k; and the Bayesian information criterion (BIC)

$$\mathrm{BIC} \equiv -2\ln\mathcal{L}_{\max} + k\ln N\,, \tag{4.2}$$

in which the penalty is proportional to the number of free parameters in the model times the logarithm of the number of data points N. The best model is the one minimizing either the AIC or the BIC criteria. Following ref. [68], the significance against a given model will be judged based on the Jeffreys' scale, which will characterize a difference ΔAIC (BIC)> 5 (> 10) as a strong (decisive) evidence against the cosmological model with higher AIC (BIC) value.

Adopting first the AIC prescription, we shall compare the different models explored here to the standard scenario, in which reionization is described via just only one parameter, τ. This *tau-only* cosmological model gives $-2\ln\mathcal{L}_{\max} = 12956.2$ [18]. As a comparison, the PCA-A case with constant fiducial model $x_e = 0.15$ (0.05) provides $-2\ln\mathcal{L}_{\max} = 12954.0$ (12953.2). Notice that both the PCA-A cases have a higher AIC value than the *tau-only* cosmology because of the larger number of parameters. The values for ΔAIC are $\Delta\mathrm{AIC} = 5.8$ and 5, respectively, and therefore there is strong evidence against these possible reionization histories. Also within the PCA-A description, we get $-2\ln\mathcal{L}_{\max} = 12956.5$ (12958.3) in the PCA-A *tanh* (*asym*) fiducial approach. These two models also provide a larger AIC than the *tau-only* scenario, and again, there will be strong (decisive) evidence against the PCA-A *tanh* (*asym*), in favor of the simplest and most economical *tau-only* reionization paradigm. In the case of the `PCHIP` approach, our results lead to $-2\ln\mathcal{L}_{\max} = 12954.5$, which also indicates strong preference for the *tau-only* scheme. We point out that all the reported values of $-2\ln\mathcal{L}_{\max}$ are taken from the corresponding MCMC chains, and not from a specific minimization algorithm. For this reason, they may not be extremely precise and they must be considered only as fair estimates of the true values of each $-2\ln\mathcal{L}_{\max}$, with possible errors of order unity, as estimated from the different parallel MCMC chains. In the case of the PCA-B parameterizations, the difference in the minimum $-2\ln\mathcal{L}_{\max}$ from the different MCMC parallel chains is too large to give even a fair estimate of the true minimum, and we decide not to claim any evidence against these two descriptions, for the reasons listed above. However, we expect that these two models are equally good in fitting the CMB data, at a comparable level with respect to the *tau-only* scenario, as their reionization histories are extremely close to the standard cosmological framework, see figure 2. Nevertheless, given the fact that the number of parameters in the PCA-B scheme is larger, the *tau-only* reionization description, with current data, will always be favored over the PCA-B parameterization.

We can also compare the different reionization descriptions among themselves using the BIC approach, as all of them have the same number of free parameters (five in total) and also the same number of data points. The result of comparing the PCA-A and `PCHIP` scenarios among themselves will always give very weak or inconclusive answers, as none of them in particular is preferred over the other possible formulations.

5 Conclusions

Unraveling the reionization period, which is still a poorly known period in the evolution of our universe, is one of the most important goals of current and future cosmological probes. This is a mandatory step, not only towards a complete understanding of star formation and evolution, but also to answer questions such as the nature of the dark matter component [70–84], constraining dark matter properties or the abundance of accreting massive primordial

JCAP04(2018)024

black holes [33–52]. Currently, the most accurate measurement of the reionization period comes from cosmic microwave background data through a redshift-integrated quantity: the reionization optical depth τ. The latest measurements of the Planck collaboration provide a value of $\tau = 0.055 \pm 0.009$ [15, 16], which shows a very good agreement with observations of Lyman-α emitters at $z \simeq 7$ [3–7]. However, this measured value of τ may correspond to very different reionization histories.

The most commonly exploited model for the time evolution of the free electron fraction, $x_e(z)$, uses a step-like transition, implemented via a hyperbolic tangent [19]. Recently, there have been several studies in the literature claiming that Planck 2015 data may prefer a high-redshift ($z > 15$) component to the reionization optical depth, implying a clear departure from the hyperbolic tangent picture. Here we consider a number of possible reionization scenarios, some of them previously explored in the literature, such as the principal component analysis (PCA) approach of refs. [13, 20–25, 29], or the `PCHIP` framework [30]. We find that the claimed need for an early reionization component from present data is highly debatable, as it is only motivated by a particular set of reionization descriptions. In other possible reionization prescriptions, equally allowed by data, we do not find such a preference. To assess this, we have applied the frequentist Akaike information criterion (AIC), which provides an unbiased model comparison method. The AIC results show that there is strong evidence from current data against more complicated reionization scenarios, always favoring the minimal scenario with the symmetric hyperbolic tangent function and described by one single parameter, the reionization optical depth τ. In other words, current Planck CMB analyses are unable to provide more information beyond that based on a single value of the τ. Upcoming data from the Planck mission will help in further disentangling the reionization history of our universe.

JCAP04(2018)024

Acknowledgments

This work makes use of the publicly available `CosmoMC` [67] and `CAMB` [56] codes and of the Planck data release 2015 Likelihood Code [66]. OM and PVD would like to thank the Fermilab Theoretical Physics Department for hospitality. OM and PVD are supported by PROMETEO II/2014/050, by the Spanish Grants SEV-2014-0398 and FPA2014–57816-P of MINECO and by the European Union's Horizon 2020 research and innovation program under the Marie Skłodowska-Curie grant agreements No. 690575 and 674896. The work of SG was supported by the Spanish grants FPA2014-58183-P, Multidark CSD2009-00064 and SEV-2014-0398 (MINECO), and PROMETEOII/2014/084 (Generalitat Valenciana).

This manuscript has been authored in part by Fermi Research Alliance, LLC under Contract No. DE-AC02-07CH11359 with the U.S. Department of Energy, Office of Science, Office of High Energy Physics. The United States Government retains and the publisher, by accepting the article for publication, acknowledges that the United States Government retains a non-exclusive, paid-up, irrevocable, world-wide license to publish or reproduce the published form of this manuscript, or allow others to do so, for United States Government purposes. This work made extensive use of the NASA Astrophysics Data System and `arXiv.org` preprint server.

References

[1] X.-H. Fan, M.A. Strauss, R.H. Becker, R.L. White, J.E. Gunn, G.R. Knapp et al., *Constraining the evolution of the ionizing background and the epoch of reionization with z 6 quasars. 2. a sample of 19 quasars*, *Astron. J.* **132** (2006) 117 [astro-ph/0512082] [INSPIRE].

[2] G.D. Becker, J.S. Bolton, P. Madau, M. Pettini, E.V. Ryan-Weber and B.P. Venemans, *Evidence of patchy hydrogen reionization from an extreme Lyα trough below redshift six*, *Mon. Not. Roy. Astron. Soc.* **447** (2015) 3402 [arXiv:1407.4850] [INSPIRE].

[3] D.P. Stark, R.S. Ellis, K. Chiu, M. Ouchi and A. Bunker, *Keck Spectroscopy of Faint $3 < z < 7$ Lyman Break Galaxies: - I. New constraints on cosmic reionisation from the luminosity and redshift-dependent fraction of Lyman-α emission*, *Mon. Not. Roy. Astron. Soc.* **408** (2010) 1628 [arXiv:1003.5244] [INSPIRE].

[4] T. Treu, K.B. Schmidt, M. Trenti, L.D. Bradley and M. Stiavelli, *The Changing Lyα Optical Depth in the Range $6 < z < 9$ from the MOSFIRE Spectroscopy of Y-dropouts*, *Astrophys. J.* **775** (2013) L29 [arXiv:1308.5985] [INSPIRE].

[5] L. Pentericci et al., *New observations of $z \sim 7$ galaxies: Evidence for a patchy reionization*, *Astrophys. J.* **793** (2014) 113 [arXiv:1403.5466] [INSPIRE].

[6] M.A. Schenker, R.S. Ellis, N.P. Konidaris and D.P. Stark, *Line Emitting Galaxies Beyond a Redshift of 7: An Improved Method for Estimating the Evolving Neutrality of the Intergalactic Medium*, *Astrophys. J.* **795** (2014) 20 [arXiv:1404.4632] [INSPIRE].

[7] V. Tilvi, C. Papovich, S.L. Finkelstein, J. Long, M. Song, M. Dickinson et al., *Rapid Decline of Lyα Emission Toward the Reionization Era*, *Astrophys. J.* **794** (2014) 5 [arXiv:1405.4869] [INSPIRE].

[8] F.Y. Wang, Z.G. Dai and E.W. Liang, *Gamma-ray Burst Cosmology*, *New Astron. Rev.* **67** (2015) 1 [arXiv:1504.00735] [INSPIRE].

[9] S. Gallerani, A. Ferrara, T.R. Choudhury, X. Fan, R. Salvaterra and P. Dayal, *Constraining cosmic reionization with quasar, gamma ray burst and Lya emitter observations*, *Mem. Soc. Astron. Ital. Suppl.* **14** (2010) 47 [arXiv:0912.2693] [INSPIRE].

[10] M. Kaplinghat, M. Chu, Z. Haiman, G. Holder, L. Knox and C. Skordis, *Probing the reionization history of the universe using the cosmic microwave background polarization*, *Astrophys. J.* **583** (2003) 24 [astro-ph/0207591] [INSPIRE].

[11] Z. Haiman and G.P. Holder, *The Reionization history at high redshifts. 1. Physical models and new constraints from CMB polarization*, *Astrophys. J.* **595** (2003) 1 [astro-ph/0302403] [INSPIRE].

[12] G. Holder, Z. Haiman, M. Kaplinghat and L. Knox, *The Reionization history at high redshifts. 2. Estimating the optical depth to Thomson scattering from CMB polarization*, *Astrophys. J.* **595** (2003) 13 [astro-ph/0302404] [INSPIRE].

[13] W. Hu and G.P. Holder, *Model - independent reionization observables in the CMB*, *Phys. Rev.* **D 68** (2003) 023001 [astro-ph/0303400] [INSPIRE].

[14] C.L. Reichardt, *Observing the Epoch of Reionization with the Cosmic Microwave Background*, eds. A. Mesinger, in *Understanding the Epoch of Cosmic Reionization*, Astrophysics and Space Science Library, vol. **423** Springer, Cham [arXiv:1511.01117] [INSPIRE].

[15] Planck collaboration, N. Aghanim et al., *Planck intermediate results. XLVI. Reduction of large-scale systematic effects in HFI polarization maps and estimation of the reionization optical depth*, *Astron. Astrophys.* **596** (2016) A107 [arXiv:1605.02985] [INSPIRE].

[16] Planck collaboration, R. Adam et al., *Planck intermediate results. XLVII. Planck constraints on reionization history*, *Astron. Astrophys.* **596** (2016) A108 [arXiv:1605.03507] [INSPIRE].

JCAP04(2018)024

[17] WMAP collaboration, G. Hinshaw et al., *Nine-Year Wilkinson Microwave Anisotropy Probe (WMAP) Observations: Cosmological Parameter Results*, *Astrophys. J. Suppl.* **208** (2013) 19 [arXiv:1212.5226] [INSPIRE].

[18] PLANCK collaboration, P.A.R. Ade et al., *Planck 2015 results. XIII. Cosmological parameters*, *Astron. Astrophys.* **594** (2016) A13 [arXiv:1502.01589] [INSPIRE].

[19] A. Lewis, *Cosmological parameters from WMAP 5-year temperature maps*, *Phys. Rev.* **D 78** (2008) 023002 [arXiv:0804.3865] [INSPIRE].

[20] M.J. Mortonson and W. Hu, *Model-independent constraints on reionization from large-scale CMB polarization*, *Astrophys. J.* **672** (2008) 737 [arXiv:0705.1132] [INSPIRE].

[21] M.J. Mortonson and W. Hu, *Impact of reionization on CMB polarization tests of slow-roll inflation*, *Phys. Rev.* **D 77** (2008) 043506 [arXiv:0710.4162] [INSPIRE].

[22] M.J. Mortonson and W. Hu, *Reionization constraints from five-year WMAP data*, *Astrophys. J.* **686** (2008) L53 [arXiv:0804.2631] [INSPIRE].

[23] M.J. Mortonson, C. Dvorkin, H.V. Peiris and W. Hu, *CMB polarization features from inflation versus reionization*, *Phys. Rev.* **D 79** (2009) 103519 [arXiv:0903.4920] [INSPIRE].

[24] M.J. Mortonson and W. Hu, *Evidence for horizon-scale power from CMB polarization*, *Phys. Rev.* **D 80** (2009) 027301 [arXiv:0906.3016] [INSPIRE].

[25] S. Mitra, T.R. Choudhury and A. Ferrara, *Reionization constraints using Principal Component Analysis*, *Mon. Not. Roy. Astron. Soc.* **413** (2011) 1569 [arXiv:1011.2213] [INSPIRE].

[26] A. Lewis, J. Weller and R. Battye, *The Cosmic Microwave Background and the Ionization History of the Universe*, *Mon. Not. Roy. Astron. Soc.* **373** (2006) 561 [astro-ph/0606552] [INSPIRE].

[27] S. Pandolfi, A. Cooray, E. Giusarma, E.W. Kolb, A. Melchiorri, O. Mena et al., *Harrison-Z'eldovich primordial spectrum is consistent with observations*, *Phys. Rev.* **D 81** (2010) 123509 [arXiv:1003.4763] [INSPIRE].

[28] S. Pandolfi, E. Giusarma, E.W. Kolb, M. Lattanzi, A. Melchiorri, O. Mena et al., *Impact of general reionization scenarios on extraction of inflationary parameters*, *Phys. Rev.* **D 82** (2010) 123527 [arXiv:1009.5433] [INSPIRE].

[29] C.H. Heinrich, V. Miranda and W. Hu, *Complete Reionization Constraints from Planck 2015 Polarization*, *Phys. Rev.* **D 95** (2017) 023513 [arXiv:1609.04788] [INSPIRE].

[30] D.K. Hazra and G.F. Smoot, *Witnessing the reionization history using Cosmic Microwave Background observation from Planck*, *JCAP* **11** (2017) 028 [arXiv:1708.04913] [INSPIRE].

[31] S. Mitra, T.R. Choudhury and B. Ratra, *First study of reionization in the Planck 2015 normalized closed ΛCDM inflation model*, arXiv:1712.00018 [INSPIRE].

[32] J.P. Gardner et al., *The James Webb Space Telescope*, *Space Sci. Rev.* **123** (2006) 485 [astro-ph/0606175] [INSPIRE].

[33] E. Pierpaoli, *Decaying particles and the reionization history of the universe*, *Phys. Rev. Lett.* **92** (2004) 031301 [astro-ph/0310375] [INSPIRE].

[34] M. Mapelli, A. Ferrara and E. Pierpaoli, *Impact of dark matter decays and annihilations on reionzation*, *Mon. Not. Roy. Astron. Soc.* **369** (2006) 1719 [astro-ph/0603237] [INSPIRE].

[35] A. Natarajan and D.J. Schwarz, *The effect of early dark matter halos on reionization*, *Phys. Rev.* **D 78** (2008) 103524 [*Erratum ibid.* **D 81** (2010) 089905] [arXiv:0805.3945] [INSPIRE].

[36] A. Natarajan and D.J. Schwarz, *Dark matter annihilation and its effect on CMB and Hydrogen 21 cm observations*, *Phys. Rev.* **D 80** (2009) 043529 [arXiv:0903.4485] [INSPIRE].

JCAP04(2018)024

[37] A.V. Belikov and D. Hooper, *How Dark Matter Reionized The Universe*, *Phys. Rev.* **D 80** (2009) 035007 [arXiv:0904.1210] [INSPIRE].

[38] G. Huetsi, A. Hektor and M. Raidal, *Constraints on leptonically annihilating Dark Matter from reionization and extragalactic gamma background*, *Astron. Astrophys.* **505** (2009) 999 [arXiv:0906.4550] [INSPIRE].

[39] M. Cirelli, F. Iocco and P. Panci, *Constraints on Dark Matter annihilations from reionization and heating of the intergalactic gas*, *JCAP* **10** (2009) 009 [arXiv:0907.0719] [INSPIRE].

[40] T. Kanzaki, M. Kawasaki and K. Nakayama, *Effects of Dark Matter Annihilation on the Cosmic Microwave Background*, *Prog. Theor. Phys.* **123** (2010) 853 [arXiv:0907.3985] [INSPIRE].

[41] A. Natarajan and D.J. Schwarz, *Distinguishing standard reionization from dark matter models*, *Phys. Rev.* **D 81** (2010) 123510 [arXiv:1002.4405] [INSPIRE].

[42] G. Giesen, J. Lesgourgues, B. Audren and Y. Ali-Haimoud, *CMB photons shedding light on dark matter*, *JCAP* **12** (2012) 008 [arXiv:1209.0247] [INSPIRE].

[43] R. Diamanti, L. Lopez-Honorez, O. Mena, S. Palomares-Ruiz and A.C. Vincent, *Constraining Dark Matter Late-Time Energy Injection: Decays and P-Wave Annihilations*, *JCAP* **02** (2014) 017 [arXiv:1308.2578] [INSPIRE].

[44] L. Lopez-Honorez, O. Mena, S. Palomares-Ruiz and A.C. Vincent, *Constraints on dark matter annihilation from CMB observationsbefore Planck*, *JCAP* **07** (2013) 046 [arXiv:1303.5094] [INSPIRE].

[45] L. Lopez-Honorez, O. Mena, Á. Moliné, S. Palomares-Ruiz and A.C. Vincent, *The 21 cm signal and the interplay between dark matter annihilations and astrophysical processes*, *JCAP* **08** (2016) 004 [arXiv:1603.06795] [INSPIRE].

[46] V. Poulin, P.D. Serpico and J. Lesgourgues, *A fresh look at linear cosmological constraints on a decaying dark matter component*, *JCAP* **08** (2016) 036 [arXiv:1606.02073] [INSPIRE].

[47] V. Poulin, P.D. Serpico and J. Lesgourgues, *Dark Matter annihilations in halos and high-redshift sources of reionization of the universe*, *JCAP* **12** (2015) 041 [arXiv:1508.01370] [INSPIRE].

[48] M. Ricotti, J.P. Ostriker and K.J. Mack, *Effect of Primordial Black Holes on the Cosmic Microwave Background and Cosmological Parameter Estimates*, *Astrophys. J.* **680** (2008) 829 [arXiv:0709.0524] [INSPIRE].

[49] B. Horowitz, *Revisiting Primordial Black Holes Constraints from Ionization History*, arXiv:1612.07264 [INSPIRE].

[50] Y. Ali-Haïmoud and M. Kamionkowski, *Cosmic microwave background limits on accreting primordial black holes*, *Phys. Rev.* **D 95** (2017) 043534 [arXiv:1612.05644] [INSPIRE].

[51] D. Aloni, K. Blum and R. Flauger, *Cosmic microwave background constraints on primordial black hole dark matter*, *JCAP* **05** (2017) 017 [arXiv:1612.06811] [INSPIRE].

[52] V. Poulin, P.D. Serpico, F. Calore, S. Clesse and K. Kohri, *CMB bounds on disk-accreting massive primordial black holes*, *Phys. Rev.* **D 96** (2017) 083524 [arXiv:1707.04206] [INSPIRE].

[53] E.W. Kolb and M.S. Turner, *The Early Universe*, *Front. Phys.* **69** (1990) 1 [INSPIRE].

[54] M. Stiavelli, *From First Light to Reionization: The End of the Dark Ages*, Wiley Series in Cosmology (2009).

[55] H. Mo, F. C. van den Bosch and S. White, *Galaxy Formation and Evolution*, Cambridge University Press, Cambridge, U.K. (2010).

[56] A. Lewis, A. Challinor and A. Lasenby, *Efficient computation of CMB anisotropies in closed FRW models*, *Astrophys. J.* **538** (2000) 473 [astro-ph/9911177] [INSPIRE].

JCAP04(2018)024

[57] M. Douspis, N. Aghanim, S. Ilić and M. Langer, *A new parameterization of the reionisation history*, *Astron. Astrophys.* **580** (2015) L4 [arXiv:1509.02785] [INSPIRE].

[58] M. Tegmark, A. Taylor and A. Heavens, *Karhunen-Loeve eigenvalue problems in cosmology: How should we tackle large data sets?*, *Astrophys. J.* **480** (1997) 22 [astro-ph/9603021] [INSPIRE].

[59] F. Fritsch and R. Carlson, *Monotone Piecewise Cubic Interpolation*, *SIAM J. Numer. Anal.* **17** (1980) 238.

[60] F. Fritsch and J. Butland, *A Method for Constructing Local Monotone Piecewise Cubic Interpolants*, *SIAM J. Sci. and Stat. Comput.* **5** (1984) 300.

[61] S. Gariazzo, C. Giunti and M. Laveder, *Light Sterile Neutrinos and Inflationary Freedom*, *JCAP* **04** (2015) 023 [arXiv:1412.7405] [INSPIRE].

[62] E. Di Valentino, S. Gariazzo, E. Giusarma and O. Mena, *Robustness of cosmological axion mass limits*, *Phys. Rev.* **D 91** (2015) 123505 [arXiv:1503.00911] [INSPIRE].

[63] S. Gariazzo, L. Lopez-Honorez and O. Mena, *Primordial Power Spectrum features and f_{NL} constraints*, *Phys. Rev.* **D 92** (2015) 063510 [arXiv:1506.05251] [INSPIRE].

[64] E. Di Valentino, S. Gariazzo, M. Gerbino, E. Giusarma and O. Mena, *Dark Radiation and Inflationary Freedom after Planck 2015*, *Phys. Rev.* **D 93** (2016) 083523 [arXiv:1601.07557] [INSPIRE].

[65] Planck collaboration, R. Adam et al., *Planck 2015 results. I. Overview of products and scientific results*, *Astron. Astrophys.* **594** (2016) A1 [arXiv:1502.01582] [INSPIRE].

[66] Planck collaboration, N. Aghanim et al., *Planck 2015 results. XI. CMB power spectra, likelihoods and robustness of parameters*, *Astron. Astrophys.* **594** (2016) A11 [arXiv:1507.02704] [INSPIRE].

[67] A. Lewis and S. Bridle, *Cosmological parameters from CMB and other data: A Monte Carlo approach*, *Phys. Rev.* **D 66** (2002) 103511 [astro-ph/0205436] [INSPIRE].

[68] A.R. Liddle, *Information criteria for astrophysical model selection*, *Mon. Not. Roy. Astron. Soc.* **377** (2007) L74 [astro-ph/0701113] [INSPIRE].

[69] R. Trotta, *Bayes in the sky: Bayesian inference and model selection in cosmology*, *Contemp. Phys.* **49** (2008) 71 [arXiv:0803.4089] [INSPIRE].

[70] R. Barkana, Z. Haiman and J.P. Ostriker, *Constraints on warm dark matter from cosmological reionization*, *Astrophys. J.* **558** (2001) 482 [astro-ph/0102304] [INSPIRE].

[71] N. Yoshida, A. Sokasian, L. Hernquist and V. Springel, *Early structure formation and reionization in a warm dark matter cosmology*, *Astrophys. J.* **591** (2003) L1 [astro-ph/0303622] [INSPIRE].

[72] R.S. Somerville, J.S. Bullock and M. Livio, *The epoch of reionization in models with reduced small scale power*, *Astrophys. J.* **593** (2003) 616 [astro-ph/0303481] [INSPIRE].

[73] B. Yue and X. Chen, *Reionization in the Warm Dark Matter Model*, *Astrophys. J.* **747** (2012) 127 [arXiv:1201.3686] [INSPIRE].

[74] F. Pacucci, A. Mesinger and Z. Haiman, *Focusing on Warm Dark Matter with Lensed High-redshift Galaxies*, *Mon. Not. Roy. Astron. Soc.* **435** (2013) L53 [arXiv:1306.0009] [INSPIRE].

[75] A. Mesinger, A. Ewall-Wice and J. Hewitt, *Reionization and beyond: detecting the peaks of the cosmological 21 cm signal*, *Mon. Not. Roy. Astron. Soc.* **439** (2014) 3262 [arXiv:1310.0465] [INSPIRE].

JCAP04(2018)024

[76] C. Schultz, J. Oñorbe, K.N. Abazajian and J.S. Bullock, *The High-z Universe Confronts Warm Dark Matter: Galaxy Counts, Reionization and the Nature of Dark Matter*, *Mon. Not. Roy. Astron. Soc.* **442** (2014) 1597 [arXiv:1401.3769] [INSPIRE].

[77] P. Dayal, T.R. Choudhury, V. Bromm and F. Pacucci, *Reionization and Galaxy Formation in Warm Dark Matter Cosmologies*, *Astrophys. J.* **836** (2017) 16 [arXiv:1501.02823] [INSPIRE].

[78] A. Lapi and L. Danese, *Cold or Warm? Constraining Dark Matter with Primeval Galaxies and Cosmic Reionization after Planck*, *JCAP* **09** (2015) 003 [arXiv:1508.02147] [INSPIRE].

[79] S. Bose, C.S. Frenk, J. Hou, C.G. Lacey and M.R. Lovell, *Reionization in sterile neutrino cosmologies*, *Mon. Not. Roy. Astron. Soc.* **463** (2016) 3848 [arXiv:1605.03179] [INSPIRE].

[80] S. Bose, W.A. Hellwing, C.S. Frenk, A. Jenkins, M.R. Lovell, J.C. Helly et al., *Substructure and galaxy formation in the Copernicus Complexio warm dark matter simulations*, *Mon. Not. Roy. Astron. Soc.* **464** (2017) 4520 [arXiv:1604.07409] [INSPIRE].

[81] P.S. Corasaniti, S. Agarwal, D.J.E. Marsh and S. Das, *Constraints on dark matter scenarios from measurements of the galaxy luminosity function at high redshifts*, *Phys. Rev.* **D 95** (2017) 083512 [arXiv:1611.05892] [INSPIRE].

[82] N. Menci, A. Grazian, M. Castellano and N.G. Sanchez, *A Stringent Limit on the Warm Dark Matter Particle Masses from the Abundance of z=6 Galaxies in the Hubble Frontier Fields*, *Astrophys. J.* **825** (2016) L1 [arXiv:1606.02530] [INSPIRE].

[83] L. Lopez-Honorez, O. Mena, S. Palomares-Ruiz and P. Villanueva-Domingo, *Warm dark matter and the ionization history of the Universe*, *Phys. Rev.* **D 96** (2017) 103539 [arXiv:1703.02302] [INSPIRE].

[84] P. Villanueva-Domingo, N.Y. Gnedin and O. Mena, *Warm Dark Matter and Cosmic Reionization*, *Astrophys. J.* **852** (2018) 139 [arXiv:1708.08277] [INSPIRE].

JCAP04(2018)024

Journal of Cosmology and Astroparticle Physics
An IOP and SISSA journal

A fresh look into the interacting dark matter scenario

Miguel Escudero,[a] **Laura Lopez-Honorez,**[b,c] **Olga Mena,**[a] **Sergio Palomares-Ruiz**[a] **and Pablo Villanueva-Domingo**[a]

[a]Instituto de Física Corpuscular (IFIC), CSIC-Universitat de Valencia, Apartado de Correos 22085, E-46071, Spain
[b]Service de Physique Théorique, CP225, Université Libre de Bruxelles, Bld du Triomphe, Pleinlaan 2, B-1050 Brussels, Belgium
[c]Theoretische Natuurkunde, Vrije Universiteit Brussel and The International Solvay Institutes, Pleinlaan 2, B-1050 Brussels, Belgium

E-mail: miguel.escudero@ific.uv.es, llopezho@ulb.ac.be, olga.mena@ific.uv.es, sergio.palomares.ruiz@ific.uv.es, pablo.villanueva@ific.uv.es

Received March 29, 2018
Revised May 11, 2018
Accepted May 21, 2018
Published June 5, 2018

Abstract. The elastic scattering between dark matter particles and radiation represents an attractive possibility to solve a number of discrepancies between observations and standard cold dark matter predictions, as the induced collisional damping would imply a suppression of small-scale structures. We consider this scenario and confront it with measurements of the ionization history of the Universe at several redshifts and with recent estimates of the counts of Milky Way satellite galaxies. We derive a conservative upper bound on the dark matter-photon elastic scattering cross section of $\sigma_{\gamma\mathrm{DM}} < 8\times10^{-10}\,\sigma_T\ (m_{\mathrm{DM}}/\mathrm{GeV})$ at 95% CL, about one order of magnitude tighter than previous constraints from satellite number counts. Due to the strong degeneracies with astrophysical parameters, the bound on the dark matter-photon scattering cross section derived here is driven by the estimate of the number of Milky Way satellite galaxies. Finally, we also argue that future 21 cm probes could help in disentangling among possible non-cold dark matter candidates, such as interacting and warm dark matter scenarios. Let us emphasize that bounds of similar magnitude to the ones obtained here could be also derived for models with dark matter-neutrino interactions and would be as constraining as the tightest limits on such scenarios.

Keywords: particle physics - cosmology connection, dwarfs galaxies, reionization, dark matter theory

ArXiv ePrint: 1803.08427

 https://doi.org/10.1088/1475-7516/2018/06/007

JCAP06(2018)007

Contents

1 Introduction

The nature of the dark matter (DM) of our Universe still remains uncertain [1–6]. Despite the fact that the existence of non-relativistic, cold DM (CDM) is in excellent agreement with cosmic microwave background (CMB) and large scale structure (LSS) data [7, 8], there are a number of observations at small scales, which may indicate a departure from this picture. This is commonly referred to as the "small-scale crisis" of the standard CDM paradigm [9], which arises from the fact that CDM numerical predictions for the abundances and the kinematics of gravitationally bound structures show some discrepancies with observations [10–14]. One of these discrepancies is the so-called "missing satellite problem": the fact that there are fewer observed satellites around our galaxy than the number predicted in CDM simulations [10, 11] (see however the recent ref. [15] for a different perspective and reanalysis of this long-standing CDM problem). A number of dedicated simulations to set light on these issues have been carried out by different groups [16–19].

One very interesting possibility, extensively explored in the literature, is the case of the existence of DM candidates with non-negligible velocity dispersion at early times, which would result in the suppression of small-scale structures due to their free-streaming nature. Among this type of scenarios, warm DM (WDM) candidates with masses in the keV range could provide a solution to the missing satellite problem [19–37]. Indeed, the WDM hypothesis has received much attention due to claims of the detection of a monochromatic line at (3.5–3.6) keV in X-ray data from galaxy clusters, the galactic center and the cosmic X-ray

JCAP06(2018)007

background [38–41], which could potentially point to the radiative decay of a WDM keV sterile neutrino ($\nu_s \to \gamma\nu$). However, the most recent Lyman-α (Lyα) forest constraints suggest $m_{\rm WDM} > (3\text{–}5)\,{\rm keV}$ [42, 43] (for a thermal relic). In the case of sterile neutrino production via non-resonant active-sterile neutrino oscillations [44], thermal equilibrium would never be reached, but one can relate the limit for thermal relics to the one for non-resonantly produced sterile neutrinos [45], resulting in $m_s \gtrsim (20\text{–}30)\,{\rm keV}$.

Another very appealing scenario to solve the small-scale problem is to consider a DM candidate that interacts with relativistic particles (IDM for short) of the Standard Model (SM) [46–49] (i.e., photons or neutrinos, or from a hidden sector [50–55]), with potential self-interactions [52, 56–67] (see also ref. [68] for a generic treatment of the IDM and WDM effects under the name "non-cold" DM scenarios). Elastic scatterings between the DM particles and photons or neutrinos would give rise to collisional damping [69–71], which would erase small-scale structures and thus, could provide a mechanism to alleviate the aforementioned problems.

In the following, we shall focus on a generic IDM model involving DM-photon interactions, characterized by the elastic scattering cross section $\sigma_{\gamma{\rm DM}}$. Even if the suppression of small-scale fluctuations in the IDM and WDM scenarios results from different physics (that is, collisional damping and free-streaming, respectively) it is possible to establish an approximate relation between the DM parameters that drive the small-scale suppression in these two scenarios (i.e., $\sigma_{\gamma{\rm DM}}$ and $m_{\rm WDM}$). Both the IDM and the WDM schemes have been exhaustively confronted against different cosmological observations (CMB fluctuations and spectral distortions, galaxy clustering and Lyα forest power spectrum) [42, 43, 46–49, 68, 71–93].

Notice that the DM model featuring a velocity-independent DM-γ scattering cross section considered in our work would correspond to millicharged DM. Indeed, the DM-γ cross section can be expressed as

$$\sigma_{\gamma{\rm DM}} = \epsilon^2 \sigma_T \left(\frac{m_e}{m_{\rm DM}}\right)^2 , \tag{1.1}$$

where $\epsilon = |q|/e$ with q the DM electric charge and m_e the electron mass. Stringent limits on such a model can be obtained using CMB and Lyα data [94] (see also ref. [95] for a compilation of limits),

$$\epsilon < 1.8 \times 10^{-6} \left(\frac{m_{\rm DM}}{\rm GeV}\right)^{1/2} , \tag{1.2}$$

which are valid for $m_{\rm DM} \gtrsim {\rm MeV}$.

In this work, we revisit the constraints on these non-CDM scenarios from the comparison of the predicted number of Milky Way (MW) satellite galaxies to the number estimated from actual observations. We consider the MW satellites recently discovered by the Dark Energy Survey (DES) [96, 97], in addition to the eleven classical objects plus those detected by the Sloan Digital Sky Survey (SDSS) [98, 99]. The additional satellites, together with the assessment of the probability for a subhalo to form a galaxy [15], change the expected bounds on the DM-photon elastic scattering cross section as compared to the earlier analysis of ref. [49], which we discuss. Moreover, we also study the impact, within these scenarios, of the small-scale suppression on the ionization history of the Universe. Because of the reduction of power at small scales, reionization would be delayed with respect to the standard CDM case [100–103]. Whereas many works in the literature have been devoted to test the impact of WDM scenarios on reionization-related observables [101–116], the modification of the ionization history of the Universe produced in IDM scenarios has only been recently addressed within a model with DM-hidden sector interactions [67]. Here, we consider measurements

JCAP06(2018)007

of the optical depth from the last scattering surface to reionization and of the ionization fraction at several redshifts. Given the current precision on these reionization observables and the (not yet fully understood) reionization efficiencies and thresholds, satellite galaxies counts turn out to provide the most powerful probe (among those used here) for testing IDM (as well as WDM) models.

A similar analysis could be performed for a DM coupling to dark radiation[1] or neutrinos. Unfortunately, the information necessary to perform the analyses in this work is not publicly available. Notice, though, that ref. [48] shows the strong (qualitative and quantitative) similarities between the DM-neutrino and DM-photon interaction models. We will use those results to provide a rough estimate of the bounds on DM-neutrino interactions that could be obtained using the same method as the one presented here.

The structure of the paper is as follows. In section 2, we describe the halo mass function obtained from numerical simulations of WDM and IDM scenarios and discuss the relation between $\sigma_{\gamma\mathrm{DM}}$ and m_{WDM}, based on similar small-scale suppression. This will be later used in the computation of the ionization history of the Universe in section 3, where we discuss how we calculate the evolution of the ionized fraction of the Universe and present the measurements we consider. In section 4, we discuss the main ingredients entering the computation of the number of MW satellites in WDM and IDM scenarios and indicate the current observational data. Finally, in section 5, we show the constraints on the DM-photon cross section and on the WDM mass, using the different data sets individually and when combined. In that section, even if it is not the main focus of this paper, we also briefly discuss the prospects from future measurements of the 21 cm signal of neutral hydrogen and how these observations could be used to test and disentangle from each other non-CDM scenarios, as the ones studied in this work. Finally, in section 6, we summarize our results and draw our conclusions.

2 Halo mass function of non-standard dark matter scenarios

When studying the number of satellites of the MW or the ionization history of the Universe, the density perturbations at small scales have long gone non-linear and one has to make use of the results from high resolution N-body simulations in order to account for the properties of DM halos. The halo mass function, that counts the number of halos per unit halo mass and volume at a given redshift, can be written as [118]

$$\frac{dn}{dM} = -\frac{1}{2}\,\frac{\rho_m}{M^2}\,f(\nu)\,\frac{d\ln\sigma^2}{d\ln M}\,, \tag{2.1}$$

where n is the halo number density, $\rho_m = \Omega_m\,\rho_c$ is the average matter density in the Universe at $z = 0$ and $\sigma^2 = \sigma^2(M, z)$ is the variance of density perturbations, which is a function of the halo mass M and redshift. The first-crossing distribution, $f(\nu)$, is expected to be a universal function of $\nu \equiv \delta_c^2/\sigma^2(M, z)$, with $\delta_c = 1.686$, the linearly extrapolated density for collapse at

[1] Notice that in ref. [52], an attempt to model the halo mass function of ETHOS simulations is studied making use of a sharp power law cut-off, similarly to WDM. The authors, however, point out that this approximation ceases to be valid at low halo masses, as ETHOS models have more power in the primordial power spectrum in comparison with WDM at those scales. Ref. [117] precisely goes beyond such an approximation, providing the fit (2.11) for the DM-photon scattering case. Notice as well that the imprint of an ETHOS model on satellite number counts was considered in ref. [52], while its imprint on reionization observables was studied in ref. [67].

JCAP06(2018)007

$z = 0$. From the Press-Schechter formalism [118, 119], but considering an ellipsoidal collapse model, the Sheth-Tormen (ST) first-crossing distribution was obtained as [120–122]

$$f(\nu) = A\sqrt{\frac{2\,q\,\nu}{\pi}}\left(1 + (q\,\nu)^{-p}\right)\, e^{-q\,\nu/2}\,, \tag{2.2}$$

with $p = 0.3$, $q = 0.707$ and $A = 0.3222$. For the standard CDM scenario, we consider this first-crossing distribution.[2]

As for the non-CDM scenarios we consider, we use the halo mass functions that match IDM and WDM simulations, as reported in refs. [26, 123]. The dependence in the particular DM cosmological model is partially encoded in the variance of density perturbations. The redshift dependence is driven by the linear growth function, $D(z)$ normalized to 1 at $z = 0$, so that the root-mean-square (rms) density fluctuation is $\sigma(M, z) = \sigma(M, z = 0)\, D(z)$. The variance at $z = 0$, $\sigma(M) \equiv \sigma(M, z = 0)$, at a given scale R can be expressed as

$$\sigma_X^2(M(R)) = \int \frac{d^3k}{(2\pi)^3}\, P_X(k)\, W^2(kR)\,, \tag{2.3}$$

where $P_X(k)$ is the linear power spectrum at $z = 0$ for a given $X = \{\text{CDM, IDM or WDM}\}$ cosmology and W is the Fourier transform of a filter function, which is defined as a top-hat (TH) function in real space,

$$W_{\rm TH}(kR) = \frac{3}{kR}\,\left(\sin(kR) - kR\cos(kR)\right)\ . \tag{2.4}$$

In this case, the mass M associated to the scale R is given by $M = \frac{4\pi}{3}\,\rho_m\,R^3$.

In order to parameterize the small scale suppression of the power spectrum within a given model $X = \{\text{IDM or WDM}\}$ with respect to the CDM case, one can express the ratio of CDM and X power spectra in terms of the transfer function T_X, defined as[3]

$$P_X(k) = P_{\rm CDM}(k)\, T_X^2(k)\,, \tag{2.5}$$

which can be parameterized in terms of a finite set of parameters and physical inputs, such as the WDM mass or the DM-photon elastic scattering cross section in IDM scenarios (see also ref. [68] for a recent generalization to a larger set of non-CDM models). Here we consider the fits obtained in ref. [20] for WDM and in ref. [70] for IDM using the full perturbation evolution through a Boltzmann solver code. In those works the transfer function is expressed as

$$T_X(k) = \left(1 + (\alpha_X k)^{2\mu}\right)^{-5/\mu}\,, \tag{2.6}$$

where μ is a dimensionless exponent which is obtained to be $\mu = 1.2$ and α_X is the breaking scale, whose parameterization in terms of the model parameters will be specified in the next subsections.

In order to describe the suppression in the linear regime, one can consider the half-mode mass $M_{\rm hm}$, defined as the mass scale for which $T_X/T_{\rm CDM} = 1/2$ (i.e., $P_X/P_{\rm CDM} = 1/4$).

[2] Note, however, that the values of the parameters in eq. (2.2) are different from the default ones in the `21cmFAST` code (used throughout this work) and thus, have been correspondingly modified.

[3] Note that this is not to be confused with the usual transfer function used in $P_{\rm CDM}(k)$, which encodes the information on the evolution of density perturbations at different scales with respect to the primordial power spectrum, in the standard CDM scenario.

JCAP06(2018)007

Using the general fit to the transfer function, eq. (2.6), the half-mode length $\lambda_{\rm hm}$ ($\lambda \equiv 2\pi/k$) and the half-mode mass $M_{\rm hm}$ can be easily derived as

$$\lambda_{\rm hm} = 2\,\pi\,\alpha_X \left(2^{\mu/5} - 1\right)^{-1/(2\,\mu)} ,$$
$$M_{\rm hm} \equiv \frac{4\,\pi}{3}\,\rho_m \left(\frac{\lambda_{\rm hm}}{2}\right)^3 . \tag{2.7}$$

2.1 Warm dark matter scenarios

In the case of WDM scenarios, refs. [26, 48] obtained the breaking scale, $\alpha_{\rm WDM}$, parameterized as [20]

$$\alpha_{\rm WDM} = 0.048 \left(\frac{\rm keV}{m_{\rm WDM}}\right)^{1.15} \left(\frac{\Omega_{\rm WDM}}{0.4}\right)^{0.15} \left(\frac{h}{0.65}\right)^{1.3} {\rm Mpc}/h\,, \tag{2.8}$$

in terms of the WDM mass $m_{\rm WDM}$.

In order to match the results of N-body simulations, the WDM halo mass function can be expressed as

$$\frac{dn^{\rm WDM}}{dM} = \left(1 + \frac{M_{\rm hm}}{b\,M}\right)^a \frac{dn^{\rm ST,\,WDM}}{dM}\,, \tag{2.9}$$

where an additional mass-dependent correction to the standard ST formalism, governed by two parameters, a and b, had to be introduced to reproduce the results of simulations [26]. The function $\frac{dn^{\rm ST,\,WDM}}{dM}$ refers to the halo mass function obtained with a ST first-crossing distribution, as defined in eq. (2.2), and a linear matter power spectrum corresponding to the WDM case. It was shown by ref. [48] that the agreement with WDM simulations was largely improved for $b = 0.5$.[4] Therefore, in the following, when considering the WDM halo mass functions, we shall refer to eq. (2.9) with $a = -0.6$ and $b = 0.5$.

2.2 Interacting dark matter scenarios

DM-photon interactions would give rise to large collisional damping effects that would also suppress the linear matter power spectrum at small scales [49, 70, 71, 81, 83]. In ref. [70], such a reduction of the power at small scales was accounted for by means of eq. (2.6) with $\mu = 1.2$, and parameterizing the breaking scale in terms of the DM-photon elastic scattering cross section,

$$\alpha_{\rm IDM} = 0.073 \left[10^8 \left(\frac{\sigma_{\gamma{\rm DM}}}{\sigma_T}\right)\left(\frac{\rm GeV}{m_{\rm DM}}\right)\right]^{0.48} \left(\frac{\Omega_{\rm WDM}}{0.4}\right)^{0.15} \left(\frac{h}{0.65}\right)^{1.3} {\rm Mpc}/h\,, \tag{2.10}$$

where $\sigma_T = 6.65 \times 10^{-25}$ cm^2 is the Thompson cross section. Notice that the suppression in the power spectrum at small scales can also be accounted for by DM-neutrino interactions, described with the same parameterization for the transfer function, with a small correction in the breaking scale, $\alpha_{\nu{\rm DM}} \simeq 0.8 \times \alpha_{\gamma{\rm DM}}$ [48].

In figure 1, we show the results of the fitting formula for two benchmark models. The curves for the transfer functions, obtained via eq. (2.6) (using eqs. (2.8) and (2.10) for the WDM and IDM scenarios, respectively) are compared to the transfer function for the IDM case, computed numerically by means of the Boltzmann solver code CLASS [124], where we have introduced the DM-photon interactions as described in refs. [70, 81]. Notice that this parameterization provides an accurate description of the IDM transfer function until the

[4] Notice there was a typo in ref. [48], as clarified in ref. [123].

JCAP06(2018)007

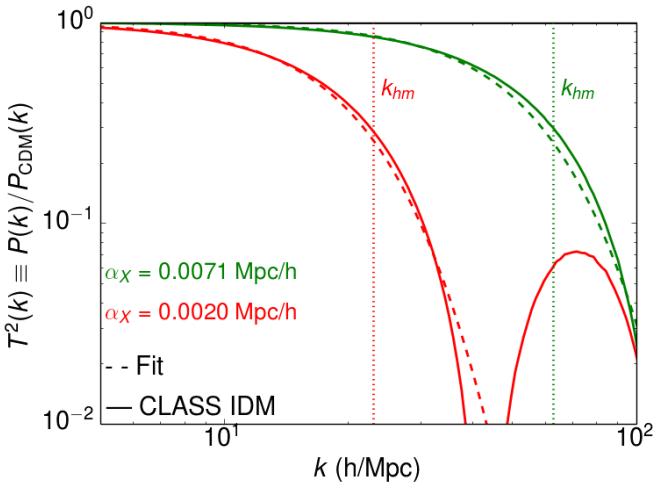

Figure 1. Transfer functions for the IDM scenario calculated with the Boltzmann solver CLASS [124] (solid curves) and for the WDM and IDM scenarios using the fitting formula in eq. (2.6), with eqs. (2.8) and (2.10) (dashed curves). We compare the results for two cases (see table 1) corresponding to the same half-mode length (i.e., the same half-mode mass $M_{\rm hm}$) or, equivalently, to the same breaking scale $\alpha_X = 0.0020\,{\rm Mpc}/h$ (leftmost red curves) and $\alpha_X = 0.0071\,{\rm Mpc}/h$ (rightmost green curves). The corresponding values for the DM-photon elastic scattering cross section in IDM and the DM mass in WDM scenarios are: $\sigma_{\gamma{\rm DM}} = 6.3 \times 10^{-10}\,\sigma_T\,(m_{\rm DM}/{\rm GeV})$ and $m_{\rm WDM} = 2.15\,{\rm keV}$ (leftmost red curves) and $\sigma_{\gamma{\rm DM}} = 7.9 \times 10^{-11}\,\sigma_T\,(m_{\rm DM}/{\rm GeV})$ and $m_{\rm WDM} = 5.17\,{\rm keV}$ (rightmost green curves). The wave-mode number corresponding to the half-mode length in each case is depicted by the dotted vertical lines. Notice that the agreement is very good until the typical damping oscillatory effects in IDM models start to dominate and create oscillations in the power spectrum.

damped oscillatory effects at small scales appear. However, the accuracy of this description is enough for our purposes, as we are mostly interested in the region where the difference between IDM and CDM is maximal, and at the scale where the damped oscillations appear, the height of the second maximum is already suppressed by more than one order of magnitude (see figure 1 and also, e.g., ref. [70]).

Even if the fits for the power spectrum in WDM and IDM look very similar for masses above the half-mode mass, the oscillations in the power spectrum that appear at small scales in IDM scenarios introduce differences in the description of the number density of halos. As was noticed in ref. [48], as a consequence of these oscillations, the number of low-mass structures in IDM is larger than in WDM scenarios and in order to reproduce the IDM results for masses below the half-mode mass, and extra mass-dependent correction must be introduced to the halo mass function [123],

$$\frac{dn^{\rm IDM}}{dM} = \left(1 + \frac{M_{\rm hm}}{b\,M}\right)^a \left(1 + \frac{M_{\rm hm}}{g\,M}\right)^c \frac{dn^{\rm ST,\,CDM}}{dM}\,, \tag{2.11}$$

with $a = -1$, $b = 0.33$, $g = 1$, $c = 0.6$ and $\frac{dn^{\rm ST,\,CDM}}{dM}$ refers to the standard ST first-crossing distribution as defined in eq. (2.2) and considering the CDM linear power spectrum

JCAP06(2018)007

for the variance of density perturbations. This approach has been shown to provide an excellent match to numerical simulations at $z = 0$ for $\sigma_{\gamma \mathrm{DM}} = 2.0 \times 10^{-9}\, \sigma_T\, (m_{\mathrm{DM}}/\mathrm{GeV})$. Notice, though, that a wider range of DM-photon scattering cross sections were considered in ref. [48] where the universal dependence (i. e., independent of the value of value of the cross section) for the IDM halo mass function was pointed out to exist (see also ref. [125], where the fit in eq. (2.11) appears to describe the halo mass function of all simulated models). It is thus reasonable to assume that eq. (2.11) represents a good description of all the models considered in this work and it is the one we implement in our numerical calculations. Let us also emphasize that the fit to the halo mass function depends on the parameters describing the IDM transfer function μ and α_{IDM} in M_{hm}.

As both IDM and WDM scenarios result in a suppression of the small-scale matter power spectrum, it is possible to establish an approximate connection among these two schemes above the half-mode mass. By equating eqs. (2.8) and (2.10) one gets the correspondence

$$\left(\frac{\sigma_{\gamma \mathrm{DM}}}{\sigma_T}\right)\left(\frac{\mathrm{GeV}}{m_{\mathrm{DM}}}\right) \simeq 4.1 \times 10^{-9} \left(\frac{\mathrm{keV}}{m_{\mathrm{WDM}}}\right)^{2.4}, \tag{2.12}$$

which relates the DM-photon elastic scattering cross section in IDM scenarios to the DM mass in the WDM case that give rise to similar suppression of the linear power spectrum. This would help to map the constraints obtained in IDM scenarios to those corresponding to WDM scenarios, and viceversa, when scales not much smaller than the half-mode length are being tested. In our calculations, for IDM scenarios we focus on the range $\sigma_{\gamma \mathrm{DM}} \in [10^{-11}\text{–}10^{-8}]\, \sigma_T \times (m_{\mathrm{DM}}/\mathrm{GeV})$, which according to the $m_{\mathrm{DM}} - \sigma_{\gamma \mathrm{DM}}$ relation above, corresponds roughly to $m_{\mathrm{DM}} \in [1\text{–}12]\,\mathrm{keV}$ in WDM scenarios.

Notice, though, that ref. [48] shows the strong (qualitative and quantitative) similarities between the DM-neutrino and DM-photon interaction models. We will use those results to provide a rough estimate of the bounds on DM-neutrino interactions that could be obtained using the same method as the one presented here.

Also notice that ref. [48] showed indications that models with DM-neutrino interactions could be described in a very similar manner. In particular, from the performed simulations at $z = 0$, the cases of $\sigma_{\gamma \mathrm{DM}} = 2.9 \times 10^{-9}\, \sigma_T\, (m_{\mathrm{DM}}/\mathrm{GeV})$ and of $\sigma_{\nu \mathrm{DM}} = 2.0 \times 10^{-9}\, \sigma_T\, (m_{\mathrm{DM}}/\mathrm{GeV})$ (for fixed half-mode mass) appear to result in very similar halo mass functions. We will consider this correspondence after deriving the bounds on IDM scenarios with DM-γ elastic scattering.

3 Ionization history of the universe

As mentioned in the introductory section, the properties of the DM component could have a significant impact on the ionization history of the Universe. These effects can be exploited to constrain both the IDM and the WDM scenarios described above by studying the evolution of different reionization observables, such as the total ionized fraction $\bar{x}_i$ at different redshifts or the optical depth to reionization τ (see, e.g., refs. [67, 100–102, 104–107, 110, 112, 126–128] for previous analyses in this direction).

3.1 Simulation and astrophysical parameters of the ionization history

For the purpose of studying constraints from the ionization history of the Universe, we make use of the publicly available code `21cmFast`, based on excursion set formalism, perturbation

JCAP06(2018)007

theory and analytic prescriptions [129]. The code generates semi-analytic simulations of the evolved density, peculiar velocity, halo and ionization fields. While the main purpose of the code is the study of variations in the 21 cm signal due to changes in a given set of astrophysical and cosmological parameters, we use it here with the purpose of evaluating the ionization fraction evolution before and around the epoch of reionization (EoR) in different DM scenarios. We have adapted the default WDM implementation available in `21cmFast`, in particular in the definition of the transfer function and of the halo mass function, so as to account for the IDM and WDM descriptions provided in section 2.

Let us now describe the simplifying assumptions and ionization parameters considered in `21cmFast` to evaluate the ionized fraction. The total ionized fraction $\bar{x}_i$, is given by the covering factor of the fully ionized HII regions $Q_{\rm HII}$, plus a contribution from the averaged ionized fraction of the *neutral* intergalactic medium (IGM), x_e [130]

$$\bar{x}_i \simeq Q_{\rm HII} + (1 - Q_{\rm HII})\, x_e \ . \tag{3.1}$$

Notice that the most relevant contribution to $\bar{x}_i$ at the epoch of reionization comes from $Q_{\rm HII}$. In `21cmFast`, the latter is characterized by[5]

$$Q_{\rm HII} = \frac{\zeta_{\rm UV} f_{\rm coll}\left(> M_{\rm vir}^{\rm min}\right)}{1 - x_e} \, , \tag{3.2}$$

where $\zeta_{\rm UV}$ is the UV ionization efficiency, which will be discussed below, and $f_{\rm coll}(> M_{\rm vir}^{\rm min})$ denotes the fraction of mass collapsed into halos with mass large enough to host star-forming galaxies (i.e., $M > M_{\rm vir}^{\rm min}$, see below). The latter is defined in terms of the halo mass function for a given cosmology X, introduced in section 2, as

$$f_{\rm coll}^{X}(> M_{\rm vir}^{\rm min}) = \int_{M_{\rm vir}^{\rm min}} \frac{M}{\rho_{m,0}} \frac{dn^X}{dM}\, dM \ . \tag{3.3}$$

On the other hand, the evolution of the local ionized fraction of the *neutral* IGM, $x_e(\mathbf{x}, z)$ results from

$$\frac{dx_e(\mathbf{x}, z)}{dz} = \frac{dt}{dz}\left(\Lambda_{\rm ion} - \alpha_{\rm A}\, C\, x_e^2\, n_b\, \mathfrak{f}_{\rm H}\right) \, , \tag{3.4}$$

where $n_b = \bar{n}_{b,0}(1+z)^3(1+\bar{\delta}_b(\mathbf{x}, z))$ is the baryon number density, $\Lambda_{\rm ion}$ the ionization rate, $\alpha_{\rm A}$ the case-A recombination coefficient, $C \equiv \langle n_e^2\rangle/\langle n_e\rangle^2$ is the clumping factor (set to one as default), with n_e the electron number density, and $\mathfrak{f}_{\rm H} = n_{\rm H}/n_b$ is the hydrogen number fraction. Eq. (3.4) is solved numerically by means of the `21cmFAST` code, briefly described above. Once the ionization history is at hand, one can compute the optical depth to reionization τ, defined as

$$\tau = \sigma_T \int \bar{x}_i\, n_b\, dl \, , \tag{3.5}$$

where σ_T is the Thomson cross section and dl is the line-of-sight proper distance.

Besides the DM parameters $m_{\rm DM}$ and $\sigma_{\gamma{\rm DM}}$, astrophysical parameters such as the ionization efficiency of UV photons, $\zeta_{\rm UV}$, and the minimum virial temperature, $T_{\rm vir}^{\rm min}$ (or equivalently the minimum virial mass $M_{\rm vir}^{\rm min}$, see below), have a strong impact on the evolution of

[5] In `21cmFast` the different fields, including ionization, are resolved on a grid. Except for parameters such as $\zeta_{\rm UV}$ and $T_{\rm vir}$, described below, we use the `21cmFAST` default settings for our simulations corresponding to $(200\ {\rm Mpc})^3$ comoving box with a 900^3 grid.

JCAP06(2018)007

$\bar{x}_i$.[6] It has already been pointed out that these parameters show degeneracies with the DM properties, affecting the small-scale matter power suppression (see, e.g., refs. [100, 103]). The UV ionizing efficiency $\zeta_{\rm UV}$ is assumed to be directly proportional to the fraction of ionizing photons escaping their host galaxy $f_{\rm esc}$, the number of ionizing photons per stellar baryons inside stars N_γ and the fraction of baryons that form stars $f_\star$ (see, e.g., ref. [130]). Let us emphasize that $\zeta_{\rm UV}$ is assumed to be constant with redshift. The criterion encoded in the `21cmFast` code for a region to be considered ionized is

$$\zeta_{\rm UV} f_{\rm coll} \left(> M_{\rm vir}^{\rm min}\right) > 1 - x_e \ . \tag{3.6}$$

Here, we allow $\zeta_{\rm UV}$ to vary in the range $\zeta_{\rm UV} \in [5, 80]$ (see, e.g., refs. [103, 132] for previous analyses using similar ranges). Also, in eqs. (3.3) and (3.6), the minimum virial halo mass, $M_{\rm vir}^{\rm min}$, can be related to the threshold temperature for halos to host star-forming galaxies, $T_{\rm vir}^{\rm min}$, as [133]

$$M_{\rm vir}^{\rm min}(z) \simeq 10^8 \left(\frac{T_{\rm vir}^{\rm min}}{2\times 10^4\,{\rm K}}\right)^{3/2} \left(\frac{1+z}{10}\right)^{-3/2} M_\odot \ . \tag{3.7}$$

The minimum value considered in this work is $T_{\rm vir}^{\rm min} = 10^4\,{\rm K}$, as lower temperatures have been shown to be insufficient to efficiently cool the halo gas through atomic cooling [134–138], while we take an upper limit of $T_{\rm vir}^{\rm min} \sim 2\times 10^5\,{\rm K}$ [130, 139]. We take the same threshold temperature $T_{\rm vir}^{\rm min}$ for halos hosting ionizing and X-ray sources.

For illustrative purposes, in figure 2 we show the resulting ionization history for different benchmark scenarios (see table 1), which are allowed at 95% confidence level (CL), to be discussed in section 5.3: IDM (solid curves), WDM (dashed curves) and CDM (dotted curves), for two values of the ionization efficiency and of the minimum virial temperature: $\zeta_{\rm UV} = 30$ with $T_{\rm vir}^{\rm min} = 5\times 10^4\,{\rm K}$ (green curves) and $\zeta_{\rm UV} = 55$ with $T_{\rm vir}^{\rm min} = 10^5\,{\rm K}$ (red curves). The chosen values for the DM-photon elastic scattering cross section and the WDM mass are such that the half-mode mass is the same in the IDM and WDM scenarios. As can be seen from the figure (solid and dashed curves of each color), this results into very similar ionization histories, although WDM scenarios give rise to a slightly more delayed reionization than in the corresponding IDM scenarios. This is related to the extra amount of power at small scales in the IDM case with respect to the WDM case due to the oscillating matter power spectrum at scales smaller than $\lambda_{\rm hm}$. As mentioned above, this effect is at the origin of the slightly modified description of the halo mass function of the IDM scenario in eq. (2.11), compared to the WDM case in eq. (2.9) [48]. All in all, distinguishing these two scenarios using this type of observables would be a very challenging task (if possible at all).

3.2 Ionization history measurements

To jointly constrain the ionization history of the Universe and the DM properties, we exploit two sets of observables. First of all, we use measurements of the optical depth from the last-scattering surface to reionization, τ, which provides information on the integrated ionization history of the Universe and affects the CMB photon temperature and polarization spectra. Indeed, the most accurate measurements of τ are obtained by means of CMB data and

[6] The value of $\zeta_{\rm X}$, the number of X-ray photons per solar mass in stars (that represents the X-ray efficiency) has been fixed to $10^{56}\,M_\odot^{-1}$, which approximately corresponds to $N_{\rm X} \simeq 0.1$ X-ray photons per stellar baryon. Note that, if varied within an order of magnitude, in consistency with the (0.5–8) keV integrated luminosity at $z = 0$ [131], our results do not depend on the value of $\zeta_{\rm X}$. Nevertheless, a larger contribution from X-rays could have important consequences in more extreme scenarios [130].

JCAP06(2018)007

	α_X [Mpc/h]	$M_{\rm hm}$ [$M_\odot$]	$\zeta_{\rm UV}$	$T_{\rm vir}^{\rm min}$ [K]	τ
$\sigma_{\gamma \rm DM} = 6.3 \times 10^{-10} (\sigma_T \times m_{\rm DM}/{\rm GeV})$	0.0071	6.9×10^8	55	10^5	0.061
$m_{\rm WDM} = 2.15\,{\rm keV}$					0.059
$\sigma_{\gamma \rm DM} = 7.9 \times 10^{-11} (\sigma_T \times m_{\rm DM}/{\rm GeV})$	0.0020	3.5×10^7	30	5×10^4	0.064
$m_{\rm WDM} = 5.17\,{\rm keV}$					0.063

Table 1. IDM and WDM benchmark models, corresponding to the same $M_{\rm hm}$. See figures 2 and 7 for the ionization histories and the 21 cm signals expected for these two models.

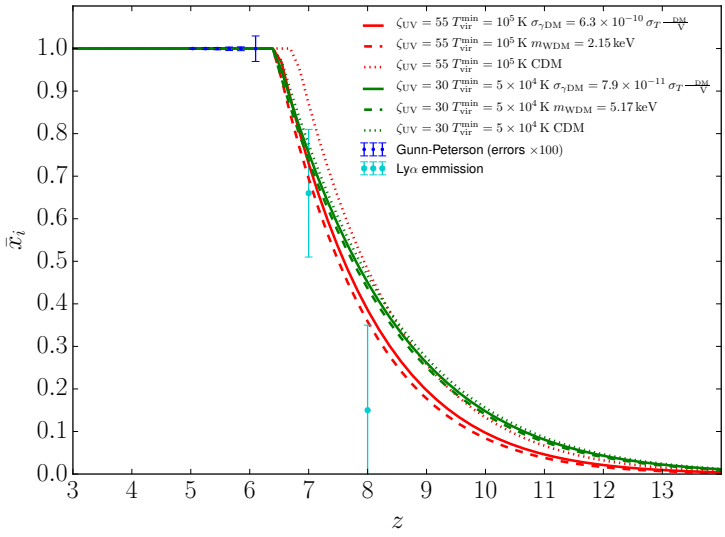

Figure 2. Ionization history for IDM (solid curves), WDM (dashed curves) and CDM (dotted curves) scenarios for two combinations of values of the ionization efficiency and the minimum virial temperature: $\zeta_{\rm UV} = 30$ and $T_{\rm vir}^{\rm min} = 5 \times 10^4\,{\rm K}$ (green curves), and $\zeta_{\rm UV} = 55$ and $T_{\rm vir}^{\rm min} = 10^5\,{\rm K}$ (red curves). The parameters of the IDM and WDM scenarios are also indicated (see table 1). The blue and cyan points and the associated error bars correspond to the low- and high-redshift $\bar{x}_i$ measurements considered in section 3 (see table 2). Notice that the errors associated to Gunn-Peterson effect measurements (in blue) have been magnified by a factor of 100 to be visible.

consequently, for our numerical analyses, we impose a Gaussian prior on τ using the Planck measurement $\tau = 0.055 \pm 0.009$ [140]. We first calculate the redshift evolution of the total ionized fraction, $\bar{x}_i(z)$, using the `21cmFAST` code [129, 141], as previously explained. Then, we determine the value of τ for each of the models studied here by means of the Boltzmann solver code CAMB (Code for Anisotropies in the Microwave Background) [142], that has been modified to allow for any possible ionization history $\bar{x}_i(z)$, including those corresponding to WDM or IDM scenarios.

Different astrophysical observations can provide very valuable information on the evolution of the global ionization fraction. At low redshifts, measurements of the Gunn-Peterson optical depth from bright quasars at six different redshifts, $z = 5.03$, 5.25, 5.45, 4.65, 5.85,

JCAP06(2018)007

Data	Redshift	$x_{\rm HII}$	Reference
Gunn-Peterson effect	5.03	$0.9999451^{+0.0000142}_{-0.0000165}$	[143]
	5.25	$0.9999330^{+0.0000207}_{-0.0000244}$	
	5.45	$0.9999333^{+0.0000247}_{-0.0000301}$	
	5.65	$0.9999140^{+0.0000365}_{-0.0000460}$	
	5.85	$0.9998800^{+0.0000408}_{-0.0000490}$	
	6.10	0.99957 ± 0.00030	
Dark gaps in quasar spectra	5.6	>0.91	[144]
	5.9	>0.89	
Lyα Emission in Galaxies (High redshift)	7	0.66 ± 0.15	[159]
	8	0.15 ± 0.20	

Table 2. Set of $\bar{x}_i$ data used in this work (see also ref. [160]).

6.10 [143], as well as the distribution of dark gaps in quasar spectra at $z = 5.6$ and $z = 5.9$ [144], indicate that reionization has to be completed by $z \sim 6$. We consider this *low-z* set of measurements to further constrain the different model parameters.[7]

On the other hand, we also use data from Lyα emission in star-forming galaxies at earlier times ($z \gtrsim 7$). Extrapolating the behavior at lower redshifts [145–158], these results indicate that reionization is not complete at those epochs. Concretely, in this work, we consider data at $z = 7$ and $z = 8$ [159], which use the models of ref. [147], and we refer to them as the *high-z* data set. A compilation of all data can be found in ref. [160].

Therefore, in practice, we compute three different χ^2 functions, one for each type of data (τ measurements, Gunn-Peterson optical depth and dark gaps in quasar spectra data, and high-z constraints from Lyα emission) and then we add them up. Table 2 shows the results of these measurements, together with their associated errors, for the Gunn-Peterson and high-redshift Lyα emission.

4 Number of Milky Way satellite galaxies

As previously discussed, the standard CDM framework may be facing a problem at sub-galactic scales, the so-called "missing satellite problem". More specifically, the current number of observed satellite galaxies is $N_{\rm gal} \sim 50$ [97] and extrapolations to the entire MW virial volume show that $N_{\rm gal} \sim 150$ [161] are expected to be present, while CDM N-body simulations [14, 162, 163] predict that there should be $N_{\rm sub} \sim 1000$ dark subhalos with $M_{\rm sub} > 10^7\, M_\odot$. Nevertheless, this can be explained by the suppression of galaxy formation efficiency for low mass subhalos [164–166]. Therefore, the number of observed satellite galaxies does not seem to be in contradiction with numerical DM-only simulations, once the effects of baryons are included. Indeed, we will use these arguments to set a bound on the maximum amount of suppression which is allowed by current satellite counts. In what follows, we shall review the observational status and our treatment of the MW satellite galaxy counts.

[7] Notice that in our previous analyses [103], we did not consider the 95% CL constraints from the low redshift data set. Instead, we considered these measurements as lower limits.

JCAP06(2018)007

4.1 Observational Status

The current number of discovered satellite galaxies in the MW is 54, out of which 11 are the so-called classical ones, 17 have been discovered by DES [96, 97], 17 by SDSS [98, 99] and 9 have been found in other surveys (see appendix A of ref. [161] for a comprehensive catalog). Extrapolation to full sky of the total number of dwarf satellite galaxies in the MW has been a subject of intense study [161, 167–169]. We shall make use of the latest estimation [161], which accounts for the latest DES discoveries and newer simulations, and leads to the constrain $N_{\rm gal} > 85$ at 95% CL across the entire sky. Finally, it is worth to note that the estimate of the number of satellites in the MW from ref. [161] has been obtained from radial extrapolations of the subhalo distribution from CDM simulations. Nevertheless, the radial subhalo distribution has been shown to be fairly universal and independent of the DM properties [112]. Therefore, in the following, we will apply the bound

$$N_{\rm gal} > 85 \quad \text{at } 95\% \text{ CL} \,. \tag{4.1}$$

4.2 Number of subhalos in IDM scenarios

In order to set constraints on the IDM cross section, we now compute the number of satellite galaxies in the MW in terms of $\sigma_{\gamma \rm DM}$. The most sophisticated and accurate way of performing this calculation is through N-body simulations, and this approach has been followed in the past for IDM [47, 49] (see also refs. [28, 170] for the WDM case). Here, instead, we follow an analytical approach along the same lines of the recent ref. [15], circumventing the computationally expensive N-body simulations. This method requires as inputs the subhalo mass function for IDM cosmologies, and the probability for a subhalo to host a galaxy, $f_{\rm lum}(M)$. The number of subhalos is defined as [15]

$$N_{\rm sub} = \int_{M_{\rm min}}^{M_{\rm host}} \frac{dN}{dM}\, dM \,, \tag{4.2}$$

where $M_{\rm min}$ is the minimum subhalo mass considered, $M_{\rm host}$ is the mass of the host galaxy (in our case the MW) and dN/dM is the subhalo mass function. To obtain the number of satellite galaxies (namely, luminous subhalos) a correction to the above expression is required, so that the probability that a subhalo of a given mass hosts a luminous galaxy, $f_{\rm lum}(M)$, is accounted for and hence [15],

$$N_{\rm gal} = \int_{M_{\rm min}}^{M_{\rm host}} \frac{dN}{dM}\, f_{\rm lum}(M)\, dM \,. \tag{4.3}$$

From N-body simulations within the CDM scenario, a fit to the subhalo mass function has been obtained in ref. [171],

$$\frac{dN^{\rm CDM}}{dM^{\rm peak}} = K_0 \left(\frac{M^{\rm peak}}{M_\odot}\right)^{-\chi} \frac{M_{\rm host}}{M_\odot} \,, \tag{4.4}$$

where $K_0 = 1.88 \times 10^{-3}\, M_\odot^{-1}$ and $\chi = 1.87$ are fitting parameters and $M^{\rm peak}$ represents M_{200} at peak (i.e., the maximum mass of a subhalo achieved over its history enclosed by a volume that is $200\,\rho_c$, with ρ_c the critical density of the Universe). Note that the number of subhalos also depends on the mass of the host halo. In the particular case of the MW, the range of values for the MW mass [172] introduces an additional uncertainty, which we take into account.

JCAP06(2018)007

For the case of IDM scenarios, to the best of our knowledge, the only available N-body simulations are those from ref. [47], but unfortunately they did not provide a fit to the IDM subhalo mass function. Nevertheless, WDM simulations have shown that the suppression in the halo mass [26] and subhalo [28] mass functions are fairly similar, agreeing within 40%. Furthermore, the subhalo suppression is always more pronounced, as expected for non-CDM scenarios with reduced power at small scales. Therefore, following a conservative approach, for the IDM subhalo mass function we use the same parametric form of suppression, with respect to CDM, as given for halos in eq. (2.11), namely,

$$\frac{dN}{dM}^{\rm IDM} = \left(1+\frac{M_{\rm hm}}{b\,M}\right)^{a}\left(1+\frac{M_{\rm hm}}{g\,M}\right)^{c}\frac{dN}{dM}^{\rm CDM}\,, \tag{4.5}$$

with $a=-1$, $b=0.33$, $g=1$, $c=0.6$ and M is the mass at $z=0$, which is different from $M^{\rm peak}$ due to the effect of tidal stripping. They are related with the scaling relation $(M/M_\odot)=(M^{\rm peak}/M_\odot)^{0.965}$, which we obtain from a fit to the high-resolution halo catalog of the ELVIS simulation [163].

This is a conservative approach, as adopting this suppression should lead to a larger number of subhalos/galaxies than those resulting from dedicated IDM simulations. For the sake of comparison between IDM and WDM scenarios, we use of the following description of the WDM subhalo mass function [28]:

$$\frac{dN}{dM}^{\rm WDM} = \left(1+g_s\frac{M_{\rm hm}}{M}\right)^{-b_s}\frac{dN}{dM}^{\rm CDM}\,, \tag{4.6}$$

where $g_s=2.7$, $b_s=0.99$.

Assuming all DM subhalos to host luminous galaxies would largely overestimate the number of visible satellites [173–175]. This is the reason why we have introduced the function $f_{\rm lum}$ in eq. (4.3). We shall follow the results of ref. [171] for its description, bearing in mind they were obtained from a CDM merger history. In particular, the fraction of DM halos that host luminous galaxies, $f_{\rm lum}$, depends on the ionization model. Indeed, UV photons able to ionize hydrogen prevent sufficient cooling and gas accretion for star formation. The importance of this effect is actually encapsulated in the parameter $T_{\rm vir}^{\rm min}$, introduced in section 3. Here, we directly use the results of ref. [171] that explored possible scenarios with reionization redshifts $z_{\rm re}=14.4$, 11.3 and 9.3. Their most conservative choice, giving rise to the largest number of satellite galaxies, is a model with a reionization redshift of $z_{\rm re}=9.3$, and we focus on this particular realization.[8] The form of $f_{\rm lum}$ is a fast-rising function at a particular value of the subhalo mass (close to a step-function) which depends on the reionization redshift, reaching $f_{\rm lum}\sim 0.5$ at $M\sim 2\times10^8\,M_\odot$ for $z_{\rm re}=9.3$ (see figure 12 of ref. [171]).

In the next section, we use the results above in order to constraint IDM scenarios. In section 5.2, we also provide a direct comparison between the results of the analytic approach followed here and those obtained in ref. [47], based on IDM simulations. They are consistent with each other, which establishes the validity of the method we follow.

[8] A higher reionization redshift reduces the probability for a halo of reaching the critical size for H_2 and atomic cooling before reionization, reducing the probability for star-formation in such a halo and therefore suppressing the final number of satellite galaxies. In this regard, our numbers are conservative as the reionization redshift in this work is lower than the one used in ref. [171] to obtain $f_{\rm lum}$.

JCAP06(2018)007

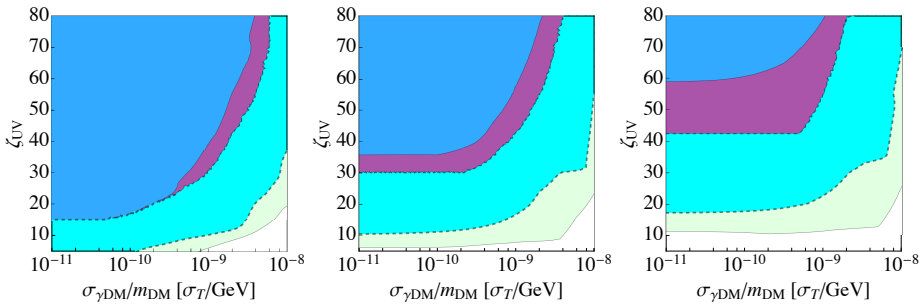

Figure 3. Constraints at 95% CL in the $(\sigma_{\gamma\mathrm{DM}}/m_{\mathrm{DM}}, \zeta_{\mathrm{UV}})$ plane, from τ and $\bar{x}_i$ measurements, for $T_{\mathrm{vir}}^{\mathrm{min}} = 10^4$, 5×10^4 and 10^5 K (from left to right). The cyan (dark blue) contours denote the 95% CL allowed regions from high-z (low-z) $\bar{x}_i$ data. The light green regions below these contours represent the 95% CL constraints from τ measurements. The dark purple regions denote the joint constraints from all three measurements.

5 Results and Prospects

5.1 Reionization constraints

The results from the analyses of the ionization history data are depicted in figure 3, where we show the 95% CL bounds arising from the three different χ^2 analyses in the $((\sigma_{\gamma\mathrm{DM}}/m_{\mathrm{DM}}), \zeta_{\mathrm{UV}})$ plane. We show one contour for each type of data (τ measurements in light green, Gunn-Peterson optical depth plus dark gaps in quasar spectra data at low-z in blue, and high-z constraints from Lyα emission in cyan). We also show the combined 95% CL region in dark purple. From left to right, the three panels illustrate the constraints for a value of the minimum virial temperature of $T_{\mathrm{vir}}^{\mathrm{min}} = 10^4$, 5×10^4 and 10^5 K.

First of all, notice that the τ measurement, being an integrated quantity, can only set modest constraints on the parameter space, as can be seen from the green contours in figure 3 (see also ref. [67] for a related discussion). Furthermore, the larger the minimum virial temperature, the worse its constraining power, as even if larger values of $T_{\mathrm{vir}}^{\mathrm{min}}$ imply lower values of τ, this effect can be easily compensated with a higher ionization efficiency, ζ_{UV}. Even for the lowest $T_{\mathrm{vir}}^{\mathrm{min}} = 10^4$ K we consider (left panel), a larger value of $\sigma_{\gamma\mathrm{DM}}$ (i.e., a more important suppression of power at small scales that would delay reionization) could be compensated by a larger UV ionizing efficiency ζ_{UV}. This shows the strong (positive) correlation of these two parameters. Indeed, a similar correlation appears for the high-z, Lyα emission data (cyan contours) for all values of $T_{\mathrm{vir}}^{\mathrm{min}}$: the smaller $T_{\mathrm{vir}}^{\mathrm{min}}$ (i.e., the smaller the minimum mass for star formation and thus the earlier the period of reionization), the larger the value of ζ_{UV} needed to recover consistency with data.

In addition, with the low-z data set, which indicates $\bar{x}_i \simeq 1$ with a high degree of precision (see table 2), one can further constrain the parameter space (see dark blue regions in figure 3). In order to explain these data, a large ionization efficiency $\zeta_{\mathrm{UV}} > 30$ is required to ensure that reionization is complete by $z \simeq 5 - 6$. As it might not be possible to compensate the delayed reionization caused by a large DM-photon cross section due to the suppression of power at small scales, this results into an upper bound on the cross section, $\sigma_{\gamma\mathrm{DM}}/\sigma_T \lesssim 4 \times 10^{-9}\,(m_{\mathrm{DM}}/\mathrm{GeV})$ at 95% CL, for all values of $T_{\mathrm{vir}}^{\mathrm{min}}$. Indeed, it appears that low and high-z data sets constrain different regions of the parameter space. Therefore, when these

JCAP06(2018)007

data sets are combined (see the dark purple contours in figure 3), upper (lower) bounds on the interacting DM cross section (UV efficiency) can be obtained. We would like to stress this point, as the combination of more precise low-z and high-z measurements of the ionization history could set strong limits to IDM scenarios or to any other non-CDM cosmologies. In this regard, 21 cm probes, which are expected to map the HI along the Universe's history and therefore cover a wide redshift range, may help in testing this type of scenarios (see section 5.4).

5.2 Milky Way satellites constraints

We focus now on the constraints from MW satellite galaxies. By means of eq. (4.3) with the CDM subhalo mass functions, and using the IDM subhalo suppression, eq. (4.5), we have calculated the number of satellite galaxies in the MW as a function of the photon-DM elastic scattering cross section. Imposing the aforementioned 95% CL lower limit in the number of satellite galaxies (i.e., $N_{\rm gal} > 85$ [161]), we obtain the bounds on the IDM cross section depicted by the blue curve in figure 4. Notice that we show the results as a function of the MW mass $M_{\rm MW}^{200}$, within its expected mass range [172]. The most conservative 95% CL upper limit on the IDM cross section is found for the highest value of $M_{\rm MW}^{200}$ considered here (i.e., $(\sigma_{\gamma \rm DM}/\sigma_T) < 8 \times 10^{-10}$ $(m_{\rm DM}/{\rm GeV})$). For the sake of completeness, we also show the 95% CL lower bounds on the WDM mass by the red curve in figure 4. The most conservative 95% CL lower limit corresponds to $m_{\rm WDM} > 2.8\,{\rm keV}$ (for a thermal candidate). Notice that these results imply an order of magnitude improvement on the DM-photon elastic scattering cross section over those previously obtained in ref. [47], while the bound on the WDM mass we find is very similar to the results from N-body simulations from ref. [170].

Let us now compare our results with those of previous analyses of MW satellite galaxies. While a direct comparison of the bounds from MW number counts derived here to the ones obtained in ref. [47] is non-trivial, we nevertheless make a comparison to clearly state the validity of our method. In ref. [47], the cumulative number count of MW satellites was studied as a function of their maximal circular velocity, $V_{\rm max}$, the latter being a measure of their mass. In contrast, our method relies on the subhalo mass M. This implies that, for a direct comparison, we would need a relationship between $V_{\rm max}$ and M for IDM, which is still missing in the literature. Furthermore, due to the finite resolution, ref. [47] only considered subhalos with a maximum peak velocity $V_{\rm max} \gtrsim 8\,{\rm km/s}$, while there are known satellites with $V_{\rm max} \sim 5.7\,{\rm km/s}$ [176]. We know, however, from WDM simulations [28] (that show a similar matter power suppression to that of IDM) that $V_{\rm max} = 8\,{\rm km/s}$ corresponds to $M_{\rm sub} \sim 10^8\,M_\odot$. As a result, the total number of satellites with $V_{\rm max} > 8\,{\rm km/s}$ is expected to be $N_{\rm sub}(V_{\rm max} > 8\,{\rm km/s}) > 40$ at 95% CL [177]. Finally, since the simulations in ref. [47] only considered DM, they did not include the luminosity function of subhalos discussed above. This is the reason for using here the fraction of DM halos that host luminous galaxies $f_{\rm lum}(M)$ from CDM simulations (see section 4.2 for the derivation of the constraints in section 5.2).

All in all, in order to make a fair comparison with previous estimates, *(a)* we shall compare subhalos and not galaxies; *(b)* we shall require that the minimum mass of the subhalos to be considered satisfies $M_{\rm sub}^{\rm min} \sim 10^8\,M_\odot$; and *(c)* we should impose $N_{\rm sub} > 40$. The comparison of our results to those of ref. [47] under these conditions is illustrated in figure 5. The red dashed curve shows our results for a minimum subhalo mass $M_{\rm sub} \sim 10^8\,M_\odot$, see eq. (4.3), which roughly corresponds to $V_{\rm max} = 8\,{\rm km/s}$. We also illustrate with the blue region the results we would obtain for a minimum subhalo mass within the interval $M_{\rm sub}^{\rm min} \in [7 \times 10^7,\, 2 \times 10^8]\,M_\odot$. This blue region should be compared with the results based

JCAP06(2018)007

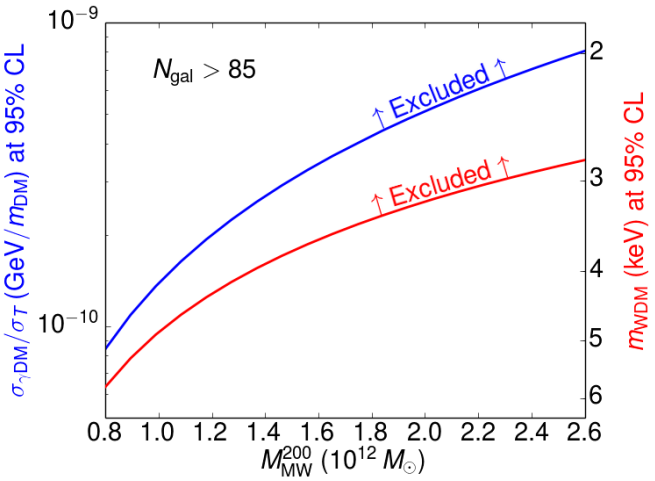

Figure 4. The top blue (bottom red) curve shows the 95% CL upper (lower) limits on the DM-photon cross section (WDM mass) as a function of the MW mass. The y-axes are calibrated so that the models have the same transfer function up to the first damped oscillatory mode in the IDM and WDM matter power spectra (see eq. (2.5) and figure 1).

on IDM N-body simulations previously obtained in ref. [47], shown here with the red solid line. As the agreement between the two approaches is fairly good, the method used here to derive bounds on the IDM cross section using MW number counts is well justified.

5.3 Combination of constraints

In figure 6 we depict the 95% CL bounds from the global χ^2 analysis (profiling over $T_{\rm vir}^{\rm min}$), by combining low-z (Gunn-Peterson and dark gaps in quasar spectra data) and high-z $\bar{x}_i$ measurements together with the constraints on the reionization optical depth τ from the Planck satellite, in the $((\sigma_{\gamma \rm DM}), \zeta_{\rm UV})$ plane. Notice the large degeneracy between the DM-photon cross section and the UV efficiency, already discussed in section 5.1 and also present in figure 3. We have superimposed the allowed regions from the MW satellite number counts likelihood. Note that for our estimates of the number of satellite galaxies, we have considered the most conservative reionization scenario from ref. [171] to describe $f_{\rm lum}$, with $z_{\rm re} = 9.3$, and that different reionization redshifts would correspond to different values of $T_{\rm vir}^{\rm min}$ (if all other parameters are fixed). From this perspective, we can assume to have already approximately marginalized with respect to $T_{\rm vir}^{\rm min}$ (and $\zeta_{\rm UV}$) and thus, these bounds only depend on the IDM cross section. We report the 95% CL exclusion region derived from satellite counts assuming a MW mass of $M_{\rm MW}^{200} = 0.8 \times 10^{12}\ M_\odot$ (shaded blue region) and $M_{\rm MW}^{200} = 2.6 \times 10^{12}\ M_\odot$ (shaded orange region). These former bounds turn out to be the most stringent ones and help alleviating the strong degeneracy between $\sigma_{\gamma \rm DM}$ and $\zeta_{\rm UV}$ present with τ and $\bar{x}_i$ data. Therefore, within the limited number of parameters considered in this work, the preferred values of $\zeta_{\rm UV}$ in IDM scenarios approximately coincide with those in the standard CDM case [130, 132].

JCAP06(2018)007

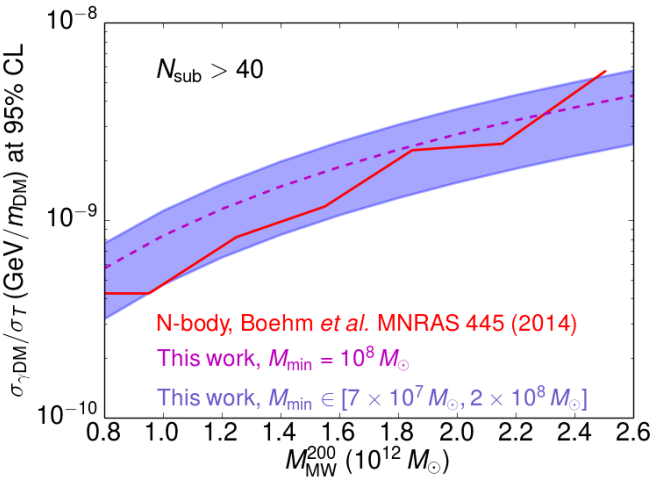

Figure 5. Upper limits on the DM-photon elastic scattering cross section as a function of the MW mass, obtained at 95% CL. They are calculated following the method described in section 4.2 by setting $N_{\rm sub} > 40$, considering subhalos with masses above the range $M^{\rm min}_{\rm sub} \in [7\times10^7, 2\times10^8]\ M_\odot$ (blue contour) and also by fixing the subhalo mass to $M_{\rm sub} \sim 10^8\,M_\odot$ (dashed curve). For comparison purposes, we also report the constraints from N-body simulations from ref. [47] with the red solid line.

Recall, however, that the DM model featuring a velocity-independent DM-γ scattering cross section considered in our work would correspond to millicharged DM. The stringent limits on this model obtained in ref. [94] translate into the constraint

$$\sigma_{\gamma{\rm DM}} < 8.5\times10^{-19}\,\sigma_T\left(\frac{\rm GeV}{m_{\rm DM}}\right), \tag{5.1}$$

valid for $m_{\rm DM} \gtrsim$MeV, and which is several orders of magnitude more constraining than the limit that we have derived from satellite number count. Now, the effects of DM-photon scattering on the observables considered here are expected to be very similar to those of DM-neutrino interactions. Indeed, the suppression of power at small scales has been shown to be very similar in these two scenarios for the same halo half-mode mass [48]. Lacking dedicated fits for the halo mass function in the DM-neutrino scenario, a rough estimation of the limits on $\sigma_{\nu{\rm DM}}$ can be obtained by rescaling the bounds derived here in terms of the half-mode mass. Noting that very similar half-mode masses are obtained for $\sigma_{\nu{\rm DM}} \sim 1.5\times\sigma_{\gamma{\rm DM}}$ (see section 2), the limits on $\sigma_{\nu{\rm DM}}$ are expected to be in the range 10^{-9} to $10^{-10}\times\sigma_T\,(m_{\rm DM}/{\rm GeV})$, which is similar to the constraints from Lyα, $\sigma_{\nu{\rm DM}} \lesssim 1.5\times10^{-9}\,\sigma_T\,(m_{\rm DM}/{\rm GeV})$ [83].

5.4 Imprint of IDM and WDM scenarios on the 21 cm signal

Finally, let us briefly discuss the IDM signature in other future cosmological observations. New insights on the EoR ($z = 6$–12) and the cosmic dawn ($z \sim 30$) will be provided by the study of the redshifted 21 cm signal (in emission or absorption) from the primordial IGM, associated to the transition between singlet and triplet hyperfine levels of the hydrogen ground

JCAP06(2018)007

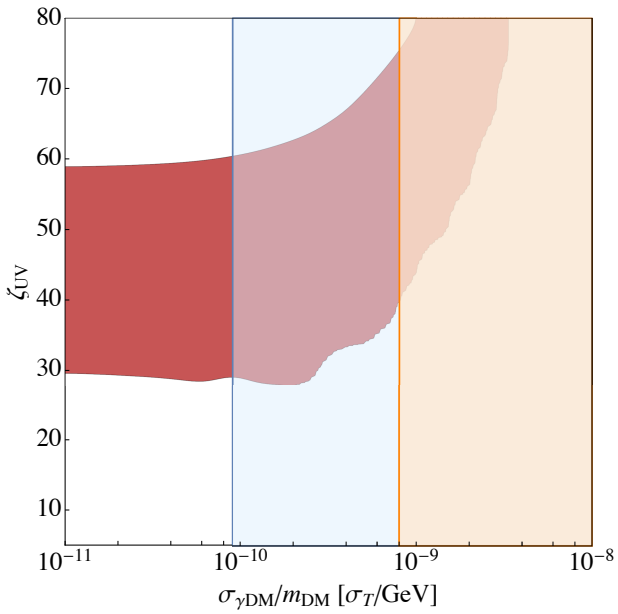

Figure 6. Global constraints, at 95% CL, on the $(\sigma_{\gamma\rm DM}/m_{\rm DM}, \zeta_{\rm UV})$ plane. We depict the allowed region from the combination of τ and $\bar{x}_i$ data, after profiling over $T_{\rm vir}^{\rm min}$ (red contour); and the excluded region from satellite counts, assuming a MW mass of $M_{\rm MW}^{200} = 0.8 \times 10^{12}\ M_\odot$ (shaded blue region) and $M_{\rm MW}^{200} = 2.6 \times 10^{12}\ M_\odot$ (shaded orange region).

state. The observation of the 21 cm line signal represents several advantages compared to traditional cosmic and astrophysical probes (see, e.g., refs. [178, 179]). Given that hydrogen is the most abundant element in the Universe, this signal traces the baryonic matter density. By measuring the collective emission from large regions without resolving individual galaxies (intensity mapping), three-dimensional maps of the 21 cm signal could also be obtained. The first generation of radio interferometers testing the 21 cm signal includes the Low Frequency Array (LOFAR) [180], the MIT EoR experiment [181], the Murchison Widefield Array (MWA) [182, 183] and the Precision Array for Probing the Epoch of Reionization (PAPER) [184] projects, which have already provided upper bounds on the 21 cm signal power spectrum [184, 185]. However, these first-generation experiments may not be able to make a definitive detection of the 21 cm signal [186]. The next generation of instruments, such as the Hydrogen Epoch of Reionization Array (HERA) [186, 187] and the Square Kilometer Array (SKA) [188] will benefit from a larger collecting area and are therefore expected to provide significant measurements of the 21 cm power spectrum. All these experiments will have to deal with foregrounds, that are ~ 5 times stronger than the 21 cm cosmological signal (see, e.g., ref. [186] for a summary of different avenues to solve the foregrounds issue).

At this point, let us also mention the recent detection claim of the sky-averaged global 21 cm signal at a redshift $z \sim 18$ by the Experiment to Detect the Global Epoch of Reionization Signatures (EDGES) [189]. The reported absorption in the measured 21 cm global signal appears to be deeper than that expected in standard CDM scenarios and therefore

JCAP06(2018)007

it cannot be explained by any mechanism that gives rise to heating of the IGM (e.g., DM annihilations [190, 191]). The IDM and WDM scenarios under study in this paper are also unlikely to explain this deep absorption, as they will only shift the absorption dip to later times, leaving unchanged the amplitude of the dip (see lower panels of figure 7). In any case, the EDGES measurement would still need confirmation from observations in other instruments, such as the Large Aperture Experiment to Detect the Dark Ages (LEDA) [192] or via the detection of the 21 cm power spectrum in the redshift range covered by HERA or SKA.

The brightness of a patch of the IGM relative to the CMB is expressed in terms of the differential brightness temperature, δT_b, and can be written as [179, 193–195]

$$\frac{\delta T_b(\nu)}{\mathrm{mK}} \simeq 27 x_{\mathrm{HI}}(1+\delta_b)\left(1-\frac{T_{\mathrm{CMB}}}{T_{\mathrm{S}}}\right)\left(\frac{H}{H+\frac{\partial v_r}{\partial r}}\right)\left(\frac{1+z}{10}\right)^{1/2}\left(\frac{0.15}{\Omega_m h^2}\right)^{1/2}\left(\frac{\Omega_b h^2}{0.023}\right), \tag{5.2}$$

where x_{HI} represents the fraction of neutral hydrogen, δ_b is the baryon overdensity, $\Omega_b h^2$ and $\Omega_m h^2$ refer to the current baryon and matter contribution to the Universe's mass-energy content, $H(z)$ is the Hubble parameter and $\partial v_r/\partial r$ is the comoving gradient of the peculiar velocity along the line of sight. The above expression is exact if $\partial v_r/\partial r$ is constant over the width of the 21 cm line and $\partial v_r/\partial r \ll H$. The ratio of the populations of the two ground state hyperfine levels of hydrogen is quantified by the spin temperature, T_{S}, which is determined by three competing effects [196]: 1) absorption and stimulated emission of CMB photons; 2) atomic collisions, which are important at high redshifts, well before the EoR; and 3) resonant scattering of Lyα photons that turn on with the first sources, the so-called Wouthuysen-Field effect [197, 198]. The differential brightness temperature power spectrum is defined as

$$\langle \widetilde{\delta}_{21}(\mathbf{k},z)\,\widetilde{\delta}^{*}_{21}\left(\mathbf{k}',z\right)\rangle \equiv (2\pi)^3\,\delta^{D}\left(\mathbf{k}-\mathbf{k}'\right)\,P_{21}(k,z)\,, \tag{5.3}$$

where δ^D is the Dirac delta function, the brackets denote an ensemble average, and $\widetilde{\delta}_{21}(\mathbf{k},z)$ refers to the Fourier transform of $\delta_{21}(\mathbf{x},z) = \delta T_b(\mathbf{x},z)/\overline{\delta T_b}(z) - 1$ where $\overline{\delta T_b}(z)$ is the sky-averaged differential brightness temperature. The power spectrum $P_{21}(k,z)$ carries information about the correlations in the spin temperature field and is expected to provide the highest signal-to-noise ratio measurement of the 21 cm line around the EoR in the near future. The dimensionless 21 cm differential brightness temperature power spectrum, is defined as

$$\Delta^2_{21}(k,z) = \frac{k^3}{2\pi^2}\,P_{21}(k,z)\,. \tag{5.4}$$

In figure 7, we show the 21 cm power spectrum, $\Delta^2_{21}(k,z)$, multiplied by $\overline{\delta T_b}^2$, as a function of redshift at a fixed scale of $k = 0.2\,\mathrm{h/Mpc}$ (top panels) and the corresponding $\overline{\delta T_b}(z)$ (bottom panels) for CDM (dotted curves) and for the WDM (dashed curves) and IDM (by the solid curves) benchmark scenarios described in table 1. These curves have been obtained with the public code `21cmFast` [129]. One can see that, for the redshift range shown in figure 7 several typical features appear in both $\Delta^2_{21}(z)$ and $\overline{\delta T_b}$. They are directly related to the physical processes driving the 21 cm emission or absorption (see, e.g., refs. [109, 179, 195]). The power spectra (top panels) show a three-peak structure related, from left to right, to the EoR, the epoch of X-ray heating and the Lyα coupling. The sky-averaged signal appears to be in absorption until X-ray heating processes and in emission until the end of EoR. The expected sensitivities of the HERA350 configuration to 21 cm power spectrum measurements [186] are also shown for the IDM power spectrum in one of

JCAP06(2018)007

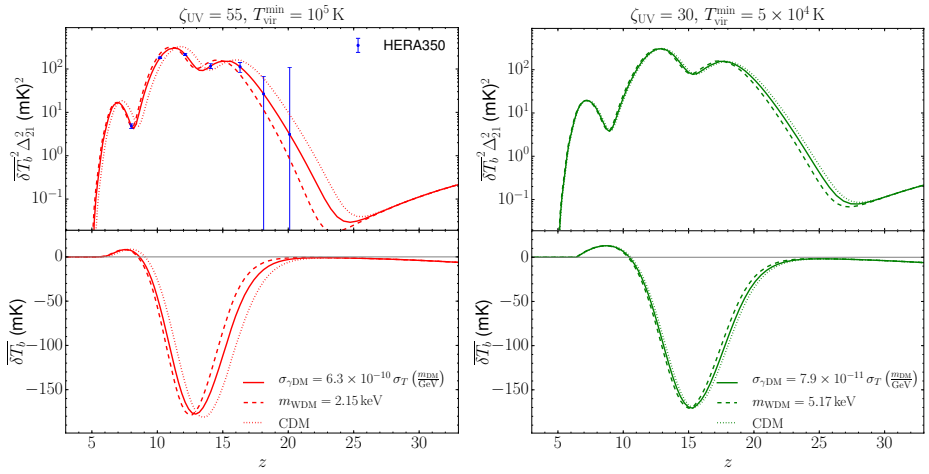

Figure 7. The top panels show the power spectrum of the redshifted 21 cm signal, $\Delta_{21}(z)$, as a function of redshift, z, at a fixed scale of $k = 0.2\,{\rm h/Mpc}$. The bottom panels depict the associated sky averaged differential brightness temperature, $\delta T_b(z)$. We illustrate the results for CDM (dotted curves), WDM (dashed curves) and IDM (solid curves) scenarios, for the parameter values specified in table 1. The IDM and WDM scenarios with a very strong (weak) suppression at small scales are depicted in the left (right) panel. In the left panel we also show the expected sensitivities for the IDM power spectrum from the HERA350 configuration (blue bars) [186].

our benchmark models. These sensitivities have been obtained with the publicly available code `21cmSense` [187, 199].[9] We consider in all cases, a total observing time of 1080 hours and a bandwidth of 8 MHz, being both the default parameters in `21cmSense`. The error bars have been computed for $z = 8$, 10, 12, 14, 16 and 20 and include thermal noise plus sample variance. The sensitivity is very good for $z \lesssim 16$, especially around the X-ray heating and the EoR peaks. The left (right) panel of figure 7, corresponds to a WDM/IDM scenario that produces a strong (weak) small scale suppression (see table 1), within the allowed region by the measurements discussed in this work. We also show the results for the CDM case, obtained for the very same astrophysical parameters. Overall, WDM and IDM scenarios give rise to a delay in structure formation that shifts to later times the typical features in the 21 cm sky-averaged signal and power spectrum. The same effect was observed when we discussed reionization in section 5.1 and it is more pronounced for the WDM case.

For a fixed value of the half-mode mass, there is a fall of power in Δ_{21}^2 for IDM and WDM models, and a corresponding vanishing $\overline{\delta T_b}$, at very similar redshift, $z \sim 8$, driven by the end of reionization, as expected from figure 2. However, comparing IDM and WDM scenarios, the difference in the shifts of the second (X-ray heating) and third (Lyα coupling) peaks is more pronounced than in the first peak (EoR). Therefore, the differences between IDM and WDM cannot be simply compensated by a shift in the redshift evolution of the 21 cm signal (as it is the case, for instance, when changing $T_{\rm vir}^{\rm min}$ [191]). The larger number of low mass halos in the IDM case shifts the different milestone epochs of the 21 cm signal in a non-trivial and different way from the WDM case. This is very interesting, as points to a distinctive

[9] https://github.com/jpober/21cmSense.

JCAP06(2018)007

signature to disentangle these two scenarios, otherwise difficult to distinguish. Thus, in principle, barring out of the discussion astrophysical uncertainties, one could potentially be able to differentiate between IDM and WDM scenarios by studying the redshift interval between the reionization and the X-ray heating processes, although a dedicated analysis is beyond the scope of this paper. Obviously, for very small (large) values of the IDM cross section (WDM mass), distinguishing any of these scenarios (WDM, IDM and CDM) from each other would be even more challenging (see the right panels of figure 7).

6 Summary and conclusions

A number of observational probes of our Universe at galactic and subgalactic scales may require a modification to the standard CDM paradigm. These small-scale measurements indicate that *(a)* dwarf galaxies are hosted by halos that are less massive than those predicted in the CDM numerical simulations, and *(b)* the observed number of satellite galaxies that orbit close to the MW is smaller than that predicted within standard CDM cosmology. Possible avenues to overcome these problems have been proposed in the literature [36, 37], ranging from lowering the total mass of the satellites by baryon or supernovae feedback effects [16–18], by changes in the numerical simulations [27] or by modifying the DM model sector. Focusing on this last solution, possible modifications to the standard CDM paradigm include IDM scenarios (see, e.g., ref. [49]) and WDM candidates (such as sterile neutrinos) [25, 28, 34], which attracted recently more attention due to possible hints in X-ray data [38–41]. Here, we have focused on IDM scenarios (and its comparison with WDM scenarios), as they provide a possible solution to the small-scale crisis via collisional damping effects that would suppress the amount of small-scale structures. Nevertheless, the suppression of small structures would also directly impact on different cosmological observables. In this work we consider the impact of these non-CDM scenarios on reionization-related observables, along with constraints from the number of observed satellite galaxies of the MW.

After describing the halo mass function obtained from numerical simulations in the case of IDM (and WDM) scenarios (section 2), we first study the effects on the ionization history of the Universe within this kind of scenarios (figure 2), parameterized by the ratio of the DM-photon elastic scattering cross section, $\sigma_{\gamma\mathrm{DM}}$: the IDM collisional damping would wash out small-scale overdensities, delaying the onset of reionization and thus, would affect reionization-related observables. We have considered three different types of measurements in order to constrain the IDM scenario. Namely, for our analyses we include the CMB Planck integrated optical depth τ, the Gunn-Peterson optical depth low-z data and high-z constraints from Lyα emission (section 3). Nevertheless, the effects of collisional damping in IDM scenarios are somewhat degenerate with a number of (uncertain) astrophysical parameters governing the ionization processes in the Universe, as the minimum virial temperature $T_{\mathrm{vir}}^{\mathrm{min}}$ and the UV ionization efficiency, ζ_{UV}. Indeed, we have explicitly shown the degeneracy between ζ_{UV} and $\sigma_{\gamma\mathrm{DM}}$ (figure 3). Although current data are not precise enough to disentangle it, the combination of future low-z Gunn-Peterson and high-z measurements of the ionization history provides a promising tool to discard IDM scenarios. All in all, at present, the combination of reionization observables allows us to set an upper bound on IDM cross section, $\sigma_{\gamma\mathrm{DM}} < 4 \times 10^{-9}\, \sigma_T \times (m_{\mathrm{DM}}/\mathrm{GeV})$ at 95% CL.

These constraints are complemented by studying the predicted number of MW satellites as a function of the IDM cross section, which are also compared with the results in WDM scenarios using the DM mass as the free parameter (section 4). We profit here from the

JCAP06(2018)007

recent updates in the statistics of MW satellite galaxy number counts: the eleven classical MW satellites, the seventeen objects discovered by DES [96, 97], the seventeen satellites detected by SDSS [98, 99] and the nine objects found in other surveys [161]. Using the latest estimation for the number of satellite galaxies, $N_{\rm gal}$, of the MW, which accounts for the latest discoveries and recent N-body simulations, a lower bound was obtained, $N_{\rm gal} > 85$ at 95% CL [161]. This result is confronted with the predictions for IDM (and WDM) scenarios in order to constrain the IDM cross section (and WDM mass). For these estimates, we follow the analytical approach of ref. [15] and take into account the probability of a subhalo to actually host a galaxy (section 4). Our most conservative 95% CL upper limit on the IDM cross section is found for the highest value of the MW mass we consider ($M^{200}_{\rm MW} = 2.6 \times 10^{12}\ M_\odot$), $\sigma_{\gamma \rm DM} < 8 \times 10^{-10}\, \sigma_T\ (m_{\rm DM}/{\rm GeV})$ (figure 4), which implies an order of magnitude improvement over the limits on the DM-photon elastic scattering cross section obtained in ref. [47]. Nevertheless, we have also shown that under the same assumptions and using the same set of data, we can approximately recover the results of this previous work (figure 5). In case that the MW mass is $M^{200}_{\rm MW} = 0.8 \times 10^{12}\ M_\odot$, the resulting 95% CL upper limit on the IDM cross section is found to be $\sigma_{\gamma \rm DM} < 9 \times 10^{-11}\, \sigma_T\ (m_{\rm DM}/{\rm GeV})$. Note that recent analyses using Gaia data point toward the lower side range of MW masses that we consider [200–203].

Throughout this paper, we have also discussed the impact of another non-CDM scenario, as it is the case of WDM candidates. This scenario could also potentially solve discrepancies observed at galactic and subgalactic scales. Due to their free-streaming, WDM particles would also lead to a suppression in the small-scale power spectrum. Indeed, it is possible to establish an approximate connection between the power spectrum in these two non-CDM scenarios (figure 1), in terms of the scale at which the transfer function is reduced by half, although the connection between the number of low-mass halos requires additional corrections (section 2). Therefore, in a similar way we can obtain an upper limit on the IDM cross section, we can also obtain a lower limit on the WDM mass. Using MW satellite galaxy counts and similarly as done for IDM, we get $m_{\rm WDM} > 2.8\,{\rm keV}$ at 95% CL for a thermal candidate (or $m_s > 16\,{\rm keV}$ at 95% CL for a non-resonantly produced sterile neutrino) for $M^{200}_{\rm MW} = 2.6 \times 10^{12}\ M_\odot$ (figure 4).

These results indicate that currently, among the different data sets used in this analysis, the most restricting one for the non-CDM scenarios considered is the estimated number of MW satellite galaxies (figure 6). Notice, though, that since DM-photon interactions of the type considered in this work imply DM-nucleon interactions with a Rutherford-like cross section, Lyα and CMB data set more stringent constraints on the latter than the bounds obtained here. We argue, however, that the method use could be applied to any other IDM model with DM-radiation interaction. In particular, in the case of DM-neutrino interactions, the bounds derived in this work are among the most constraining limits on such scenario.

Note that the approximate connection that can be established between IDM and WDM scenarios also implies that they give rise to very similar effects in the observables we have considered and thus, the IDM cross section is (almost) fully degenerate with the WDM mass. Therefore, distinguishing them using this type of data would be a very challenging task. Nevertheless, we have also briefly discussed the potential distinctive signatures of these scenarios in future cosmological measurements of the 21 cm hydrogen line (section 5.4), which will probe the Universe evolution beyond the EoR. In particular, IDM scenarios could give rise to a larger relative shift in redshift between the characteristic features of the 21 cm power spectrum and of the sky-averaged global brightness temperature than WDM scenarios with

JCAP06(2018)007

the same half-mode mass. Therefore, future, very large radio interferometers, as HERA or SKA, may also be important tools to shed light on the nature of DM particles and on their precise clustering and interacting properties.

Acknowledgments

We would like to thank J. Pober for providing us with the HERA350 configuration files, C. Bœhm for discussions and P. Champion for useful cross-checks. ME is supported by Spanish Grant FPU13/03111 of MECD. LLH is supported by the Fonds National de la Recherche Scientifique, by the Belgian Federal Science Policy Office through the Interuniversity Attraction Pole P7/37 and by the Vrije Universiteit Brussel through the Strategic Research Program *High-Energy Physics*. ME, OM, PVD are supported by PROMETEO II/2014/050 and by the Spanish Grants FPA2014-57816-P and FPA2017-85985-P of the MINECO. SPR is supported by a Ramón y Cajal contract, by the Spanish MINECO under grants FPA2017-84543-P and FPA2014-54459-P and by the Generalitat Valenciana under grant PROMETEOII/2014/049. ME, OM, SPR and PVD are also supported by the MINECO Grant SEV-2014-0398 and by the European Union's Horizon 2020 research and innovation program under the Marie Skłodowska-Curie grant agreements No. 690575 and 674896. SPR is also partially supported by the Portuguese FCT through the CFTP-FCT Unit 777 (PEst-OE/FIS/UI0777/2013).

References

[1] G. Bertone, D. Hooper and J. Silk, *Particle dark matter: Evidence, candidates and constraints*, *Phys. Rept.* **405** (2005) 279 [hep-ph/0404175] [INSPIRE].

[2] L. Bergström, *Dark Matter Candidates*, *New J. Phys.* **11** (2009) 105006 [arXiv:0903.4849] [INSPIRE].

[3] H. Baer, K.-Y. Choi, J.E. Kim and L. Roszkowski, *Dark matter production in the early Universe: beyond the thermal WIMP paradigm*, *Phys. Rept.* **555** (2015) 1 [arXiv:1407.0017] [INSPIRE].

[4] N. Bernal, M. Heikinheimo, T. Tenkanen, K. Tuominen and V. Vaskonen, *The Dawn of FIMP Dark Matter: A Review of Models and Constraints*, *Int. J. Mod. Phys.* **A 32** (2017) 1730023 [arXiv:1706.07442] [INSPIRE].

[5] L. Roszkowski, E.M. Sessolo and S. Trojanowski, *WIMP dark matter candidates and searches — current issues and future prospects*, *Rept. Prog. Phys.* **81** (2018) 066201 [arXiv:1707.06277] [INSPIRE].

[6] M.R. Buckley and A.H.G. Peter, *Gravitational probes of dark matter physics*, arXiv:1712.06615 [INSPIRE].

[7] Planck collaboration, P.A.R. Ade et al., *Planck 2015 results. XIII. Cosmological parameters*, *Astron. Astrophys.* **594** (2016) A13 [arXiv:1502.01589] [INSPIRE].

[8] BOSS collaboration, S. Alam et al., *The clustering of galaxies in the completed SDSS-III Baryon Oscillation Spectroscopic Survey: cosmological analysis of the DR12 galaxy sample*, *Mon. Not. Roy. Astron. Soc.* **470** (2017) 2617 [arXiv:1607.03155] [INSPIRE].

[9] J.S. Bullock and M. Boylan-Kolchin, *Small-Scale Challenges to the ΛCDM Paradigm*, *Ann. Rev. Astron. Astrophys.* **55** (2017) 343 [arXiv:1707.04256] [INSPIRE].

[10] A.A. Klypin, A.V. Kravtsov, O. Valenzuela and F. Prada, *Where are the missing Galactic satellites?*, *Astrophys. J.* **522** (1999) 82 [astro-ph/9901240] [INSPIRE].

JCAP06(2018)007

[11] B. Moore, S. Ghigna, F. Governato, G. Lake, T.R. Quinn, J. Stadel et al., *Dark matter substructure within galactic halos*, *Astrophys. J.* **524** (1999) L19 [astro-ph/9907411] [INSPIRE].

[12] M. Boylan-Kolchin, J.S. Bullock and M. Kaplinghat, *The Milky Way's bright satellites as an apparent failure of LCDM*, *Mon. Not. Roy. Astron. Soc.* **422** (2012) 1203 [arXiv:1111.2048] [INSPIRE].

[13] B. Moore, T.R. Quinn, F. Governato, J. Stadel and G. Lake, *Cold collapse and the core catastrophe*, *Mon. Not. Roy. Astron. Soc.* **310** (1999) 1147 [astro-ph/9903164] [INSPIRE].

[14] V. Springel, J. Wang, M. Vogelsberger, A. Ludlow, A. Jenkins, A. Helmi et al., *The Aquarius Project: the subhalos of galactic halos*, *Mon. Not. Roy. Astron. Soc.* **391** (2008) 1685 [arXiv:0809.0898] [INSPIRE].

[15] S.Y. Kim, A.H.G. Peter and J.R. Hargis, *There is No Missing Satellites Problem*, arXiv:1711.06267 [INSPIRE].

[16] T. Sawala, C.S. Frenk, R.A. Crain, A. Jenkins, J. Schaye, T. Theuns et al., *The abundance of (not just) dark matter haloes*, *Mon. Not. Roy. Astron. Soc.* **431** (2013) 1366 [arXiv:1206.6495] [INSPIRE].

[17] T. Sawala et al., *The APOSTLE simulations: solutions to the Local Group's cosmic puzzles*, *Mon. Not. Roy. Astron. Soc.* **457** (2016) 1931 [arXiv:1511.01098] [INSPIRE].

[18] A. Fattahi, J.F. Navarro, T. Sawala, C.S. Frenk, L.V. Sales, K. Oman et al., *The cold dark matter content of Galactic dwarf spheroidals: no cores, no failures, no problem*, arXiv:1607.06479 [INSPIRE].

[19] T. Nakama, J. Chluba and M. Kamionkowski, *Shedding light on the small-scale crisis with CMB spectral distortions*, *Phys. Rev.* **D 95** (2017) 121302 [arXiv:1703.10559] [INSPIRE].

[20] P. Bode, J.P. Ostriker and N. Turok, *Halo formation in warm dark matter models*, *Astrophys. J.* **556** (2001) 93 [astro-ph/0010389] [INSPIRE].

[21] A. Knebe, J.E.G. Devriendt, A. Mahmood and J. Silk, *Merger histories in WDM structure formation scenarios*, *Mon. Not. Roy. Astron. Soc.* **329** (2002) 813 [astro-ph/0105316] [INSPIRE].

[22] P. Colin, O. Valenzuela and V. Avila-Reese, *On the Structure of Dark Matter Halos at the Damping Scale of the Power Spectrum with and without Relict Velocities*, *Astrophys. J.* **673** (2008) 203 [arXiv:0709.4027] [INSPIRE].

[23] J. Zavala, Y.P. Jing, A. Faltenbacher, G. Yepes, Y. Hoffman, S. Gottlober et al., *The velocity function in the local environment from LCDM and LWDM constrained simulations*, *Astrophys. J.* **700** (2009) 1779 [arXiv:0906.0585] [INSPIRE].

[24] R.E. Smith and K. Markovic, *Testing the Warm Dark Matter paradigm with large-scale structures*, *Phys. Rev.* **D 84** (2011) 063507 [arXiv:1103.2134] [INSPIRE].

[25] M.R. Lovell, V. Eke, C.S. Frenk, L. Gao, A. Jenkins, T. Theuns et al., *The Haloes of Bright Satellite Galaxies in a Warm Dark Matter Universe*, *Mon. Not. Roy. Astron. Soc.* **420** (2012) 2318 [arXiv:1104.2929] [INSPIRE].

[26] A. Schneider, R.E. Smith, A.V. Maccio and B. Moore, *Nonlinear Evolution of Cosmological Structures in Warm Dark Matter Models*, *Mon. Not. Roy. Astron. Soc.* **424** (2012) 684 [arXiv:1112.0330] [INSPIRE].

[27] E. Polisensky and M. Ricotti, *Massive Milky Way Satellites in Cold and Warm Dark Matter: dependence on Cosmology*, *Mon. Not. Roy. Astron. Soc.* **437** (2014) 2922 [arXiv:1310.0430] [INSPIRE].

JCAP06(2018)007

[28] M.R. Lovell, C.S. Frenk, V.R. Eke, A. Jenkins, L. Gao and T. Theuns, *The properties of warm dark matter haloes*, *Mon. Not. Roy. Astron. Soc.* **439** (2014) 300 [arXiv:1308.1399] [INSPIRE].

[29] R. Kennedy, C. Frenk, S. Cole and A. Benson, *Constraining the warm dark matter particle mass with Milky Way satellites*, *Mon. Not. Roy. Astron. Soc.* **442** (2014) 2487 [arXiv:1310.7739] [INSPIRE].

[30] C. Destri, H.J. de Vega and N.G. Sanchez, *Warm dark matter primordial spectra and the onset of structure formation at redshift z*, *Phys. Rev.* **D 88** (2013) 083512 [arXiv:1308.1109] [INSPIRE].

[31] R.E. Angulo, O. Hahn and T. Abel, *The Warm DM halo mass function below the cut-off scale*, *Mon. Not. Roy. Astron. Soc.* **434** (2013) 3337 [arXiv:1304.2406] [INSPIRE].

[32] A.J. Benson, A. Farahi, S. Cole, L.A. Moustakas, A. Jenkins, M. Lovell et al., *Dark Matter Halo Merger Histories Beyond Cold Dark Matter: I - Methods and Application to Warm Dark Matter*, *Mon. Not. Roy. Astron. Soc.* **428** (2013) 1774 [arXiv:1209.3018] [INSPIRE].

[33] A. Kamada, N. Yoshida, K. Kohri and T. Takahashi, *Structure of Dark Matter Halos in Warm Dark Matter models and in models with Long-Lived Charged Massive Particles*, *JCAP* **03** (2013) 008 [arXiv:1301.2744] [INSPIRE].

[34] M.R. Lovell, S. Bose, A. Boyarsky, S. Cole, C.S. Frenk, V. Gonzalez-Perez et al., *Satellite galaxies in semi-analytic models of galaxy formation with sterile neutrino dark matter*, *Mon. Not. Roy. Astron. Soc.* **461** (2016) 60 [arXiv:1511.04078] [INSPIRE].

[35] A.D. Ludlow, S. Bose, R.E. Angulo, L. Wang, W.A. Hellwing, J.F. Navarro et al., *The mass-concentration-redshift relation of cold and warm dark matter haloes*, *Mon. Not. Roy. Astron. Soc.* **460** (2016) 1214 [arXiv:1601.02624] [INSPIRE].

[36] L. Wang, V. Gonzalez-Perez, L. Xie, A.P. Cooper, C.S. Frenk, L. Gao et al., *The galaxy population in cold and warm dark matter cosmologies*, *Mon. Not. Roy. Astron. Soc.* **468** (2017) 4579 [arXiv:1612.04540] [INSPIRE].

[37] M.R. Lovell, V. Gonzalez-Perez, S. Bose, A. Boyarsky, S. Cole, C.S. Frenk et al., *Addressing the too big to fail problem with baryon physics and sterile neutrino dark matter*, *Mon. Not. Roy. Astron. Soc.* **468** (2017) 2836 [arXiv:1611.00005] [INSPIRE].

[38] E. Bulbul, M. Markevitch, A. Foster, R.K. Smith, M. Loewenstein and S.W. Randall, *Detection of An Unidentified Emission Line in the Stacked X-ray spectrum of Galaxy Clusters*, *Astrophys. J.* **789** (2014) 13 [arXiv:1402.2301] [INSPIRE].

[39] A. Boyarsky, O. Ruchayskiy, D. Iakubovskyi and J. Franse, *Unidentified Line in X-Ray Spectra of the Andromeda Galaxy and Perseus Galaxy Cluster*, *Phys. Rev. Lett.* **113** (2014) 251301 [arXiv:1402.4119] [INSPIRE].

[40] A. Boyarsky, J. Franse, D. Iakubovskyi and O. Ruchayskiy, *Checking the Dark Matter Origin of a 3.53 keV Line with the Milky Way Center*, *Phys. Rev. Lett.* **115** (2015) 161301 [arXiv:1408.2503] [INSPIRE].

[41] N. Cappelluti, E. Bulbul, A. Foster, P. Natarajan, M.C. Urry, M.W. Bautz et al., *Searching for the 3.5 keV Line in the Deep Fields with Chandra: the 10 Ms observations*, *Astrophys. J.* **854** (2018) 179 [arXiv:1701.07932] [INSPIRE].

[42] V. Iršič et al., *New Constraints on the free-streaming of warm dark matter from intermediate and small scale Lyman-α forest data*, *Phys. Rev.* **D 96** (2017) 023522 [arXiv:1702.01764] [INSPIRE].

[43] C. Yèche, N. Palanque-Delabrouille, J. Baur and H. du Mas des Bourboux, *Constraints on neutrino masses from Lyman-alpha forest power spectrum with BOSS and XQ-100*, *JCAP* **06** (2017) 047 [arXiv:1702.03314] [INSPIRE].

JCAP06(2018)007

[44] S. Dodelson and L.M. Widrow, *Sterile-neutrinos as dark matter*, *Phys. Rev. Lett.* **72** (1994) 17 [hep-ph/9303287] [INSPIRE].

[45] B. Bozek, M. Boylan-Kolchin, S. Horiuchi, S. Garrison-Kimmel, K. Abazajian and J.S. Bullock, *Resonant Sterile Neutrino Dark Matter in the Local and High-z Universe*, *Mon. Not. Roy. Astron. Soc.* **459** (2016) 1489 [arXiv:1512.04544] [INSPIRE].

[46] C. Bœhm, H. Mathis, J. Devriendt and J. Silk, *Non-linear evolution of suppressed dark matter primordial power spectra*, *Mon. Not. Roy. Astron. Soc.* **360** (2005) 282 [astro-ph/0309652] [INSPIRE].

[47] C. Bœhm, J.A. Schewtschenko, R.J. Wilkinson, C.M. Baugh and S. Pascoli, *Using the Milky Way satellites to study interactions between cold dark matter and radiation*, *Mon. Not. Roy. Astron. Soc.* **445** (2014) L31 [arXiv:1404.7012] [INSPIRE].

[48] J.A. Schewtschenko, R.J. Wilkinson, C.M. Baugh, C. Bœhm and S. Pascoli, *Dark matter-radiation interactions: the impact on dark matter haloes*, *Mon. Not. Roy. Astron. Soc.* **449** (2015) 3587 [arXiv:1412.4905] [INSPIRE].

[49] J.A. Schewtschenko, C.M. Baugh, R.J. Wilkinson, C. Bœhm, S. Pascoli and T. Sawala, *Dark matter-radiation interactions: the structure of Milky Way satellite galaxies*, *Mon. Not. Roy. Astron. Soc.* **461** (2016) 2282 [arXiv:1512.06774] [INSPIRE].

[50] F.-Y. Cyr-Racine, R. de Putter, A. Raccanelli and K. Sigurdson, *Constraints on Large-Scale Dark Acoustic Oscillations from Cosmology*, *Phys. Rev.* **D 89** (2014) 063517 [arXiv:1310.3278] [INSPIRE].

[51] M.R. Buckley, J. Zavala, F.-Y. Cyr-Racine, K. Sigurdson and M. Vogelsberger, *Scattering, Damping and Acoustic Oscillations: simulating the Structure of Dark Matter Halos with Relativistic Force Carriers*, *Phys. Rev.* **D 90** (2014) 043524 [arXiv:1405.2075] [INSPIRE].

[52] M. Vogelsberger, J. Zavala, F.-Y. Cyr-Racine, C. Pfrommer, T. Bringmann and K. Sigurdson, *ETHOS — an effective theory of structure formation: dark matter physics as a possible explanation of the small-scale CDM problems*, *Mon. Not. Roy. Astron. Soc.* **460** (2016) 1399 [arXiv:1512.05349] [INSPIRE].

[53] F.-Y. Cyr-Racine, K. Sigurdson, J. Zavala, T. Bringmann, M. Vogelsberger and C. Pfrommer, *ETHOS — an effective theory of structure formation: from dark particle physics to the matter distribution of the Universe*, *Phys. Rev.* **D 93** (2016) 123527 [arXiv:1512.05344] [INSPIRE].

[54] L.G. van den Aarssen, T. Bringmann and C. Pfrommer, *Is dark matter with long-range interactions a solution to all small-scale problems of ΛCDM cosmology?*, *Phys. Rev. Lett.* **109** (2012) 231301 [arXiv:1205.5809] [INSPIRE].

[55] T. Bringmann, H.T. Ihle, J. Kersten and P. Walia, *Suppressing structure formation at dwarf galaxy scales and below: late kinetic decoupling as a compelling alternative to warm dark matter*, *Phys. Rev.* **D 94** (2016) 103529 [arXiv:1603.04884] [INSPIRE].

[56] A.A. de Laix, R.J. Scherrer and R.K. Schaefer, *Constraints of selfinteracting dark matter*, *Astrophys. J.* **452** (1995) 495 [astro-ph/9502087] [INSPIRE].

[57] D.N. Spergel and P.J. Steinhardt, *Observational evidence for selfinteracting cold dark matter*, *Phys. Rev. Lett.* **84** (2000) 3760 [astro-ph/9909386] [INSPIRE].

[58] C.S. Kochanek and M.J. White, *A Quantitative study of interacting dark matter in halos*, *Astrophys. J.* **543** (2000) 514 [astro-ph/0003483] [INSPIRE].

[59] J.L. Feng, M. Kaplinghat, H. Tu and H.-B. Yu, *Hidden Charged Dark Matter*, *JCAP* **07** (2009) 004 [arXiv:0905.3039] [INSPIRE].

[60] A. Loeb and N. Weiner, *Cores in Dwarf Galaxies from Dark Matter with a Yukawa Potential*, *Phys. Rev. Lett.* **106** (2011) 171302 [arXiv:1011.6374] [INSPIRE].

JCAP06(2018)007

[61] M. Vogelsberger, J. Zavala and A. Loeb, *Subhaloes in Self-Interacting Galactic Dark Matter Haloes*, *Mon. Not. Roy. Astron. Soc.* **423** (2012) 3740 [arXiv:1201.5892] [INSPIRE].

[62] M. Rocha, A.H.G. Peter, J.S. Bullock, M. Kaplinghat, S. Garrison-Kimmel, J. Onorbe et al., *Cosmological Simulations with Self-Interacting Dark Matter I: Constant Density Cores and Substructure*, *Mon. Not. Roy. Astron. Soc.* **430** (2013) 81 [arXiv:1208.3025] [INSPIRE].

[63] A.H.G. Peter, M. Rocha, J.S. Bullock and M. Kaplinghat, *Cosmological Simulations with Self-Interacting Dark Matter II: Halo Shapes vs. Observations*, *Mon. Not. Roy. Astron. Soc.* **430** (2013) 105 [arXiv:1208.3026] [INSPIRE].

[64] B. Dasgupta and J. Kopp, *Cosmologically Safe eV-Scale Sterile Neutrinos and Improved Dark Matter Structure*, *Phys. Rev. Lett.* **112** (2014) 031803 [arXiv:1310.6337] [INSPIRE].

[65] M. Vogelsberger, J. Zavala, C. Simpson and A. Jenkins, *Dwarf galaxies in CDM and SIDM with baryons: observational probes of the nature of dark matter*, *Mon. Not. Roy. Astron. Soc.* **444** (2014) 3684 [arXiv:1405.5216] [INSPIRE].

[66] J.F. Cherry, A. Friedland and I.M. Shoemaker, *Neutrino Portal Dark Matter: From Dwarf Galaxies to IceCube*, arXiv:1411.1071 [INSPIRE].

[67] M.R. Lovell, J. Zavala, M. Vogelsberger, X. Shen, F.-Y. Cyr-Racine, C. Pfrommer et al., *ETHOS — an effective theory of structure formation: predictions for the high-redshift Universe — abundance of galaxies and reionization*, *Mon. Not. Roy. Astron. Soc.* **477** (2018) 2526 [arXiv:1711.10497] [INSPIRE].

[68] R. Murgia, A. Merle, M. Viel, M. Totzauer and A. Schneider, *"Non-cold" dark matter at small scales: a general approach*, *JCAP* **11** (2017) 046 [arXiv:1704.07838] [INSPIRE].

[69] C. Bœhm, P. Fayet and R. Schaeffer, *Constraining dark matter candidates from structure formation*, *Phys. Lett.* **B 518** (2001) 8 [astro-ph/0012504] [INSPIRE].

[70] C. Bœhm, A. Riazuelo, S.H. Hansen and R. Schaeffer, *Interacting dark matter disguised as warm dark matter*, *Phys. Rev.* **D 66** (2002) 083505 [astro-ph/0112522] [INSPIRE].

[71] C. Bœhm and R. Schaeffer, *Constraints on dark matter interactions from structure formation: damping lengths*, *Astron. Astrophys.* **438** (2005) 419 [astro-ph/0410591] [INSPIRE].

[72] M. Viel, J. Lesgourgues, M.G. Haehnelt, S. Matarrese and A. Riotto, *Constraining warm dark matter candidates including sterile neutrinos and light gravitinos with WMAP and the Lyman-alpha forest*, *Phys. Rev.* **D 71** (2005) 063534 [astro-ph/0501562] [INSPIRE].

[73] U. Seljak, A. Makarov, P. McDonald and H. Trac, *Can sterile neutrinos be the dark matter?*, *Phys. Rev. Lett.* **97** (2006) 191303 [astro-ph/0602430] [INSPIRE].

[74] M. Viel, J. Lesgourgues, M.G. Haehnelt, S. Matarrese and A. Riotto, *Can sterile neutrinos be ruled out as warm dark matter candidates?*, *Phys. Rev. Lett.* **97** (2006) 071301 [astro-ph/0605706] [INSPIRE].

[75] G. Mangano, A. Melchiorri, P. Serra, A. Cooray and M. Kamionkowski, *Cosmological bounds on dark matter-neutrino interactions*, *Phys. Rev.* **D 74** (2006) 043517 [astro-ph/0606190] [INSPIRE].

[76] M. Viel, G.D. Becker, J.S. Bolton, M.G. Haehnelt, M. Rauch and W.L.W. Sargent, *How cold is cold dark matter? Small scales constraints from the flux power spectrum of the high-redshift Lyman-alpha forest*, *Phys. Rev. Lett.* **100** (2008) 041304 [arXiv:0709.0131] [INSPIRE].

[77] A. Boyarsky, J. Lesgourgues, O. Ruchayskiy and M. Viel, *Lyman-alpha constraints on warm and on warm-plus-cold dark matter models*, *JCAP* **05** (2009) 012 [arXiv:0812.0010] [INSPIRE].

[78] P. Serra, F. Zalamea, A. Cooray, G. Mangano and A. Melchiorri, *Constraints on neutrino — dark matter interactions from cosmic microwave background and large scale structure data*, *Phys. Rev.* **D 81** (2010) 043507 [arXiv:0911.4411] [INSPIRE].

JCAP06(2018)007

[79] S.D. McDermott, H.-B. Yu and K.M. Zurek, *Turning off the Lights: How Dark is Dark Matter?*, *Phys. Rev.* **D 83** (2011) 063509 [arXiv:1011.2907] [INSPIRE].

[80] M. Viel, G.D. Becker, J.S. Bolton and M.G. Haehnelt, *Warm dark matter as a solution to the small scale crisis: new constraints from high redshift Lyman-α forest data*, *Phys. Rev.* **D 88** (2013) 043502 [arXiv:1306.2314] [INSPIRE].

[81] R.J. Wilkinson, J. Lesgourgues and C. Bœhm, *Using the CMB angular power spectrum to study Dark Matter-photon interactions*, *JCAP* **04** (2014) 026 [arXiv:1309.7588] [INSPIRE].

[82] A.D. Dolgov, S.L. Dubovsky, G.I. Rubtsov and I.I. Tkachev, *Constraints on millicharged particles from Planck data*, *Phys. Rev.* **D 88** (2013) 117701 [arXiv:1310.2376] [INSPIRE].

[83] R.J. Wilkinson, C. Bœhm and J. Lesgourgues, *Constraining Dark Matter-Neutrino Interactions using the CMB and Large-Scale Structure*, *JCAP* **05** (2014) 011 [arXiv:1401.7597] [INSPIRE].

[84] A. Schneider, *Structure formation with suppressed small-scale perturbations*, *Mon. Not. Roy. Astron. Soc.* **451** (2015) 3117 [arXiv:1412.2133] [INSPIRE].

[85] M. Escudero, O. Mena, A.C. Vincent, R.J. Wilkinson and C. Bœhm, *Exploring dark matter microphysics with galaxy surveys*, *JCAP* **09** (2015) 034 [arXiv:1505.06735] [INSPIRE].

[86] Y. Ali-Haïmoud, J. Chluba and M. Kamionkowski, *Constraints on Dark Matter Interactions with Standard Model Particles from Cosmic Microwave Background Spectral Distortions*, *Phys. Rev. Lett.* **115** (2015) 071304 [arXiv:1506.04745] [INSPIRE].

[87] J. Baur, N. Palanque-Delabrouille, C. Yèche, C. Magneville and M. Viel, *Lyman-alpha Forests cool Warm Dark Matter*, *JCAP* **08** (2016) 012 [arXiv:1512.01981] [INSPIRE].

[88] R. Diamanti, S. Ando, S. Gariazzo, O. Mena and C. Weniger, *Cold dark matter plus not-so-clumpy dark relics*, *JCAP* **06** (2017) 008 [arXiv:1701.03128] [INSPIRE].

[89] S. Gariazzo, M. Escudero, R. Diamanti and O. Mena, *Cosmological searches for a noncold dark matter component*, *Phys. Rev.* **D 96** (2017) 043501 [arXiv:1704.02991] [INSPIRE].

[90] J.A.D. Diacoumis and Y.Y.Y. Wong, *Using CMB spectral distortions to distinguish between dark matter solutions to the small-scale crisis*, *JCAP* **09** (2017) 011 [arXiv:1707.07050] [INSPIRE].

[91] E. Di Valentino, C. Bœehm, E. Hivon and F.R. Bouchet, *Reducing the H_0 and σ_8 tensions with Dark Matter-neutrino interactions*, *Phys. Rev.* **D 97** (2018) 043513 [arXiv:1710.02559] [INSPIRE].

[92] A. Olivares-Del Campo, C. Bœhm, S. Palomares-Ruiz and S. Pascoli, *Dark matter-neutrino interactions through the lens of their cosmological implications*, *Phys. Rev.* **D 97** (2018) 075039 [arXiv:1711.05283] [INSPIRE].

[93] J. Stadler and C. Bœhm, *Constraints on γ-CDM interactions matching the Planck data precision*, arXiv:1802.06589 [INSPIRE].

[94] C. Dvorkin, K. Blum and M. Kamionkowski, *Constraining Dark Matter-Baryon Scattering with Linear Cosmology*, *Phys. Rev.* **D 89** (2014) 023519 [arXiv:1311.2937] [INSPIRE].

[95] N. Vinyoles and H. Vogel, *Minicharged Particles from the Sun: A Cutting-Edge Bound*, *JCAP* **03** (2016) 002 [arXiv:1511.01122] [INSPIRE].

[96] DES collaboration, K. Bechtol et al., *Eight New Milky Way Companions Discovered in First-Year Dark Energy Survey Data*, *Astrophys. J.* **807** (2015) 50 [arXiv:1503.02584] [INSPIRE].

[97] DES collaboration, A. Drlica-Wagner et al., *Eight Ultra-faint Galaxy Candidates Discovered in Year Two of the Dark Energy Survey*, *Astrophys. J.* **813** (2015) 109 [arXiv:1508.03622] [INSPIRE].

JCAP06(2018)007

[98] SDSS collaboration, C.P. Ahn et al., *The Ninth Data Release of the Sloan Digital Sky Survey: First Spectroscopic Data from the SDSS-III Baryon Oscillation Spectroscopic Survey*, *Astrophys. J. Suppl.* **203** (2012) 21 [arXiv:1207.7137] [INSPIRE].

[99] S.E. Koposov, J. Yoo, H.-W. Rix, D.H. Weinberg, A.V. Maccio and J. Miralda-Escude, *A quantitative explanation of the observed population of Milky Way satellite galaxies*, *Astrophys. J.* **696** (2009) 2179 [arXiv:0901.2116] [INSPIRE].

[100] M. Sitwell, A. Mesinger, Y.-Z. Ma and K. Sigurdson, *The Imprint of Warm Dark Matter on the Cosmological 21-cm Signal*, *Mon. Not. Roy. Astron. Soc.* **438** (2014) 2664 [arXiv:1310.0029] [INSPIRE].

[101] P. Dayal, A. Mesinger and F. Pacucci, *Early galaxy formation in warm dark matter cosmologies*, *Astrophys. J.* **806** (2015) 67 [arXiv:1408.1102] [INSPIRE].

[102] S. Bose, C.S. Frenk, J. Hou, C.G. Lacey and M.R. Lovell, *Reionization in sterile neutrino cosmologies*, *Mon. Not. Roy. Astron. Soc.* **463** (2016) 3848 [arXiv:1605.03179] [INSPIRE].

[103] L. Lopez-Honorez, O. Mena, S. Palomares-Ruiz and P. Villanueva-Domingo, *Warm dark matter and the ionization history of the Universe*, *Phys. Rev.* **D 96** (2017) 103539 [arXiv:1703.02302] [INSPIRE].

[104] R. Barkana, Z. Haiman and J.P. Ostriker, *Constraints on warm dark matter from cosmological reionization*, *Astrophys. J.* **558** (2001) 482 [astro-ph/0102304] [INSPIRE].

[105] N. Yoshida, A. Sokasian, L. Hernquist and V. Springel, *Early structure formation and reionization in a warm dark matter cosmology*, *Astrophys. J.* **591** (2003) L1 [astro-ph/0303622] [INSPIRE].

[106] R.S. Somerville, J.S. Bullock and M. Livio, *The epoch of reionization in models with reduced small scale power*, *Astrophys. J.* **593** (2003) 616 [astro-ph/0303481] [INSPIRE].

[107] B. Yue and X. Chen, *Reionization in the Warm Dark Matter Model*, *Astrophys. J.* **747** (2012) 127 [arXiv:1201.3686] [INSPIRE].

[108] F. Pacucci, A. Mesinger and Z. Haiman, *Focusing on Warm Dark Matter with Lensed High-redshift Galaxies*, *Mon. Not. Roy. Astron. Soc.* **435** (2013) L53 [arXiv:1306.0009] [INSPIRE].

[109] A. Mesinger, A. Ewall-Wice and J. Hewitt, *Reionization and beyond: detecting the peaks of the cosmological 21 cm signal*, *Mon. Not. Roy. Astron. Soc.* **439** (2014) 3262 [arXiv:1310.0465] [INSPIRE].

[110] C. Schultz, J. Oñorbe, K.N. Abazajian and J.S. Bullock, *The High-z Universe Confronts Warm Dark Matter: Galaxy Counts, Reionization and the Nature of Dark Matter*, *Mon. Not. Roy. Astron. Soc.* **442** (2014) 1597 [arXiv:1401.3769] [INSPIRE].

[111] A. Lapi and L. Danese, *Cold or Warm? Constraining Dark Matter with Primeval Galaxies and Cosmic Reionization after Planck*, *JCAP* **09** (2015) 003 [arXiv:1508.02147] [INSPIRE].

[112] S. Bose, W.A. Hellwing, C.S. Frenk, A. Jenkins, M.R. Lovell, J.C. Helly et al., *Substructure and galaxy formation in the Copernicus Complexio warm dark matter simulations*, *Mon. Not. Roy. Astron. Soc.* **464** (2017) 4520 [arXiv:1604.07409] [INSPIRE].

[113] P.S. Corasaniti, S. Agarwal, D.J.E. Marsh and S. Das, *Constraints on dark matter scenarios from measurements of the galaxy luminosity function at high redshifts*, *Phys. Rev.* **D 95** (2017) 083512 [arXiv:1611.05892] [INSPIRE].

[114] N. Menci, A. Grazian, M. Castellano and N.G. Sanchez, *A Stringent Limit on the Warm Dark Matter Particle Masses from the Abundance of z=6 Galaxies in the Hubble Frontier Fields*, *Astrophys. J.* **825** (2016) L1 [arXiv:1606.02530] [INSPIRE].

JCAP06(2018)007

[115] P. Villanueva-Domingo, N.Y. Gnedin and O. Mena, *Warm Dark Matter and Cosmic Reionization*, *Astrophys. J.* **852** (2018) 139 [arXiv:1708.08277] [INSPIRE].

[116] S. Das, R. Mondal, V. Rentala and S. Suresh, *On dark matter-dark radiation interaction and cosmic reionization*, arXiv:1712.03976 [INSPIRE].

[117] Á. Moliné, M.A. Sánchez-Conde, S. Palomares-Ruiz and F. Prada, *Characterization of subhalo structural properties and implications for dark matter annihilation signals*, *Mon. Not. Roy. Astron. Soc.* **466** (2017) 4974 [arXiv:1603.04057] [INSPIRE].

[118] W.H. Press and P. Schechter, *Formation of galaxies and clusters of galaxies by selfsimilar gravitational condensation*, *Astrophys. J.* **187** (1974) 425 [INSPIRE].

[119] J.R. Bond, S. Cole, G. Efstathiou and N. Kaiser, *Excursion set mass functions for hierarchical Gaussian fluctuations*, *Astrophys. J.* **379** (1991) 440 [INSPIRE].

[120] R.K. Sheth and G. Tormen, *Large scale bias and the peak background split*, *Mon. Not. Roy. Astron. Soc.* **308** (1999) 119 [astro-ph/9901122] [INSPIRE].

[121] R.K. Sheth, H.J. Mo and G. Tormen, *Ellipsoidal collapse and an improved model for the number and spatial distribution of dark matter haloes*, *Mon. Not. Roy. Astron. Soc.* **323** (2001) 1 [astro-ph/9907024] [INSPIRE].

[122] R.K. Sheth and G. Tormen, *An Excursion set model of hierarchical clustering : Ellipsoidal collapse and the moving barrier*, *Mon. Not. Roy. Astron. Soc.* **329** (2002) 61 [astro-ph/0105113] [INSPIRE].

[123] Á. Moliné, J.A. Schewtschenko, S. Palomares-Ruiz, C. Bœhm and C.M. Baugh, *Isotropic extragalactic flux from dark matter annihilations: lessons from interacting dark matter scenarios*, *JCAP* **08** (2016) 069 [arXiv:1602.07282] [INSPIRE].

[124] J. Lesgourgues, *The Cosmic Linear Anisotropy Solving System (CLASS) I: overview*, arXiv:1104.2932 [INSPIRE].

[125] J.A. Schewtschenko, *Cosmological Simulations with Dark Matter from beyond the Standard Model*, Ph.D. thesis, Durham University (2016).

[126] S. Bose, W.A. Hellwing, C.S. Frenk, A. Jenkins, M.R. Lovell, J.C. Helly et al., *The COpernicus COmplexio: Statistical Properties of Warm Dark Matter Haloes*, *Mon. Not. Roy. Astron. Soc.* **455** (2016) 318 [arXiv:1507.01998] [INSPIRE].

[127] P. Dayal, T.R. Choudhury, V. Bromm and F. Pacucci, *Reionization and Galaxy Formation in Warm Dark Matter Cosmologies*, *Astrophys. J.* **836** (2017) 16 [arXiv:1501.02823] [INSPIRE].

[128] A. Rudakovskiy and D. Iakubovskyi, *Influence of 7keV sterile neutrino dark matter on the process of reionization*, *JCAP* **06** (2016) 017 [arXiv:1604.01341] [INSPIRE].

[129] A. Mesinger, S. Furlanetto and R. Cen, *21cmFAST: A Fast, Semi-Numerical Simulation of the High-Redshift 21-cm Signal*, *Mon. Not. Roy. Astron. Soc.* **411** (2011) 955 [arXiv:1003.3878] [INSPIRE].

[130] A. Mesinger, A. Ferrara and D.S. Spiegel, *Signatures of X-rays in the early Universe*, *Mon. Not. Roy. Astron. Soc.* **431** (2013) 621 [arXiv:1210.7319] [INSPIRE].

[131] S. Mineo, M. Gilfanov and R. Sunyaev, *X-ray emission from star-forming galaxies - I. High-mass X-ray binaries*, *Mon. Not. Roy. Astron. Soc.* **419** (2012) 2095 [arXiv:1105.4610] [INSPIRE].

[132] A. Liu, J.R. Pritchard, R. Allison, A.R. Parsons, U. Seljak and B.D. Sherwin, *Eliminating the optical depth nuisance from the CMB with 21 cm cosmology*, *Phys. Rev.* **D 93** (2016) 043013 [arXiv:1509.08463] [INSPIRE].

[133] R. Barkana and A. Loeb, *In the beginning: The First sources of light and the reionization of the Universe*, *Phys. Rept.* **349** (2001) 125 [astro-ph/0010468] [INSPIRE].

JCAP06(2018)007

[134] A.E. Evrard, *Formation and evolution of X-ray clusters — A hydrodynamic simulation of the intracluster medium*, *Astrophys. J.* **363** (1990) 349 [INSPIRE].

[135] A. Blanchard, D. Vall-Gabaud and G.A. Mamon, *The origin of the galaxy luminosity function and the thermal evolution of the intergalactic medium*, *Astron. Astrophys.* **264** (1992) 365.

[136] M. Tegmark, J. Silk, M.J. Rees, A. Blanchard, T. Abel and F. Palla, *How small were the first cosmological objects?*, *Astrophys. J.* **474** (1997) 1 [astro-ph/9603007] [INSPIRE].

[137] Z. Haiman, T. Abel and M.J. Rees, *The radiative feedback of the first cosmological objects*, *Astrophys. J.* **534** (2000) 11 [astro-ph/9903336] [INSPIRE].

[138] B. Ciardi, A. Ferrara, F. Governato and A. Jenkins, *Inhomogeneous reionization regulated by radiative and stellar feedbacks*, *Mon. Not. Roy. Astron. Soc.* **314** (2000) 611 [astro-ph/9907189] [INSPIRE].

[139] B. Greig and A. Mesinger, *21CMMC: an MCMC analysis tool enabling astrophysical parameter studies of the cosmic 21 cm signal*, *Mon. Not. Roy. Astron. Soc.* **449** (2015) 4246 [arXiv:1501.06576] [INSPIRE].

[140] Planck collaboration, N. Aghanim et al., *Planck intermediate results. XLVI. Reduction of large-scale systematic effects in HFI polarization maps and estimation of the reionization optical depth*, *Astron. Astrophys.* **596** (2016) A107 [arXiv:1605.02985] [INSPIRE].

[141] A. Mesinger and S. Furlanetto, *Efficient Simulations of Early Structure Formation and Reionization*, *Astrophys. J.* **669** (2007) 663 [arXiv:0704.0946] [INSPIRE].

[142] A. Lewis, A. Challinor and A. Lasenby, *Efficient computation of CMB anisotropies in closed FRW models*, *Astrophys. J.* **538** (2000) 473 [astro-ph/9911177] [INSPIRE].

[143] X.-H. Fan, M.A. Strauss, R.H. Becker, R.L. White, J.E. Gunn, G.R. Knapp et al., *Constraining the evolution of the ionizing background and the epoch of reionization with z 6 quasars. 2. a sample of 19 quasars*, *Astron. J.* **132** (2006) 117 [astro-ph/0512082] [INSPIRE].

[144] I. McGreer, A. Mesinger and V. D'Odorico, *Model-independent evidence in favour of an end to reionization by $z \approx 6$* , *Mon. Not. Roy. Astron. Soc.* **447** (2015) 499 [arXiv:1411.5375] [INSPIRE].

[145] M.R. Santos, *Probing reionization with Lyman-alpha emission lines*, *Mon. Not. Roy. Astron. Soc.* **349** (2004) 1137 [astro-ph/0308196] [INSPIRE].

[146] S. Malhotra and J.E. Rhoads, *Luminosity functions of Lyman-alpha emitters at $z = 6.5$ and $z = 5.7$: evidence against reionization at $z = 6$*, *Astrophys. J.* **617** (2004) L5 [astro-ph/0407408] [INSPIRE].

[147] M. McQuinn, L. Hernquist, M. Zaldarriaga and S. Dutta, *Studying Reionization with Ly-alpha Emitters*, *Mon. Not. Roy. Astron. Soc.* **381** (2007) 75 [arXiv:0704.2239] [INSPIRE].

[148] A. Mesinger and S. Furlanetto, *Lyman-alpha Emitters During the Early Stages of Reionization*, *Mon. Not. Roy. Astron. Soc.* **386** (2008) 1990 [arXiv:0708.0006] [INSPIRE].

[149] D.P. Stark, R.S. Ellis, K. Chiu, M. Ouchi and A. Bunker, *Keck Spectroscopy of Faint $3 < z < 7$ Lyman Break Galaxies: - I. New constraints on cosmic reionisation from the luminosity and redshift-dependent fraction of Lyman-alpha emission*, *Mon. Not. Roy. Astron. Soc.* **408** (2010) 1628 [arXiv:1003.5244] [INSPIRE].

[150] D.P. Stark, R.S. Ellis and M. Ouchi, *Keck Spectroscopy of Faint $3 < z < 7$ Lyman Break Galaxies — II. A High Fraction of Line Emitters at Redshift Six*, *Astrophys. J.* **728** (2011) L2 [arXiv:1009.5471] [INSPIRE].

[151] A. Fontana et al., *The lack of intense Lyman alpha in ultradeep spectra of z=7 candidates in GOODS-S: imprint of reionization?*, *Astrophys. J.* **725** (2010) L205 [arXiv:1010.2754] [INSPIRE].

JCAP06(2018)007

[152] M. Dijkstra, A. Mesinger and S. Wyithe, *The Detectability of Lyman Alpha Emission from Galaxies during the Epoch of Reionization*, *Mon. Not. Roy. Astron. Soc.* **414** (2011) 2139 [arXiv:1101.5160] [INSPIRE].

[153] L. Pentericci et al., *Spectroscopic confirmation of z 7 LBGs: probing the earliest galaxies and the epoch of reionization*, *Astrophys. J.* **743** (2011) 132 [arXiv:1107.1376] [INSPIRE].

[154] Y. Ono et al., *Spectroscopic Confirmation of Three z-Dropout Galaxies at z = 6.844 - 7.213: Demographics of Lyman-Alpha Emission in z 7 Galaxies*, *Astrophys. J.* **744** (2012) 83 [arXiv:1107.3159] [INSPIRE].

[155] J. Caruana, A.J. Bunker, S.M. Wilkins, E.R. Stanway, M. Lacy, M.J. Jarvis et al., *No Evidence for Lyman-alpha Emission in Spectroscopy of $z > 7$ Candidate Galaxies*, *Mon. Not. Roy. Astron. Soc.* **427** (2012) 3055 [arXiv:1208.5987] [INSPIRE].

[156] T. Treu, K.B. Schmidt, M. Trenti, L.D. Bradley and M. Stiavelli, *The Changing Lyα Optical Depth in the Range $6 < z < 9$ from the MOSFIRE Spectroscopy of Y-dropouts*, *Astrophys. J.* **775** (2013) L29 [arXiv:1308.5985] [INSPIRE].

[157] J. Caruana, A.J. Bunker, S.M. Wilkins, E.R. Stanway, S. Lorenzoni, M.J. Jarvis et al., *Spectroscopy of $z \sim 7$ candidate galaxies: using Lyman α to constrain the neutral fraction of hydrogen in the high-redshift universe*, *Mon. Not. Roy. Astron. Soc.* **443** (2014) 2831 [arXiv:1311.0057] [INSPIRE].

[158] V. Tilvi, C. Papovich, S.L. Finkelstein, J. Long, M. Song, M. Dickinson et al., *Rapid Decline of Lyα Emission Toward the Reionization Era*, *Astrophys. J.* **794** (2014) 5 [arXiv:1405.4869] [INSPIRE].

[159] M.A. Schenker, R.S. Ellis, N.P. Konidaris and D.P. Stark, *Line Emitting Galaxies Beyond a Redshift of 7: An Improved Method for Estimating the Evolving Neutrality of the Intergalactic Medium*, *Astrophys. J.* **795** (2014) 20 [arXiv:1404.4632] [INSPIRE].

[160] R.J. Bouwens, G.D. Illingworth, P.A. Oesch, J. Caruana, B. Holwerda, R. Smit et al., *Reionization after Planck: The Derived Growth of the Cosmic Ionizing Emissivity now matches the Growth of the Galaxy UV Luminosity Density*, *Astrophys. J.* **811** (2015) 140 [arXiv:1503.08228] [INSPIRE].

[161] O. Newton, M. Cautun, A. Jenkins, C.S. Frenk and J. Helly, *The total satellite population of the Milky Way*, arXiv:1708.04247 [INSPIRE].

[162] B.F. Griffen et al., *The Caterpillar Project: a Large Suite of Milky way Sized Halos*, *Astrophys. J.* **818** (2016) 10 [arXiv:1509.01255] [INSPIRE].

[163] S. Garrison-Kimmel, M. Boylan-Kolchin, J. Bullock and K. Lee, *ELVIS: Exploring the Local Volume in Simulations*, *Mon. Not. Roy. Astron. Soc.* **438** (2014) 2578 [arXiv:1310.6746] [INSPIRE].

[164] P.S. Behroozi, R.H. Wechsler and C. Conroy, *The Average Star Formation Histories of Galaxies in Dark Matter Halos from z =0-8*, *Astrophys. J.* **770** (2013) 57 [arXiv:1207.6105] [INSPIRE].

[165] A.M. Brooks and A. Zolotov, *Why Baryons Matter: The Kinematics of Dwarf Spheroidal Satellites*, *Astrophys. J.* **786** (2014) 87 [arXiv:1207.2468] [INSPIRE].

[166] B.P. Moster, T. Naab and S.D.M. White, *Galactic star formation and accretion histories from matching galaxies to dark matter haloes*, *Mon. Not. Roy. Astron. Soc.* **428** (2013) 3121 [arXiv:1205.5807] [INSPIRE].

[167] S. Koposov et al., *The Luminosity Function of the Milky Way Satellites*, *Astrophys. J.* **686** (2008) 279 [arXiv:0706.2687] [INSPIRE].

JCAP06(2018)007

[168] E.J. Tollerud, J.S. Bullock, L.E. Strigari and B. Willman, *Hundreds of Milky Way Satellites? Luminosity Bias in the Satellite Luminosity Function*, *Astrophys. J.* **688** (2008) 277 [arXiv:0806.4381] [INSPIRE].

[169] J.R. Hargis, B. Willman and A.H.G. Peter, *Too Many, Too Few, or Just Right? The Predicted Number and Distribution of Milky Way Dwarf Galaxies*, *Astrophys. J.* **795** (2014) L13 [arXiv:1407.4470] [INSPIRE].

[170] P. Jethwa, D. Erkal and V. Belokurov, *The upper bound on the lowest mass halo*, *Mon. Not. Roy. Astron. Soc.* **473** (2018) 2060 [arXiv:1612.07834] [INSPIRE].

[171] G.A. Dooley, A.H.G. Peter, T. Yang, B. Willman, B.F. Griffen and A. Frebel, *An observer's guide to the (Local Group) dwarf galaxies: predictions for their own dwarf satellite populations*, *Mon. Not. Roy. Astron. Soc.* **471** (2017) 4894 [arXiv:1610.00708] [INSPIRE].

[172] W. Wang, J. Han, A.P. Cooper, S. Cole, C. Frenk and B. Lowing, *Estimating the dark matter halo mass of our Milky Way using dynamical tracers*, *Mon. Not. Roy. Astron. Soc.* **453** (2015) 377 [arXiv:1502.03477] [INSPIRE].

[173] J.S. Bullock, A.V. Kravtsov and D.H. Weinberg, *Reionization and the abundance of galactic satellites*, *Astrophys. J.* **539** (2000) 517 [astro-ph/0002214] [INSPIRE].

[174] R.S. Somerville, *Can photoionization squelching resolve the sub-structure crisis?*, *Astrophys. J.* **572** (2002) L23 [astro-ph/0107507] [INSPIRE].

[175] A.J. Benson, C.S. Frenk, C.G. Lacey, C.M. Baugh and S. Cole, *The effects of photoionization on galaxy formation. 2. Satellites in the local group*, *Mon. Not. Roy. Astron. Soc.* **333** (2002) 177 [astro-ph/0108218] [INSPIRE].

[176] J. Wolf, G.D. Martinez, J.S. Bullock, M. Kaplinghat, M. Geha, R.R. Muñoz et al., *Accurate Masses for Dispersion-supported Galaxies*, *Mon. Not. Roy. Astron. Soc.* **406** (2010) 1220 [arXiv:0908.2995] [INSPIRE].

[177] B. Willman, *In Pursuit of the Least Luminous Galaxies*, *Adv. Astron.* **2010** (2010) 285454 [arXiv:0907.4758] [INSPIRE].

[178] Y. Mao, M. Tegmark, M. McQuinn, M. Zaldarriaga and O. Zahn, *How accurately can 21 cm tomography constrain cosmology?*, *Phys. Rev.* **D 78** (2008) 023529 [arXiv:0802.1710] [INSPIRE].

[179] J.R. Pritchard and A. Loeb, *21-cm cosmology*, *Rept. Prog. Phys.* **75** (2012) 086901 [arXiv:1109.6012] [INSPIRE].

[180] M.P. van Haarlem et al., *LOFAR: The LOw-Frequency ARray*, *Astron. Astrophys.* **556** (2013) A2 [arXiv:1305.3550] [INSPIRE].

[181] MITEoR collaboration, H. Zheng et al., *MITEoR: a scalable interferometer for precision 21 cm cosmology*, *Mon. Not. Roy. Astron. Soc.* **445** (2014) 1084 [arXiv:1405.5527] [INSPIRE].

[182] J.D. Bowman and A.E.E. Rogers, *A lower limit of $dz > 0.06$ for the duration of the reionization epoch*, *Nature* **468** (2010) 796 [arXiv:1209.1117] [INSPIRE].

[183] S.J. Tingay et al., *The Murchison Widefield Array: the Square Kilometre Array Precursor at low radio frequencies*, *Publ. Astron. Soc. Austral.* **30** (2013) 7 [arXiv:1206.6945] [INSPIRE].

[184] A.R. Parsons et al., *The Precision Array for Probing the Epoch of Reionization: 8 Station Results*, *Astron. J.* **139** (2010) 1468 [arXiv:0904.2334] [INSPIRE].

[185] Z.S. Ali et al., *PAPER-64 Constraints on Reionization: The 21cm Power Spectrum at $z = 8.4$*, *Astrophys. J.* **809** (2015) 61 [arXiv:1502.06016] [INSPIRE].

[186] D.R. DeBoer et al., *Hydrogen Epoch of Reionization Array (HERA)*, *Publ. Astron. Soc. Pac.* **129** (2017) 045001 [arXiv:1606.07473] [INSPIRE].

JCAP06(2018)007

[187] J.C. Pober et al., *What Next-Generation 21 cm Power Spectrum Measurements Can Teach Us About the Epoch of Reionization*, *Astrophys. J.* **782** (2014) 66 [arXiv:1310.7031] [INSPIRE].

[188] SKA collaboration, P. Dewdney et al., *SKA baseline description*, https://www.skatelescope.org/wp-content/uploads/2014/03/SKA-TEL-SKO-0000308_SKA1_System_Baseline_v2_DescriptionRev01-part-1-signed.pdf (2015).

[189] J.D. Bowman, A.E.E. Rogers, R.A. Monsalve, T.J. Mozdzen and N. Mahesh, *An absorption profile centred at 78 megahertz in the sky-averaged spectrum*, *Nature* **555** (2018) 67 [INSPIRE].

[190] C. Evoli, A. Mesinger and A. Ferrara, *Unveiling the nature of dark matter with high redshift 21 cm line experiments*, *JCAP* **11** (2014) 024 [arXiv:1408.1109] [INSPIRE].

[191] L. Lopez-Honorez, O. Mena, Á. Moliné, S. Palomares-Ruiz and A.C. Vincent, *The 21 cm signal and the interplay between dark matter annihilations and astrophysical processes*, *JCAP* **08** (2016) 004 [arXiv:1603.06795] [INSPIRE].

[192] G. Bernardi, J.T.L. Zwart, D. Price, L.J. Greenhill, A. Mesinger, J. Dowell et al., *Bayesian constraints on the global 21-cm signal from the Cosmic Dawn*, *Mon. Not. Roy. Astron. Soc.* **461** (2016) 2847 [arXiv:1606.06006] [INSPIRE].

[193] P. Madau, A. Meiksin and M.J. Rees, *21-CM tomography of the intergalactic medium at high redshift*, *Astrophys. J.* **475** (1997) 429 [astro-ph/9608010] [INSPIRE].

[194] S. Furlanetto, S.P. Oh and F. Briggs, *Cosmology at Low Frequencies: The 21 cm Transition and the High-Redshift Universe*, *Phys. Rept.* **433** (2006) 181 [astro-ph/0608032] [INSPIRE].

[195] S.R. Furlanetto, *The 21-cm Line as a Probe of Reionization*, in *Understanding the Epoch of Cosmic Reionization: Challenges and Progress*, A. Mesinger eds., vol. 423, pp. 247–280, Springer International Publishing (2016) [arXiv:1511.01131] [INSPIRE].

[196] C.M. Hirata, *Wouthuysen-Field coupling strength and application to high-redshift 21 cm radiation*, *Mon. Not. Roy. Astron. Soc.* **367** (2006) 259 [astro-ph/0507102] [INSPIRE].

[197] S.A. Wouthuysen, *On the excitation mechanism of the 21-cm (radio-frequency) interstellar hydrogen emission line*, *Astrophys. J.* **57** (1952) 31.

[198] G.B. Field, *Excitation of the Hydrogen 21 cm Line*, *Proc. IRE* **46** (1958) 240.

[199] J.C. Pober, A.R. Parsons, D.R. DeBoer, P. McDonald, M. McQuinn, J.E. Aguirre et al., *The Baryon Acoustic Oscillation Broadband and Broad-beam Array: Design Overview and Sensitivity Forecasts*, *Astron. J.* **145** (2013) 65 [arXiv:1210.2413] [INSPIRE].

[200] GAIA collaboration, A. Helmi et al., *Gaia Data Release 2: Kinematics of globular clusters and dwarf galaxies around the Milky Way*, arXiv:1804.09381.

[201] L. Posti and A. Helmi, *Mass and shape of the Milky Way's dark matter halo with globular clusters from Gaia and Hubble*, arXiv:1805.01408.

[202] T.K. Fritz et al., *Gaia DR2 Proper Motions of Dwarf Galaxies within 420 kpc: Orbits, Milky Way Mass, Tidal Influences, Planar Alignments, and Group Infall*, arXiv:1805.00908.

[203] L.L. Watkins, R.P. van der Marel, S.T. Sohn and N.W. Evans, *Evidence for an Intermediate-Mass Milky Way from Gaia DR2 Halo Globular Cluster Motions*, arXiv:1804.11348.

JCAP06(2018)007

PHYSICAL REVIEW D **99,** 023522 (2019)

Dark matter microphysics and 21 cm observations

Laura Lopez-Honorez,[1,2,*] Olga Mena,[3,†] and Pablo Villanueva-Domingo[3,‡]
[1]*Service de Physique Théorique, CP225, Université Libre de Bruxelles, Bld du Triomphe, 1050 Brussels, Belgium*
[2]*Vrije Universiteit Brussel and The International Solvay Institutes, Pleinlaan 2, 1050 Brussels, Belgium*
[3]*Instituto de Física Corpuscular (IFIC), CSIC-Universitat de Valencia, Apartado de Correos 22085, E-46071, Spain*

(Received 20 November 2018; published 22 January 2019)

Dark matter interactions with massless or very light standard model particles, as photons or neutrinos, may lead to a suppression of the matter power spectrum at small scales and of the number of low mass haloes. Bounds on the dark matter scattering cross section with light degrees of freedom in such interacting dark matter (IDM) scenarios have been obtained from e.g., early time cosmic microwave background physics and large scale structure observations. Here we scrutinize dark matter microphysics in light of the claimed 21 cm EDGES 78 MHz absorption signal. IDM is expected to delay the 21 cm absorption features due to collisional damping effects. We identify the astrophysical conditions under which the existing constraints on the dark matter scattering cross section could be largely improved due to the IDM imprint on the 21 cm signal, providing also an explicit comparison to the WDM scenario.

DOI: 10.1103/PhysRevD.99.023522

I. INTRODUCTION

Interacting dark matter (IDM) with standard model light or massless degrees of freedom, such as photons and neutrinos, gives rise to a suppression of the small-scale matter power spectrum [1–4] (see also Refs. [5–12] for interactions with new (dark) light degrees of freedom). This damping is similar to the one caused by the free streaming of warm dark matter (WDM). In IDM scenarios, in contrast, the suppression of the small-scale overdensities is due to collisional damping [13–15]. These two alternatives to the standard ΛCDM model fall into the category of *noncold dark matter* scenarios [16] (NCDM). Such dark matter models can provide some solutions to the ΛCDM (where dark matter is made of purely cold and collisionless dark matter particles) *small scale crisis* (see, e.g., the review of Ref. [17]). A large number of studies in the literature have been devoted to constrain the NCDM picture by means of cosmological probes, such as cosmic microwave background (CMB) fluctuations and spectral distortions, galaxy clustering and Lyman-α forest power spectrum, the number of Milky Way satellites, the reionization history, or gravitational lensing [1–4,15,16,18–65].

In this regard, the 21 cm signal offers a new cosmological probe, complementary to the existing ones, that could open a new window on the early universe and can further test the imprint of NCDM (see, e.g., [66,67] for early work on the subject). Here we will focus on the cosmic dawn period and in particular on the first claimed detection of an absorption feature in the sky-averaged global 21 cm signal at a redshift $z \sim 17$ by the experiment to Detect the Global Epoch of Reionization Signatures (EDGES) [68]. The measured amplitude of the dip in the 21 cm global signal appears to be much deeper than that expected in standard CDM scenarios and therefore requires new physics to heat the radio background or cool the gas temperature. This has triggered a surge of interest from the dark matter community trying to relate this effect to dark matter decay and annihilation [69–72][1] and investigating the dark matter scenarios that could account for the signal [76–81], see also [82–84]. There are however other possible interpretations of the EDGES signal that do not involve new physics. In particular, the signal could be explained with a different modeling of the foregrounds [85] or with the existence of a systematic artifact within the ground plane which may also produce an absorption feature [86].

While NCDM scenarios are unlikely to explain the large absorption amplitude, they delay structure formation and, therefore, might delay the onset of reionization and of UV and x-ray emission, see e.g., [45,46,60,66]. As a result a shift to later times in the typical features in the 21 cm sky-averaged global signal and power spectrum is observed in the context of non-cold dark matter [60,66,87–89]. Consequently, it is timely to study the compatibility

*llopezho@ulb.ac.be
†olga.mena@ific.uv.es
‡pablo.villanueva@ific.uv.es

[1]See also the previous works of Refs. [73–75].

between the observation reported by EDGES, located at a redshift around $z \simeq 17$ and the IDM scenario. We follow two possible avenues. The first of them relies on exploiting the non-negligible Lyman-α coupling between the gas and the spin temperature characterizing the 21 cm signal at $z \simeq 20$ [88,89]. The second one consists in imposing the minimum in the absorption feature to happen before $z \simeq 17$ [87]. For both strategies, a number of degeneracies between the details of dark matter microphysics and the astrophysical parameters will appear. We will briefly discuss their impact on the constraints on NCDM scenarios.

Universal fits to the halo mass functions from N-body simulations for the IDM scenarios have been obtained in [3,90,91]. In particular, here we will use the results of [90] derived for IDM scenarios involving dark matter-photon scatterings. A possible particle physics model related to this cosmological scenario is the case of millicharged dark matter [65,92,93]. IDM scenarios including dark matter-neutrino scatterings have been shown to give rise to a very similar damping in the power spectrum and also to a very similar mass function as for dark matter-photon scatterings, see Refs. [3,14] and the Appendix A. Unfortunately, in the latter case, no publicly available dedicated analysis provides the necessary fits to the associated halo mass functions necessary for our study. We therefore use the IDM scattering on photons as a toy model to evaluate the impact of the EDGES signal on the more general case of IDM with light degrees of freedom. In order to ease comparison with previous studies, we shall also study the case of thermal warm dark matter (WDM) with mass in the keV range (see Refs. [35,36,44–59,94–112] and the most recent works of Refs. [87,89]).

The structure of the paper is as follows. We start in Sec. II by describing the physics of the 21 cm global signature. We account for the effect of IDM in the 21 cm global signature in Sec. III, presenting the constraints on the dark matter photon elastic cross sections arising from (i) the presence of a rich Lyman-α background at $z \simeq 20$ (see Sec. III A), and (ii) the location of the EDGES minimum (see Sec. III B). Finally, we summarize our results and conclude in Sec. IV.

II. THE 21 CM SIGNAL

A. The differential brightness temperature

The brightness of a patch of neutral hydrogen (HI) relative to the CMB at a given redshift z is expressed in terms of the differential brightness temperature, δT_b. The sky-averaged δT_b scales as [113–116]

$$\frac{\delta T_b(\nu)}{\mathrm{mK}} \simeq 27 x_{\mathrm{HI}} \left(1 - \frac{T_{\mathrm{CMB}}}{T_{\mathrm{S}}}\right) \left(\frac{1+z}{10}\right)^{1/2} \times \left(\frac{0.15}{\Omega_m h^2}\right)^{1/2} \left(\frac{\Omega_b h^2}{0.023}\right), \tag{2.1}$$

where $\nu = \nu_{21}/(1+z)$ with $\nu_{21} = 1420$ MHz, x_{HI} represents the fraction of neutral hydrogen and $\Omega_b h^2$ and $\Omega_m h^2$ refer to the current baryon and matter contributions to the universe's mass-energy content. The ratio of the populations of the two ground state hyperfine levels of hydrogen is quantified by the spin temperature, T_{S}, which is determined by three competing effects [117]: (1) absorption and stimulated emission of CMB photons coupling the spin temperature to the CMB temperature T_{CMB} in contrast with (2) atomic collisions (which are important at high redshifts $z \gtrsim 30$); and 3) resonant scattering of Lyman-α photons that couple the spin temperature to the gas kinetic temperature T_k. The latter effect is the so-called Wouthuysen-Field effect [118,119] that turns on with the first sources. Assuming that the Lyman-α color temperature is $T_\alpha \simeq T_k$ [115], the spin temperature results from:

$$\left(1 - \frac{T_{\mathrm{CMB}}}{T_{\mathrm{S}}}\right) = \frac{x_{\mathrm{tot}}}{1 + x_{\mathrm{tot}}} \left(1 - \frac{T_{\mathrm{CMB}}}{T_k}\right) \tag{2.2}$$

with $x_{\mathrm{tot}} = x_\alpha + x_c$ and x_c and x_α are the coupling coefficients for collisions and Lyman-α scatterings.

At the low redshifts of interest here, collision coupling effects can be safely neglected and therefore, $x_{\mathrm{tot}} = x_\alpha$. The Lyman-$\alpha$ coupling is defined as

$$x_\alpha = \frac{16\pi^2 T_\star e^2 f_\alpha}{27 A_{10} T_\gamma m_e c} S_\alpha J_\alpha, \tag{2.3}$$

where $T_\star = h\nu_{21} = 68.2$ mK is the hyperfine energy splitting, e and m_e the charge and mass of the electron, f_α is the oscillator strength of the Lyman-α transition, A_{10} is the spontaneous decay rate of the 21 cm transition, J_α is the specific intensity of the background radiation evaluated at the Lyman-α frequency and S_α is an order unity correction factor which accounts for the detailed shape of the spectrum near the resonance [120]. In particular, in the framework considered here, $S_\alpha \lesssim 1$ and the Lyman-α flux gets two types of contributions. One results from the x-ray excitation of HI ($J_{\alpha X}$), while the other one results from direct stellar emission of UV photons between Lyman-α and the Lyman-α limit $J_{\alpha\star}$, thus $J_\alpha = J_{\alpha X} + J_{\alpha\star}$ [121]. We will see in Sec. II B that for the x-ray efficiencies considered here, $J_{\alpha X}$ only represents a small contribution to the total Lyα flux. On the other hand, the direct stellar emission contribution to J_α is computed assuming by default a Pop II stars spectral model. This gives rise to the emission of 9690 photons per baryon between Lyman-α and the Lyman limit, see Appendix B (see also [122]). Notice from Eq. (2.2) that, when $x_{\mathrm{tot}} = x_\alpha = 1$, δT_b will be at the half of the value that it would have if T_S were completely coupled to T_k, which happens when $x_\alpha \gg 1$. The authors of Ref. [89], following the EDGES results [68], have imposed that x_α should be one or larger at redshift $z \simeq 20$. We shall apply this constraint in our numerical analyses of IDM scenarios, see Sec. III A.

In order to extract the imprint of NCDM on the 21 cm signal, we profit from the publicly available tool 21CMFAST. The main purpose of the code is the study of variations in the 21 cm signal due to changes in a given set of astrophysical and cosmological parameters. We make use of the output values of x_α and of T_S and $x_{\rm HI}$ to extract the differential brightness temperature as in Eq. (2.1). We perform our simulations in a box of 300 Mpc of size with a 128^3 grid, since high-resolution computations are not required for extracting only the global 21 cm signal. In practice, we use a version of the 21CMFAST code adapted to account for the IDM and the WDM as detailed in Ref. [60]. We have modified the default WDM scenario implementation modifying the definition of both the transfer function and the halo mass function according to the prescription given in the Appendix A. This halo mass function plays an important role in the evaluation of the production rate of ultraviolet (UV), x-rays, and Lyman-α radiation, responsible of the ionization, heating and Lyman-α coupling respectively. These production rates are proportional to the star formation rate $\dot{\rho}_\star$. In 21CMFAST, this quantity is evaluated in terms of the growth of the fraction of mass collapsed in haloes which are able to host star-forming galaxies, $f_{\rm coll}(> M_{\rm vir}^{\rm min})$, defined as

$$f_{\rm coll}(> M_{\rm vir}^{\rm min}) = \frac{1}{\rho_{m,0}} \int_{M_{\rm vir}^{\rm min}}^{\infty} M \frac{dn}{dM} dM, \qquad (2.4)$$

where $\rho_{m,0}$ is the current matter density and dn/dM is the halo mass function. For the NCDM cosmologies, the halo mass function is always suppressed at small masses compared to the CDM scenario, giving rise to a smaller $f_{\rm coll}$, at fixed redshift, as illustrated in Fig. 1, see also [1,66,123].[2] With the purple area we show the case of CDM with threshold masses $M_{\rm vir}^{\rm min}$ between $10^6\ M_\odot$ (upper curve) and $3\times10^7\ M_\odot$ (lower curve) at $z = 20$ or equivalently $T_{\rm vir}^{\rm min}$ between 10^3 and 10^4 K, see Eq. (2.5). The upper purple curve for CDM can be compared to case of NCDM scenarios in the form of WDM (red, blue, and cyan continuous curves) and of IDM (red, blue, and cyan dotted curves) for the same $M_{\rm vir}^{\rm min} = 10^6\ M_\odot$ at $z = 20$ ($T_{\rm vir}^{\rm min} = 10^3$ K). The IDM scattering cross sections are normalized in terms of the Thompson cross section $\sigma_T = 6.65\times10^{-25}$ cm^2.

Overall, in the framework considered here, the NCDM modification of $f_{\rm coll}$ will result into a delayed reionization, heating and Lyman-α coupling, giving rise to an absorption feature in the 21 cm signal located at lower redshifts with respect to CDM scenarios [45,46,60,66]. Notice also that curves of a fixed color in Fig. 1 correspond to IDM and WDM models giving rise to a fixed value of the half-mode mass or breaking scale of the linear power spectrum, see Eqs. (A6), (A7), and (A9) in Appendix A. For fixed half-mode mass, the suppression of the $f_{\rm coll}$ is always more severe in the WDM scenarios than in the IDM scenarios due to a relatively larger number of low mass haloes in the IDM case, see [90]. The rate at which $f_{\rm coll}$ increases with redshift is also different between IDM and WDM. These features might help to discriminate between NCDM models using both the 21 cm global signal and its power spectrum [60].

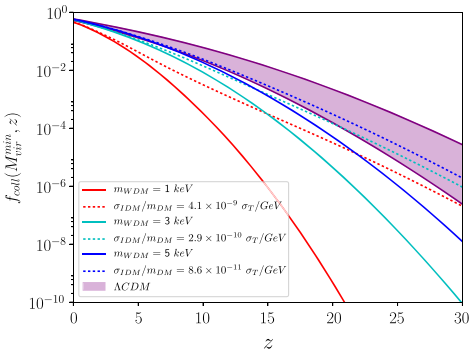

FIG. 1. Fraction of mass collapsed into haloes of mass larger than $M_{\rm vir}^{\rm min}(z = 20) \simeq 10^6\ M_\odot$ (corresponding to $T_{\rm vir}^{\rm min} = 10^3$ K) as a function of the redshift. The continuous lines depict the WDM cases that are compared with IDM scenarios, shown with dotted curves. Continuous and dotted curves of the same colors correspond to a fixed value of the half-mode mass. The purple region illustrates the change in the CDM collapsed fraction (using the Sheth-Tormen mass function) for $T_{\rm vir}^{\rm min}$ varying within the range of 10^3 to 10^4 K.

B. The astrophysical parameters

The minimum virial mass $M_{\rm vir}^{\rm min}$ from which haloes begin to efficiently form stars [see Eq. (2.4)] is related to the threshold temperature $T_{\rm vir}^{\rm min}$ as [125]

$$M_{\rm vir}^{\rm min}(z) = 10^8 \left(\frac{T_{\rm vir}^{\rm min}}{1.98\times10^4\ {\rm K}}\frac{0.6}{\mu}\right)^{3/2} \left(\frac{1+z}{10}\right)^{-3/2} M_\odot/h, \qquad (2.5)$$

where μ is the mean molecular weight and it is equal to 1.2 (0.6) for a neutral (fully ionized) primordial gas. The value of the minimum virial temperature depends on the cooling mechanism considered. The lower threshold to make the atomic cooling channel effective is $T_{\rm vir}^{\rm min} = 10^4$ K [126–130], corresponding to $M_{\rm vir}^{\rm min} = 3\times10^7\ M_\odot$ at $z = 20$ for $\mu = 0.6$. In contrast, the molecular H_2 cooling channel can be effective down to temperatures of $T_{\rm vir}^{\rm min} = 10^3$ K

[2]Let us emphasize that our prescription for WDM differs from one of [66]. Here we follow the fits to the results of simulations from [100] for WDM which was directly compared to the results of IDM simulations in [3,91,124]. Reference [66] followed an earlier prescription introduced by [47].

corresponding to $M_{\rm vir}^{\rm min} = 10^6\ M_\odot$ at $z = 20$. The hydrogen molecules could be destroyed by photons in the Lyman-Werner band. Nevertheless, several hydrodynamical works in the literature [131,132] have shown that in the presence of a large soft UV background, molecular cooling could be highly effective, i.e., metal-enriched star formation is not restricted to atomic cooling. Furthermore, molecular cooling could cool down the gas in haloes associated to virial temperatures much lower than the ones required for atomic cooling. Consequently, in the following, we shall consider $T_{\rm vir}^{\rm min} = 10^3$ K as the minimum threshold temperature for star formation and we assume the same threshold temperature $T_{\rm vir}^{\rm min}$ for haloes hosting ionizing and x-ray sources. This parameter plays a crucial role in extracting the constraints from the 21 cm absorption signal in both CDM and NCDM scenarios, see also [87,88]. The impact of varying $T_{\rm vir}^{\rm min}$ in the 10^3 K to 10^4 K range within the CDM paradigm is illustrated in Fig. 1 with the purple area. The lower value of the threshold parameter corresponds to higher values of the faction of collapsed haloes at a given redshift.

The comoving star formation rate density is described by $\dot{\rho}_\star = f_* \rho_{b,0} \dot{f}_{\rm coll}(> M_{\rm vir}^{\rm min})$, where f_*, the fraction of baryons that are converted into stars, considered here as a constant parameter (neglecting any dependence on the halo masses or redshift). As f_* controls the amplitude of the star formation rate density, it also sets the amplitude of both the ionizing and heating rates, as well as the Lyman-α flux. This parameter is quite uncertain as no observations of low mass haloes of mass $10^6 - 10^8\ M_\odot$ at redshift $z \sim 20$ are available. Nevertheless, several previous works, based on radiation-hydrodynamic simulations of high-redshift galaxies in a neutral medium [132–135] or based on the comparison of the star formation rate density to the one derived from UV luminosity function measurements [89,136,137], have found values of $f_* \sim \mathcal{O}(0.01)$. In the following, we therefore consider $f_* = 0.01$, leaving for the discussion in Sec. IV the impact in our results of slightly larger values of f_*.

Finally, in order to characterize the overall normalization of the x-ray luminosity, 21CMFAST makes use of the x-ray efficiency parameter ζ_X, expressed in units of $M_\odot^{-1}$. This parameter is varied here within the range $\zeta_X = [1\text{–}5] \times 10^{56}/M_\odot$. One can relate this parameter to the integrated x-ray soft band emissivity (below 2 keV) per unit of star formation rate escaping the galaxy $L_{X<2\,\rm keV}/\mathrm{SFR}$, varied in the range $\log_{10}(L_{X<2\,\rm keV}/\mathrm{SFR}) \in [39.5, 40.2]$ erg/s/$(M_\odot/\mathrm{yr})$.[3] This range is similar to one extracted from observations of the hot interstellar medium, which lead to $\log_{10}(L_{X<2\,\rm keV}/\mathrm{SFR}) \sim [39,40]$ erg/s/$(M_\odot/\mathrm{yr})$ [139], and also to the one adopted in Ref. [87] (see also Ref. [140]).

[3]The emissivity $L_{X<2\,\rm keV}/\mathrm{SFR}$ corresponds to the following combination of parameters: $\alpha_X \zeta_X h_p \int (\nu/\nu_0)^{-\alpha_X} d\nu$ where h_p is the Planck constant, α_X is the spectral slope parameter and ν_0 is the obscuration frequency cutoff parameter (see the 21CMMC code [138] based on 21CMFAST). The integral goes from ν_0 to 2 keV. We took $\alpha_X = 1.2$ and $\nu_0 = 7.2 \times 10^{12}$ Hz (corresponding to an energy of 300 eV), that are the default values in the 21CMFAST code.

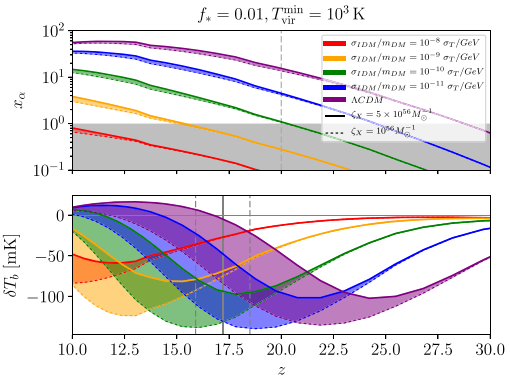

FIG. 2. Coupling coefficient for Lyman-α scattering (top) and sky-averaged 21 cm brightness temperature (bottom) as a function of the redshift for several possible values of the scattering dark matter-photon cross section over the dark matter particle mass. We have fixed $f_* = 0.01$ and $T_{\rm vir}^{\rm min} = 10^3$ K. The width of the bands refers to the change in δT_b and x_α due to different values of ζ_X.

III. IMPRINT OF THE IDM ON THE 21 CM SIGNAL

Noncold dark matter scenarios are expected to delay structure formation and therefore the absorption feature in the 21 cm signal at cosmic dawn. This effect is illustrated for the IDM model under study in Fig. 2, where we show the coupling coefficient for Lyman-α scattering x_α (top), and the sky-averaged 21 cm brightness temperature (bottom). The different colors correspond to different values of the dark matter-photon scattering cross sections over the dark matter particle mass, $\sigma_{\rm IDM}/\sigma_T(\mathrm{GeV}/m_{\rm DM})$. As can be noticed, large cross sections, inducing a stronger suppression at small scales, also induce a stronger suppression of the Lyman-α coupling at a given redshift (see the top panel of Fig. 2) and a larger shift toward smaller redshifts of the 21 cm features (see the bottom panel of Fig. 2). We also illustrate, with a vertical line, the position of the minimum of absorption reported by the EDGES experiment (at $\nu = 78$ MHz corresponding to $z = 17.2$). The dashed lines correspond to the largest signal redshift range at the minimum of absorption within the 99% CL interval reported by Ref. [68].

Figure 2 also shows the impact of varying the x-ray heating efficiency ζ_X in the $10^{56}\ M_\odot^{-1} - 5 \times 10^{56}\ M_\odot^{-1}$ range with the width of the colored bands. We see from the top panel of Fig. 2 that the range of ζ_X considered here, the Lyman-α flux resulting from x-ray excitation

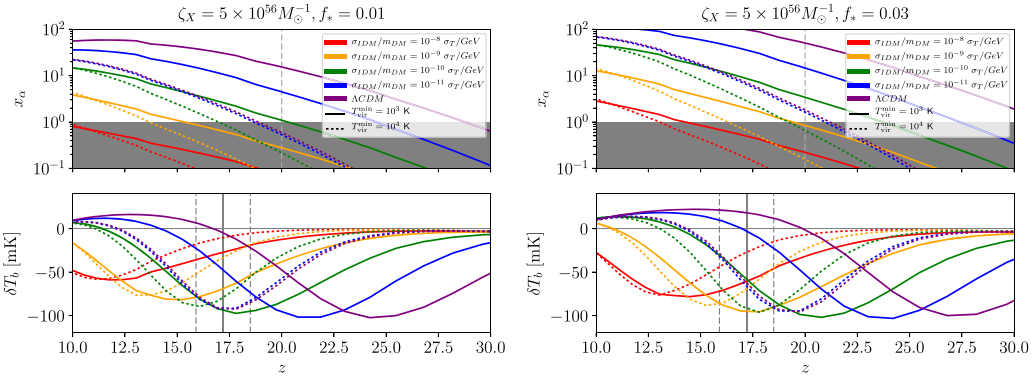

FIG. 3. Top panels: Lyman-α coupling coefficient x_α versus redshift for different values of the astrophysical parameter $T_{\rm vir}^{\rm min}$ and for several possible values of the scattering dark matter-photon cross-section over the dark matter mass. Cases within the shaded region are highly disfavoured by the condition given by Eq. (3.1). Bottom panels: sky-averaged 21 cm brightness temperature. The solid (dashed) lines indicates the mean redshift (range in redshift) associated to the EDGES signal. We have fixed $\zeta_X = 5 \times 10^{56}\ M_\odot$ and $f_* = 0.01$ ($f_* = 0.03$) in left (right) panel.

($J_{\alpha X} \propto \zeta_X$) is usually a negligible contribution to the Lyman-α coupling at the redshift at which $x_\alpha \sim 1$. On the bottom panel of Fig. 2, we see the impact of the x-ray heating parameter ζ_X on the differential brightness temperature. Here the impact is more significant. The deepest absorption dip corresponds to $\zeta_X = 10^{56}\ M_\odot^{-1}$, while the shallowest one is obtained for $\zeta_X = 5 \times 10^{56}\ M_\odot^{-1}$. Notice also that a larger value of ζ_X implies an earlier minimum, i.e., the x-ray heating of the IGM occurs earlier in time. As a result, in order to extract conservative constraints on the NCDM parameters from the redshift at which the absorption minimum is located, we shall consider the value $\zeta_X = 5 \times 10^{56}/M_\odot$, see Sec. III B. Even if a larger value of the x-ray efficiency parameter will make harder to match the observed depth of the EDGES signal, we recall here that our analyses are driven by the location (and not the amplitude) of the dip.

Figure 3 illustrates the equivalent to Fig. 2 with ζ_X fixed to $5 \times 10^{56}\ M_\odot^{-1}$ and considering this time $T_{\rm vir}^{\rm min} = 10^3$ K (continuous curves) as well as $T_{\rm vir}^{\rm min} = 10^4$ K (dotted curves). Going from left to right panel of Fig. 3 we increase the value of f_* by a factor of 3. Based on these plots, we discuss in the next two subsections the constraints that could be derived on NCDM scenarios following two different approaches. Notice that none of our predictions in Figs. 2 and 3 show the flat bottom present in the EDGES signal (see, e.g., Fig. 1 of [68]). Instead, these models have a more gradual evolution around the minimum. Together with the fact that we are unable to obtain the amplitude of 500 mK of the EDGES absorption dip, this shows that standard astrophysical predictions, even within NCDM models, cannot reproduce all the features of the EDGES profile, see, e.g., [141,142] for more details.

A. Constraints from the Lyman-α background

In order to account for the EDGES results, the authors of Ref. [89] based their analyses on the assumption that a sufficiently strong Lyman-α background is present by $z \sim 20$. They imposed

$$x_\alpha(z = 20) \gtrsim 1. \tag{3.1}$$

This limit results from the observation that the absorption signal reported by the EDGES experiment is equal to half of the maximum amplitude of absorption at $z \simeq 20$. We shall follow this assumption here, applying this condition to our simulations within NCDM models. Let us first focus on the top left panel of Fig. 3, which shows the Lyman-α coupling coefficient x_α as a function of the redshift for $f_* = 0.01$. The condition reported in (3.1) disfavors the cosmological scenarios associated to a prediction of $x_\alpha(z)$ lying within the shaded area at $z = 20$.

The astrophysical parameter $T_{\rm vir}^{\rm min}$ has a significant impact on the Lyman-α coupling coefficient x_α. Larger virial temperature shifts star formation to lower redshifts, giving rise to a lower Lyman-α background at a given redshift. In a similar way, a large value of the IDM scattering cross section implies a longer delay in structure formation. As a result, one can deduce from Fig. 3 (left panel) that, for molecular cooling ($T_{\rm vir}^{\rm min} = 10^3$ K), the scattering cross section must be below $10^{-10}\sigma_T \times (m_{\rm DM}/{\rm GeV})$. If one assumes instead that the only efficient cooling mechanism is atomic cooling with $T_{\rm vir}^{\rm min} \geq 10^4$ K, the limits on the IDM scattering cross section become much tighter, excluding scattering cross section lower than $10^{-11}\sigma_T \times (m_{\rm DM}/{\rm GeV})$. Our most conservative bound (assuming $f_* = 0.01$) is therefore $\sigma_{\rm IDM} \lesssim 10^{-10}\sigma_T \times (m_{\rm DM}/{\rm GeV})$. This constraint is stronger than

the 95% CL upper limit of $\sigma_{\rm IDM} < 8 \times 10^{-10}\sigma_T \times (m_{\rm DM}/{\rm GeV})$ reported in Ref. [60], based on observations of Milky Way satellite galaxy number counts and assuming a mass for our galaxy of $M_{\rm MW} = 2.6 \times 10^{12}\ M_\odot$.

Notice that the Lyman-α coupling coefficient x_α is directly proportional to the fraction of baryons converted into stars (f_*), here considered as constant. The left (right) panels of Fig. 3 have been simulated with $f_* = 0.01$ ($f_* = 0.03$). Notice that larger values of f_* increase the Lyman-α coupling at a fixed redshift, weakening the bound on IDM scenarios resulting from Eq. (3.1). In the case of $f_* = 0.03$, the limits quoted above are translated into $\sigma_{\rm IDM} \lesssim 10^{-9}\sigma_T \times (m_{\rm DM}/{\rm GeV})$ and $\sigma_{\rm IDM} \lesssim 10^{-10}\sigma_T \times (m_{\rm DM}/{\rm GeV})$ for $T_{\rm vir}^{\rm min} = 10^3$ K and $T_{\rm vir}^{\rm min} = 10^4$ K respectively.

B. Constraints from the position of the absorption minimum in the 21 cm global signature

Another possible avenue to constrain NCDM models using the EDGES observations is based on the location of the minimum of the absorption. Reference [87] imposed that it should be located at a redshift higher than $z = 17.2$ and studied the resulting bounds on a large set of NCDM models. We show in the bottom panels of Fig. 3 the effect of the IDM scenario considered here on the global sky-averaged 21 cm brightness temperature obtained by means of Eq. (2.1).

Let us focus first in the $f_* = 0.01$ case (i.e., left panel). Considering atomic cooling (dotted curves with $T_{\rm vir}^{\rm min} = 10^4$ K), it appears that for scattering cross sections larger than $\sim 10^{-11}\sigma_T \times (m_{\rm DM}/{\rm GeV})$ the absorption minimum takes place at redshifts lower than $z = 17.2$. Such cross sections should therefore be regarded as disfavored. Considering molecular cooling softens this constraint by $\sim$ one order of magnitude (see the continuous curves for $T_{\rm vir}^{\rm min} = 10^3$ K). Notice that we have considered a conservative x-ray efficiency of $\zeta_X = 5 \times 10^{56}\ M_\odot^{-1}$ for all curves. Considering lower values of ζ_X will give rise to a later x-ray heating and thus a minimum of absorption located at lower redshifts.

If instead, we consider a larger fraction of baryons converted into stars, $f_* = 0.03$, (see the bottom right panel), and $T_{\rm vir}^{\rm min} = 10^3$ (10^4) K, the limit on the IDM interactions is relaxed, excluding cross sections above $\sim 10^{-9}$ $(10^{-10})\sigma_T \times (m_{\rm DM}/{\rm GeV})$. This is due to the fact that both the x-ray and the Lyman-α emission rates are directly proportional to f_*. Increasing f_* implies an earlier Lyman-α coupling and x-ray heating periods, displacing the minimum of the absorption in the 21 cm signal to a larger redshift.

IV. DISCUSSION AND CONCLUSIONS

Interacting dark matter (IDM) models, in which dark matter is not made out of purely cold, pressureless particles, are an interesting alternative to the standard CDM paradigm and provide a possible avenue to alleviate the so-called small-scale crisis of the ΛCDM. The IDM could be scattering off light or massless degrees of freedom such as photons or neutrinos. Here we have considered the case of dark matter scattering on photons, characterized by the size of the scattering rate over the DM mass, $\sigma_{\rm IDM}/m_{\rm DM}$. The reason for this choice is driven by the availability of a fitting function for the halo mass function relevant for our study. Let us emphasize though that scatterings on neutrinos are expected to give rise to a similar imprint on the 21 cm signal.

Several studies have constrained IDM models based on their suppression of clustering at small scales, exploiting galaxy power spectrum, gravitational lensing, CMB, number of Milky Way dwarf galaxies and Lyman-α forest observations, among others. Here we focus on the imprint of IDM on the 21 cm signal arising from cosmic dawn. Based on a modified version of the 21CMFAST code, our simulations show that IDM delays the formation of haloes capable of star formation, shifting the timing of the 21 cm signal features compared to the standard CDM scenario. A similar effect has been reported in the case of other NCDM models [45,46,60,66]. In this paper, we have considered two possible ways to test the IDM properties against the 21 cm signal. First, following Ref. [89], a significant Lyman-α coupling between the gas and the spin temperature characterizing the 21 cm signal should be present at $z = 20$. Second, as argued in Ref. [87], the location of the absorption minimum in the EDGES signal at $z = 17.2$ implies that any scenario with sufficiently enough delayed structure formation could be discarded.

We have first identified which are the most relevant astrophysical parameters showing large degeneracies with the IDM scattering cross section over the mass $\sigma_{\rm IDM}/m_{\rm DM}$. Namely, the fraction of baryons into stars f_*, the threshold temperature for haloes to host star-forming galaxies $T_{\rm vir}^{\rm min}$ and the x-ray efficiency, ζ_X, have been shown to interfere with the eventual extraction of a nonzero $\sigma_{\rm IDM}$. Fortunately, the parameter ζ_X only plays a significant role in extracting the location of the absorption minimum, and we have adopted the conservative value of $\zeta_X = 5 \times 10^{56}\ M_\odot^{-1}$ (corresponding to an integrated soft band x-ray emissivity of $L_{X<2\,{\rm keV}}/{\rm SFR} = 10^{40.2}$ erg/s/$(M_\odot/{\rm yr})$). We also considered a lower limit on the threshold virial temperature of $T_{\rm vir}^{\rm min} = 10^3$ K (corresponding to molecular cooling) as well as a constant value of $f_* < 0.03$.

Our results are summarized on the left panel of Fig. 4 in the case of $f_* = 0.01$. The top panels shows the Lyman-α coupling coefficient x_α at $z = 20$ for $T_{\rm vir}^{\rm min} = 10^3$ (10^4) K with the top blue (bottom red) curve as a function of the IDM scattering cross section. Notice that the $x_\alpha(z = 20)$ curves saturate to a maximum value at low enough values of the scattering cross section. This corresponds to the limiting $x_\alpha(z = 20)$ value that one would get in the CDM scenario (indicated with the horizontal dotted lines). In

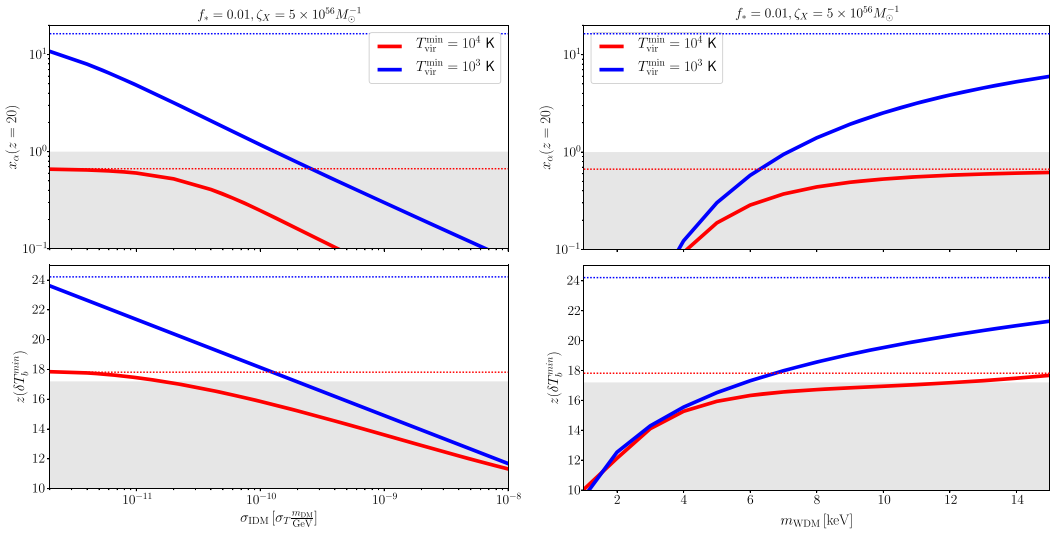

FIG. 4. Left, top (bottom) panel: Lyman-α coupling coefficient x_α at $z = 20$ (redshift of the absorption minimum in the sky-averaged 21 cm brightness temperature) versus the scattering dark matter-photon cross-section for $T_{\rm vir}^{\rm min} = 10^4$ K (atomic cooling) and for $T_{\rm vir}^{\rm min} = 10^3$ K (molecular cooling). Right panels: the same but for WDM models, as a function of the WDM mass $m_{\rm WDM}$. IDM/WDM scenarios lying in the shaded regions are highly disfavoured by the two conditions exploited here, see text for details. We have fixed $f_* = 0.01$ and $\zeta_X = 5 \times 10^{56}\ M_\odot^{-1}$. Dashed lines stand for the results in the CDM scenario.

addition, the shaded region refers to the parameter space in which the condition $x_\alpha(z = 20) > 1$ can not be satisfied and can therefore be considered as disfavored by the condition given by Eq. (3.1). As a result, for $f_* = 0.01$ and $\zeta_X = 5 \times 10^{56}\ M_\odot^{-1}$, a value of $\sigma_{\rm IDM} > 10^{-10}\sigma_T \times (m_{\rm DM}/{\rm GeV})$ fails to satisfy the condition $x_\alpha(z{=}20){>}1$ when considering molecular cooling ($T_{\rm vir}^{\rm min} = 10^3$ K). This improves the previous bound derived on such IDM model in Ref. [60]. When considering higher threshold temperatures for efficient cooling, the bounds gets tighter, disfavoring even the canonical CDM scenario if $T_{\rm vir}^{\rm min} = 10^4$ K. All these limits would be relaxed if the fraction of baryons converted into stars is larger, as it was illustrated in Fig. 3 for $f_* = 0.03$. For instance, for $T_{\rm vir}^{\rm min} = 10^3$ K, the limit would be reduced by one order of magnitude (i.e., $\sigma_{\rm IDM} < 10^{-9}\sigma_T \times (m_{\rm DM}/{\rm GeV})$).

In the bottom left panel of Fig. 4, we show the redshift at which the sky-averaged 21 cm brightness temperature exhibits its minimum of absorption at cosmic dawn, $z(\delta T_b^{\rm min})$, as a function of the IDM scattering cross section. Again $z(\delta T_b^{\rm min})$ saturates for low enough scattering cross-section to a value corresponding to the CDM limit denoted with a dotted horizontal line. The shaded area denotes the region in which this minimum is located below $z = 17.2$. More concretely, in order to derive the curves shown in the bottom panels of Fig. 4, we have fitted the brightness temperature curves obtained from our simulations to the flattened Gaussian shape that the EDGES collaboration uses to model the 21 cm absorption profile [68]. This procedure allows us to extract the central frequency for each possible value of $\sigma_{\rm IDM}/m_{\rm DM}$, $T_{\rm vir}^{\rm min}$ and f_*, and also to constrain the model by imposing that this mean frequency ν_0 of our flattened gaussian fits should lie at frequencies below the lower 99% confidence interval (including estimates of systematic uncertainties) reported by the EDGES collaboration for the $\nu_0 = 78$ MHz parameter.[4] From Fig. 4, the position of the minimum of absorption disfavors the region $\sigma_{\rm IDM} > 10^{-10}\sigma_T \times (m_{\rm DM}/{\rm GeV})$ ($\sigma_{\rm IDM} > 10^{-11}\sigma_T \times (m_{\rm DM}/{\rm GeV})$) for $T_{\rm vir}^{\rm min} = 10^3$ K ($T_{\rm vir}^{\rm min} = 10^4$ K). As in the case of the $x_\alpha(z = 20) > 1$ condition, these limits would be relaxed by one order of magnitude in the case of a value of $f_* = 0.03$. Also, for the astrophysical parameters considered here, we see that the constraints from the Lyman-α coupling condition are typically tighter than those arising from the position of the minimum of absorption. Nevertheless, the uncertainty on the limits derived using the Lyman-α coupling criterion of Eq. (3.1) is more difficult to quantify than the one related to the position of the minimum of absorption. Indeed, using Eq. (3.1), we are not using any specific parameter of the fit

[4]It should be noted that we cannot reproduce precisely the values of other parameters quoted by EDGES of the fits due to the lack of flat bottom and large amplitude in our predictions.

to derive the exclusion region, but a statement on the general shape. Also, notice that there could be a small variation of the limits depending on the redshift at which one assumes that $x_\alpha = 1$. Here $z = 20$ has been taken, but small variations in the range $z = 20 \pm 0.5$ would agree with the δT_b obtained varying the signal parameters within the 99% CL range reported by EDGES. In contrast, the dip-position criterion based on the 99% CL of the location observed by EDGES appears thus to be more robust. Finally, the dip location and x_α criterion are sensitive to different astrophysics parameters. For example, the dip location very much depends on ζ_X while, as can be seen in Fig. 2, x_α is quite insensitive to this parameter at $z \sim 20$. Still, the limits on the DM properties from the two methods show an excellent agreement for $T_{\rm vir}^{\rm min} = 10^3$ K.

Summarizing, for $f_* \simeq 0.01$, $\zeta_X < 5 \times 10^{56}\ M_\odot^{-1}$ and $T_{\rm vir}^{\rm min} > 10^3$ K, the bounds on $\sigma_{\rm IDM}/m_{\rm DM}$ derived in this work imply an order of magnitude improvement over the most constraining existing limits in the literature [2,60]. Larger values of f_* may compromise these upgraded limits. In order to ease the comparison to other studies on NCDM scenarios, we provide the results obtained following the same methodology in a thermal warm dark matter scenario involving light dark matter particles with a mass $m_{\rm WDM}$ of a few keV. The prescription considered here to describe the suppression of the halo mass function at small halo masses is given in the Appendix A. We show the obtained dependence of $x_\alpha(z = 20)$ and $z(\delta T_b^{\rm min})$ in the right panel of Fig. 4. From this figure with $f_* = 0.01$ and $\zeta_X = 5 \times 10^{56}\ M_\odot^{-1}$, we can infer a lower limit in the WDM mass around $m_{\rm WDM} > 6$ keV ($m_{\rm WDM} > 12$ keV) if $T_{\rm vir}^{\rm min} = 10^3$ K ($T_{\rm vir}^{\rm min} = 10^4$ K). These tight limits are similar to those derived in Refs. [87,89] for slightly different WDM implementations and astrophysical parameters. As a final comment, it should be noted that IDM cross sections or WDM masses in these allowed regions could be not sufficient to solve the small-scale problems, since they predict a similar amount of substructures than the CDM case (see e.g., Table II of [143] for the WDM prescription). However, increasing f_* to 0.03 would relax the constraints by about one order of magnitude (recall the discussion about Fig. 3), being therefore these NCDM scenarios still suitable to deal with the subgalactic issues.

ACKNOWLEDGMENTS

L. L. H. is supported by the FNRS, by the Strategic Research Program *High Energy Physics* and by the Research Council of the Vrije Universiteit Brussel. O. M. and P. V. D. are supported by PROMETEO II/2014/050, by the Spanish MINECO Grants No. FPA2014–57816-P, No. FPA2017-85985-P, and No. SEV-2014-0398 and by the European Union's Horizon 2020 research and innovation program under the Marie Sklodowska-Curie Grant Agreements No. 690575 and 674896.

APPENDIX A: HALO MASS FUNCTIONS

The halo mass function, that counts the number of haloes per unit halo mass and volume at a given redshift, can be written as [144]

$$\frac{dn}{dM} = -\frac{1}{2}\frac{\rho_m}{M^2} f(\nu) \frac{d\ln\sigma^2}{d\ln M}, \tag{A1}$$

where n is the halo number density, $\rho_m = \Omega_m \rho_c$ is the average matter density in the Universe at $z = 0$ and $\sigma^2 = \sigma^2(M, z)$ is the variance of density perturbations, which is a function of the halo mass M and redshift. The first-crossing distribution, $f(\nu)$, is expected to be a universal function of $\nu \equiv \delta_c^2/\sigma^2(M, z)$, with $\delta_c = 1.686$, the linearly extrapolated density for collapse at $z = 0$. The Sheth-Tormen (ST) first-crossing distribution reads as [145–147]:

$$f(\nu) = A\sqrt{\frac{2q\nu}{\pi}}(1 + (q\nu)^{-p})e^{-q\nu/2}, \tag{A2}$$

with $p = 0.3$, $q = 0.707$ and $A = 0.3222$. For the standard CDM scenario, we consider this first-crossing distribution. The variance at $z = 0$, $\sigma(M) \equiv \sigma(M, z = 0)$, at a given scale R can be expressed as

$$\sigma_X^2(M(R)) = \int \frac{d^3k}{(2\pi)^3} P_X(k) W^2(kR), \tag{A3}$$

where $P_X(k)$ is the linear power spectrum at $z = 0$ for a given $X = \{\text{CDM, IDM or WDM}\}$ cosmology and W is the Fourier transform of a filter function that we consider to be a top-hat (TH) function in real space (see, e.g., [16,87] for the possibility of using a sharp-k window function for NCDM). The redshift dependence is driven by the linear growth function, $D(z)$ normalized to 1 at $z = 0$, so that the root-mean-square (rms) density fluctuation is $\sigma(M, z) = \sigma(M, z = 0)D(z)$.

The transfer function T_X for a NCDM scenario X is defined as

$$P_X(k) = P_{\rm CDM}(k) T_X^2(k), \tag{A4}$$

where $P_{\rm CDM}(k)$ is the linear power spectrum in ΛCDM. Here we use the prescription of Refs. [14,94]:

$$T_X(k) = (1 + (\alpha_X k)^{2\mu})^{-5/\mu}, \tag{A5}$$

where $\mu = 1.2$ is a dimensionless exponent and α_X is a breaking scale. The latter takes the form:

$$\alpha_{\rm WDM} = 0.048 \left(\frac{\rm keV}{m_{\rm WDM}}\right)^{1.15} \left(\frac{\Omega_{\rm WDM}}{0.4}\right)^{0.15} \left(\frac{h}{0.65}\right)^{1.3} {\rm Mpc}/h, \tag{A6}$$

$$\alpha_{\gamma\mathrm{DM}} = 0.073\left[10^8\left(\frac{\sigma_{\mathrm{IDM}}}{\sigma_T}\right)\left(\frac{\mathrm{GeV}}{m_{\mathrm{DM}}}\right)\right]^{0.48}\left(\frac{\Omega_{\mathrm{WDM}}}{0.4}\right)^{0.15} \times \left(\frac{h}{0.65}\right)^{1.3}\mathrm{Mpc}/h. \quad \text{(A7)}$$

for WDM scenarios [3,100] and IDM involving dark matter-photon scattering [14] respectively. For DM-neutrino interactions, described with the same parametrization of the transfer function, one gets a breaking scale $\alpha_{\nu\mathrm{DM}} \simeq 0.8 \times \alpha_{\gamma\mathrm{DM}}$ for a fixed value of the scattering cross section [3].

The halo mass function defined as in Eq. (A1) is well suited for CDM but it needs to be adapted for the NCDM case. In order to match the results from N-body simulations, the WDM halo mass function can be expressed as [100]

$$\frac{dn^{\mathrm{WDM}}}{dM} = \left(1+\frac{M_{\mathrm{hm}}}{bM}\right)^a \frac{dn^{\mathrm{ST,WDM}}}{dM}, \quad \text{(A8)}$$

where an additional mass-dependent correction to the standard ST formalism appears. We use $a = -0.6$ and $b = 0.5$, as obtained in [3,90]. The function $\frac{dn^{\mathrm{ST,WDM}}}{dM}$ in Eq. (A8) refers to the halo mass function obtained with a ST first-crossing distribution, as defined in Eq. (A2), and a linear matter power spectrum corresponding to the WDM case. In order to describe the suppression in the linear regime, one can consider the half-mode mass M_{hm}, defined as the mass scale for which $T_X/T_{\mathrm{CDM}} = 1/2$ (i.e., $P_X/P_{\mathrm{CDM}} = 1/4$). Using the general fit to the transfer function, Eq. (A5), the half-mode mass M_{hm} can be easily derived as

$$M_{\mathrm{hm}} \equiv \frac{4\pi}{3}\rho_m(\pi\alpha_X)^3(2^{\mu/5}-1)^{-3/(2\mu)}. \quad \text{(A9)}$$

For what concerns the IDM models, the number of low-mass structures appears to be larger than in WDM scenarios [3] (see also [7]). In order to reproduce the IDM results for masses below the half-mode mass, an extra mass-dependent correction must be introduced to the halo mass function [90]:

$$\frac{dn^{\mathrm{IDM}}}{dM} = \left(1+\frac{M_{\mathrm{hm}}}{bM}\right)^a\left(1+\frac{M_{\mathrm{hm}}}{gM}\right)^c \frac{dn^{\mathrm{ST,CDM}}}{dM}, \quad \text{(A10)}$$

with $a = -1$, $b = 0.33$, $g = 1$, $c = 0.6$ and $\frac{dn^{\mathrm{ST,CDM}}}{dM}$ refers to the standard ST first-crossing distribution as defined in Eq. (A2) with the CDM linear power spectrum for the variance of density perturbations.

APPENDIX B: LYMAN-α EMISSIVITY

The Lyman-α flux from direct stellar emission of UV photons, $J_{\alpha\star}$, is given by the sum over the Lyman-n levels which can lead to a $2p \to 1s$ transition through a decaying cascade. Due to the optical thickness of the IGM, photons which redshift to a Lyman resonance are absorbed by the medium. A photon which reaches a Lyman-n resonance at redshift z has to be emitted at a redshift below $1 + z_{\mathrm{max},n} = \frac{1-(n+1)^{-2}}{1-n^{-2}}(1+z)$. If $f_{\mathrm{rec}}(n)$ is the recycled fraction of the level n, i.e., the probability of generating a Lyman-α photon from the n level [148], the total Lyman-α flux can be written as

$$J_{\alpha\star} = \frac{c(1+z)^2}{4\pi}\sum_{n=2}^{n_{\mathrm{max}}} f_{\mathrm{rec}}(n)\int_z^{z_{\mathrm{max},n}} dz' \frac{\epsilon_\alpha(\nu_n', z')}{H(z')}, \quad \text{(B1)}$$

where the emission frequency is $\nu_n' = \nu_n\frac{1+z'}{1+z}$, being $\nu_n = \nu_{\mathrm{LL}}(1-n^{-2})$ and ν_{LL} the Lyman limit frequency. The comoving emissivity ϵ_α can be written as proportional to the comoving star formation rate $\dot{\rho}_{\star,0}$:

$$\epsilon_\alpha(\nu, z) = \varepsilon(\nu)\frac{\dot{\rho}_{\star,0}(z)}{\mu m_p} = \varepsilon(\nu) f_* \bar{n}_{b,0}\dot{f}_{\mathrm{coll}}(z), \quad \text{(B2)}$$

where $\bar{n}_{b,0}$ is the comoving number density of baryons. Assuming that only Population-II stars contribute to this emissivity, the spectral distribution $\varepsilon(\nu)$ is given by a separate power law between each Lyman-n and Lyman-$n+1$ levels:

$$\varepsilon(\nu) = N_n\frac{(\beta_n+1)\nu_\alpha^{\beta_n}}{(\nu_{n+1}^{\beta_n+1}-\nu_n^{\beta_n+1})}\left(\frac{\nu}{\nu_\alpha}\right)^{\beta_n}, \quad \text{(B3)}$$

for $\nu_n \le \nu \le \nu_{n+1}$, with N_n the number of photons emitted between the n and $n+1$ resonances and β_n the spectral index [122]. The function above is normalized as $\int_{\nu_n}^{\nu_{n+1}} d\nu\varepsilon(\nu) = N_n$, with $\int_{\nu_\alpha}^{\nu_{\mathrm{LL}}} d\nu\varepsilon(\nu) = \sum_n N_n \simeq 9690$ the total number of photons emitted between the Lyman-α and the Lyman limit. Although we keep this normalization as constant through our analysis, notice that changes in the number of photons which contribute to the Lyman-α flux could have a deep impact in the 21 cm signal [141].

[1] C. Boehm, H. Mathis, J. Devriendt, and J. Silk, Mon. Not. R. Astron. Soc. **360**, 282 (2005).
[2] C. Bœhm, J. A. Schewtschenko, R. J. Wilkinson, C. M. Baugh, and S. Pascoli, Mon. Not. R. Astron. Soc. **445**, L31 (2014).
[3] J. A. Schewtschenko, R. J. Wilkinson, C. M. Baugh, C. Bœhm, and S. Pascoli, Mon. Not. R. Astron. Soc. **449**, 3587 (2015).
[4] J. A. Schewtschenko, C. M. Baugh, R. J. Wilkinson, C. Bœhm, S. Pascoli, and T. Sawala, Mon. Not. R. Astron. Soc. **461**, 2282 (2016).
[5] F.-Y. Cyr-Racine, R. de Putter, A. Raccanelli, and K. Sigurdson, Phys. Rev. D **89**, 063517 (2014).
[6] M. R. Buckley, J. Zavala, F.-Y. Cyr-Racine, K. Sigurdson, and M. Vogelsberger, Phys. Rev. D **90**, 043524 (2014).
[7] M. Vogelsberger, J. Zavala, F.-Y. Cyr-Racine, C. Pfrommer, T. Bringmann, and K. Sigurdson, Mon. Not. R. Astron. Soc. **460**, 1399 (2016).
[8] F.-Y. Cyr-Racine, K. Sigurdson, J. Zavala, T. Bringmann, M. Vogelsberger, and C. Pfrommer, Phys. Rev. D **93**, 123527 (2016).
[9] L. G. van den Aarssen, T. Bringmann, and C. Pfrommer, Phys. Rev. Lett. **109**, 231301 (2012).
[10] T. Bringmann, H. T. Ihle, J. Kersten, and P. Walia, Phys. Rev. D **94**, 103529 (2016).
[11] T. Binder, L. Covi, A. Kamada, H. Murayama, T. Takahashi, and N. Yoshida, J. Cosmol. Astropart. Phys. 11 (2016) 043.
[12] A. Kamada and T. Takahashi, J. Cosmol. Astropart. Phys. 01 (2018) 047.
[13] C. Bœhm, P. Fayet, and R. Schaeffer, Phys. Lett. B **518**, 8 (2001).
[14] C. Bœhm, A. Riazuelo, S. H. Hansen, and R. Schaeffer, Phys. Rev. D **66**, 083505 (2002).
[15] C. Bœhm and R. Schaeffer, Astron. Astrophys. **438**, 419 (2005).
[16] R. Murgia, A. Merle, M. Viel, M. Totzauer, and A. Schneider, J. Cosmol. Astropart. Phys. 11 (2017) 046.
[17] J. S. Bullock and M. Boylan-Kolchin, Annu. Rev. Astron. Astrophys. **55**, 343 (2017).
[18] M. Viel, G. D. Becker, J. S. Bolton, and M. G. Haehnelt, Phys. Rev. D **88**, 043502 (2013).
[19] M. Viel, J. Lesgourgues, M. G. Haehnelt, S. Matarrese, and A. Riotto, Phys. Rev. D **71**, 063534 (2005).
[20] U. Seljak, A. Makarov, P. McDonald, and H. Trac, Phys. Rev. Lett. **97**, 191303 (2006).
[21] M. Viel, J. Lesgourgues, M. G. Haehnelt, S. Matarrese, and A. Riotto, Phys. Rev. Lett. **97**, 071301 (2006).
[22] G. Mangano, A. Melchiorri, P. Serra, A. Cooray, and M. Kamionkowski, Phys. Rev. D **74**, 043517 (2006).
[23] M. Viel, G. D. Becker, J. S. Bolton, M. G. Haehnelt, M. Rauch, and W. L. W. Sargent, Phys. Rev. Lett. **100**, 041304 (2008).
[24] A. Boyarsky, J. Lesgourgues, O. Ruchayskiy, and M. Viel, J. Cosmol. Astropart. Phys. 05 (2009) 012.
[25] P. Serra, F. Zalamea, A. Cooray, G. Mangano, and A. Melchiorri, Phys. Rev. D **81**, 043507 (2010).
[26] S. D. McDermott, H.-B. Yu, and K. M. Zurek, Phys. Rev. D **83**, 063509 (2011).
[27] R. J. Wilkinson, J. Lesgourgues, and C. Bœhm, J. Cosmol. Astropart. Phys. 04 (2014) 026.
[28] A. D. Dolgov, S. L. Dubovsky, G. I. Rubtsov, and I. I. Tkachev, Phys. Rev. D **88**, 117701 (2013).
[29] R. J. Wilkinson, C. Bœhm, and J. Lesgourgues, J. Cosmol. Astropart. Phys. 05 (2014) 011.
[30] A. Schneider, Mon. Not. R. Astron. Soc. **451**, 3117 (2015).
[31] M. Escudero, O. Mena, A. C. Vincent, R. J. Wilkinson, and C. Bœhm, J. Cosmol. Astropart. Phys. 09 (2015) 034.
[32] Y. Ali-Haïmoud, J. Chluba, and M. Kamionkowski, Phys. Rev. Lett. **115**, 071304 (2015).
[33] J. Baur, N. Palanque-Delabrouille, C. Yèche, C. Magneville, and M. Viel, J. Cosmol. Astropart. Phys. 08 (2016) 012.
[34] R. Diamanti, S. Ando, S. Gariazzo, O. Mena, and C. Weniger, J. Cosmol. Astropart. Phys. 06 (2017) 008.
[35] V. Irsic *et al.*, Phys. Rev. D **96**, 023522 (2017).
[36] C. Yèche, N. Palanque-Delabrouille, J. Baur, and H. du Mas des Bourboux, J. Cosmol. Astropart. Phys. 06 (2017) 047.
[37] S. Gariazzo, M. Escudero, R. Diamanti, and O. Mena, Phys. Rev. D **96**, 043501 (2017).
[38] J. A. D. Diacoumis and Y. Y. Y. Wong, J. Cosmol. Astropart. Phys. 09 (2017) 011.
[39] E. Di Valentino, C. Bœhm, E. Hivon, and F. R. Bouchet, Phys. Rev. D **97**, 043513 (2018).
[40] A. O.-D. Campo, C. Bœhm, S. Palomares-Ruiz, and S. Pascoli, Phys. Rev. D **97**, 075939 (2018).
[41] J. Stadler and C. Bœhm, J. Cosmol. Astropart. Phys. 10 (2018) 009.
[42] A. D. Rivero, C. Dvorkin, F.-Y. Cyr-Racine, J. Zavala, and M. Vogelsberger, Phys. Rev. D **98**, 103517 (2018).
[43] M. R. Lovell, J. Zavala, M. Vogelsberger, X. Shen, F.-Y. Cyr-Racine, C. Pfrommer, K. Sigurdson, M. Boylan-Kolchin, and A. Pillepich, Mon. Not. R. Astron. Soc. **477**, 2886 (2018).
[44] P. Dayal, A. Mesinger, and F. Pacucci, Astrophys. J. **806**, 67 (2015).
[45] S. Bose, C. S. Frenk, J. Hou, C. G. Lacey, and M. R. Lovell, Mon. Not. R. Astron. Soc. **463**, 3848 (2016).
[46] L. Lopez-Honorez, O. Mena, S. Palomares-Ruiz, and P. Villanueva-Domingo, Phys. Rev. D **96**, 103539 (2017).
[47] R. Barkana, Z. Haiman, and J. P. Ostriker, Astrophys. J. **558**, 482 (2001).
[48] N. Yoshida, A. Sokasian, L. Hernquist, and V. Springel, Astrophys. J. **591**, L1 (2003).
[49] R. S. Somerville, J. S. Bullock, and M. Livio, Astrophys. J. **593**, 616 (2003).
[50] B. Yue and X. Chen, Astrophys. J. **747**, 127 (2012).
[51] F. Pacucci, A. Mesinger, and Z. Haiman, Mon. Not. R. Astron. Soc. **435**, L53 (2013).
[52] A. Mesinger, A. Ewall-Wice, and J. Hewitt, Mon. Not. R. Astron. Soc. **439**, 3262 (2014).
[53] C. Schultz, J. Oñorbe, K. N. Abazajian, and J. S. Bullock, Mon. Not. R. Astron. Soc. **442**, 1597 (2014).
[54] A. Lapi and L. Danese, J. Cosmol. Astropart. Phys. 09 (2015) 003.
[55] S. Bose, W. A. Hellwing, C. S. Frenk, A. Jenkins, M. R. Lovell, J. C. Helly, B. Li, V. Gonzalez-Perez, and L. Gao, Mon. Not. R. Astron. Soc. **464**, 4520 (2017).
[56] P. S. Corasaniti, S. Agarwal, D. J. E. Marsh, and S. Das, Phys. Rev. D **95**, 083512 (2017).

[57] N. Menci, A. Grazian, M. Castellano, and N. G. Sanchez, Astrophys. J. **825**, L1 (2016).
[58] P. Villanueva-Domingo, N. Y. Gnedin, and O. Mena, Astrophys. J. **852**, 139 (2018).
[59] S. Das, R. Mondal, V. Rentala, and S. Suresh, J. Cosmol. Astropart. Phys. 08 (2018) 045.
[60] M. Escudero, L. Lopez-Honorez, O. Mena, S. Palomares-Ruiz, and P. Villanueva-Domingo, J. Cosmol. Astropart. Phys. 06 (2018) 007.
[61] P. Dayal, T. R. Choudhury, V. Bromm, and F. Pacucci, Astrophys. J. **836**, 16 (2017).
[62] P. Dayal, T. R. Choudhury, F. Pacucci, and V. Bromm, Mon. Not. R. Astron. Soc. **472**, 4414 (2017).
[63] A. Harada and A. Kamada, J. Cosmol. Astropart. Phys. 01 (2016) 031.
[64] A. Kamada, K. T. Inoue, and T. Takahashi, Phys. Rev. D **94**, 023522 (2016).
[65] A. Kamada, K. Kohri, T. Takahashi, and N. Yoshida, Phys. Rev. D **95**, 023502 (2017).
[66] M. Sitwell, A. Mesinger, Y.-Z. Ma, and K. Sigurdson, Mon. Not. R. Astron. Soc. **438**, 2664 (2014).
[67] I. P. Carucci, F. Villaescusa-Navarro, M. Viel, and A. Lapi, J. Cosmol. Astropart. Phys. 07 (2015) 047.
[68] J. D. Bowman, A. E. E. Rogers, R. A. Monsalve, T. J. Mozdzen, and N. Mahesh, Nature (London) **555**, 67 (2018).
[69] A. Berlin, D. Hooper, G. Krnjaic, and S. D. McDermott, Phys. Rev. Lett. **121**, 011102 (2018).
[70] G. D'Amico, P. Panci, and A. Strumia, Phys. Rev. Lett. **121**, 011103 (2018).
[71] H. Liu and T. R. Slatyer, Phys. Rev. D **98**, 023501 (2018).
[72] A. Mitridate and A. Podo, J. Cosmol. Astropart. Phys. 05 (2018) 069.
[73] M. Valdés, C. Evoli, A. Mesinger, A. Ferrara, and N. Yoshida, Mon. Not. R. Astron. Soc. **429**, 1705 (2013).
[74] C. Evoli, A. Mesinger, and A. Ferrara, J. Cosmol. Astropart. Phys. 11 (2014) 024.
[75] L. Lopez-Honorez, O. Mena, A. Moliné, S. Palomares-Ruiz, and A. C. Vincent, J. Cosmol. Astropart. Phys. 08 (2016) 004.
[76] M. Pospelov, J. Pradler, J. T. Ruderman, and A. Urbano, Phys. Rev. Lett. **121**, 031103 (2018).
[77] D. Aristizabal Sierra and C. S. Fong, Phys. Lett. B **784**, 130 (2018).
[78] K. K. Boddy, V. Gluscevic, V. Poulin, E. D. Kovetz, M. Kamionkowski, and R. Barkana, Phys. Rev. D **98**, 123506 (2018).
[79] E. D. Kovetz, V. Poulin, V. Gluscevic, K. K. Boddy, R. Barkana, and M. Kamionkowski, Phys. Rev. D **98**, 103529 (2018).
[80] R. Barkana, N. J. Outmezguine, D. Redigolo, and T. Volansky, Phys. Rev. D **98**, 103005 (2018).
[81] R. Barkana, Nature (London) **555**, 71 (2018).
[82] A. Hektor, G. Hütsi, L. Marzola, and V. Vaskonen, Phys. Lett. B **785**, 429 (2018).
[83] A. Hektor, G. Hütsi, L. Marzola, M. Raidal, V. Vaskonen, and H. Veermäe, Phys. Rev. D **98**, 023503 (2018).
[84] S. Fraser *et al.*, Phys. Lett. B **785**, 159 (2018).
[85] R. Hills, G. Kulkarni, P. D. Meerburg, and E. Puchwein, Nature (London) **564**, E32 (2018).
[86] R. F. Bradley, K. Tauscher, D. Rapetti, and J. O. Burns, arXiv:1810.09015.
[87] A. Schneider, Phys. Rev. D **98**, 063021 (2018).
[88] M. Safarzadeh, E. Scannapieco, and A. Babul, Astrophys. J. **859**, L18 (2018).
[89] A. Lidz and L. Hui, Phys. Rev. D **98**, 023011 (2018).
[90] Á. Moliné, J. A. Schewtschenko, S. Palomares-Ruiz, C. Bœhm, and C. M. Baugh, J. Cosmol. Astropart. Phys. 08 (2016) 069.
[91] J. A. Schewtschenko, Cosmological simulations with Dark Matter from beyond the Standard Model, Ph.D. thesis, Durham U., 2016.
[92] C. Dvorkin, K. Blum, and M. Kamionkowski, Phys. Rev. D **89**, 023519 (2014).
[93] N. Vinyoles and H. Vogel, J. Cosmol. Astropart. Phys. 03 (2016) 002.
[94] P. Bode, J. P. Ostriker, and N. Turok, Astrophys. J. **556**, 93 (2001).
[95] A. Knebe, J. E. G. Devriendt, A. Mahmood, and J. Silk, Mon. Not. R. Astron. Soc. **329**, 813 (2002).
[96] P. Colin, O. Valenzuela, and V. Avila-Reese, Astrophys. J. **673**, 203 (2008).
[97] J. Zavala, Y. P. Jing, A. Faltenbacher, G. Yepes, Y. Hoffman, S. Gottlöber, and B. Catinella, Astrophys. J. **700**, 1779 (2009).
[98] R. E. Smith and K. Markovic, Phys. Rev. D **84**, 063507 (2011).
[99] M. R. Lovell, V. Eke, C. S. Frenk, L. Gao, A. Jenkins, T. Theuns, J. Wang, S. D. M. White, A. Boyarsky, and O. Ruchayskiy, Mon. Not. R. Astron. Soc. **420**, 2318 (2012).
[100] A. Schneider, R. E. Smith, A. V. Macciò, and B. Moore, Mon. Not. R. Astron. Soc. **424**, 684 (2012).
[101] E. Polisensky and M. Ricotti, Mon. Not. R. Astron. Soc. **437**, 2922 (2014).
[102] M. R. Lovell, C. S. Frenk, V. R. Eke, A. Jenkins, L. Gao, and T. Theuns, Mon. Not. R. Astron. Soc. **439**, 300 (2014).
[103] R. Kennedy, C. Frenk, S. Cole, and A. Benson, Mon. Not. R. Astron. Soc. **442**, 2487 (2014).
[104] C. Destri, H. J. de Vega, and N. G. Sánchez, Phys. Rev. D **88**, 083512 (2013).
[105] R. E. Angulo, O. Hahn, and T. Abel, Mon. Not. R. Astron. Soc. **434**, 3337 (2013).
[106] A. J. Benson, A. Farahi, S. Cole, L. A. Moustakas, A. Jenkins, M. Lovell, R. Kennedy, J. Helly, and C. Frenk, Mon. Not. R. Astron. Soc. **428**, 1774 (2013).
[107] A. Kamada, N. Yoshida, K. Kohri, and T. Takahashi, J. Cosmol. Astropart. Phys. 03 (2013) 008.
[108] M. R. Lovell, S. Bose, A. Boyarsky, S. Cole, C. S. Frenk, V. Gonzalez-Perez, R. Kennedy, O. Ruchayskiy, and A. Smith, Mon. Not. R. Astron. Soc. **461**, 60 (2016).
[109] A. D. Ludlow, S. Bose, R. E. Angulo, L. Wang, W. A. Hellwing, J. F. Navarro, S. Cole, and C. S. Frenk, Mon. Not. R. Astron. Soc. **460**, 1214 (2016).
[110] L. Wang, V. Gonzalez-Perez, L. Xie, A. P. Cooper, C. S. Frenk, L. Gao, W. A. Hellwing, J. Helly, M. R. Lovell, and L. Jiang, Mon. Not. R. Astron. Soc. **468**, 4579 (2017).
[111] M. R. Lovell, V. Gonzalez-Perez, S. Bose, A. Boyarsky, S. Cole, C. S. Frenk, and O. Ruchayskiy, Mon. Not. R. Astron. Soc. **468**, 2836 (2017).
[112] T. Nakama, J. Chluba, and M. Kamionkowski, Phys. Rev. D **95**, 121302 (2017).

[113] P. Madau, A. Meiksin, and M. J. Rees, Astrophys. J. **475**, 429 (1997).
[114] S. Furlanetto, S. P. Oh, and F. Briggs, Phys. Rep. **433**, 181 (2006).
[115] J. R. Pritchard and A. Loeb, Rep. Prog. Phys. **75**, 086901 (2012).
[116] S. R. Furlanetto, in *Understanding the Epoch of Cosmic Reionization: Challenges and Progress*, edited by A. Mesinger (Springer International Publishing, Scuola Normale Superiore, Pisa PI, Italy, 2016), Vol. 423, pp. 247–280.
[117] C. M. Hirata, Mon. Not. R. Astron. Soc. **367**, 259 (2006).
[118] S. A. Wouthuysen, Astrophys. J. **57**, 31 (1952).
[119] G. B. Field, Proc. IRE **46**, 240 (1958).
[120] X.-L. Chen and J. Miralda-Escude, Astrophys. J. **602**, 1 (2004).
[121] A. Mesinger, S. Furlanetto, and R. Cen, Mon. Not. R. Astron. Soc. **411**, 955 (2011).
[122] R. Barkana and A. Loeb, Astrophys. J. **626**, 1 (2005).
[123] R. S. de Souza, A. Mesinger, A. Ferrara, Z. Haiman, R. Perna, and N. Yoshida, Mon. Not. R. Astron. Soc. **432**, 3218 (2013).
[124] Á. Moliné, M. A. Sánchez-Conde, S. Palomares-Ruiz, and F. Prada, Mon. Not. R. Astron. Soc. **466**, 4974 (2017).
[125] R. Barkana and A. Loeb, Phys. Rep. **349**, 125 (2001).
[126] A. E. Evrard, Astrophys. J. **363**, 349 (1990).
[127] A. Blanchard, D. Valls-Gabaud, and G. A. Mamon, Astron. Astrophys. **264**, 365 (1992).
[128] M. Tegmark, J. Silk, M. J. Rees, A. Blanchard, T. Abel, and F. Palla, Astrophys. J. **474**, 1 (1997).
[129] Z. Haiman, T. Abel, and M. J. Rees, Astrophys. J. **534**, 11 (2000).
[130] B. Ciardi, A. Ferrara, F. Governato, and A. Jenkins, Mon. Not. R. Astron. Soc. **314**, 611 (2000).
[131] J. H. Wise and T. Abel, Astrophys. J. **671**, 1559 (2007).
[132] J. H. Wise, V. G. Demchenko, M. T. Halicek, M. L. Norman, M. J. Turk, T. Abel, and B. D. Smith, Mon. Not. R. Astron. Soc. **442**, 2560 (2014).
[133] H. Xu, J. H. Wise, M. L. Norman, K. Ahn, and B. W. O'Shea, Astrophys. J. **833**, 84 (2016).
[134] X. Ma, P. F. Hopkins, S. Garrison-Kimmel, C.-A. Faucher-Giguère, E. Quataert, M. Boylan-Kolchin, C. C. Hayward, R. Feldmann, and D. Kereš, Mon. Not. R. Astron. Soc. **478**, 1694 (2018).
[135] J. Rosdahl, H. Katz, J. Blaizot, T. Kimm, L. Michel-Dansac, T. Garel, M. Haehnelt, P. Ocvirk, and R. Teyssier, Mon. Not. R. Astron. Soc. **479**, 994 (2018).
[136] N. Mashian, P. A. Oesch, and A. Loeb, Mon. Not. R. Astron. Soc. **455**, 2101 (2016).
[137] N. Leite, C. Evoli, M. D'Angelo, B. Ciardi, G. Sigl, and A. Ferrara, Mon. Not. R. Astron. Soc. **469**, 416 (2017).
[138] B. Greig and A. Mesinger, Mon. Not. R. Astron. Soc. **449**, 4246 (2015).
[139] S. Mineo, M. Gilfanov, and R. Sunyaev, Mon. Not. R. Astron. Soc. **426**, 1870 (2012).
[140] R. A. Monsalve, B. Greig, J. D. Bowman, A. Mesinger, A. E. E. Rogers, T. J. Mozdzen, N. S. Kern, and N. Mahesh, Astrophys. J. **863**, 11 (2018).
[141] S. Witte, P. Villanueva-Domingo, S. Gariazzo, O. Mena, and S. Palomares-Ruiz, Phys. Rev. D **97**, 103533 (2018).
[142] A. A. Kaurov, T. Venumadhav, L. Dai, and M. Zaldarriaga, Astrophys. J. **864**, L15 (2018).
[143] S. Y. Kim, A. H. G. Peter, and J. R. Hargis, Phys. Rev. Lett. **121**, 211302 (2018).
[144] W. H. Press and P. Schechter, Astrophys. J. **187**, 425 (1974).
[145] R. K. Sheth and G. Tormen, Mon. Not. R. Astron. Soc. **308**, 119 (1999).
[146] R. K. Sheth, H. J. Mo, and G. Tormen, Mon. Not. R. Astron. Soc. **323**, 1 (2001).
[147] R. K. Sheth and G. Tormen, Mon. Not. R. Astron. Soc. **329**, 61 (2002).
[148] J. R. Pritchard and S. R. Furlanetto, Mon. Not. R. Astron. Soc. **367**, 1057 (2006).

PHYSICAL REVIEW D **100,** 043540 (2019)

Constraining the primordial black hole abundance with 21-cm cosmology

Olga Mena, Sergio Palomares-Ruiz, Pablo Villanueva-Domingo, and Samuel J. Witte
Instituto de Física Corpuscular (IFIC), CSIC-Universitat de València, Apartado de Correos 22085 E-46071, Spain

(Received 26 June 2019; published 29 August 2019)

The discoveries of a number of binary black hole mergers by LIGO and VIRGO have reinvigorated the interest that primordial black holes (PBHs) of tens of solar masses could contribute non-negligibly to the dark matter energy density. Should even a small population of PBHs with masses $\gtrsim\mathcal{O}(M_\odot)$ exist, they could profoundly impact the properties of the intergalactic medium and provide insight into novel processes at work in the early Universe. We demonstrate here that observations of the 21-cm transition in neutral hydrogen during the epochs of reionization and cosmic dawn will likely provide one of the most stringent tests of solar mass PBHs. In the context of 21-cm cosmology, PBHs give rise to three distinct observable effects: (i) the modification to the primordial power spectrum (and thus also the halo mass function) induced by Poisson noise, (ii) a uniform heating and ionization of the intergalactic medium via x-rays produced during accretion, and (iii) a local modification to the temperature and density of the ambient medium surrounding isolated PBHs. Using a four-parameter astrophysical model, we show that experiments like SKA and HERA could potentially improve upon existing constraints derived using observations of the cosmic microwave background by more than 1 order of magnitude.

DOI: 10.1103/PhysRevD.100.043540

I. INTRODUCTION

The canonical cosmological model assumes that dark matter is composed of a cold gas of weakly interacting particles. Despite its simplicity, this minimal scenario provides an excellent fit to both cosmic microwave background (CMB) and large-scale structure measurements [1–4]. However, a precise understanding of the fundamental nature of dark matter is missing and remains at the forefront in the current list of unsolved problems in modern physics.

Although dark matter is usually interpreted in terms of a new elementary particle, other alternatives exist. Black holes (BHs) produced prior to big bang nucleosynthesis, i.e., primordial black holes (PBHs), represent such an alternative—remarkably, this solution is as old as particle dark matter [5]. In particular, this scenario has recently attracted much attention [6–12] in the context of the LIGO and VIRGO discoveries of several binary BH mergers [13–17].

The idea that PBHs could be formed by strong accretion during the radiation-dominated epoch was first introduced five decades ago [18]. It was later suggested that initial fluctuations in the early Universe could give rise to a large number of gravitationally collapsed objects with masses above the Planck mass [19], that however, would not grow substantially by accretion [20]. Very light PBHs would not survive until the present epoch, though the prediction that any BH should emit particles with a black body spectrum [21,22] implies that PBHs with masses below $10^{-18}\ M_\odot$ (with $M_\odot$ the Sun's mass) would have evaporated on cosmological timescales [21–23]. While the evaporation of such light PBHs would have interesting observational consequences [24–26], only heavier PBHs could constitute a non-negligible fraction of the dark matter content of the Universe [5] (see, e.g., Refs. [27–29] for recent reviews). Alternative mechanisms for the formation of PBHs have also been proposed, such as the collapse of domain walls [30–32] or cosmic strings [33–35], first-order phase transitions [36–43], or fragmentation of scalar condensates [44–46]. Today, the most studied mechanism of PBH formation is gravitational collapse [47–51] of the fluctuations predicted in inflationary scenarios [48,49,52–58].

Following the recent observations of BH mergers by the LIGO and VIRGO experiments [13–17], PBHs of several solar masses or heavier have been extensively examined and constrained by a number of different means (see, e.g., Refs. [7,25,28,29,59–66] for compilations of constraints, also at other mass scales): gravitational lensing [67–70], dynamical constraints [12,63,71–74], radio and x-rays measurements [75–78], and spectral and anisotropy distortions of the CMB [79–88]. If energy is injected into the intergalactic medium (IGM) via the accretion of matter onto PBHs, the ionization and thermal evolution of the Universe could be affected and thus, both the spectral shape [52,53,89,90] and the anisotropies of the CMB [60,60,81–86,91]. Namely, the work of Ref. [85] excludes PBH with masses $\gtrsim 2\ M_\odot$ as the sole component of dark matter, although uncertainties associated with the accretion make the determination of a robust upper limit difficult. Moreover, Poisson-noise fluctuations could become too

large to be consistent with the power spectrum on scales of the Lyman-α forest, setting an upper limit on PBH masses near a few times $10^4\ M_\odot$ [92], which has been recently improved to $M_{\rm PBH} \lesssim 60\ M_\odot$ [93].

The presence of PBHs could also change the process known as reionization, during which the first sources in the Universe emitted ultraviolet photons that ionized the neutral hydrogen. Collectively, observations from the CMB observations, Lyman-α emission in star-forming galaxies, and of the Gunn-Peterson optical depth from bright quasars indicate that the Universe should be fully ionized by $z \sim 6$. Nevertheless, only observations of the CMB are currently sensitive to the early part of reionization and to the epoch during which the first stars formed (referred to as the cosmic dawn). The CMB, however, is only sensitive to a cumulative line-of-sight effect (observed via modifications to the integrated optical depth), and thus cannot provide detailed information about the state of the IGM during these epochs. The only proposed method for understanding the nature of the Universe on these timescales is 21-cm cosmology, which attempts to observe the hyperfine transition between the singlet and triplet levels of neutral hydrogen. To date, only one experiment working has claimed a putative signal; using a single dish radio telescope, the EDGES (Experiment to Detect the Reionization Step) Collaboration [94] claimed detection of a large absorption dip in the globally averaged signal, appearing around $z \sim 17$, but whose amplitude cannot be explained within the standard ΛCDM scenario. Determining the validity of this signal, however, is notoriously challenging, as foregrounds at these frequencies are expected to be at least $\sim 10^4$ times larger than the signal of interest. Thus, the 21-cm contribution can only be discriminated by systematically removing spectrally smooth foreground components from the observation. Next-generation radio interferometers such as HERA (Hydrogen Epoch of Reionization Array) [95] and SKA (Square Kilometer Array) [96] will also attempt to observe these epochs. A major advantage of using an interferometer in these observations is that one also has direct information on the scales over which foregrounds emanate, allowing for a more robust removal of foregrounds and providing additional spatial information on the 21-cm signal.

The field of 21-cm cosmology should be considered particularly important for those in the field of particle physics, as the wealth of available information might allow physicists to probe any new process which, e.g., modifies structure formation, the energy in the IGM, star formation and evolution, and photon propagation. Studies have been performed in the context of various dark matter candidates, for example, illustrating unprecedented sensitivity to a wide array of dark matter candidates [97–117]. Existing works looking into the effects of PBHs in 21-cm cosmology have independently focused on understanding the effects arising from PBH accretion on the globally averaged signal [118], Poisson-noise on the power spectrum [119,120], and local modifications to the medium around PBHs on the globally averaged signal and the angular power spectrum [121,122]. In this work, we compare and contrast these three effects in the context of $\gtrsim \mathcal{O}(M_\odot)$ PBHs, illustrating that the only process relevant for $M_{\rm PBH} \lesssim 10^3\ M_\odot$ is the heating and ionization of the IGM arising from x-rays produced during accretion. Using the 21-cm power spectrum, which offers a far more robust and powerful probe the globally averaged signature, we illustrate the near-future sensitivity of both HERA and SKA.

The structure of the paper is as follows. In Sec. II, we review the basics of 21-cm cosmology, in particular focusing on the computation of the 21-cm brightness temperature and power spectrum. In Sec. III, we discuss the impact that PBHs have on the observable 21-cm signal; in particular we study global heating and ionization as a consequence of accretion around PBHs (Sec. III A), and how the process of accretion heats and ionizes the local medium surrounding the PBH (Sec. III B), and we also address how Poisson-noise induced in the power spectrum by the discrete nature of PBHs modifies the signal arising in minihalos (Sec. III C). We comment on the sensitivity analysis in Sec. IV, and then present the results and conclude in Sec. V.

II. 21-CM COSMOLOGY

Below, we present a brief overview of the fundamentals of 21-cm cosmology. A more extensive overview can be found, e.g., in Refs. [123–126].

The intensity of the redshifted 21-cm line provides direct information about the fraction of neutral hydrogen residing in excited and ground states. This is conventionally characterized by the so-called spin temperature T_S and is formally defined as

$$\frac{n_1}{n_0} = 3e^{-T_0/T_S}, \tag{2.1}$$

where n_0 and n_1 are the number density of neutral hydrogen atoms in the ground (singlet) and excited (triplet) states, $k_B T_0 = h\nu_0$ is the energy of the 21-cm photon, and the factor of 3 comes from the degeneracy of the triplet excited state. The spin temperature of the 21-cm line is controlled by three processes: (i) absorption of and stimulated emission induced by a background radiation field, (ii) collisions of neutral hydrogen with hydrogen atoms, free protons, or free electrons, and (iii) indirect excitations/de-excitations induced by scattering with ambient Lyman-α photons. Consequently, the spin temperature can be expressed directly in terms of temperatures characterizing the efficiency of each of these processes,

$$T_S = \frac{T_{\rm R} + y_k T_k + y_\alpha T_\alpha}{1 + y_k + y_\alpha}, \tag{2.2}$$

where T_R, T_k, and T_α are the temperature of the background radiation, kinetic temperature of the gas, and the temperature associated with the intensity of the Lyman-α emission (for all environments of interest, it is sufficient to take $T_\alpha \simeq T_k$), and y_k and y_α are their respective couplings.

The collisional coupling, y_k, is given by

$$y_k = \frac{T_0}{A_{10}T_k} n_H (x_H C_{HH} + (1-x_H)C_{eH} + (1-x_H)C_{pH}), \tag{2.3}$$

where $A_{10} = 2.85 \times 10^{-15}$ s^{-1} is the Einstein coefficient of spontaneous emission rate, n_H is the hydrogen comoving number density, x_H is the neutral fraction of hydrogen, and C_{HH}, C_{eH}, and C_{pH} are the de-excitation rates due to collisions between a hydrogen atom and another hydrogen atom, an electron, or a proton, respectively. These quantities are computed using the fitting formulas of Ref. [127].

The Lyman-α coupling, y_α, can be written in terms of the Lyman-α flux J_α,

$$y_\alpha = \frac{16\pi^2 e^2 f_{12}}{27 m_e c A_{10}} \frac{T_0}{T_k} J_\alpha, \tag{2.4}$$

where e and m_e are the charge and mass of the electron, and $f_{12} = 0.416$ is the oscillator strength of the Lyman-α transition.

Rather than working directly with observed intensity, it is conventional for radio astronomers to use the effective brightness temperature, $T_b(\nu)$, which is proportional to the specific intensity (or spectral radiance) of a black body in the Rayleigh-Jeans limit, $\nu \ll T_b(\nu)$. The change in intensity relative to the background radiation field is thus given by the differential brightness temperature,

$$\delta T_b(\nu) = \frac{T_S - T_R}{1+z}(1 - e^{-\tau_{\nu_0}}), \tag{2.5}$$

where τ_{ν_0} is the optical depth of the 21-cm line. Throughout this work, we will implicitly assume the background radiation field to simply be the CMB, $T_R = T_{CMB}$. We note, however, that in the light of the abnormally deep absorption trough observed by EDGES [94], several scenarios predicting an unexpected excess of radio background have been explored [106,128–135] (see, however, Ref. [136]).

III. THE EFFECTS OF PRIMORDIAL BLACK HOLES

The existence of a population of $M_{PBH} \gtrsim M_\odot$ PBHs has the potential to modify the 21-cm signal in a number of different ways. In order to understand exactly how and where these effects would arise, let us consider for the moment a single isolated PBH. Matter surrounding the PBH is accreted at some rate $\dot{M}_{PBH}$. The in-falling matter heats and ionizes in a localized region surrounding the PBH. Some of the energy gained via accretion is radiated by the newly formed plasma, primarily in the form x-rays produced by thermal synchrotron and bremsstrahlung emission, and modified by comptonization. Additionally, energy resulting from the in-fall of matter can be viscously dissipated, directly heating the accreting matter rather than radiating x-rays. This type of energy dissipation is at the heart of the so-called advection-dominated accretion flow (ADAF) (see, e.g., Ref. [137] for a review). It has recently been argued [85] that accretion onto $\sim\mathcal{O}(M_\odot)$ PBHs at high redshifts is likely to proceed via a thick inflated disk, best described within the ADAF framework—we will thus follow Ref. [85] in adopting this formalism. Typically, ADAF accreting models radiate extremely inefficiently (i.e., only a small fraction of the accreted energy is radiated and escapes into the IGM), while the remainder is dissipated locally in the form of heat through viscous interactions of the plasma. The relative efficiency with which x-rays are emitted in the IGM can be characterized by a parameter ϵ ($\epsilon \to 1$ being the limit that the accretion medium radiates perfectly, and $\epsilon \to 0$ being the limit in which most of the accreted energy goes into local heating via advection), which depends intimately on the geometry and strength of accretion. X-rays that escape into the medium have a large mean free path and would deposit their energy approximately uniformly on all scales, affecting both the temperature and ionization fraction of the IGM. On the other hand, the remainder of the energy is deposited locally (and is eventually swallowed by the PBH), modifying the temperature and ionization profile of the medium directly surrounding the PBH. Thus, accretion onto a single BH modifies the state of the IGM both globally (Sec. III A) and locally (Sec. III B), effects which for the sake of simplicity we treat separately in what follows.

In addition to the effects arising from accretion, the presence of a large population of PBHs can modify structure formation. The discrete nature of massive PBHs implies that shot noise fluctuations in the PBH number density are not necessarily negligible. These fluctuations manifest as isocurvature perturbations in the linear matter power spectrum, leading to an enhancement in structure at small scales [92]. For viable populations of PBHs (i.e., those evading current constraints), the effect is only expected to be pronounced for halos below the star-forming limit—these halos are typically referred to as minihalos. Within the context of ΛCDM, minihalos contribute minimally to the 21-cm signal [138] (the signal is expected to be at the level of $\mathcal{O}(1)$ mK in ΛCDM). However, it has been argued that the enhancement in the number density of these halos by a population of PBHs can make their contribution observable [119,120]. We address this claim in Sec. III C and show that the contribution of minihalos is typically suppressed when the global effects of accretion are self-consistently included in the calculation.

A. Global heating and ionization

Here we address the global impact of accretion by PBHs on the IGM, i.e., the effect that arises from radiation that escapes the local vicinity of PBHs and deposits its energy approximately uniformly in the IGM. In what follows we consider the simplifying assumption of a monochromatic mass function for PBHs, broadly used in the literature. Note, however, that this is not necessarily a realistic assumption, since many mechanisms of PBH formation in the early Universe would generically lead to extended mass distributions, which could bias the obtained constraints [28,63,64,66].

The rate of energy injected into the medium per unit volume is given by [82,85]

$$\left(\frac{dE}{dVdt}\right)_{\rm inj} = L_{\rm acc} n_{\rm PBH} = L_{\rm acc} \frac{f_{\rm PBH}\rho_{\rm DM}}{M_{\rm PBH}}, \quad (3.1)$$

where $L_{\rm acc}$ is the luminosity of radiation emitted from matter accreting onto a PBH of mass $M_{\rm PBH}$, $n_{\rm PBH}$ is the number density of PBHs of mass $M_{\rm PBH}$, $\rho_{\rm DM}$ is the density of dark matter, and $f_{\rm PBH}$ is the fraction of dark matter that comprises PBHs of mass $M_{\rm PBH}$. The accretion luminosity can be expressed in terms of the product of the accretion rate $\dot{M}_{\rm PBH}$ and the radiative efficiency ϵ,

$$L_{\rm acc} = \epsilon \dot{M}_{\rm PBH}. \quad (3.2)$$

In general, both the accretion rate and the radiative efficiency are complicated unknown functions of both the PBH properties and the evolution of the medium. However, various approximations have been developed that can be used to estimate each of these functions.

We begin by addressing the radiative efficiency factor ϵ in Eq. (3.2), which describes the fraction of energy radiated away into the IGM. In principle, it depends on the accretion rate, accretion geometry, and the properties of the medium. Here, we assume that the radiative cooling is inefficient and the dynamics of the accreting gas are controlled by advective currents (ADAF) [137,139–145]. It is worth noting that if the radiative cooling is efficient and forms a thin accretion disk (rather than the thick disk or tori that may appear in the ADAF scenario), the radiative efficiency could be orders of magnitude larger [146]. For the efficiency function, we adopt the fitting formula obtained in Ref. [145],

$$\epsilon = \epsilon_0 \left(\frac{100\dot{M}_{\rm PBH}}{\dot{M}_{\rm Edd}}\right)^a, \quad (3.3)$$

where $\dot{M}_{\rm Edd} = 10 L_{\rm Edd} = 10 \times 4\pi G M_{\rm PBH} m_p/\sigma_{\rm T} \simeq 1.28 \times 10^{39} (M_{\rm PBH}/M_\odot)$ ergs/s is the Eddington rate (and $L_{\rm Edd}$ is the Eddington luminosity), and the functional form and coefficients are indicated in Table I, assuming the viscous parameter to be $\alpha = 0.1$ and the parameter which dictates the fraction of dissipation that heats the electrons directly to be $\delta = 0.1$. Larger (smaller) values of δ are expected to increase (decrease) the radiative efficiency by a factor of a few in the most extreme scenarios.

TABLE I. Fit coefficients characterizing the radiative efficiency of ADAF accretion, described by Eq. (3.3), in terms of the net accretion rate. From Ref. [145], for $\delta = 0.1$ and for the viscous parameter $\alpha = 0.1$.

$\dot{M}_{\rm PBH}/\dot{M}_{\rm Edd}$	ϵ_0	a
$\lesssim 9.4 \times 10^{-5}$	0.12	0.59
9.4×10^{-5}–5×10^{-3}	0.026	0.27
5×10^{-3}–6.6×10^{-3}	0.50	4.53

We now shift our attention to the accretion rate. Accretion onto a point mass moving through some homogeneous medium was first studied by Hoyle and Lyttleton in the first half of the 20th century [147–150]. Nevertheless, this early treatment only considered the gravitational effects (neglecting, for example, the thermodynamic pressure), and was thus only useful as a first-step approximation within a particular limiting regime (far away from the point source and with a reasonably large relative velocity). Bondi and Hoyle were later able to correct for the previously neglected effect of pressure and calculated an exact solution to the problem of spherical accretion onto a stationary point mass in a homogenous medium [151],

$$\dot{M}_{\rm Bondi-Hoyle} = 4\pi\lambda\rho_\infty \frac{(GM_{\rm PBH})^2}{c_{s,\infty}^3}, \quad (3.4)$$

where ρ_∞ and $c_{s,\infty}$ are the density and speed of sound far away from the point source, G is the gravitational constant, and λ is an $\mathcal{O}(1)$ parameter quantifying nongravitational effects [151], which also allows to treat nonspherical accretion. Given that simulations suggest that radiative outflows reduce the amount of matter that ultimately accretes in the inner region, potentially reducing the observed luminosity by a factor of $\mathcal{O}(100)$ [145], we account for this by taking λ to be 0.01.

In order to address the problem of accretion onto a BH moving with respect to the ambient medium with relative velocity $v_{\rm rel}$, Bondi suggested the substitution of $c_{s,\infty}$ by an effective velocity $\sqrt{c_{s,\infty}^2 + v_{\rm rel}^2}$ [152]. The relative velocity between PBHs and the ambient medium can be described by the relative velocity between dark matter and baryons. Unfortunately, deriving the relative dark matter-baryon velocity at scales relevant for accretion is nontrivial [153,154]. On linear scales, the velocity field is Gaussian and thus, the modulus of the three-velocity field follows a Maxwellian distribution, with the square root of the variance approximated as [82]

$$\sqrt{\langle v_L^2 \rangle} \simeq \min\left[1, \frac{1+z}{1000}\right] \times 30 \text{ km/s}. \tag{3.5}$$

The accretion luminosity is the result of averaging over the distribution of the relative velocities of PBHs with respect to the ambient gas. The accretion rate is inversely proportional to $(c_{s,\infty}^2 + v_{\rm rel}^2)^{3/2}$ (after the substitution above) [60,82] and, for the usual (simplified) case considered in the literature, the individual PBH accretion luminosity is proportional to the square of the accretion rate (i.e., $L_{\rm acc} \propto \dot{M}_{\rm PBH}^2$). It is important to emphasize that this applies only to scenarios in which $\epsilon \propto \dot{M}_{\rm PBH}$. Generalizing the accretion rate to scenarios in which the radiative efficiency has an arbitrary power law dependence (i.e., $\epsilon \propto \dot{M}_{\rm PBH}^a$) is obtained by expressing the effective velocity as

$$\begin{aligned} v_{\rm eff} &\equiv \left\langle \frac{1}{(c_{s,\infty}^2 + v_{\rm rel}^2)^{3(1+a)/2}} \right\rangle^{-\frac{1}{3(1+a)}} \\ &= c_{s,\infty}\left[\left(\frac{3}{2}\right)^{\frac{3}{2}} U\left(\frac{3}{2}, 1-\frac{3a}{2}, \frac{3}{2}\mathcal{M}^{-2}\right)\mathcal{M}^{-3}\right]^{-\frac{1}{3(1+a)}}, \end{aligned} \tag{3.6}$$

with $\mathcal{M} \equiv \frac{\sqrt{\langle v_L^2 \rangle}}{c_{s,\infty}}$ and $U(x;y;z)$ the confluent hypergeometric function of second kind, or Tricomi's function. Up to first order, the two limiting cases are

$$v_{\rm eff} \simeq \begin{cases} c_{s,\infty}\mathcal{M}^{1/(1+a)}\left[3\sqrt{\frac{3}{2\pi}}B\left(\frac{3a}{2}, \frac{3}{2}\right)\right]^{-\frac{1}{3(1+a)}}, & \mathcal{M} \gg 1 \\ c_{s,\infty}, & \mathcal{M} \ll 1, \end{cases} \tag{3.7}$$

with $B(x,y)$ the beta function. Notice that this expression reproduces the limiting case in which $a = 1$ found in Refs. [60,82].

Therefore, using the effective velocity rather than the speed of sound, the accretion rate can be written as

$$\dot{M}_{\rm PBH} = 4\pi\lambda\rho_\infty \frac{(GM_{\rm PBH})^2}{v_{\rm eff}^3}. \tag{3.8}$$

Even if more accurate expressions have been obtained [155], this modified accretion rate provides a reasonable description of the problem. It is worth noting that the Bondi accretion rate is strictly valid only for spherical accretion. It was recently argued, however, that accretion onto PBHs with $M_{\rm PBH} \gtrsim M_\odot$ likely results in the formation of an accretion disk [85]. Note that this statement ran contrary to previous assumptions that PBH accretion was spherical [60,82–84]. Given that there exists a relatively large amount of uncertainty in the dynamics of disk accretion, some of which serves to increase and some of which serves to decrease the relative accretion rate [155–157], Eq. (3.8) can likely be thought of as a reasonable ball-park estimate. Therefore, despite all these caveats regarding the potential legitimacy of Eqs. (3.6) and (3.8), though, we will follow previous works [82,85] in adopting the expression of $v_{\rm eff}$ for $a = 1$.

Finally, it is important to note that the quantity of interest is not the rate of energy injected into the medium, given in Eq. (3.1), but rather the rate of energy deposited into the medium. These two quantities are related by functions known as energy deposition factors,

$$\left(\frac{dE_c}{dVdt}\right)_{\rm dep} = f_c(z)\left(\frac{dE}{dVdt}\right)_{\rm inj} \equiv n_b \epsilon_c^{\rm PBH}, \tag{3.9}$$

where $\epsilon_c^{\rm PBH}$ represents the energy deposition rate per baryon, and the subscript c denotes the channel in which energy is deposited—i.e., ionization of hydrogen (HI) or helium (HeI), heating of the medium (heat), or excitations (Lyα). These energy deposition factors are computed by using the following expression:

$$f_c(z) = \frac{H(z)\int \frac{d\ln(1+z')}{H(z')}\int d\omega T_c(z,z',\omega) L_{\rm acc}(z',\omega)}{\int d\omega L_{\rm acc}(z,\omega)}, \tag{3.10}$$

where the $T_c(z,z',\omega)$ are the transfer functions taken from Ref. [158]. As is done in Ref. [85], the spectrum of the luminosity is taken from ADAF models of Ref. [137]; namely, we adopt a simple parametrization given by

$$L(\omega) \propto \Theta(\omega - \omega_{\rm min})\omega^\beta \exp(-\omega/\omega_s), \tag{3.11}$$

where $\omega_{\rm min} \equiv (10\ M_\odot/M_{\rm PBH})^{1/2}$ eV, $\omega_s \sim \mathcal{O}(m_e)$ (taken explicitly to be $\omega_s = 200$ keV), and $\beta = -1$ (with reasonable values of $\beta \in [-1.3, -0.7]$). In principle, the exact form of the spectrum changes with the accretion rate. However, the results found here are largely independent of these details.

Equations (3.2) and (3.11) provide the ingredients necessary to compute the energy injected into the IGM from a population of PBHs as a function of redshift, and Eq. (3.10) describes how and where the energy is deposited. With this in hand, we now turn to incorporating this energy injection into the equations governing the evolution of the ionization fraction, the gas temperature, and the Lyman-α flux.

The quantity $x_e(\mathbf{x}, z)$, governing the evolution of the local ionized fraction of the neutral IGM, is given by

$$\frac{dx_e}{dz} = \frac{dt}{dz}(\Lambda_{\rm ion} - \alpha_{\rm A} C x_e^2 n_b \mathfrak{f}_{\rm H}), \tag{3.12}$$

where $n_b = \bar{n}_{b,0}(1+z)^3(1+\delta_b(\mathbf{x}, z))$ is the baryon number density, $\Lambda_{\rm ion}$ is the ionization rate, $\alpha_{\rm A}$ is the case-A

recombination coefficient, $\mathfrak{f}_H = n_H/n_b$ is the hydrogen number fraction, and $C \equiv \langle n_e^2\rangle/\langle n_e\rangle^2$ is the clumping factor (set to one as default), with n_e the electron number density. Ionization from the PBH accretion mechanism would lead to an additional contribution of the form

$$\Lambda_{\rm ion}^{\rm PBH} = \mathfrak{f}_H \frac{\epsilon_{\rm HI}^{\rm PBH}}{E_{\rm HI}} + \mathfrak{f}_{\rm He} \frac{\epsilon_{\rm HeI}^{\rm PBH}}{E_{\rm HeI}}, \tag{3.13}$$

where $\mathfrak{f}_H = n_H/n_b$ and $\mathfrak{f}_{\rm He} = n_{\rm He}/n_b$ are the hydrogen and helium number fractions, and $E_{\rm HI,HeI}$ are the ionization energies for hydrogen and helium. Here, we neglect the effect of secondary ionizations.[1] The evolution of the kinetic temperature of the gas T_k is computed via

$$\frac{dT_k}{dz} = \frac{2T_k}{3n_b}\frac{dn_b}{dz} - \frac{T_k}{1+x_e}\frac{dx_e}{dz} + \frac{2}{3k_B(1+x_e)}\frac{dt}{dz}\sum_j \epsilon_{{\rm heat},j}, \tag{3.14}$$

where the last term accounts for the heating/cooling processes, with $\epsilon_{{\rm heat},j}$ the heating rate per baryon for the process j (Compton cooling, x-ray heating, and PBH heating).

Finally, there is also a contribution to the Lyman-α flux resulting from collisional excitations due to energy deposition by PBH accretion in the IGM, which can be written as

$$J_{\alpha,{\rm PBH}} = \frac{cn_b}{4\pi}\frac{\epsilon_{{\rm Ly}\alpha}^{\rm PBH}}{h\nu_\alpha}\frac{1}{H(z)\nu_\alpha}, \tag{3.15}$$

where ν_α is the emission frequency of a Lyman-α photon.

The aforementioned modifications to the free electron fraction, temperature of the gas, and Lyman-α flux are incorporated by modifying the publicly available codes COSMOREC/RECFAST++ [159–161], relevant at high redshifts when astrophysical mechanisms can be neglected, and 21CMFAST [162], relevant at low redshifts when astrophysical mechanisms, such as ionization and heating from stars and x-ray binaries, are relevant. Figures 1 and 2 show the redshift evolution of the free electron fraction and the kinetic gas temperature for a population of PBHs with mass $M_{\rm PBH} = 100\ M_\odot$ and different relative abundances $f_{\rm PBH}$.[2] Notice that the effect of PBHs accretion on the free electron fraction in Fig. 1 is clearly visible: the presence of the extra heating and ionization terms from PBHs accretion changes the redshift evolution of x_e, increasing this quantity from the early recombination era, below $z \sim 1000$, until the late reionization era. The kinetic gas temperature would also be increased by the presence of the energy injection in the IGM (see Fig. 2). Similar to the case in which there is energy injection from dark matter annihilations [99,101], PBH accretion leads to an earlier and more uniform heating of the IGM, which is larger for an increasing fraction of dark matter in the form of PBHs, until stellar sources turn on and start to ionize the

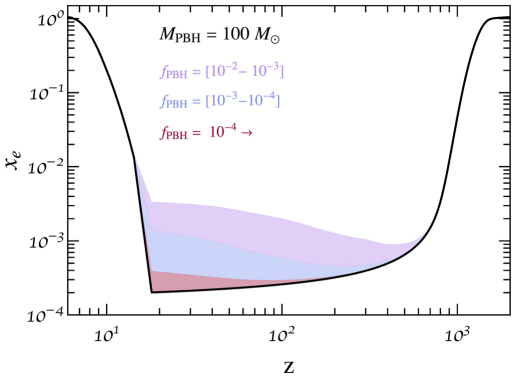

FIG. 1. Free electron fraction, x_e, as a function of redshift, including the contribution of a monochromatic PBH population with mass $M_{\rm PBH} = 100\ M_\odot$, for different PBH dark matter fractions $f_{\rm PBH} = (10^{-2}, 10^{-3}, 10^{-4}, \lesssim 10^{-4})$. The standard scenario with $f_{\rm PBH} = 0$ is denoted by the solid black line. We use fiducial astrophysical parameters: $(\zeta_{\rm UV}, \zeta_{\rm X}, T_{\rm min}, N_\alpha) = (50, 2\times 10^{56}\ M_\odot^{-1}, 5\times 10^4\ {\rm K}, 4000)$; see Sec IV A.

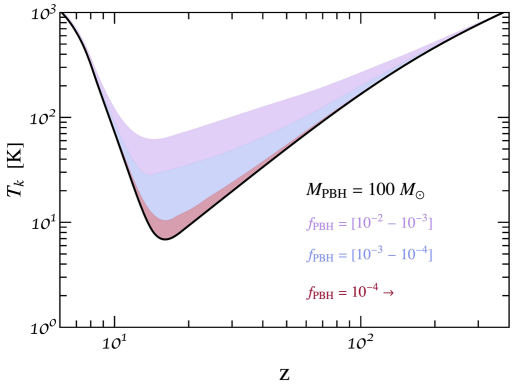

FIG. 2. Kinetic temperature of the gas, T_k, as a function of redshift, including the contribution of a monochromatic PBH population with mass $M_{\rm PBH} = 100\ M_\odot$, for different PBH dark matter fractions $f_{\rm PBH} = (10^{-2}, 10^{-3}, 10^{-4}, \lesssim 10^{-4})$. The standard scenario with $f_{\rm PBH} = 0$ is denoted by the solid black line. We use fiducial astrophysical parameters: $(\zeta_{\rm UV}, \zeta_{\rm X}, T_{\rm min}, N_\alpha) = (50, 2\times 10^{56}\ M_\odot^{-1}, 5\times 10^4\ {\rm K}, 4000)$; see Sec. IV A.

[1]Since the differential brightness temperature is proportional to the neutral hydrogen fraction, rather than the free electron fraction, the effect of ionizations from PBH accretion is expected to be significantly subdominant to that of heating. Thus, neglecting secondary ionizations is a safe assumption.

[2]This range of values is simply intended to illustrate the dependence of these observables on $f_{\rm PBH}$. Note that the cases with the largest abundances are in tension with CMB constraints [85].

medium (around $z \sim 15$ in Fig. 1).[3] These results illustrate that even small abundances of PBHs could have dramatic effects on the properties of the IGM.

Before continuing, we would like to emphasize that the treatment of accretion adopted in this work is rather conservative. For the redshifts relevant for 21-cm cosmology, the conditions necessary for the formation of accretion disks around PBHs seem likely. Within the context of disk accreting models, ADAF accretion is among the lowest in the radiative efficiency of x-rays. Adopting a larger radiative luminosity or accretion rate would correspondingly enhance the observable signatures associated with global heating and ionization of the IGM.

1. Global 21-cm line signal

Since the optical depth at the frequencies of interest is small, one can expand the exponential term in Eq. (2.5) and express the global differential brightness temperature as

$$\delta T_b(\nu) \simeq 27 x_{\rm H}(1+\delta_b)\left(1-\frac{T_{\rm CMB}}{T_S}\right)\left(\frac{1}{1+H^{-1}\partial v_r/\partial r}\right) \times \left(\frac{1+z}{10}\right)^{1/2}\left(\frac{0.15}{\Omega_{\rm m}h^2}\right)^{1/2}\left(\frac{\Omega_{\rm b}h^2}{0.023}\right) \text{ mK}, \quad (3.16)$$

where δ_b is the baryonic overdensity, H is the Hubble parameter, $\partial v_r/\partial r$ is the peculiar velocity gradient along the line of sight, which introduces redshift space distortions, and $\Omega_{\rm m}$ and $\Omega_{\rm b}$ are the matter and baryon abundances of the Universe. A number of current and future experiments is devoted to detect the 21-cm global signal averaged over all directions in the sky. Examples are EDGES and the future LEDA (Large Aperture Experiment to Detect the Dark Ages) [163] and DARE (Moon space observatory Dark Ages Radio Experiment) [164]. The observation of an absorption profile located at a redshift of $z \sim 17$ has been recently claimed by the EDGES experiment, with an amplitude which is twice the maximum predicted within the context of the ΛCDM model [94]. This has motivated a larger number of studies in the literature [102–106, 110–112,115,117,118,128–135,165–178].

To compute the redshift evolution of the 21-cm global signal, we use the publicly available code 21CMFAST [162]. Nevertheless, the code only evolves the IGM for redshifts $z \lesssim 35$. Thus, initial conditions for the mean ionization fraction x_e and for the gas temperature T_k are required inputs. We produce these inputs using a modified version of COSMOREC/RECFAST++ [159–161].[4] The cumulative effect of a population of 100 $M_\odot$ PBHs on the global differential

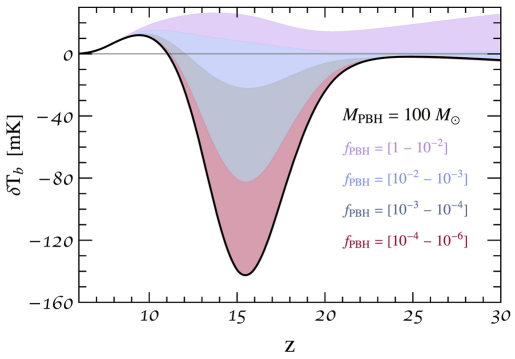

FIG. 3. Global 21-cm differential brightness temperature for various values of $f_{\rm PBH}$, assuming $M_{\rm PBH} = 100\ M_\odot$ and different ranges for the PBH dark matter fraction. The standard scenario with $f_{\rm PBH} = 0$ is denoted by the solid black lines. We use fiducial astrophysical parameters: $(\zeta_{\rm UV}, \zeta_{\rm X}, T_{\rm min}, N_\alpha) = (50, 2 \times 10^{56}\ M_\odot^{-1}, 5 \times 10^4\ {\rm K}, 4000)$; see Section IV A.

21-cm brightness temperature is shown in Fig. 3 for various PBH abundances. As discussed above, accretion onto PBHs significant increases both the free electron fraction and the temperature of the IGM (as shown in Figs. 1 and 2). Consequently, the effect of PBHs on the 21-cm global differential brightness temperature can be summarized as a suppression of the absorption trough before x-ray heating dominates the signal. Notice the difference with the standard scenario, $f_{\rm PBH} = 0$, depicted by the solid black lines in Fig. 3.

It is also possible to measure the power spectrum of the differential brightness temperature, i.e., to extract the fluctuations in the all-sky averaged differential brightness temperature. This method could in principle provide a cleaner foreground removal. Indeed, this is the major goal of experiments such as GMRT (Giant Metrewave Radio Telescope), LOFAR (LOw Frequency ARray), MWA (Murchison Widefield Array), and PAPER (Precision Array for Probing the Epoch of Reionization), which have improved the upper limits at $z = 8.4$ [179]. As previously stated, future high-redshift 21-cm experiments include SKA and HERA.[5] The dimensionless 21-cm power spectrum is given by

$$\langle \tilde{\delta}_{21}(\mathbf{k}, z)\tilde{\delta}^*_{21}(\mathbf{k}', z)\rangle \equiv (2\pi)^3 \delta^D(\mathbf{k}-\mathbf{k}')P_{21}(k, z), \quad (3.17)$$

[3]Note that although the spatial and redshift PBH distribution follows that of matter, it is different from the distribution of x-ray sources, i.e., star-forming halos beyond a threshold for atomic cooling.

[4]Notice that these initial values are different from the ones in the default tables, as the presence of PBHs would change significantly the recombination process and its outputs.

[5]The 21-cm line will also be observed at lower redshifts, predominately in the postreionization era ($z \lesssim 3$), via the so-called intensity mapping technique, which will attempt to shed light on the spatial distribution emanating from dense clumps of neutral hydrogen [180–183]. This is the target of the GBT-HIM project [184], CHIME (Canadian Hydrogen Intensity Mapping Experiment) [185], the TIANLAI project [186], and SKA-MID frequency (see, e.g., Ref. [187]).

where δ^D is the Dirac delta function, the brackets indicate average quantities, and $\tilde{\delta}_{21}(\mathbf{k}, z)$ is the Fourier transform of $\delta_{21}(\mathbf{x}, z) = \delta T_b(\mathbf{x}, z)/\overline{\delta T_b}(z) - 1$. In what follows, we shall work with the 21-cm differential brightness temperature power spectrum, $\Delta^2_{21}(k, z) = (k^3/2\pi^2)P_{21}(k, z)$, and show results for $\overline{\delta T_b}^2(z)\Delta^2_{21}(k, z)$ in Sec. IV A.

B. Local heating and ionization

As mentioned in the previous section, within the ADAF framework only a small fraction of the energy gained via accretion is radiated into the medium. In this section, we attempt to model the contribution to the 21-cm line from the local environment of the PBH, estimating the radial profiles.

1. Radial profiles

The difficulty in estimating the true contribution to the 21-cm signal from the local medium surrounding PBHs arises from the fact that solving for the radial density, ρ, velocity, v, temperature, T, and ionization profiles, x_e, of the accreting medium is nontrivial and can only be solved analytically in very specific scenarios and certain regions of the parameter space (for an analytic solution at small radii within the ADAF framework, see, e.g., Ref. [188]). As will be shown below, the dominant contribution to the 21-cm signal comes from radii near the Bondi radius (the Bondi radius, to be defined, approximately demarcates where the solutions asymptote to the IGM value). This motivates one to study the simple solution to the problem of static spherically symmetric accretion around a point, in which we neglect heating from the radiated emission (likely a valid approximation for the ADAF framework since the efficiency is small) and viscosity (an assumption which certainly breaks down near the BH, but which plays a less significant role as one approaches the IGM).

In this static spherically symmetric case, the fluid equations for determining the radial profiles are given by

$$4\pi r^2 \rho |v| = \dot{M}_{\rm PBH} = \text{constant}, \tag{3.18}$$

$$v\frac{dv}{dr} = -\frac{1}{\rho}\frac{dP}{dr} - \frac{GM_{\rm PBH}}{r^2}, \tag{3.19}$$

$$\Lambda_{\rm ion}(1 - x_e) = \alpha_{\rm B} n_{\rm H} x_e^2, \tag{3.20}$$

where $\alpha_{\rm B}$ is the case-B recombination coefficient, $P = \rho(1 + x_e)T/m_p$ is the pressure, and m_p is the mass of the proton (we neglect the helium contribution in this computation for the sake of simplicity). The first of these equations arises from integrating the continuity equation, the second one is the Euler equation (accounting for momentum conservation), and the final one determines the balance between ionization and recombination. As in Sec. III A, we adopt the Bondi-Hoyle accretion rate given in Eq. (3.8). The relevant scales are the Bondi velocity, defined as in Eq. (3.6), and the Bondi radius

$$r_{\rm B} = \frac{GM_{\rm PBH}}{v_{\rm eff}^2}. \tag{3.21}$$

Note that these definitions differ from those originally defined by Bondi, a consequence of the fact that we have modified the accretion rate via the substitution $c_s \to v_{\rm eff}$, as discussed above. For reference, a value of $v_{\rm eff} \sim c_s$ and $T_k \sim T_{\rm ad} \propto (1 + z)^2$ lead to a Bondi radius of $r_{\rm B} \sim 3 \times 10^{-5}(M_{\rm PBH}/M_\odot)(30/(1 + z))^2$ kpc. For distances greater than the Bondi radius, the effects of accretion are negligible, asymptoting to their background values.

As mentioned in Sec. III A, the accretion of matter onto the central BH leads to a highly energetic radiation flux which is capable of ionizing the surrounding medium. In order to solve Eq. (3.20), it is necessary to identify the flux of ionizing photons as a function of the radial distance to the BH. Here, we assume that most of the radiation is produced at very small radii (where the surrounding medium can reach temperatures in excess of 10^9 K), and thus, one can write the flux in terms of the comoving distance coordinate r from the source by using a point source approximation

$$F(E, r, z) = \frac{L_{\rm acc}(E, z)}{4\pi r^2} e^{-\tau_{\rm ion}(E,r,z)}, \tag{3.22}$$

where $L_{\rm acc}(E, z)$ is the accretion luminosity given by combining Eqs. (3.2) and (3.11). The ionization optical depth $\tau_{\rm ion}$ is given by

$$\tau_{\rm ion}(E, r, z) = \int_0^r n_{\rm H}(z)\sigma(E)x_{\rm HI}(r, z), \tag{3.23}$$

where the ionization cross section $\sigma(E)$ is taken to be the fitting function obtained in Ref. [189]. For most of the radii of interest, the optical depth is found to be negligible. The local ionization rate is given by

$$\Lambda_{\rm ion} = \int_{E_0}^{\infty} \frac{dE}{E}\sigma(E)F(E, r, z)\left[1 + \frac{E - E_{\rm th}}{E_{\rm th}} f_{\rm ion}(E, x_e)\right], \tag{3.24}$$

where $E_{\rm th}$ is the ground level energy of the hydrogen. We parametrize the energy deposition function $f_{\rm ion}$[6] using different fitting formulas for $E \leq 0.5$ keV [190] and $E > 0.5$ keV [191].

[6]Note that this is conceptually the same as parameter defined in Eq. (3.10). However, in the case of local ionization, it is appropriate to apply the on-the-spot approximation, and thus the functional forms and dependencies of these parameters are different.

Since, at the scales of interest, we can safely neglect heating/cooling effects, we get the usual adiabatic relation between the temperature and the density $T \propto \rho^{2/3}$. The set of Eqs. (3.18)–(3.20) can be easily solved numerically given the boundary conditions ρ_∞ and T_∞, which we take as the IGM values, that depend on both $M_{\rm PBH}$ and $f_{\rm PBH}$, and are calculated using the formalism presented in the previous section (Sec. III A).

Is is important to bear in mind that after obtaining the temperature and density profiles, one must resolve the radiative transfer equation radially in order to obtain the differential brightness temperature. For these small enough length scales, the time evolution and expansion of the Universe can be neglected, leading to the following kinetic equation in terms of the brightness temperature at a frequency ν, $T_{b,\nu}$,

$$\frac{dT_{b,\nu}(r)}{dr} = -\kappa_\nu(r)[T_{b,\nu}(r) - T_S(r)], \tag{3.25}$$

with κ_ν being the absorption coefficient

$$\begin{aligned}\kappa_\nu(r) &= \frac{h\nu_0}{4\pi}\phi_\nu[B_{01}n_0(r) - B_{10}n_1(r)] \\ &\simeq \frac{3c^2A_{10}}{32\pi\nu_0^2}x_{\rm H}(r)n_{\rm H}\phi_\nu\frac{T_0}{T_S(r)},\end{aligned} \tag{3.26}$$

where B_{01}, B_{10}, and A_{10} are the Einstein coefficients between the triplet and singlet states, and ϕ_ν is the line profile, given by the Doppler broadening

$$\phi_\nu = \frac{1}{\sqrt{\pi}\Delta\nu_{\rm D}}e^{-(\nu-\nu_0)^2/\Delta\nu_{\rm D}^2}, \tag{3.27}$$

with $\Delta\nu_{\rm D} = \nu_0\sqrt{2T_k/m_p}$.

The brightness temperature along a line of sight at a radial distance r from the PBH, Eq. (3.25), can be formally solved with the boundary condition at $r = 0$, leading to

$$T_{b,\nu}(r) = T_{b,\nu}(0)e^{-\tau_\nu(0,r)} + \int_0^r dr'\kappa_\nu(r')T_S(r')e^{-\tau_\nu(r',r)}, \tag{3.28}$$

with the optical depth $\tau_\nu(r', r)$ defined as

$$\tau_\nu(r', r) = \int_{r'}^r dr''\kappa_\nu(r''). \tag{3.29}$$

At distances near the PBH the medium would be fully ionized, leading to a vanishing κ_ν. Therefore, it is appropriate to adopt the boundary condition $T_{b,\nu}(0) = T_{\rm CMB}$. Defining the differential brightness temperature as $\delta T_{b,\nu}(r) \equiv (T_{b,\nu}(r) - T_{\rm CMB})/(1+z)$, we get

$$\delta T_{b,\nu}(r) = \int_0^r dr'\kappa_\nu(r')\frac{T_S(r') - T_{\rm CMB}}{1+z}e^{-\tau_\nu(r',r)}. \tag{3.30}$$

The spin temperature can be calculated using Eq. (2.2), with the collisional coupling coefficient, y_k, defined in Eq. (2.3) and the Lyman-α coefficient, y_α, in Eq. (2.4). The Lyman-α flux in y_α contains two contributions, $J_\alpha(r) = J_\alpha^{\rm loc}(r) + J_\alpha^{\rm back}$. The first of these comes from the local emission in the local medium, given by

$$\begin{aligned}J_\alpha^{\rm loc}(r) = \frac{f_\alpha(x_e)c}{4\pi H\nu_\alpha h\nu_\alpha}n_{\rm H}(z,r)x_{\rm H}(r,z)\int_{E_0}^\infty dE\left(\frac{E-E_{\rm th}}{E}\right) \\ \times\sigma(E)F(E,r,z).\end{aligned} \tag{3.31}$$

We parametrize the energy deposition fraction $f_\alpha(x_e)$ using the fitting formula obtained in Ref. [191], given by $f_\alpha = 0.48(1 - x_e^{0.27})^{1.52}$. The second component to the Lyman-α flux comes from the background contribution, which is given the mean average over the IGM, produced by a combination of stellar sources and distant PBHs. This global flux $J_\alpha^{\rm back}$ for a given astrophysical model is computed by implementing the formalism of Sec. III A into 21CMFAST, as discussed in the previous section. Thus, the Lyman-α coupling coefficient can then be determined summing both components.

In Fig. 4, we show radial profiles of the density (top-left panel), gas temperature (purple line in the top-right panel), spin temperature (blue and red lines in the top-right panel), and the collisional (y_k, solid lines in the bottom panel) and Lyman-α (y_α, dashed lines in the bottom panel) couplings at various redshifts for $M_{\rm PBH} = 1\ M_\odot$. As designed, both the density profiles and the kinetic temperature profiles asymptote to the IGM values, which have been taken from the customized version of 21CMFAST (see Sec. IV A for more details). The subsequent 21-cm temperature profile, computed using the values in Fig. 4, is depicted in Fig. 5. Note that the contribution must be truncated at large radii to avoid double counting the IGM contribution—we define this truncation to occur when the temperature profile is within 1% of its asymptotic value, although the results are insensitive to a reasonable choice of this value. Note that the suppression of y_α (bottom panel in Fig. 4) between $z = 20$ and $z = 10$ can be explained by its dependence with the inverse of the temperature of the gas, $y_\alpha \propto T_k^{-1}$, which has been already heated significantly by this epoch.

2. Averaged 21-cm line signal

The prescription provided above allows one to compute the 21-cm profile for an individual PBH. Nevertheless, the observable quantity of interest is the contribution to the global 21-cm line from all the PBHs in the Universe. Here, we rederive the formula that allows one to compute the globally averaged brightness temperature $\overline{T_b}$ from the radial 21-cm profile [138]. The brightness temperature is related to the flux per unit frequency and solid angle $\frac{dF}{d\nu d\Omega}$ arising from a PBH of mass $M_{\rm PBH}$ by

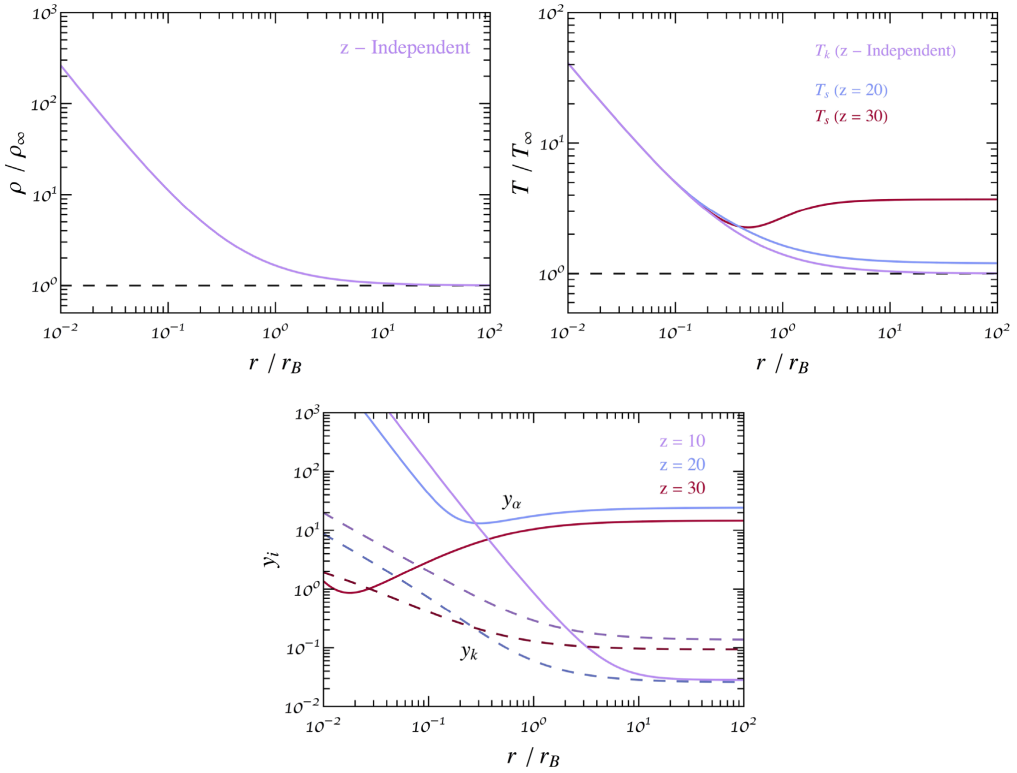

FIG. 4. Radial profiles for the local density (top-left panel), kinetic and spin temperatures (top-right panel), and coupling coefficients (bottom panel) y_k (dashed lines) and y_α (solid lines), displayed at various redshifts, for a PBH of mass $M_{\rm PBH} = 1\ M_\odot$. The dashed lines in the upper panels represent the IGM values.

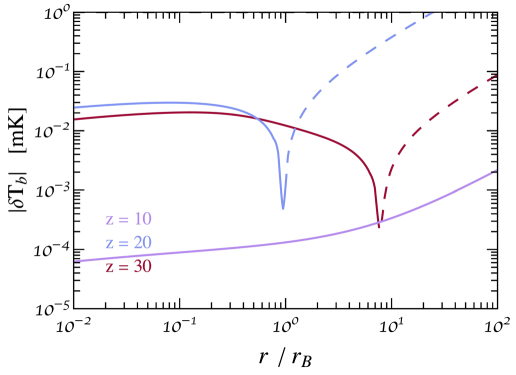

FIG. 5. Radial profile of the absolute value of the 21-cm differential brightness temperature, $\delta\bar{T}_b$, for a PBH of mass $M_{\rm PBH} = 1\ M_\odot$, at redshifts $z = 10$, 20, and 30. Dashed (solid) lines denote radii at which the signal would be seen in absorption (emission).

$$\frac{dF}{d\nu d\Omega} = \frac{2\nu^2}{c^2} T_{b,\nu}. \tag{3.32}$$

The averaged value of this quantity on a frequency interval $d\nu$ and a solid angle $d\Omega$ can be written as

$$\overline{\frac{dF}{d\nu d\Omega}} d\nu d\Omega = \langle F \rangle n_{\rm PBH} dV, \tag{3.33}$$

where dV is the differential comoving volume, $n_{\rm PBH}$ is the number density of PBHs, and $\langle F \rangle$ is the area-averaged flux for a single PBH,

$$\langle F \rangle = \frac{1}{A} \int dAF, \tag{3.34}$$

with $A = \pi r_{\rm max}^2$, and where $r_{\rm max}$ is the maximum radius at which the PBH influences the IGM (defined as above—specifically, this is the radius at which T_k is within 1% of the asymptotic value). Using the fact that $|d\nu/dz| = \nu_0/(1+z)^2$ and writing the differential comoving volume

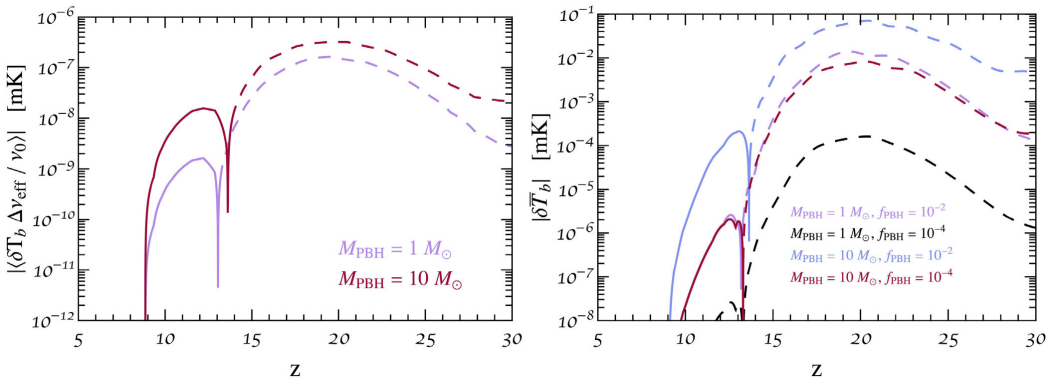

FIG. 6. Left panel: area-averaged differential brightness temperature times $\Delta\nu_{\rm eff}/\nu_0$ for one single PBH of mass $M_{\rm PBH} = 1\ M_\odot$ and $M_{\rm PBH} = 10\ M_\odot$, and assuming $f_{\rm PBH} = 10^{-2}$. Right panel: cumulative local contributions of a monochromatic population of PBHs to the globally averaged brightness temperature for mass $M_{\rm PBH} = 1\ M_\odot$ and $M_{\rm PBH} = 10\ M_\odot$, and dark matter fractions $f_{\rm PBH} = 10^{-2}$ and $f_{\rm PBH} = 10^{-4}$. In both panels, dashed (solid) lines represent when the 21-cm signal would be seen in absorption (emission), i.e., $\delta T_b < 0$ ($\delta T_b > 0$).

as $dV = D^2 dD d\Omega$, where D is the comoving distance, we find

$$\frac{\overline{dF}}{d\nu d\Omega} = \frac{c(1+z)^2}{\nu_0 H(z)} D^2 \langle F\rangle n_{\rm PBH}, \tag{3.35}$$

where we have used $dD/dz = c/H(z)$. The integrated flux over frequency and solid angle is then given by

$$F = \int d\nu d\Omega \frac{dF}{d\nu d\Omega} = \Delta\Omega \Delta\nu_{\rm eff} \left.\frac{dF}{d\nu d\Omega}\right|_{\nu_0}, \tag{3.36}$$

where $\Delta\Omega = A/D_A^2$ is the solid angle subtended by the halo around the PBH, with $D_A = D/(1+z)$ the angular diameter distance, and $\Delta\nu_{\rm eff} = ((1+z)\phi_\nu(\nu_0))^{-1} = \sqrt{\pi}\Delta\nu_{\rm D}/(1+z)$ [138]. One can then revert to the averaged brightness temperature using

$$\frac{\overline{dF}}{d\nu d\Omega} = \frac{2\nu_0^2}{c^2}\bar{T}_b. \tag{3.37}$$

From Eqs. (3.35) and (3.37), we find the globally averaged brightness temperature to be given by

$$\bar{T}_b = \frac{c(1+z)^4}{\nu_0 H(z)} n_{\rm PBH} \langle \Delta\nu_{\rm eff} T_{b,\nu_0}\rangle A. \tag{3.38}$$

For the area-averaged differential brightness temperature $\delta\bar{T}_b$, Eq. (3.38) is applied but replacing T_{b,ν_0} by $\delta T_{b,\nu_0}$ computed from Eq. (3.30). We depict in Fig. 6 the area-averaged 21-cm signal for one single PBH as a function of redshift (left panel), and the globally averaged signal (right panel), for various values of $M_{\rm PBH}$ and $f_{\rm PBH}$. The dashed and solid lines in the left panel indicate when the signal would be seen in absorption or emission. Interestingly, and perhaps counterintuitively, the global contribution is often negative (i.e., it is seen in absorption). At first glance this appears strange, as the process of accretion heats and ionizes the medium—thus, one might naively expect to see this contribution in emission. However, the asymptotic signal is observed in absorption during this epoch and, while the process of accretion does heat the local medium, the density rises faster than the temperature [recall that $\rho(r) \propto T(r)^{3/2}$]. Thus, there exists a range of radii near the Bondi radius for which the kinetic temperature has not yet been heated above the background temperature, but for which the density has noticeably increased—the net effect is an amplification of a slightly suppressed absorption dip.

The large drop in the signal for $z \lesssim 10$ in Fig. 6 appears because stellar sources have begun ionizing the medium. We emphasize that for the masses and dark matter fractions adopted here, the local contribution is never greater than 0.1 mK. Given that the usual IGM signals for these epochs range between 1 and 100 mK (see Sec. IV A), the local contribution from PBHs is negligible for the models of interest.

3. Comment on the local contribution

Before continuing, a discussion on the treatment and impact of the local contribution is in order. We begin by addressing a number of concerns regarding the formalism adopted in the section above.

It should be emphasized that the spherically symmetric treatment of accretion adopted here neglects a number of potentially important features. First, our formalism only accounts for the adiabatic evolution of the medium, leading to the relation $T \propto \rho^{2/3}$. Thus, we have neglected the local heating of the gas by the highly energetic radiation

generated during accretion. This heating term is proportional to the luminosity and, therefore, to the radiative efficiency and the PBH mass. However, the effect of such a heating would be the enhancement of the local temperature, which would suppress the absorption signal that arises near the Bondi radius, subsequently reducing the global contribution to the 21-cm signal. Thus, from this point of view, neglecting the heating term is a conservative assumption. We have also chosen to neglect viscosity in our treatment, despite the fact that viscosity is known to play an important role in ADAF accretion [141,145]. We believe that this choice is justified as the derived signal seems to be dominated by the behavior at larger radius, where the effects of viscosity are reduced. Nevertheless, a more rigorous numerical treatment would be required to verify this statement.

Another concern about the adopted formalism is the assumption of the static solution of an isolated PBH in a uniform background. In reality, this is almost certainly not the case. The matter accreted onto the PBH must come from the IGM. We have implicitly assumed, however, that the asymptotic condition of the IGM remains unaltered by the presence of the PBH. Conceptually, one would expect that an underdensity at $r \gtrsim r_{\rm B}$ is necessary in order to counteract the overdensity observed for $r \lesssim r_{\rm B}$. Neglecting momentarily the effects of heating and ionization, the contribution of the underdensity should identically cancel that of the overdensity. The fact that the signal is predominately seen in absorption indicates that it is dominated by the state of the IGM near the Bondi radius, where not properly accounting for these changes in density could be important. Thus, it is entirely possible that the observed absorption feature is actually artificial and arises from the fact that we have not correctly accounted for the influence of the PBH on the IGM. Nevertheless, this implies that our formalism is likely to significantly overestimate the true contribution of local accretion, again suggesting the estimate is conservative.

Before continuing, it is important to address why the results found here differ by orders of magnitude from previous PBH calculations [121,122]. We think there are multiple reasons for this discrepancy,[7] which we outline below.

First, note that the assumed PBH luminosity in Ref. [122] is near the Eddington limit (specifically they adopt a luminosity of $L = 0.1 L_{\rm Edd}$). Such a large luminosity is not consistent with ADAF accretion, but rather solutions in which one forms a thin disk that radiates extremely efficiently ($\epsilon \sim 1$). In the event that only the radiative efficiency is modified, local heating would be reduced and global heating enhanced. However, there also exists a significant difference in the normalization of the luminosity, as the dimensionless accretion rate adopted in our framework is roughly $L/L_{\rm Edd} \sim 10^{-10}$. The difference in adopted luminosity changes the relative importance of heating, implying that within our formalism one cannot neglect the derivative terms in the accretion equations, whereas for large luminosities these terms may be subdominant to local heating. Next, it is slightly concerning that Ref. [122] seeks a static solution to the local profile on scales comparable to and higher than the Hubble length (note that $r_{\rm H} = c/H(z) \simeq 4.6 \times 10^4 [30/(1+z)]^{3/2}$ kpc). Hence, the expansion of the Universe can no longer be neglected, and thus the static framework is applied out of the range of validity. This does not appear to be a problem with the ADAF framework, as the smaller luminosities imply smaller scales of interest.

Finally, it is important to note that one should not directly apply Eq. (3.16) to obtain the brightness temperature profile around the PBH. Equation (3.16) is only valid when considering large scales; namely, it is valid when one can neglect the radial dependence of both the spin temperature and the optical depth, and when the optical depth is exclusively given by the optical depth of the IGM. Here, neither of these statements is true, and thus one must solve the radiative transfer equation as a function of the radial coordinate using Eq. (3.30) (as was done in previous works, see, e.g., Refs. [119,138]). This profoundly impacts the strength of the signal. In Fig. 7, we illustrate, using the formalism of the previous section, that incorrectly applying Eq. (3.16) leads to an enhancement of the signal by roughly $\sim$2 orders of magnitude.

Therefore, we conclude that it is unlikely that the local contribution from PBHs could significantly add to the 21-cm signal. Nevertheless, it is likely the case that complex high-resolution simulations will need to be performed for this contribution to be truly understood.

C. Shot noise

Since PBHs are point sources, they contribute to the power spectrum as Poisson white noise (i.e., they contribute in a scale-independent manner) [92]. The associated perturbations are isocurvature modes and thus, their contribution only affects scales smaller than those corresponding to the matter-radiation equality era, $k > k_{\rm eq} \equiv a_{\rm eq} H_{\rm eq}$, being negligible at larger scales. Approximating the isocurvature transfer function as $T_{\rm iso} = 3/2(1+z_{\rm eq})$ for $k > k_{\rm eq}$ and 0 otherwise, where $z_{\rm eq}$ is the redshift of

[7] In addition to the differences in formalism, discussed below, the de-excitation rates (taken from Ref. [127]) appear to be incorrectly transcribed in Ref. [122]. Most notably, the *logarithms* in the e-H de-excitation rate should be base 10, rather than natural logs. We have verified, using the formalism of Ref. [122], that this mistake does indeed enter the calculations. Implementing the correct de-excitation rate into the same formalism completely removes the absorption dip responsible for the majority of the signal (see Fig. 6 of Ref. [122]), and thus significantly alters the contribution of minihalos to the global 21-cm signal. The check we have performed agrees with the result of Ref. [121], which appears to have a formalism nearly identical to that of Ref. [122], but without the artificial absorption dip.

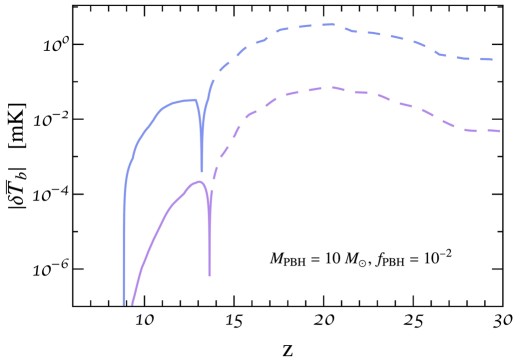

FIG. 7. Contribution to differential brightness temperature, $\delta\bar{T}_b$, from local heating induced by accretion onto a population of PBHs with $M_{\rm PBH} = 10\ M_\odot$, assuming $f_{\rm PBH} = 10^{-2}$, computed by resolving the radiative transfer equation locally, Eq. (3.30), (purple line) and by incorrectly applying Eq. (3.16) (blue line).

matter-radiation equality [192], this term can be written as [92]

$$\Delta P = T_{\rm iso}^2 \frac{f_{\rm PBH}^2}{n_{\rm PBH}} D^2(z) = \frac{9(1+z_{\rm eq})^2 f_{\rm PBH} M_{\rm PBH}}{4\Omega_{\rm DM}\rho_c} D^2(z) \simeq 2.5\times 10^{-2} f_{\rm PBH}\left(\frac{M_{\rm PBH}}{30\ M_\odot}\right) D^2(z)\ {\rm Mpc}^3, \qquad k > k_{\rm eq}, \tag{3.39}$$

where $\Omega_{\rm DM}$ is the fraction of dark matter energy density over the critical density ρ_c and $D(z)$ is the linear growth factor of density perturbations. The inclusion of this contribution modifies the halo mass function on small scales. For the masses studied here (namely $M_\odot \lesssim M_{\rm PBH} \lesssim 10^3\ M_\odot$), however, the effects are only important for halos which are not large enough to cool and collapse to form stars (such halos are known as "minihalos"). Since star-forming halos are expected to produce the dominant 21-cm signal in the epochs of interest, one is naively driven to conclude that the Poisson noise in the power spectrum is not relevant and can be neglected (even though, we have included it in the calculation of the global signal). It was recently argued [119,120], however, that the enhanced number density of minihalos arising from the shot noise induced by $\sim\mathcal{O}(M_\odot)$ PBHs could sufficiently elevate the contribution of minihalos to a discernible level. We briefly outline the formalism for estimating the minihalo contribution below and show that the computation of Ref. [119] failed to self-consistently account for the heating of the IGM induced by PBH accretion. Correctly accounting for this effect tends to suppress the minihalo contribution to the point where it can be neglected.

1. Brightness temperature inside minihalos

A dark matter halo at redshift z can be characterized by one parameter, the overdensity $\Delta_c(z)$ relative to the critical density $\rho_c(z)$, so that its mass $M_{\rm h}$ and virial radius $R_{\rm vir}$ are related by

$$M_{\rm h} = \frac{4\pi}{3}\Delta_c(z)\rho_c(z)R_{\rm vir}^3. \tag{3.40}$$

Here, we use the virial overdensity based on spherical collapse [193]

$$\Delta_c(z) = 18\pi^2 + 82(\Omega_{{\rm m},z} - 1) - 39(\Omega_{{\rm m},z} - 1)^2, \tag{3.41}$$

where

$$\Omega_{{\rm m},z} = \frac{\Omega_{\rm m}(1+z)^3}{\Omega_{\rm m}(1+z)^3 + \Omega_\Lambda}. \tag{3.42}$$

In the calculation below, we assume the neutral hydrogen fraction, $x_{\rm H}$, to be given by the IGM value, and the kinetic temperature in the halo by $T_k = T_{\rm vir}$, where the virial temperature of a truncated isothermal halo is [194]

$$T_{\rm vir}(M_{\rm h}, z) \simeq 4.8\times 10^4\ {\rm K}\left(\frac{\mu}{1.22}\right)\left(\frac{M_{\rm h}}{10^8\ M_\odot h^{-1}}\right)^{2/3} \times \left(\frac{\Omega_{\rm m}}{\Omega_{{\rm m},z}}\frac{\Delta_c(z)}{18\pi^2}\right)^{1/3}\left(\frac{1+z}{10}\right), \tag{3.43}$$

being $\mu = 1.22$ the mean molecular weight of neutral IGM. The average number density of neutral hydrogen of the halo is

$$\bar{n}_{\rm H}(M_{\rm h}, z) = \frac{\mathfrak{f}_{\rm H}}{m_p}\left(\frac{\Omega_{\rm b}}{\Omega_{\rm m}}\right)\left(\frac{3M_{\rm h}}{4\pi R_{\rm vir}^3}\right) = \mathfrak{f}_{\rm H}\left(\frac{\Omega_{\rm b}}{\Omega_{\rm m}}\right)\left(\frac{\rho_c(z)\Delta_c(z)}{m_p}\right), \tag{3.44}$$

where ρ_b the baryon energy density. For the sake of consistency with the constant temperature assumption, we consider that neutral hydrogen in halos follows a truncated (singular) isothermal distribution, normalized to provide the mean value given in Eq. (3.44),

$$n_{\rm H}(M_{\rm h}, z, r) = \frac{1}{3}\bar{n}_{\rm H}(M_{\rm h}, z)\left(\frac{R_{\rm vir}}{r}\right)^2. \tag{3.45}$$

We have also verified that reasonable modifications to this assumption (e.g., taking an NFW profile [195] or a truncated nonsingular isothermal profile [194]) give rise to only small changes on the cumulative minihalo signal.

Since the flux of Lyman-α photons predominantly arises from star formation, the spin temperature *inside* minihalos, whose virial temperatures are below threshold for atomic

hydrogen cooling, is dictated exclusively by the collisional coupling, y_k, given by Eq. (2.3). The brightness temperature for photons with frequency ν through a minihalo of given mass and redshift is obtained by solving the radiative transfer equation. Here, however, one has to be careful so as to not double count factors contained in the IGM contribution. To clarify, consider decomposing the IGM and minihalo contribution to the spin temperature such that

$$\tau = \tau_{\rm IGM} + \tau_{\rm mh}, \tag{3.46}$$

$$T_S = T_{\rm S,IGM} + T_{\rm S,mh}, \tag{3.47}$$

where $\tau_{\rm IGM}$ and $\tau_{\rm mh}$ are the optical depth of the IGM and the minihalo, respectively, and we define

$$\tau_{\rm mh}, T_{\rm S,mh} \neq 0 \quad \text{for } |r| \leq R_{\rm vir}, \tag{3.48}$$

$$\tau_{\rm IGM}, T_{\rm S,IGM} \neq 0 \quad \text{for } |r| > R_{\rm vir}, \tag{3.49}$$

where r is the radial distance from the center of a minihalo with maximum radius $R_{\rm vir}$. The general solution to the radiative transfer equation (neglecting scattering) is given by

$$T_b = T_{\rm CMB} e^{-\tau} + \int d\tau T_S(\tau) e^{-\tau}. \tag{3.50}$$

Using Eqs. (3.46)–(3.49), one finds

$$T_b = T_{\rm CMB} e^{-(\tau_{\rm IGM}+\tau_{\rm mh})} + \int ds \frac{d\tau_{\rm IGM}}{ds} T_{\rm S,IGM} e^{-(\tau_{\rm IGM}+\tau_{\rm mh})} + \int ds \frac{d\tau_{\rm mh}}{ds} T_{\rm S,mh} e^{-(\tau_{\rm IGM}+\tau_{\rm mh})}, \tag{3.51}$$

where s is the line-of-sight. In order to avoid double counting, one must subtract off the contribution of the IGM, given by

$$T_{\rm b,IGM} = T_{\rm CMB} e^{-\tau_{\rm IGM}} + \int ds \frac{d\tau_{\rm IGM}}{ds} T_{\rm S,IGM} e^{-\tau_{\rm IGM}}, \tag{3.52}$$

implying the solution for the minihalo brightness temperature is given by

$$T_{\rm b,mh}(\nu) = T_{\rm CMB} e^{-\tau_{\rm IGM}} (e^{-\tau_{\rm mh}(\nu,\infty)} - 1) + \int_{-\infty}^{\infty} ds T_S(\ell) e^{-(\tau_{\rm IGM}+\tau_{\rm mh}(\nu,s))} \frac{d\tau_{\rm mh}(\nu,s)}{ds}, \tag{3.53}$$

where we have added some explicit dependences. The optical depth of the minihalo, $\tau_{\rm mh}(\nu, s)$, is given by

$$\tau_{\rm mh}(\nu, s) = \frac{3A_{10}T_0}{32\pi\nu_0^2} \int_{-\infty}^{s} ds' \frac{n_{\rm H}(\ell)\phi(\nu,\ell)}{T_S(\ell)}, \tag{3.54}$$

and s and ℓ are radial comoving distances, s being the component along the line-of-sight and ℓ connecting s to the center of the minihalo, $\ell^2 = s^2 + b^2 R_{\rm vir}^2$ [196], with b the impact parameter. One might be inclined to obtain the differential brightness temperature by subtracting $T_{\rm CMB}$ from Eq. (3.53); however, note that it is given by

$$\delta T_b = \frac{T_b - T_{\rm CMB}}{1+z} = \frac{T_{\rm b,IGM} + T_{\rm b,mh} - T_{\rm CMB}}{1+z} = \frac{\delta T_{\rm b,IGM} + T_{\rm b,mh}}{1+z}, \tag{3.55}$$

and thus the proper contribution to the total differential brightness temperature is simply given by Eq. (3.53).

Obtaining the global contribution from all minihalos can be done in a similar manner to what was shown in Sec. III B. Specifically, one can use Eq. (3.38), but with the generalization that $n_{\rm PBH} \to \int dM_{\rm h} dn/dM_{\rm h}$, i.e.,

$$\delta\bar{T}_b = \frac{c(1+z)^4}{\nu_0 H(z)} \int_{M_{\rm min}}^{M_{\rm max}} dM_{\rm h} \frac{dn}{dM_{\rm h}} \langle \Delta\nu_{\rm eff} \delta T_{b,\nu_0} \rangle A, \tag{3.56}$$

where, in analogy to the area-averaged signal in Sec. III B, the brackets represent the average over the minihalo cross section [c.f., Eq. (3.34)], $A = \pi R_{\rm vir}^2$. The integration of Eq. (3.56) is bounded from above by the mass threshold for star formation, which we take as the one corresponding to a virial temperature, Eq. (3.43), of $T_{\rm min} = 10^4$ K. The lower limit of the integral is chosen as the maximum between the PBH mass and the Jeans mass $M_{\rm J}$ (although for all cases of interest here, $M_{\rm PBH} < M_{\rm J}$), which is given by the mass enclosed in a region with diameter of the Jeans length, $\lambda_{\rm J} = \sqrt{(5\pi T_k)/(3G\bar{\rho}\mu m_p)}$,

$$M_{\rm J}(z) = \frac{4\pi}{3}\bar{\rho}\left(\frac{\lambda_{\rm J}}{2}\right)^3 \simeq 2.2 \times 10^9 \, M_\odot \left(\frac{T_k}{10^4 \, \rm K}\right)^{3/2} \times \left(\frac{1.22}{\mu}\right)^{3/2} \left(\frac{10}{1+z}\right)^{3/2}, \tag{3.57}$$

where $\bar{\rho}$ is the mean matter density prior to collapse. Here, we calculate T_k using the formalism presented in Sec. III A.

The number density of halos per unit mass is given by the halo mass function,

$$\frac{dn}{dM_{\rm h}} = \frac{\rho_{\rm m}}{M_{\rm h}} \frac{d\ln\sigma^{-1}}{dM_{\rm h}} f(\sigma), \tag{3.58}$$

where $f(\sigma)$ represents the fraction of mass that has collapsed to form halos per unit interval in $\ln\sigma^{-1}$, with σ the root-mean-square of the matter density fluctuation smoothed with a real-space top hat filter over the virial radius,

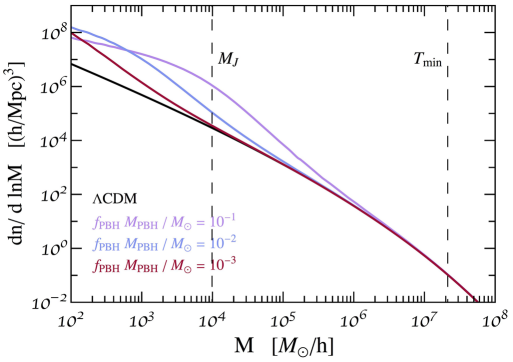

FIG. 8. Halo mass function for several PBH cases at $z = 20$. Dotted and dashed vertical lines represent the Jeans mass, assuming a ΛCDM cosmology (i.e., not additional heating from PBH accretion), and the minimum halo mass for star formation, respectively, which limit the range of integration in Eq. (3.56).

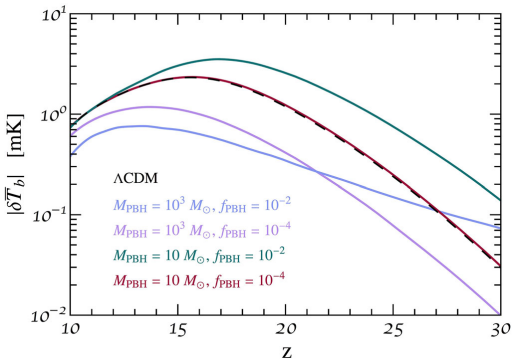

FIG. 9. Collective contribution of minihalos to the globally averaged 21-cm differential brightness temperature, $\delta\bar{T}_b$, for various PBH masses and dark matter fractions, and compared with the minihalo contribution in ΛCDM (black dashed line), as a function of redshift.

$$\sigma^2(M_{\rm h}, z) = \frac{D^2(z)}{D^2(0)} \int_0^\infty \frac{dk}{k} \frac{k^3 P(k)}{2\pi^2} |W(k; M_{\rm h})|^2, \qquad (3.59)$$

where $D(z)$ is the growth factor of linear perturbations, $P(k)$ is the linear matter power spectrum [here, modified by including the shot noise term from the PBH population, Eq. (3.39)], and $W(k; M_{\rm h})$ is the Fourier transform of the real-space top hat filter. Here we use the Sheth-Tormen halo mass function [197,198],

$$f(\sigma) = A\sqrt{\frac{2a}{\pi}}\left[1 + \left(\frac{\sigma^2}{a\delta_c^2}\right)^p\right] \frac{\delta_c}{\sigma} e^{-\frac{a\delta_c^2}{2\sigma^2}}, \qquad (3.60)$$

with fit coefficients $A = 0.3222$, $a = 0.707$, and $p = 0.3$, and the critical collapse density $\delta_c = 1.686$. The halo mass function at $z = 20$ for several PBH cases is depicted in Fig. 8. Note that, since the additional shot noise contribution from PBH to the matter power spectrum depends on the combination $f_{\rm PBH} M_{\rm PBH}$ [see Eq. (3.39)], so does the modification of the halo mass function with respect to the standard ΛCDM case.

Using Eqs. (3.53), (3.56), and (3.58), one can calculate the globally averaged 21-cm signal from the cumulative population of minihalos. In Fig. 9, we depict the contribution of minihalos assuming a monochromatic population of PBHs with mass of either 10 $M_\odot$ or 10^3 $M_\odot$ and a dark matter fraction of $f_{\rm PBH} = 10^{-2}$ or $f_{\rm PBH} = 10^{-4}$. Notice that the redshift dependence of the minihalo contribution can be rather nontrivial, as the T_k dependence of the Jeans mass is modified by the accretion model, and the mass derivative of the halo mass function can be either enhanced or suppressed relative to ΛCDM at this mass scale. We can see that the enhancement on the formation of structures due to the Poisson noise would produce a larger signal in the case $M_{\rm PBH} = 10\ M_\odot$ and $f_{\rm PBH} = 10^{-2}$. However, contrary to previous claims [119,120], the other cases shown in Fig. 9 are not enhanced but suppressed. For small PBH masses and low values of $f_{\rm PBH}$, the minihalo contribution saturates to the standard ΛCDM prediction; that is to say, the number density of minihalos is negligibly modified, and the result is equivalent to that of ΛCDM. Meanwhile, the signal is suppressed for models with larger values of $M_{\rm PBH} \times f_{\rm PBH}$, where the enhancement of the halo mass function is significant. The reason for the discrepancy between the result presented here and that found in Refs. [119,120] lies on the treatment of the Jeans mass. In those previous works, only adiabatic cooling was considered for the evolution of the IGM temperature, while here the heating by standard x-ray sources and by accretion onto the population of PBHs (see Sec. III A) has also been included. This implies a larger Jeans mass and thus a reduction of the relevant mass range of integration in Eq. (3.56). For instance, for the models depicted in Fig. 2, x-ray radiation would heat up the temperature around an order of magnitude with respect to the adiabatic cooling case at $z \sim 10$, increasing therefore the Jeans mass by a factor of $10^{3/2} \sim 30$.

IV. METHODOLOGY

A. Numerical simulations

As already mentioned above, in order to compute the redshift evolution of both the 21-cm global signal and power spectrum we make use of the publicly available package 21CMFASTV1.2 [162]. This code produces realizations of the evolved density, ionization, peculiar velocity, and spin temperature fields from semianalytic calculations. It depends on a number of parameters describing the different processes taking place at the reionization

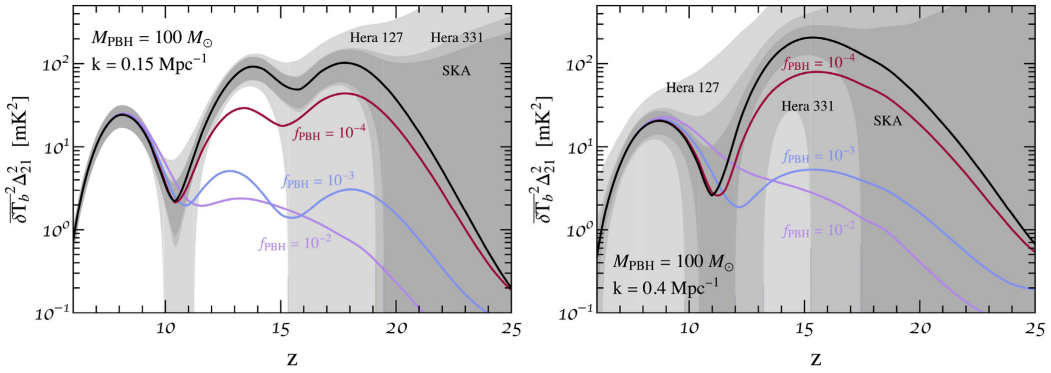

FIG. 10. A 21-cm power spectrum as a function of redshift z, for two values of the scale: $k = 0.15$ Mpc^{-1} (left panel) and $k = 0.4$ Mpc^{-1} (right panel). We consider a monochromatic PBH mass distribution with $M_{\rm PBH} = 100\ M_\odot$ and the fiducial astrophysical parameters. We illustrate primordial black hole fractions of $f_{\rm PBH} = 10^{-2}$, 10^{-3}, and 10^{-4}. Errors for the future HERA and SKA radio interferometers for the standard scenario (with $f_{\rm PBH} = 0$, denoted by the solid black lines) are also depicted. See text for details.

period. We use here a minimal set of four parameters: the UV ionization efficiency, $\xi_{\rm UV}$, the number of x-ray photons per solar mass, $\xi_{\rm X}$, the minimum virial temperature of halos hosting galaxies, $T_{\rm min}$, and the number of photons per stellar baryon between Lyman-α and the Lyman limit, N_α.[8] The phenomenological parameter $\xi_{\rm UV}$ is assumed to be proportional to: (i) the fraction of ionizing photons escaping their host galaxies, (ii) the number of ionizing photons per stellar baryons inside stars, and (iii) the fraction of baryons that form stars. The efficiency for ionization, heating, and Lyman-α production by x-ray sources depends on the total x-ray emission rate, which is proportional to the star formation rate and to the number of x-ray photons per solar mass in stars, $\xi_{\rm X}$.[9] The temperature $T_{\rm min}$ is the minimum of the virial temperature of a halo, below which gas cannot cool efficiently, and thus star formation is suppressed.[10] In the following, we present various examples of the 21-cm signal using a fiducial ΛCDM model defined by $(\xi_{\rm UV}, \xi_{\rm X}, T_{\rm min}, N_\alpha) = (50, 2\times10^{56}\ M_\odot, 5\times10^4\ {\rm K}, 4000)$.

In Fig. 3, we showed the global differential 21-cm brightness temperature for a population of 100 $M_\odot$ PBHs, for a range of abundances, as a function of redshift. In Fig. 10, we depict the 21-cm power spectrum as a function of redshift at scales $k = 0.15$ Mpc^{-1} (left panel) and $k = 0.4$ Mpc^{-1} (right panel), which are expected to be reasonably free from foregrounds [206]. Notice that the 21 cm power spectrum in the standard scenario (solid black curves) exhibits three characteristic peaks, associated to the epochs of reionization, heating from x-ray sources and Lyman-α pumping [162,207,208], from lower to higher redshifts. The presence of PBHs is translated into a suppression of the x-ray heating peak in the power spectrum, which is obviously more pronounced as one increases $f_{\rm PBH}$. Additionally, the Lyman-α pumping peak could even disappear for $f_{\rm PBH} \gtrsim 10^{-2}$. In Fig. 11, we show the 21-cm power spectrum as a function of the scale for two fixed redshifts: $z = 12.2$ (left panel) and $z = 17.5$ (right panel). The red areas indicate the scales where the signal is expected to be contaminated by foregrounds. The effect of PBHs arises primarily from an increase in the flux of x-rays, which can induce both scale-dependent and redshift-dependent features in the power spectrum.

In Figs. 10 and 11, we also include the forecasted errors associated to future HERA and SKA measurements of the 21-cm power spectrum. These errors have been estimated by means of the publicly available code 21cmSense[11] [209,210] (see also Ref. [211]). The total noise is given by

$$\overline{\delta\Delta^2_{T+S}}(k,z) = \left(\sum\nolimits_i \frac{1}{(\Delta^2_{N,i} + \bar{\Delta}^2_{21})^2}\right)^{-1/2}, \quad (4.1)$$

[8]The default value of N_α in 21cmFast is obtained by assuming Pop II stars [199] and normalizing their emissivity to ∼4400 ionizing photons per stellar baryon.

[9]A value of $\xi_{\rm X} = 10^{56}\ M_\odot^{-1}$ implies $N_{\rm X} \simeq 0.1$ x-ray photons per stellar baryon.

[10]Note that the definition of the virial temperature here is taken to be as defined in Ref. [200], which differs from Eq. (3.43) by a factor of 2.44. This difference arises from the fact that in Eq. (3.43) we consider $\mu = 1.22$ and that the virial temperature depends upon the adopted halo profile, although these changes do not significantly impact any of the results of this section. The default value in the 21cmFast code is $T_{\rm min} = 10^4$ K, which has been identified in the literature with the atomic cooling threshold [201–205], and using Ref. [200], it corresponds to a minimum halo mass of $M_{\rm min} \simeq 8\times10^7\ M_\odot$ at a redshift $z = 10$.

[11]https://github.com/jpober/21cmSense.

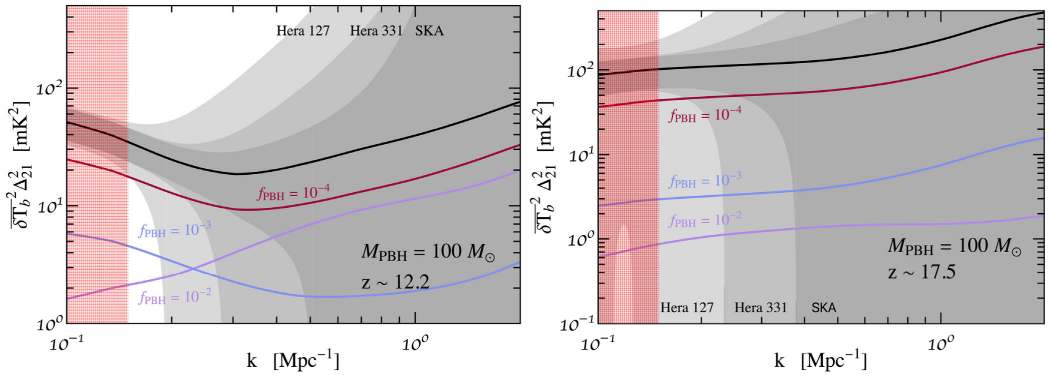

FIG. 11. A 21-cm power spectrum as a function of the scale, for two fixed redshifts: $z = 12.2$ (left panel) and $z = 17.5$ (right panel). The parameters are the same as in Fig. 10. The red areas denote the scales where foregrounds dominate over the signal.

with two contributions, one from thermal noise (N) plus a second one, a sample variance error (S), $\bar{\Delta}^2_{21} \equiv \overline{\delta T_b}^2 \Delta^2_{21}$. The thermal noise depends on the solid angle, the integrated observation time, and the temperature of the system. We focus here on the future HERA [95] and SKA-low frequency [96] experiments. We consider both the intermediate and final HERA configurations, with 127 and 331 antennas, which we refer to henceforth as Hera 127 and Hera 331. For SKA-low frequency, we follow the design presented in the SKA System Baseline Design Document [96]. Finally, we assume an exposure of 1080 hours and a bandwidth of 8 MHz, as these are the default values for these parameters in 21CMSENSE.

One of the fundamental difficulties associated with full statistical 21-cm analyses arises from the fact that consistent and accurate theoretical predictions for the 21-cm signal require time consuming semianalytical (or even fully hydrodynamical) simulations. Restricting our attention momentarily to a single PBH mass, obtaining a coherent interpolation over a five-dimensional parameter space (defined by $f_{\rm PBH}$, $\zeta_{\rm UV}$, $\zeta_{\rm X}$, $T_{\rm min}$, and N_α) requires enormous amounts of computing time. Recently, various groups have developed techniques which rely on simplified calculations (at the expense of numerical accuracy), principle component decompositions, and machine learning algorithms, to reduce the computational expense involved in obtaining a comprehensive 21-cm parameter scan (see, e.g., Refs. [212–217]).

In this work, we circumvent this numerical issue by exploiting a class of feed-forward neural networks known as multilayer perceptrons (MLPs). Specifically, for a fixed PBH mass, we compute the full 21-cm power spectrum for ~600 choices of astrophysical parameters (constrained to the range defined in Table II) and construct MLPs with two hidden layers, each containing ~50 hidden nodes, to emulate the output of 21CMFAST for arbitrary choices of parameters. The MLP is trained on ~70% of the computed power spectra while the remaining 30% are simultaneously used to ensure the neural network is not over-learning. We find that this procedure reproduces the computed datasets (both the trained dataset and test dataset), as well as various power spectra computed with randomly generated points in parameter space after the training of the neural network. We choose to assess the relative accuracy of the neural net by defining an accuracy statistic, which later serves as the quantity directly entering our likelihood, as

$$\alpha_{\rm err} \equiv \left| \frac{\bar{\Delta}^2_{21}(k,z) - \Delta^2_{21,NN}(k,z)}{\sqrt{\overline{\delta\Delta^2_{T+S}}^2(k,z) + (0.4 \times \bar{\Delta}^2_{21}(k,z))^2}} \right|, \quad (4.2)$$

where $\bar{\Delta}^2_{21}(k,z)$ is the power spectrum computed by 21CMFAST, and $\Delta^2_{21,NN}(k,z)$ is the power spectrum as computed by the neural net. Following Ref. [218], we have chosen to add in quadrature an additional modeling error (here we conservatively adopt a 40% error, although we note that this factor is somewhat *ad hoc*) that is intended to capture the approximate level of disagreement between 21CMFAST calculations and full hydrodynamic simulations. Using Eq. (4.2), one finds that the mean error of the neural net is $\lesssim 1\%$.

TABLE II. Model parameters and priors adopted in the sensitivity analysis.

	Minimum value	Maximum value	Prior type
$f_{\rm PBH}$	10^{-8}	1	Log
$\zeta_{\rm UV}$	10	100	Log
$\zeta_{\rm X}$	$2 \times 10^{55}\ M_\odot^{-1}$	$2 \times 10^{57}\ M_\odot^{-1}$	Log
$T_{\rm min}$	10^4 K	10^5 K	Log
N_α	4×10^2	4×10^4	Log

B. Statistics

We adopt a multivariate Gaussian likelihood with a diagonal covariance matrix, the elements of which are set using Eq. (4.2), and further assume that measurements are obtained in six log-spaced bins in k-space from $k = 0.15\ \mathrm{Mpc}^{-1}$ to $k = 1\ \mathrm{Mpc}^{-1}$ and 9 log-spaced measurements in redshift from $z \sim 8.3$ to $z \sim 19.5$. While it is likely that experiments such as SKA will be capable of achieving far better resolution in both k- and z-space, adopting a finer grid without properly accounting for correlated errors risks the possibility of significantly overestimating the sensitivity of these experiments.

We adopt the four-parameter astrophysical model discussed in Sec. IV A (implying a total of five model parameters for each fixed value of M_{PBH}), where the priors on each parameter are as given in Table II. For each fixed value of M_{PBH}, we perform a Markov chain Monte Carlo (MCMC), assuming the true measurement is given by a fiducial astrophysical model with $f_{\mathrm{PBH}} = 0$.

V. RESULTS AND CONCLUSIONS

The 2σ upper limits as derived from the MCMC analysis described in Sec. IV B and are shown in Fig. 12 for HERA (red line), assuming 331 antennas, and SKA (green line). Also shown in Fig. 12 are current constraints from microlensing surveys [219–221] (blue line), and the CMB [82,83,85] (purple and black lines), where the purple contour denotes the bound derived assuming an identical accretion model to the one adopted here. As discussed in the introduction, there exist additional constraints in this region; however, these are not shown for clarity. The MCMC analysis was only performed for PBH masses in the range $(1\text{–}10^3)\ M_\odot$; however, this is a consequence of the computational difficulty associated with 21-cm analyses. In principle, these experiments will be sensitive to both smaller and larger masses, and the relative importance of the shot noise, minihalos, and the modification to the IGM, in general, varies with mass.

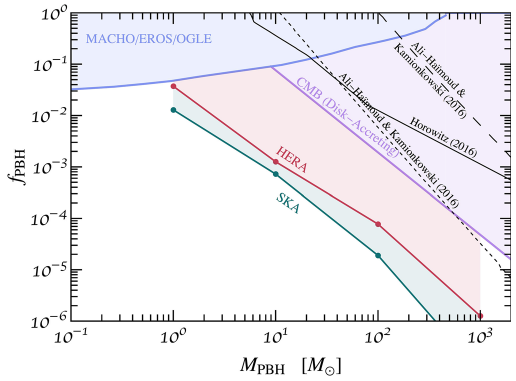

FIG. 12. Estimated 2σ sensitivity of SKA (green line) and HERA with 331 antennas (red line) for a monochromatic distribution of PBHs in the mass range $M_\odot \leq M_{\mathrm{PBH}} \leq 10^3\ M_\odot$. Results are compared to various limits derived from microlensing surveys [219–221] (blue line) and the CMB [82,83,85] (purple and black lines).

The results shown in Fig. 12 suggest that near-future 21-cm experiments will be able to increase the sensitivity to $\mathcal{O}(M_\odot)$ PBHs relative to that of the CMB by more than 1 order of magnitude. Moreover, 21-cm surveys provide a highly complementary probe that is sensitive to the dynamics of accretion at much lower redshifts. Thus, should a positive detection be made with both probes, one may be able to shed light on the dynamics and evolution of accretion in these systems. For completeness, we also show in Fig. 13 the result of the MCMC performed for $M_{\mathrm{PBH}} = 10^3\ M_\odot$ using the SKA telescope array. Figure 13 illustrates that many of the astrophysical parameters adopted in this analysis could be well constrained by these experiments.

In this work, we have focused on understanding the sensitivity that near-future radio interferometers may have to a population of $\gtrsim\mathcal{O}(M_\odot)$ PBHs using the 21-cm power spectrum. In particular, we have jointly analyzed three effects: namely, heating and ionization arising from accretion on both local and global scales, and the signal arising from minihalos (whose number density is enhanced with respect to that of ΛCDM, a consequence of having non-negligible Poissonian noise in the distribution of PBHs). Contrary to previous claims in the literature [121,122], we find that the local effect of accretion is negligible for all redshifts, masses, and PBH fractions discussed in this work. Moreover, for the PBH masses studied here, the addition of shot noise to the power spectrum modifies the halo mass function below the mass threshold for efficient star formation. Consequently, this term would only be relevant if minihalos gave sizable contributions, or if one considers extremely heavy PBHs (however, it is worth noting that there unavoidably exists uncertainty in the high redshift halo mass function within ΛCDM which could produce degenerate effects to minihalos). While previous work has claimed that the enhanced number density of minihalos, produced by viable populations of PBHs, could give rise to an observable signal [119,120], we show here that these calculations had not self-consistently accounted for the global heating of the IGM, which significantly raises the Jeans mass and tends to suppress the minihalo contribution. Thus, the dominant effect on the 21-cm power spectrum arises exclusively from the modifications to the heating and ionization of the IGM. We find experiments like HERA and SKA could significantly improve upon existing limits from the CMB, should observations be inconsistent with a $f_{\mathrm{PBH}} = 0$ cosmology (i.e., no PBHs).

Finally, we emphasize that 21-cm observations will have access to much more information than just the two-point correlation function. Should foregrounds be removed to a

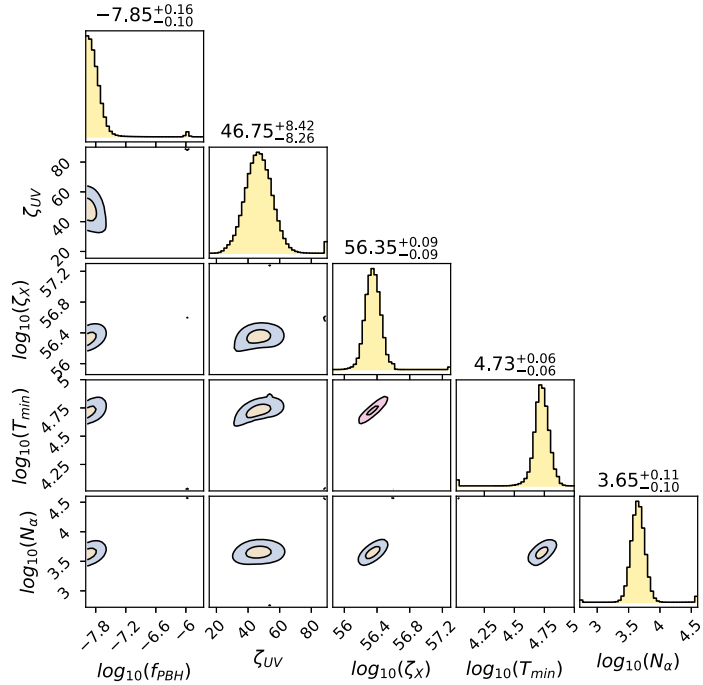

FIG. 13. Parameter sensitivity for SKA MCMC, assuming a monochromatic PBH mass distribution with $M_{\rm PBH} = 10^3\ M_\odot$, depicted with 1σ and 2σ contours. The numbers above each panel denote the maximum of the posterior and the upper/lower 1σ confidence interval on these values.

sufficiently high degree, these experiments may be able to exploit higher dimensional n-point correlation functions, or perhaps one could exploit the power of convolutional neural nets to shed light of the highly non-Gaussian behavior of neutral hydrogen during these epochs.

ACKNOWLEDGMENTS

O. M., P. V. D., and S. W. are supported by the Spanish Grant No. FPA2017-85985-P of the MINECO. S. P. R. is supported by a Ramón y Cajal contract, by the Spanish MINECO under Grant No. FPA2017-84543-P, and partially, by the Portuguese FCT through the CFTP-FCT Unit 777 (UID/FIS/00777/2019). All the authors also acknowledge support from the European Union's Horizon 2020 research and innovation program under the Marie Skłodowska-Curie Grants No. 690575 and No. 674896. This work was also supported by the Spanish MINECO Grant No. SEV-2014-0398.

[1] R. Adam *et al.* (Planck Collaboration), Astron. Astrophys. **594**, A1 (2016).
[2] P. A. R. Ade *et al.* (Planck Collaboration), Astron. Astrophys. **594**, A13 (2016).
[3] N. Aghanim *et al.* (Planck Collaboration), Astron. Astrophys. **594**, A11 (2016).
[4] S. Alam *et al.* (BOSS Collaboration), Mon. Not. R. Astron. Soc. **470**, 2617 (2017).
[5] G. F. Chapline, Nature (London) **253**, 251 (1975).
[6] S. Bird, I. Cholis, J. B. Muñoz, Y. Ali-Haïmoud, M. Kamionkowski, E. D. Kovetz, A. Raccanelli, and A. G. Riess, Phys. Rev. Lett. **116**, 201301 (2016).
[7] S. Clesse and J. García-Bellido, Phys. Dark Universe **15**, 142 (2017).
[8] S. Clesse and J. García-Bellido, Phys. Dark Universe **18**, 105 (2017).

[9] M. Sasaki, T. Suyama, T. Tanaka, and S. Yokoyama, Phys. Rev. Lett. **117**, 061101 (2016); **121**, 059901(E) (2018).
[10] M. Raidal, V. Vaskonen, and H. Veermäe, J. Cosmol. Astropart. Phys. 09 (2017) 037.
[11] Y. Ali-Haïmoud, E. D. Kovetz, and M. Kamionkowski, Phys. Rev. D **96**, 123523 (2017).
[12] B. J. Kavanagh, D. Gaggero, and G. Bertone, Phys. Rev. D **98**, 023536 (2018).
[13] B. P. Abbott *et al.* (LIGO Scientific and Virgo Collaborations), Phys. Rev. Lett. **116**, 061102 (2016).
[14] B. P. Abbott *et al.* (LIGO Scientific and Virgo Collaborations), Phys. Rev. X **6**, 041015 (2016); **8**, 039903(E) (2018).
[15] B. P. Abbott *et al.* (LIGO Scientific and Virgo Collaborations), Phys. Rev. Lett. **118**, 221101 (2017); **121**, 129901 (E) (2018).
[16] B. P. Abbott *et al.* (LIGO Scientific and Virgo Collaborations), Phys. Rev. Lett. **116**, 241103 (2016).
[17] B. P. Abbott *et al.* (LIGO Scientific and Virgo Collaborations), Phys. Rev. Lett. **119**, 141101 (2017).
[18] Y. B. Zel'dovich and I. D. Novikov, Sov. Astron. **10**, 602 (1967).
[19] S. Hawking, Mon. Not. R. Astron. Soc. **152**, 75 (1971).
[20] B. J. Carr and S. W. Hawking, Mon. Not. R. Astron. Soc. **168**, 399 (1974).
[21] S. W. Hawking, Nature (London) **248**, 30 (1974).
[22] S. W. Hawking, Commun. Math. Phys. **43**, 199 (1975).
[23] D. N. Page, Phys. Rev. D **13**, 198 (1976).
[24] M. Yu. Khlopov, Res. Astron. Astrophys. **10**, 495 (2010).
[25] B. J. Carr, K. Kohri, Y. Sendouda, and J. Yokoyama, Phys. Rev. D **81**, 104019 (2010).
[26] X. Calmet, B. Carr, and E. Winstanley, *Quantum Black Holes*, Springer Briefs in Physics (Springer, Berlin, 2014).
[27] K. M. Belotsky, A. D. Dmitriev, E. A. Esipova, V. A. Gani, A. V. Grobov, M. Yu. Khlopov, A. A. Kirillov, S. G. Rubin, and I. V. Svadkovsky, Mod. Phys. Lett. A **29**, 1440005 (2014).
[28] B. Carr, F. Kuhnel, and M. Sandstad, Phys. Rev. D **94**, 083504 (2016).
[29] M. Sasaki, T. Suyama, T. Tanaka, and S. Yokoyama, Classical Quantum Gravity **35**, 063001 (2018).
[30] K. Sato, M. Sasaki, H. Kodama, and K.-i. Maeda, Prog. Theor. Phys. **65**, 1443 (1981).
[31] K.-i. Maeda, K. Sato, M. Sasaki, and H. Kodama, Phys. Lett. **108B**, 98 (1982).
[32] V. A. Berezin, V. A. Kuzmin, and I. I. Tkachev, Phys. Lett. **120B**, 91 (1983).
[33] C. J. Hogan, Phys. Lett. **143B**, 87 (1984).
[34] S. W. Hawking, Phys. Lett. B **231**, 237 (1989).
[35] A. Polnarev and R. Zembowicz, Phys. Rev. D **43**, 1106 (1991).
[36] M. Crawford and D. N. Schramm, Nature (London) **298**, 538 (1982).
[37] S. W. Hawking, I. G. Moss, and J. M. Stewart, Phys. Rev. D **26**, 2681 (1982).
[38] H. Kodama, M. Sasaki, and K. Sato, Prog. Theor. Phys. **68**, 1979 (1982).
[39] L. J. Hall and S. Hsu, Phys. Rev. Lett. **64**, 2848 (1990).
[40] I. G. Moss, Phys. Rev. D **50**, 676 (1994).
[41] R. V. Konoplich, S. G. Rubin, A. S. Sakharov, and M. Yu. Khlopov, Yad. Fiz. **62**, 1705 (1999) [Phys. At. Nucl. **62**, 1593 (1999)].
[42] K. Jedamzik and J. C. Niemeyer, Phys. Rev. D **59**, 124014 (1999).
[43] M. Yu. Khlopov, R. V. Konoplich, S. G. Rubin, and A. S. Sakharov, Gravitation Cosmol. **6**, 153 (2000).
[44] E. Cotner and A. Kusenko, Phys. Rev. Lett. **119**, 031103 (2017).
[45] E. Cotner and A. Kusenko, Phys. Rev. D **96**, 103002 (2017).
[46] E. Cotner, A. Kusenko, and V. Takhistov, Phys. Rev. D **98**, 083513 (2018).
[47] B. J. Carr, Astrophys. J. **201**, 1 (1975).
[48] P. Ivanov, P. Naselsky, and I. Novikov, Phys. Rev. D **50**, 7173 (1994).
[49] J. Yokoyama, Astron. Astrophys. **318**, 673 (1997).
[50] M. Shibata and M. Sasaki, Phys. Rev. D **60**, 084002 (1999).
[51] S. Young, C. T. Byrnes, and M. Sasaki, J. Cosmol. Astropart. Phys. 07 (2014) 045.
[52] B. J. Carr and J. E. Lidsey, Phys. Rev. D **48**, 543 (1993).
[53] B. J. Carr, J. H. Gilbert, and J. E. Lidsey, Phys. Rev. D **50**, 4853 (1994).
[54] J. García-Bellido, A. D. Linde, and D. Wands, Phys. Rev. D **54**, 6040 (1996).
[55] A. Taruya, Phys. Rev. D **59**, 103505 (1999).
[56] A. M. Green and K. A. Malik, Phys. Rev. D **64**, 021301 (2001).
[57] B. A. Bassett and S. Tsujikawa, Phys. Rev. D **63**, 123503 (2001).
[58] S. Pi, Y.-l. Zhang, Q.-G. Huang, and M. Sasaki, J. Cosmol. Astropart. Phys. 05 (2018) 042.
[59] K. J. Mack, J. P. Ostriker, and M. Ricotti, Astrophys. J. **665**, 1277 (2007).
[60] M. Ricotti, J. P. Ostriker, and K. J. Mack, Astrophys. J. **680**, 829 (2008).
[61] A. S. Josan, A. M. Green, and K. A. Malik, Phys. Rev. D **79**, 103520 (2009).
[62] F. Capela, M. Pshirkov, and P. Tinyakov, Phys. Rev. D **87**, 123524 (2013).
[63] A. M. Green, Phys. Rev. D **94**, 063530 (2016).
[64] N. Bellomo, J. L. Bernal, A. Raccanelli, and L. Verde, J. Cosmol. Astropart. Phys. 01 (2018) 004.
[65] F. Kühnel and K. Freese, Phys. Rev. D **95**, 083508 (2017).
[66] B. Carr, M. Raidal, T. Tenkanen, V. Vaskonen, and H. Veermäe, Phys. Rev. D **96**, 023514 (2017).
[67] A. M. Green, Phys. Rev. D **96**, 043020 (2017).
[68] J. García-Bellido and S. Clesse, Phys. Dark Universe **19**, 144 (2018).
[69] M. Zumalacarregui and U. Seljak, Phys. Rev. Lett. **121**, 141101 (2018).
[70] J. García-Bellido, S. Clesse, and P. Fleury, Phys. Dark Universe **20**, 95 (2018).
[71] M. A. Monroy-Rodríguez and C. Allen, Astrophys. J. **790**, 159 (2014).
[72] T. D. Brandt, Astrophys. J. **824**, L31 (2016).
[73] T. S. Li *et al.* (DES Collaboration), Astrophys. J. **838**, 8 (2017).

[74] S. M. Koushiappas and A. Loeb, Phys. Rev. Lett. **119**, 041102 (2017).
[75] D. Gaggero, G. Bertone, F. Calore, R. M. T. Connors, M. Lovell, S. Markoff, and E. Storm, Phys. Rev. Lett. **118**, 241101 (2017).
[76] Y. Inoue and A. Kusenko, J. Cosmol. Astropart. Phys. 10 (2017) 034.
[77] A. Hektor, G. Hütsi, and M. Raidal, Astron. Astrophys. **618**, A139 (2018).
[78] J. Manshanden, D. Gaggero, G. Bertone, R. M. T. Connors, and M. Ricotti, J. Cosmol. Astropart. Phys. 06 (2019) 026.
[79] Y. Tada and S. Yokoyama, Phys. Rev. D **91**, 123534 (2015).
[80] S. Young and C. T. Byrnes, J. Cosmol. Astropart. Phys. 04 (2015) 034.
[81] L. Chen, Q.-G. Huang, and K. Wang, J. Cosmol. Astropart. Phys. 12 (2016) 044.
[82] Y. Ali-Haïmoud and M. Kamionkowski, Phys. Rev. D **95**, 043534 (2017).
[83] B. Horowitz, arXiv:1612.07264.
[84] D. Aloni, K. Blum, and R. Flauger, J. Cosmol. Astropart. Phys. 05 (2017) 017.
[85] V. Poulin, P. D. Serpico, F. Calore, S. Clesse, and K. Kohri, Phys. Rev. D **96**, 083524 (2017).
[86] J. L. Bernal, N. Bellomo, A. Raccanelli, and L. Verde, J. Cosmol. Astropart. Phys. 10 (2017) 052.
[87] T. Nakama, B. Carr, and J. Silk, Phys. Rev. D **97**, 043525 (2018).
[88] H. Deng, A. Vilenkin, and M. Yamada, J. Cosmol. Astropart. Phys. 07 (2018) 059.
[89] J. Chluba, A. L. Erickcek, and I. Ben-Dayan, Astrophys. J. **758**, 76 (2012).
[90] K. Kohri, T. Nakama, and T. Suyama, Phys. Rev. D **90**, 083514 (2014).
[91] B. J. Carr, Mon. Not. R. Astron. Soc. **194**, 639 (1981).
[92] N. Afshordi, P. McDonald, and D. N. Spergel, Astrophys. J. **594**, L71 (2003).
[93] R. Murgia, G. Scelfo, M. Viel, and A. Raccanelli, arXiv:1903.10509.
[94] J. D. Bowman, A. E. E. Rogers, R. A. Monsalve, T. J. Mozdzen, and N. Mahesh, Nature (London) **555**, 67 (2018).
[95] A. P. Beardsley, M. F. Morales, A. Lidz, M. Malloy, and P. M. Sutter, Astrophys. J. **800**, 128 (2015).
[96] G. Mellema *et al.*, Exp. Astron. **36**, 235 (2013).
[97] M. Valdés, C. Evoli, A. Mesinger, A. Ferrara, and N. Yoshida, Mon. Not. R. Astron. Soc. **429**, 1705 (2013).
[98] M. Sitwell, A. Mesinger, Y.-Z. Ma, and K. Sigurdson, Mon. Not. R. Astron. Soc. **438**, 2664 (2014).
[99] C. Evoli, A. Mesinger, and A. Ferrara, J. Cosmol. Astropart. Phys. 11 (2014) 024.
[100] I. P. Carucci, F. Villaescusa-Navarro, M. Viel, and A. Lapi, J. Cosmol. Astropart. Phys. 07 (2015) 047.
[101] L. Lopez-Honorez, O. Mena, Á. Moliné, S. Palomares-Ruiz, and A. C. Vincent, J. Cosmol. Astropart. Phys. 08 (2016) 004.
[102] A. Berlin, D. Hooper, G. Krnjaic, and S. D. McDermott, Phys. Rev. Lett. **121**, 011102 (2018).
[103] G. D'Amico, P. Panci, and A. Strumia, Phys. Rev. Lett. **121**, 011103 (2018).
[104] H. Liu and T. R. Slatyer, Phys. Rev. D **98**, 023501 (2018).
[105] A. Mitridate and A. Podo, J. Cosmol. Astropart. Phys. 05 (2018) 069.
[106] M. Pospelov, J. Pradler, J. T. Ruderman, and A. Urbano, Phys. Rev. Lett. **121**, 031103 (2018).
[107] D. Aristizabal Sierra and C. S. Fong, Phys. Lett. B **784**, 130 (2018).
[108] K. K. Boddy, V. Gluscevic, V. Poulin, E. D. Kovetz, M. Kamionkowski, and R. Barkana, Phys. Rev. D **98**, 123506 (2018).
[109] E. D. Kovetz, V. Poulin, V. Gluscevic, K. K. Boddy, R. Barkana, and M. Kamionkowski, Phys. Rev. D **98**, 103529 (2018).
[110] R. Barkana, N. J. Outmezguine, D. Redigolo, and T. Volansky, Phys. Rev. D **98**, 103005 (2018).
[111] R. Barkana, Nature (London) **555**, 71 (2018).
[112] A. Fialkov, R. Barkana, and A. Cohen, Phys. Rev. Lett. **121**, 011101 (2018).
[113] M. Escudero, L. Lopez-Honorez, O. Mena, S. Palomares-Ruiz, and P. Villanueva-Domingo, J. Cosmol. Astropart. Phys. 06 (2018) 007.
[114] A. Schneider, Phys. Rev. D **98**, 063021 (2018).
[115] M. Safarzadeh, E. Scannapieco, and A. Babul, Astrophys. J. **859**, L18 (2018).
[116] A. Lidz and L. Hui, Phys. Rev. D **98**, 023011 (2018).
[117] L. Lopez-Honorez, O. Mena, and P. Villanueva-Domingo, Phys. Rev. D **99**, 023522 (2019).
[118] A. Hektor, G. Hutsi, L. Marzola, M. Raidal, V. Vaskonen, and H. Veermäe, Phys. Rev. D **98**, 023503 (2018).
[119] J.-O. Gong and N. Kitajima, J. Cosmol. Astropart. Phys. 08 (2017) 017.
[120] J.-O. Gong and N. Kitajima, J. Cosmol. Astropart. Phys. 11 (2018) 041.
[121] H. Tashiro and N. Sugiyama, Mon. Not. R. Astron. Soc. **435**, 3001 (2013).
[122] J. L. Bernal, A. Raccanelli, L. Verde, and J. Silk, J. Cosmol. Astropart. Phys. 05 (2018) 017.
[123] P. Madau, A. Meiksin, and M. J. Rees, Astrophys. J. **475**, 429 (1997).
[124] S. Furlanetto, S. P. Oh, and F. Briggs, Phys. Rep. **433**, 181 (2006).
[125] J. R. Pritchard and A. Loeb, Rep. Prog. Phys. **75**, 086901 (2012).
[126] S. R. Furlanetto, *Understanding the Epoch of Cosmic Reionization: Challenges and Progress*, edited by Andrei Mesinger (Springer International Publishing, New York, 2015).
[127] M. Kuhlen, P. Madau, and R. Montgomery, Astrophys. J. **637**, L1 (2006).
[128] C. Feng and G. Holder, Astrophys. J. **858**, L17 (2018).
[129] A. Ewall-Wice, T. C. Chang, J. Lazio, O. Dore, M. Seiffert, and R. A. Monsalve, Astrophys. J. **868**, 63 (2018).
[130] S. Fraser *et al.*, Phys. Lett. B **785**, 159 (2018).
[131] J. Mirocha and S. R. Furlanetto, Mon. Not. R. Astron. Soc. **483**, 1980 (2019).
[132] J. Dowell and G. B. Taylor, Astrophys. J. **858**, L9 (2018).
[133] R. Jana, B. B. Nath, and P. L. Biermann, Mon. Not. R. Astron. Soc. **483**, 5329 (2019).

[134] A. Fialkov and R. Barkana, Mon. Not. R. Astron. Soc. **486**, 1763 (2019).
[135] A. Ewall-Wice, T.-C. Chang, and T. J. W. Lazio, arXiv:1903.06788.
[136] P. Sharma, Mon. Not. R. Astron. Soc. **481**, L6 (2018).
[137] F. Yuan and R. Narayan, Annu. Rev. Astron. Astrophys. **52**, 529 (2014).
[138] I. T. Iliev, P. R. Shapiro, A. Ferrara, and H. Martel, Astrophys. J. **572**, L123 (2002).
[139] S. Ichimaru, Astrophys. J. **214**, 840 (1977).
[140] M. J. Rees, E. S. Phinney, M. C. Begelman, and R. D. Blandford, Nature (London) **295**, 17 (1982).
[141] R. Narayan and I. Yi, Astrophys. J. **428**, L13 (1994).
[142] R. D. Blandford and M. C. Begelman, Mon. Not. R. Astron. Soc. **303**, L1 (1999).
[143] R. Narayan, in *Lighthouses of the Universe*, edited by M. Gilfanov, R. Sunyaev *et al.* (Springer-Verlag, Berlin, 2002).
[144] S. Pellegrini, Astrophys. J. **624**, 155 (2005); **636**, 564(E) (2006).
[145] F.-G. Xie and F. Yuan, Mon. Not. R. Astron. Soc. **427**, 1580 (2012).
[146] N. I. Shakura and R. A. Sunyaev, Astron. Astrophys. **24**, 337 (1973).
[147] F. Hoyle and R. A. Lyttleton, *Mathematical Proceedings of the Cambridge Philosophical Society* (Cambridge University Press, Cambridge, United Kingdom, 1939), Vol. 35, pp. 405–415.
[148] F. Hoyle and R. A. Lyttleton, *Mathematical Proceedings of the Cambridge Philosophical Society* (Cambridge University Press, Cambridge, United Kingdom, 1940), Vol. 36, pp. 325–330.
[149] F. Hoyle and R. A. Lyttleton, *Mathematical Proceedings of the Cambridge Philosophical Society* (Cambridge University Press, Cambridge, United Kingdom, 1940), Vol. 36, pp. 424–437.
[150] F. Hoyle and R. A. Lyttleton, Mon. Not. R. Astron. Soc. **101**, 227 (1941).
[151] H. Bondi and F. Hoyle, Mon. Not. R. Astron. Soc. **104**, 273 (1944).
[152] H. Bondi, Mon. Not. R. Astron. Soc. **112**, 195 (1952).
[153] D. Tseliakhovich and C. Hirata, Phys. Rev. D **82**, 083520 (2010).
[154] C. Dvorkin, K. Blum, and M. Kamionkowski, Phys. Rev. D **89**, 023519 (2014).
[155] I. El Mellah and F. Casse, Mon. Not. R. Astron. Soc. **454**, 2657 (2015).
[156] M. R. Krumholz, C. F. McKee, and R. I. Klein, Astrophys. J. **618**, 757 (2005).
[157] M. R. Krumholz, C. F. McKee, and R. I. Klein, Astrophys. J. **638**, 369 (2006).
[158] T. R. Slatyer, Phys. Rev. D **93**, 023521 (2016).
[159] J. Chluba and R. M. Thomas, Mon. Not. R. Astron. Soc. **412**, 748 (2011).
[160] Y. Ali-Haïmoud and C. M. Hirata, Phys. Rev. D **82**, 063521 (2010).
[161] J. Chluba, G. M. Vasil, and L. J. Dursi, Mon. Not. R. Astron. Soc. **407**, 599 (2010).
[162] A. Mesinger, S. Furlanetto, and R. Cen, Mon. Not. R. Astron. Soc. **411**, 955 (2011).
[163] L. J. Greenhill and G. Bernardi, arXiv:1201.1700.
[164] J. O. Burns, T. J. W. Lazio, S. D. Bale, J. D. Bowman, R. F. Bradley, C. L. Carilli, S. R. Furlanetto, G. J. A. Harker, A. Loeb, and J. R. Pritchard, Adv. Space Res. **49**, 433 (2012).
[165] J. B. Muñoz and A. Loeb, Nature (London) **557**, 684 (2018).
[166] S. McGaugh, Res. Notes AAS **2**, 37 (2018).
[167] Z. Kang, arXiv:1803.04928.
[168] Y. Yang, Phys. Rev. D **98**, 103503 (2018).
[169] A. A. Costa, R. C. G. Landim, B. Wang, and E. Abdalla, Eur. Phys. J. C **78**, 746 (2018).
[170] T. R. Slatyer and C.-L. Wu, Phys. Rev. D **98**, 023013 (2018).
[171] A. Falkowski and K. Petraki, arXiv:1803.10096.
[172] J. B. Muñoz, C. Dvorkin, and A. Loeb, Phys. Rev. Lett. **121**, 121301 (2018).
[173] J. C. Hill and E. J. Baxter, J. Cosmol. Astropart. Phys. 08 (2018) 037.
[174] S. J. Clark, B. Dutta, Y. Gao, Y.-Z. Ma, and L. E. Strigari, Phys. Rev. D **98**, 043006 (2018).
[175] K. Cheung, J.-L. Kuo, K.-W. Ng, and Y.-L. S. Tsai, Phys. Lett. B **789**, 137 (2019).
[176] S. Hirano and V. Bromm, Mon. Not. R. Astron. Soc. **480**, L85 (2018).
[177] M. S. Mahdawi and G. R. Farrar, J. Cosmol. Astropart. Phys. 10 (2018) 007.
[178] S. Witte, P. Villanueva-Domingo, S. Gariazzo, O. Mena, and S. Palomares-Ruiz, Phys. Rev. D **97**, 103533 (2018).
[179] Z. S. Ali *et al.*, Astrophys. J. **809**, 61 (2015).
[180] S. Wyithe, A. Loeb, and P. Geil, Mon. Not. R. Astron. Soc. **383**, 1195 (2008).
[181] T.-C. Chang, U.-L. Pen, J. B. Peterson, and P. McDonald, Phys. Rev. Lett. **100**, 091303 (2008).
[182] A. Loeb and S. Wyithe, Phys. Rev. Lett. **100**, 161301 (2008).
[183] F. Villaescusa-Navarro, M. Viel, K. K. Datta, and T. R. Choudhury, J. Cosmol. Astropart. Phys. 09 (2014) 050.
[184] T.-C. Chang *et al.* (GBT-HIM Team), *American Astronomical Society Meeting Abstracts*, Vol. 227 (American Astronomical Society, Washington DC, USA, 2016).
[185] K. Bandura, G. E. Addison, M. Amiri, J. R. Bond, D. Campbell-Wilson, L. Connor, J.-F. Cliche, G. Davis, M. Deng, and N. Denman, in *Ground-Based and Airborne Telescopes V,* Society of Photo-Optical Instrumentation Engineers (SPIE) Conference Series Vol. 9145 (Society of Photo-Optical Instrumentation Engineers, Washington, USA, 2014), p. 914522.
[186] X. Chen, IAU Gen. Assem. **22**, 2252187 (2015).
[187] P. Bull, P. G. Ferreira, P. Patel, and M. G. Santos, Astrophys. J. **803**, 21 (2015).
[188] R. Narayan and I. Yi, Astrophys. J. **452**, 710 (1995).
[189] A. A. Zdziarski and R. Svensson, Astrophys. J. **344**, 551 (1989).
[190] M. Dijkstra, Z. Haiman, and A. Loeb, Astrophys. J. **613**, 646 (2004).
[191] J. M. Shull and M. E. van Steenberg, Astrophys. J. **298**, 268 (1985).
[192] J. A. Peacock, *Cosmological Physics* (Cambridge University Press, Cambridge, United Kingdom, 1999).

[193] G. L. Bryan and M. L. Norman, Astrophys. J. **495**, 80 (1998).
[194] P. R. Shapiro and I. T. Iliev, Mon. Not. R. Astron. Soc. **307**, 203 (1999).
[195] J. F. Navarro, C. S. Frenk, and S. D. M. White, Astrophys. J. **490**, 493 (1997).
[196] S. Chongchitnan and J. Silk, Mon. Not. R. Astron. Soc. **426**, L21 (2012).
[197] R. K. Sheth and G. Tormen, Mon. Not. R. Astron. Soc. **308**, 119 (1999).
[198] R. K. Sheth, H. J. Mo, and G. Tormen, Mon. Not. R. Astron. Soc. **323**, 1 (2001).
[199] R. Barkana and A. Loeb, Astrophys. J. **626**, 1 (2005).
[200] R. Barkana and A. Loeb, Phys. Rep. **349**, 125 (2001).
[201] A. E. Evrard, Astrophys. J. **363**, 349 (1990).
[202] A. Blanchard, D. Vall-Gabaud, and G. A. Mamon, Astron. Astrophys. **264**, 365 (1992).
[203] M. Tegmark, J. Silk, M. J. Rees, A. Blanchard, T. Abel, and F. Palla, Astrophys. J. **474**, 1 (1997).
[204] B. Ciardi, A. Ferrara, and T. Abel, Astrophys. J. **533**, 594 (2000).
[205] Z. Haiman, T. Abel, and M. J. Rees, Astrophys. J. **534**, 11 (2000).
[206] J. C. Pober *et al.*, Astrophys. J. **768**, L36 (2013).
[207] J. R. Pritchard and S. R. Furlanetto, Mon. Not. R. Astron. Soc. **376**, 1680 (2007).
[208] S. Baek, B. Semelin, P. Di Matteo, Y. Revaz, and F. Combes, Astron. Astrophys. **523**, A4 (2010).
[209] J. C. Pober *et al.*, Astrophys. J. **782**, 66 (2014).
[210] J. C. Pober, A. R. Parsons, D. R. DeBoer, P. McDonald, M. McQuinn, J. E. Aguirre, Z. Ali, R. F. Bradley, T.-C. Chang, and M. F. Morales, Astron. J. **145**, 65 (2013).
[211] A. Parsons, M. McQuinn, D. Jacobs, J. Aguirre, and J. Pober, Astrophys. J. **753**, 81 (2012).
[212] N. S. Kern, A. Liu, A. R. Parsons, A. Mesinger, and B. Greig, Astrophys. J. **848**, 23 (2017).
[213] H. Shimabukuro and B. Semelin, Mon. Not. R. Astron. Soc. **468**, 3869 (2017).
[214] N. Gillet, A. Mesinger, B. Greig, A. Liu, and G. Ucci, Mon. Not. R. Astron. Soc. **484**, 282 (2019).
[215] P. La Plante and M. Ntampaka, Astrophys. J. **880**, 110 (2019).
[216] W. D. Jennings, C. A. Watkinson, F. B. Abdalla, and J. D. McEwen, Mon. Not. R. Astron. Soc. **483**, 2907 (2019).
[217] A. Doussot, E. Eames, and B. Semelin, arXiv:1904.04106.
[218] B. Greig and A. Mesinger, Mon. Not. R. Astron. Soc. **449**, 4246 (2015).
[219] R. A. Allsman *et al.* (MACHO Collaboration), Astrophys. J. **550**, L169 (2001).
[220] P. Tisserand *et al.* (EROS-2 Collaboration), Astron. Astrophys. **469**, 387 (2007).
[221] L. Wyrzykowski *et al.*, Mon. Not. R. Astron. Soc. **416**, 2949 (2011).

The Astrophysical Journal, 907:44 (14pp), 2021 January 20 https://doi.org/10.3847/1538-4357/abd245

Removing Astrophysics in 21 cm Maps with Neural Networks

Pablo Villanueva-Domingo[1] and Francisco Villaescusa-Navarro[2,3]
[1] Instituto de Física Corpuscular (IFIC), CSIC-Universitat de Valencia, Apartado de Correos 22085, E-46071, Spain; pablo.villanueva@ific.uv.es
[2] Department of Astrophysical Sciences, Princeton University, Peyton Hall, Princeton, NJ 08544, USA; fvillaescusa@princeton.edu
[3] Center for Computational Astrophysics, Flatiron Institute, 162 5th Avenue, New York, NY 10010, USA
Received 2020 July 28; revised 2020 December 7; accepted 2020 December 8; published 2021 January 27

Abstract

Measuring temperature fluctuations in the 21 cm signal from the epoch of reionization and the cosmic dawn is one of the most promising ways to study the universe at high redshifts. Unfortunately, the 21 cm signal is affected by both cosmology and astrophysics processes in a nontrivial manner. We run a suite of 1000 numerical simulations with different values of the main astrophysical parameters. From these simulations we produce tens of thousands of 21 cm maps at redshifts $10 \leqslant z \leqslant 20$. We train a convolutional neural network to remove the effects of astrophysics from the 21 cm maps and output maps of the underlying matter field. We show that our model is able to generate 2D matter fields not only that resemble the true ones visually but whose statistical properties agree with the true ones within a few percent down to scales $\simeq 2$ Mpc^{-1}. We demonstrate that our neural network retains astrophysical information that can be used to constrain the value of the astrophysical parameters. Finally, we use saliency maps to try to understand which features of the 21 cm maps the network is using in order to determine the value of the astrophysical parameters.

Unified Astronomy Thesaurus concepts: Cosmology (343); Cold dark matter (265); Dark matter (353); Dark matter distribution (356); H I line emission (690); Intergalactic medium (813); Cosmological evolution (336); Convolutional neural networks (1938); Large-scale structure of the universe (902)

1. Introduction

Measuring the cosmological 21 cm signal represents one of the most promising probes to gain insight into the evolution of the intergalactic medium (IGM), as well as an observational challenge. On the one hand, detecting the global average temperature is the main goal of several current and future experiments, such as Experiment to Detect the Global EoR Signature (EDGES; Bowman et al. 2018), Large Aperture Experiment to Detect the Dark Ages (LEDA; Greenhill & Bernardi 2012), and Dark Ages Polarimeter PathfindER (DAPPER; Burns et al. 2019). The observation of an absorption profile located at a redshift of $z \sim 17$ has been recently claimed by the EDGES experiment, with an amplitude that is twice the maximum predicted within the context of the ΛCDM model (Bowman et al. 2018). This has motivated a large number of studies in the literature (see, e.g., Barkana 2018; Fialkov et al. 2018; Muñoz & Loeb 2018; Pospelov et al. 2018; Witte et al. 2018; Ewall-Wice et al. 2019; Fialkov & Barkana 2019; Lopez-Honorez et al. 2019; Mirocha & Furlanetto 2019).

Meanwhile, other experiments are devoted to observing the fluctuations of the differential brightness temperature, which allows better foreground removal and contains additional information beyond that from the global signal. Among them, there are some examples that have already collected data, such as Giant Metrewave Radio Telescope (GMRT), LOw Frequency ARray (LOFAR; van Haarlem et al. 2013), Murchison Widefield Array (MWA; Bowman et al. 2013), and Precision Array for Probing the Epoch of Reionization (PAPER; Ali et al. 2015), while others like Hydrogen Epoch of Reionization Array (HERA; DeBoer et al. 2017) or Square Kilometer Array (SKA; Mellema et al. 2013) are expected to be completed within this decade.

The aim of these experiments is to shed light on the poorly known astrophysics that shaped the reionization of the universe. The amplitude, time dependence, and spatial distribution of the 21 cm signal not only arise from astrophysics but also are sensitive to cosmology. Therefore, 21 cm maps can be used to improve our knowledge not only of astrophysics but also about cosmology. Unfortunately, the signatures left by astrophysics and cosmology on the 21 cm signal are coupled in a nontrivial manner: the spatial distribution of matter, with its peaks (halos), positions, and sizes (masses), is mainly driven by cosmology. In those halos, gas is able to cool down and form stars and black holes. The radiation from those objects ionizes neutral hydrogen, creating bubbles that can expand tens of megaparsecs. The 21 cm signal is sensitive to all these astrophysical processes.

Ideally, we would like to constrain both cosmology and astrophysics from 21 cm observations. Lots of work has been done in extracting this information from either the power spectrum or other summary statistics (Mao et al. 2008; Mesinger et al. 2013; Sitwell et al. 2014; Greig & Mesinger 2015; Liu & Parsons 2016; Cohen et al. 2018; Majumdar et al. 2018; Watkinson et al. 2018; Muñoz 2019a, 2019b; Park et al. 2019). In this work we take a different route and try to *undo* the effects of astrophysics on 21 cm maps. By doing that, we will obtain a map with the spatial distribution of matter in the high-redshift universe. Those maps will be an invaluable source of information. First, they will represent a picture of the universe at high redshift, allowing us to cross-check the validity of the ΛCDM model. Second, since those maps will be obtained at high redshift, the power spectrum will be able to retrieve all cosmological information down to very small scales. Third, those maps can be used for cross-correlation studies with different tracers, e.g., high-redshift galaxies, to learn about the halo–galaxy connection. Fourth, those maps will allow us to better reconstruct the effect of astrophysics and its correlation with the matter field.

The Astrophysical Journal, 907:44 (14pp), 2021 January 20

In this paper, we make use of machine learning techniques to *undo* the effects of astrophysics and produce 2D matter density fields in real space from 21 cm maps in redshift space. In particular, we made use of deep convolutional neural networks. Recently, artificial neural networks have been broadly applied to cosmology, and specifically to study the 21 cm signal. Examples of this are extracting the global signal from different foreground models (Choudhury et al. 2020), generating accurate HI fields and 21 cm maps by means of Generative Adversarial Networks (Zamudio-Fernandez et al. 2019; Feder et al. 2020; List & Lewis 2020), and emulating reionization simulations to extract information about the underlying astrophysical processes, by means of the 21 cm power spectrum (Kern et al. 2017; Shimabukuro & Semelin 2017; Schmit & Pritchard 2018) or by studying the tomography of the HI fields, directly from 21 cm maps (Hassan et al. 2017; Gillet et al. 2019; Hassan et al. 2020; Kwon et al. 2020).[4]

Our goal is to train a neural network to output the projected dark matter field in real space, from a 21 cm map in redshift space generated with given astrophysics. Therefore, we want to undo the effects of both astrophysics and redshift-space distortions. By feeding the network with 21 cm maps produced by different values of the astrophysical parameters and different realizations (due to cosmic variance), we are forcing the model to learn to undo the effects of astrophysics, within their range of variation. We focus on the redshift range between 20 and 10, where astrophysical heating and Lyα coupling become important. For lower redshifts, however, the map between density fluctuations and brightness temperature becomes more complex, and the results of the network worsen, as we shall further show.

We have run 1000 numerical simulations with different values of three of the most relevant astrophysical parameters, making use of the publicly available code `21cmFAST` (Mesinger et al. 2011; Park et al. 2019). From these simulations we then extract 120 2D slices per simulation of 21 cm and matter maps that we use as training, validation, and test sets for our neural network.

The paper is organized as follows. In Section 2, we briefly describe the fundamentals of the 21 cm signal and the relevant astrophysical parameters that can leave an imprint on it. We discuss the methods we use in Section 3. We then present the main results of this work in Section 4. Finally, we draw the main conclusions in Section 5.

2. The 21 cm Signal

2.1. Fundamentals of the 21 cm Signal

In this work we have made use of the publicly available code `21cmFAST` (Mesinger et al. 2011; Park et al. 2019) to compute the matter density and 21 cm maps. We start by reviewing some basic aspects of this redshifted line that are implemented in the code (see, e.g., Madau et al. 1997; Furlanetto et al. 2006; Pritchard & Loeb 2012; Furlanetto 2015; Mesinger 2019 for comprehensive reviews). This line arises from the spin-flip transition in the hyperfine structure of the hydrogen atom. The intensity of the line depends on the ratio between the excited and ground states of the 1s level of neutral hydrogen. This ratio is conventionally characterized by the so-called spin temperature T_S and is formally defined through the following equation:

$$\frac{n_1}{n_0} = 3\, e^{-T_0/T_S}, \tag{1}$$

where n_0 and n_1 are the number density of neutral hydrogen atoms in the ground (singlet) and excited (triplet) states, $T_0 = h\nu_0/k_B = 0.068$ K is the energy splitting of the hyperfine transition, and the factor of 3 comes from the degeneracy of the triplet excited state.

Three main processes can modify the population of the excited and ground levels and determine therefore the spin temperature: (i) absorption and stimulated emission induced by a background radiation field, namely, the cosmic microwave background (CMB); (ii) collisions of neutral hydrogen atoms with other hydrogen atoms, free protons, or free electrons; and (iii) indirect spin-flip transitions produced by scattering with Lyα photons, the so-called Wouthuysen–Field effect (Wouthuysen 1952; Field 1958). The spin temperature can be expressed as a weighted sum over the temperatures that characterize the efficiency of each of these processes:

$$T_S = \frac{T_{\rm CMB} + y_k\, T_k + y_\alpha\, T_\alpha}{1 + y_k + y_\alpha}, \tag{2}$$

where $T_{\rm CMB}$, T_k, and T_α are the temperature of the CMB, the kinetic temperature of the gas, and the color temperature, respectively. The latter is associated with the intensity of the Lyα emission, and for most cases of interest, $T_\alpha \simeq T_k$ (although `21cmFAST` computes it properly by an iterative procedure). The strengths of the different processes are given by the coupling coefficients, y_k for collisions and y_α for Lyα scatttering (see, e.g., Furlanetto et al. 2006; Pritchard & Loeb 2012 for more details).

It is customary to express the intensity of the 21 cm line relative to the CMB in terms of the differential brightness temperature δT_b. Taking into account absorption and emission of 21 cm photons in the expanding IGM, it is possible to write the solution of the radiative transfer equation as

$$\delta T_b = \frac{T_S - T_{\rm CMB}}{1+z}(1 - e^{-\tau_{\nu_0}}), \tag{3}$$

where τ_{ν_0} is the optical depth of the 21 cm line. Since the value of the optical depth, at the redshifts of interest, is always small, we can safely expand the exponential term and express the differential brightness temperature as (Furlanetto et al. 2006; Pritchard & Loeb 2012)

$$\begin{aligned}\delta T_b \simeq\ & 27 x_{\rm HI}(1+\delta)\left(1 - \frac{T_{\rm CMB}}{T_S}\right) \\ & \times \left(\frac{1}{1 + H^{-1}\partial v_r/\partial r}\right)\left(\frac{1+z}{10}\right)^{1/2} \\ & \times \left(\frac{0.15}{\Omega_{\rm m}h^2}\right)^{1/2}\left(\frac{\Omega_{\rm b}h^2}{0.023}\right){\rm mK},\end{aligned} \tag{4}$$

where $\delta = \rho/\bar{\rho} - 1$ is the matter overdensity, H is the Hubble parameter, $\partial v_r/\partial r$ is the velocity gradient along the line of sight, and $\Omega_{\rm m}$ and $\Omega_{\rm b}$ are the matter and baryon abundances of the universe at $z = 0$. We see in Equation (4) that δT_b depends directly on δ, providing an indirect measurement of the

[4] For a comprehensive list of applications of neural networks (and machine learning in general) to cosmology, see https://github.com/georgestein/ml-in-cosmology.

Table 1
Astrophysical Parameters Considered in the 1000 21cmFAST Simulations

Parameter	Range	Units	Description
$L_{X\leqslant 2\mathrm{keV}}/\mathrm{SFR}$	$10^{40}-10^{41}$	erg s^{-1} $M_\odot^{-1}$ yr	Luminosity of X-rays per star formation rate
M_{min}	10^8-10^9	$M_\odot$	Minimum mass of a halo to host star formation
$N_{\gamma/b_\star}$	10^3-10^4	—	Number of ionizing photons per baryon

Note. The parameter values are arranged in a Latin hypercube.

underlying matter density field. Nevertheless, it also depends on several other quantities related to the ionization and thermal state of the hydrogen, such as the neutral fraction x_{HI}, the temperature of the gas, and the Lyα background field, through the spin temperature T_S. Therefore, the link between the 21 cm field δT_b and the density field δ is not trivial.

We emphasize that the above equation holds at every spatial location, $\boldsymbol{x}$. The quantity expected to be observed is $\delta T_b(\boldsymbol{x})$, and without knowing quantities like $x_{\mathrm{HI}}(\boldsymbol{x})$ and $T_S(\boldsymbol{x})$, it is not possible to determine the value of $\delta(\boldsymbol{x})$. Fortunately, there are nontrivial spatial correlations between those fields and the underlying matter field. A neural network may be able to identify these correlations and use them to infer the value of $\delta(\boldsymbol{x})$ from $\delta T_b(\boldsymbol{x})$. This is the purpose of this work.

2.2. Astrophysical Parameters

Now we turn our attention to the relevant astrophysical processes that can leave an imprint on the thermal history of the universe and, consequently, affect the amplitude and spatial distribution of the 21 cm signal. Here we assume a minimal model with three free parameters. We refer the reader to Mesinger et al. (2011) and Park et al. (2019) for more details on the astrophysical parameterization.

First, we assume that only the most massive halos are able to cool down the gas to trigger star formation. Therefore, low-mass halos do not form stars and do not contribute to the X-ray and UV radiation. Following the 21cmFAST parameterization (Mesinger et al. 2011; Park et al. 2019), we take an exponential cutoff for the mass integration $\exp(-M_{\mathrm{min}}/M_h)$, with M_h the mass of the halo and M_{min} the threshold mass, assumed to be redshift independent. This minimum mass could be related to a virial temperature of the halo of $\sim 10^4$ K, where the threshold of atomic cooling lies, which corresponds to $\sim 10^8\, M_\odot$. Reasonable values for M_{min} lie within $10^8 \lesssim M_{\mathrm{min}}/M_\odot \lesssim 10^9$.

One of the most important processes that affects the 21 cm signal is the X-ray emission from astrophysical sources, such as high-mass X-ray binaries (HMXBs), which are able to heat up the gas of the IGM. Since the specific properties of the heating sources at high redshift are not well known yet, we assume a power-law profile for the X-ray emissivity, with L_X^0 being the normalization and α_X the spectral index. We fix $\alpha_X = 1$, consistent with HMXB.[5] Notice that not all photons will affect the IGM. On the one hand, only X-rays with energy $\lesssim 2$ keV are absorbed in the IGM, as photons with energies above this threshold have mean free paths larger than the Hubble length. On the other hand, low-energy photons below some threshold E_0 (taken as 0.5 keV) are absorbed locally in the galaxy and are not able to escape to the IGM. The relevant luminosity that determines the heating of the IGM is therefore given by the integration of the emissivity over the range mentioned above:

$$\frac{L_{X\leqslant 2\,\mathrm{keV}}}{\mathrm{SFR}} = \int_{E_0}^{2\,\mathrm{keV}} dE\, \frac{L_X^0}{\mathrm{SFR}}\, E^{-\alpha_X}, \tag{5}$$

where SFR is the star formation rate. Therefore, we employ $L_{X\leqslant 2\mathrm{keV}}/\mathrm{SFR}$ as a free parameter. This is a rather important quantity since it determines how quickly and abruptly the gas is heated, affecting the amplitude and width of the 21 cm absorption profile. We let it vary in a physical relevant range between 10^{40} and 10^{41} ergs s^{-1} $M_\odot^{-1}$ yr.

Lastly, we consider the modeling of the UV radiation, which is important for two reasons. First of all, UV photons redshifting to Lyman resonances in the high-z universe can cascade to the Lyα line and couple the spin temperature to the kinetic temperature of the gas (the so-called Wouthuysen–Field effect), driving the 21 cm signal to an absorption period. Second, when the emission of UV photons is efficient enough, the H II regions around galaxies can grow and merge, ionizing the full IGM, which is known as the epoch of reionization. Since the 21 cm signal is proportional to the fraction of neutral hydrogen, it is very sensitive to the reionization epoch and therefore to the number of ionizing photons. We account for the normalization of the UV luminosity by means of the number of UV photons per stellar baryon $N_{\gamma/b_\star}$, which we consider can range from $\sim 10^3$ to 10^4. We follow the default 21cmFAST parameterization, where the spectrum normalization between the Lyα and Lyman limit is proportional to the value of $N_{\gamma/b_\star}$, assuming Population II stars. Note that other choices of astrophysical parameters would also be meaningful, such as the fraction of baryons into stars, assumed here to be $f_* = 0.05$. Given that we focus on $z \gtrsim 10$ and the degenerations between some astrophysical parameters, the above choice seems appropriate. Furthermore, it presents the advantage of being easy to interpret regarding their impact on the 21 cm signal and IGM history.

Table 1 summarizes the three free astrophysical parameters and their ranges of variation considered. Notice that for more realistic scenarios we may consider additional free parameters (Greig & Mesinger 2015; Park et al. 2019), but for the sake of simplicity here we restrict to this minimal choice. It is convenient to note that adding more parameters may worsen the performance of the network, since neural networks usually generalize badly. There is no guarantee to maintain the effectiveness to predict the density fields in that case. Hence, this has to be regarded as a proof of concept, rather than a conclusive work.

[5] We do not expect this choice to have a strong impact on the results, given that several degeneracies between the astrophysical parameters are present, and thus small changes in the spectral index may be countered by variations in, e.g., the luminosity.

3. Methods

In this section, we describe the numerical simulations run, the architecture of the neural network used, and some caveats of the training process.

3.1. Simulations

We use the publicly available code `21cmFAST`[6] (Mesinger et al. 2011; Park et al. 2019) to generate the 21 cm and matter density fields at different redshifts. From an initial linear Gaussian field, this software employs several semianalytical approximations to evolve the density field, produce a map of collapsed regions, and compute the 21 cm brightness temperature. The 21 cm cubes are generated taking into account redshift-space distortions. The 3D box of the simulations contains 200^3 voxels, with a physical length of 300 Mpc, having therefore a spatial resolution of 1.5 Mpc. To generate the density field, second-order Lagrangian perturbation theory (2LPT) has been employed (Scoccimarro 1998).

We run 1000 simulations of 3D boxes (*coeval* cubes in the `21cmFAST` terminology) with different initial random seeds[7] varying the value of the most relevant astrophysical parameters, discussed in Section 2.2: the threshold mass to host star formation in galaxies, $M_{\rm min}$; the X-ray luminosity over star formation rate, $L_{X\leqslant 2{\rm keV}}/{\rm SFR}$; and the number of ionizing photons per baryon, $N_{\gamma/b_\star}$. The values of the astrophysical parameters are laid down from a Latin hypercube with 1000 elements that spans the range outlined in Table 1.

Since the effects arising from varying cosmological parameters are expected to be much smaller than the ones from astrophysics, we fix the value of those to the constraints from the Planck Collaboration (Aghanim et al. 2020). Notice that while the 21 cm field is highly affected by the different astrophysical processes, the matter density field is not, since `21cmFAST` does not account for back-reaction of gas into dark matter.

For simplicity and computational efficiency, we work with 2D maps instead of 3D fields. For each simulation we take 20 2D slices orthogonal to the line of sight, in order to account for redshift-space distortions in the 21 cm field. Each slice contains $200 \times 200 \times 4$ voxels, which we project along the line of sight (i.e., summing the 4 voxels over the third dimension, where the redshift-space distortions lie) to obtain 2D maps with 200×200 pixels. Each map represents thus a region of the universe with dimensions $300 \times 300 \times 6\,{\rm Mpc}^3$. We do that for each field in the simulation, namely, the brightness temperature and the density field. We have verified that producing maps with slightly larger or smaller width along the line of sight does not change our conclusions.

Figure 1 shows an example of 21 cm and matter density fields at three different redshifts from one simulation. The effects of some of the cosmic processes introduced in Section 2 become patent. At $z \sim 20$, the 21 cm radiation is in the absorption regime, since the newborn galaxies start to emit UV radiation that redshifts toward Lyman frequencies and produces the Wouthuysen–Field effect. As new galaxies are formed, the UV radiation field increases and the Lyα coupling becomes more important, reaching large amplitudes (in absolute value) at $z \sim 15$. At redshifts $z \sim 10$, the X-ray heating has become efficient enough to raise the temperature of the IGM and therefore reduce the absorption of the brightness temperature. Moreover, the ionizing radiation starts to spread abroad and expands the H II regions around the overdensities, appearing as the bright spots in the δT_b panel. Note that this chronology strongly depends on the specific value of the astrophysical parameters; different values would lead to different timings of these evolutionary phases. On the other hand, the matter density field evolves quasi-linearly over time at high redshifts, entering into a nonlinear regime at lower redshifts and on smaller scales.

3.2. Network Architecture

We now outline the details of the model employed. As stated before, the goal is to undo the effect of astrophysics on 21 cm maps at redshifts $z \in [10-20]$, to recover the spatial distribution of the underlying matter field. We achieve this by training a deep convolutional neural network using the U-Net architecture (Ronneberger et al. 2015), first proposed in the context of biomedical image segmentation.[8] This kind of architecture has already applied to cosmological fields (see, e.g., Giusarma et al. 2019; He et al. 2019). Figure 2 shows a scheme of the network architecture, while each layer and block are detailed in Table 2. We define a *unit layer* as the composition of a 2D convolutional layer, a batch normalization (BN), and a rectified linear unit (ReLU). Summarizing, the U-Net architecture consists of a contracting path, or encoder, followed by an expanding path, or decoder:

1. The *contracting path* is composed by the application of three contracting blocks, each of them composed by two unit layers followed by a 2×2 max pooling operation. This reduces the spatial size by half.
2. The *expanding path* consists of the application of three expanding blocks, each of them composed by two unit layers followed by a transposed convolution layer for upsampling. The output of each upsampling is concatenated with the result from the contracting block (before pooling) of the same level, by means of *skip connections*. Finally, there is a final block of two unit layers plus a final convolutional layer.

For each convolutional layer, 3×3 filters are employed, stride 1, applying a zero-padding with size 1. For the transpose convolutional layers, the filters also have a 3×3 kernel, with stride 2 and padding 1. The network employed here has a total of $15 \times ({\rm Conv2D} \times {\rm ReLU} \times {\rm BN}) + 3\ {\rm MaxPool} + 3$ transposed convolution $= 51$ layers and $\sim$8.5 millions of parameters. Notice that the U-Net architecture is similar to the well-known Autoencoders (see, e.g., Goodfellow et al. 2016), with the main difference being that here layers between the encoder and the decoder are linked by means of the skip connections. This aspect is missing in typical Autoencoders, which are designed to recover an image with information only from the bottleneck. Notice also that, in general, Autoencoders aim at producing the same output as the input, while this is not our purpose here.

[6] https://github.com/andreimesinger/21cmFAST

[7] We have repeated the whole analysis of this paper using simulations with the same initial random seed. In this case, the network is able to reconstruct the dark matter field with a much higher accuracy. Notice that in this case the network will have to predict always the same output, so this is a much simpler task than the one we are trying to accomplish here.

[8] Our implementation of the specific CNN architecture is based on the one in https://github.com/Hsankesara/DeepResearch/tree/master/UNet.

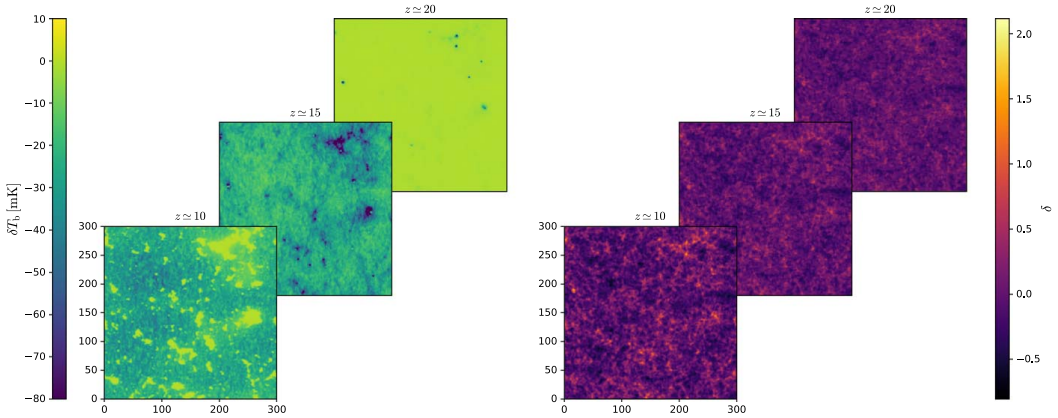

Figure 1. 2D slices of the differential brightness temperature δT_b in redshift space (left) and the matter density field in real space δ (right) at redshifts 10, 15, and 20. The purpose of this work is to train neural networks that find the mapping between the 21 cm and dark matter maps.

3.3. Training of the CNN

As mentioned above, we make use of two different fields simulated by `21cmFAST`: (1) the 21 cm field δT_b (the input) and (2) the matter density δ (the output). We have employed maps from the 1000 numerical simulations to train, validate, and test the network. A total of 70% of the maps are used for training, while 15% are used for validation and the last 15% for testing. We employ simulations at a fixed redshift for training. As stated before, we extract 20 2D slices from the 3D box, having therefore 20 slices per simulation. Moreover, we employ data augmentation to mock new data and to force the network to learn the symmetries of the problem, e.g., rotational and parity invariance. We apply all eight possible rigid transformations in 2D to each slice: four rigid rotations with their respective reflections. Therefore, from each simulation box, we obtain $20 \times 8 = 160$ slices for δT_b and the same for δ.

We have trained our network throughout 40 epochs[9] with a batch size of 30, employing an Adam optimizer (Kingma & Ba 2014) with a learning rate of 10^{-3} and values 0.5 and 0.999 for the β parameters.[10] Although the Adam optimizer already adapts the learning rate during the training, a scheduler has been applied in order to improve the convergence, reducing the learning rate by a factor of 10 if the validation loss does not decrease after 10 epochs. For the loss function, we choose the mean squared error. We apply L2 regularization, with a weight decay value of 10^{-4}. Our network and codes used for training, validation, and testing are publicly available.[11]

We have explored the impact of variations in the architecture and hyperparameters on the final results. We have checked that, with enough epochs, the results are insensitive to remove the first concatenation of the U-Net. Similarly, a deeper network (i.e., including more unit layers, with corresponding pooling and concatenation links) does not produce any noticeable gain. Neither including more channels (i.e., enhancing the depth) nor using different activation functions, such as Leaky ReLU, leads to a significant improvement. Placing the batch normalization layer after the activation function does not have any impact on the results, giving equally good results.

[9] We have verified that our results do not improve when training for more epochs.

[10] These are common hyperparameters, widely employed in deep learning literature. For definitions and detailed explanations, see, e.g., Goodfellow et al. (2016).

[11] https://github.com/PabloVD/21cmDeepLearning

4. Results

In this section we present the results of our analysis. Before quantifying the performance of the neural network, we can visually overview the success of the model at a sample of 2D slices from the same simulation in Figure 3.

We train our network using pairs of 21 cm and matter density maps from the training set. Once the network has been trained, we input a 21 cm map from the test set (which the network has not seen before; bottom left panel), and the network produces an output (top right panel) that aims at matching the real underlying density field (top left panel). At a glance, the predicted field emulates with high accuracy the true field. This is confirmed looking at the logarithm of the absolute error $\log_{10}(|\delta_{\rm true}(r) - \delta_{\rm pred}(r)|)$ (bottom right), which, however, takes larger values at the overdense spots in the δ maps, as one could naively expect.

In the following subsections we make use of different summary statistics to quantify the performance of the network. In the next subsections, we show results for a network trained with fields at $z \simeq 15$, except in Sections 4.4 and 4.5, where we compare the outputs at other times.

4.1. Power Spectrum and Cross-correlation Coefficient

One of the most commonly used statistics in cosmology is the *two-point correlation function*

$$\xi(r) = \langle \delta(x)\delta(x+r) \rangle, \tag{6}$$

or its Fourier transform, the *power spectrum*

$$P(k) = \int d^2r \xi(r) e^{ik\cdot r}. \tag{7}$$

Notice that in our definition we employ a differential element of area d^2r instead of volume since we are working with 2D slices. We compute numerically the power spectra from our fields, making use of the Python package `powerbox`

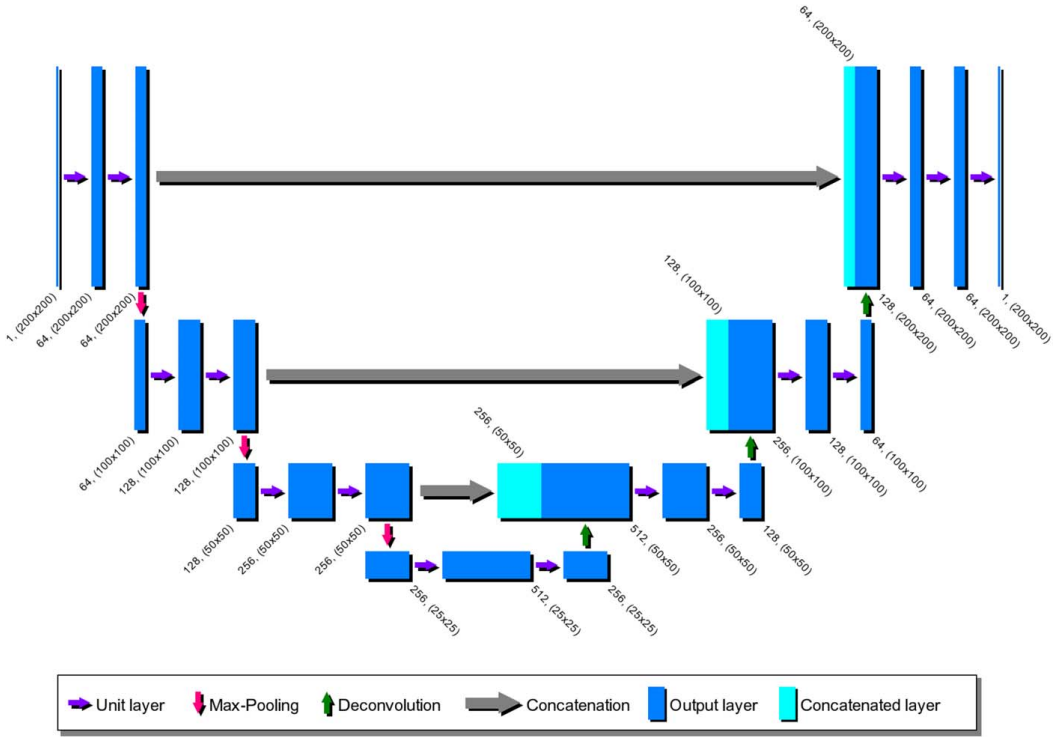

Figure 2. Scheme of the architecture employed in this work. The numbers associated with each output layer represent the number of channels (depth) and the spatial dimensions.

Table 2
Different Blocks Used in the Architecture of Our Neural Network

Block	Layers
Unit layer	Convolution layer
	Batch normalization
	ReLU
Contracting block	Unit layer
	Unit layer
	Max pooling
Expanding block	Unit layer
	Unit layer
	Transpose convolution
	Concatenation
Final block	Unit layer
	Unit layer
	Convolution layer

(Murray 2018). In the left panel of Figure 4 we show the mean power spectrum over 100 samples of the testing data set, with the bands representing the standard deviation among the testing slices. We can see that the power spectrum of the prediction from the CNN (blue line) reproduces with high accuracy that of the real density field (red line). The prediction slightly worsens at small scales, presenting a 2σ tension at $k \simeq 2$ Mpc^{-1}. To better quantify the deviation in the amplitude between both power spectra, we compute the *transfer function* $T(k)$, defined as

$$T(k) = \sqrt{\frac{P_{\rm pred}(k)}{P_{\rm true}(k)}}, \tag{8}$$

with $P_{\rm true}(k)$ and $P_{\rm pred}(k)$ being the (auto-correlated) power spectra for the true and predicted fields, respectively. The top right panel of Figure 4 depicts this quantity as a function of scale, along with its standard deviation region, showing that for all the scales the transfer function is very close to 1, especially on the largest scales, where the perfect correlation case $T(k) = 1$ is covered by the standard deviation region. Our model is able to recover the correct amplitude of the power spectrum within 5% and 8% down to $k \simeq 0.7\,{\rm Mpc}^{-1}$ and $k \simeq 2\,{\rm Mpc}^{-1}$, respectively.

While the above transfer function informs us on the correlation between mode amplitudes, it is insensitive to mode phases. In order to quantify the accuracy on that, we made use of the cross-correlation coefficient, $r(k)$, defined as

$$r(k) = \frac{P_{\rm true\times pred}(k)}{\sqrt{P_{\rm true}(k)P_{\rm pred}(k)}}, \tag{9}$$

with $P_{\rm true\times pred}(k)$ being the cross-power spectrum between the true and the predicted fields. With this definition, a perfect match between the prediction and the true field would

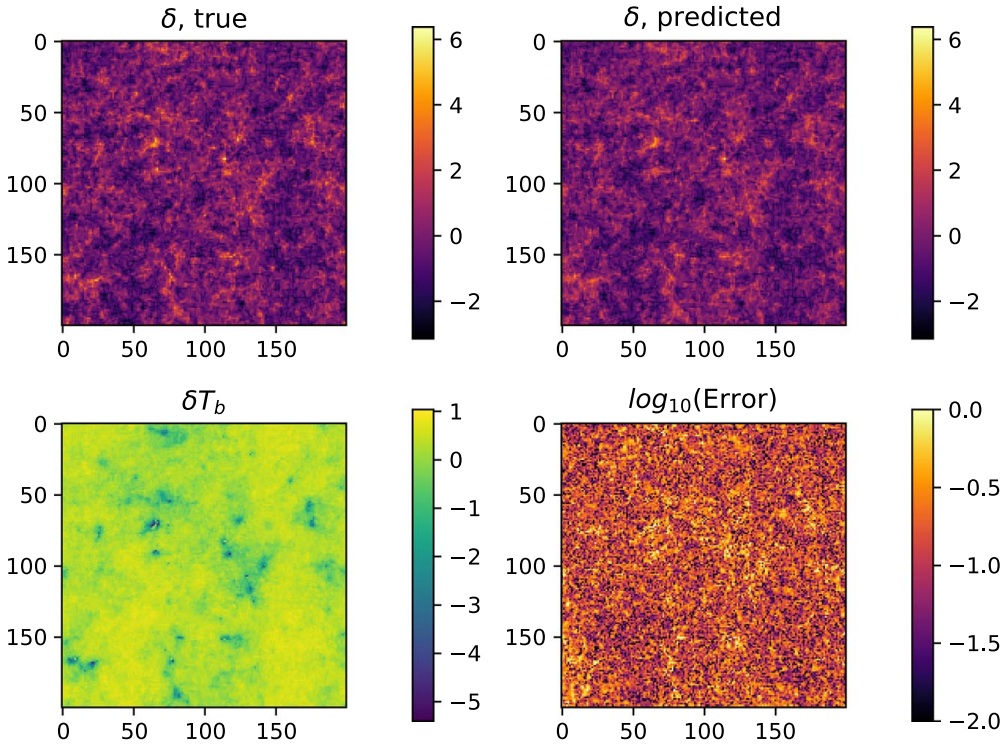

Figure 3. We train a neural network to output 2D matter density fields from 21 cm maps. The 21 cm maps have different values of the astrophysical parameters. Once the network is trained, we input a 21 cm map from the test set (bottom left), which outputs the matter density field of the top right panel. The true matter density map is shown in the top left panel. Residuals between predicting and true are displayed in the bottom right panel. As can be seen, the network produces matter fields that visually resemble very well the true ones. All results shown here are at $z = 15$.

correspond to $r = 1$. In the bottom right panel of Figure 4 we show $r(k)$ as a function of scale, which is also close to 1 for all scales, especially at $k \lesssim 3 \times 10^{-1}$ Mpc^{-1}, implying that there is a strong phase correlation between the prediction and the true fields. This can also be seen directly in Figure 3. Similarly to the transfer function, our network matches the results from the true fields within 5% and 8% down to $k \simeq 0.7$ Mpc^{-1} and $k \simeq 2\,h$Mpc^{-1}, respectively.

We note that the standard deviation of our results, both for the transfer function and for the cross-correlation coefficient, increases on large scales. This reflects the effect of cosmic variance, which is larger on large scales. The deviations we find in both the transfer function and cross-correlation coefficient on small scales may be due to different effects. For instance, at small scales, nonlinearities are more important, and the network could have more trouble mapping the density and the 21 cm field at that regime. Another reason may be that the effects of astrophysics strongly dominate on these scales, and they destroy the spatial correlations with the matter field. The different modifications of the network architecture mentioned at the end of Section 3.3 were not able to improve the performance. One could in principle presume that a deeper and wider network, with a much finer tuning of the hyperparameters, may improve our results. However, it may be that the effect of astrophysics smooths out correlations at small scales and significant improvement would not be attainable.

4.2. Probability Distribution Function

We now consider a different statistic that contains information complementary to that of the power spectrum: the probability distribution function (pdf). Although the initial distribution that leaves the seeds of the overdensities is taken as Gaussian centered around $\delta = 0$, the evolution under nonlinear dynamics modifies the shape of the pdf. Figure 5 depicts the pdf's for the true and predicted density fields, showing the resemblance between both cases. The pdf is computed in each sample image, with the solid lines and shaded regions showing the mean and standard deviation, respectively, among the different testing images. We find a very good agreement between both pdf's, both in the peak and on the tails. To have a more quantitative insight of this similarity, the moments of both distributions have been computed, finding that the mean, variance, and skewness of the pdf's coincide within the percent error, while the kurtosis presents a relative deviation of less than ∼10%, with the predicted pdf presenting slightly less pronounced tails than the target one.

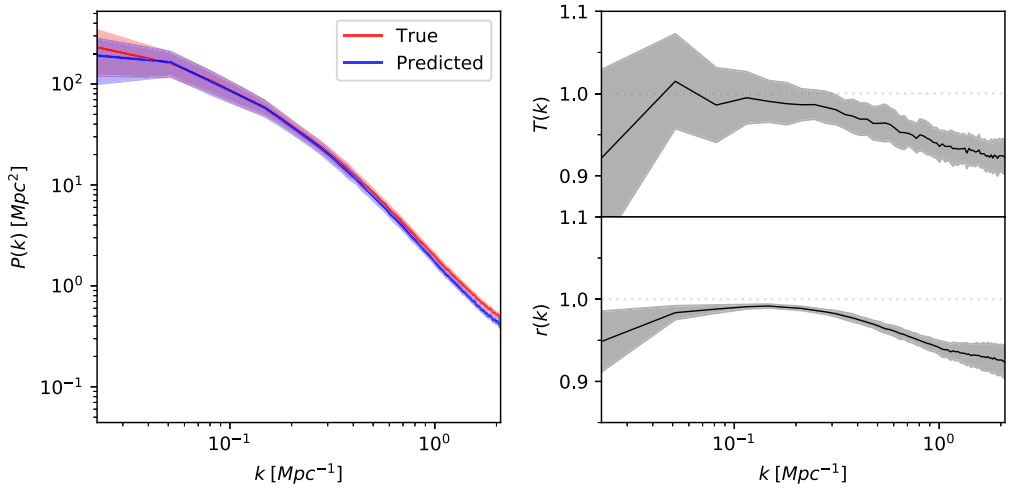

Figure 4. Once the network has been trained, we use it to produce matter density fields from 100 21 cm maps from the test set. The blue line in the left panel shows the mean of the power spectrum of these output maps, while its band represents the standard deviation. The red line and band display the results for the power spectrum of the true maps. The right panels show the transfer function (top right), defined in Equation (8), and the cross-correlation coefficient (bottom right), defined in Equation (9). Our network is able to reconstruct the amplitudes and phases of the modes of the matter field within a few percent down to very small scales.

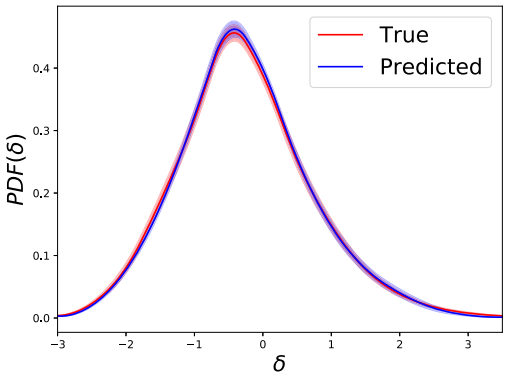

Figure 5. The pdf for the true (red) and predicted (blue) normalized density fields, with their corresponding standard deviation regions.

This shows that our network is able to capture the underlying distribution of the matter field, which at these redshifts starts developing non-Gaussian tails.

4.3. Astrophysical Information Embedded in the Network

We have shown in the previous sections that our network is able to learn the mapping between the 21 cm and density maps. To do so, it has to remove, or undo, the astrophysical processes. Thus, it is expected that different layers of the network carry out information about astrophysics, which the network will use to remove their effects. In order to check this, we have made use of an additional neural network to perform regression to the astrophysical parameters.

Specifically, we employ the result of the encoder, until the third max pooling layer, to quantify the amount of information encoded in the contracting part of the U-Net. The procedure is as follows. First, a 21 cm map is input to the network. Next, we take the output of the encoder and pass it to another neural network that predicts the value of the three astrophysical parameters of the input 21 cm map. While the encoder of the U-Net is fixed, i.e., its weights are kept fixed, the weights of the second network are tuned via gradient descent to match the value of the astrophysical parameters of the input 21 cm map.

Table 3
Architecture of the Convolutional Neural Network Employed to Predict the Value of the Astrophysical Parameters from 21 cm Maps

Block	Output Size	Weights
Input	$1 \times 200 \times 200$	—
Encoder	$256 \times 25 \times 25$	Fixed/trainable
Unit layer	$512 \times 13 \times 13$	Trainable
Unit layer	$1028 \times 7 \times 7$	Trainable
Unit layer	$1028 \times 4 \times 4$	Trainable
Fully connected	100	Trainable
ReLU	100	—
Fully connected	3	Trainable

Note. The Encoder is the contracting path of the U-Net shown in Figure 2.

This second network has the following architecture: three unit layers (i.e., three 2D convolutional layers, each of them followed by a batch normalization and an ReLu activation), employing stride 2 for the downsampling instead of pooling. The output is flattened and passed through a fully connected layer with ReLU as the activation function and a dropout of 0.2. Finally, a last fully connected layer provides the three values for the astrophysical parameters. A scheme of the architecture is shown in Table 3. We employ the same loss function and optimizer as used with the U-Net. We train for 20 epochs and do not observe significant improvements for larger trainings.

The top panels of Figure 6 show the predicted values of the astrophysical parameters versus their true values at $z \simeq 15$. We

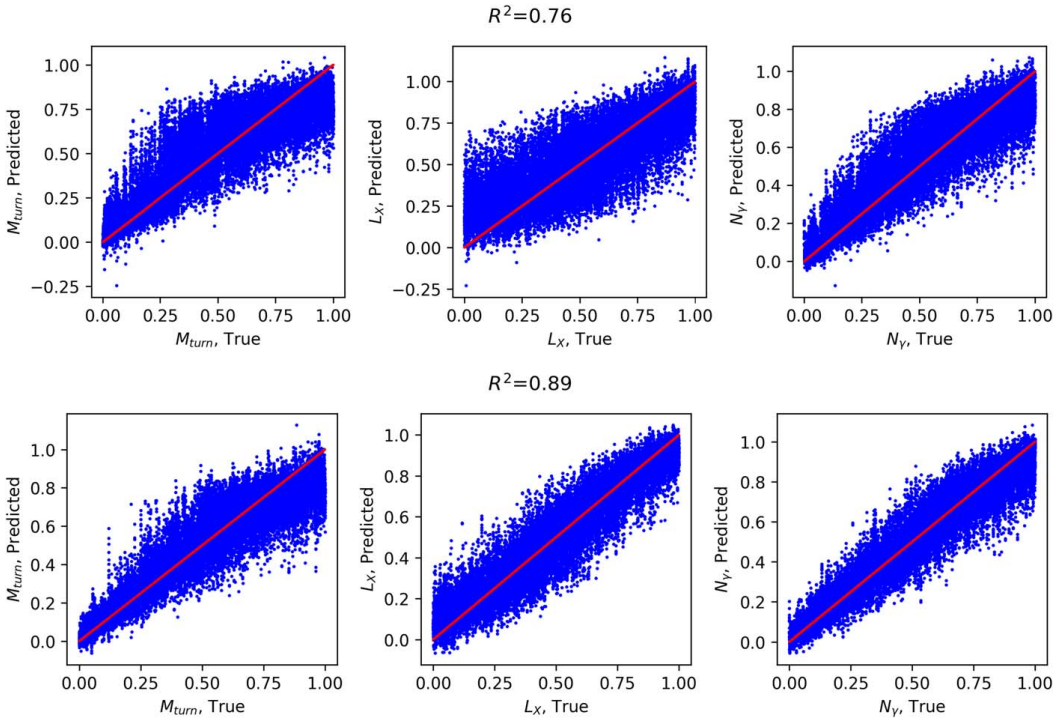

Figure 6. Our network is trained to output the matter field from 21 cm maps with different astrophysics. Thus, it is expected that the network will embed astrophysical information, which it will use to undo its effects on 21 cm maps. We used a second neural network, which takes as input the output of the encoder part of the U-Net and performs regression to the value of the astrophysical parameters. Results are shown in the top row. Notice that the weights of the encoder are fixed. We have repeated the same exercise but training also the weights of the encoder to perform regression; results are shown in the bottom row. We find that the encoder part of the U-Net indeed contains astrophysical information, although not as much as if the encoder were trained to perform parameter regression. Parameter values are normalized with respect to the mean. Results are shown at $z \simeq 15$.

find that the network is able to approximate the proper mean value for each parameter, although with a large dispersion, having a linear correlation coefficient of $R^2 = 0.76$. We note that this information is contained in the encoder arm of the U-Net, which has been previously trained to reproduce the density fields, i.e., the encoder part is not trained again with the loss function of the astrophysical parameters.

The above experiment points out that our network indeed contains astrophysical information that can be used to regress the value of the astrophysical parameters. However, the network is not trained to achieve that, so it is expected that a network specifically trained to perform parameter regression may perform better. In order to verify that, we have repeated the above experiments but training also the weights of the U-Net encoder.

The results of such tests are shown in the bottom row of Figure 6, where the linear correlation coefficient is enhanced up to $R^2 = 0.89$ and the accuracy of the network has improved significantly. This suggests that the encoder trained to predict the matter density field does not carry all the possible astrophysical information. We note that more astrophysical information may be embedded into the decoder part, which we are not quantifying here. However, it may be that, rather than learning directly the astrophysical information, the U-Net is able to reproduce the density field by other means.

We have verified that different variations on the architecture, such as adding or removing convolutional, pooling, or fully connected layers, do not significantly improve our results.

Notice that previous works have already employed neural networks to predict the underlying astrophysical models (Hassan et al. 2017; Kern et al. 2017; Shimabukuro & Semelin 2017; Schmit & Pritchard 2018; Gillet et al. 2019; Hassan et al. 2020), obtaining much better accuracies than the ones shown here. However, these works employ inputs at several redshifts, as opposed to our case, since we want to explore the amount of astrophysical information encoded in the U-Net. Nonetheless, as we show in the next section, we can recover the astrophysical parameters with high accuracy at lower redshifts.

4.4. Redshift Dependence

In the previous subsections we have focused our analysis at $z \simeq 15$. Here we investigate the dependence on redshift of our results.

We have checked that at higher redshifts, $z \simeq 20$, we still recover the different statistics considered with a similar accuracy to that at $z \simeq 15$. However, at lower redshifts, the

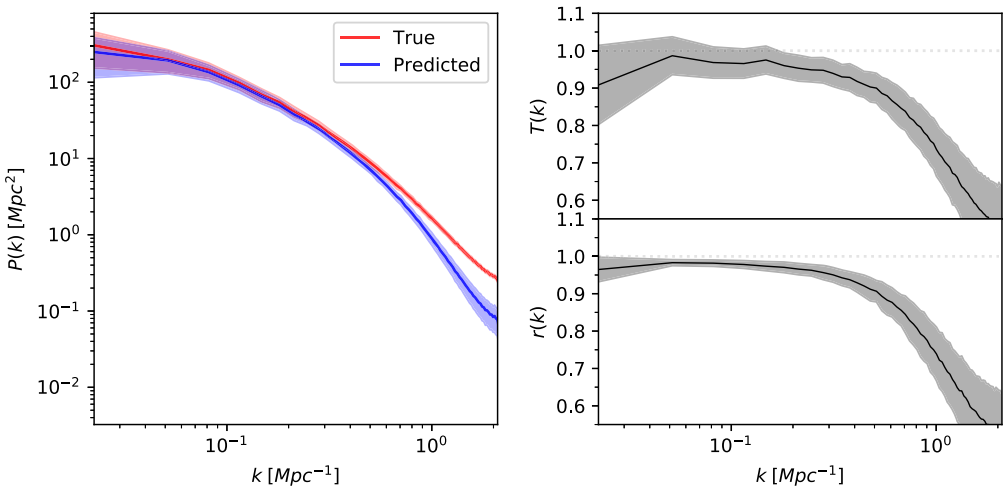

Figure 7. Same as Figure 4, but at $z \simeq 10$.

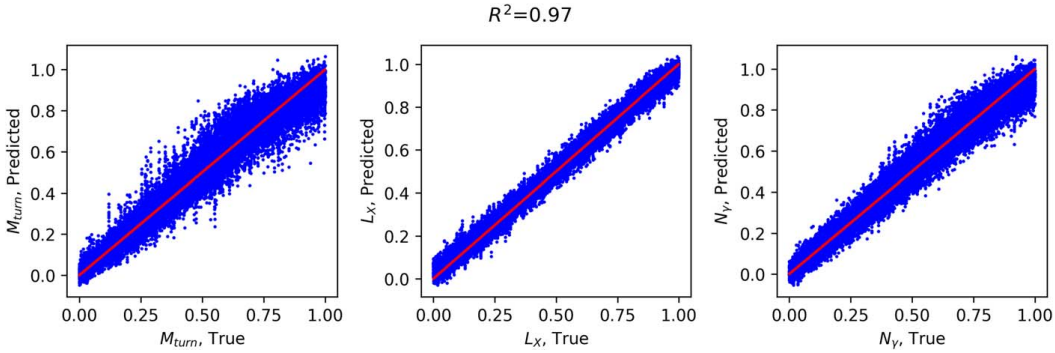

Figure 8. Same as the bottom panel of Figure 6, but at $z \simeq 10$.

performance of the U-Net worsens significantly. To illustrate this, we show results for the power spectrum, transfer function, and cross-correlation coefficient at $z \simeq 10$ in Figure 7. Although the amplitude of the power spectrum is still well recovered on large scales, it is further suppressed for wavenumbers lower than $\simeq 3 \times 10^{-1}$ Mpc^{-1}. Both $T(k)$ and $r(k)$ depart significantly from 1 on small scales.

We believe that the reason for the worse performance is mainly driven by the presence of reionization processes. At these low redshifts, the release of UV radiation from galactic sources is efficient enough to ionize a significant portion of the universe, forming H II bubbles around each source. These bubbles start to grow and overlap at this epoch, although they may not be completely ionized yet. In an analogous way, temperature inhomogeneities driven by the heating processes may become more important at these stages too, which contribute to the 21 cm maps. Therefore, the link between the differential brightness temperature and the matter density field gets weaker, and δ cannot be recovered as accurately as in previous times, when the astrophysical processes were not so advanced.

However, while it is more difficult to reproduce the matter density field from the brightness temperature, we find that the astrophysical parameters can be predicted with much higher accuracy, as we show in Figure 8 for maps at $z \simeq 10$. For this regression, we retrain the same neural network of the previous section, training at the same time the U-Net encoder and the final layers, as this was shown to achieve better results.

The linear correlation coefficient reaches now $R^2 = 0.97$. This better behavior happens for the same reason that we find worse results in the U-Net. The astrophysical processes are more advanced at these stages of the cosmic history. Reionization and heating processes leave significant imprints in the brightness temperature field, which are now more patent and strongly dependent on the astrophysical model. This allows the network performing regression to identify the underlying model more easily, while it is harder to find correlations with the underlying matter field. It is worth noting that this accuracy has been achieved employing only one redshift, being comparable to or even better than other cases in the literature (e.g., Gillet et al. 2019) where inputs at several redshifts have been used. The above results suggest the trend at lower

redshifts and scales that the 21 cm signal keeps astrophysical information to the detriment of the density field. It remains as an open question whether there is a limiting scale up to which the maximum information achievable can be extracted, regardless of the training and tuning of the neural network.

4.5. Saliency Maps

Although neural networks have been shown to be very successful at finding correlations and extracting information from the data, understanding what operations or features they are looking up is not an easy task. Saliency maps provide a way to quantify what pixels in the original image are the ones that have the largest influence on the output of the network (Simonyan et al. 2013). Here, we employ this method with the neural network devoted to predict the value of the astrophysical parameters, in order to try to understand what the network is looking at. Since training the encoder together with the top layers of the net provided better results, we employ that version of the astrophysical network for this test.

The saliency maps are generated as follows. First, with the neural network trained, we input a 21 cm map. Next, three saliency maps are generated by computing the derivative of the output, with respect to the input. In our case, the output is just the value of the astrophysical parameters, while our input is the 21 cm brightness temperature in each pixel of the image.

The pixels whose gradient is large (in modulus) are the ones whose variations will most largely impact the output of the network. For example, in typical classification problems in computer vision, this procedure usually tends to produce larger gradients for pixels where the object to be classified is located. The algorithm that we follow for producing the saliency maps is the so-called Vanilla Gradient. Although there are further improvements on this basic idea, the Vanilla Gradient has been shown to be robust and fast, also avoiding some problems that other techniques may present (Adebayo et al. 2018).

Figure 9 shows samples of 21 cm maps from our simulations. The red circles in the images show the locations of the pixels with the largest absolute values of the saliency maps for $M_{\rm turn}$. Darker points indicate larger gradients in modulus. Top panels show results at $z \simeq 15$, while bottom panels correspond to $z \simeq 10$. We find that the outputs of the saliency maps are redshift dependent. At $z \simeq 15$, we can clearly see in the top panel of Figure 9 that the brightest pixels of the saliency map (red points) correspond to regions in the 21 cm field relatively far from the overdensities, presenting therefore less absorption. Instead of looking at the radiative sources, as one could naively expect, the neural network seems to extract most of the astrophysical information from the underdense regions around them. On the other hand, at lower redshifts $z \simeq 10$ (bottom panel of Figure 9), when the astrophysical processes are more advanced, the neural network pays more attention to regions, or the edges of these regions, that are more heated and ionized, where the astrophysical processes are leaving stronger signatures. Nonetheless, in both cases the saliency maps highlight neutral regions far away from the sources. We note that further work is needed in order to extract more robust conclusions on where the network information is coming from.

The above results stand only for the parameter $M_{\rm turn}$, but in principle the saliency maps for the other parameters may present differences among them, since the different astrophysical processes may induce distinct features on the brightness temperature. However, we find the saliency maps for the three parameters to be pretty similar (Figure 10), which indicates that the neural network employs the same pixels of the input image for predicting any of the parameters. Nonetheless, the magnitude of the gradients varies among the different parameters. As can be seen in Figure 10, the points in the N_γ saliency map are redder and more clustered, meaning that this parameter could be more sensitive to variations of the pixels in the input image.

All these results present a step forward toward the search for an optimal estimator to extract astrophysical information from 21 cm maps. However, further research is needed in order to get a better understanding on that estimator and its properties.

5. Conclusions

Brightness temperature fluctuations in 21 cm maps contain a rich amount of information on both cosmology and astrophysics. Unfortunately, they are coupled in a nontrivial way. In this paper we have used deep convolutional neural networks to recover 2D images of the underlying matter field (in real space) from 21 cm maps in redshift space. Being able to generate 2D matter density fields at high redshifts will be beneficial for several reasons: (1) the power spectrum will allow us to extract most of the cosmological information down to pretty small scales, (2) they can be used to improve our knowledge on the halo–galaxy connection, and (3) they will allow us to better understand the impact of astrophysics on 21 cm maps.

We have run a set of 1000 numerical simulations, varying the value of three astrophysical parameters in a wide range. The values of those parameters are laid down in a Latin hypercube. From each simulation we generate both 21 cm maps and their corresponding matter density fields.

We have trained U-Net architecture to find the mapping between 21 cm maps and 2D matter density fields. Since each 21 cm map is affected by astrophysics in a different manner, the network is forced to undo astrophysical effects.

We find that at $z = 15$ our network is able to generate 2D density maps whose power spectra agree with the true ones at $\simeq$8% down to $k \simeq 2\ {\rm Mpc}^{-1}$, with a much better performance on larger scales. Similar results hold for the cross-correlation coefficient, showing that the network is able to reconstruct both mode amplitudes and phases with high accuracy. Other statistics of the generated maps, e.g., the one-point pdf, are also in excellent agreement with those of the true maps.

At lower redshifts our results become worse, likely due to the effect of nonlinearities in the matter field, but mainly because astrophysics effects become so large that the spatial correlations between the 21 cm and matter field are largely affected and become weaker.

It is expected that different layers of our network carry out information on astrophysics, as that is needed to undo their effects. We have verified this by taking the output of the U-Net encoder part and performing regression to the value of the astrophysical parameters through a secondary neural network. We find that this setup allows us to place constraints on the value of the astrophysical parameters, pointing out the presence of astrophysical information in the network.

That information is, however, not the maximum available. We have tested this by retraining the above model, but not keeping fixed the value of the encoder weights (i.e., training the encoder weights at the same time as the second network). In that case we are able to get more accurate constraints on the parameters. This indicates that while the network carries out

The Astrophysical Journal, 907:44 (14pp), 2021 January 20 Villanueva-Domingo & Villaescusa-Navarro

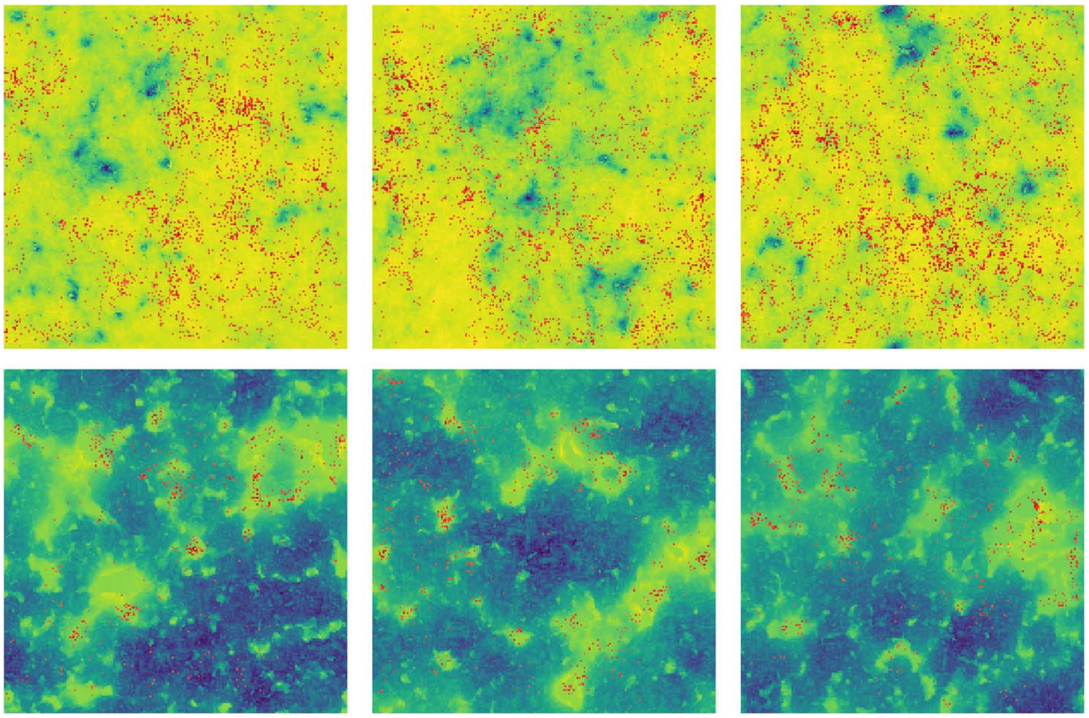

Figure 9. Samples of 21 cm brightness temperature δT_b maps at $z \simeq 15$ (top) and $z \simeq 10$ (bottom). The brightest pixels of their respective saliency maps for $M_{\rm turn}$ are superimposed as red pixels. The saliency maps are computed from the gradient of the outputs (the astrophysical parameters) with respect to the input image. Brighter pixels in the saliency map denote regions that have more impact on the output of the neural network. The maps for the other astrophysical parameters are very similar at $z \simeq 15$, although they differ at lower redshifts, as can be seen in Figure 10. While at $z \simeq 15$ the network seems to be looking at regions away from the sources, at lower redshifts the network appears to focus its attention on the heated and ionized regions.

astrophysical information, the encoder part does not maximize it for the regression task. The decoder part may contain additional astrophysical information, or the network does not need to maximize regression information to perform the mapping to the matter field.

Finally, we have made use of saliency maps to investigate the features and pixels the network is giving more weight when performing regression to the parameters. For simplicity, we use the network where the encoder is trained at the same time as the secondary network. At redshifts $z \simeq 15$, we find that the network is most sensitive to the 21 cm pixels that are far away from sources, while at lower redshifts the network seems to be focusing most of its attention on the heated and ionized regions around the sources (albeit not completely ionized yet). The usage of saliency maps, or other tools developed to interpret neural network behavior, is an important step toward identifying the best statistics to extract information from 21 cm maps.

It is important to emphasize the simplifying assumptions we have made in this work. First of all, our 21 cm maps do not include any instrumental noise. In real observations, this noise will significantly affect the temperature fluctuations of the 21 cm maps. Residual foreground removal is also expected to affect the 21 cm signal on large scales. However, these effects would mainly impact the power spectrum at small scales, where the network is not as reliable. One may deal with this issue imposing a cut at the scales where we trust the recovered statistics. Nevertheless, a complete analysis including noises and foreground would be mandatory in order to apply this network to cosmological observations.

We have used `21cmFAST` to generate the density and 21 cm fields, with a minimal choice of three free astrophysical parameters. Full hydrodynamic simulation may produce slightly different results with more complex patterns for the 21 cm field and its relation to the underlying matter field. Furthermore, the density fluctuations are computed using second-order Lagrangian perturbation theory, which suppresses power at small scales with respect to full N-body simulations. This may affect the performance of the network at these scales when more accurate density simulations are employed. Finally, while in this work we have changed the value of the astrophysical parameters within a wide range, we have kept fixed the cosmology. Whereas it is expected that changes in cosmology within current bounds will have a much smaller effect than astrophysics, it should be explicitly tested how much this affects our results.

All the above effects will degrade the accuracy with which we can recover the underlying matter density field. On the other hand, we have performed our analysis on 2D, where some information is lost owing to projection effects. A neural network trained to find the mapping between the 3D 21 cm and

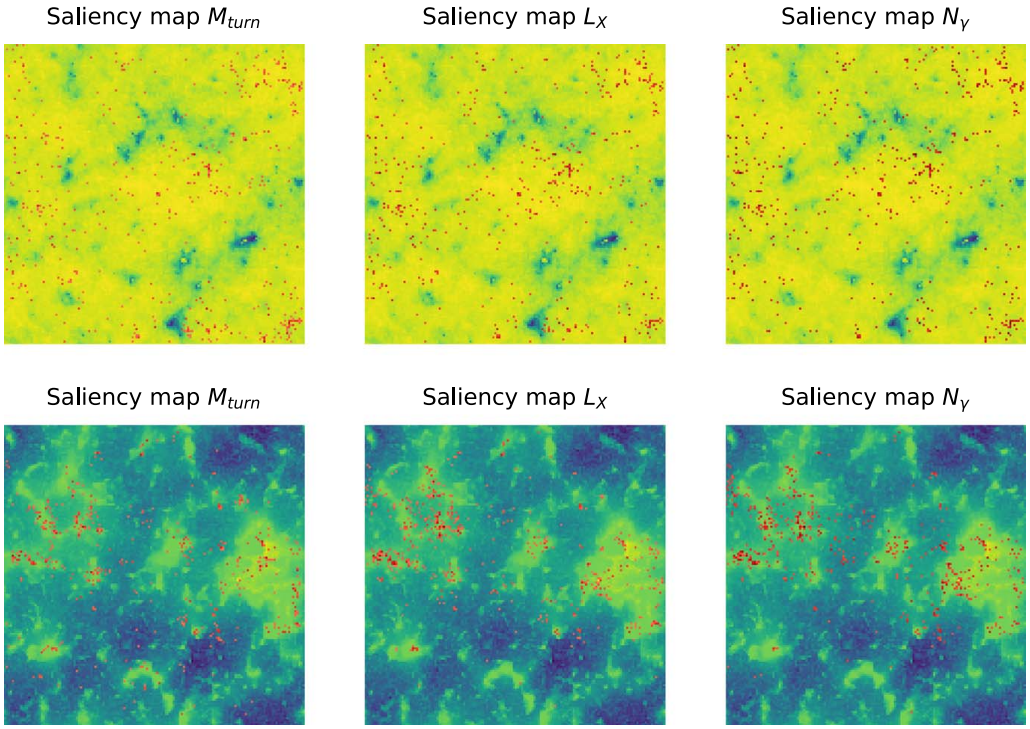

Figure 10. 21 cm maps, together with the brightest pixels of their corresponding saliency maps (red circles), for each astrophysical parameter at $z \simeq 15$ (top) and at $z \simeq 10$ (bottom). The network seems to be looking at the same regions when performing regression to the three different astrophysical parameters.

matter fields may improve our results. Furthermore, our neural network has trained using maps at a single redshift; using maps, or 3D fields, at different redshifts may improve the overall performance of the network, in particular at lower redshifts. We leave for future work a quantification of all these different issues.

Data Availability

The codes and networks underlying this article are available at https://github.com/PabloVD/21cmDeepLearning.

P.V.D. thanks the Department of Astrophysical Sciences of Princeton University for its hospitality during the early stages of this work. This work has made use of the Tiger cluster of Princeton University. We thank Gabriella Contardo, Yin Li, Shirley Ho, and David Spergel for useful conversations. F.V.N. acknowledges funding from the WFIRST program through NNG26PJ30C and NNN12AA01C. P.V.D. is supported by the Spanish MINECO grants SEV-2014-0398 and FPA2017-85985-P and by PROMETEO/2019/083.

ORCID iDs

Pablo Villanueva-Domingo https://orcid.org/0000-0002-0936-4279
Francisco Villaescusa-Navarro https://orcid.org/0000-0002-4816-0455

References

Adebayo, J., Gilmer, J., Muelly, M., et al. 2018, arXiv:1810.03292
Aghanim, N., Akrami, Y., Ashdown, M., et al. 2020, A&A, 641, A6
Ali, Z. S., Parsons, A. R., Zheng, H., et al. 2015, ApJ, 809, 61
Barkana, R. 2018, Natur, 555, 71
Bowman, J. D., Cairns, I., Kaplan, D. L., et al. 2013, PASA, 30, e031
Bowman, J. D., Rogers, A. E. E., Monsalve, R. A., Mozdzen, T. J., & Mahesh, N. 2018, Natur, 555, 67
Burns, J. O., Bale, S., & Bradley, R. F. 2019, AAS Meeting, 234, 212.02
Choudhury, M., Datta, A., & Chakraborty, A. 2020, MNRAS, 491, 4031
Cohen, A., Fialkov, A., & Barkana, R. 2018, MNRAS, 478, 2193
DeBoer, D. R., Parsons, A. R., Aguirre, J. E., et al. 2017, PASP, 129, 045001
Ewall-Wice, A., Chang, T.-C., & Lazio, T. J. W. 2019, Mon. Not. R. Astron. Soc., 492, 6086
Feder, R. M., Berger, P., & Stein, G. 2020, PhRvD, 102, 103504
Fialkov, A., & Barkana, R. 2019, MNRAS, 486, 1763
Fialkov, A., Barkana, R., & Cohen, A. 2018, PhRvL, 121, 011101
Field, G. B. 1958, PIRE, 46, 240
Furlanetto, S. R. 2015, Understanding the Epoch of Cosmic Reionization: Challenges and Progress (Berlin: Springer)
Furlanetto, S., Oh, S. P., & Briggs, F. 2006, PhR, 433, 181
Gillet, N., Mesinger, A., Greig, B., Liu, A., & Ucci, G. 2019, MNRAS, 484, 282
Giusarma, E., Hurtado, M. R., Villaescusa-Navarro, F., et al. 2019, arXiv:1910.04255
Goodfellow, I., Bengio, Y., & Courville, A. 2016, Deep Learning (Cambridge, MA: MIT Press)
Greenhill, L. J., & Bernardi, G. 2012, arXiv:1201.1700
Greig, B., & Mesinger, A. 2015, MNRAS, 449, 4246
Hassan, S., Andrianomena, S., & Doughty, C. 2020, MNRAS, 494, 5761
Hassan, S., Liu, A., Kohn, S., et al. 2017, in IAU Symp. 333, 47
He, S., Li, Y., Feng, Y., et al. 2019, PNAS, 116, 13825

Kern, N. S., Liu, A., Parsons, A. R., Mesinger, A., & Greig, B. 2017, ApJ, 848, 23
Kingma, D. P., & Ba, J. 2014, arXiv:1502.03167
Kwon, Y., Hong, S. E., & Park, I. 2020, JKPS, 77, 49
List, F., & Lewis, G. F. 2020, MNRAS, 493, 5913
Liu, A., & Parsons, A. R. 2016, MNRAS, 457, 1864
Lopez-Honorez, L., Mena, O., & Villanueva-Domingo, P. 2019, PhRvD, 99, 023522
Madau, P., Meiksin, A., & Rees, M. J. 1997, ApJ, 475, 429
Majumdar, S., Pritchard, J. R., Mondal, R., et al. 2018, MNRAS, 476, 4007
Mao, Y., Tegmark, M., McQuinn, M., Zaldarriaga, M., & Zahn, O. 2008, PhRvD, 78, 023529
Mellema, G., et al. 2013, ExA, 36, 235
Mesinger, A. (ed.) 2019, The Cosmic 21 cm Revolution (Bristol: IOP Publishing), 2514
Mesinger, A., Ferrara, A., & Spiegel, D. S. 2013, MNRAS, 431, 621
Mesinger, A., Furlanetto, S., & Cen, R. 2011, MNRAS, 411, 955
Mirocha, J., & Furlanetto, S. R. 2019, MNRAS, 483, 1980
Muñoz, J. B. 2019a, PhRvD, 100, 063538
Muñoz, J. B. 2019b, PhRvL, 123, 131301
Muñoz, J. B., & Loeb, A. 2018, Natur, 557, 684
Murray, S. G. 2018, JOSS, 3, 850
Park, J., Mesinger, A., Greig, B., & Gillet, N. 2019, MNRAS, 484, 933
Pospelov, M., Pradler, J., Ruderman, J. T., & Urbano, A. 2018, PhRvL, 121, 031103
Pritchard, J. R., & Loeb, A. 2012, RPPh, 75, 086901
Ronneberger, O., Fischer, P., & Brox, T. 2015, arXiv:1505.04597
Schmit, C. J., & Pritchard, J. R. 2018, MNRAS, 475, 1213
Scoccimarro, R. 1998, MNRAS, 299, 1097
Shimabukuro, H., & Semelin, B. 2017, MNRAS, 468, 3869
Simonyan, K., Vedaldi, A., & Zisserman, A. 2013, arXiv:1312.6034
Sitwell, M., Mesinger, A., Ma, Y.-Z., & Sigurdson, K. 2014, MNRAS, 438, 2664
van Haarlem, M. P., Wise, M. W., Gunst, A. W., et al. 2013, A&A, 556, A2
Watkinson, C. A., Giri, S. K., Ross, H. E., et al. 2018, MNRAS, 482, 2653
Witte, S., Villanueva-Domingo, P., Gariazzo, S., Mena, O., & Palomares-Ruiz, S. 2018, PhRvD, 97, 103533
Wouthuysen, S. A. 1952, AJ, 57, 31
Zamudio-Fernandez, J., Okan, A., Villaescusa-Navarro, F., et al. 2019, arXiv:1904.12846

Part III

Resumen de la tesis

Resumen de la tesis

1 Introducción

Durante las últimas décadas, el enorme desarrollo de la cosmología nos ha permitido alcanzar una profunda comprensión de nuestro universo, culminando en el establecimiento del paradigma estándar cosmológico ΛCDM. Este modelo asume diversos componentes para explicar la evolución del universo y las estructuras que observamos. Por un lado, la conocida como energía oscura, que conforma cerca de un 70% de la energía actual. Esta presenta un comportamiento en la evolución cósmica equivalente a la constante cosmológica Λ, lo que causa la expansión acelerada del universo detectada a partir de supernovas lejanas. Por otra parte, diversas observaciones astrofísicas a lo largo del siglo XX, especialmente de las curvas de rotación galácticas y de cumúlos galácticos, hicieron evidente la presencia de un cierto tipo de materia no interactiva ni radiativa, conocida como materia oscura (*Dark Matter*, DM), que comprende cerca de un 25% de la energía cosmológica. Además, la mayor parte de observaciones sugieren que esta materia es relativamente fría, sin dispersión de velocidades térmica apreciable, siendo pues conocida como materia oscura fría (*Cold Dark Matter*, CDM). Finalmente, la materia bariónica del Modelo Estándar de física de partículas tan solo contribuye en un 5% a la fracción energética actual. Este paradigma cosmológico es capaz de explicar con precisión tanto observaciones de galaxias y supernovas lejanas como las anisotropías del Fondo Cósmico de Microondas (*Cosmic Microwave Background*, CMB) y la nucleosíntesis primordial. Pese a ello, la naturaleza de la materia oscura y de la energía oscura permanecen esencialmente desconocidas.

Las observaciones de las anisotropías del CMB, el remanente fósil de fotones del universo primigenio, nos ofrecen información muy precisa sobre los diversos componentes del universo temprano, así como acerca del crecimiento de las perturbaciones primordiales. Por otra parte, los catálogos galácticos han permitido crear mapas cósmicos del universo cercano con gran detalle, los cuales permiten conocer cómo se distribuye la materia e

inferir los procesos que han llevado a la formación de las estructuras cosmológicas que vemos actualmente. Sin embargo, entre el desacoplamiento del CMB y las galaxias de nuestro vecindario, existe un gran intervalo temporal esencialmente incierto y desconocido. Durante la época de dominación de materia, las regiones más densas del universo comienzan a colapsar formando las primeras estructuras cosmológicas. Este proceso se acrecienta durante las Edades Oscuras, periodo tras la Recombinación conocido así debido a la ausencia de fuentes de luz (estelares y primordiales) que permitan observarlo directamente. Con el paso del tiempo, llega un momento en que las inhomogeneidades son tan grandes que producen halos suficientemente masivos como para que la materia de su interior se enfríe y colapse formando estrellas. La época del nacimiento de las primeras estrellas se conoce como el Amanecer Cósmico, e implica la emisión por parte de las primeras galaxias de gran cantidad de radiación energética, en forma de rayos UV y X, que puede ser absorbida por los átomos del Medio Intergaláctico (*Intergalactic Medium*, IGM). Esto se espera que caliente el gas difuso presente entre las galaxias y lo ionice. Cuando la formación estelar es lo suficientemente alta, el medio circundante alrededor de las galaxias se ioniza completamente, formando burbujas de hidrógeno ionizado que se expanden durante la Época de Reionización (*Epoch of Reionization*, EoR), hasta que todo el medio intergaláctico alcance un estado ionizado. Si bien esta cronología cósmica es generalmente aceptada, todavía son desconocidos los detalles, duración y extensión de cada periodo. Aunque la observación del espectro de cuásares y galaxias, así como la polarización del CMB, pueden proporcionar cierta información relativa a la extensión y la consumación de la EoR, aún carecemos de una evaluación precisa de la historia de ionización del medio intergaláctico.

La señal cosmológica de 21 cm se constituye como una prometedora herramienta para entender la evolución del universo. Esta radiación emerge de la transición hiperfina del hidrógeno neutro, y dada la gran abundancia de este elemento en el universo, podría permitir realizar un cartografiado de la distribución de materia en función del tiempo. Dada su sensibilidad respecto al estado térmico del medio, su detección aportaría valiosa información sobre la época de formación de primeras galaxias durante el Amanecer Cósmico. Además, dado que solo está presente en átomos neutros, proporcionaría un medio para poder conocer con precisión la historia de ionización durante la EoR. Por otra parte, la señal de 21 cm podría servir como una herramienta excepcional para ahondar en la naturaleza de la materia oscura. Aunque el modelo de materia oscura fría es el aceptado generalmente, existen otros candidatos bien motivados teóricamente que podrían proporcionar la materia oscura presente en el universo. Estos modelos de materia oscura alternativos podrían producir un impacto en la evolución del medio

intergaláctico y tener por tanto efectos observables. Es por ello que la precisa determinación de las distintas épocas de la cronología cósmica resulta de gran importancia para acotar los distintos escenarios posibles de materia oscura. En esta tesis, se examina el potencial de la señal de 21 cm, junto con otras medidas del estado de ionización del medio intergaláctico, con el fin de acotar la composición, naturaleza y evolución de la materia oscura.

2 Candidatos alternativos de materia oscura

El caso paradigmático de materia oscura fría considera partículas masivas débilmente interactivas (*Weakly Interacting Massive Particles*, WIMP), con masas usualmente del orden del GeV o superior, que estuvieron en equilibrio con el plasma cósmico en el universo primigenio. Estas interacciones dejarían de ser eficientes para mantener el acoplamiento con las partículas del Modelo Estándar en cierto momento, dejando un remanente que no interactúa con el resto de materia bariónica y radiación. Si bien esta hipótesis está bien motivada y es capaz de aportar la abundancia de materia oscura observada, las partículas constituyentes no han sido observadas en experimentos dedicados a su detección. Por otra parte, modelos de materia oscura fría presentan diversas discordancias con observaciones cosmológicas a escalas pequeñas, que pueden resumirse en el hecho de que simulaciones de materia oscura fría predicen más subestructuras de las halladas en las observaciones. Pese a que estos problemas podrían ser solucionados recurriendo a ciertos efectos astrofísicos, como retroalimentación estelar o de supernovas, otra posibilidad consiste en considerar modelos alternativos de materia oscura capaces de solucionar dichas discrepancias.

Una de las propuestas más atractivas se basa en la *materia oscura templada* (*Warm Dark Matter*, WDM), cuyas partículas tendrían una masa del orden del keV. Ejemplos de este tipo de materia oscura podrían ser los gravitinos de teorías supersimétricas, o bien neutrinos estériles, presentes en muchas extensiones del Modelo Estándar de partículas. Debido a su masa, su dispersión de velocidades y su temperatura serían notablemente mayores a las del caso frío. Esto sería relevante en el crecimiento de las fluctuaciones de materia, actuando como una presión efectiva, y contrarrestando el colapso gravitatorio en escalas pequeñas. Como consecuencia, estructuras con tamaños por debajo de una cierta escala serían fundamentalmente suprimidas. Esta escala actuaría como una escala de Jeans efectiva, y estaría determinada principalmente por la masa de la materia oscura templada y su abundancia. En estos modelos, la cantidad de halos de masas bajas sería reducida, explicando así algunas de las discrepancias presentes con la materia oscura fría. Este hecho tendría a su vez un impacto en la

evolución del medio intergaláctico, ya que produciría menos galaxias de las esperadas, retrasando ciertos periodos de la cronología, como el amanecer cósmico o la reionización. Por ello, es de esperar que el análisis de observables del estado de ionización y de la señal de 21 cm sean sensibles a dichos efectos, y puedan potencialmente constreñir modelos de materia oscura templada.

Otra candidato alternativo podría tratarse de *materia oscura interactiva* (*Interacting Dark Matter*, IDM) con radiación. Pese a que hay cotas muy restrictivas respecto a las interacciones de la materia oscura con fotones, no es posible excluirlas por completo. Colisiones elásticas de partículas de materia oscura interactiva con fotones en el universo temprano producirían un acoplamiento de los primeros a los segundos, reduciendo las fluctuaciones de la materia oscura interactiva a escalas pequeñas, e imprimiéndoles en cierta manera el espectro oscilatorio típico de las perturbaciones adiabáticas de la radiación. En consecuencia, esto resultaría en una supresión del número de estructuras cosmológicas en pequeñas escalas, de una manera similar al caso de materia oscura templada, lo que ha sido propuesto como solución a algunas de las discordancias del escenario de materia oscura fría con los datos. De la misma manera, el número de halos que albergase formación estelar se reduciría, y por tanto, observaciones de la absorción y emisión en 21 cm y límites sobre la historia de ionización serían capaces de acotar el espacio de parámetros de la materia oscura interactiva compatible con los datos.

Finalmente, cabe la posibilidad de que los constituyentes de la materia oscura no sean partículas microscópicas, sino objetos astrofísicos macroscópicos masivos, conocidos como MACHOs. La mayoría de estos candidatos, como podrían ser planetas gigantes y enanas marrones, son descartados por no ser capaces de originar las fluctuaciones primordiales patentes en el CMB y la cantidad de bariones en la nucleosíntesis primordial. No obstante, el colapso de *agujeros negros primordiales* (*Primordial Black Holes*, PBHs) durante el universo temprano sería consistente con dichas restricciones, por su naturaleza previa a la formación estelar, y podrían formar parte de al menos una fracción de la materia oscura. Esta hipótesis recobró especial atención tras las observaciones por parte de las colaboraciones LIGO y VIRGO de diversos eventos de emisión de ondas gravitatorias originadas en la fusión de agujeros negros de varias masas solares [41]. Contrariamente a los agujeros negros astrofísicos estándares, limitados a masas iguales o superiores a $\sim 3M_{\odot}$, los agujeros negros primordiales podrían ser formados en principio con cualquier masa. Estos objetos podrían además actuar como germen de los agujeros negros supermasivos observados en los centros de la mayoría de las galaxias, cuyas masas son difícilmente explicables mediante mecanismos de acrecimiento estándares, a no ser que partiesen de una

masa inicial anterior a la época de formación estelar. Uno de los aspectos más interesantes de los agujeros negros primordiales como candidatos de la materia oscura es la gran cantidad de efectos observables que su existencia implicaría, permitiendo acotar su abundancia hasta niveles potencialmente muy bajos. Ejemplos de ello son efectos de lente gravitatoria, la emisión de partículas debido a su evaporación, la inyección de energía en el medio circundante por el acrecimiento de materia, o el incremento en las fluctuaciones primordiales debido a su carácter discreto. Estos dos últimos efectos podrían afectar potencialmente a la evolución del medio intergaláctico, y por tanto, a la línea de 21 cm.

3 Metodología

La mayor parte de la tesis se focaliza en explorar diversos modelos de materia oscura alternativos al estándar de materia oscura fría mediante simulaciones de la evolución del universo, con el fin de contrastarlos con datos observacionales para acotar sus propiedades. Para ello, se han llevado a cabo simulaciones del crecimiento de las fluctuaciones del campo de materia y la formación de halos, así como de la evolución térmica, y de ionización del medio intergaláctico. En la mayor parte de los artículos incluidos, se ha hecho uso del programa de acceso libre `21cmFAST` [378], que emplea una serie de aproximaciones semi-analíticas para calcular la evolución del medio intergaláctico. Esencialmente, este código resuelve la evolución del campo de densidad empleando teoría de perturbaciones lagrangiana de segundo orden. A partir del mapa de densidad, el programa calcula las regiones ionizadas alrededor de las zonas con mayor densidad, siguiendo la prescripción de Furlanetto-Zaldarriaga-Hernquist (FZH) [509], la cual se basa en la aplicación del formalismo de conjunto de excursiones (*excursion set formalism*) [175]. Estas simulaciones concuerdan con cálculos más rigurosos empleando simulaciones hidrodinámicas o de N cuerpos para escalas relativamente grandes, a partir de ~ 1 Mpc. Sin embargo, para el análisis presentado en la Ref. [2], se han empleado simulaciones hidrodinámicas más precisas, basadas en el programa de Reionización Cósmica en Computadoras (*Cosmic Reionization on Computers*, CROC) [514], que emplean un tratamiento preciso de la evolución de la densidad, del transporte radiativo, y por tanto, un cálculo más robusto del campo de ionización. Ambos métodos asumen diversos modelos astrofísicos cuyos parámetros no están bien determinados por las observaciones, y por tanto, los resultados finales son sensibles a la elección específica de dichos parámetros.

Para el análisis de resultados y el contraste con datos observacionales, se emplea tanto un enfoque probabilista frecuentista, basado en el máximo

de la función de verosimilitud (o, equivalentemente, en el mínimo del χ^2), como métodos bayesianos, muestreando la función de probabilidad posterior mediante Cadenas de Markov de Monte Carlo (*Monte Carlo Markov Chains*, MCMC). Finalmente, en la Ref. [7], se hacen uso de métodos de aprendizaje profundo (*deep learning*), empleando redes neuronales convolucionales.

4 Resultados de la tesis

Esta sección comprende un resumen de los trabajos de investigación originales que conforman el cuerpo de la tesis doctoral. A continuación, se presentan la motivación y los resultados más relevantes de cada artículo.

4.1 Materia oscura cálida e historia de ionización del Universo

En la Ref. [1] se estudia el impacto de modelos de materia oscura templada en la evolución térmica y de ionización del medio intergaláctico. Debido al efecto de dispersión de velocidades de partículas con masas $\sim$ keV, la formación de estructuras es suprimida en escalas pequeñas con respecto al caso estándar de materia oscura fría. Esto implica una reducción en el número de halos de baja masa que pueden albergar formación estelar, capaces de emitir radiación UV y rayos X responsables de ionizar y calentar el medio intergaláctico. La disminución del número de tales fuentes conduce a un retraso del amanecer cósmico, de la época de calentamiento y de la EoR. Haciendo uso de simulaciones semi-analíticas, la evolución de la temperatura cinética y de la fracción de ionización se calcula en varios escenarios de materia oscura templada, variando la masa de sus partículas entre 1 y 4 keV, un rango motivado físicamente para tratar de resolver los problemas a pequeña escala presentes con la materia oscura fría. Dado que la historia térmica del medio intergaláctico es muy sensible a los procesos estelares y radiativos involucrados, también consideramos diferentes escenarios astrofísicos. Se modifican tres parámetros astrofísicos: la temperatura virial mínima (relacionada con la masa mínima del halo para producir formación estelar), la eficiencia de ionización de rayos UV y la eficiencia de calentamiento de los rayos X (relacionada con la luminosidad en rayos X de fuentes astrofísicas, como binarias de rayos X).

Los resultados obtenidos en lo que respecta a la fracción de ionización de las simulaciones se han confrontado con límites observacionales sobre el estado de ionización durante la EoR. Entre los tipos de datos tenidos en cuenta, se hallan las restricciones y los límites inferiores de la fracción de

ionización en el rango de desplazamientos al rojo (*redshifts*) $8 \geq z \gtrsim 6$ de espectros de cuásares y las galaxias emisoras de radiación Lyα. Por otro lado, también empleamos la profundidad óptica de Thomson inferida de las anisotropías del CMB, obtenida mediante la integral de la fracción de ionización sobre el redshift, en lugar de una restricción dependiente del corrimiento al rojo. Se muestra que los límites que emplean solo datos de CMB son menos restrictivos que los obtenidos usando el estado de ionización a un tiempo dado, dado que la profundidad óptica de Thomson es una cantidad integrada, y no una función del tiempo.

Encontramos que algunos parámetros astrofísicos están fuertemente degenerados entre ellos, y a su vez, con la masa de la materia oscura templada. Más específicamente, el retraso de la EoR presente en un modelo de materia oscura templada puede ser contrarrestado aproximadamente por una alta eficiencia de ionización (que impulsa una reionización más temprana) o por una temperatura virial mínima más baja (lo que permite que halos de menor masa formen estrellas y contribuyan a emitir más radiación ionizante). Por esa razón, los límites inferiores de la masa de la materia oscura templada obtenidos por este método son más débiles que aquellos inferidos a partir del bosque de Lyα, aunque son capaces de limitar masas de la materia oscura templada menores de ~ 1 keV.

4.2 Materia oscura cálida y reionización cósmica

Con el fin de profundizar en la fenomenología de la materia oscura templada, en la Ref. [2] se continúa investigando el impacto de estos modelos en la evolución cosmológica y la formación de estructuras. En este caso, se emplean precisas simulaciones hidrodinámicas, en lugar de cálculos semi-analíticos, proporcionando así resultados más fiables. Hacemos uso de simulaciones basadas en el programa *Cosmic Reionization on Computers* (CROC) [514], que representan la vanguardia en el modelado numérico de la EoR. En las condiciones iniciales de cada simulación, el espectro de potencias es modificado adecuadamente para incluir la supresión característica de escenarios de materia oscura templada. Se asume una masa de las partículas de $m_{\rm WDM} = 3$ keV, valor que se encuentra alrededor de las restricciones obtenidas mediante el bosque de Lyα.

Se calculan diferentes observables de reionización para explorar el impacto de la escala de supresión de estructuras, como la función de masa de los halos y las funciones de luminosidad UV de la galaxia, que muestran una supresión (en masas bajas y magnitudes altas, respectivamente) con respecto al caso estándar. Los telescopios actuales no parecen ser capaces de discriminar entre estos casos de materia oscura fría y templada. Sin

embargo, el futuro telescopio *James Webb Space Telescope* (JWST) sería capaz de alcanzar el extremo de la función de luminosidad de galaxias de magnitudes débiles, siendo apto para restringir tales masas de la materia oscura templada. También se discute el efecto en la función de distribución de probabilidad cumulativa para la profundidad óptica Lyα efectiva $\tau_{\rm GP}$ en el medio intergaláctico posterior a la reionización. En comparación con el escenario de materia oscura fría en un tiempo dado, el caso de materia oscura templada presenta distribuciones con colas más extendidas hacia valores de $\tau_{\rm GP}$ altos, que corresponden a regiones de alta densidad, ya que se ionizan posteriormente. Comparando con los datos observacionales del bosque de Lyα, el caso de materia oscura fría resulta preferido respecto al caso de materia oscura templada, aunque no está claro si el ajuste de los parámetros astrofísicos en el escenario de materia oscura templada podría mejorar su concordancia con los datos. Por último, también se calcula el espectro de potencias de la línea de 21 cm, que en el caso de materia oscura templada muestra un balance entre una supresión debida a la dispersión térmica de velocidades, y un realzamiento dado por la reionización retardada. Esto conduce a un comportamiento no trivial, que lo hace difícilmente detectable por la primera generación de experimentos de 21 cm.

4.3 ¿Hubo un componente de reionización temprano en nuestro universo?

La historia de ionización del universo durante la EoR está lejos de encontrarse bien determinada. Aunque la mayoría de los límites son consistentes con un proceso de reionización relativamente rápido que termina a redshifts $z \sim 6$, aún puede ser posible una contribución temprana, por ejemplo, de escenarios de materia oscura no canónicos que inyecten energía en el medio, como materia oscura desintegrándose o agujeros negros primordiales. En la Ref. [3], esta cuestión se examina a la luz de los datos de Planck del CMB. La historia de ionización se modela para que sea coherente con el espectro de polarización EE del CMB, que es sensible a la reionización en multipolos bajos. Se emplean varios métodos para emular la evolución de la fracción de ionización x_e. En primer lugar, se consideran dos parametrizaciones funcionales frecuentes en la literatura, como la parametrización simétrica y la asimétrica en z. Por otro lado, se aplica una reconstrucción de x_e basada en el Análisis de Componentes Principales (*Principal Component Analysis*, PCA), extrayendo los modos propios de la matriz de Fisher de los componentes C_l del espectro EE. Se espera que aquellos con las varianzas más pequeñas contengan la información cosmológica más valiosa. Un subconjunto de estas funciones propias se emplea como base para escribir como su combinación el historial de ionización alrededor de un modelo por defecto

dado, ya sea asumiendo un valor constante o una de las parametrizaciones mencionadas anteriormente. Finalmente, se emplea un tercer método basado en el polinomio de interpolación de Hermite cúbico por partes (*Piecewise Cubic Hermite Interpolating Polynomial*, PCHIP), considerando como parámetros libres la fracción ionizada en varios z diferentes, que se interpolan suavemente a través del PCHIP.

Comparamos los diferentes enfoques para recuperar la evolución de la ionización con un análisis empleando Cadenas de Markov de Monte Carlo (MCMC), que muestra que algunos de ellos prefieren un componente de reionización temprano, incluido algún patrón oscilatorio, como el uso de la combinación de PCA sumada a un modelo por defecto. Sin embargo, cuando se incluye la combinación PCA como argumento de la parametrización, explotando su forma funcional, la evolución de x_e resultante es más suave y no muestra un inicio temprano. La aplicación de los criterios frecuentista de información de Akaike y de información bayesiano confirman que ninguna de las formulaciones en particular es preferida por los datos sobre el resto, y por lo tanto, que los datos de CMB no indican una reionización temprana, contrariamente a afirmaciones anteriores en la literatura [554].

4.4 Una nueva mirada al escenario de la materia oscura interactiva

En la Ref. [4], los modelos fenomenológicos de materia oscura que involucran la dispersión elástica con fotones, conocidos como materia oscura interactiva, se discuten en el contexto de la evolución térmica del medio intergaláctico y del número de galaxias satélites de la Vía Láctea. En el caso de la materia oscura interactiva, el acoplamiento entre partículas de materia oscura y fotones produce un efecto de amortiguación debido a las colisiones, induciendo una supresión y un patrón oscilatorio en las escalas más pequeñas en el espectro de potencias, de manera similar a los inducidos por el acoplamiento barión-fotón en el caso estándar. Este efecto puede reducir el número de estructuras a pequeña escala y halos de baja masa, de manera similar a lo que ocurre con la materia oscura templada. La magnitud de este amortiguamiento está determinada por la sección eficaz de dispersión elástica sobre la masa, $\sigma_{\gamma\mathrm{DM}}/m_{\mathrm{DM}}$.

Se han realizado simulaciones semi-analíticas del estado térmico y de ionización del medio intergaláctico para investigar el impacto de escenarios con materia oscura interactiva. La supresión del crecimiento de estructuras debido a la amortiguación de colisiones retrasa la formación de las primeras estrellas y galaxias, retardando todos los procesos astrofísicos como el calentamiento por rayos X y la reionización. Análogamente a lo visto en la

sección 4.1 (Ref. [1]) con respecto a la masa de la materia oscura templada, la sección eficaz de la materia oscura interactiva está fuertemente degenerada con varios parámetros astrofísicos, principalmente con la eficiencia de ionización y la temperatura virial mínima. Por otro lado, se calcula el número de subhalos esperados, que en un escenario de materia oscura interactiva se reduce con respecto al escenario de materia oscura fría. Este hecho permite acotar la sección eficaz elástica al comparar las predicciones teóricas con las galaxias satélite de la Vía Láctea observadas. Sin embargo, la restricción a partir de las galaxias satélite depende en gran medida de la masa total asumida de la Vía Láctea, que no está completamente determinada con certeza. Dentro de su rango de masa esperado, los límites de la sección eficaz pueden variar hasta un orden de magnitud. Combinando este límite superior con los límites de la historia de ionización del medio intergaláctico, se pueden romper algunas degeneraciones astrofísicas.

4.5 Microfísica de materia oscura y observaciones de 21 cm

La colaboración de EDGES presentó la supuesta primera detección de la señal global de 21 cm, presentando un espectro de absorción con una amplitud de aproximadamente 500 mK, que duplica las expectativas en el caso estándar ΛCDM. Esto resulta ser difícilmente explicable solo a partir de distintos modelos astrofísicos, posiblemente requiriendo escenarios no estándar con un mecanismo de enfriamiento adicional para explicar esta absorción, como materia oscura interaccionando con bariones. Sin embargo, la localización en el tiempo de la señal de absorción medida por EDGES, perfectamente consistente con las predicciones estándar en escenarios ΛCDM, se puede emplear para restringir otros escenarios no canónicos de materia oscura que pueden afectar la evolución del medio intergaláctico. En la Ref. [5], se explotan dos aspectos de la ubicación temporal de la señal de EDGES para restringir modelos de materia oscura interactiva y templada, que son capaces de retrasar el inicio de la formación estelar durante el amanecer cósmico.

Por un lado, se exige que el mínimo de la temperatura global de brillo de 21 cm calculada a partir de simulaciones aparezca no más tarde del pico de absorción de EDGES, situado en $z \simeq 17$. Por otro lado, al examinar el comienzo del régimen de absorción en los datos de EDGES, se puede inferir cuándo el acoplamiento Lyα debe ser lo suficientemente fuerte como para acoplar la temperatura de espín con la temperatura cinética del medio intergaláctico. Siguiendo estas ideas, para ser coherente con los datos, se puede suponer que el coeficiente de acoplamiento Lyα debe alcanzar el

orden uno a $z \simeq 20$. Por tanto, es posible descartar los modelos materia oscura interactiva y templada que presentan una época de absorción demasiado retrasada y no pueden cumplir las condiciones anteriores. Ambos criterios mencionados permiten extraer restricciones competitivas en la masa de la materia oscura templada y en la sección eficaz de la interactiva. Estos límites son fuertemente dependientes del escenario astrofísico específico, debilitando los límites en escenarios con bajas temperaturas viriales. No obstante, asumiendo el escenario predeterminado de estrellas de población II (de baja metalicidad) con una temperatura virial de 10^4 K como fuente de radiación Lyα, los límites obtenidos mediante este método pueden mejorar en gran medida aquellos obtenidos a partir de otros análisis.

4.6 Restringiendo la abundancia de agujeros negros primordiales con cosmología de 21 cm

En la Ref. [6] se estudia en detalle los efectos cosmológicos de la existencia de agujeros negros primordiales como parte de la materia oscura en la señal cosmológica de 21 cm. Hay dos consecuencias principales de agujeros negros de origen primitivo de masa solar o superior para la evolución del medio intergaláctico. Por un lado, la presencia de agujeros negros primordiales en el universo temprano implicaría una contribución adicional al espectro de potencias de la materia dado por un espectro de ruido blanco de Poisson, independiente de la escala, debido a su naturaleza discreta, evolucionando como un modo de isocurvatura. Esto magnificaría la formación de estructuras a pequeña escala, donde este término se vuelve dominante con respecto a las fluctuaciones adiabáticas estándares. Por lo tanto, este incremento afectaría principalmente a los minihalos, aquellos halos de baja masa que no son lo suficientemente masivos para iniciar la formación de estrellas. La temperatura de brillo promedio de 21 cm esperada proveniente de estos minihalos es calculada, que difiere de la señal global estándar del medio intergaláctico. En el artículo se demuestra que, incluso con el incremento en el espectro de potencias a pequeñas escalas debido a la contribución de Poisson, no sería suficiente para producir una señal detectable, contrariamente a lo que se ha afirmado anteriormente en la literatura [316, 317].

Por otro lado, al igual que los agujeros negros astrofísicos estándares, los agujeros negros primordiales acrecerían materia circundante debido a su atracción gravitatoria. Durante la caída hacia el PBH, las partículas podrían acelerarse enormemente, liberando radiación UV y de rayos X al ambiente circundante. Estos fotones inyectarían energía en el medio cuando se absorbieran, calentándolo e ionizándolo aún más. En el artículo, calculamos la señal de 21 cm que surge del entorno local de los PBH, mostrando que

estaría muy por debajo de las sensibilidades observables. Sin embargo, la radiación energética puede escapar de los alrededores cercanos de los agujeros negros primordiales y depositarse en el medio intergaláctico, afectando notablemente la señal global de 21 cm y el espectro de potencias. Debido a la ionización adicional y al medio más caliente, se suprimiría la amplitud de absorción de la temperatura de brillo y sus fluctuaciones, implicando una transición a un régimen de emisión en los casos más extremos. Realizamos un análisis MCMC con simulaciones semi-analíticas de la señal del medio intergaláctico de 21 cm, variando la fracción de agujeros negros primordiales como materia oscura, $f_{\rm PBH}$, y su masa, $M_{\rm PBH}$, junto con cuatro parámetros astrofísicos. Las sensibilidades esperadas de los próximos interferómetros HERA y SKA se emplean para explorar la región del espacio de parámetros de agujeros negros primordiales que puede ser testada por tales experimentos. Finalmente, mostramos que los límites actuales en la abundancia de agujeros negros primordiales en el rango de $1 - 10^3 M_\odot$, provenientes del efecto de lente gravitatoria y el impacto de la acrecimiento en el CMB, podrían mejorarse potencialmente hasta en dos órdenes de magnitud con observaciones del espectro de potencias de 21 cm.

4.7 Eliminando la astrofísica en mapas de 21 cm con redes neuronales

La línea de 21 cm se erige como una prometedora herramienta para mapear la distribución de materia en el universo, dado que permite localizar la ubicación del hidrógeno neutro en los cúmulos de materia oscura. Esto podría permitir lograr mapas tomográficos de densidad en 3D del medio intergaláctico. Sin embargo, la relación entre la distribución de hidrógeno neutro y densidad de materia oscura no es unívoca, ya que la temperatura de brillo depende en gran medida del estado térmico y de ionización del medio. Además, una vez que la reionización es muy avanzada, la señal de las regiones de hidrógeno ionizado se suprime en su mayor parte. En la Ref. [7], se trata de recuperar el campo de densidad de materia subyacente a partir de un mapa de 21 cm, utilizando métodos de aprendizaje automático. En concreto, se entrena una red neural convolucional basada en la arquitectura U-Net [576] con 1000 simulaciones numéricas del campo de temperatura de brillo y sus correspondientes mapas de densidad, con el objetivo de aprender a recuperar este último a partir del mapa de 21 cm. Estas simulaciones incluyen diferentes condiciones iniciales para cada realización, variando también tres parámetros astrofísicos relevantes, con el fin de volverse robustos a distintos escenarios astrofísicos.

Se demuestra que, una vez entrenada, la red neuronal es capaz de extraer con éxito el campo de densidad de un mapa de 21 cm dado. Para probar su precisión, se calculan varios estadísticos del campo de densidad de materia, como el espectro de potencias, el coeficiente de correlación cruzada o la función de distribución de probabilidad, coincidiendo las predicciones con las correspondientes de los mapas reales con alta precisión hasta escalas tan pequeñas como $k \sim 2$ Mpc $^{-1}$. La red se puede aplicar a mapas en diferentes momentos de la evolución cósmica, aunque su rendimiento empeora con instantes más recientes, $z \sim 10$, cuando la reionización ya está en curso y el vínculo entre la distribución de hidrógeno neutro y materia oscura se vuelve más difuso. Además, parte de las capas entrenadas de la red se emplean para predecir los parámetros astrofísicos subyacentes, lo que muestra que la red neuronal realmente aprende información astrofísica, con el fin de sustraerla de la señal de 21 cm para predecir el campo de densidad.

5 Conclusiones

Los trabajos de investigación incluidos en la presente tesis doctoral pretenden ejemplificar diversos enfoques para estudiar la naturaleza y propiedades de la materia oscura a partir del estudio de la evolución del medio intergaláctico. Diferentes modelos alternativos de materia oscura son considerados, como materia oscura templada, interactiva y agujeros negros primordiales, los cuales presentan diferentes efectos en la formación de estructuras y en la historia térmica. Los casos de materia oscura templada e interactiva presentan una supresión en las fluctuaciones a pequeñas escalas, dada por la dispersión de velocidades térmica y por el amortiguamiento colisional, respectivamente, retrasando la formación de estructuras cosmológicas y con ello todos los procesos astrofísicos. Por otra parte, agujeros negros primordiales de masa solar o mayor pueden acrecer materia, radiando e inyectando posteriormente energía en el medio, calentándolo e ionizándolo. Todos estos efectos dejarían un gran impacto en la evolución del medio intergaláctico, afectando a la época de formación de primeras estrellas, y a la EoR. Como se ha mostrado, tests observacionales del progreso de la reionización, como las anisotropías del CMB y los espectros de absorción de quásares lejanos, podrían por tanto ser capaces de conferir cotas sobre los diferentes modelos de materia oscura. Las restricciones sobre el espacio de parámetros de la materia oscura obtenidas de este modo son, sin embargo, altamente sensibles al modelado astrofísico del medio intergaláctico, y una precisa determinación de los distintos procesos y fuentes astrofísicas es necesaria para obtener límites robustos. Datos de la historia de ionización como el CMB también pueden aplicarse a casos donde un modelo específico

no es asumido, estudiando por ejemplo procesos de reionización temprana, que podrían ser inducidos por partículas de materia oscura que inyectasen energía en el medio.

Especial atención merece la señal cosmológica de 21 cm, dada su gran sensibilidad al estado térmico y de ionización del medio, siendo un observable de gran interés. Empleando la localización temporal de la señal global de absorción detectada por EDGES, es posible acotar diversos modelos de materia oscura como templada e interactiva, mejorando algunas de las restricciones actuales mediante otros métodos. Sin embargo, aún más prometedor resulta el espectro de potencias de 21 cm, el cual sería capaz de arrojar información sobre las inhomogeneidades del medio intergaláctico, además de ser más fácilmente separable de los contaminantes astrofísicos, que pueden exceder en varios órdenes de magnitud la señal cosmológica. Como ejemplo de su potencial, se han calculado las posibles futuras cotas sobre la abundancia de agujeros negros primordiales como materia oscura asumiendo la sensibilidad de detección de la siguiente generación de radiointerferómetros, como SKA, mostrando que dichas restricciones podrían mejorar en varios órdenes de magnitud las presentes actualmente en el mismo rango de masas mediante otros métodos.

Además, se presentan aplicaciones de aprendizaje automático en cosmología, con el fin de obtener el campo de densidad de materia subyacente y los parámetros astrofísicos a partir de un mapa de 21 cm dado. Esto muestra, por un lado, el gran potencial de la señal hiperfina del hidrógeno como herramienta para estudiar el crecimiento de las inhomogeneidades y la formación y distribución de estructuras. Y por otra parte, la gran capacidad y aplicaciones que pueden tener los métodos basados en redes neuronales para extraer información cosmológica, la cual puede ser inalcanzable de otro modo.